On Protein Corona Formation: Understanding Nano-Bio Interactions Toward Engineering Optical Nanomaterials

By

Rebecca L. Pinals

A dissertation submitted in partial satisfaction of the

requirements for the degree of

Doctor of Philosophy

in

Chemical Engineering

in the

Graduate Division

of the

University of California, Berkeley

Committee in charge:

Professor Markita P. Landry, Chair
Professor David Schaffer
Professor Wenjun Zhang
Professor Amy Herr

Spring 2021

On Protein Corona Formation: Understanding Nano-Bio Interactions Toward Engineering Optical Nanomaterials

Rebecca L. Pinals

Abstract

On Protein Corona Formation: Understanding Nano-Bio Interactions Toward Engineering Optical Nanomaterials

by

Rebecca L. Pinals

Doctor of Philosophy in Chemical Engineering

University of California, Berkeley

Professor Markita P. Landry, Chair

Engineered nanoparticles have emerged as a promising platform upon which to develop biological sensing, imaging, and delivery tools. Yet, a paramount challenge toward implementing such technologies is understanding how these engineered nanoparticles are *affecting* and *being affected by* the complex bioenvironments in which they are applied. Introducing a nanoparticle into a biological system rapidly establishes a nano-bio interface, as biomolecules, most notably proteins, adsorb to the nanoparticle surface to form the "corona". The abruptness of protein adsorption on foreign nanoparticle surfaces causes proteins to interact in atypical modes, contrary to normal biomolecular interactions governed by precise genetic control, and often produces undesirable outcomes such as protein denaturation. Further, protein corona formation unpredictably changes the nanoparticle identity and fate, as the adsorbed proteins mask original surface characteristics and endow new biochemical properties to the nanoparticle. As a result, how the nanoparticle-corona complex interacts with biological machinery is impacted and *in vivo* circulation, bioaccumulation, and biocompatibility outcomes are drastically modified. Consequently, protein corona formation can disrupt the nanoparticle's designated function by attenuating or eliminating nanoparticle efficacy relative to its *in vitro* performance. Conversely, the protein corona can be taken advantage of, with an engineered protein corona that facilitates new sensing modalities or stealth transport in targeted delivery applications, with improved nanoparticle functionality or therapeutic effect to follow. In both cases, the protein corona displayed on the nanoparticle surface is a principal design parameter for ensuring successful applications of nanotechnologies in biological systems.

In this dissertation, I develop a framework of analysis to quantitatively characterize protein corona formation that occurs on nanoparticle substrates in different biological environments. I adopt a primarily experimental approach, with complementary physics-based and statistical modeling, toward investigating these nano-bio interfacial interactions. I begin with a multimodal characterization of protein corona composition, driving forces of formation, and kinetics in relevant biological media. These studies primarily focus on protein adsorption to single-stranded DNA-functionalized single-walled carbon nanotube (ssDNA-SWCNT) probes. ssDNA-SWCNTs are an appealing tool for biological sensing and imaging because they operate at spatiotemporal scales necessary to capture information on complex biological systems, such as neurotransmitter signaling in the brain. However, it is of note that the methods of corona characterization and

framework of understanding are generalizable to different nanoparticles in different bioenvironments. To probe the protein corona composition, I have optimized a platform to isolate nanoparticle-bound corona proteins and to determine abundance and differential enrichment vs. depletion of corona proteins by mass spectrometry-based proteomics. This analysis provides protein corona compositional maps for nanoparticles that underscore the selectivity of corona formation, reveal key proteins and protein functional roles implicated in corona formation, and enable analysis of protein physicochemical properties governing adsorption to nanoparticle surfaces. By varying incubation conditions of ssDNA-SWCNTs in biofluids, I investigate the role different interactions have on driving selective protein corona formation dependent on corona layer, including electrostatic and hydrophobic forces. These experimental studies are complemented by mathematical modeling, with a colloid thermodynamic framework to describe how the nanoparticle and protein interact in solution, and classification modeling, with a supervised learning approach to move toward predicting nano-bio interactions. To study the dynamic exchange of biomolecules on the SWCNT surface, I have developed a multiplexed fluorescence assay that enables real-time tracking of biomolecule adsorption and desorption events, with corresponding kinetic modeling of this exchange process. From these dynamic corona studies, I provide insight on the general translatability of whole-biofluid nano-bio interactions to single-protein experiments, while highlighting the role of cooperativity effects driving certain protein-nanoparticle interactions. Moreover, this corona exchange assay can be readily extended to examine various biomolecules binding on nanoparticles and enables study in solution rather than in a surface-immobilized, less biologically relevant, setting. Understanding the protein corona composition, driving forces of formation, and dynamics under relevant solution conditions informs design and synthesis of nanotechnology-based tools applied in protein-rich environments.

Although corona formation can impair nanobiotechnology efficacy, it also presents an opportunity to create improved protein-nanoparticle architectures by exploiting selective protein adsorption to the nanoparticle surface. Toward this end, I leverage the fundamental understanding of nano-bio interactions developed in the first portion of this dissertation to design and develop a novel nanosensor for viral protein detection. This nanosensor harnesses SWCNTs to provide the optical signal readout, together with proteins that possess intrinsic recognition ability for the analyte of interest: the ACE2 cell membrane protein is used to bind to the SARS-CoV-2 spike protein analyte. The resulting ACE2-SWCNT nanosensors are thus developed and validated in a proof-of-principle study to create hybrid nano-bio constructs for rapid, label-free protein detection. Notably, this sensing platform is intended to enable rapid detection of live virus (denoting current viral infection) with a near-infrared signal readout that is transmissible through biological media (detecting virus in unprocessed patient samples such as saliva and nasal fluid). As such, further development of this nanosensor construct is envisioned to yield an accessible, point-of-care testing platform.

In sum, this work develops techniques and analyses to characterize the protein corona and subsequently employs this knowledge toward rational design of nanobiotechnologies. The holistic approach developed herein represents a step toward generalized corona formation rules and understanding that will aid the translation of sensing, imaging, and delivery nanotechnologies into biological application.

To Avi Pinals, you are missed.

Contents

List of Figures

List of Tables

Acknowledgments

Thank you to my advisor, Professor Markita Landry, for being an outstanding mentor and role model. Her research and career advice throughout my time in graduate school has been key to my development as a scientist. She tirelessly provided encouragement through the ups and downs of research and consistently empowered me to apply for opportunities that I felt otherwise unqualified for. I am grateful for the freedom Markita granted me in designing my project direction, and with this, how she entertained my ramblings on thermodynamics and branching side projects that came about.

Thank you to my other dissertation committee members, Professors David Schaffer, Wenjun Zhang, and Amy Herr, who provided feedback on this work. I am additionally grateful I had the opportunity to work with Professors Clay Radke and Roya Maboudian and I thank them for their mentorship. I greatly appreciate Carlet Altamirano and Sigrid Allen for orchestrating the graduate degree process and research funding. My work has been funded by the National Science Foundation Graduate Research Fellowship Program.

Thank you to the entirety of the Landry Lab for being an exceptional group of people to do science and graduate school with. In particular, thank you to Linda Chio, Gozde Demirer, and Nat Goh for all being constant sources of encouragement, great friends, and the best people to take boba breaks with. Thank you to Darwin Yang for answering my many questions and being keen to pursue side projects with me, some of which ended up being useful. Thank you to Travis Del Bonis O'Donnell and Ian McFarlane for being wonderful mentors and all-around science gurus throughout my time in lab. Thank you to other lab friends/collaborators including Alison Lui, the sensors squad (Nicole Navarro, Francis Ledesma, Sanghwa Jeong), Sarah Yang, Daniel Rosenberg, Jeff Wang, and Nick Ouassil. Additionally, thank you to my mentees for their work on various projects (some of which unfortunately did not fit into this dissertation), including Tanya Chaudhary, Dorothy Li, Xingcheng (Cindy) Zhou, and Wendy Cao. Finally, thanks to Liz Voke, who will carry the protein corona torch when I graduate and from whom I expect excellent things to come.

Thank you to my incredible 2016 cohort and other members of the Chemical and Biomolecular Engineering Department for making graduate school such a blast. Our small-but-mighty cohort bonded over late night study sessions, nights out, our post-prelims Lake Tahoe trip, and more. Specifically, thank you to Danna Nozik as my first Berkeley housemate; together we braved first-semester classes, prelims, fighting off ants from residing in our modem, and tying a couch in the back of a Zipcar without it falling out.

Beyond the lab and department, thank you to the various scientific communities I have been involved in during graduate school, including the awesome Women in Mathematical Biology group (Professors Adriana Dawes, Calina Copos, Britt Bannish, Minghao Rostami, and Kelsey Gasior), the Women Chemists Committee/Merck community (specifically my mentor Ania Fryszkowska), the CAS Future Leaders, the Bay Area Scientists in Schools volunteer group (the liquid nitrogen ice cream trick will never get old), and the Graduate Women of Engineering.

Thank you to my friends and family for your constant support and love throughout the PhD marathon. My family-away-from home has been the Alligator House, including members past and

present – Constance, Matt, Tammy, Parry, Sarah, Pete, Julie, and Kyle. I have greatly appreciated the company and the conversations, on science and beyond, extending from our Saturday night feasts to our group backpacking trips, and everything in between. In particular, Sarah Berlinger and I became fast friends at the beginning of graduate school due to our matching floral dress patterns, mutual love of dessert (her making it and me licking the frosting bowl afterwards), and aligned research interests in interfacial phenomena (read: stuff sticking to other stuff). Thank you for embarking on the graduate school journey with me, through the highs and lows. Thank you to my friends from back home – Jonah and Nikolay (for superb camping trips in Joshua Tree and Zion, filled with equally superb conversation) and Roni (my rock since 2nd grade and an all-around rockstar of an individual).

Thank you to my parents, Diane and David, for instilling in me a sense of curiosity and for your ever-persistent support, even in my decision to move across the country to California for graduate school. Dad, thank you for insisting that I try to fix things myself first and for initiating fun musical collaborations, whether it is a song from Kevin Burke's Open House or a Bach duet with harmonica and violin. Mom, thank you for reminding me that sometimes you just need to dance and for always being a phone call away. Thank you to my older sister Lisa for paving the way into engineering and for being a constant inspiration to me. I feel incredibly lucky to have a sister who is not only brilliant at math and coding, but also a silly and lovely human being. Thank you to my grandparents, Bob and Ella, for inspiring and supporting me in my scientific pursuits, and for passing on to me your love of the scientific lab where you two first met. Thank you to my grandmother, Connie, for reminding me the importance of dessert and a smile. Finally, thank you to Andrew Crothers. Although I am not entirely sure if it was my Toy Story Halloween costume or my love of transport phenomena that first caught your eye, I am exceedingly happy that you asked me on a bike ride that turned out to be our first date. Thank you for keeping me challenged yet grounded throughout the PhD journey. Your kindness, love of science and engineering, unwavering support, and pesto pasta have been key contributors to my happiness in graduate school. I, too, am excited for all of the adventures of our future.

1 Introduction

1.1 Nanotechnologies to Probe and Modify Biological Systems

As material dimensions are confined to the nanoscale, new properties emerge: surfaces structures dominate over bulk characteristics, continuum concepts may break down, and quantum confinement effects give rise to unique properties.[1–3] Such characteristics render nanoparticles capable of gaining unprecedented access to biomolecular phenomena, with the requisite spatial, temporal, and chemical resolution to provide fundamental insight into biological systems and processes.[4,5] Accordingly, engineered nanoparticles are a promising technology for furthering our knowledge of how biological systems both function and malfunction, and for addressing global health problems.[6–9] Nanoparticles have been employed in biological systems to serve as sensors and imaging agents toward fundamental research purposes and disease diagnostics in the clinic, exploiting the distinct nanoscale properties of these confined systems for readout modalities including optical, electric, magnetic, and plasmonic detection.[1,5,10–13,4] By virtue of their small size and tunable physicochemical properties, nanoparticles have also been applied as delivery agents to protect fragile cargoes (such as genomic material) during transport, while being composed of biodegradable components to ensure biological compatibility post-delivery.[9,14–16] Historically, such delivery vehicles were first realized during the 1960s, with the discovery of the liposome nanoparticle structure.[17,18] More recently, we have witnessed the rapid development of SARS-CoV-2 mRNA-based vaccines, with the mRNA packaged inside of lipid nanoparticles for effective delivery of the otherwise unstable cargo.[19–23] For delivery, nanoparticles also offer the potential benefits of treatment specificity and biological barrier passage, with the intention to limit off-target effects and toxicity, such as in the case of cancer therapeutic doxorubicin encapsulated in liposome carriers.[24,17,14,25,15]

Nanobiotechnologies generally consist of two components: (i) a nanoparticle, to serve as a signal-transducing element (sensing/imaging) or carrier (delivery), and (ii) a tethered moiety, to act as a molecular recognition element (sensing/imaging) or cargo (delivery). Nanoparticles can be synthesized to have tunable and environment-sensitive signals, such as fluorescence dependent on size and surface chemistry.[26–28] Single-walled carbon nanotubes (SWCNTs) are one such example of a signal transduction element, upon which this dissertation will mainly focus. SWCNTs are an allotrope of carbon with physical and optical properties that are readily harnessed to effectively monitor and modulate biological systems.[29,27,10] Like other nanoparticles, SWCNT dimensions are on the nanoscale, with approximate diameters and lengths of ~1 nm and ~100-1000 nm, respectively. This high aspect ratio provides a large surface area upon which tethered moieties can be loaded for various purposes. However, SWCNTs are composed solely of carbon and are therefore extremely hydrophobic. To apply SWCNTs in aqueous bioenvironments, we take advantage of noncovalent surface modification with amphiphilic polymers and molecules, whereby the hydrophobic portion stabilizes the SWCNT surface, and the hydrophilic portion interacts with the surrounding aqueous solution.[30–32] This simultaneously enables aqueous suspension and can confer added functionality toward sensing, imaging, and delivery outcomes. Noncovalent functionalization is primarily chosen over covalent linkage to fully retain the innate optical SWCNT properties: due to the sp^2-hybridized graphitic lattice and cylindrical geometry resulting in radial quantum confinement, SWCNTs possess an intrinsic bandgap in the near-

infrared region.[27,33,34] SWCNT fluorescence emission falls within the "tissue transparency window" (1000-1300 nm), enabling imaging through optically occluded biological media such as biofluids and tissues.[27,33] Moreover, the fluorescence is highly sensitive to localized perturbations, allowing use of SWCNTs as signal transducers to sense changes in their surroundings that manifest as either a fluorescence intensity increase or decrease, or a solvatochromic shift in the emission wavelength.[27,33] The semiconductor nature of SWCNTs bestows indefinite photostability that is unachievable by conventional fluorophores.[27,35,36]

Complementary to the nanoparticle substrate, the tethered moiety varies by application, such as a ligand with intrinsic molecular recognition capabilities or where such capabilities are conferred only upon nanoparticle-surface immobilization. The former case has been explored in using targeting ligands on nanoparticle surfaces for delivery, yet less so in the case of nanoparticle-based sensors.[17,37,38] For SWCNT-based sensors, this idea of surface-constrained polymers adopting an analyte-specific binding pocket has been termed "corona phase molecular recognition".[32,39,40] In particular, this dissertation will use a SWCNT-based nanosensor developed by this route as a case study: a dopamine nanosensor was recently developed using a screening-based approach to determine that a single-stranded DNA (ssDNA) functionalized SWCNT, specifically with a repeated sequence of guanine and thymine $(GT)_x$, exhibited a sizeable turn-on fluorescence response in the presence of the neuromodulator dopamine.[40] This $(GT)_x$-SWCNT dopamine nanosensor has since been optimized and applied in various cellular and tissue environments.[41–44] More broadly, such nanotechnologies enrich the toolbox of strategies with which biological systems can be investigated and adapted, providing fundamental insights on how highly complex biological systems function and routes toward more targeted disease diagnostics and treatments.

1.2 Protein Corona Formation as Relevant to Applied Nanobiotechnologies*

Although engineered nanoparticles are increasingly used for biological sensing, imaging, and delivery, the critical – yet often overlooked – challenge with these nanoscale tools is understanding the mechanisms of interaction between the nanoparticle and the biological system they are designed to query or alter.[45,46] Nanotechnologies are generally developed and validated *in vitro*, absent from the complexity of biological environments.[47] However, when nanoparticles are introduced into biological systems, proteins spontaneously adsorb to the nanoparticle surfaces, leading to the formation of the "protein corona".[48] Binding of proteins to pristine nanoparticles can adversely affect the structure and function of the bound proteins,[49,50] and carries the additional consequence of masking and re-defining the nanoparticle identity.[45,51] Accordingly, *in vivo* trafficking, biodistribution, clearance, and biocompatibility of the nanoparticle-corona complex become unpredictable.[45,51–53] These corona-mediated alterations manifest as decreased nanoparticle efficacy or loss of *in vitro*-validated results, whereby the nanoparticle no longer carries out its designated function (Figure 1-1).[54,55] Furthermore, the protein corona is dynamic in nature.[45,56] Rapid protein binding events on the nanoparticle surface, in conjunction with

* Portions of section 1.2 published as Pinals, R. L.; Yang, D.; Rosenberg, D. J.; Chaudhary, T.; Crothers, A. R.; Iavarone, A. T.; Hammel, M.; Landry, M. P. Quantitative Protein Corona Composition and Dynamics on Carbon Nanotubes in Biological Environments. *Angewandte Chemie International Edition* **2020**, *59* (52), 23668–23677. https://doi.org/10.1002/anie.202008175.

differential protein affinities in the corona, give rise to further complications in understanding the timescales over which nanoparticles retain their corona-free attributes within biological environments.

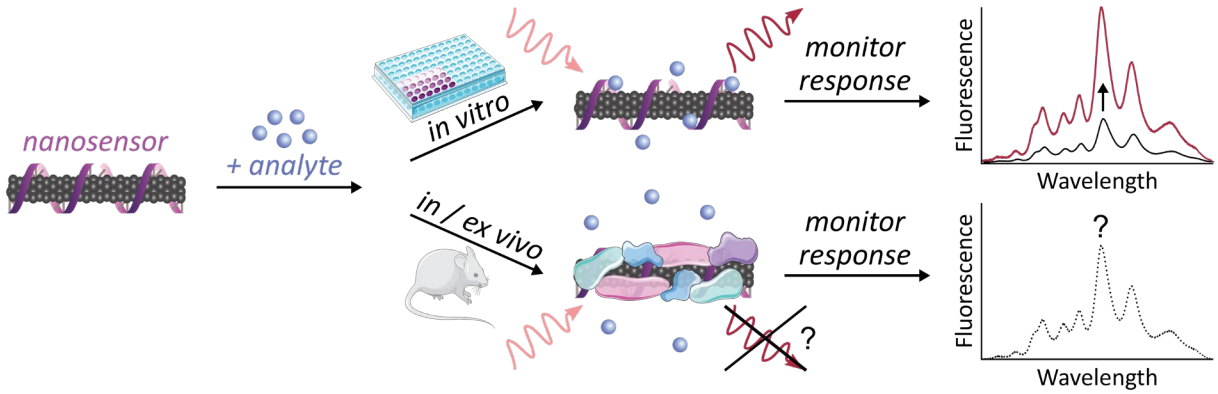

Figure 1-1. Protein corona formation unpredictably affects performance of nanoparticle-based sensors applied in biological environments.

Corona formation as a function of nanoparticle type, biological environment, and time remains poorly understood.[57] Prior work investigates the roles of nanoparticle surface charge and chemistry, among other factors, in governing protein corona formation,[58–61] revealing the variation and complexity of protein corona formation across nanoparticle types and bioenvironments (as will be explored in section 1.3).[46,62] Consequent work has sought to mitigate corona formation by nanoparticle-surface passivation with polymers such as polyethylene glycol (PEG) to abrogate protein adsorption and sterically stabilize the nanoparticle. Of note, PEGylation of liposomes, a model nanoparticle for delivery, has been demonstrated to decrease protein adsorption and maintain some functionality of surface-exposed targeting moieties.[63–65] Yet, such strategies can display variable efficacy depending on the underlying nanoparticle and bioenvironmental factors.[66,67]

Interfacing functional nanomaterials with biological systems is central to the field of nanobiotechnology. However, unpredictable nano-bio interfacial interactions present a critical challenge in effectively translating nanotechnologies from *in vitro* development to *in vivo* application, thus limiting the widespread biological deployment of nanoparticle-based probes and carriers.[11,68,69] To provide some context of this translational gap, we can consider cancer nanomedicine: there are anywhere from 0.5-1 million published research papers on cancer and nanoparticles as of April 2021. A meta-analysis gave rise to an estimate of <1% nanoparticle-based cancer therapeutic delivery to tumors.[68] Then, on the clinical side, there are only around 15 nanoparticle-based cancer nanomedicines approved globally, noting that many of these are re-formulations of pre-existing cancer drugs.[14,69–71] Numerous reasons are reported as to why such cancer nanomedicines underperform or fail, including biofouling, instability, unfavorable immune response, untimely clearance, lack of biological barrier traversal, and off-target effects including toxicity. Most, if not all, of these failures can be traced back to our poor understanding of the nano-bio interface. [69,71] While cancer nanomedicine illustrates one example, the ubiquitous and fascinating problem of protein corona formation is demonstrated across intended biological applications of nanoparticles and accordingly will be the focus of this dissertation.

1.3 Factors Influencing Protein Corona Formation[†]

Nanoparticle physicochemical properties and the surrounding bioenvironment are inherent variables affecting protein corona formation. Many studies classify the protein corona around specific nanoparticles in particular biological systems of interest, although findings often lack generality or are contradictory as to which nanoparticle or protein properties drive protein corona composition, dynamics, and subsequent biological outcomes. Additionally, the protein corona is dependent upon a convolution of parameters carrying varying weights, and often these parameters are difficult to decouple without meticulous experimental design. Therefore, although general parameters are summarized in Figure 1-2, we note that these generalities may not always hold depending on the intricacies of the nanoparticle-biosystem under consideration. In the following sections, recent literature is summarized highlighting key parameters governing protein corona formation on nanoparticles. To extend experimental data into broader design rules, recent work has involved ensemble machine learning approaches to develop predictive models of protein corona fingerprints formed on nanoparticles based on protein, nanoparticle, and solution characteristics.[72] Such models could better inform corona-based design.

1.3.1 Nanoparticle Characteristics Influencing Protein Corona Formation

Nanoparticle surface properties are most significant in governing protein corona formation, as compared to the nanoparticle core.[61,73,74] These nanoparticle surface features include: (i) electrostatic charge, (ii) hydrophobicity, and (iii) surface structure. These attributes are functions of nanoparticle surface chemistry and ligand functionalization.

1.3.1.1 Electrostatic Charge

Nanoparticle charge affects protein corona composition and packing density.[75–79] Many studies conclude that proteins possessing opposite charges from the nanoparticles are enriched in the corona. As most proteins are negatively charged at physiological pH, it is often found that cationic nanoparticles adsorb the highest number of proteins.[75–77,80,81] However, there are examples in which proteins are able to overcome electrostatically adverse conditions and adsorb by nonelectrostatic driving forces.[82–84] It is important to consider that even if nanoparticles are synthesized with appropriate surface chemistries, these nanosurfaces may only retain these engineered features transiently within biosystems.[61] Nanoparticle charge thus impacts surface packing, where higher magnitude charge leads to more proteins in the corona.[73] Other studies conclude that more cationic surfaces increase conformational changes of adsorbed proteins.[84] These results are contradictory, in that post-adsorptive protein structural changes generally take place under lower surface packing densities, where proteins have more accessible area to spread out and denature on the surface.[85,86] It is unlikely that such conformational changes would be able to occur in a highly crowded corona environment. Beyond the individual nanoparticle, surface charge also directly impacts colloidal stability because neutral surfaces (or surfaces neutralized by

---

[†] Sections 1.3-1.4 published as Pinals, R. L.; Chio, L.; Ledesma, F.; Landry, M. P. Engineering at the Nano-Bio Interface: Harnessing the Protein Corona towards Nanoparticle Design and Function. *Analyst* **2020**, *145* (15), 5090–5112. https://doi.org/10.1039/D0AN00633E.

protein and ion adsorption) tend to aggregate in the absence of intervening electrostatic repulsions.[87] As will be discussed below, the surrounding solution ionic strength determines the importance of electrostatic interactions, as these interactions are screened and play less of a role in high-salt systems. Accordingly, nanoparticles must be designed in such a manner that they are not only colloidally stable as a homogeneous solution, but retain colloidal stability in the presence of proteins in the surrounding bulk and surface-adsorbed state.[75]

Manipulating nanoparticle charge offers a useful means to tune nanoparticle interactions with biological cells, with regards to cell internalization and toxicity:[88] positively charged nanoparticles have enhanced cell internalization due to interactions with the negatively charged cell membrane,[89–93] especially enhanced for the case of cancer cells.[76] Yet, if positively charged nanoparticles bind too many proteins, this leads to colloidal instability, aggregation, and downstream toxicity.[75,94]

1.3.1.2 Hydrophobicity

Nanoparticle surface chemistry also dictates hydrophobicity, where hydrophobic nanoparticles exhibit increased protein adsorption capacity,[73,95] more irreversible protein adsorption,[78,87,95] and cause more protein conformational changes.[87,95] Nanoparticles with hydrophobic surfaces are more likely to produce deleterious effects on protein structures, as protein unfolding is driven by the favorable interactions of the protein hydrophobic core with the nanoparticle surface.[95] Frequently, such unfolding is irreversible, leading to larger scale aggregates, nonfunctional nanoparticles, and immune activation/clearance.[81,87] Again, these conclusions of high packing density and high conformational changes are at odds with each other, for the same reasons as specified for electrostatic charge.

1.3.1.3 Surface Structure

Features of nanoparticle surface topography that impact protein corona formation include surface roughness, porosity, and sterics. A rough or porous surface creates more available surface area for proteins to coat and so allows proteins to minimize lateral repulsive forces in the adsorbed state. Functionalization with polymers, targeting ligands, or other moieties that extend outward into solution also affects nanoparticle surface topography. The grafting density and conformation of such attached ligands impacts accessibility of proteins to the nanoparticle surface.[96,97] Based on the principles of both hydrophobicity and surface structure, corona mitigation techniques often involve surface-grafting of hydrophilic polymers such as polyethylene glycol (PEG) to abrogate protein adsorption and sterically stabilize the nanoparticle.[61,98,99] Higher antiadhesive polymer coverage is associated with alleviated protein corona formation, while lower coverage or linear conformations are less effective in deterring protein binding.[97,100,101] Combining these concepts of surface roughness and sterically stabilizing polymers, Piloni *et al.* demonstrated that a patchy polymer-grafted nanoparticle reduced protein adsorption in comparison to a smooth polymer-grafted surface by six-fold (protein content per nanoparticle).[102]

Beyond surface characteristics, other nanoparticle factors that impact corona formation include: (iv) size, (v) curvature or shape, (vi) stiffness, and, to a much lesser extent, (vii) core material composition.

1.3.1.4 Size

Size is found to quantitatively, though not qualitatively, impact corona formation: larger nanoparticles present more high surface free energy, net exposed area and permit higher protein loading per nanoparticle,[77,103] although the corona constituents are often no different than those on smaller nanoparticles of identical material properties.[87] Moreover, smaller nanoparticles possess a higher surface area to volume ratio, hence smaller nanoparticles adsorb more proteins on an area normalized basis. Optimizing the metric of protein loading on a nanoparticle number or area basis depends on the desired application, as will be discussed in subsequent sections. Further, increasing nanoparticle size decreases surface curvature (though dependent on the geometry), therefore there exists a threshold above which larger particles do not necessarily adsorb more proteins.[104]

Another important consideration is the effect of nanoparticle size on targeting and localization efficiencies: biological barrier crossing efficiency and mechanism are both size-dependent, where successful crossing scales inversely with size.[92,105] Here, it is critical to consider the hydrodynamic, *in situ* nanoparticle-corona complex size; an adsorbed protein corona may add up to hundreds of nanometers to *in vitro* particle size.[106] Biological barriers range from vasculature walls to cell membranes, with typical cutoff dimensions including <6 nm for renal clearance[79] vs. >300 nm for liver or spleen filtration,[107] ~20-200 nm for tumor penetration and retention,[107–109] <50-100 nm for blood-brain barrier (BBB) crossing and extracellular matrix (ECM) navigation,[110,111] and 10-100 nm for cell internalization.[92] On the cellular level, Shadmani *et al.* applied a mathematical model based on diffusion of membrane-mobile receptors to examine how protein corona formation impacts internalization of gold nanoparticles by receptor-mediated endocytosis.[105] From this model, optimal values for nanoparticle-corona radius (40 nm bare diameter increasing to 60 nm upon corona formation) and targeting ligand density (~1500 μm^{-2} on a 100 nm gold nanoparticle) are described to minimize endocytosis time through a balance of membrane tension energy and ligand-receptor interaction density, demonstrating how *in silico* models are useful for nanoparticle design.

1.3.1.5 Curvature/Shape

Reiterating the earlier discussion of lateral interactions, now considering nanoparticle shape, a higher curvature surface minimizes adverse lateral protein-protein interactions. Thus, a more curved nanoparticle surface would be expected to adsorb more proteins if unfavorable protein-protein interactions are preeminent (e.g. lateral, repulsive electrostatic interactions). However, if favorable nanoparticle-protein interactions dominate (e.g. attractive dispersion forces), a flatter surface would be advantageous to facilitate more adsorption. This latter case is manifested as higher protein adsorption (per unit surface area) on higher aspect ratio nanoparticles, such as nanorods relative to nanospheres.[112] Other studies find that curvature impacts adsorbed protein orientation to result in lower packing.[113] Therefore, no generalizable rules can be deduced with regards to the effect of nanoparticle shape on protein adsorption. Once applied *in vivo*, shape also dictates how nanoparticles behave within convective flow, such as how they interact with bounding walls, and internalization efficiencies and mechanisms, since membrane bending energy is dependent on nanoparticle form factor.[92]

1.3.1.6 Stiffness

As with shape, nanoparticle stiffness has been shown to affect modes of cell internalization and bioaccumulation: less stiff nanoparticles generally exhibit lower cell internalization across many cell types, and correspondingly longer circulation times due to the more difficult uptake and clearance by macrophages.[91,114,115] Stiffness here refers to the nanomaterial's ability to resist deformation under applied force, related to the material's Young's Modulus and geometry. Yet, the impact of nanoparticle stiffness on protein corona formation remains relatively under-studied. While proteins are considered soft matter and may be expected to increase the inherent nanoparticle softness, this may not be the dominant factor, as higher protein adsorption often leads to the opposite downstream outcomes as those reported for less stiff nanoparticles. The effect of nanoparticle stiffness on protein adsorption remains an open question.

1.3.1.7 Core Composition

Finally, while the core material composition does influence corona formation to some extent,[77] the core is mostly shielded from direct exposure with the biofluid and thus plays a minor role in determining protein corona formation. However, use of exogenous nanoparticle core materials can lead to immune activation and toxicity during attempted clearance.[79]

1.3.2 Biological Environment Factors Influencing Protein Corona Formation

In addition to the influence of innate nanoparticle variables on protein corona formation, the bioenvironment of the intended application must be taken into account. Environmental parameters include: (i) biomolecular components, (ii) solution conditions, and (iii) surrounding dynamics.

1.3.2.1 Biomolecular Components

Native biomolecule concentration and composition within a biological environment influences the consequent protein corona formed on nanoparticles. Higher protein concentration in the surrounding fluid frequently leads to more protein adsorption on nanoparticles, as suggested by ideal-solution thermodynamics, and witnessed experimentally.[116,117] Nonetheless, relative corona protein concentration does not necessarily correlate with native circulating protein concentration due to preferential protein partitioning into surface vs. bulk solution phases.[82,118] More complex mechanisms often govern protein corona formation, giving rise to surprising magnitudes of protein enrichment or depletion on nanoparticles relative to the native biofluid. A frequent example of this phenomenon is the Vroman effect, where highly abundant proteins initially adsorbed to nanoparticles competitively exchange with and are eventually replaced by lower abundance, higher surface-affinity proteins.[84,116,119] Cooperative adsorption is another mechanism leading to corona composition unanticipated from circulating concentrations, where initially bound corona proteins provide a scaffold promoting successive protein adsorption.[119,120] Regarding native biomolecule composition, the observed corona in the presence of proteases may be a convolution of protease degradation of and exchange with the existing corona.[121] These higher order mechanisms offer an explanation as to why corona constituents and kinetics resulting from single protein adsorption experiments are often not representative of whole biofluid experiments.[82] These findings also stress the importance of testing nanoparticles within physiologically relevant biological fluids. A prominent example is the proliferous use of blood serum (absent of blood coagulation proteins) instead of blood plasma (which contains blood coagulation proteins) to test

nanoparticles designed for intravenous administration, where coronas formed from plasma proteins have been shown to be different from those of serum and more strongly adhered.[77,109,119,122] An additional consideration in terms of biomolecule composition arises in that nanoparticles may be subject to harsh conditions such as enzymatic degradation in the gastrointestinal tract[123] and cancer cells,[121] or immobilized, tenacious biomolecules in the mucus layer[123] and brain extracellular matrix.[124] Presence of these biomolecules introduce physical obstacles to penetration and routes to irreversible corona formation with subsequent toxicity. It is of further consequence that disease states alter endogenous protein concentrations and compositions, which leads to deleterious effects if the same such protein is pre-conjugated on nanoparticles for targeting purposes.[125]

1.3.2.2 Solution Conditions

Corona formation is a function of surrounding conditions, such as temperature, ionic strength, and pH. Increasing temperature increases the weighting of the entropic term within the net Gibbs free energy change of adsorption ($\Delta G = \Delta H - T\Delta S$). This results in proteins that are entropically favorable to adsorb ($+\Delta S$) becoming more favorable at higher temperature ($-\Delta G$), and vice versa.[82,103] Within this analysis, it is key to note that each term is the net system, therefore a function of the protein, nanoparticle, and solution initial and final states during binding. For solution ionic strength, electrostatic forces scale inversely with the square-root of salt ionic strength in solution. These electrostatic forces originate from interactions between electric double layers surrounding the charged colloidal nanoparticles and proteins. This underscores how nanoparticle surface charge is inherently coupled with solution ionic strength, and the two parameters must be co-designed appropriately. In high ionic strength conditions (high salt concentration), nanoparticles and proteins do not "see" each other in solution until they are in closer proximity. Closer approach between entities bearing the same electrostatic charge results in more protein adsorption. In addition, once adsorbed, charge shielding ensures less unfavorable lateral repulsions between adsorbed proteins (again, most bearing the same negative charge at physiological pH). Both phenomena imply more protein adsorption with more salt present. However, when ionic strength becomes too elevated, charge screening leads to undesirable protein-nanoparticle complex aggregation.[87,109] Accordingly, ionic strength and even ionic composition are important considerations in protein adsorption and potential downstream toxicity due to aggregation, such as high free calcium ion concentrations in the brain microenvironment leading to nanoparticle aggregation.[111] pH is another relevant solution condition in that it governs the protonation state of surface chemistries on the nanoparticle, again influencing aggregation tendency,[111] and impacts adsorbed protein extent and stability. As the solution pH approaches the protein isoelectric point, proteins become less stable in solution and tend to self-aggregate or adsorb to available nanoparticle surfaces.[126] In terms of corona stability, the pH range that the nanoparticle will encounter is crucial to consider as a design parameter, as biological compartments cover a significant pH range at the organ and cell levels, and can differ as a function of disease state, such as the acidic pH of tumors.[116,127] Many protein or peptide drugs externally loaded on nanoparticles may not survive severe conditions,[123] or their expected release profile can be negatively impacted.[110]

1.3.2.3 Dynamics

Finally, temporal dynamics and hydrodynamics should be considered for protein corona formation. Protein adsorption occurs within seconds of contact with biofluids,[119] and may either display a dynamic nature, with fast and reversible protein association/dissociation events on the nanoparticle surface, or enter an irreversibly aggregated state.[85,87,128] Proteins adsorbed directly to the nanoparticle surface are termed the "hard", inner corona, characterized by a longer (if not indefinite) residence time in the corona phase and often more prominent conformational changes.[84,86,116,119] Proteins interacting predominantly with other adsorbed proteins, instead of directly with the nanoparticle surface, constitute the "soft", outer corona, and frequently maintain their native conformation as they undergo continuous exchange with proteins in the surrounding media.[106,116] Protein corona composition is impacted by the contact time and history of nanoparticles in biofluids: the former, reiterating the likes of the Vroman effect, and the latter, in that nanoparticles evolve to carry a "fingerprint" of adsorbed proteins as they progress from one biological compartment to the next.[80,129]

Nanoparticles must endure flow conditions during transit, navigating channels or regions of characteristic tortuosity, permeability, and hydrodynamics. A classic example of nanoparticles maneuvering through a highly tortuous path is within the porous extracellular matrix (ECM) of the brain, relevant for neurosensors or brain-targeted therapeutics.[110,124] The ECM is a mesh-like structural and biochemical scaffold for brain cells, with channels of widths ~40-200 nm, that acts as an adhesive and steric barrier for nanoparticles attempting to pass.[110,111] Work within the Nance lab has pioneered brain-penetrating nanoparticles, with design principles to ensure that the nanoparticles exhibit minimized electrostatic, hydrophobic, or hydrogen bonding interactions with the ECM.[124] Toward nanoparticle permeability, crossing of biological barriers is of paramount importance. Again, considering the brain, the blood-brain barrier (BBB) functions as a selective barrier to protectively isolate the brain from an influx of potentially harmful entities within blood circulation, as will be discussed in section 7.5.3. It must also be taken into consideration that the brain's tortuous ECM and selective BBB vary with pathology and developmental age.[124,130] Finally, regarding hydrodynamics, dynamic flow can result in a more rapidly formed and compositionally diverse corona.[119,131] From a design perspective, shear stresses imposed on nanoparticle-loaded cargoes must be considered *a priori*: the required stability of the corona-nanoparticle complex will depend on whether the dominant transport mechanism will be passive diffusion or active convection.[119]

In sum, a host of intrinsic nanoparticle-based and extrinsic bioenvironmental factors affect protein corona formation (Figure 1-2). These relevant factors should be considered beforehand to aid appropriate experimental design and implementation toward rational nanobiotechnology design. There are frequent discrepancies between *in vitro* and *in vivo* corona characterizations that arise from negligence of these factors, such as flow dynamics present in circulation that are absent for *in vitro* tests.[80,132,133]

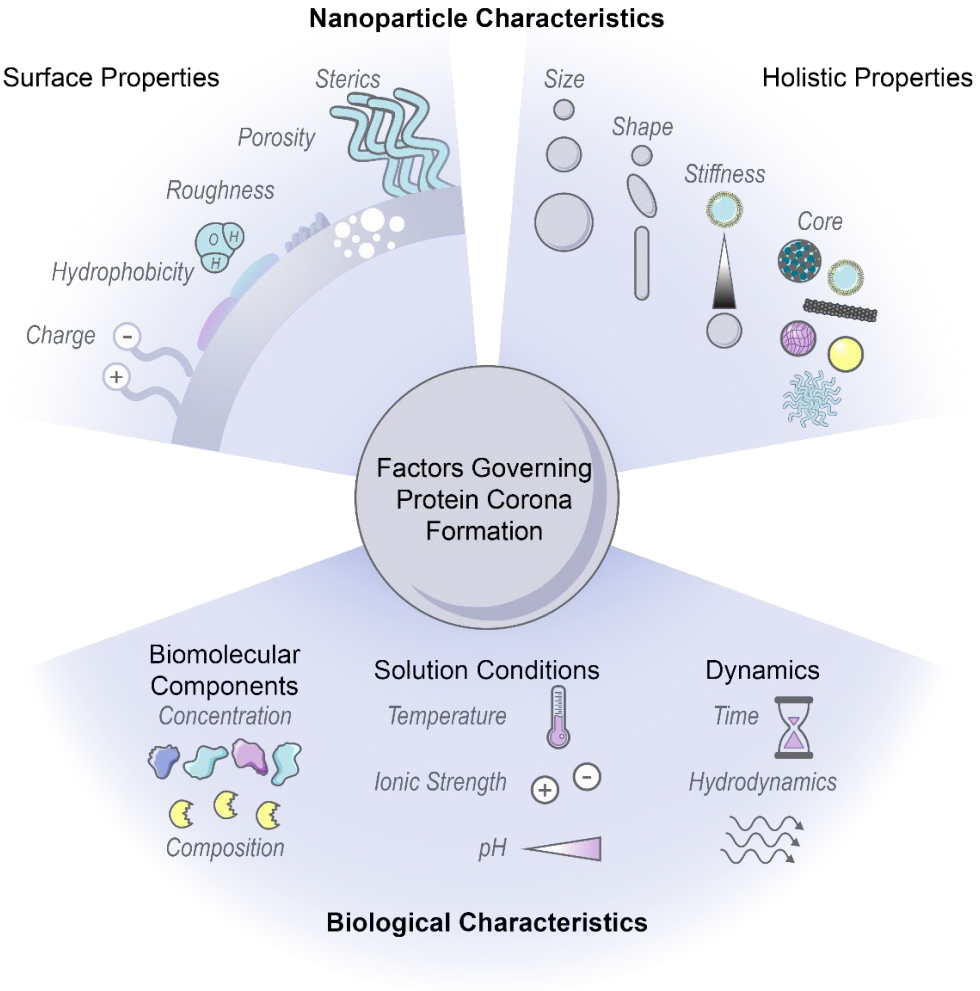

Figure 1-2. Factors governing protein corona formation include intrinsic nanoparticle characteristics and extrinsic biological characteristics. Intrinsic nanoparticle properties (top) can be employed as design handles during rational nanoparticle-corona design and extrinsic biofactors (bottom) must be carefully considered to ensure the complex will function properly within the intended biological environment.

1.4 Nanoparticle-Corona Characterization Methods

Understanding the protein corona necessitates characterization of the physical, biological, and dynamic properties of the protein-nanoparticle complex, alongside testing in suitable *ex vivo* or *in vivo* systems (Figure 1-3). Many requisite bioanalytical methods are well-established for this purpose and can be directly applied or adapted to study corona formation and outcomes.[134] We also highlight novel methodologies being developed toward this.

1.4.1 Physical Property Characterization

Techniques commonly applied to assess in-solution physical properties of protein corona formation include: zeta potential to assess surface charge;[77,104,110] dynamic light scattering

(DLS)[77,104,110] or fluorescence correlation spectroscopy (FCS)[87,135] for hydrodynamic size; absorbance spectroscopy for colloidal morphology and concentration;[61,77,136] fluorescence quenching to track adsorption,[118] with Stern-Volmer analysis of the mechanism;[113,125] and fluorescence microscopy to confirm adsorption via colocalization.[123,126,137] Although zeta potential is not rigorously equivalent to the electric surface potential nor the Stern potential and there are implicit geometry assumptions in the calculation, zeta potential still provides a proxy for colloidal charge and stability, where often the zeta potential tends to zero in the presence of destabilizing protein adsorbates. Small-angle x-ray scattering (SAXS) has recently been applied to acquire in-solution colloidal morphology of nanoparticle-corona systems, including protein-nanoparticle complexation to verify binding and higher order aggregate formation to examine potential routes of *in vivo* toxicity.[80,82,138] Diffusion nuclear magnetic resonance (NMR) has also been employed to infer protein adsorption on nanoparticles via increasing hydrodynamic radius, offering the advantage of *in situ* characterization in turbid bioenvironments by virtue of not being an optics-based measurement.[139] Regarding the aforementioned techniques used to measure protein-nanoparticle size (DLS, FCS, etc.), the readout must be carefully interpreted. Large increases in hydrodynamic size may indicate aggregation of the nanoparticles in the presence of proteins via polymer bridging or other noncovalent interactions, rather than formation of protein multilayers on individual nanoparticles.[87,131,135] Surface techniques are also applied to assess dried-state physical properties of protein corona formation, including: electron microscopy (EM),[110,140,141] atomic force microscopy (AFM),[95,142] and energy dispersive X-ray spectroscopy (EDS mapping)[143] for size and morphology. However, these methods all require drying samples on a substrate for observation, which results in conclusions not representative of the solubilized system. Recent work has also implemented cryogenic transmission electron microscopy (cryo-TEM) to enable visualization of protein-nanoparticle morphology in a closer-to-native state.[132,144]

To study the composition of corona constituents, the protein-nanoparticle complexes are first isolated from non-binding entities, typically accomplished by some variation of a pull-down assay.[14] After corona proteins are unbound from the nanoparticle, characterization methods to identify the protein constituents include gel electrophoresis (GE)[123,125,145] and proteomic mass spectrometry (MS).[61,86,106] Separation techniques to isolate the soft, more loosely bound corona from the hard corona are currently in development, such as asymmetric field-flow fractionation by Weber *et al*.[146] The Sutherland lab has also developed an *in situ* click-chemistry reaction to separately characterize the soft and hard coronas formed on model nanoparticles.[86] To gauge whether corona loading or mitigation strategies are successful, net protein adsorption can be measured by protein assays such as the bicinchoninic assay (BCA) for protein loading,[61,110,147] gel electrophoresis again, immunoblotting (e.g. Western blots),[121] and enzyme-linked immunosorbent assays (ELISAs).[121] The accuracy of colorimetric protein assays such as BCA in the presence of nanoparticles must be critically assessed prior to experiments, as nanoparticles often interfere by adsorbing the reporter molecule or absorbing the output light used to quantify protein concentration. Moreover, the specific chemistry of the assay will determine whether proteins in solution, in the adsorbed state, or both are being measured.

1.4.2 Biological Property Characterization

Techniques applied to assess biological function in the corona include: circular dichroism (CD)[113,133] and solution NMR[148,149] spectroscopy for bound protein structure and conformation; Förster resonance energy transfer (FRET) for measurement of protein-protein interactions[123] and

conformational changes;[116] nano differential scanning fluorimetry (nanoDSF) for protein stability and conformational changes;[126] and immunoblotting to evaluate accessibility and function in the corona.[125,143,150] To study corona structural organization and functionality at the nanoparticle surface, Herda *et al.* developed a method to characterize adsorbed protein orientation by exploiting antibody-conjugated gold nanoparticles to map available epitopes.[140] When they applied this method for transferrin proteins covalently conjugated to PEGylated silicon dioxide nanoparticles, they found that only ~4% of corona proteins adopt the correct orientation to facilitate receptor binding, highlighting the need for more homogenous and controlled protein grafting methodologies. Recently, the Chan lab developed a modified-ELISA workflow to similarly probe protein corona organization and binding functionality when adsorbed from blood serum onto gold nanoparticles, establishing that merely a third of the adsorbed proteins remain functional for binding to their target proteins.[151] Imaging advances have led to the development of various techniques to assess protein interactions on surfaces, including single molecule high resolution imaging with photobleaching (SHRImP) by Warning *et al.* to measure protein conformational changes on a surface.[85]

1.4.3 Dynamic Property Characterization

Methods to study dynamics of protein corona formation include: isothermal titration calorimetry (ITC) to extract thermodynamic binding energies and equilibrium parameters,[97,103,152] as reviewed extensively elsewhere,[153] and surface plasmon resonance (SPR),[86,106,154] biolayer interferometry (BLI),[155] and quartz crystal microbalance with dissipation monitoring (QCM-d)[113] to determine binding kinetics. Recently, Kari *et al.* designed a custom biosensor system for *in situ* determination of protein corona structure and composition by coupling SPR and proteomic MS, enabling differentiation of the hard and soft corona formed on liposomes under physiologically relevant conditions.[106] Super-resolution microscopy presents a single-molecule technique with requisite sensitivities to monitor individual protein-nanoparticle binding events, avoiding ensemble-averaged methods of studying corona formation.[156] However, it is important to note that application of surface techniques such as SPR and microscopy to study nanoparticles again requires surface immobilization of the nanoparticles. Surface immobilization introduces topographical constraints that affect kinetics and transport, giving rise to sampling artifacts and changing the in-solution nanoparticle properties. Ideally, protein-nanoparticle complexes are studied in solution with physiologically relevant parameters that are known to affect corona formation (including ionic strength, temperature, pH, etc.). Accordingly, in-solution kinetic corona methods have been developed, including fluorescence assays to monitor protein fall-off[145] and exchange[118] on solubilized nanoparticle surfaces. To expand upon the use of surface charge changes as a proxy for protein corona formation, Zhao and colleagues measured in-solution protein binding dynamics onto nanoparticles using pulsed streaming potential, resulting in knowledge of adsorption rates and equilibria under varying buffer conditions.[157] Further, Weiss *et al.* have developed a microfluidic system to simulate a flow environment, with control over fluid flow and shear applied to nanoparticles and proteins.[119] This microfluidic system has elucidated the more complex corona formed in dynamic rather than static conditions.

While prior studies provide insight into bio-corona formation, numerous techniques and model fits are ill-applied and present conclusions not representative of the system. The protein corona is often treated as existing at thermodynamic equilibrium, despite a body of literature providing evidence otherwise.[158–160] One frequent manifestation of this equilibrium assumption is the erroneous

application of the Langmuir adsorption isotherm to mechanistically describe proteins adsorbing to nanoparticles, despite the fact that many of the model conditions are not satisfied.[161] A key point here is that Langmuir-like binding profile does not necessitate that the binding mechanism is indeed a Langmuir isotherm: this profile shape for protein-surface adsorption processes often emerges as the result of adsorption-induced protein spreading/denaturation, reorientation, and aggregation as a function of bulk protein concentration,[116] in contrast to originating from the dynamic equilibrium adsorption process required for Langmuirian adsorption.[161] Therefore, while the Langmuir isotherm does provide a simple functional form that may fit data, it should only be applied in extraction of relative binding affinity measures rather than true thermodynamic parameters or underlying adsorption mechanisms. For instance, ITC is often a method applied with intent to assess protein-nanoparticle binding events. Instead, ITC often measures a convolution of protein binding to individual nanoparticles, to aggregated nanoparticles, and nanoparticle aggregation.[82] Aggregation is a kinetically controlled, non-equilibrium process that violates the central assumption of ITC that each titration step is equilibrated, observed as visible aggregation and baseline drifting during the run. Accordingly, the reported free energies and equilibria values must be taken with the perspective that these are whole-system energy changes, often with higher-order processes occurring simultaneously. The suitability of such models and experimental methodologies to describe certain nanoparticle-protein corona formation processes should be carefully considered prior to application.

Finally, molecular dynamics (MD) simulations provide insight into fundamental interactions driving adsorption to surfaces and protein structural changes upon adsorption, as reviewed extensively elsewhere.[162–164] Atomistic MD models convey a detailed picture of protein-nanoparticle interactions, including the individual amino acids responsible for association.[165] Alternatively, coarse-grained MD models trade such detail for access to longer time and length scales, increasing approximately an order of magnitude from the millisecond and nanometer scales in atomistic models.[162] Although coarse-grained models are inherently lower resolution, such as lacking physicochemical details of the nanoparticle surface,[166] these models can facilitate the study of protein-protein interactions and adsorption onto smaller nanoparticles, with explicit curvature effects. Both scenarios are unfeasible in atomistic models, which instead highlight interfacial phenomena in dilute protein settings. Some particular MD studies of interest involving protein-nanoparticle systems include: atomistic MD simulations of amyloidogenic peptides on gold nanoparticles (modeled as a gold surface)[165] and plasma proteins on model nanomaterials;[84,95] hybrid MD simulations, with an atomistic nanoparticle description and a coarse-grained, solvent-explicit protein description;[78] and multiscale MD simulations, adopting coarse-grained or meso-scale models for single vs. simultaneous protein adsorption on small gold nanoparticles, respectively.[167] MD simulations extend our understanding of dynamic protein-nanoparticle interactions, yet require further refinement and validation against experimental results prior to use as purely predictive tools, due to the underlying complexity of nanoparticles interacting with proteins.[162]

1.4.4 Biological Outcome Characterization

Toward applied nanoparticle-corona technologies, *in vivo* studies provide compelling evidence for sustained engineered nanoparticle function or therapeutic efficacy within complex bioenvironments. Animal models such as mice and rats provide the means to study not only function, but also systems-level clearance profiles, bioaccumulation, and toxicity.[101,123,143] *Ex vivo*

organ slices enable measurement of nanoparticle diffusion by particle tracking studies, providing insight into unfavorable adhesive interactions with the surrounding biological matrix.[99] At the cellular level, fluorescence (often confocal) microscopy,[99,123,125] immunofluorescence,[110,143] and flow cytometry[99,100,125] provide information on cellular uptake, spatial localization, cell morphology, and cytotoxicity. As an intermediate between achieving *in vitro* experimental control and assessing *in vivo* translatability, transwells offer a useful cellular model for biological barriers such as the blood-brain barrier[129] and three-dimensional organoids or tumor spheroids offer a scaled-down organ model for assessing efficacy and toxicity.[75,168]

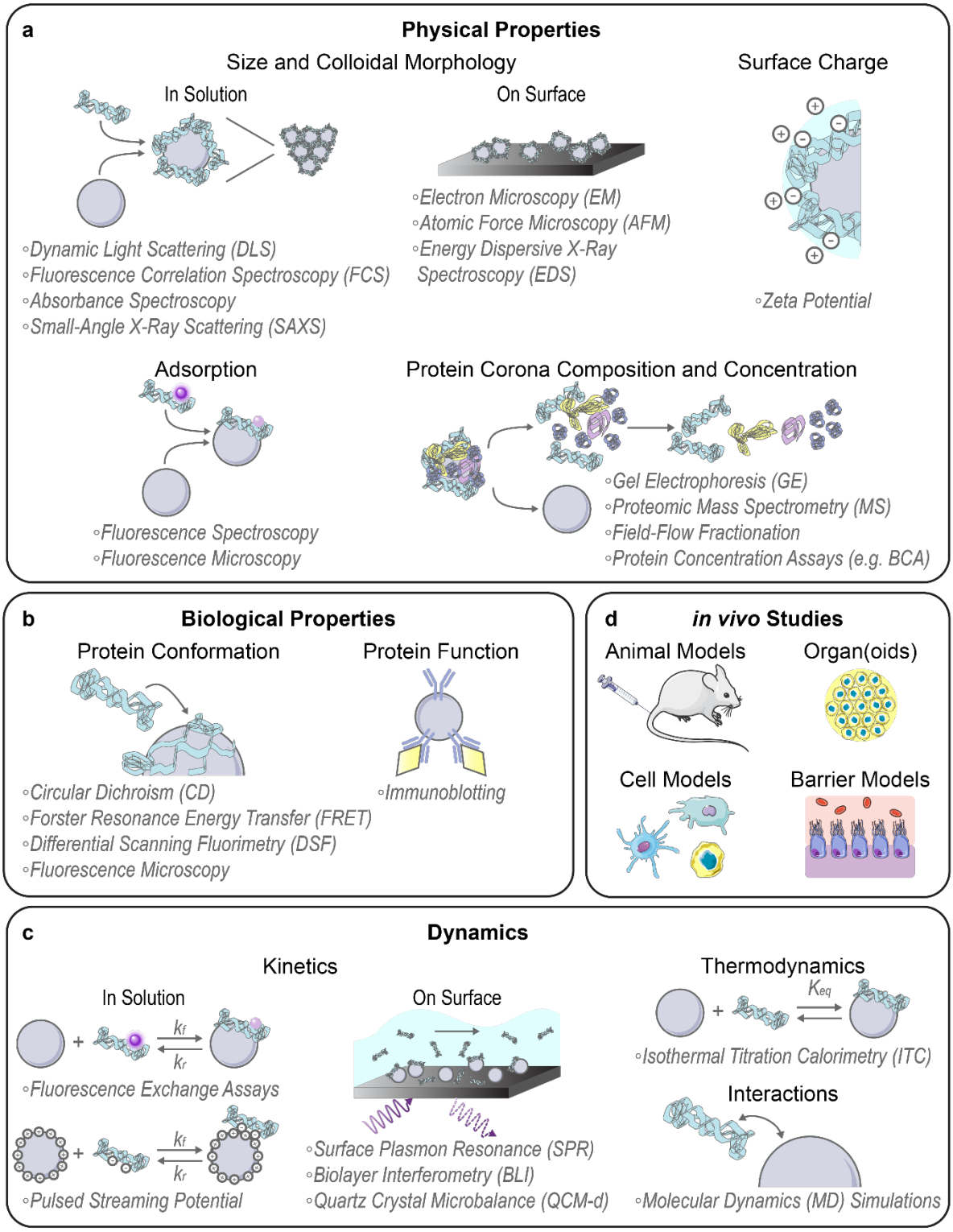

Figure 1-3. Modes of characterizing protein-nanoparticle complex formation and performance. (a) Physical properties include complex size and colloidal morphology (preferably characterized in solution over on surface), surface charge, corona adsorption, and corona composition and amount. (b) Biological properties include surface-adsorbed protein conformation and function.

(c) Dynamics include kinetics (preferably characterized in solution over on surface), thermodynamics, and interactions. (d) *in vivo* function can be assessed in model organisms, organs or organoids, cells, and cellular barriers.

1.5 Scope of Dissertation

This dissertation contains seven chapters, in addition to this introduction and concluding remarks at the end. Each chapter maintains the central theme of understanding and harnessing nano-bio interactions, from various perspectives and for various means. The following discussion serves to provide transitions between the dissertation sections.

Chapter 2 presents a fundamental understanding of the protein corona composition, driving forces, dynamics, and morphology on carbon nanotube-based nanosensors. The aim was to answer three crucial questions: *(i) what proteins coat a nanoparticle upon exposure to a biological system, (ii) how does this binding process occur, and (iii) why are these particular proteins adsorbing to the nanoparticle?* Existing studies correlating nanoparticle properties to corona formation mainly describe systems of spherical model nanoparticles in blood plasma and solely answer the question of *what* is coating the nanoparticles without rigorously delving into the underlying mechanistic *how* and *why*. This study primarily focuses on protein interactions with the SWCNT-based probes that our lab develops, however, the experimental platform and framework of analysis are generalizable to various nanoparticles in different biological environments. The model system of polystyrene nanoparticles in blood plasma is used as a means of platform validation, however, the study is an impactful addition to the body of protein corona literature due to the quantitative nature of the study, resultant analysis, and application to a new nanoparticle system (DNA-functionalized SWCNTs) in an understudied biofluid (cerebrospinal fluid of the brain).

Chapter 3 elaborates on the study of protein corona formation dynamics. We develop an assay to measure the dynamic exchange of the biomolecular corona on SWCNTs in solution, in real-time. This corona exchange assay overcomes limitations of pre-existing techniques, namely, (i) the need for nanoparticle immobilization to apply conventional surface-analysis techniques and (ii) the lack of tracking both biomolecular entities involved in the surface exchange. Initial assay development and validation is focused on monitoring the exchange of ssDNA initially on the SWCNT surface upon addition of proteins in the surrounding bulk biofluid. This chapter provides insight into assay development, application in a case study of two length ssDNA sequences, development of a simple kinetic model description of the ssDNA/protein exchange process on the SWCNT surface, and the extension to exchange between various biomolecules such as phospholipids and peptoids.

Chapter 4 expounds on the interactions driving protein corona formation on nanoparticles by adopting a physics-based modeling approach. We use colloid theory to mathematically model the thermodynamic potential of mean force between different proteins in solution and nanoparticles of varying geometry. Solvation, dispersion, and electrostatic forces describe these interactions from which the total potential of mean force is calculated. Although assumptions are required to simplify the binding partners, this theoretical description gives insight into important interactions governing how the protein and nanoparticle first “see” each other in solution as they come in closer proximity.

Chapter 5 continues this analysis toward protein corona formation driving forces on ssDNA-SWCNTs, providing an extension of the linear regression analysis pursued in Chapter 2 to further evaluate the various physicochemical protein properties driving adsorption. Protein corona compositional data is derived from Chapter 2 and analyzed by various supervised learning models, from which a random forest classification scheme is ultimately adopted. This study provides insight into protein characteristics that are heavily implicated in corona formation. Additionally, the classifier is used to predict new proteins expected to display intrinsic adsorptive interactions with the SWCNT surface, as this will be useful in rational nanosensor design (detailed further in Chapter 8). "Hit" proteins determined by this developed classifier are experimentally validated by applying the corona exchange assay detailed in Chapter 3.

Chapter 6 serves as a departure from the focus of prior chapters on protein/ssDNA-SWCNT interactions. The dissertation theme of how biomolecules modulate the inherent characteristics of nanoparticles is continued, as the graphene substrate geometry is expanded from the quasi-one-dimensional carbon nanotube to the two-dimensional graphene quantum dot (GQD). Initial project goals involved the intended development and application of a GQD-based nanosensor platform. However, this in the end became a more fundamental study due to limitations of this graphene substrate as a nanosensor, namely, fluorescence in the UV-low-visible range, instability in salt conditions, and lack of response to screened libraries of biologically relevant small molecule analytes. The study describes the complexation of various types of GQDs with biomolecules (mainly ssDNA of varying sequence and length), with experimental validation and complementary molecular dynamics simulations to provide insight on these nano-bio interactions.

Chapter 7 provides a transition to consider a corona-based design approach. Although formation of the nanoparticle-corona complex can pose an obstacle toward effectively deploying nanotechnologies (as explored in many of the preceding chapters), corona formation presents a unique opportunity as a functional handle to tune and enhance auxiliary nanoparticle properties. The review of recent literature presented in this chapter is mainly within the context of nanoparticle-based delivery applications, as this constitutes the majority of prior work. However, the following chapter applies this similar idea toward a nanoparticle-based sensing application.

Finally, Chapter 8 applies this idea of rational, corona-mediated nanoparticle design in the development of a rapid SARS-CoV-2 nanosensor. Leveraging the insight gained from the fundamental study of protein-nanotube interactions, a hybrid nano-bio construct is designed and created, exploiting the natural recognition ability of a cell membrane receptor protein (ACE2) for the SARS-CoV-2 spike protein protruding from the virion surface. ACE2 as the molecular recognition domain is tethered to SWCNTs that serve as the signal transducing elements, providing an optical readout upon SARS-CoV-2 spike protein binding. This study presents a proof-of-concept nanosensor construct, with promising initial results regarding nanosensor selectivity and function in complex patient samples, such as saliva, upon nanosensor passivation to mitigate unfavorable biofouling. Moreover, the experimental framework of probing the mechanisms of protein-nanotube interactions developed in the preceding chapters is applied to guide nanosensor synthesis and validation. This study opens doors to label-free protein detection, and specifically for viral sensing, with the ultimate intention of being incorporated into an accessible, point-of-care format and to function in minimally processed patient biofluids.

2 Quantitative Protein Corona Composition, Driving Forces, and Dynamics on Carbon Nanotubes in Biological Environments

2.1 Chapter Abstract

When nanoparticles enter biological environments, proteins adsorb to form the "protein corona" which alters nanoparticle biodistribution and toxicity. Herein, we measure protein corona formation on DNA-functionalized single-walled carbon nanotubes (ssDNA-SWCNTs), a nanoparticle used widely for sensing and delivery, in blood plasma and cerebrospinal fluid. We characterize corona composition by mass spectrometry, revealing high-abundance corona proteins involved in lipid binding, complement activation, and coagulation. We investigate roles of electrostatic and entropic interactions driving selective corona formation. Lastly, we study real-time protein binding on ssDNA-SWCNTs, obtaining agreement between enriched proteins binding strongly and depleted proteins binding marginally, while highlighting cooperative adsorption mechanisms. Knowledge of protein corona composition, formation mechanisms, and dynamics informs nanoparticle translation from *in vitro* design to *in vivo* application.‡

2.2 Introduction

Engineered nanoparticles are prominently used for sensing and imaging applications in biological systems due to their distinctive optical and physical properties.[10,16] A key challenge with these nanoscale tools is understanding the mechanisms of interaction between the nanoprobe and the biological system they are designed to query.[45,46] As detailed in the Introduction (section 1), an incomplete understanding of protein corona formation remains as a paramount barrier to successfully implementing nanotechnologies within biological environments.

Although many studies classify protein corona composition around specific nanoparticle systems, significant debate persists as to which protein and nanoparticle characteristics are most important in determining corona composition, and how different biological environments contribute to compositional and temporal corona heterogeneity.[46,169] While prior studies clarify different aspects of bio-corona formation, system constraints such as surface-immobilization or treating the protein corona as existing at thermodynamic equilibrium make it difficult to reliably translate results to real biofluid systems.[45,158,159] Additionally, many nanosensor technologies are tested for biofouling and biocompatibility in blood serum, a blood-based fluid rich in albumin, the most abundant blood plasma protein, and devoid of blood clotting proteins. The assumptions that serum is a representative biofluid for confirming *in vivo* function and that protein abundance in a native biofluid determines its relative abundance in a nanoparticle corona both stand to be refined.

Understanding protein corona formation is essential to design nanoparticles that are robust and stable in biological environments. Our work focuses on single-walled carbon nanotubes

---

‡ Published as Pinals, R. L.; Yang, D.; Rosenberg, D. J.; Chaudhary, T.; Crothers, A. R.; Iavarone, A. T.; Hammel, M.; Landry, M. P. Quantitative Protein Corona Composition and Dynamics on Carbon Nanotubes in Biological Environments. *Angewandte Chemie International Edition* **2020**, *59* (52), 23668–23677. https://doi.org/10.1002/anie.202008175.

(SWCNTs), a nanoparticle class that possesses unique optical and physical properties ideal for biological imaging, molecular sensing, and delivery applications.[10,32,41,170] To apply hydrophobic SWCNTs in aqueous biological systems, noncovalent functionalization with amphiphilic polymers imparts water solubility to the SWCNT, while retaining the near-infrared-emissive electronic structure.[32] Select polymers confer molecular recognition functionality when adsorbed to the SWCNT surface, such as single-stranded DNA (ssDNA). Specifically, ssDNA sequences $(GT)_6$ or $(GT)_{15}$ adsorbed to SWCNTs are implemented to image the neurotransmitter dopamine in the brain at spatiotemporal scales of relevance to endogenous neuromodulation.[40–42] ssDNA-functionalized SWCNTs have further been applied in intravenous *in vivo* scenarios, to monitor endolysosomal lipid accumulation[171] and nitric oxide production.[172] To design and apply these and other SWCNT-based nanotechnologies in biological systems, it is crucial to understand the composition, dynamics, and dominant mechanisms of protein corona formation.

Herein, we explore protein corona formation probed with a selective adsorption assay generalizable to different types of nanoparticles and biofluids. We focus on two nanoparticles: a model system of commonly studied polystyrene nanoparticles (PNPs)[47,56,58,159,173] and a newer system of noncovalently functionalized SWCNTs. Protein adsorption on these nanoparticles is assessed in two biofluids: blood plasma, a standard biofluid relevant for blood circulation applications, and cerebrospinal fluid (CSF), an understudied biofluid relevant for central nervous system studies. An understanding of the corona formed on SWCNTs in CSF has not been investigated and is imperative for developing SWCNT-based applications in the brain, including mapping of the brain extracellular space[174] and vasculature,[175] neurotransmitter imaging,[41,176] and delivery to the brain.[170] Corona composition characterized by quantitative, label-free mass spectrometry analysis reveals key protein corona contributors and isolation of protein factors governing corona formation. We identify interactions driving protein adsorption, where hydrophobic interactions dominate formation of the inner corona, while electrostatic interactions govern formation of the outer corona. To quantify the time-dependent protein corona formation process, we assess binding thermodynamics and kinetics by measuring adsorption of key proteins to $(GT)_{15}$-SWCNTs via isothermal titration calorimetry (ITC) and a corona exchange assay.[118] Finally, the protein-SWCNT complex structure is ascertained by small-angle x-ray scattering (SAXS), demonstrating changing mass fractal morphology of ssDNA-SWCNTs in the presence of a high-binding protein (fibrinogen) otherwise absent with the low-binding protein (albumin). Overall, we present a holistic experimental approach and analysis methodology to understand the complexities of protein corona formation, and apply this framework to examine an understudied system of interest: SWCNT-based probes in the brain.

2.3 Results and Discussion

2.3.1 Protein Corona Composition

Protein corona composition was studied on $(GT)_{15}$-functionalized SWCNTs (see synthesis in section 2.5.1; average 1 nm diameter, 500 nm length) and PNPs (100 nm diameter) in blood plasma (normal human, pooled donors; Innovative Research Inc.) and cerebrospinal fluid (CSF; normal human, pooled donors; Lee Biosolutions). Selective adsorption of proteins onto nanoparticles was evaluated by (i) incubating nanoparticles with biofluid for 1 h, (ii) isolating protein-nanoparticle complexes by centrifugation, (iii) removing unbound proteins by washing, (iv) eluting bound proteins from nanoparticles with surfactant and reducing agent, and (v) characterizing proteins by

two-dimensional polyacrylamide gel electrophoretic separation (2D PAGE) or liquid chromatography-tandem mass spectrometry (LC-MS/MS) (Figure 2-7; see methods in section 2.5.5).[58] Following workflow validation (Figure 2-7 and Figure 2-8), protein coronas were studied on these two distinct nanoparticle surfaces (PNPs and $(GT)_{15}$-SWCNTs) in two biofluids (plasma and CSF). PAGE analysis confirmed that proteins showed selective enrichment or depletion fingerprints on nanoparticles (Figure 2-9). More in-depth protein corona composition studies were subsequently undertaken by performing in-solution trypsin digestion of proteins eluted from nanoparticles, followed by protein characterization with label-free, quantitative LC-MS/MS. Analysis by LC-MS/MS provides (i) molar corona protein abundances via comparison to an internal standard and (ii) enrichment or depletion in each nanoparticle corona, relative to protein concentrations in the native biofluid (see details in section 2.5.6). Protein abundances, fold changes, and functional classes for protein coronas formed on PNPs and $(GT)_{15}$-SWCNTs are represented graphically in Figure 2-1 (plasma) and Figure 2-2 (CSF) (full protein lists in Figure 2-10 and Figure 2-11). The twenty most abundant proteins in the nanoparticle coronas are summarized in Table 2-1(plasma) and Table 2-2 (CSF).

2.3.1.1 Blood Plasma Protein Corona Composition

Our LC-MS/MS analysis highlights the significant enrichment vs. depletion of specific plasma proteins in the nanoparticle coronas (Figure 2-1). First, plasma proteins identified in the PNP corona are corroborated by previous literature.[56,58] Of note for $(GT)_{15}$-SWCNTs, serum albumin is the most abundant protein in plasma (55% w/v in plasma), yet does not appreciably adsorb: albumin is in low abundance and significantly depleted in the corona, with a 1300-fold lower bound concentration relative to native plasma. Broadly, corona proteins on PNPs are more diverse in functional classes than corona proteins on $(GT)_{15}$-SWCNTs, representing a range of endogenous functions including adaptive immune response and transport, for which proteins are largely absent on $(GT)_{15}$-SWCNTs. We quantify these protein functional roles implicated in corona formation by regressing ln-fold change against protein class using effect-coding while controlling for sample-to-sample variability (Figure 2-12 and Figure 2-13). The dissimilarities from this analysis highlight the less selective association of proteins to PNPs in comparison to $(GT)_{15}$-SWCNTs, where this ability of $(GT)_{15}$-SWCNTs to resist nonspecific protein biofouling is promising toward SWCNT-based biotechnology applications.

In particular, plasma proteins enhanced on $(GT)_{15}$-SWCNTs are involved in (i) lipid binding/transport (150%-fold change over the average of all protein classes) and (ii) complement activation (140%-fold change). These LC-MS/MS results suggest that, due to corona formation, $(GT)_{15}$-SWCNTs will have reduced non-specific cellular uptake (high clusterin adsorption[173]), prolonged circulation in blood (overall high apolipoprotein adsorption[47]), and minimal activation of the adaptive immune response (low immunoglobulin representation) compared to other nanoparticles (i.e. PNPs). Detrimental responses, however, may include activating the innate immune response (high complement C3 and other complement protein adsorption[177,178]) and eliciting inflammatory responses (high fibrinogen adsorption[47,50,158]) (see extended discussion in section 2.6.2).

We further compared the plasma corona formed on $(GT)_{15}$-SWCNTs to that on $(GT)_6$-SWCNTs, where the adsorbed ssDNA differs in length (30 vs. 12 nucleotides) and morphology (helical vs. ring wrapping).[42] Plasma proteins identified in the $(GT)_6$-SWCNT corona approximately match

those in the $(GT)_{15}$-SWCNT corona (Figure 2-10 and Table 2-5), and the analogous regression of protein functional classes suggests that the SWCNT surface, rather than the initial ssDNA corona, determines protein adsorption selectivity (Figure 2-12 and Figure 2-14). Surface passivation with ssDNA does, however, lead to distinct results compared to prior protein corona characterization on pristine or carboxylated SWCNTs,[179,180] where adsorption of albumin and immunoglobulins is seemingly prohibited by an initial ssDNA corona.

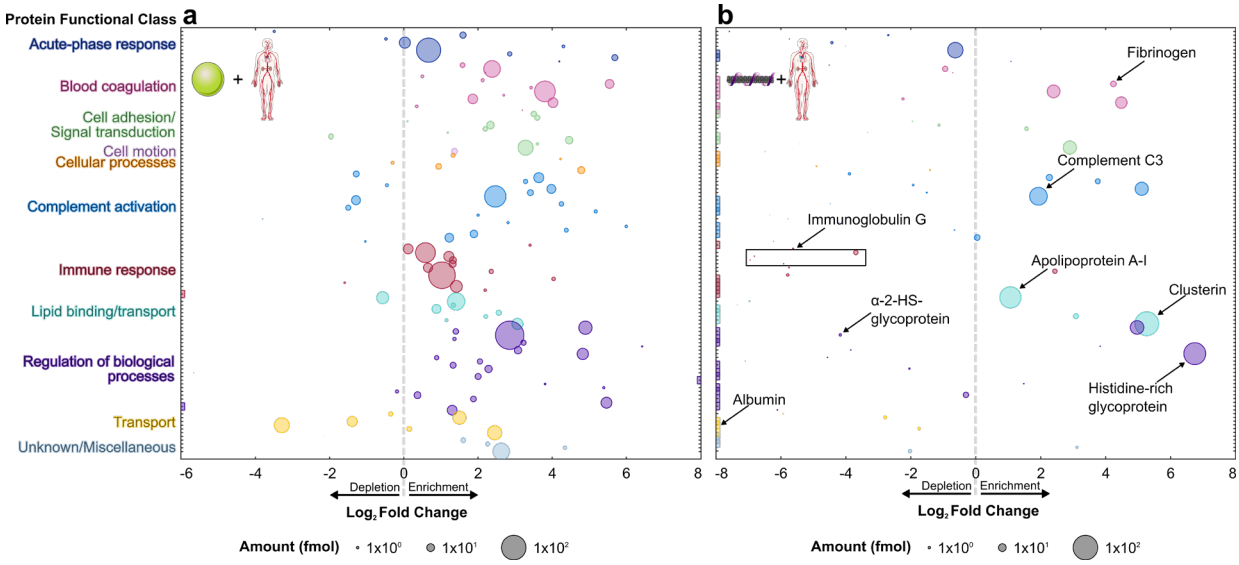

Figure 2-1. Blood plasma protein corona compositional map determined by proteomic mass spectrometry. Protein corona formed from blood plasma on (a) PNPs and (b) $(GT)_{15}$-SWCNTs. Full protein lists are available in SI (Figure 2-10). Circle size corresponds to protein abundance (femtomolar). Proteins are grouped by functional class according to color (PANTHER).[41] Log_2 fold change is in comparison to the biofluid alone, for example, log_2 fold change of zero indicates the same relative amount of protein exists in the corona as in bulk solution of the native biofluid, while < 0 is depletion and > 0 is enrichment. Names are included for proteins of interest or proteins used for subsequent experiments. Colored boxes at x-axis limits indicate no protein detected in either corona ($x < 2^{-6}$ or 2^{-8}) or biofluid ($x > 2^{8}$). Data represent experimental triplicate for plasma with nanoparticles, technical triplicate for plasma alone.

Table 2-1. Top 20 most abundant proteins identified by proteomic mass spectrometry in plasma nanoparticle coronas.

	Plasma	PNPs in plasma	$(GT)_{15}$-SWCNTs in plasma
1	Serum albumin	Alpha-2-HS-glycoprotein	Clusterin
2	Haptoglobin	Ig kappa constant	Histidine-rich glycoprotein
3	Ig kappa constant	Haptoglobin	Apolipoprotein A-I
4	Ig heavy constant gamma	Complement C3	Complement C3
5	Serotransferrin	Kininogen-1	Haptoglobin
6	Apolipoprotein A-I	Ig heavy constant gamma 1	A disintegrin and metalloproteinase with thrombospondin motifs 12
7	Complement C4	Apolipoprotein A-II	Complement C1r subcomponent
8	Telomeric repeat-binding factor 2-interacting protein	tRNA-dihydrouridine(47) synthase [NAD(P)(+)]-like	Vitronectin
9	Alpha-1-antitrypsin	Beta-2-glycoprotein 1	Kininogen-1
10	Alpha-2-HS-glycoprotein	Vitronectin	Prothrombin
11	Apolipoprotein A-II	Serum albumin	C4b-binding protein alpha chain
12	Ig heavy constant alpha 1	Vitamin D-binding protein	Complement factor H
13	Integrin alpha-7	A disintegrin and metalloproteinase with thrombospondin motifs 12	Fibrinogen alpha chain
14	Alpha-2-macroglobulin	Hemopexin	Protein AMBP
15	Complement C3	Apolipoprotein A-I	Beta-2-glycoprotein 1
16	Complement C5	Ig lambda-like polypeptide 5	Apolipoprotein E
17	Hemopexin	Histidine-rich glycoprotein	Complement C1q subcomponent subunit B
18	Alpha-1-acid glycoprotein 1	Clusterin	Ig heavy constant gamma 1
19	Ig heavy constant mu	Alpha-1-antitrypsin	Ig J chain
20	Beta-2-glycoprotein 1	Serum paraoxonase/arylesterase 1	Galectin-3-binding protein

2.3.1.2 Cerebrospinal Fluid Protein Corona Composition

We repeated our assay and analysis to study protein corona formation from CSF on PNPs and $(GT)_{15}$-SWCNTs (Figure 2-2). Highly abundant proteins in the CSF corona formed on $(GT)_{15}$-SWCNTs include complement C3 as the most abundant (26-fold enriched relative to native CSF), clusterin as the 2nd most abundant (15-fold enriched), and histidine-rich glycoprotein as the 3rd most abundant (41-fold enriched). Again, serum albumin is remarkably absent, with over 2.5 million-fold lower bound concentration relative to native CSF. Notably, the reproducible outlier of galectin-3-binding protein (G3BP) emerges, which is the 4th most abundant and most strongly enriched (80-fold) protein on the $(GT)_{15}$-SWCNT surface. Identification of highly adsorbing and potentially interfering proteins could enable *a priori* design of future nanosensors to either promote selective or mitigate unfavorable protein adsorption.

LC-MS/MS analysis of the CSF-based protein corona revealed proteins across a range of functional classes for both nanoparticles (Figure 2-12). Protein classes that have higher than average fold change on $(GT)_{15}$-SWCNTs are coagulation proteins (441% higher fold change than

average), complement proteins (213% higher), and cell adhesion/signal transduction proteins (486% higher).

Many proteins have the same corona representation on $(GT)_{15}$-SWCNTs across plasma and CSF, including clusterin, histidine-rich glycoprotein, and complement C3. Conversely, certain proteins show distinctive behaviors in the $(GT)_{15}$-SWCNT corona formed from different biofluids, such as serotransferrin missing from the plasma corona and present in the CSF corona, despite serotransferrin's higher native concentration in plasma. These discrepancies point to mechanisms such as adsorption cooperativity and the Vroman effect,[158] whereby surface adsorption is dictated by relative affinities and abundances of all protein constituents in the bulk to determine the end-state corona. We also find that while plasma protein content in the corona vs. native biofluid is positively correlated for plasma proteins on PNPs ($R^2 = 0.461$), this scaling does not hold for either $(GT)_{15}$-SWCNTs ($R^2 = 0.101$) or $(GT)_6$-SWCNTs ($R^2 = 0.072$) in either biofluid (Figure 2-16). This again suggests complex mechanisms driving selective corona adsorption on SWCNTs and, depending on the biofluid, also PNPs.

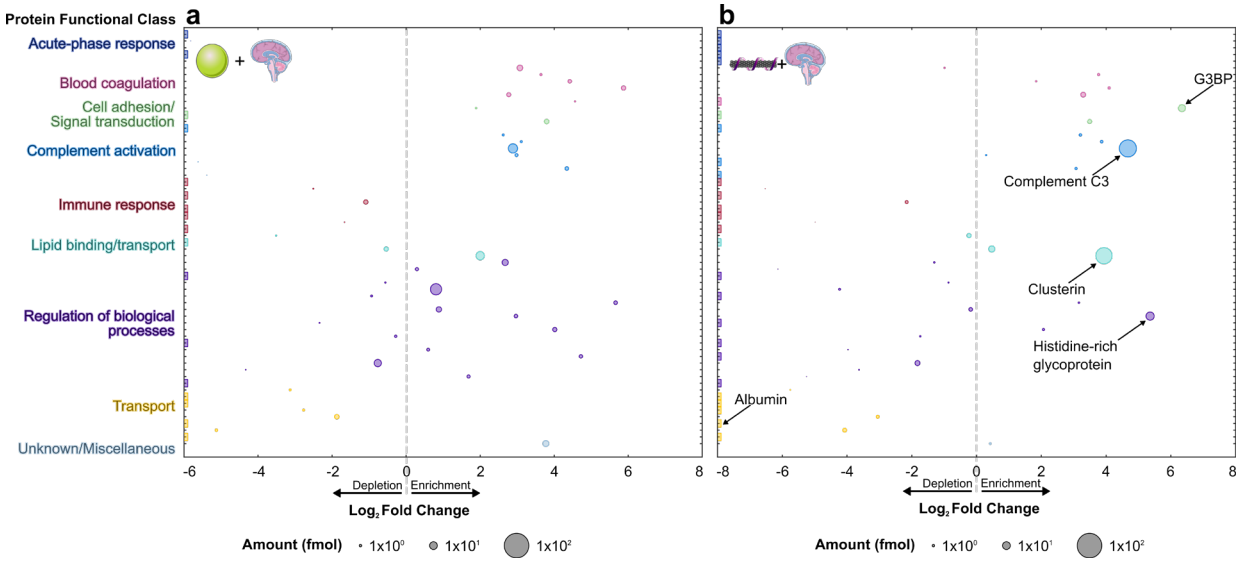

Figure 2-2. Cerebrospinal fluid (CSF) protein corona compositional map determined by proteomic mass spectrometry. Protein corona formed from CSF on (a) PNPs and (b) $(GT)_{15}$-SWCNTs. Full protein lists are available in SI (Figure 2-11). Circle size corresponds to protein abundance (femtomolar). Proteins are grouped by functional class according to color (PANTHER).[41] Log_2 fold change is in comparison to the biofluid alone, for example, fold change of zero indicates the same relative amount of protein exists in the corona as in bulk solution of the native biofluid, while < 0 is depletion and > 0 is enrichment. Names are included for proteins of interest or proteins used for subsequent experiments. Colored boxes at x-axis limits indicate no protein detected in either corona ($x < 2^{-6}$ or 2^{-8}) or biofluid ($x > 2^8$). Data represent technical triplicate for CSF with and without nanoparticles.

Table 2-2. Top 20 most abundant proteins identified by proteomic mass spectrometry in CSF nanoparticle coronas.

	CSF	PNPs in CSF	$(GT)_{15}$-SWCNTs in CSF
1	Serum albumin	Cystatin-C	Complement C3
2	Transthyretin	Complement C3	Clusterin
3	Alpha-1-antitrypsin	Clusterin	Histidine-rich glycoprotein
4	Prostaglandin-H2 D-isomerase	Prostaglandin-H2 D-isomerase	Galectin-3-binding protein
5	Serotransferrin	Alpha-2-HS-glycoprotein	Apolipoprotein E
6	Cystatin-C	Collagen alpha-2(XI) chain	Prostaglandin-H2 D-isomerase
7	Alpha-1-acid glycoprotein 1	Beta-2-glycoprotein 1	Kininogen-1
8	Hemoglobin subunit alpha	Gelsolin	Apolipoprotein A-I
9	Ig heavy constant gamma 1	Serotransferrin	Vitronectin
10	Vitamin D-binding protein	Vitronectin	Transthyretin
11	Ceruloplasmin	Ig heavy constant gamma 1	Gelsolin
12	Hemopexin	Apolipoprotein E	Ig heavy constant gamma 1
13	Apolipoprotein E	Fibulin-1	Serotransferrin
14	Ig kappa constant	Major prion protein	Complement C1s subcomponent
15	Apolipoprotein A-I	Kininogen-1	Complement C1q subcomponent subunit B
16	Hemoglobin subunit beta	EGF-containing fibulin-like extracellular matrix protein 1	Fibulin-1
17	Haptoglobin	Complement factor H	Complement factor H
18	Clusterin	Histidine-rich glycoprotein	Major prion protein
19	Suppression of tumorigenicity 18 protein	Fibrinogen beta chain	Fibrinogen alpha chain
20	Gelsolin	ProSAAS	Cystatin-C

2.3.2 Protein Corona Formation Mechanisms

2.3.2.1 Molecular Phenomena Involved in Protein Corona Formation

To evaluate the nanoscale mechanisms involved in corona formation, we linearly regressed the ln-fold change against physicochemical protein properties including mass, post-translational modification frequency, binding site frequency, and amino acid percent compositions (Figure 2-3 and Figure 2-15; see section 2.5.7).[72,181] Statistically, the calculated regression coefficients quantify the fractional difference of the fold change for a protein with a unit increase of the independent variable, holding all other independent variables constant. Thermodynamically, the regression coefficients quantify the free energy change of a protein adsorbing into the corona per unit of the independent variable in units of k_bT (see derivation in section 2.6.3). Proteins often denature upon surface adsorption, exposing otherwise solvent-inaccessible residues.[158,161,180,182,183] Accordingly, we include all amino acid groups in the regression analysis rather than only solvent-exposed groups. Future work should isolate the roles residue accessibility and/or protein structure play on corona formation.

This regression analysis reveals that PNPs are generally agnostic to physicochemical properties of proteins entering the corona, except for a slight favorable interaction associated with the aromatic phenylalanine residue and unfavorable interaction with tyrosine. In contrast, the plasma corona formed on $(GT)_{15}$-SWCNTs is selective, showing unfavorable interactions with non-aromatic, hydrophobic amino acids (-0.53 k_bT/%hydrophobic), despite the extremely hydrophobic SWCNT surface. However, we find aromatic residues are enhanced in the $(GT)_{15}$-SWCNT plasma corona, namely phenylalanine (0.57 k_bT/%F), tyrosine (0.22 k_bT/%Y), and tryptophan (0.39 k_bT/%W). Regarding basic residues, lysine (and to a lesser extent, arginine) content is also associated with unfavorable interactions with $(GT)_{15}$-SWCNTs (-0.63 k_bT/%K), which is surprising in that positively charged proteins are expected to have favorable electrostatic interactions with the negatively charged, solvent-exposed phosphate backbone of ssDNA on the SWCNT. Moreover, more negatively charged, acidic residue content led to enhancement in the protein corona (0.31 k_bT/%acidic). This result indicates that protein charges are effectively screened by salt in solution and/or that proteins interact directly with the solvent-accessible SWCNT surface. The latter hypothesis is supported by the low initial ssDNA coverage on the SWCNT (~1-25%)[118,184,185] and the small fraction of ssDNA removed from the SWCNT during protein adsorption (~1-5%).[118] Direct protein interaction with the SWCNT surface could also explain the enhancement of aromatic residues, as they would favorably interact via π-π stacking directly with the graphitic SWCNT surface.

Apart from the favorable aromatic residue contribution, $(GT)_{15}$-SWCNTs have strikingly different interactions with proteins in CSF. In CSF, unlike in plasma, acidic residues are associated with unfavorable interactions with SWCNTs (-0.52 k_bT/%acidic), whereas positively charged arginine (and to a lesser extent, lysine) have favorable interactions (1.53 k_bT/%R). The tendency of ssDNA-SWCNTs in CSF to interact favorably with positively charged residues and unfavorably with negatively charged residues suggests that the negatively charged ssDNA wrapping is less screened electrostatically by other adsorbed proteins (seeing as net ionic strength in both biofluids is comparable), or that more ssDNA remains immobilized on the SWCNT surface following protein exposure in CSF than in plasma (as shown experimentally, Figure 2-17). In sum, these regression results emphasize the non-intuitive nature of corona formation, in that seemingly important properties for corona formation such as in-solution protein stability are not predictive of presence in a nanoparticle corona.

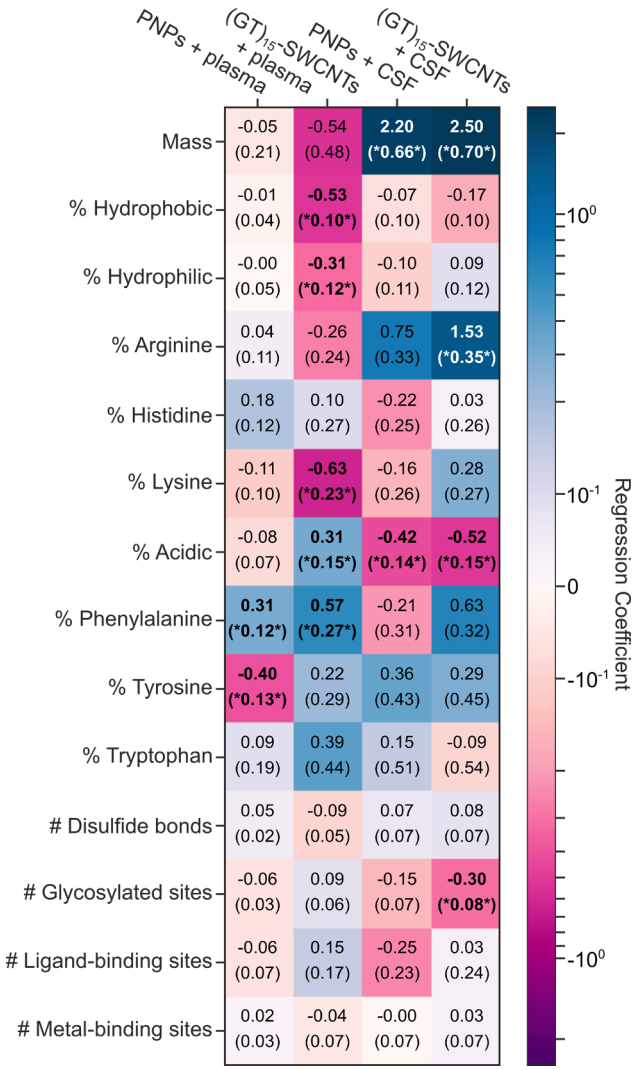

Figure 2-3. Molecular attributes of proteins that govern protein corona formation for each nanoparticle-biofluid pairing. Ln-fold change regression coefficients for molecular attributes of proteins (rows) for each nanoparticle-biofluid pairing (columns). Cells are colored from dark purple (negative effect on fold change) to white (no effect) to dark blue (positive effect). Standard errors of the coefficients are given in parenthesis. Results that have false-discovery-rate-corrected p-values below 0.1 are bolded and noted with asterisks. Amino acid groupings include: non-aromatic hydrophobic (sum of alanine, valine, isoleucine, leucine, and methionine content), hydrophilic (sum of serine, threonine, asparagine, and glutamine content), and acidic (sum of aspartic acid and glutamic acid content).

2.3.2.2 Driving Forces of Protein Corona Formation

To gain further insight on interactions driving protein adsorption to nanoparticles, incubation conditions of $(GT)_{15}$-SWCNTs exposed to plasma were varied and corona proteins were characterized by 2D PAGE. Specifically, conditions varied include dynamics (to probe corona stability), ionic strength (to probe electrostatic interactions), and temperature (to probe entropic contributions) (Figure 2-4). Under dynamic protein-nanoparticle incubation, proteins in the outer

adsorbed plane undergo shear and are removed. Remaining proteins are postulated to represent the inner, more tightly bound "hard" corona proteins that interact more strongly with the nanoparticle surface, while removed proteins represent the outer, more loosely bound "soft" corona proteins that interact with other adsorbed proteins. We note that in both cases, the proteins are co-precipitated with the nanoparticles for characterization. For $(GT)_{15}$-SWCNTs, apolipoproteins A-I, clusterin, complement C3, fibrinogen, and alpha-1-antitrypsin compose the hard corona, while some soft corona proteins of interest include albumin and haptoglobin. Elimination of salt during incubation increases the role of repulsive electrostatic forces by removing ionic charge screening. This absence of charge screening means that proteins and nanoparticles do not approach as closely in solution and that lateral electrostatic interactions of surface-adsorbed proteins increase, both of which result in less protein adsorption.[186] For $(GT)_{15}$-SWCNTs, the three hard-corona proteins (apolipoprotein A-I, complement C3, and fibrinogen) still enter the corona despite the lack of charge shielding. This result points to the role of non-electrostatic forces facilitating formation of the hard corona, likely hydrophobic interactions, that drive protein-SWCNT adsorption even under electrostatically adverse conditions of electric double-layer repulsion (as supported by zeta potential measurements of nanoparticles and plasma proteins, separately, Figure 2-8). In addition, most soft corona proteins are missing in the no salt incubation, underscoring the need for charge-screening for soft corona formation. Finally, higher temperature incubation increases weighting of the entropic contribution to the overall free energy change of protein binding. Entropic contributions originate from the solvent (positive, as hydration shells of the protein and surface are released to bulk) and protein (negative, from the adsorbate losing degrees of freedom and potentially positive if proteins unfold upon adsorption).[187] At physiological temperature, hard-corona proteins are still able to adsorb to $(GT)_{15}$-SWCNTs, indicating that adsorption of these proteins is entropically favorable and/or enthalpically driven. Enthalpic contributions arise from noncovalent interactions between proteins and the SWCNT surface, and hydrogen bond formation within the bulk solvent as proteins leave solution to enter the adsorbed state. Thus, hard-corona proteins undergo high affinity binding to $(GT)_{15}$-SWCNTs despite dynamic perturbation, low ionic strength, and increased temperature incubation conditions.

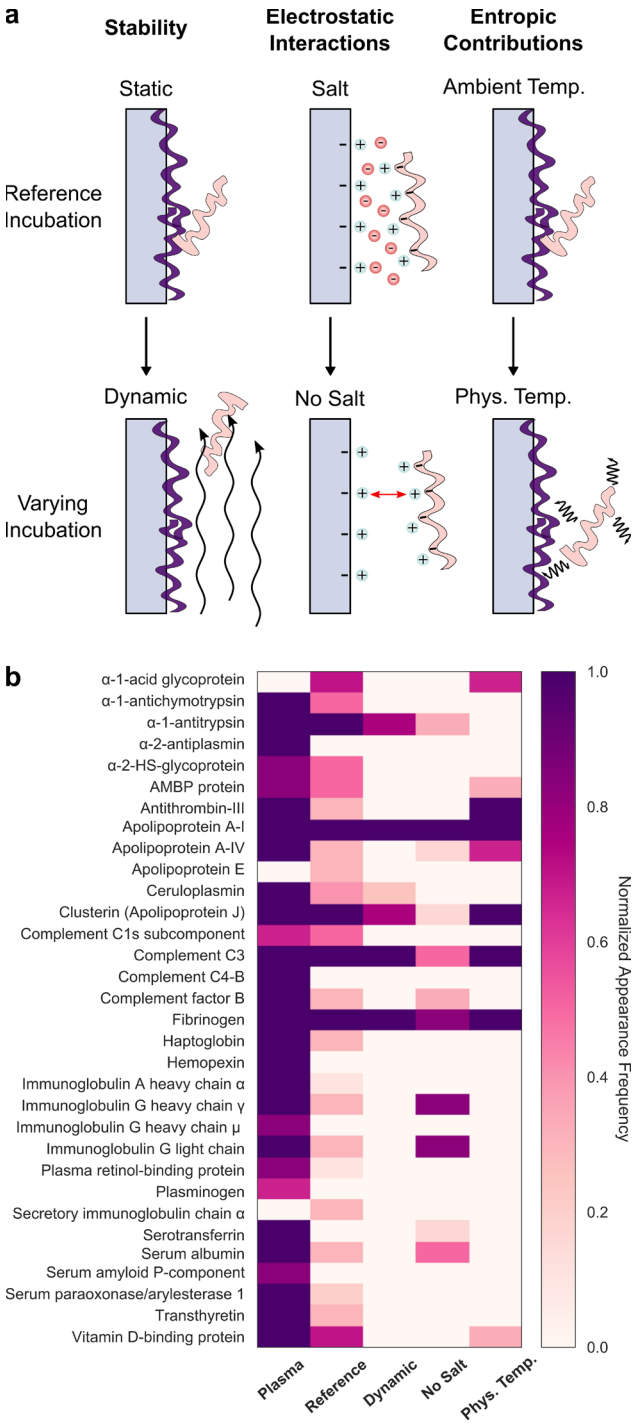

Figure 2-4. Effect of varying incubation parameters to probe corona stability, electrostatic interactions, and entropic contributions to corona formation of plasma proteins on $(GT)_{15}$-SWCNTs. (a) Schematics depicting incubation conditions affecting corona adsorption, with reference conditions (top) vs. varied conditions (bottom). (b) Proteins present in native plasma (left-most column) as compared to the plasma corona formed on $(GT)_{15}$-SWCNTs under reference conditions (static, phosphate-buffered saline, and 25°C incubation) and varying incubation conditions, including dynamic (on orbital shaker; to probe corona stability), no salt

(water; to probe ionic effects), and temperature (37°C; to probe entropic contributions). Color indicates normalized appearance frequency of protein in corona characterized by 2D PAGE (N ≥ 3 experimental replicates; see details in section 2.5.8).

2.3.3 Protein Corona Dynamics

Beyond probing corona composition at the end point of adsorption, we investigated corona formation dynamics to understand the time-dependent process and overall system energetics driving corona formation. Toward this end, isothermal titration calorimetry (ITC) was applied to probe the thermodynamics of protein adsorption to SWCNT surfaces.[48,67,188] We studied binding of $(GT)_{15}$-SWCNTs with two proteins identified by LC-MS/MS with opposite binding affinities: albumin, selected as a model low-binding protein, and fibrinogen, a model high-binding protein. ITC results confirm that fibrinogen preferentially adsorbs to $(GT)_{15}$-SWCNTs and albumin does not, as evidenced by the binding curve in the former and absence of changing heats upon injection in the latter (Figure 2-18). From the ITC binding curve of fibrinogen with $(GT)_{15}$-SWCNTs, the change in enthalpy is -565.2 kJ/mol and the change in entropy is -1.756 kJ/K-mol. This favorable enthalpic term outweighs the net unfavorable entropic terms to ultimately drive formation as a spontaneous, energetically favorable process: the net change in free energy is -41.91 kJ/mol. However, these ITC results must be interpreted with the consideration that the equilibrium requirement for this thermodynamic analysis is not rigorously held (see extended discussion in section 2.6.4).[45,158,159] This binding profile shape for protein-surface adsorption processes often emerges as a result of adsorption-induced protein spreading/denaturation, reorientation, and aggregation as functions of bulk protein concentration, in contrast to originating from the dynamic equilibrium between the fluid and surface-adsorbed phases required for Langmuirian adsorption.[161,182,183,189] Thus, although these binding curves confirm compositional findings of the relative binding affinities, it should be noted that ITC is not a suitable methodology to study all nanoparticle-protein systems and these limitations must be reflected in interpreting these energetics as overall changes in system energies, rather than a true deconvolution of protein-nanoparticle binding interactions.

We next implemented a real-time kinetic binding assay to study dynamic protein interactions with SWCNTs.[118] Briefly, multiplexed fluorescence enables tracking each entity involved in the corona formation process, with cyanine 5 (Cy5)-tagged ssDNA originally on the SWCNT surface exchanging with protein added to solution. We implemented this platform to track the binding of key plasma corona proteins to $(GT)_{15}$-SWCNTs and $(GT)_6$-SWCNTs (Figure 2-5a-b), with desorption of Cy5-tagged ssDNA originally on the SWCNT measured as an increase in Cy5 fluorescence and used as a proxy for protein adsorption to SWCNT. Specifically, we assayed the protein panel: clusterin, apolipoprotein A-I, fibrinogen, and complement C3, which are predicted to adsorb in high abundance to $(GT)_{15}$-SWCNTs, and alpha-2-HS glycoprotein, immunoglobulin G, and albumin, which are predicted to adsorb less to $(GT)_{15}$-SWCNTs based on LC-MS/MS compositional analysis (see expected ordering in Table 2-1). Interestingly, the order of protein adsorption from this corona exchange assay was: fibrinogen > apolipoprotein A-I > alpha-2-HS glycoprotein > immunoglobulin G ≈ clusterin > complement C3 > albumin (Figure 2-5a). While this result affirms the high affinity of fibrinogen and apolipoprotein A-I vs. low affinity of albumin to $(GT)_{15}$-SWCNTs, some of the single-protein end states do not match the relative ordering of protein abundances from the full-biofluid LC-MS/MS experiments. Accordingly, higher order

interactions such as the Vroman effect are further supported in affecting protein adsorption in the full-biofluid experiments, absent in the single-protein experiments. Moreover, these time-dependent dynamics reveal that the rates of protein binding are distinct among proteins, even though some converge to the same final value (such as alpha-2-HS glycoprotein and clusterin). A comparison of this same protein panel binding to $(GT)_6$-SWCNTs is provided because the shorter ssDNA strand is displaced more readily, offering a greater spread between protein species (Figure 2-5b; see expected ordering in Table 2-5). The dynamics of protein adsorption recapitulate similar high- vs. low-binding propensities, yet, complement C3 and clusterin again display significantly less adsorption than expected based on LC-MS/MS results, signifying that these proteins enter the corona with cooperative binding mechanisms (e.g. C3 binding to other surface-adsorbed proteins[190]) rather than by high binding affinity to the SWCNT surface on their own. To build a physical picture of protein-SWCNT association, we next expand to structural studies of these protein-nanoparticle complexes.

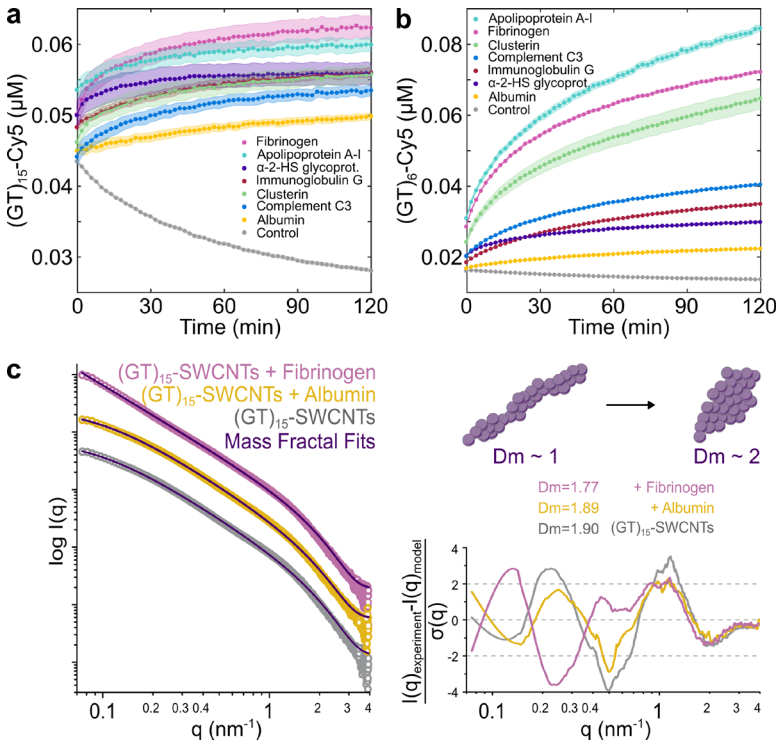

Figure 2-5. Protein corona dynamics and structure assessed for binding of key proteins to ssDNA-SWCNTs. A corona exchange assay is employed to determine binding kinetics of a protein panel (each at 80 mg L^{-1} final concentration) to (a) $(GT)_{15}$-SWCNTs and (b) $(GT)_6$-SWCNTs (each at 5 mg L^{-1} final concentration). Shaded error bars indicate standard error between experimental replicates (N = 3). Small-angle x-ray scattering (SAXS) is applied to gain in-solution structural information of albumin vs. fibrinogen adsorption on $(GT)_{15}$-SWCNTs. (c) Experimental SAXS profiles for 0.5 g L^{-1} $(GT)_{15}$-SWCNTs with and without albumin or fibrinogen, each at 0.5 g L^{-1} final concentrations. Mass fractal model fits are included in purple together with fit residuals on the right. The accompanying illustration depicts the mass fractal dimension *Dm* increasing from approximately 1 (rod-like) to 2 (disk-like), with the fit *Dm* values for $(GT)_{15}$-SWCNTs in the presence and absence of proteins.

2.3.4 Protein Corona Morphology

To evaluate in-solution structural changes of the $(GT)_{15}$-SWCNTs due to protein corona formation, small-angle X-ray scattering (SAXS) was performed with two proteins, albumin and fibrinogen, as low-binding and high-binding proteins, respectively. SAXS results confirm formation of unique form factors and thus complexation for $(GT)_{15}$-SWCNTs with fibrinogen, absent for the case of albumin (Figure 2-5c), therefore recapitulating corona compositional findings.

The intrinsically disordered experimental SAXS profiles were fit using mass fractal geometries, complemented by power-law dependencies from the Porod region, as detailed in SI (Figure 2-5c, Figure 2-19, and Table 2-8).[191–193] The mass fractal radii (all R~1 nm), traditionally defined as the radius of the uniform sphere used to cover the fractal, suggest that the overall topology of the $(GT)_{15}$-SWCNTs remains constant with and without protein. The fractal dimension Dm and analogous power-law exponent p, found to be in close agreement, estimate the bulk geometries of the mass fractals, where the integer value represents the three dimensions in Euclidean space such that values of 1, 2, and 3 represent rod, disk, and sphere geometries, respectively. The decrease in fractal dimension from Dm~1.90 for $(GT)_{15}$-SWCNTs with or without albumin to Dm=1.77 for $(GT)_{15}$-SWCNTs with fibrinogen reveals an initial disk-like mass fractal geometry, then elongation to gain rod-like character in the presence of fibrinogen (Figure 2-5c). This is consistent with previous literature in which fibrinogen binds to SWCNTs in a lengthwise manner.[39,180] Furthermore, the decrease of $(GT)_{15}$-SWCNT Dm in the presence of fibrinogen signifies increasing attractive forces between the molecular entities and consequent colloidal instability.[194] Finally, the cutoff length ζ, or the maximum distance between any two points of the mass fractal, undergoes a ten-fold increase for $(GT)_{15}$-SWCNTs with fibrinogen, denoting a drastic increase in the aggregate size. Thus, SAXS confirms fibrinogen complexation with $(GT)_{15}$-SWCNTs, suggests a side-on orientation (as reiterated by TEM, Figure 2-20), and enables quantification of the changing fractal structure, pointing to the role of multilayer adsorption mechanisms and aggregate formation.

2.4 Conclusions

As engineered nanoparticles are increasingly implemented as tools to study and alter biosystems, it is crucial to develop an understanding of how these nanoparticles interact with their biological surroundings. Accordingly, we have conducted a multimodal study to characterize protein corona formation in a biologically representative in-solution state. We focus on applying $(GT)_{15}$-SWCNTs in the brain microenvironment, although the framework itself is generic to study protein corona composition on other nanoparticles and in other biofluids.

We find that while PNPs are largely agnostic to protein adsorption, $(GT)_{15}$-SWCNTs show strong preferential binding of proteins involved in lipid transport, complement activation, and blood coagulation. Importantly, enrichment of complement proteins (especially C3) on ssDNA-SWCNTs is concerning due to the potential of nanoparticle opsonization and complement pathway activation. The selectivity of proteins binding to $(GT)_{15}$-SWCNTs motivates either the rational design of sensors harnessing innate affinity for the SWCNT surface, or the development of SWCNT-based nanosensors passivated against detrimental biofouling. Additionally, $(GT)_{15}$-SWCNTs show high binding of fibrinogen and low binding of albumin, despite the prevalence of albumin binding on other nanoparticles across a body of previous literature.[195] This raises cogent

concern for the need to test nanotechnologies in blood plasma (with all protein constituents present) rather than blood serum (absent of fibrinogen), where fibrinogen may be a more important contributor to diminished *in vivo* efficacy than albumin.

We connect protein attributes that dictate protein-nanoparticle interactions to the thermodynamics and transient kinetics of protein-nanoparticle binding. Outer corona formation can be mitigated by tuning electrostatic interactions through nanoparticle design and by applying dynamic flow conditions (such as in circulating environments), whereas entropic considerations must be considered for the inner corona. Moreover, protein properties mediate adsorption differently in each biofluid, underscoring the complexity of corona formation. This phenomenon emphasizes that protein corona formation is a function of collective interactions at the nano-bio interface, rather than a property of isolated protein-nanomaterial interactions.

This work clarifies fundamental interactions for nanoscale systems in which development and optimization is done *in vitro*, with a desired application *in vivo*. Difficulties persist in the effective application of ssDNA-SWCNTs in brain imaging and delivery, including biofouling and the tendency of ssDNA-SWCNTs to aggregate in the presence of proteins. A more in-depth understanding of the protein corona could allow *a priori* prediction of biodistribution profiles and/or enable us to better understand these results in organisms. Elucidating protein corona composition, dynamics, structure, and driving forces that mediate nanoparticle-protein interactions will establish design considerations for nanosensor development and provide a framework for understanding *how* and *why* our engineered nanoparticles are affecting, and being affected by, complex bioenvironments.

2.5 Materials and Methods

2.5.1 Synthesis of SWCNT-Based Nanosensors

Single-stranded DNA with single-walled carbon nanotube (ssDNA-SWCNT) suspensions were prepared with 1 mg of mixed-chirality SWCNTs (small diameter HiPco™ SWCNTs, NanoIntegris) and 1 mg of ssDNA (custom ssDNA oligos with standard desalting, Integrated DNA Technologies, Inc.) in 1 mL of 1X phosphate-buffered saline (PBS; 137 mM NaCl, 2.7 mM KCl, 10 mM Na_2HPO_4, 1.8 mM KH_2PO_4). Solutions were bath sonicated for 10 min (Branson Ultrasonic 1800) and probe-tip sonicated for 10 min in an ice bath (3 mm probe tip at 50% amplitude, 5-6 W, Cole-Parmer Ultrasonic Processor). Samples were incubated at room temperature for 30 min then centrifuged to pellet insoluble bundles and contaminants (16.1 krcf, 30 min). Supernatant containing the product was collected. ssDNA-SWCNTs were spin-filtered to remove free ssDNA (Amicon Ultra-0.5 mL centrifugal filters with 100 kDa MWCO, Millipore Sigma) by washing with Milli-Q water two times (8 krcf, 5 min) then reversing the spin filter and centrifuging to recover sample (1 krcf, 5 min). ssDNA-SWCNT concentration was determined via sample absorbance at 632 nm (NanoVue Plus, GE Healthcare Life Sciences) and the extinction coefficient ε_{632nm}=0.036 L mg^{-1} cm^{-1}.[32] ssDNA-SWCNTs were stored at 4°C until use and then diluted to a working concentration of 100 mg L^{-1} in PBS.

2.5.2 Nanoparticle Characterization

100 nm polystyrene nanoparticles were purchased from Polysciences, Inc. (PNPs; Fluoresbrite® yellow-green fluorophore-labeled). Size was confirmed with DLS to be in accordance with manufacturer specifications (Figure 2-7b) and measured zeta potential is -59.7 ± -3.24 mV (Figure 2-8; Zetasizer Nano, Malvern Panalytical; 1.67 g L^{-1} in PBS, 700 µL volume).

ssDNA-SWCNTs were synthesized as described above. Mixed-chirality HiPco™ SWCNTs are reported by the manufacturer (NanoIntegris) to have diameters 0.8-1.2 nm (average 1 nm; measured by Unidym from TEM) and lengths 100-1,000 nm (measured by Unidym from AFM). Upon suspension with ssDNA, previous AFM work informs a diameter of ~1 nm and length distribution centered around ~500 nm,[196] yet AFM sample deposition is known to influence such measurements in a DNA sequence-dependent manner.[197] Our previous work depicts ssDNA-SWCNT morphology by TEM.[198] Measured zeta potential of $(GT)_{15}$-SWCNTs is -19.4 ± 0.945 mV (Figure 2-8; Zetasizer Nano, Malvern Panalytical; 28.67 mg L^{-1} in PBS, 700 µL volume). Absorbance and fluorescence spectra of $(GT)_{15}$-SWCNTs are presented in Figure 2-6, confirming formation of a stable SWCNT dispersion[34] and in agreement with previous literature.[42] Absorbance of 30 mg L^{-1} $(GT)_{15}$-SWCNTs in PBS was measured in a 700 µL volume, black-sided quartz cuvettes (Thorlabs, Inc.) with a UV-VIS-nIR spectrophotometer (Shimadzu UV-3600 Plus). Fluorescence was obtained with an inverted Zeiss microscope (Axio Observer.D1, 10x objective) coupled to a Princeton Instruments spectrometer (SCT 320) and liquid nitrogen cooled Princeton Instruments InGaAs detector (PyLoN-IR). Fluorescence was measured in a glass-bottom 384 well-plate format (30 µL volume sample, 10 mg L^{-1} concentration in PBS), with a 721 nm laser (OptoEngine LLC) excitation light source and 800 – 1400 nm emission wavelength range.

We have previously determined approximately 140 $(GT)_{15}$ molecules or 364 $(GT)_6$ molecules adsorbed per SWCNT.[118] Using $(GT)_{15}$ and $(GT)_6$ contact areas from MD simulations,[42] this translates to ssDNA surface coverages of 2.1% and 6.5%, respectively. Previous work reports ~20-25% surface coverage of ssDNA on SWCNTs in the saturation regime (i.e. when further ssDNA adsorption is sterically unfavorable).[184,185,199] To capture the differing experimental and modeling conditions, we report the full range of ~1-25% initial ssDNA surface coverage on the SWCNT.

2.5.3 Isolation and Characterization of Protein-Nanoparticle Complexes

Protein corona composition was studied on PNPs, $(GT)_{15}$-SWCNTs, and $(GT)_6$-SWCNTs. PNPs were vortexed prior to use (1 min in 5 s pulses). Biofluids studied were human blood plasma and human CSF (Table 2-3) obtained with informed consent from all donors and in accordance with the relevant guidelines and regulations. CSF was concentrated 10X prior to incubation to match protein to nanoparticle ratios under volume constraints (14 krcf, 30 min; Amicon Ultra-0.5 mL centrifugal filters with 3 kDa MWCO, Millipore Sigma). The ratio of protein concentration to nanoparticle surface area was maintained constant for each respective nanoparticle in different biofluids, with 26 g L^{-1} protein per m^2 nanoparticle surface area for PNPs (from previous literature[58]) and 200 g L^{-1} protein per m^2 nanoparticle surface area for $(GT)_6$- and $(GT)_{15}$-SWCNTs. Based on experimental optimization, an 8-fold higher ssDNA-SWCNT surface area relative to PNP was selected to collect enough protein material from the SWCNT corona for downstream characterization, due to significantly lower protein adsorption on SWCNTs compared to PNPs. These incubation ratios translate to 1.67 g L^{-1} PNPs with 2.67% (v/v) plasma; 0.4 g L^{-1} PNPs with

8.67% (v/v) 10X CSF; 28.67 mg L^{-1} $(GT)_{15}$-SWCNTs with 2.67% (v/v) plasma; and 12.67 mg L^{-1} $(GT)_{15}$-SWCNTs with 16% (v/v) 10X CSF. Biofluid percentages are nominal, and were adjusted on a mass basis to match the target protein per surface area ratios. Nanoparticles were incubated with biofluids in PBS, 750 µL total volume, for 1 h at ambient temperature (Figure 2-7a). Protein-nanoparticle complexes were pelleted by centrifugation (16.1 krcf, 20 min). Supernatant containing unbound proteins was removed, the pellet resuspended in PBS, and the pellet broken up by pipetting. Washing was repeated three times to ensure removal of unbound proteins.

Each step was validated for polystyrene nanoparticles (PNPs) exposed to blood plasma proteins as follows: (i) incubation of proteins with nanoparticles induced an increase in nanoparticle hydrodynamic radius as determined by dynamic light scattering (DLS), where the number distribution shifted to a larger peak center and broadened out due to nonuniform aggregate formation as protein to nanoparticle loading was increased (Figure 2-7b); (ii) proteins initiated nanoparticle aggregation, as shown by solution absorbance before and after initial pelleting (Figure 2-7c), thus facilitating nanoparticle recovery for analysis; (iii) three washing steps were sufficient to remove unbound proteins by quantifying proteins remaining in the supernatant (Figure 2-7d; also valid for all nanoparticle/biofluid combinations); and (iv) proteins were fully eluted from nanoparticles by boiling in solutions of sodium dodecyl sulfate/β-mercaptoethanol (SDS/βME, for 2D PAGE analysis; Figure 2-7e) and urea/dithiothreitol (urea/DTT, for LC-MS/MS analysis). The equivalent verification was performed with $(GT)_{15}$-SWCNTs, yet the high aspect ratio of SWCNTs precluded accurate DLS measurement. Zeta potentials of the nanoparticle/plasma mixtures were determined as a proxy of the nanoparticle-protein complex surface charge, although this measurement captures a convolution of any free proteins, free nanoparticles, and nanoparticle-protein complexes (Figure 2-8). Zeta potential measurements of plasma proteins alone and nanoparticles alone reveal that the separate entities were initially negatively charged, whereby mixing results in a broadened zeta distribution of lower average magnitude than the nanoparticles alone. The measured reduction in effective surface charge implies some degree of protein adsorption to the nanoparticles and lowering of electrostatic repulsion, contributing to the experimentally observed colloidal instability upon combining nanoparticles with plasma, in agreement with previous literature.[47]

Toward (i), the incubation solution was characterized by dynamic light scattering and zeta potential measurements in folded capillary zeta cell disposable cuvettes (Zetasizer Nano, Malvern Panalytical; 700 µL volume). PNPs are negatively charged as a result of initiator fragments from the polymerization process, yet these PNPs are conventionally considered to be a model plain nanoparticle due to no explicit functionalization.[58] $(GT)_{15}$-SWCNTs are slightly negatively charged due to the presence of the ssDNA on the surface, with the phosphate backbone extending into solution. Toward (ii), absorbance spectra were measured in a 700 µL volume, black-sided quartz cuvettes (Thorlabs, Inc.) with a UV-VIS-nIR spectrophotometer (Shimadzu UV-3600 Plus). For (iii), free protein remaining in the supernatant after centrifugation was quantified during subsequent wash steps using the Qubit Protein Assay (Thermo Fisher Scientific). Note that PNPs contribute minimally to the Qubit signal (~2%), therefore the protein mass calculated for wash 0 is slightly inflated. For (iv), eluted protein from the nanoparticle was quantified using the Pierce 660nm Assay (with Ionic Detergent Compatibility Reagent; Thermo Fisher Scientific). Elution buffer was modified from SDS/βME for 2D PAGE to urea/DTT for LC-MS/MS analysis due to SDS interference with trypsin digestion, reverse-phase HPLC, and electrospray ionization

efficiency.[200] The profile of eluted proteins was confirmed to be invariable to the elution system by 2D PAGE and S-trap (Protifi) LC-MS/MS analysis, although total eluted protein amount decreased.

Nanoparticle mass loss during pelleting and washing was estimated by measuring solution absorbance of each collected supernatant after centrifugation. This measured mass loss serves as a maximum estimate due to scattering of solubilized proteins and any remaining protein-nanoparticle aggregates that increase the absorbance baseline and impede fully accurate quantification of the nanoparticles alone. After each centrifugation step as shown in Figure 2-7a (four total), the supernatant was removed and absorbance was measured (NanoDrop™ One/OneC Microvolume UV-Vis Spectrophotometer). For PNPs, absorbance was measured at the excitation maximum of the fluorophore (441 nm) and a standard curve over the relevant absorbance range (linear fit, $R^2 = 0.9986$) was used to convert this to concentration using Beer-Lambert's Law. For $(GT)_{15}$-SWCNTs, absorbance was measured at 632 nm and the known extinction coefficient was applied similarly. Results are presented in Table 2-4, with standard deviations of technical triplicate measurements and "0" denoting absorbance reading at the noise level of the instrument (e.g. absorbance ≤ 0.0133, read for buffer). The mass loss percentage is calculated as the ratio of this measured total mass removed to the calculated initial mass added to solution. We conclude that the maximum mass loss estimates of ~12% for PNPs and ~32% for $(GT)_{15}$-SWCNTs in each biofluid are not a significant portion of the population.

As a control, in the absence of nanoparticles in the incubation step, no measurable protein was present after pelleting and denaturation, confirming that we are measuring selective protein adsorption to nanoparticles, not merely to the container, nor simply seeing the high background of proteins in biofluids. This latter point is further confirmed by the result that protein corona abundance does not scale as a function of native abundance on ssDNA-SWCNTs (Figure 2-16). Contamination of the isolated protein corona with bio-nanoparticles, such as extracellular vesicles and lipoproteins,[201] was inferred by the aforementioned control (no "protein corona" measurable in the absence of nanoparticles) and the absence of large peaks in the plasma-alone DLS (Figure 2-7b).

2.5.4 Composition Studies by Two-Dimensional Polyacrylamide Gel Electrophoretic Separation (2D PAGE)

2D PAGE was performed to identify proteins via separation by isoelectric point in the first dimension and molecular weight in the second dimension. For analysis by 2D PAGE, bound proteins were eluted from nanoparticles by heating at 95°C for 10 min in SDS/BME reducing buffer (2% SDS, 5% β-mercaptoethanol, 0.066 M Tris-HCl). 1D separation was run according to the O'Farrell protocol[202] (adapted for Bio-Rad Mini-PROTEAN Tube Cell). Briefly, 1D sample buffer (8 M urea, 2% Triton X-100, 5% β-mercaptoethanol, 2% total carrier ampholytes - 1.6% Bio-Lyte 5/7, 0.4% Bio-Lyte 3/10) was added to samples in a 1:1 or 0.07:1 volume ratio (relative to initial plasma and CSF volumes, respectively) and incubated for 10 min. 1D separation was carried out in capillary tube PAGE with gel composition of 4% acrylamide (total monomer), 8 M urea, 2% Triton X-100, 2% total carrier ampholytes, 0.02% ammonium persulfate (APS), and 0.15% Tetramethylethylenediamine (TEMED). 25 µL sample and 25 µL 1D sample overlay buffer (4 M urea, 1% total carrier ampholytes) was loaded per capillary tube gel. Upper and lower chamber buffers were 100 mM sodium hydroxide and 10 mM phosphoric acid, respectively. 1D

separation was run at 500 V for 10 min, 750 V for 3.5 h. Nanoparticles were filtered from the eluted proteins by the gel itself. Capillary gels were extruded and loaded onto 2D gels. 2D separation was run according to the Laemmli protocol[203] (adapted for Bio-Rad Mini-PROTEAN Tetra Cell). Briefly, SDS/BME reducing buffer was added to the 2D well to cover the capillary gel and incubated for 10 min. 2D separation was carried out in 1 mm vertical mini gel format with a discontinuous buffer system under denaturing conditions. Gel composition was 12% acrylamide (total monomer), 0.375 M Tris-HCl, 0.1% SDS, 0.05% APS, 0.05% TEMED for the resolving gel and 12% acrylamide (total monomer), 0.125 M Tris-HCl, 0.1% SDS, 0.05% APS, 0.1% TEMED for the stacking gel. Electrode buffer was 25 mM Tris, 192 mM glycine, and 3.5 mM SDS (pH 8.3). 2D separation was run at 200 V for 1 h. Gels were extracted and silver stained according to Bio-Rad's Silver Stain Plus protocol and identified with ExPASy's SWISS-2DPAGE database (Figure 2-9).[204]

2.5.5 Composition Studies by Liquid Chromatography-Tandem Mass Spectrometry (LC-MS/MS)

Bound proteins were eluted from nanoparticles by heating at 37°C for 60 min in urea/DTT reducing buffer (8 M urea, 5 mM DTT, 50 mM Tris-HCl, pH 8). Eluted protein concentration was determined with the EZQ Protein Quantitation Kit (Thermo Fisher Scientific). Protein solution was centrifuged to pellet the majority of nanoparticles (16 krcf, 20 min) and this supernatant was spin-filtered to concentrate and remove impurities (14 krcf, 30 min; Amicon Ultra-0.5 mL centrifugal filters with 3 kDa MWCO, Millipore Sigma; pre-rinsed). Proteins were alkylated with 15 mM iodoacetamide for 30 min in the dark. 500 mM DTT was added to quench excess iodoacetamide in a volume ratio of 3:1 and incubated for 20 min. The reaction was diluted 1:1 with 50 mM Tris-HCl pH 8 to allow enzymatic protein digestion. In-solution protein digestion was done with a ratio of 1:25 w/w Trypsin/Lys-C (Mass Spectrometry Grade, Promega) to protein, overnight at 37°C. Any remaining nanoparticles were removed by spin filtering (14 krcf, 30 min; Amicon Ultra-0.5 mL centrifugal filters with 30 kDa MWCO, Millipore Sigma; pre-rinsed). Nanoparticle removal was done after protein digestion into peptides due to the otherwise very similar sizes of nanoparticles and proteins. Peptide concentration was determined with the Pierce Peptide Quantitation Kit (Thermo Fisher Scientific) and samples were normalized to 0.1 g L^{-1} in 100 µL total volume. Peptide solutions were spiked with 50 fmol of E. coli housekeeping peptide (Hi3 Ecoli Standard, Waters) per 5 µL sample volume to allow for protein quantification. Digestion was terminated by freezing samples to -20°C. Note that biofluid-alone samples underwent these same processing steps, from denaturation to tryspin digestion. The preceding isolation steps of pelleting and washing were only necessary for nanoparticle-protein complexes, and were accordingly omitted for biofluids alone. An alternative mass spectrometry preparation technique was pursued, using S-traps (Protifi), confirming our results were not biased by the sample preparation protocol.

Proteolytically digested proteins were analyzed using a Synapt G2-S*i* mass spectrometer equipped with a nanoelectrospray ionization source and connected directly in line with an Acquity M-class ultra-performance liquid chromatography system (UPLC; Waters, Milford, MA). This instrumentation is in the California Institute for Quantitative Biosciences (QB3)/College of Chemistry Mass Spectrometry Facility at UC Berkeley. Data-independent, ion mobility-enabled mass spectra and tandem mass spectra[205–207] were acquired in the positive ion mode. Data acquisition was controlled with MassLynx software (version 4.1) and tryptic peptide identification

and quantification using a label-free approach[208–210] were performed with Progenesis QI for Proteomics software (version 4.0, Waters).

2.5.6 Proteomic Mass Spectrometry Data Interpretation

Prior to LC-MS/MS analysis, all samples were normalized on a total protein mass basis (where normalizing on a total molar basis is experimentally not feasible due to the complexity of biofluid samples). Consequently, the reported abundance of each protein species *i,* b_i, is the ratio of mole number of protein *i,* n_i, to the total protein mass:

$$b_i = \frac{n_i}{\sum_j n_j MW_j} \tag{2-1}$$

where MW_j is the molecular weight of each protein species *j.* LC-MS/MS data is then expressed as the fold change ε_i between the abundance of protein species *i* in the corona on the nanoparticle surface (phase *s*) to that in the bulk biofluid (phase *f*):

$$\varepsilon_i = \frac{b_i^s}{b_i^f} = \left(\frac{n_i^s}{n_i^f}\right)\left(\frac{\sum_j n_j^f MW_j}{\sum_j n_j^s MW_j}\right) \tag{2-2}$$

Here, the second term in parentheses is equal to 1 because all samples have the same total protein mass. Therefore, the reported fold change is the molar abundance ratio of a particular protein in the corona phase to that in the bulk biofluid phase.

2.5.7 Linear Regression Models for Corona Composition

We linearly regressed[211] the natural log of the fold change of proteins for each nanoparticle-biofluid pairing using two sets of protein descriptors. The first set of descriptors are categorical variables denoting what class a protein is in (*i.e.* 1 for a protein in a given class and 0 otherwise), namely, involved in acute-phase response, blood coagulation, cell adhesion/signal transduction, complement activation, immune response, lipid binding/transport, regulation of biological processes, transport, or miscellaneous/unknown (Figure 2-12 and Figure 2-13; grouped according to PANTHER[212]). The variables were sum-effect coded such that the coefficients quantify how a protein class deviates from the grand mean of all protein classes and the intercept of the regression is the grand mean. Because each protein is grouped into one and only one class, the categorical variables are not linearly independent and one class is excluded from the regression;[211] we chose the miscellaneous class.

The second set of descriptors are molecular and biophysical properties of the proteins: protein mass, fraction of amino acids that are non-aromatic hydrophobic (sum of alanine, valine, isoleucine, leucine, and methionine content), hydrophilic (sum of serine, threonine, asparagine, glutamine content), arginine (R), histidine (H), lysine (K), acidic (sum of aspartic acid and glutamic acid content), phenylalanine (F), tyrosine (Y), tryptophan (W), number of glycosylated sites, number of ligand binding sites, number of metal binding sites, and number of disulfide binds Figure 2-3, Figure 2-14, and Figure 2-15). Each of these descriptors is a continuous variable. The regression coefficients quantify the fractional difference in the fold change for a unit increase in

the independent variable.[211] Protein-specific information was acquired from UNIPROT.[181] Note that these particular descriptors were chosen after primary analyses that eliminated highly co-dependent descriptors. An example was choosing to include percentage of acidic/basic amino acids rather than protein isoelectric point (from ExPASy Compute pI/MW), where the isoelectric point was deemed less exact because it relies on a theoretical calculation, omits protein fragments, and necessitates an average value for multicomponent proteins. Other examples were including number of disulfide bonds as an estimate of protein stability rather than protein instability index and segmenting to percentage of hydrophobic/aromatic amino acids rather than grand average hydropathy (GRAVY) score, in both cases due to the involvement of arbitrarily set scales (from ExPASy ProtParam).

For each regression, we included the measured protein fold changes for each replicate of a nanoparticle-biofluid system and controlled for sample-to-sample variability by including a categorical variable for the specific replicate. Protein abundances that fell below the lower limit of detection in the samples from the protein corona were set to $1x10^{-5}$ fmol, corresponding to the lowest detected protein abundance of all systems. Left-censoring the data in this way provides a conservative estimate of the regression coefficients by underestimating of the magnitude and significance.[211] Calculated variance inflation factors for all variables in each independent regression was <4, indicating negligible multicollinearity between the independent variables. To avoid overestimating the statistical significance of independent variables, p-values were adjusted using the Benjamini-Hochberg false discovery rate procedure.[213] All statistical analysis was implemented in Python using the StatsModels V0.10.1 package [214](0.27-0.39). Table 2-6 and Table 2-7 provide coefficients, standard errors, false discovery rate corrected (FDRC) p-values, and R-squared values for each regression. The median R-squared of the first and second regression models for the nanoparticle-biofluid systems are 0.29 and 0.34, respectively, indicating the statistical models are descriptive rather than predictive. Nonlinear or decision tree algorithms provide more precise prediction of corona composition,[72] however, these approaches were not considered because they are not readily interpretable, which is a principle goal of our analysis.

Protein properties that were controlled for but that did not show a statistically significant effect on fold change for any nanoparticle in any biofluid include: the number of disulfide bonds (used as a proxy for protein stability), number of biomolecular binding sites, number of metal binding sites, and percentage of histidine or tryptophan. The lack of dependence on disulfide bond content and also instability index is surprising in the context of previous corona literature, which suggests that less structurally stable proteins are more surface active.[158]

2.5.8 Varying Incubation Parameters

Protein corona composition was studied under varied incubation conditions in comparison to the reference state incubation (static, PBS, and 25°C incubation). Varying incubation conditions include dynamic (on orbital shaker at medium speed; to test corona stability), no salt (water; to test ionic effects), and high temperature (37°C; to test entropic contributions). Figure 2-4 summarizes data from 2D PAGE gels, with experimental replicates of 6 for plasma alone, 10 for reference, 4 for dynamic, 6 for no salt, and 3 for high temperature. Note that the numerous replicates for the reference state were due to the frequent repetition of this condition in comparison to the varied conditions.

2.5.9 Isothermal Titration Calorimetry (ITC) Methods

ITC measurements were performed with a NanoITC (TA Instruments). Prior to each experiment, samples and buffer were degassed for 10 min and the reference cell was filled with fresh Milli-Q water. Equilibration time was set to 1 h before the experiment start and the initial and final baselines were collected for 300 s. For each experiment, 1.2 g L^{-1} protein in PBS was titrated from the syringe (250 µL total volume) into 0.1 g L^{-1} $(GT)_{15}$-SWCNTs in PBS in the cell (1 mL total volume) under constant stirring (250 rpm) at 25 °C. 10 µL of protein titrant was injected into the nanoparticle solution in the cell every 7 min, with a total of 24 injections. By standard practice, every run was initiated with a 5 µL injection to ensure no artifacts due to bubbles and was removed from analysis. All protein-nanoparticle binding experiments were accompanied by three heat-of-dilution control experiments: (1) protein injected into buffer, (2) buffer injected into nanoparticles, and (3) buffer injected into buffer (where buffer is PBS). Heat of binding of protein to nanoparticles was then calculated as: (heat from titration of protein into nanoparticles) – (1) – (2) + (3). Data processing was completed with NanoAnalyze software (TA Instruments). Baseline correction was done using the auto-fit routine. An independent binding model was applied to fit the fibrinogen data set, suitable to model weak nonspecific interactions such as those present in the system under study,[67] and a blank (constant) model was applied to fit the albumin data set.

Protein and nanoparticle concentrations and ITC setup parameters were varied in attempt of obtaining binding curves for both proteins to $(GT)_{15}$-SWCNTs. However, for albumin this was not possible within the ITC instrument's operational range, therefore albumin was concluded to not bind to $(GT)_{15}$-SWCNTs.

2.5.10 Corona Exchange Assay

Corona dynamic studies were completed as described previously.[118] Briefly, the same suspension protocol was employed for preparation of fluorophore-labeled ssDNA-SWCNT complexes, using ssDNA-Cy5 (3' Cy5-labeled custom ssDNA oligos with HPLC purification, Integrated DNA Technologies, Inc.) in place of unlabeled ssDNA. Lyophilized proteins were purchased (see details in Table 2-3) and reconstituted by adding 5 mg to 1 mL of PBS, tilting to dissolve for 15 min, filtering with 0.45 µm syringe filter (cellulose acetate membrane, VWR International), and quantifying with the Qubit Protein Assay (Thermo Fisher Scientific). Because of variation in amine-labeling of proteins, fluorescently labeled ssDNA was solely tracked, and the displacement of ssDNA from the SWCNT surface was taken as a proxy for protein adsorption. Equal volumes of 10 mg L^{-1} $(GT)_{15}$- or $(GT)_6$-Cy5-SWCNTs and 160 mg L^{-1} protein were added to a 96-well PCR plate (Bio-Rad) to a total volume of 50 µL. The plate was sealed with an optically transparent adhesive seal (Bio-Rad) and spun down on a benchtop centrifuge. Fluorescence time series readings were taken in a Bio-Rad CFX96 Real Time qPCR System, scanning the Cy5 channel every 2 min at 22.5°C. Fluorescence time series were analyzed without default background correction. Fluorescence values were converted to mass concentration using linear standard curves for ssDNA-Cy5. Note that in the case of the control, ssDNA adsorption to the SWCNT is observed, in line with previous studies.[118]

2.5.11 Structure Studies by Small-Angle X-ray Scattering (SAXS)

SAXS data was collected at SIBYLS beamline (bl12.3.1) at the Advanced Light Source of Lawrence Berkeley National Laboratory, Berkeley, California.[215] X-ray wavelength was set at λ =

0.1127 nm and the sample-to-detector distance was 2.1 m, resulting in scattering vector (q) ranging from 0.1–4 nm^{-1}. The scattering vector is defined as $q = 4\pi\sin\theta/\lambda$, with scattering angle 2θ. Data was collected using a Dectris PILATUS3X 2M detector at 20°C and processed as described previously.[216]

Immediately prior to data collection, 30 µL of each sample was added to 96-well plates kept at 10°C and transferred to the sampling position via a Tecan Evo liquid handling robot with modified pipetting needles acting as sample cells as described previously.[217] Samples were exposed to X-ray synchrotron radiation for 30 s at a 0.5 s frame rate for a total of 60 images. Each collected image was circularly integrated and normalized for beam intensity to generate a one-dimensional scattering profile by beamline-specific software. Buffer subtraction was performed for the one-dimensional scattering profile of each sample using each of two PBS buffer wells to ensure the subtraction process was not subject to instrument variations. Scattering profiles over the 30 s exposure were sequentially averaged together to eliminate any potential radiation damage effects. Averaging was performed with web-based software FrameSlice (sibyls.als.lbl.gov/ran).

2.5.12 Transmission Electron Microscopy (TEM) Methods

Holey carbon-coated grids (EMS Electron Microscopy Science) were surface-treated by glow discharge to make the support hydrophilic. Samples of $(GT)_{15}$-SWCNTs with fibrinogen or plasma were negatively stained with 1% uranyl acetate solution. For the $(GT)_{15}$-SWCNTs alone sample, no negative staining was done. 5 µl of 10 mg L^{-1} solution was drop-cast onto the grid. FEI ThemIS 60-300 STEM/TEM (National Center of Electron Microscopy, Molecular Foundry) with acceleration voltage of 60kV was used to acquire TEM images by video recording (Figure 2-20). A low acceleration voltage was chosen to minimize sample damage and increase sample contrast.

Table 2-3. Purchased biofluid and protein specifications.

Protein	Manufacturer	Lot #	Source	Form
Blood plasma	Innovative Research Inc.	#23791	Pooled normal human plasma	Biofluid
Cerebrospinal fluid	Lee Biosolutions	#07C5126	Pooled normal human CSF, from remnant lumbar puncture	Biofluid
Albumin	Sigma-Aldrich	#SLBZ2785	Human plasma	Lyophilized
Alpha-2-HS glycoprotein	Biovision Inc.	#4C08L75480	Human plasma	Lyophilized
Apolipoprotein A-I	Alfa Aesar	#927J17A	Human plasma	1 g L^{-1} in 10mM ammonium bicarbonate buffer, pH 7.4
Clusterin	R&D Systems	NEV1519031	Mouse myeloma cell line, NS0-derived human; Asp23-Arg227 (beta) & Ser228-Glu449 (alpha) with a C-terminal 6-His tag	Lyophilized
Complement C3	Mybiosource Inc.	#N30/20170	Human plasma	5 g L^{-1}
Fibrinogen	Millipore Sigma	#3169957	Human plasma	Lyophilized
Immunoglobulin G	Lee Biosolutions	#06B2334	Human plasma	Lyophilized

2.6 Chapter Supporting Information

2.6.1 Supplementary Figures and Tables

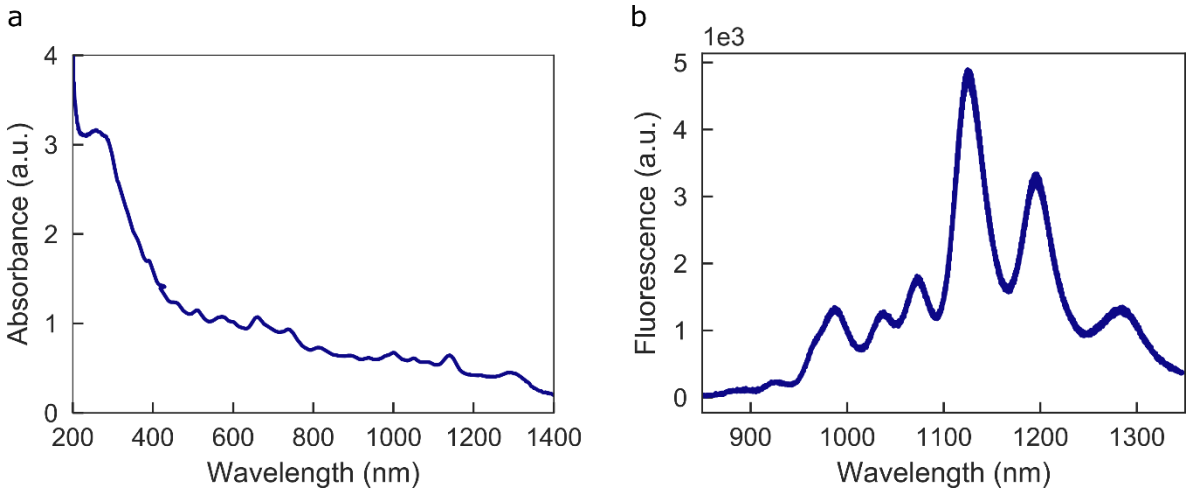

Figure 2-6. Optical characterization of $(GT)_{15}$-SWCNTs. (a) Absorbance spectrum of 30 mg L^{-1} $(GT)_{15}$-SWCNTs in PBS. (b) Fluorescence spectrum of 10 mg L^{-1} $(GT)_{15}$-SWCNTs in PBS. Stable SWCNT suspension in aqueous medium is confirmed by absorbance peaks across the visible and near-infrared range and fluorescence emission that would otherwise be quenched in a SWCNT- aggregated state.

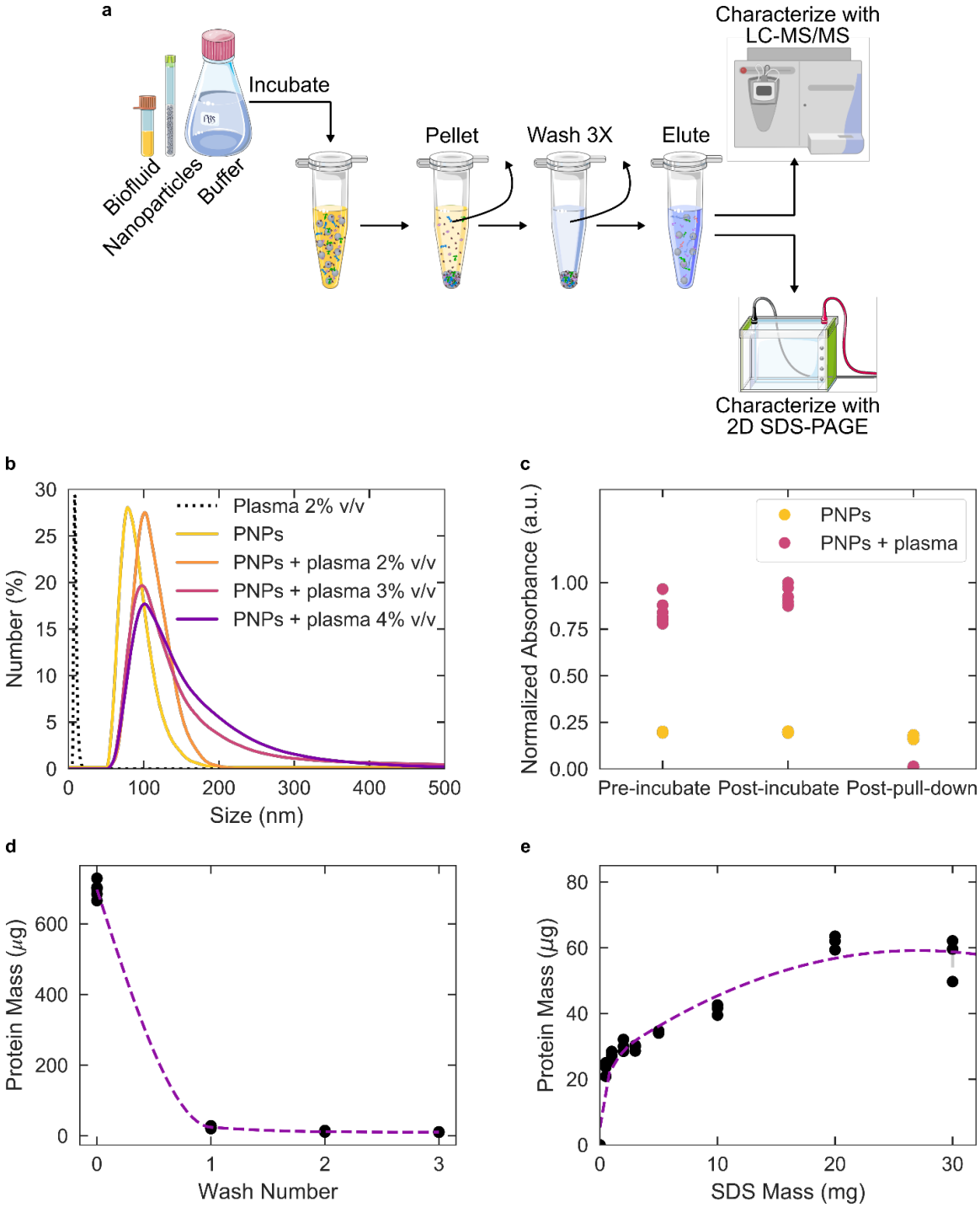

Figure 2-7. Isolation and characterization of protein-nanoparticle complexes to determine protein corona composition on nanoparticles. (a) Schematic detailing experimental procedure: nanoparticles are incubated with the desired biofluid in buffered solution, nanoparticle-protein complexes are pelleted by centrifugation and washed three times to remove non-selectively pelleted proteins, and corona proteins are eluted and characterized by two-dimensional polyacrylamide gel electrophoresis (2D PAGE) or liquid chromatography-tandem mass spectrometry (LC-MS/MS). (b) Dynamic light scattering (DLS) reveals that

plasma protein corona formation induces an increase in the hydrodynamic radius of the PNPs (1.67 g L^{-1} in PBS) via peak shifting and broadening. (c) Absorbance at PNP excitation max (441 nm) immediately after adding plasma to incubation solution, incubating for 1 hour, and after the first pelleting step demonstrates the presence of proteins facilitates isolation of nanoparticles from solution in the initial pelleting step. (d) Quantification of free protein in solution via Qubit Protein Assay for varying wash number shows nearly complete depletion of free protein by three washes. (e) Quantification of eluted protein from nanoparticles via Pierce 660 nm Protein Assay with increasing SDS reducing buffer confirms complete elution of bound proteins from nanoparticle surface prior to characterization. Error bars on (b)-(d) are ± standard error for experimental replicates of N = 6, 6, and 3, respectively.

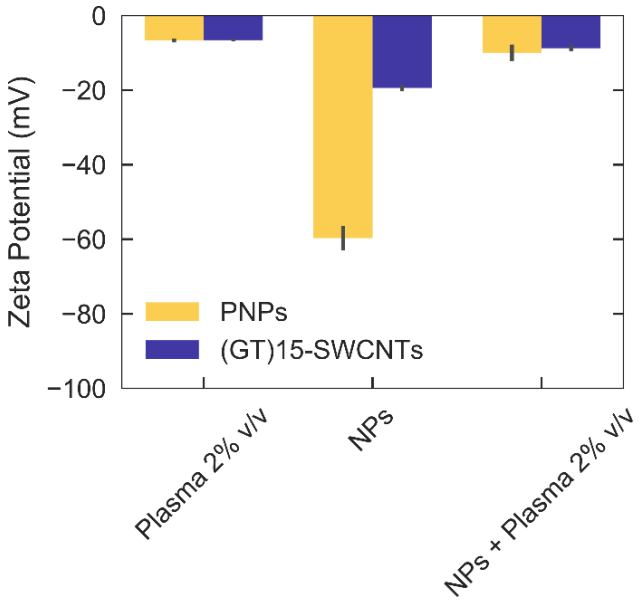

Figure 2-8. Surface charge changes induced by plasma protein corona formation. Zeta potential of native plasma, nanoparticles alone (PNPs yellow, $(GT)_{15}$-SWCNTs purple), and plasma protein-nanoparticle complexes. Lower magnitude zeta potential of protein-nanoparticle complexes indicates reduction in colloidal stability in the presence of surface-adsorbed proteins, as expected by visible aggregates formed. PNPs are 1.67 g L^{-1} and $(GT)_{15}$-SWCNTs are 28.67 mg L^{-1}, in PBS, 700 µL volume. Error bars are ± standard deviation for technical replicates (N = 3).

Table 2-4. Nanoparticle mass loss during corona isolation.

Wash	Mass [µg] PNPs (Plasma)	Mass [µg] PNPs (CSF)	Mass [µg] $(GT)_{15}$-SWCNTs (Plasma)	Mass [µg] $(GT)_{15}$-SWCNTs (CSF)
0	103.45 ± 29.40	37.51 ± 0.00	6.25 ± 0.21	3.33 ± 0.21
1	19.33 ± 1.97	0.00	0.00	0.00
2	11.37 ± 1.97	0.00	0.00	0.00
3	10.23 ± 0.00	0.00	0.00	0.00
Total Mass Removed	144.37	37.51	6.25	3.33
Initial Calculated Mass	1250	300	215	9.5
Estimated Mass Loss %	*11.55%*	*12.50%*	*29.07%*	*35.09%*

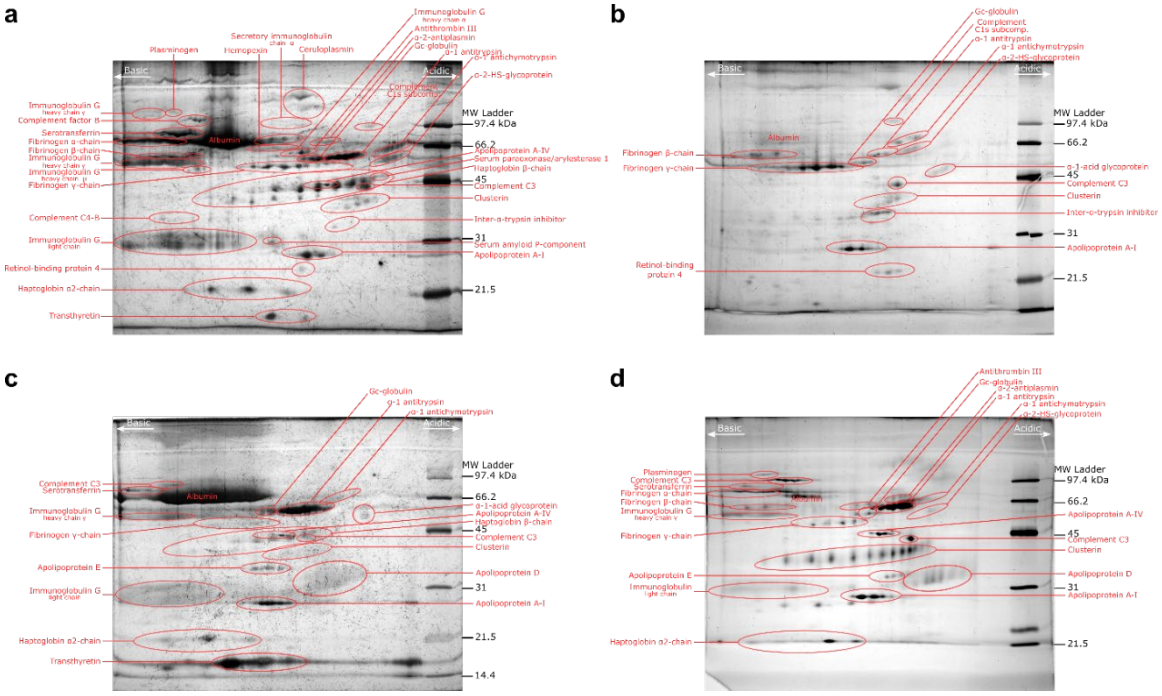

Figure 2-9. Representative 2D PAGE gels. (a) Plasma alone, (b) Plasma protein corona composition formed on $(GT)_{15}$-SWCNTs, (c) CSF alone, and (d) CSF protein corona composition formed on PNPs.

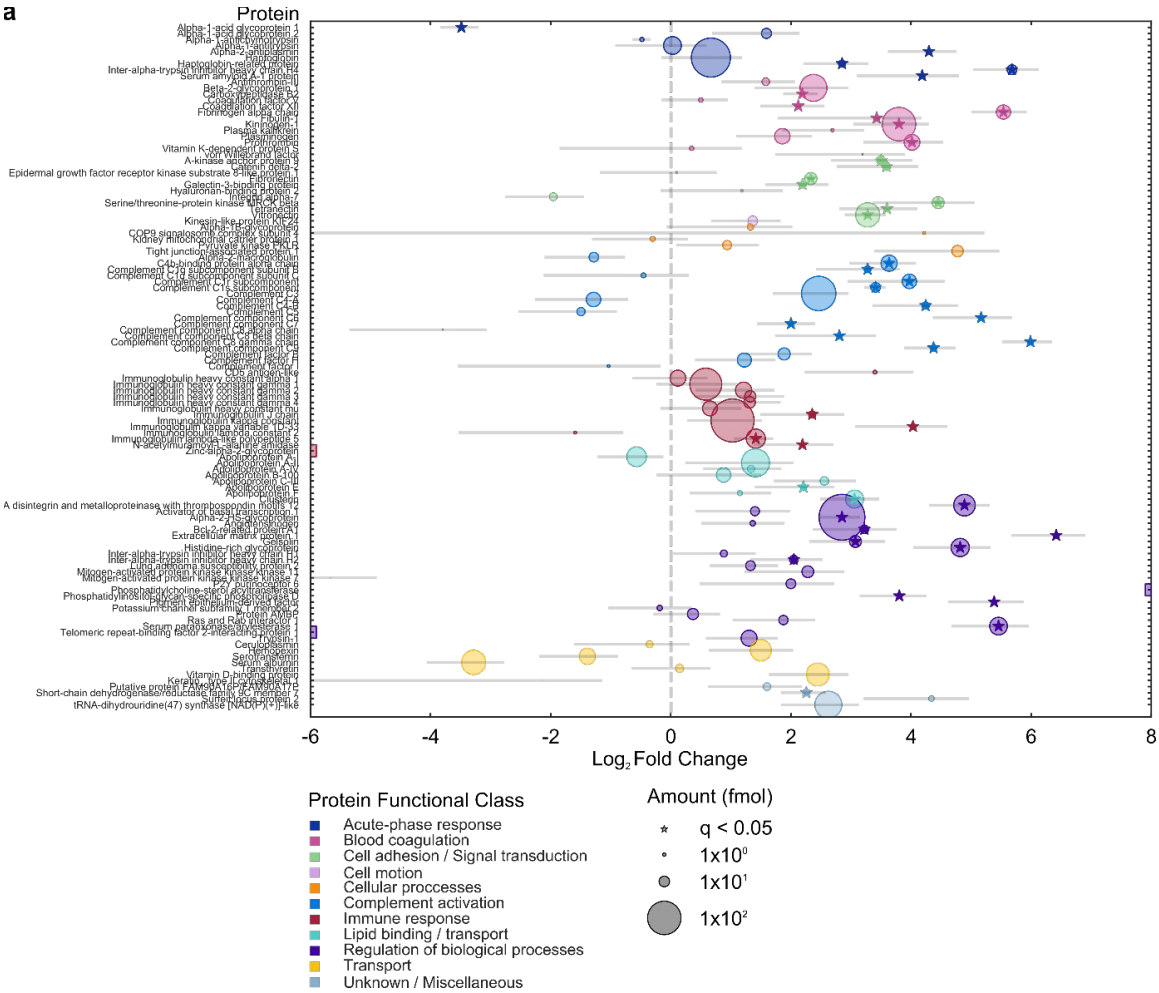
a
Protein
-6
-4
-2
0
2
4
6
8
Log2 Fold Change
Protein Functional Class
Acute-phase response
Blood coagulation
Cell adhesion / Signal transduction
Cell motion
Cellular proccesses
Complement activation
Immune response
Lipid binding / transport
Regulation of biological processes
Transport
Unknown / Miscellaneous
Amount (fmol)
q < 0.05
1x10^0
1x10^1
1x10^2

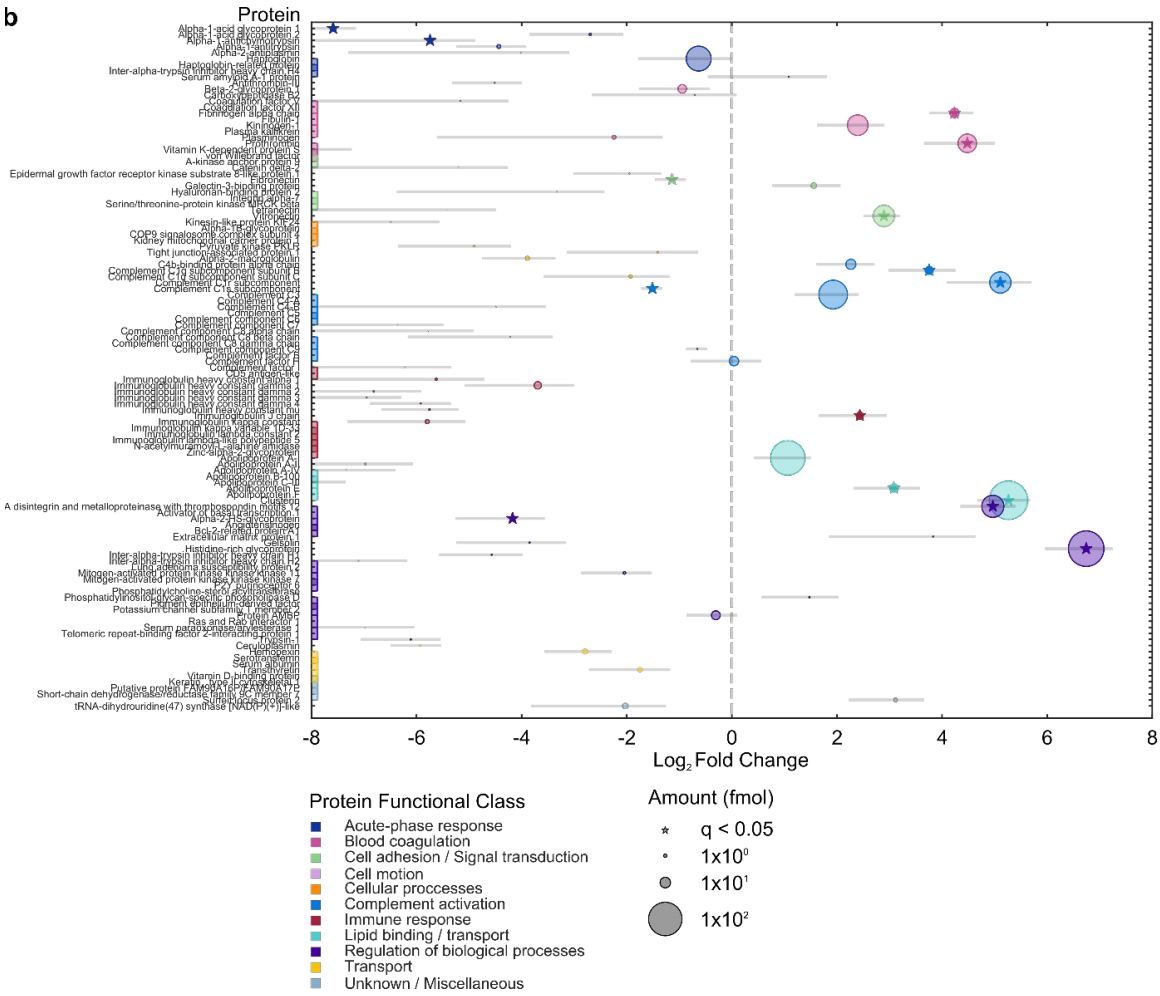
b
Protein
-8
-6
-4
-2
0
2
4
6
8
Log2 Fold Change
Protein Functional Class
Acute-phase response
Blood coagulation
Cell adhesion / Signal transduction
Cell motion
Cellular proccesses
Complement activation
Immune response
Lipid binding / transport
Regulation of biological processes
Transport
Unknown / Miscellaneous
Amount (fmol)
q < 0.05
1x10^0
1x10^1
1x10^2

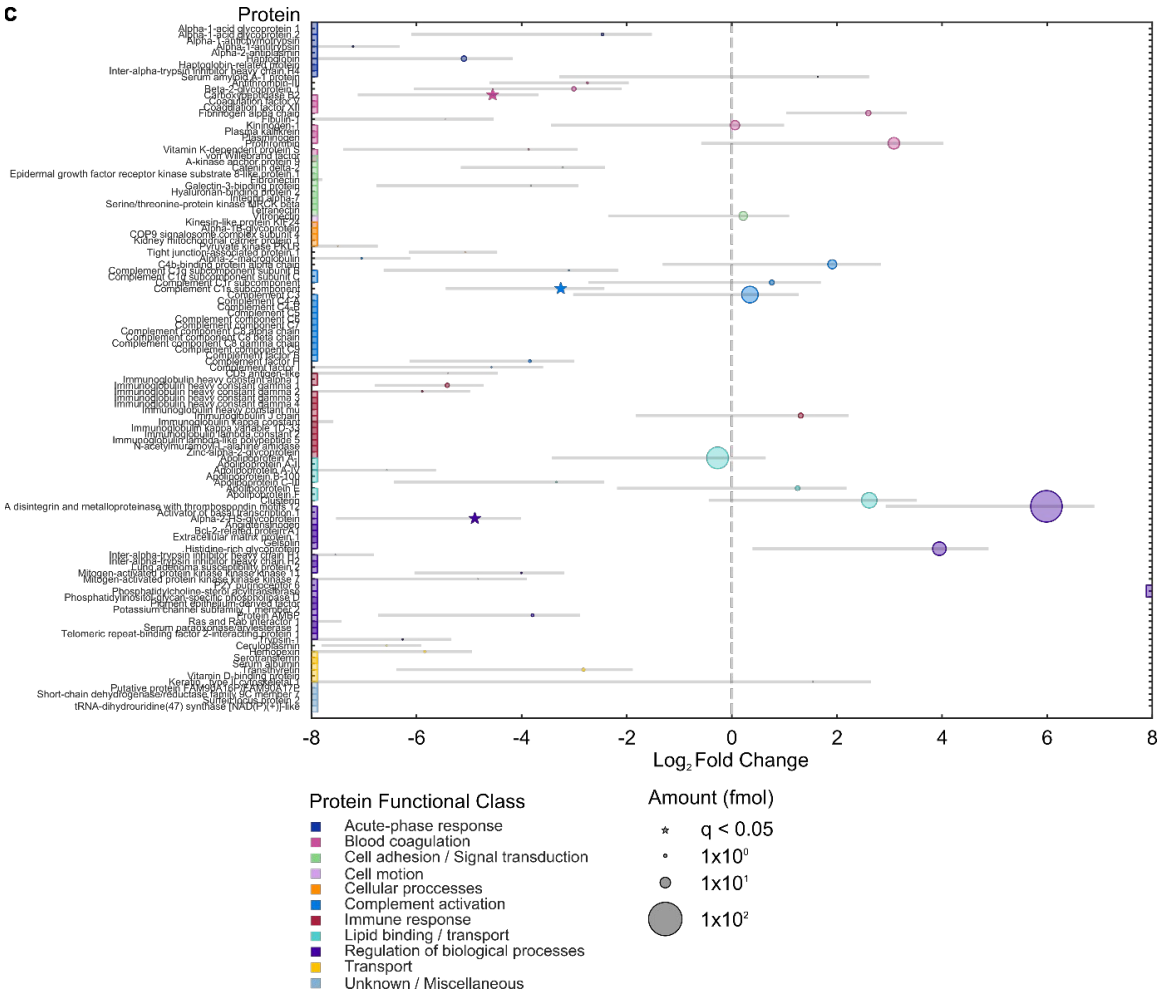

Figure 2-10. Blood plasma protein corona compositional map determined by proteomic mass spectrometry, full results. Protein corona formed from blood plasma on (a) PNPs, (b) $(GT)_{15}$-SWCNTs, and (c) $(GT)_6$-SWCNTs. Circle size corresponds to protein abundance (femtomolar). Proteins are grouped by functional class according to color (PANTHER).[212] Log_2 fold change is in comparison to the biofluid alone, e.g. log_2 fold change of zero indicates the same relative amount of protein exists in the corona as in bulk solution of the native biofluid, while < 0 is depletion and > 0 is enrichment. Names are included for proteins of interest or used for subsequent experiments. Colored boxes at x-axis limits indicate no protein detected in either corona ($x < 2^{-6}$ or 2^{-8}) or biofluid ($x > 2^8$). Error bars indicate standard error of fold change between experimental replicates (N = 3).

Table 2-5. Top 20 most abundant proteins identified by proteomic mass spectrometry in plasma $(GT)_{15}$-SWCNT and $(GT)_6$-SWCNT coronas.

	Plasma	**$(GT)_{15}$-SWCNTs in plasma**	**$(GT)_6$-SWCNTs in plasma**
1	Serum albumin	Clusterin	A disintegrin and metalloproteinase
2	Haptoglobin	Histidine-rich glycoprotein	Apolipoprotein A-I
3	Ig kappa constant	Apolipoprotein A-I	Complement C3
4	Ig heavy constant gamma	Complement C3	Clusterin
5	Serotransferrin	Haptoglobin	Histidine-rich glycoprotein
6	Apolipoprotein A-I	A disintegrin and metalloproteinase with thrombospondin motifs 12	Prothrombin
7	Complement C4	Complement C1r subcomponent	Kininogen-1
8	Telomeric repeat-binding factor 2-interacting protein	Vitronectin	C4b-binding protein alpha chain
9	Alpha-1-antitrypsin	Kininogen-1	Vitronectin
10	Alpha-2-HS-glycoprotein	Prothrombin	Haptoglobin
11	Apolipoprotein A-II	C4b-binding protein alpha chain	Fibrinogen alpha chain
12	Ig heavy constant alpha 1	Complement factor H	Ig J chain
13	Integrin alpha-7	Fibrinogen alpha chain	Complement C1r subcomponent
14	Alpha-2-macroglobulin	Protein AMBP	Apolipoprotein E
15	Complement C3	Beta-2-glycoprotein 1	Beta-2-glycoprotein 1
16	Complement C5	Apolipoprotein E	Ig heavy constant gamma 1
17	Hemopexin	Complement C1q subcomponent subunit B	Alpha-2-HS-glycoprotein
18	Alpha-1-acid glycoprotein 1	Ig heavy constant gamma 1	Transthyretin
19	Ig heavy constant mu	Ig J chain	Protein AMBP
20	Beta-2-glycoprotein 1	Galectin-3-binding protein	Alpha-1-acid glycoprotein 2

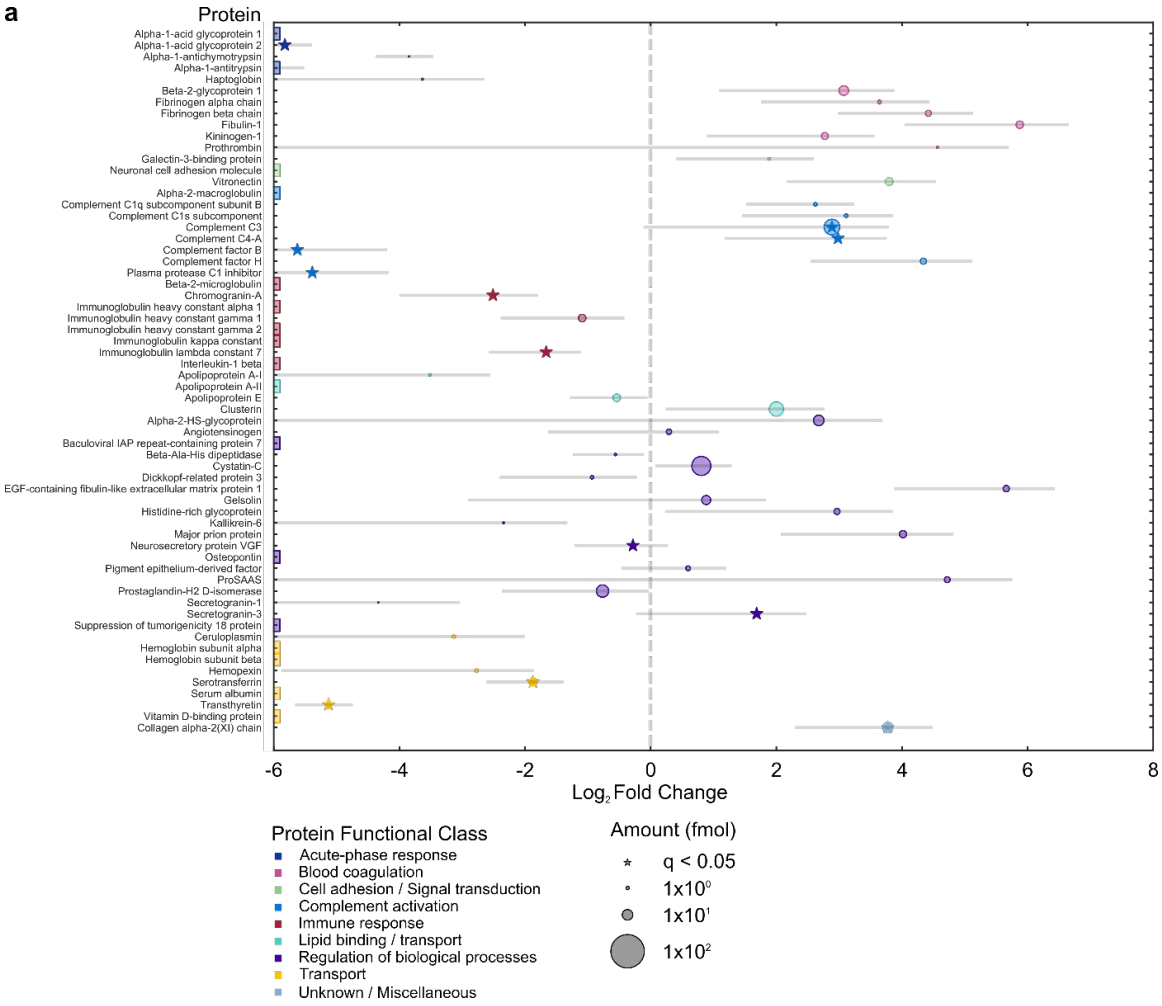
a
Protein
Alpha-1-acid glycoprotein 1
Alpha-1-acid glycoprotein 2
Alpha-1-antichymotrypsin
Alpha-1-antitrypsin
Haptoglobin
Beta-2-glycoprotein 1
Fibrinogen alpha chain
Fibrinogen beta chain
Fibulin-1
Kininogen-1
Prothrombin
Galectin-3-binding protein
Neuronal cell adhesion molecule
Vitronectin
Alpha-2-macroglobulin
Complement C1q subcomponent subunit B
Complement C1s subcomponent
Complement C3
Complement C4-A
Complement factor B
Complement factor H
Plasma protease C1 inhibitor
Beta-2-microglobulin
Chromogranin-A
Immunoglobulin heavy constant alpha 1
Immunoglobulin heavy constant gamma 1
Immunoglobulin heavy constant gamma 2
Immunoglobulin kappa constant
Immunoglobulin lambda constant 7
Interleukin-1 beta
Apolipoprotein A-I
Apolipoprotein A-II
Apolipoprotein E
Clusterin
Alpha-2-HS-glycoprotein
Angiotensinogen
Baculoviral IAP repeat-containing protein 7
Beta-Ala-His dipeptidase
Cystatin-C
Dickkopf-related protein 3
EGF-containing fibulin-like extracellular matrix protein 1
Gelsolin
Histidine-rich glycoprotein
Kallikrein-6
Major prion protein
Neurosecretory protein VGF
Osteopontin
Pigment epithelium-derived factor
ProSAAS
Prostaglandin-H2 D-isomerase
Secretogranin-1
Secretogranin-3
Suppression of tumorigenicity 18 protein
Ceruloplasmin
Hemoglobin subunit alpha
Hemoglobin subunit beta
Hemopexin
Serotransferrin
Serum albumin
Transthyretin
Vitamin D-binding protein
Collagen alpha-2(XI) chain
-6
-4
-2
0
2
4
6
8
Log2 Fold Change
Protein Functional Class
Acute-phase response
Blood coagulation
Cell adhesion / Signal transduction
Complement activation
Immune response
Lipid binding / transport
Regulation of biological processes
Transport
Unknown / Miscellaneous
Amount (fmol)
q < 0.05
1x10^0
1x10^1
1x10^2

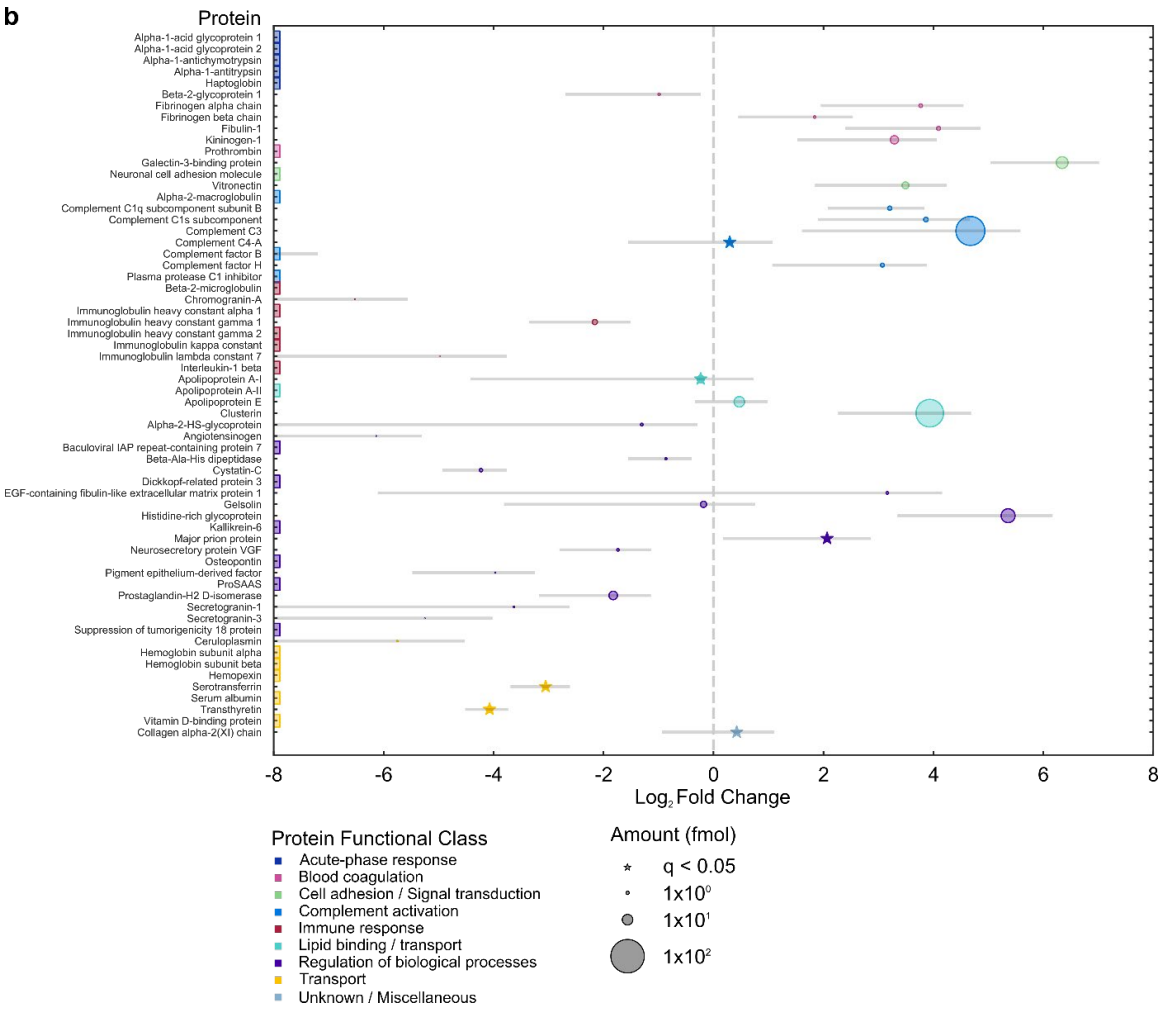

Figure 2-11. Cerebrospinal fluid (CSF) protein corona compositional map determined by proteomic mass spectrometry, full results. Protein corona formed from CSF on (a) PNPs and (b) $(GT)_{15}$-SWCNTs. Circle size corresponds to protein abundance (femtomolar). Proteins are grouped by functional class according to color (PANTHER).[212] Log_2 fold change is in comparison to the biofluid alone, e.g. fold change of zero indicates the same relative amount of protein exists in the corona as in bulk solution of the native biofluid, while < 0 is depletion and > 0 is enrichment. Names are included for proteins of interest or used for subsequent experiments. Colored boxes at x-axis limits indicate no protein detected in either corona ($x < 2^{-6}$ or 2^{-8}) or biofluid ($x > 2^{8}$). Error bars indicate standard deviation of fold change between technical replicates ($N = 3$).

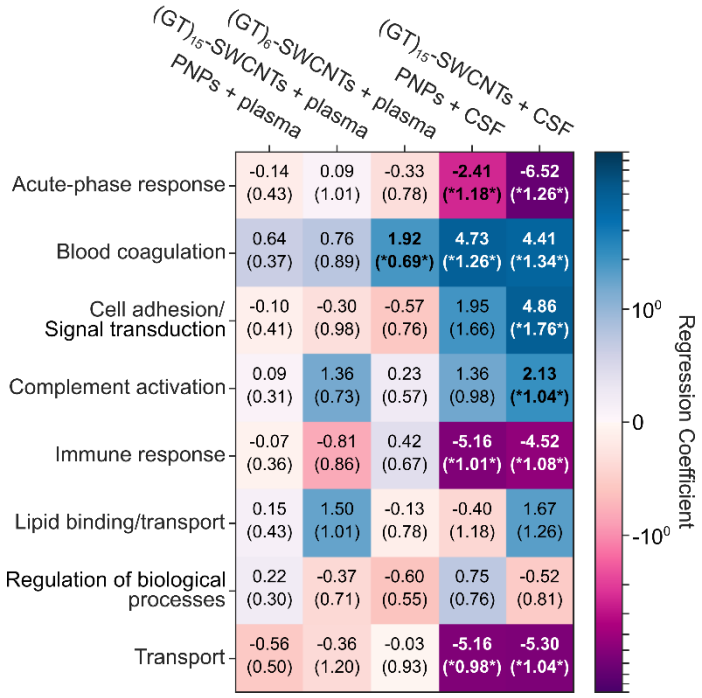

Figure 2-12. Role of protein functional class in protein corona formation for each nanoparticle-biofluid pairing. Ln-fold change, effect-coded regression coefficients of protein classes (rows) for each nanoparticle-biofluid pairing (columns). Cells are colored from dark purple (lower than the average fold change) to white (average fold change) to dark blue (higher than average fold change). Standard errors of the coefficients are given in parentheses. Results that have false-discovery-rate-corrected p-values of below 0.1 are bolded and noted with asterisks.

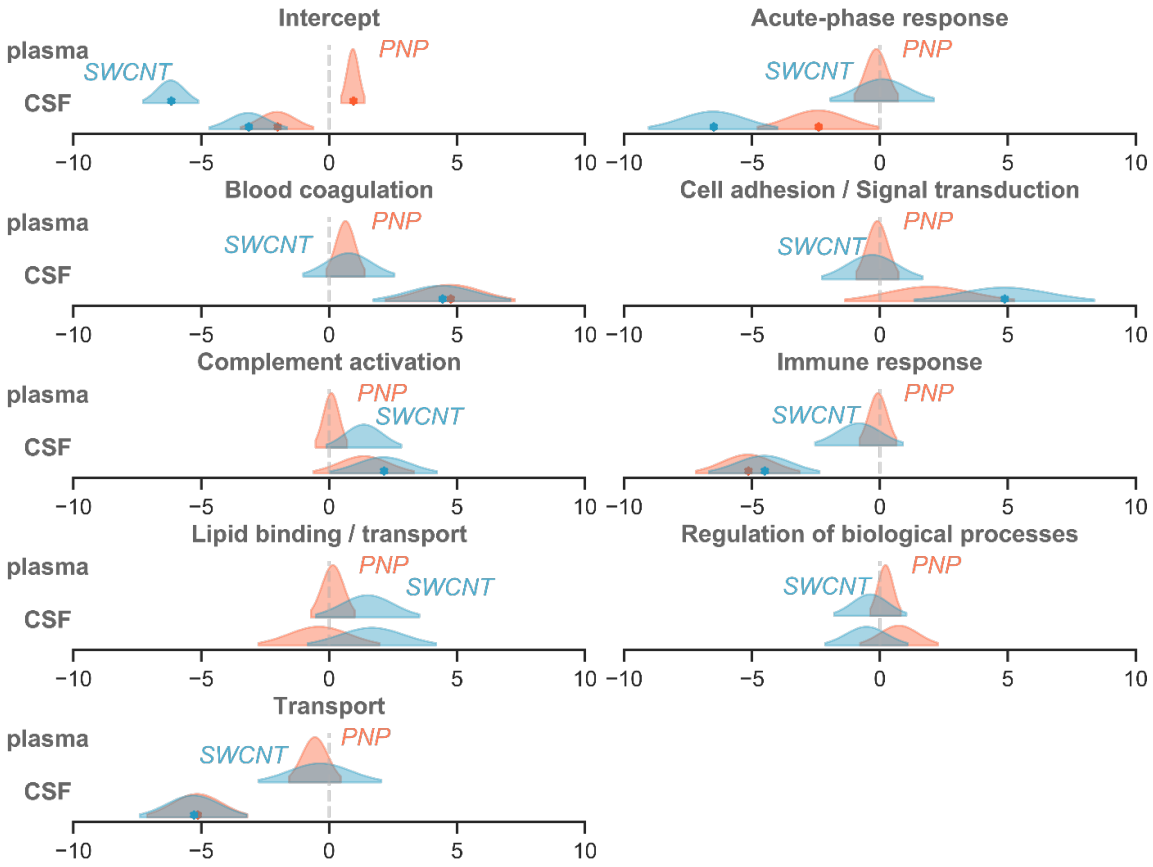

Figure 2-13. Distribution for protein class mean regression coefficients in each nanoparticle-biofluid pairing. Stars indicate false-discovery-rate adjusted p-values<0.1.

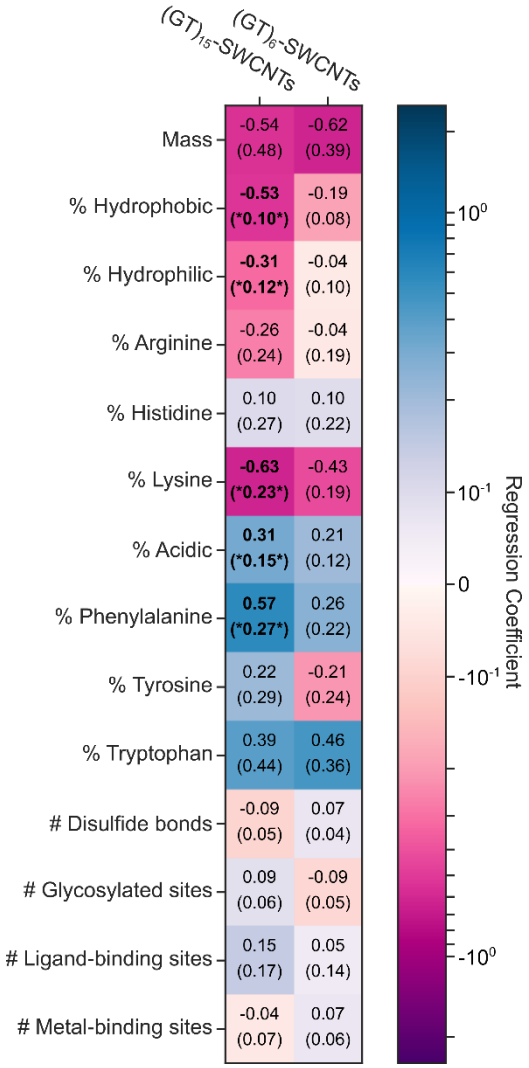

Figure 2-14. Molecular attributes of proteins that govern protein corona formation for $(GT)_x$-SWCNTs in plasma. Ln-fold change regression coefficients for molecular attributes of proteins (rows) for each nanoparticle-biofluid pairing (columns). Cells are colored from dark purple (negative effect on fold change) to white (no effect) to dark blue (positive effect). Standard errors of the coefficients are given in parenthesis. Results that have false-discovery-rate-corrected p-values below 0.1 are bolded and noted with asterisks. Amino acid groupings include: non-aromatic hydrophobic (sum of alanine, valine, isoleucine, leucine, and methionine content), hydrophilic (sum of serine, threonine, asparagine, glutamine content), and acidic (sum of aspartic acid and glutamic acid content).

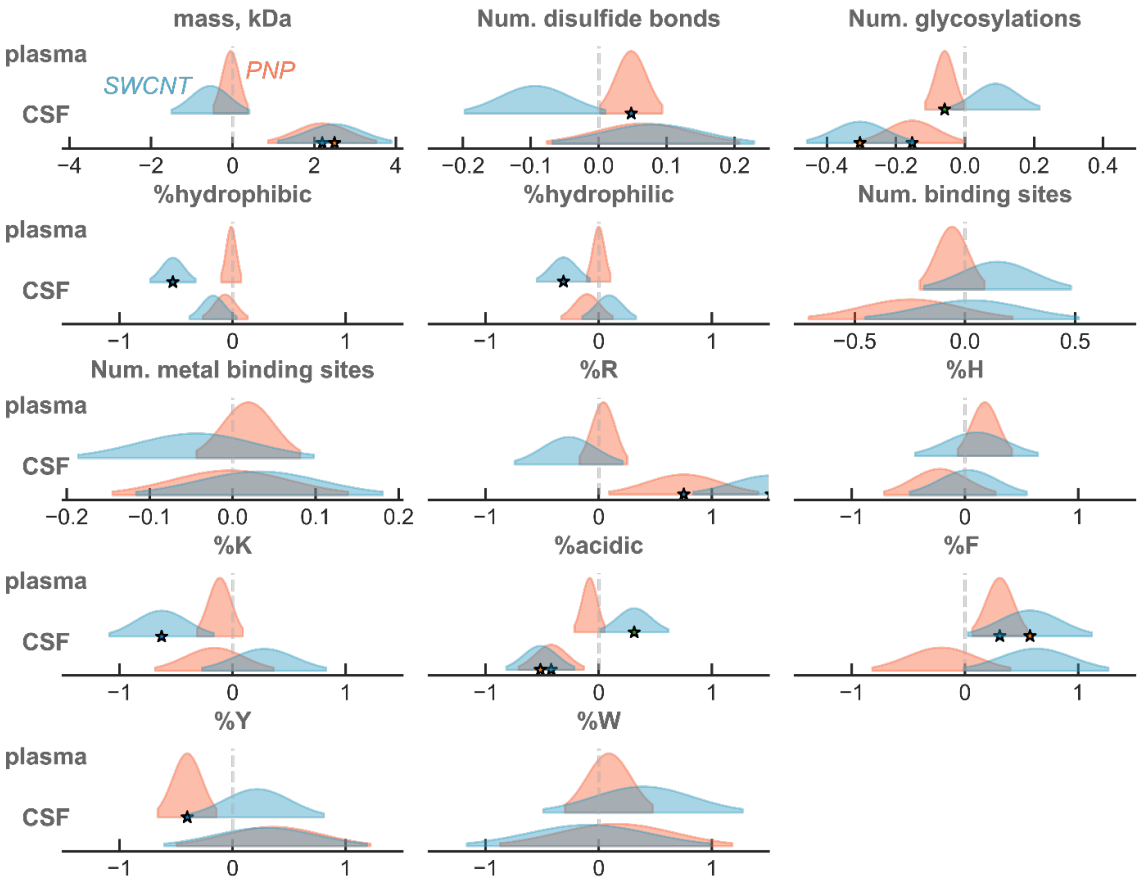

Figure 2-15. Distribution for microscale mean regression coefficients in each nanoparticle-biofluid pairing. Stars indicate false-discovery-rate adjusted p-values<0.1.

Table 2-6. Protein class regression results for each nanoparticle-biofluid pairing.

	PNPs in plasma			$(GT)_{15}$-SWCNTs in plasma		
	R-squared	**Adjusted R-squared**		**R-squared**	**Adjusted R-squared**	
	0.26	0.24		0.1	0.13	
	Parameter	**Standard Error**	**FDRC p-values**	**Parameter**	**Standard Error**	**FDRC p-values**
Intercept	0.9277	0.2270	0.0003	-6.1942	0.5380	0.0000
Sample 1	2.8743	0.3253	0.0000	4.0556	0.7711	0.0000
Sample 2	-0.0358	0.3146	0.9095	0.3037	0.7457	0.8412
Acute-phase response	-0.1393	0.4271	0.9095	0.0916	1.0124	0.9279
Blood coagulation	0.6394	0.3749	0.3267	0.7639	0.8887	0.7163
Cell adhesion / Signal transduction	-0.0981	0.4133	0.9095	-0.3003	0.9797	0.8412
Complement activation	0.0854	0.3086	0.9095	1.3564	0.7316	0.2372
Immune response	-0.0727	0.3620	0.9095	-0.8149	0.8580	0.7163
Lipid binding / transport	0.1467	0.4271	0.9095	1.5017	1.0124	0.3823
Regulation of biological processes	0.2203	0.2985	0.9095	-0.3749	0.7075	0.8412
Transport	-0.5563	0.5047	0.7460	-0.3584	1.1965	0.8412
	PNPs in CSF			$(GT)_{15}$-SWCNTs in CSF		
	R-squared	**Adjusted R-squared**		**R-squared**	**Adjusted R-squared**	
	0.32	0.28		0.35	0.31	
	Parameter	**Standard Error**	**FDRC p-values**	**Parameter**	**Standard Error**	**FDRC p-values**
Intercept	-2.0347	0.7108	0.0131	-3.1619	0.7551	0.0001
Sample 1	0.9624	0.8879	0.3850	-0.0962	0.9431	0.9939
Sample 2	0.8264	0.8915	0.3909	-0.0073	0.9470	0.9939
Acute-phase response	-2.4143	1.1830	0.0943	-6.5197	1.2566	0.0000
Blood coagulation	4.7294	1.2588	0.0009	4.4095	1.3371	0.0026
Cell adhesion / Signal transduction	1.9484	1.6552	0.3785	4.8610	1.7583	0.0117
Complement activation	1.3603	0.9806	0.3067	2.1252	1.0417	0.0675
Immune response	-5.1599	1.0141	0.0000	-4.5191	1.0772	0.0001
Lipid binding / transport	-0.3967	1.1830	0.7378	1.6716	1.2566	0.2548
Regulation of biological processes	0.7459	0.7590	0.3909	-0.5229	0.8062	0.6325
Transport	-5.1597	0.9806	0.0000	-5.3045	1.0417	0.0000

Table 2-7. Microscale regression results for each nanoparticle-biofluid pairing.

	PNPs in plasma			$(GT)_{15}$-SWCNTs in plasma		
	R-squared	**Adjusted R-squared**		**R-squared**	**Adjusted R-squared**	
	0.32	0.29		0.27	0.23	
	Parameter	**Standard Error**	**FDRC p-values**	**Parameter**	**Standard Error**	**FDRC p-values**
Intercept	2.7690	3.6300	0.7585	19.6116	8.2339	0.0607
Sample 1	2.8759	0.3147	0.0000	4.0662	0.7137	0.0000
Sample 2	-0.0427	0.3036	0.9436	0.3186	0.6886	0.6842
Mass	-0.0475	0.2109	0.9314	-0.5446	0.4785	0.4153
% hydrophobic residues (nonaromatic)	-0.0126	0.0442	0.9314	-0.5286	0.1003	0.0000
% hydrophilic residues	-0.0008	0.0520	0.9877	-0.3122	0.1179	0.0363
% arginine	0.0409	0.1051	0.9121	-0.2643	0.2385	0.4153
% histidine	0.1762	0.1197	0.4030	0.1028	0.2716	0.7053
% lysine	-0.1128	0.1015	0.5678	-0.6276	0.2302	0.0363
% acidic residues	-0.0806	0.0662	0.5447	0.3131	0.1502	0.0921
% phenylalanine	0.3077	0.1209	0.0648	0.5747	0.2743	0.0921
% tyrosine	-0.4013	0.1297	0.0184	0.2165	0.2942	0.5615
% tryptophan	0.0893	0.1940	0.9121	0.3912	0.4400	0.4942
Number of disulfide bonds	0.0477	0.0229	0.1288	-0.0938	0.0519	0.1527
Number of glycosylated sites	-0.0588	0.0280	0.1288	0.0885	0.0636	0.3124
Number of ligand binding sites	-0.0584	0.0736	0.7585	0.1473	0.1668	0.4942
Number of metal binding sites	0.0190	0.0313	0.8425	-0.0442	0.0710	0.6052
	PNPs in CSF			$(GT)_{15}$-SWCNTs in CSF		
	R-squared	**Adjusted R-squared**		**R-squared**	**Adjusted R-squared**	
	0.35	0.29		0.4	0.34	
	Parameter	**Standard Error**	**FDRC p-values**	**Parameter**	**Standard Error**	**FDRC p-values**
Intercept	-18.8198	9.7672	0.1897	-32.4292	10.2373	0.0063
Sample 1	0.7932	0.8845	0.5921	-0.4235	0.9271	0.8692
Sample 2	0.7215	0.8883	0.5921	-0.2622	0.9311	0.9097
Mass	2.1956	0.6640	0.0199	2.4973	0.6960	0.0025
% hydrophobic residues (nonaromatic)	-0.0670	0.0987	0.6048	-0.1726	0.1034	0.2361
% hydrophilic residues	-0.1034	0.1133	0.5921	0.0913	0.1187	0.7529
% arginine	0.7511	0.3295	0.1358	1.5253	0.3453	0.0003
% histidine	-0.2217	0.2464	0.5921	0.0293	0.2583	0.9097
% lysine	-0.1607	0.2616	0.6118	0.2798	0.2742	0.5836
% acidic residues	-0.4209	0.1441	0.0341	-0.5162	0.1511	0.0034
% phenylalanine	-0.2088	0.3052	0.6048	0.6294	0.3199	0.1441
% tyrosine	0.3624	0.4282	0.5921	0.2910	0.4488	0.8001
% tryptophan	0.1523	0.5128	0.8149	-0.0914	0.5375	0.9097
Number of disulfide bonds	0.0653	0.0708	0.5921	0.0801	0.0742	0.5836
Number of glycosylated sites	-0.1529	0.0733	0.1644	-0.3039	0.0769	0.0010
Number of ligand binding sites	-0.2462	0.2313	0.5921	0.0309	0.2424	0.9097
Number of metal binding sites	-0.0028	0.0709	0.9685	0.0323	0.0744	0.8692

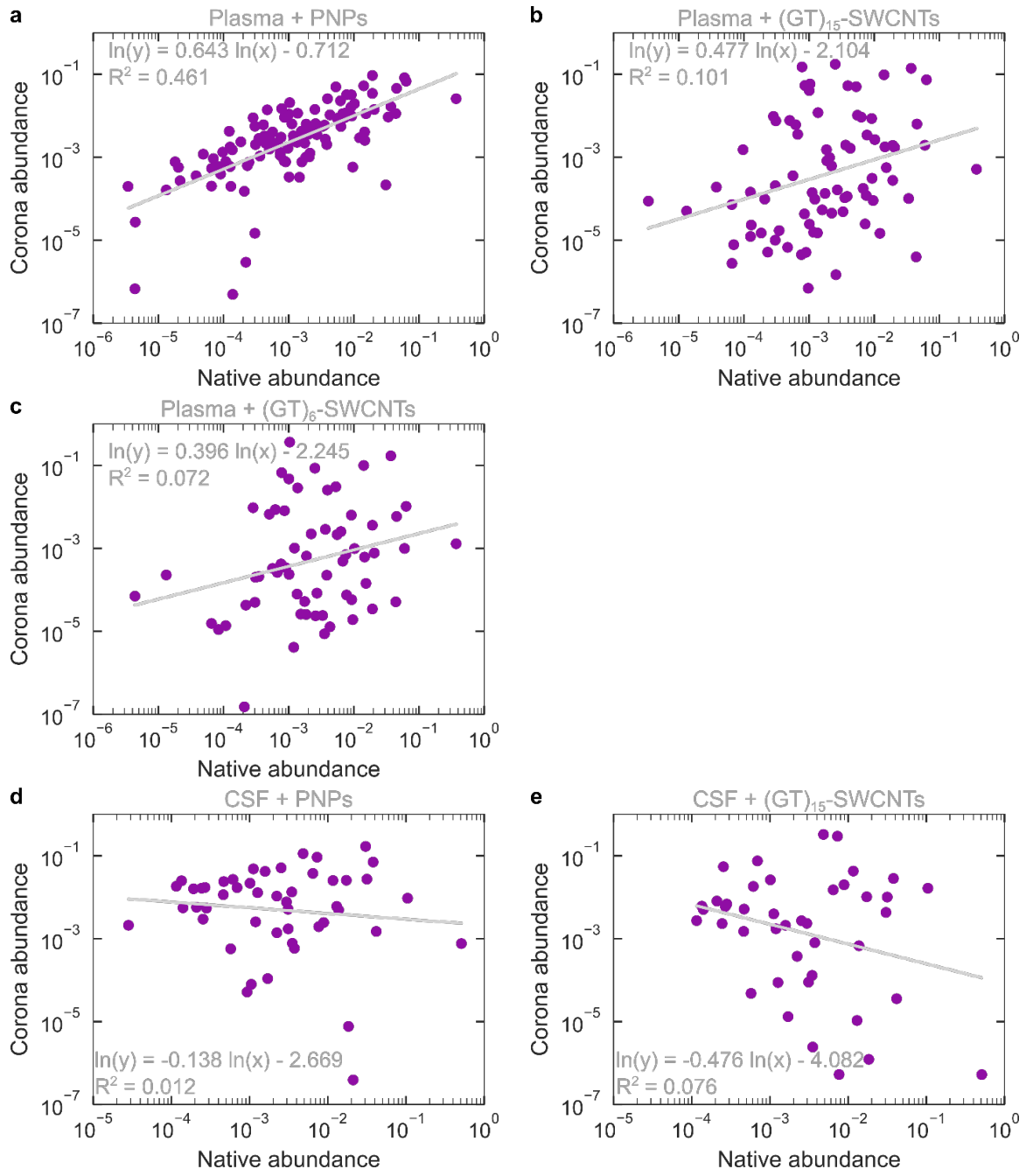
a
Plasma + PNPs
ln(y) = 0.643 ln(x) - 0.712
R² = 0.461
b
Plasma + (GT)15-SWCNTs
ln(y) = 0.477 ln(x) - 2.104
R² = 0.101
c
Plasma + (GT)6-SWCNTs
ln(y) = 0.396 ln(x) - 2.245
R² = 0.072
d
CSF + PNPs
ln(y) = -0.138 ln(x) - 2.669
R² = 0.012
e
CSF + (GT)15-SWCNTs
ln(y) = -0.476 ln(x) - 4.082
R² = 0.076
Corona abundance
Native abundance

Figure 2-16. Scaling of protein abundance in corona vs. in native biofluid. Protein mole fraction of plasma proteins in corona of (a) PNPs, (b) $(GT)_{15}$-SWCNTs, and (c) $(GT)_6$-SWCNTs, vs. protein mole fraction of plasma proteins in native biofluid. Corona abundance scaling is approximately linear for plasma proteins on PNPs ($R^2 = 0.461$) vs. highly scattered for $(GT)_{15}$-SWCNTs ($R^2 = 0.101$) and $(GT)_6$-SWCNTs ($R^2 = 0.072$). Protein mole fraction of CSF proteins in corona of (d) PNPs and (e) $(GT)_{15}$-SWCNTs vs. protein mole fraction of CSF proteins in native biofluid. Corona abundance displays a weak negative correlation with native abundance for CSF proteins on both PNPs ($R^2 = 0.012$) and $(GT)_{15}$-SWCNTs ($R^2 = 0.076$). All mole fractions are on a solvent-free basis. Note that proteins with zero corona abundance are excluded from the analysis for clarity, but the same conclusions hold when included.

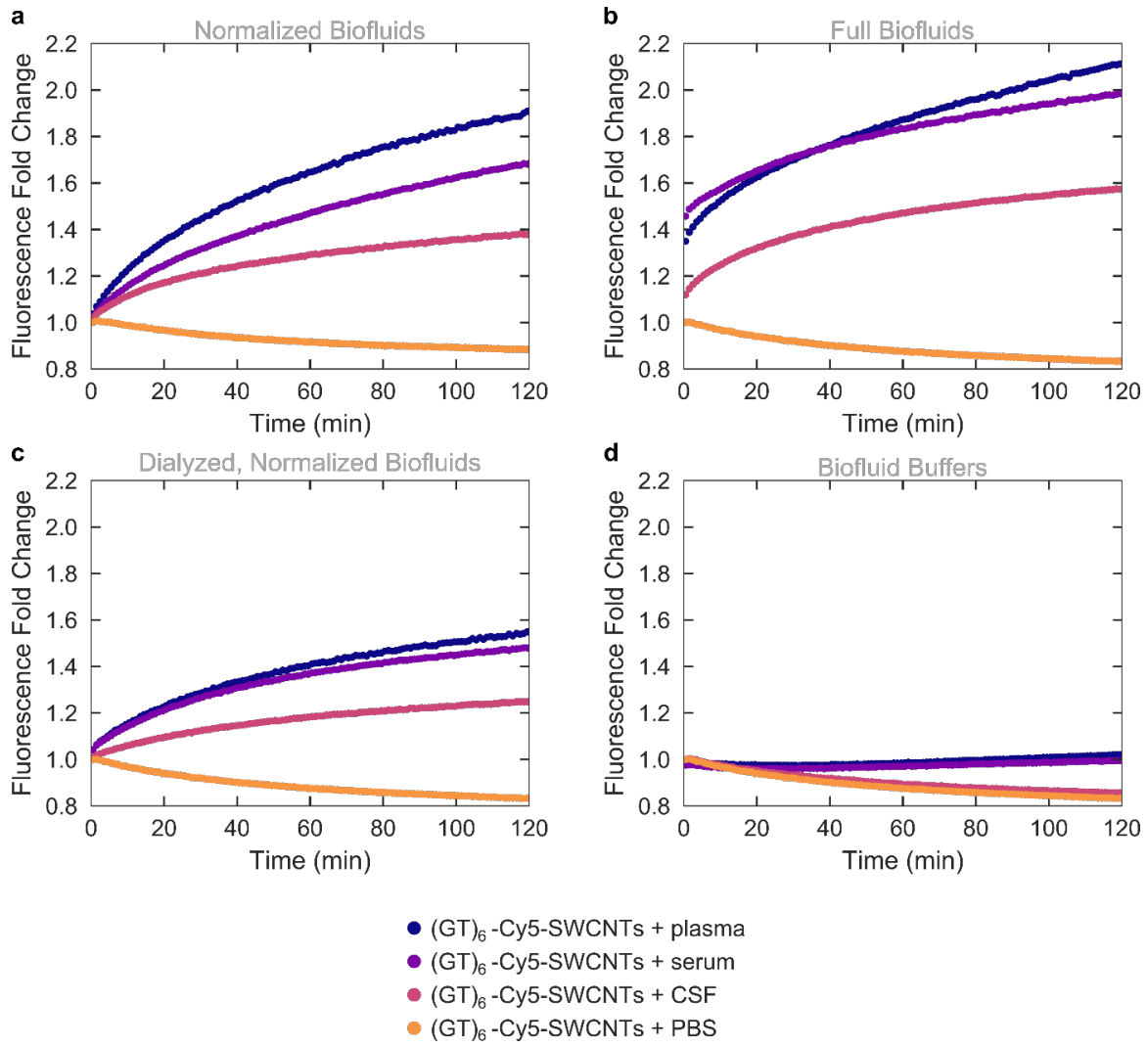

Figure 2-17. Protein corona dynamics assessed for binding of proteins in varying biofluids to $(GT)_6$-SWCNTs. A corona exchange assay is employed to track binding of proteins from the biofluids: blood plasma, blood serum, and cerebrospinal fluid (CSF) to $(GT)_6$-Cy5-SWCNTs (5 mg L^{-1} final concentration). ssDNA desorption from SWCNTs is observed as increasing fluorescence of Cy5-labeled $(GT)_6$, and taken as a proxy for protein binding.[118] (a) Biofluids normalized to 40 mg L^{-1} final protein concentration. (b) Biofluids injected as full, as-received solutions. (c) Biofluids dialyzed, with > 3 kDa portion re-suspended in PBS and normalized to 40 mg L^{-1} final protein concentration. (d) Biofluids dialyzed, with < 3 kDa portion considered the biofluid buffer. Data points are the average of experimental replicates (N = 3).

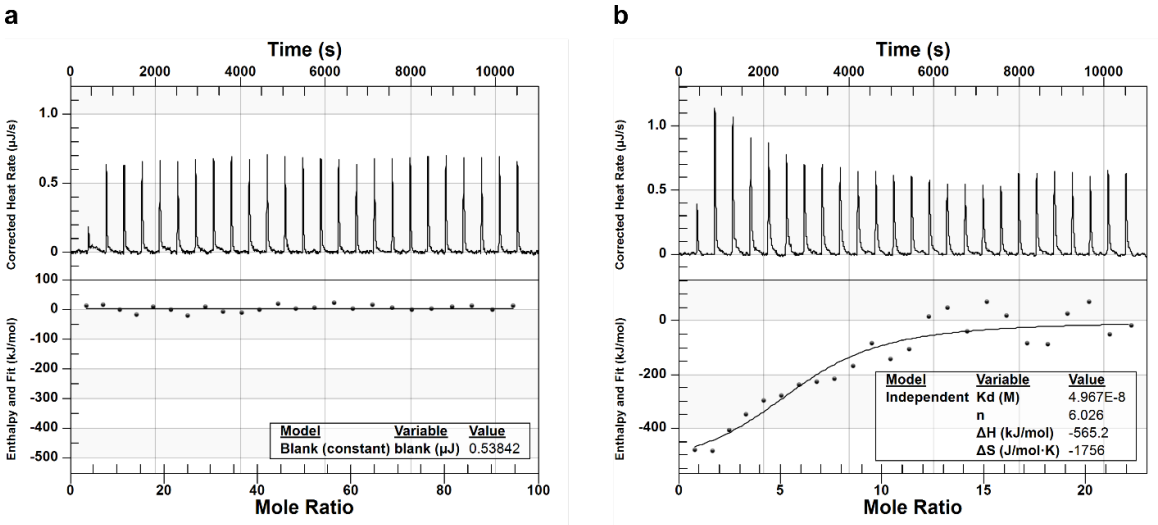

Figure 2-18. Protein corona thermodynamics assessed with ITC for binding of key proteins to $(GT)_{15}$-SWCNTs. Isothermal titration calorimetry (ITC) is employed to determine binding thermodynamics of (a) albumin and (b) fibrinogen to $(GT)_{15}$-SWCNTs. Albumin does not bind to $(GT)_{15}$-SWCNTs within experimentally accessible limits of this instrument, whereas fibrinogen does, in agreement with the corona compositional analyses from proteomic mass spectrometry and gel electrophoresis.

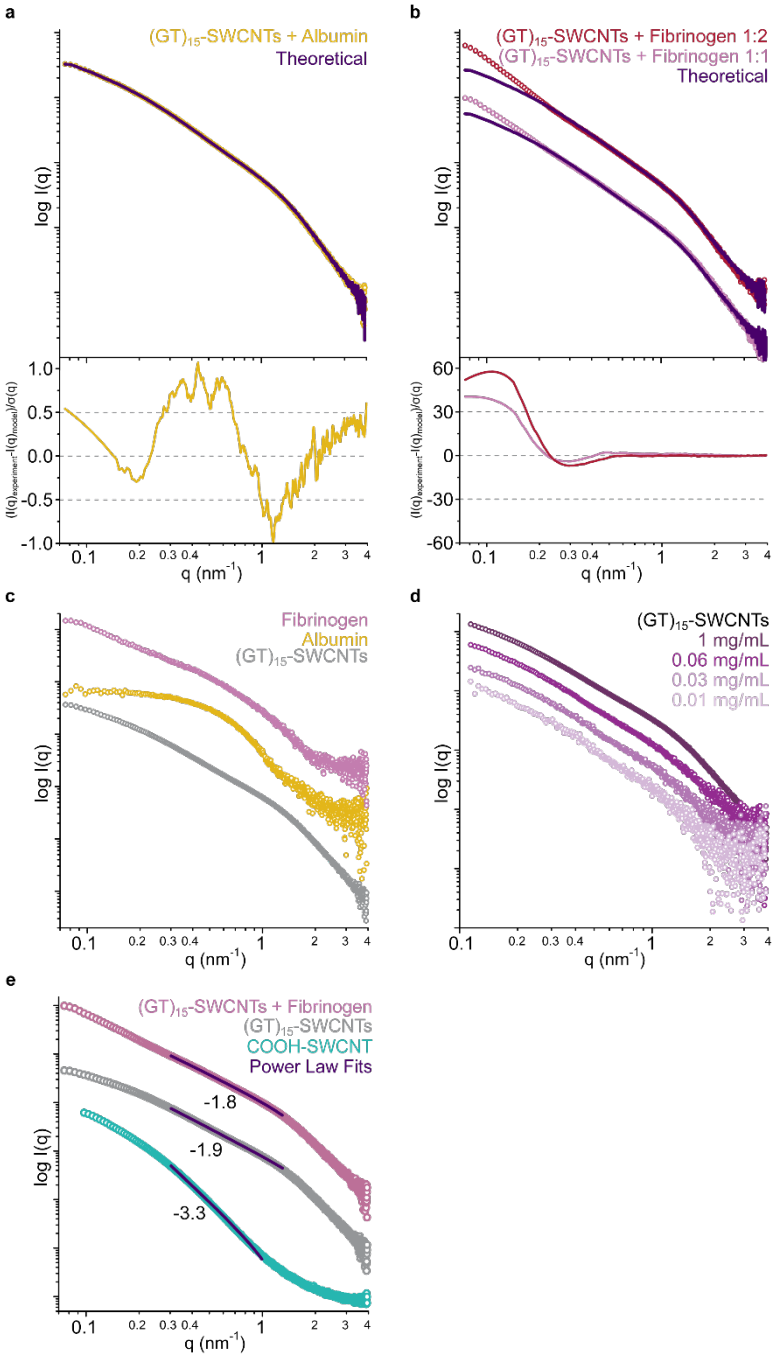
a
(GT)15-SWCNTs + Albumin
Theoretical
log I(q)
1.0
0.5
0.0
-0.5
-1.0
0.1
0.2
0.3
0.4
1
2
3
4
q (nm-1)
b
(GT)15-SWCNTs + Fibrinogen 1:2
(GT)15-SWCNTs + Fibrinogen 1:1
Theoretical
log I(q)
60
30
0
-30
-60
c
Fibrinogen
Albumin
(GT)15-SWCNTs
log I(q)
d
(GT)15-SWCNTs
1 mg/mL
0.06 mg/mL
0.03 mg/mL
0.01 mg/mL
log I(q)
e
(GT)15-SWCNTs + Fibrinogen
(GT)15-SWCNTs
COOH-SWCNT
Power Law Fits
-1.8
-1.9
-3.3
log I(q)

Figure 2-19. Protein corona structure assessed with SAXS for binding of key proteins to $(GT)_{15}$-SWCNTs. The linear combination of respective standard curves from panel c in purple and fit-residuals below, fit against the curves produced by the potential complexes of $(GT)_{15}$-SWCNTs with (a) albumin or (b) fibrinogen, at two different ratios of $(GT)_{15}$-SWCNTs to fibrinogen (1:1 is 0.5 g L^{-1} final concentrations of $(GT)_{15}$-SWCNTs and fibrinogen; 1:2 is 0.25 g L^{-1} $(GT)_{15}$-SWCNTs and 0.5 g L^{-1} fibrinogen). (c) Experimental SAXS profiles for standards of albumin, fibrinogen, and $(GT)_{15}$-SWCNTs alone, at identical concentrations to the mixing experiments (all 0.5 g L^{-1}). (d) SAXS profiles for concentration series of $(GT)_{15}$-SWCNTs alone, 0.01 – 1 g L^{-1}. (e) SAXS profiles fit to show power law dependencies in the Porod regions, including the COOH-SWCNT control without surface-adsorbed ssDNA.

Table 2-8. SAXS mass fractal modeling parameters.

Sample	Radius (nm)	Fractal Dimension (*Dm*)	Cutoff Length (nm)
$(GT)_{15}$-SWCNTs + Fibrinogen	1.05 ± 0.003	1.77	103.34 ± 9.70
$(GT)_{15}$-SWCNTs + Albumin	1.05 ± 0.003	1.90	10.60 ± 0.05
$(GT)_{15}$-SWCNTs	1.01 ± 0.002	1.89	10.91 ± 0.04

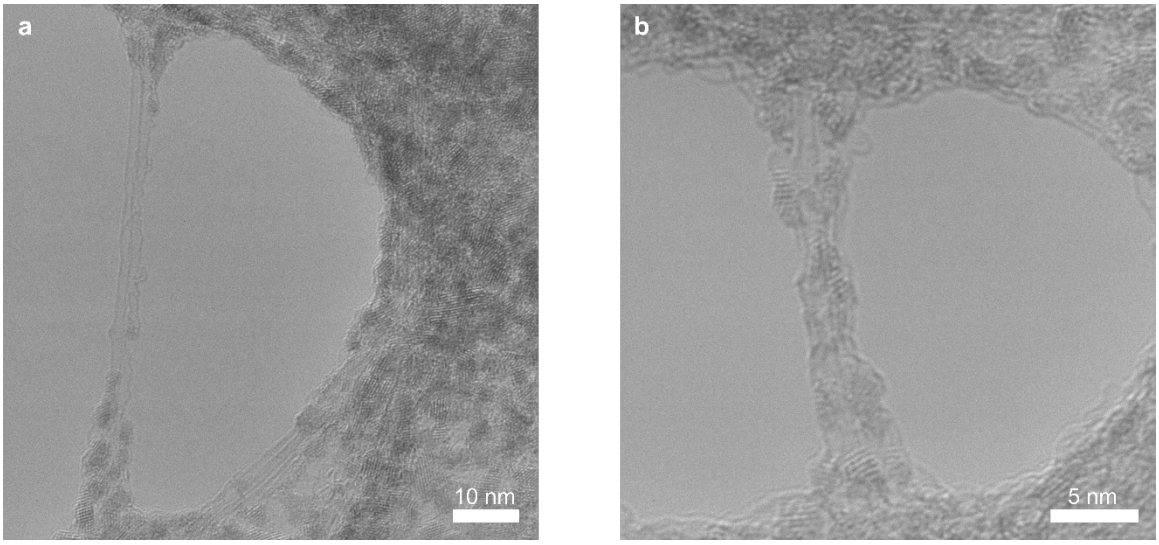

Figure 2-20. Protein corona morphology visualized by TEM for adsorption of plasma proteins to $(GT)_{15}$-SWCNTs. Transmission electron microscopy (TEM) of (a) plasma protein corona and (b) fibrinogen corona on $(GT)_{15}$-SWCNTs.

It is worth noting that the $(GT)_{15}$-SWCNTs alone seemingly exist in loose bundles, as they are still highly fluorescent at these elevated concentrations (Figure 2-21).[218] In the presence of blood plasma, these bundles seem to associate to higher order aggregates, yet remain loosely bound because the fluorescence persists (Figure 2-22) with minimal peak broadening in the absorbance spectra (Figure 2-23), indicating no inter-SWCNT energy transfer mechanisms. This finding is

reasonable in reference to previous work in which ssDNA-suspended SWCNTs persist as fluorescent, loosely packed aggregates after cell incubation.[219]

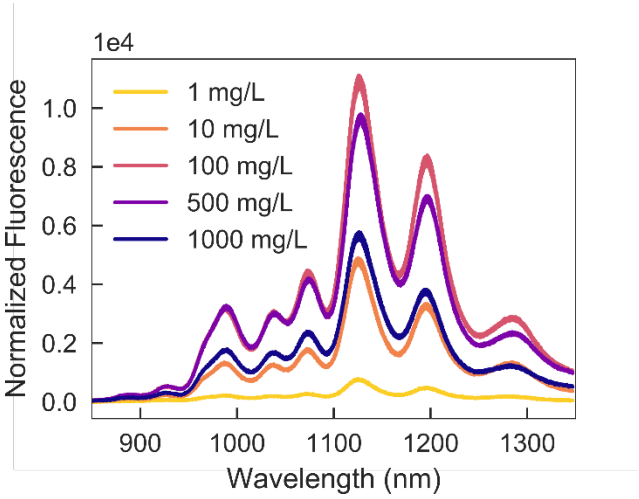

Figure 2-21. $(GT)_{15}$-SWCNTs continue to exhibit near-infrared fluorescence at high concentration. Fluorescence spectra were collected with varying concentrations of $(GT)_{15}$-SWCNTs in 0.1 M PBS.

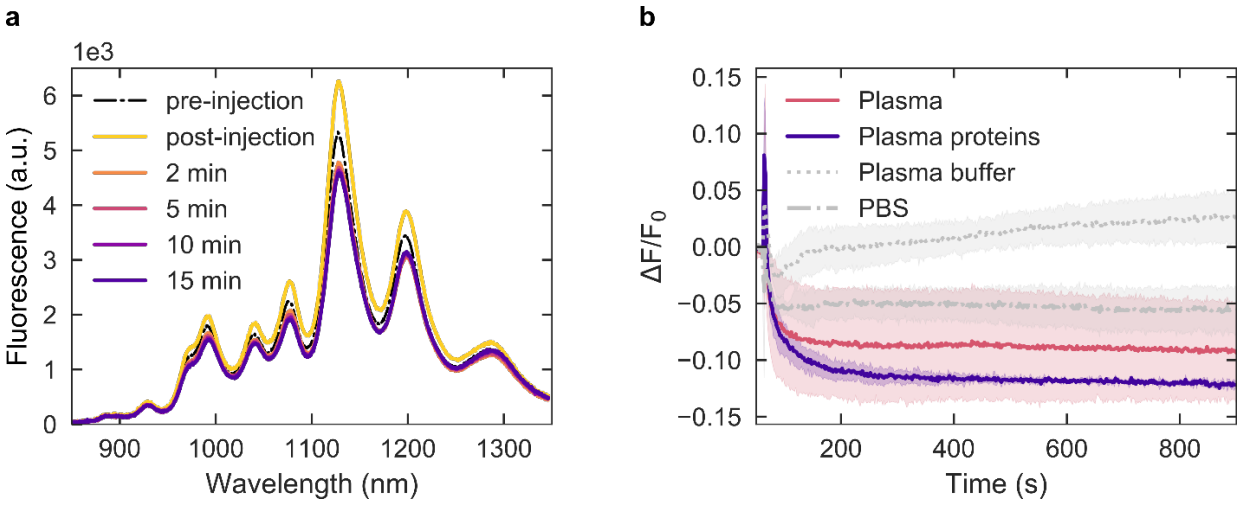

Figure 2-22. Protein corona formation impacts $(GT)_{15}$-SWCNT near-infrared fluorescence. Fluorescence spectra were collected over 15 minutes upon addition of 10% v/v plasma into 30 mg/L $(GT)_{15}$-SWCNTs in 0.1 M PBS. (a) Near-infrared spectra pre- and post-injection of plasma. (b) Integrated fluorescence fold-change for injection of plasma (10% v/v), plasma proteins (10% v/v in PBS), plasma buffer (< 3 kDa solution), and 0.1 M PBS into 30 mg/L $(GT)_{15}$-SWCNTs in 0.1 M PBS. Presence of the plasma proteins, rather than differing buffer conditions, attenuates the fluorescence signal.

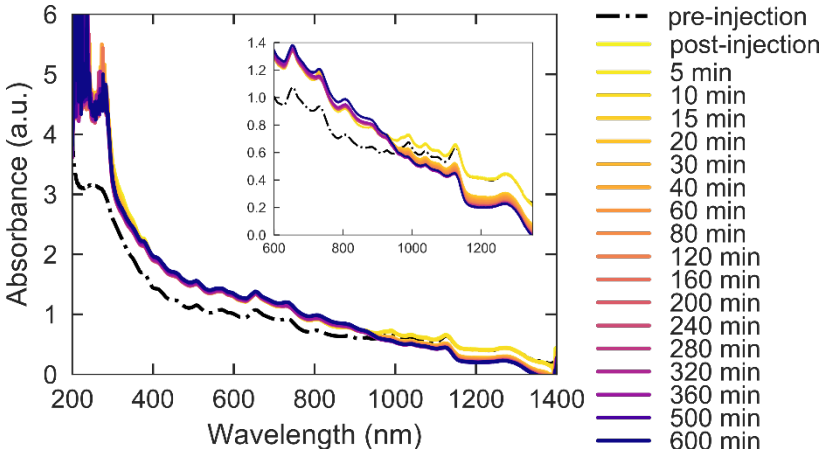

Figure 2-23. Turbidity assay reveals changing $(GT)_{15}$-SWCNT absorbance due to plasma corona formation. Absorbance spectra of $(GT)_{15}$-SWCNTs collected pre- and post-injection of plasma into solution, over a total of 10 hours with no agitation. $(GT)_{15}$-SWCNT and protein concentrations were identical to modified pull-down assay conditions (30 mg/L $(GT)_{15}$-SWCNTs with 3% v/v plasma). Immediately after injection, visible absorbance increased due to scattering of suspended particles and proteins (Tyndall effect). Near-infrared absorbance first remains static then drops at 15 minutes, indicating protein corona-induced aggregation is quenching the near-infrared optical transitions of the SWCNTs. Negligible peak-broadening implies the formation of loose aggregates. Inset is zoomed-in to transition at 955 nm between absorbance increase and decrease relative to pre-injection value.

2.6.2 Extended Discussion on Protein Corona Constituents Identified by Proteomic Mass Spectrometry

Albumin composes 55% (w/v) of proteins in blood plasma, corresponding to 35-50 g L^{-1},[220] and is often assumed to comprise a representative constituent in nanoparticle protein coronas. In consequence, many nanotechnologies are tested for functionality in serum instead of plasma.[1,47,48] Although albumin alone has been known to disperse SWCNTs in aqueous solution under sonication conditions,[53,223] here we note that albumin is likely unable to outcompete higher affinity proteins when in the presence of a complex biofluid. Accordingly, we hypothesize that albumin plays a minimal role in the full plasma protein corona and subsequent *in vivo* trafficking and fate.

The most highly enriched plasma protein, histidine-rich glycoprotein (107-fold enrichment), has been found as a representative plasma corona protein in prior studies on silica nanoparticles and is hypothesized to interact with other plasma proteins to enter the corona.[47] Another greatly enriched plasma protein, unreported in prior carbon nanoparticle corona literature, is 'a disintegrin and metalloproteinase with thrombospondin motifs 12' (ADAMTS12), which appeared in high abundance on both $(GT)_{15}$-SWCNTs (6^{th} highest abundance) and $(GT)_6$-SWNCTs (1^{st} highest abundance). ADAMTS12 is a metalloprotease with a zinc cofactor thought to possess anti-tumorigenic properties and to play a role in cell adhesion, pointing to potential applications in protein-SWCNT construct design.

Plasma proteins displaying high abundance and enrichment on $(GT)_{15}$-SWCNTs have functional roles in (i) lipid binding/transport (150% fold change over the average of all protein classes) and (ii) complement activation (140% fold change) (Figure 2-1 and Figure 2-12). A key example of a lipid binding/transport corona protein is clusterin (a.k.a. apolipoprotein J) as the most abundant plasma protein in the $(GT)_{15}$-SWCNT corona (38-fold enrichment), adsorption of which has shown promise in reducing non-specific cellular uptake of other types of nanocarriers.[173] Apolipoproteins broadly act as dysopsonins that promote prolonged circulation in the blood.[47] Hydrophobic interactions are posited to drive apolipoprotein adsorption in mimicry of native functions, such as apolipoprotein A-I (3rd most abundant) that binds and transports hydrophobic fats through aqueous environments.[56,177] We expect apolipoprotein binding, including clusterin and apolipoprotein A-I, to have a considerable impact on intracellular trafficking and fate of nanoparticles *in vivo*.[58,224] Regarding group (ii), complement C3 is the 4th most abundant plasma protein on $(GT)_{15}$-SWCNTs, with a 14-fold enrichment. This result is in agreement with previous literature that SWCNTs activate the complement system.[177,178,225] Binding of complement proteins leads to nanoparticle opsonization if the bound proteins are intact, which could be useful in developing targeted therapies, yet detrimental if longer bloodstream circulation time is desired.[46,47] The ssDNA-SWCNT surface may present an array of adsorbed corona proteins that the complement system deems as "foreign", thus activating complement systems and leading the coated SWCNT to act as an adjuvant that increases immune response. Complement proteins may bind either directly to the SWCNT surface (as was found for complement component 1q, or C1q, on double-walled carbon nanotubes[177]), or interact with other plasma proteins adsorbed on the SWCNT (where, for example, C1q binds to immunoglobulins, IgG and IgM, or fibronectin). Unfortunately, even a low degree of C1q binding can activate the complement system due to the amplification steps involved in the pathway. Yet, if the SWCNT serves to either locally sequester proteins that initiate complement activation (such as complement C3, 4th most abundant) or the corona contains down-regulators in their native state (such as complement factor H, 12th most abundant), this could in turn bypass recognition and complement activation. In contrast to the high representation of complement proteins in the corona that serve a role in the innate immune response, it is interesting to note the low corona representation of immunoglobulins (81% lower fold change than average, proteins involved in the adaptive immune response.

In addition to groups (i) and (ii), blood coagulation proteins are enhanced 76% on $(GT)_{15}$-SWNCTs in plasma, but the wide distribution of regression coefficients for these proteins precludes making statistically significant conclusions about this class (Figure 2-13). A notable enriched blood coagulation protein is fibrinogen, with 19-fold enrichment in the $(GT)_{15}$-SWCNT corona relative to concentrations in plasma. Fibrinogen's presence in the corona is unfavorable, as fibrinogen is responsible for eliciting inflammatory responses and nanoparticle aggregation.[47,50,158] Fibrinogen is a large rod-like multimeric protein with alpha, beta, and gamma subunits. Although identified on 2D PAGE, fibrinogen beta and gamma chains were absent from not only the nanoparticle-biofluid LC-MS/MS results, but also the native plasma samples. Additionally, there was no improvement using elution with 5% SDS, 50mM TEAB and purification with the S-trap mini column (Protifi). However, the fibrinogen alpha chain was present and enriched from plasma. Based on the reproducible involvement of fibrinogen in the corona from 2D PAGE results and representation of the alpha chain in LC-MS/MS results, fibrinogen was concluded to bind to $(GT)_{15}$-SWCNTs.

2.6.3 Connecting Linear Regression Model to Thermodynamics

The ideal solution chemical equilibrium constant K_P of a protein in bulk solution P adsorbing onto a nanoparticle into the protein corona P^* is equal to the ratio of the surface concentration of the protein on the nanoparticle Γ_P to the concentration of the protein in solution c_P: [226]

$$K_P = \frac{\Gamma_P}{c_P} \tag{2-3}$$

The logarithm of the chemical equilibrium constant is related to ΔG_P^o, the change in standard state Gibbs free energy for a protein adsorbing from solution to the nanoparticle surface,[226]

$$\ln K_{\mathrm{P}} = -\frac{\Delta G_P^o}{RT} \tag{2-4}$$

where R is the ideal gas constant and T is temperature. The molar abundances of P measured by LC-MS/MS from the native biofluid, n_P^f, and eluted from the nanoparticle surface, n_P^s, are related to c_P and Γ_P according to:

$$c_P = \frac{n_P^f f_P^f}{V} \tag{2-5}$$

$$\Gamma_P = \frac{n_P^s f_P^s}{S} \tag{2-6}$$

where V is the volume and S is the total surface area of the nanoparticle in the nanoparticle-biofluid solution. f_P^f and f_P^s are the fraction of moles of P that enter the LC-MS/MS relative to amount in the fluid and on the nanoparticle surface, respectively. Dilution and steps in isolating the protein-nanoparticle complexes cause f_P^f and f_P^s to vary from unity. This analysis neglects changes to the solution protein concentration due to corona formation. Rearrangement puts the LC-MS/MS measured log-fold change, $\ln(n_P^s/n_P^f)$, in terms of dilution factors and free energy changes:

$$\ln\left(\frac{n_P^s}{n_P^f}\right) = -\ln\left(\frac{V f_P^s}{S f_P^f}\right) - \frac{\Delta G_P^o}{RT} \tag{2-7}$$

In comparison, linear regression of the log-fold change gives:

$$\ln\left(\frac{n_P^s}{n_P^f}\right) = \beta_0 + \sum_{i=1} \beta_i X_{i,P} + \epsilon_P \tag{2-8}$$

where β_i is a regression coefficient corresponding to $X_{i,P}$, the ith independent variable of protein P, and ϵ_P is the disturbance term that accounts for any factors other than $X_{i,P}$ controlling the fold changes.[211] Because LC-MS/MS sample preparation should not impact proteins differently, f_P^s and

f_P^f are the same for all proteins for a set nanoparticle-biofluid system. Consequently, we can relate the chemical and statistical parameters:

$$\beta_0 = -\ln\left(\frac{V f_P^s}{S f_P^f}\right) \quad 2\text{-}9$$

$$\sum_{i=1} \beta_i X_{i,P} + \epsilon_P = -\frac{\Delta G_P^o}{RT} \quad 2\text{-}10$$

The regression coefficients β_i, therefore, relate the protein properties X_i to the Gibbs free energy change of proteins binding to the nanoparticle ΔG_P^o.

2.6.4 Extended Discussion on ITC

ITC was employed to extract relative binding parameters of protein-nanoparticle association. ITC was performed at constant pressure such that the heat absorbed or released is equivalent to the change in enthalpy (ΔH^o) upon binding. The binding curve can be fit to determine the equilibrium dissociation constant (K_d) and molar binding stoichiometry (n). This enables subsequent calculation of changes in standard state Gibbs free energy (ΔG^o) and entropy (ΔS^o) as follows:

$$\Delta G^o = RT\ln K_d = \Delta H^o - T\Delta S^o \quad 2\text{-}11$$

where R is the ideal gas constant and T is temperature. The optimized run parameters to measure heats of binding for this system require relatively high protein and nanoparticle concentrations: for each run, 10 µL of 1.2 g L^{-1} protein was added for each of 24 injections from the syringe into 1 mL of 0.1 g L^{-1} $(GT)_{15}$-SWCNTs in the cell. At these concentrations, addition of fibrinogen causes visible sample aggregation, presumably due to polymer bridging interactions of proteins adsorbed on one nanoparticle interacting with another nanoparticle. One of the key assumptions of ITC is that the system is equilibrated during each titration step. Yet, aggregation is a kinetically controlled, non-equilibrium process. As the key assumption is not held, these binding values are actually the convolution of protein binding to individual SWCNTs, fibrinogen binding to aggregated SWCNTs, and SWCNTs aggregating. We can compensate for this limitation in data processing by applying the Lumry-Eyring model,[227] in which an equilibrium reaction is coupled to a self-association reaction (i.e. aggregation), and the heats measured are separated out accordingly. This encompasses subtracting out baseline aggregation heats and arriving at an apparent binding heat. Therefore, the thermodynamic parameters are reported with consideration of these higher order processes taking place simultaneously. A further note is that baseline drift/shift were observed during these ITC experiments involving $(GT)_{15}$-SWCNTs. These changes in baseline often indicate slow non-equilibrium processes in action, further confirming the presence of aggregation. In conclusion, ITC is not a suitable methodology to study nanoparticle-protein corona formation for all systems, and these limitations must be considered during experimental design and reporting of results.

2.6.5 Extended Experimental and Modeling Details and Discussion on SAXS

Experimental SAXS profiles were collected for 0.5 g L^{-1} $(GT)_{15}$-SWCNTs with and without albumin or fibrinogen, each at 0.5 g L^{-1} final concentrations (Figure 2-5c). The linear combination of $(GT)_{15}$-SWCNTs and albumin standard curves produced a SAXS profile identical to the mixed sample of $(GT)_{15}$-SWCNTs with albumin, suggesting no interaction between the species. Dissimilarly, no calculated linear combination of the $(GT)_{15}$-SWCNTs and fibrinogen standard curves could be produced to fit the SAXS profiles of the mixed sample, indicating formation of unique form factors and thus complexation. Additionally, a clear concentration dependence is observed with an increase in the ratio of fibrinogen to $(GT)_{15}$-SWCNTs by two-fold, while albumin shows no additional binding at elevated concentrations (Figure 2-19a-b). Control SAXS profiles of albumin, fibrinogen, and $(GT)_{15}$-SWCNTs alone were collected at identical concentrations to those of the mixing experiments (Figure 2-19c). Data was collected at elevated concentrations (0.5 g L^{-1} both protein and $(GT)_{15}$-SWCNTs) to enhance SAXS signal, however, a concentration series was also performed for $(GT)_{15}$-SWCNTs to ensure that the scattering profiles do not deviate under more relevant nanoparticle conditions down to 0.01 g L^{-1} (Figure 2-19d).[41]

All $(GT)_{15}$-SWCNT samples with and without proteins were determined to be intrinsically disordered and experimental SAXS profiles were accordingly fit using mass fractal geometries. These fits were complemented by calculating power-law dependencies from the Porod region, and were both calculated using the SasView software package (www.sasview.org). Scattering intensity as a function of scattering vector $I(q)$ calculations for the mass fractal modeling (Figure 2-5) was done as follows:[228]

$$I(q) = \text{scale} * P(q)S(q) + \text{background} \tag{2-12}$$

$$P(q) = F(qR)^2 \tag{2-13}$$

$$F(\text{x}) = \frac{3[\sin(x) - x\cos(x)]}{x^3} \tag{2-14}$$

$$S(q) = \frac{\Gamma(Dm-1)\zeta^{Dm-1}}{[1+(q\zeta)2]^{\frac{Dm-1}{2}}} \frac{\sin[(Dm-1)\tan^{-1}(q\zeta)]}{q} \tag{2-15}$$

$$\text{scale} = \text{scale factor} * N\left(\frac{4}{3}\pi R^3\right)^2 (\rho_{\text{particle}} - \rho_{\text{solvent}})^2 \tag{2-16}$$

where R is the radius of the building block, Dm is the mass fractal dimension, ζ is the cut-off length, N is number of scatters, $\rho_{solvent}$ is the scattering length density of the solvent, and $\rho_{particle}$ is the scattering length density of particles. Dm relates the mass (m) to the radius as $m \sim R^{Dm}$ and is analogous to $I(q) \sim q^{-p}$ from the power-law calculations (with power-law exponent p), where $Dm = p$ when $q\zeta >> 1$.

The power-law dependencies were determined by fitting the experimental SAXS profiles (Figure 2-19e), where $0.3 \leq q \leq 1$ nm^{-1} with the following:[192]

$$I(q) = \text{scale} * q^{-p} + \text{background} \quad \text{2-17}$$

These power-law dependencies (fits listed in Figure 2-19e) recapitulate the calculated *Dm* values from the mass fractal model fits.

Three main values are derived from these mass fractal and power-law calculations: (i) radius *R* (nm), (ii) fractal dimension *Dm*, and (iii) cutoff length ζ (nm) (Table 2-8).[191–193] The radius *R* in the mass fractal analysis is traditionally defined as the radius of the uniform sphere used to cover the fractal. The fractal dimension *Dm* and analogous power-law exponent *p* estimate the overall bulk geometries of the mass fractals, where the integer values of these variables represent the three dimensions in Euclidean space. Thus, *Dm* or $p = 1$, 2, or 3 represent rod, disk, or sphere geometries, respectively. The cutoff length ζ defines the maximum distance between any two points of the mass fractal.

As another control, carboxylic acid functionalized SWCNTs (COOH-SWCNTs) were also examined via power-law scattering obtaining $p \sim 3.3$ (Figure 2-19e). This fit suggests that without ssDNA functionalization, COOH-SWCNTs form roughly spherical aggregates better modeled as a uniform density as opposed to a polymeric mass fractal. Thus, it may be inferred that ssDNA provides some semblance of order to the fine molecular structure of the system and should be the subject of further investigation.

The effect of aggregation on the scattering vector at very small angles ($q < 1$ nm^{-1}) precluded the use of the Guinier approximation and subsequent calculated metrics such as the radius of gyration (*Rg*), and the scattering intensity at $q=0$, $I(0)$, which is proportional to the molecular weight.[229] Additionally, while mathematically possible to calculate a pair-distribution function, *P(r)*, from the indirect Fourier transformation, the level of aggregation leads to non-zero values for *r=Dmax*.[230] Accordingly, we fit the whole SAXS profile to a specific mass fractal model, providing an estimate for the average cutoff length ζ, superseding the need to calculate the analogous *Dmax* value which we determined to be less accurate.

3 Corona Exchange Dynamics on Carbon Nanotubes by Multiplexed Fluorescence Monitoring

3.1 Chapter Abstract

Noncovalent adsorption of DNA on nanoparticles has led to their widespread implementation as gene delivery tools and optical probes. Yet, the behavior and stability of DNA-nanoparticle complexes once applied in biomolecule-rich, *in vivo* environments remains unpredictable, whereby biocompatibility testing usually occurs in serum. Here, we demonstrate time-resolved measurements of exchange dynamics between solution-phase and adsorbed corona-phase DNA and protein biomolecules on single-walled carbon nanotubes (SWCNTs). We capture real-time binding of fluorophore-labeled biomolecules, utilizing the SWCNT surface as a fluorescence quencher, and apply this corona exchange assay to study protein corona dynamics on ssDNA-SWCNT-based dopamine sensors. We study exchange of two blood proteins, albumin and fibrinogen, adsorbing to and competitively displacing $(GT)_6$ vs. $(GT)_{15}$ ssDNA from ssDNA-SWCNTs. We find that $(GT)_{15}$ binds to SWCNTs with a higher affinity than $(GT)_6$ and that fibrinogen interacts with ssDNA-SWCNTs more strongly than albumin. Albumin and fibrinogen cause a 52.2% and 78.2% attenuation of the dopamine nanosensor response, coinciding with 0.5% and 3.7% desorption of $(GT)_6$, respectively. Concurrently, the total surface-adsorbed fibrinogen mass is 168% greater than that of albumin. Binding profiles are fit to a competitive surface exchange model which recapitulates the experimental observation that fibrinogen has a higher affinity for SWCNTs than albumin, with a fibrinogen on-rate constant 1.61-fold greater and an off-rate constant 0.563-fold smaller than that of albumin. Our methodology presents a generic route to assess real-time corona exchange on nanoparticles in solution phase, and more broadly motivates testing of nanoparticle-based technologies in blood plasma rather than the more ubiquitously tested serum conditions.[§]

3.2 Introduction

Adsorption of polymers on single-walled carbon nanotubes (SWCNTs) has enabled developments in molecular sensing,[32] *in vivo* imaging,[10] genetic cargo delivery,[231] and chirality sorting.[232] Noncovalent SWCNT functionalization offers a route that preserves the pristine atomic structure, thus retaining the intrinsic near-infrared (nIR) fluorescence of the SWCNTs for the aforementioned applications. However, noncovalent adsorption is an inherently dynamic process, where exchange occurs between molecules in the bulk solution and molecules on the surface, into what is known as the 'corona phase'. For polymers on SWCNTs, the nature, strength, and kinetics of both the polymer binding and unbinding processes are key contributors to the success of polymer-SWCNT based technologies.[233] Understanding this exchange process is especially critical for intended uses of functionalized SWCNTs to probe biological environments. When a

---

[§] Published as Pinals, R. L.;* Yang, D.;* Lui, A.; Cao, W.; Landry, M. P. Corona Exchange Dynamics on Carbon Nanotubes by Multiplexed Fluorescence Monitoring. *J. Am. Chem. Soc.* **2020**, *142* (3), 1254–1264. https://doi.org/10.1021/jacs.9b09617.

nanoparticle is injected into a biological system, the nanoparticle surface is spontaneously and rapidly coated with proteins to form the 'protein corona'.[48] In the case of noncovalent polymer-SWCNT complexes, we hypothesize that native biomolecules compete with the original polymer to occupy the nanoparticle surface. Binding of proteins and other biomolecules to the SWCNT can disrupt the intended functionality of the nanoparticle and cause potentially adverse biocompatibility outcomes.[46,234] This phenomenon of protein corona formation leads to challenges in translating *in vitro* sensing or biomolecule delivery platforms to *in vivo* application. Moreover, the generally accepted method of simulating *in vivo* biological conditions involves testing nanotechnology performance in blood serum.[10,221] Yet, the absence of blood coagulation proteins from serum could yield a false outcome in assessing robustness of the nanotechnology and accordingly result in unpredicted failure when applied *in vivo*.

To clarify how nanoparticle-polymer conjugates behave in biologically relevant environments, it is pivotal to understand the kinetics describing molecular exchange on nanoparticle surfaces. Hence, we aim to gain a mechanistic understanding of how SWCNT-based neuromodulator sensors behave in protein-rich milieus. These sensors are based on noncovalent functionalization of $(GT)_6$ single-stranded DNA (ssDNA) on SWCNTs, resulting in a complex that exhibits ultrasensitive $\Delta F/F_o$ = 2400% and 3500% fluorescence "turn-on" responses in the presence of neuromodulators dopamine and norepinephrine, respectively.[43,42,41,40] However, the drastic enhancement of SWCNT fluorescence experienced upon *in vitro* exposure to dopamine is attenuated to $\Delta F/F_o \approx 20\%$ once the sensors are applied in brain tissue,[41] presumably due to protein adsorption and/or disruption of the ssDNA corona phase originally on the SWCNT surface.

Current methods to measure dynamic, noncovalent exchange on nanoparticles exist but are limited in scope. Most research on protein-surface interactions involves characterizing macroscopic surfaces using a series of well-developed techniques that broadly entail an input signal modulated by changing adsorbate mass on the surface as a function of time, including total internal reflection fluorescence microscopy, surface plasmon resonance, biolayer interferometry, and quartz-crystal microbalance with dissipation monitoring. To apply these surface techniques to nanoparticles, the nanoparticles must be surface immobilized, thus introducing unrealistic topographical constraints that affect ligand exchange kinetics, lead to mass transport limitations,[235] do not reproduce solution-phase nanosensor responses,[236] and cause nonselective protein adsorption to any surface left exposed during the sparse SWCNT immobilization process.[236]

An alternative method that permits the study of SWCNTs in solution takes advantage of SWCNT sensitivity to their local dielectric environment[237–239] by monitoring SWCNT fluorescence intensity changes and solvatochromic shifts upon corona exchange.[240,241] This technique is applied to study polymer-surfactant exchange kinetics,[242–245] whereby SWCNTs suspended with surfactant exhibit higher quantum yield and optical transition energy (i.e. blue-shifted spectra) compared to SWCNTs suspended with most biomolecules such as protein or ssDNA. Previous work has successfully applied measurable differences in SWCNT fluorescence spectra to study relative changes in corona surface composition.[33,184] However, this approach cannot distinguish the exchange of two biomolecules (here, ssDNA to protein), nor can it distinguish between molecular rearrangement vs. molecular desorption from the SWCNT surface. Despite the advantage of undertaking corona exchange studies in the solution phase with this approach, its low sensitivity,

non-quantitative nature, and inability to distinguish between adsorbed biomolecules nullifies its potential for monitoring ssDNA-protein exchange.

In this work, we present an assay that overcomes the limitations of previous characterization methods to study corona exchange dynamics between solution-phase and corona-phase biopolymers on SWCNTs, specifically applied to ssDNA and protein. This assay exploits the quenching of fluorophores when in close proximity to the SWCNT surface to monitor ligand binding and unbinding events.[246] While prior literature has similarly harnessed fluorophore quenching by SWCNTs to study the ssDNA-to-SWCNT binding process,[234,240,247] far less is known regarding how pre-adsorbed ssDNA and biologically native proteins exchange on the SWCNTs. To our knowledge, this method is unique in enabling real-time monitoring of SWCNT surface exchange between ssDNA and proteins, tracing the fate of all biomolecules involved in the binding exchange. We conduct multiplexed fluorescence tracking of polymer adsorption and desorption events to/from the SWCNT surface. As a case study for this assay, we focus on comparing the sorption behavior of two specific blood proteins, human serum albumin and fibrinogen, chosen because: (i) both are highly abundant in plasma, with albumin as ~55% (w/v) of blood plasma, or 35-50 mg/mL[220] and fibrinogen as ~4% (w/v) of blood plasma, or 1.5-4.5 mg/mL[248], (ii) albumin is present in both blood plasma and serum, whereas fibrinogen is a key coagulation protein present in plasma but depleted from serum, and (iii) albumin and fibrinogen are known to be interfacially active proteins prone to surface-adsorption and are implicated in the formation of many other nanoparticle coronas.[249,47,58] Binding profiles from the experimental assay in conjunction with a competitive-exchange model are used to extract kinetic parameters for each adsorbent species. Although this study specifically examines competitive adsorption of individual plasma proteins, albumin and fibrinogen, onto $(GT)_6$- and $(GT)_{15}$-SWCNTs, the assay is general to any molecules that can be fluorescently labeled and to any nanomaterial surface to which these species may adsorb and display quenched fluorescence. Binding is also compared to the orthogonal and more ubiquitously used platform monitoring solvatochromic shifting of the nIR SWCNT spectrum as a proxy for SWCNT corona coverage.[33,184] The work presented herein develops an understanding of the fundamental corona exchange mechanism, contextualizes the nature of the ligand exchange process vs. SWCNT solvatochromic shifting, and provides guidance for testing the performance of SWCNT-based systems in biologically relevant, protein-rich conditions.

3.3 Results and Discussion

3.3.1 Proteins Attenuate Dopamine Sensor Response

Noncovalent modification of single-walled carbon nanotubes (SWCNTs) with single-stranded $(GT)_6$ DNA imparts nIR fluorescence responsivity to the small molecule neurotransmitter, dopamine.[41–43] Addition of 200 μM dopamine to 5 μg/mL solution-phase $(GT)_6$-SWCNTs in phosphate buffered saline (PBS) yields an 11.5-fold increase in nanosensor fluorescence at the 1200 nm SWCNT emission peak (Figure 3-1a; see section 3.5.4). Nanosensor response was diminished in the presence of 40 μg/mL human serum albumin (HSA, Figure 3-1b) and 40 μg/mL fibrinogen (FBG, Figure 3-1c), proteins abundant in intravenous environments. Incubation of 40 μg/mL HSA or FBG with 5 μg/mL $(GT)_6$-SWCNTs reduced fluorescence response to dopamine by 52.2% or 78.2% after 40 min (Figure 3-1d), respectively. Attenuation of nanosensors was due to two effects: addition of protein led to (i) increase in baseline fluorescence intensity, likely due to protein adsorption which is predicted to be highly favorable by a thermodynamic analysis (see

section 3.6.3) and (ii) decrease in final fluorescence after addition of dopamine to $(GT)_6$-SWCNTs. HSA did not cause any wavelength shifting of the $(GT)_6$-SWCNT emission, while FBG exposure led to a redshift of 2.6 ± 0.6 nm (mean ± standard deviation of N=3 sample replicates). Although changes in both the nIR fluorescence intensity and emission wavelength could indicate protein binding, monitoring the SWCNT fluorescence alone does not provide sufficient information to correlate these phenomena.

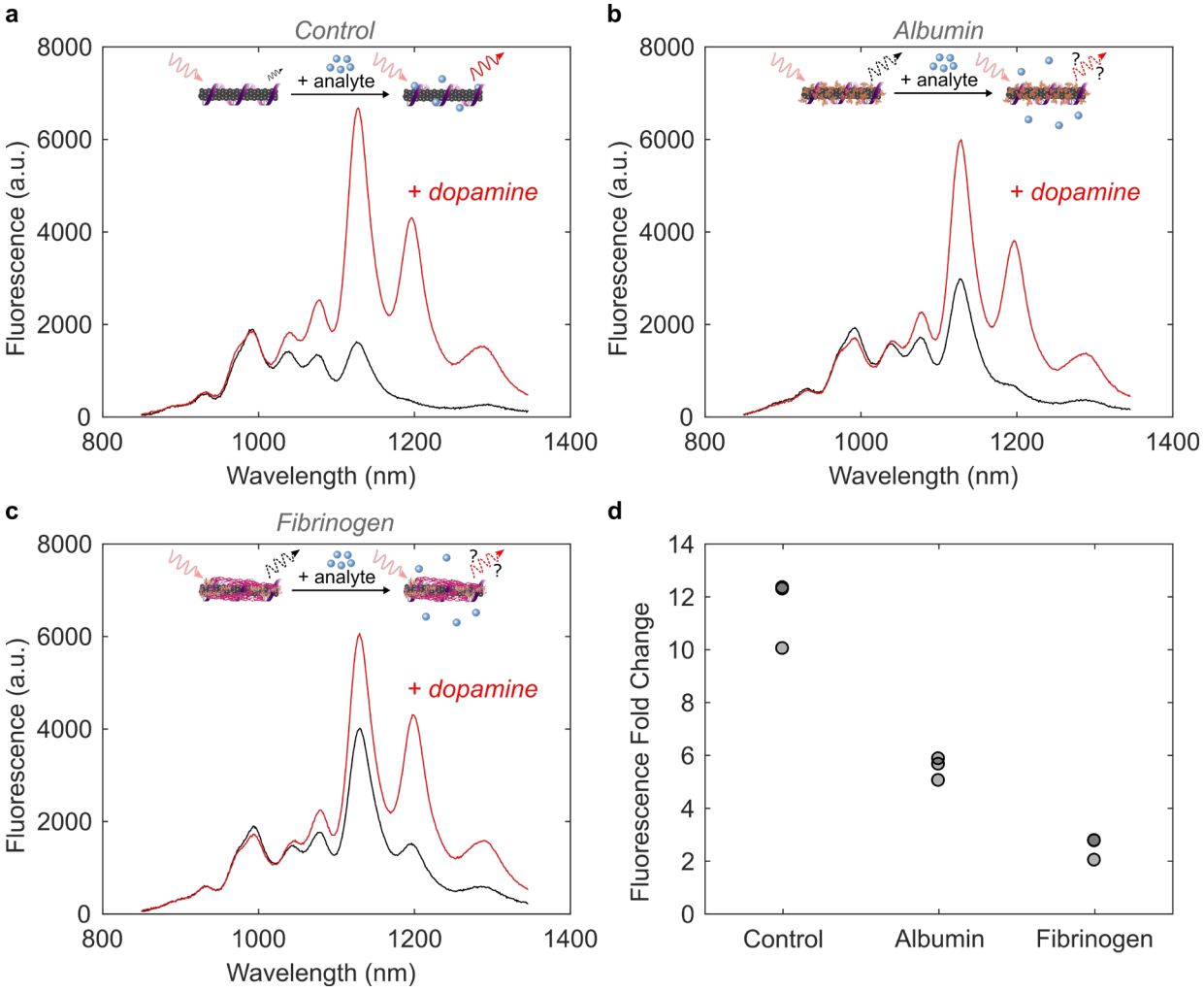

Figure 3-1. Protein adsorption attenuates $(GT)_6$-SWCNT sensor response to dopamine. (a) Near-infrared (nIR) spectra of 5 µg/mL $(GT)_6$-SWCNTs before (black) and after (red) addition of 200 µM dopamine. (b-c) nIR spectra of 5 µg/mL $(GT)_6$-SWCNTs incubated with 40 µg/mL (b) albumin or (c) fibrinogen for 40 minutes before (black) and after (red) addition of 200 µM dopamine. Insets depict influence of protein corona formation on ability of nanosensor to respond to analyte. (d) Change in $(GT)_6$-SWCNT fluorescence intensity at 1200 nm peak following 40 minutes incubation in PBS or protein solution at 40 µg/mL, then addition of 200 µM dopamine (N = 3). Nanosensor excitation was with 721 nm light.

We first implemented the solvatochromic shift assay to study surfactant-induced fluorescence changes of 5 μg/mL $(GT)_6$-SWCNTs incubated with either 40 μg/mL HSA or FBG for 40 minutes. Displacement of the biopolymer corona phase with surfactant, here 0.5% (w/v) sodium dodecylbenzene sulfonate (SDBS), causes a change in local dielectric environment that in turn leads to a blue shift in SWCNT emission wavelength and an increase in SWCNT fluorescence emission intensity. The magnitude of these observed effects is thought to provide insight on the original SWCNT-corona stability. Interestingly, FBG incubated with $(GT)_6$-SWCNTs resulted in both the largest magnitude wavelength shift and largest fold change in fluorescence intensity upon addition of SDBS (Figure 3-4). In contrast, HSA incubated with $(GT)_6$-SWCNTs did not show a significantly different wavelength shift or intensity fold change compared to the control, $(GT)_6$-SWCNTs incubated with only PBS. These results suggest albumin and fibrinogen proteins may have different binding propensities and kinetics to the SWCNT surface. However, this test fails to decouple the interactions between SWCNTs with ssDNA, protein, and then surfactant. To further study the differential attenuation of sensor response by HSA and FBG, and more thoroughly understand the exchange dynamics occurring on the SWCNT surface, we developed a method for studying SWCNT corona composition by multiplexed fluorescence monitoring.

3.3.2 Multiplexed Fluorescence Tracking Enables Real-Time Monitoring of Ligand Exchange Dynamics

Our assay leverages fluorophore quenching induced by proximity to the SWCNT surface[246] to measure surface exchange dynamics. Proteins under study were labeled with fluorescein (FAM) fluorophore (ex/em = 494/520 nm) using NHS ester conjugation to primary amine groups (see section 3.5.2). Single-stranded DNA (ssDNA) were procured with a 3' terminally labeled cyanine5 (Cy5) fluorophore (ex/em = 648/668 nm), enabling spectrally resolved multiplexed tracking of protein and ssDNA. The ssDNA-Cy5 is initially quenched on the SWCNT surface, increasing in fluorescence upon desorption from the SWCNT. This methodology has been previously implemented to study thermodynamics of fluorophore-labeled ssDNA interactions on SWCNT surfaces.[199] Conversely, the FAM-labeled protein exhibits high fluorescence when added in bulk solution, quenching upon adsorption to the SWCNT surface. In this manner, FAM-labeled protein can be injected into ssDNA-Cy5-SWCNTs in a well-plate format and fluorescence changes resulting from biomolecule exchange can be read by a fluorescence plate reader (Figure 3-2a). We first employed this method to compare the desorption rates of $(GT)_6$-Cy5 and $(GT)_{15}$-Cy5 from SWCNTs upon addition of FAM-labeled HSA and FBG. Both proteins promoted dequenching of Cy5, as compared to the addition of PBS control (Figure 3-2b-c). Dequenching was due to complete desorption of ssDNA rather than partial desorption of the 3' end, as verified by confirming that the binding profiles of 3'- vs. internally Cy5-labeled ssDNA are similar (Figure 3-5). Additionally, presence of the Cy5 tag on ssDNA did not significantly affect protein adsorption (Figure 3-6). Fibrinogen generated a 3.09 ± 0.07 Cy5 fluorescence fold increase for $(GT)_6$-Cy5-SWCNTs vs. a 1.52 ± 0.04 Cy5 fluorescence fold increase for $(GT)_{15}$-Cy5-SWCNTs. This result suggests $(GT)_{15}$ is less readily displaced from the SWCNT surface compared to the shorter $(GT)_6$ construct, a result consistent with the literature.[179,177,180]

In the same experiment, protein adsorption onto ssDNA-Cy5-SWCNTs was concurrently tracked via fluorescence quenching of the protein-conjugated FAM. Presence of residual FAM fluorophore in the FAM-protein solution was accounted for by quantifying free FAM and subtracting the

minimal change in fluorescence due to free FAM-to-SWCNT interaction (Figure 3-7, Figure 3-8, Table 3-2). Furthermore, the effect of FAM fluorophore labeling on the protein-exchange dynamics was minimal (Figure 3-9), in agreement with previous investigations demonstrating that fluorescein-labeling of proteins does not perturb protein adsorption or function, and additionally that fluorescein signals are proportional to the interfacial mass of the tagged species.[250,251,182,252] By tracking the fluorescence modulation resulting from FAM-protein interactions with ssDNA-Cy5-SWCNTs, we found that FAM-FBG exhibited a comparatively larger degree of quenching than FAM-HSA for both ssDNA-SWCNT suspensions (Figure 3-2d-e): upon addition of 40 μg/mL FAM-FBG to 5 μg/mL $(GT)_6$-SWCNTs (final concentrations), FBG induced a 42.5 ± 0.9% decrease in FAM fluorescence vs. a 25.5 ± 0.9% HSA-induced decrease in FAM fluorescence. These results consistently suggest two interaction mechanisms of ssDNA and protein with SWCNTs: (i) $(GT)_{15}$ ssDNA binds to SWCNTs with a higher affinity than $(GT)_6$ ssDNA, thus reducing protein adsorption, and (ii) FBG interacts with ssDNA-SWCNTs more strongly than HSA. The former result agrees with prior work confirming that the rate of ssDNA desorption from SWCNTs decreases with increasing oligo length,[199] also valid in the presence of competing biomolecules.[234] As such, our data suggest that FBG protein adsorption leads to more significant ssDNA desorption from SWCNTs, whereas HSA adsorbs less strongly and accordingly causes less ssDNA desorption from SWCNTs. These ssDNA-protein corona exchange trends were corroborated with polyacrylamide gel electrophoresis (PAGE) of the unbound species, where FAM-FBG adsorbed to $(GT)_6$-Cy5-SWCNTs 56.5% more than FAM-HSA and caused 5.20% greater desorption of ssDNA (Figure 3-10 and see section 3.6.2). From our corona exchange assay, it is interesting to note that protein adsorption occurs faster than ssDNA desorption. These experimental results motivate kinetic modeling of ssDNA and protein exchange on SWCNT surfaces.

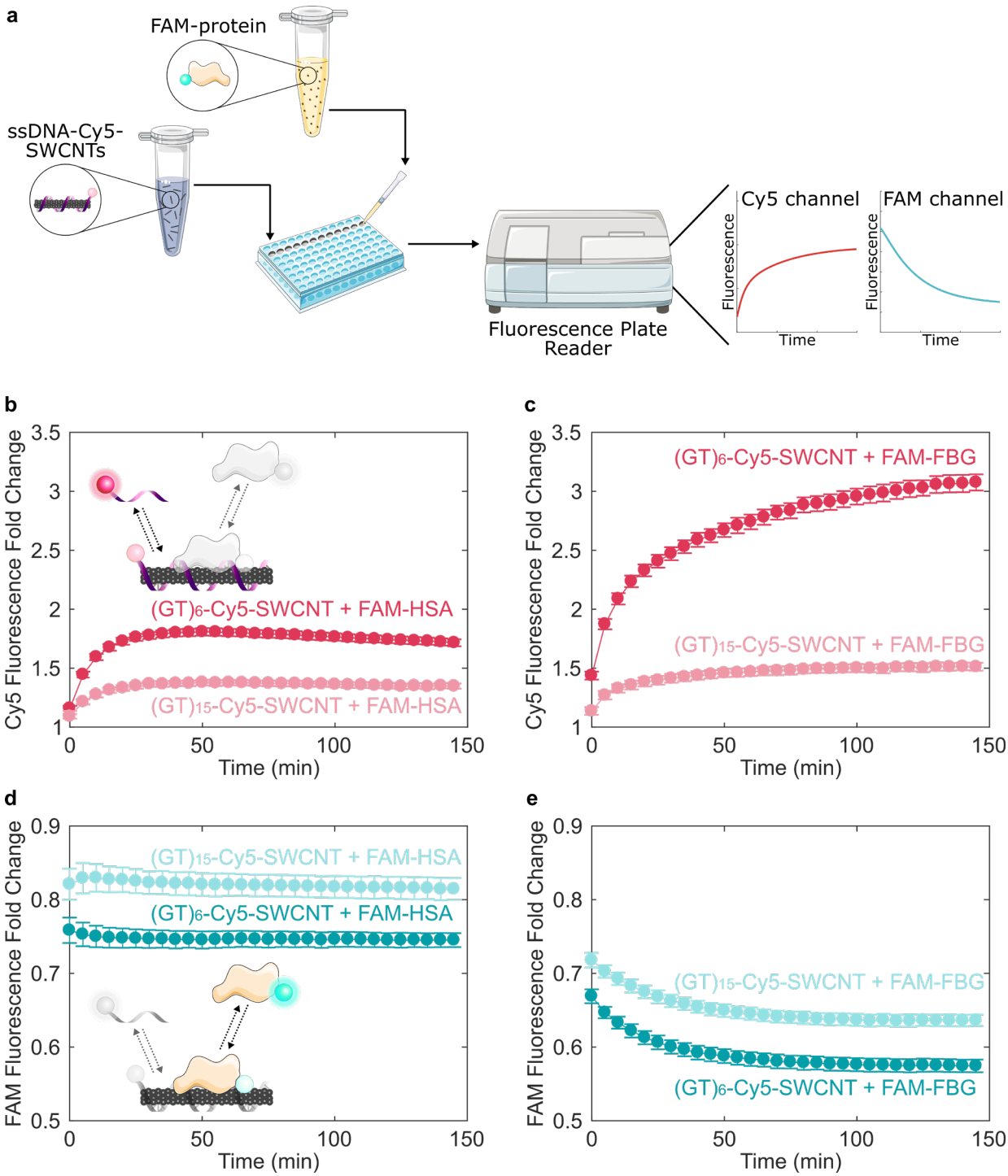

Figure 3-2. Tracking exchange of fluorophore-labeled ssDNA and protein on SWCNT surfaces demonstrates protein adsorption selectivity and ssDNA length effect. (a) Corona exchange assay workflow. ssDNA-Cy5-SWCNT solution is added to a well plate, FAM-protein solution is injected, and the ad-/de-sorption processes are monitored in separate color channels of a fluorescence plate reader (see section 3.5.3). Increase in ssDNA-Cy5 fluorescence induced by addition of 40 µg/mL (b) FAM-labeled albumin (FAM-HSA) or (c) FAM-labeled fibrinogen (FAM-FBG) to 5 µg/mL ssDNA-Cy5-SWCNT suspended with ssDNA, $(GT)_6$ or $(GT)_{15}$.

Decrease in fluorescence of (d) FAM-HSA and (e) FAM-FBG after addition of protein to $(GT)_6$- or $(GT)_{15}$-SWCNT. Error bars represent standard error between experimental replicates (N = 3).

3.3.3 Kinetic Modeling of ssDNA/Protein Competitive Binding on SWCNT Surface

To quantitatively probe differences in protein affinities for ssDNA-SWCNTs, we fit Cy5 and FAM fluorescence data to a competitive adsorption model and extracted kinetic parameters for ssDNA and proteins. Multiplexed fluorescence tracking was repeated with 5 μg/mL $(GT)_6$-Cy5-SWCNTs and concentrations of FAM-HSA and FAM-FBG ranging from 5 to 160 μg/mL. Fluorescence values were converted to mass concentration using standard curves for ssDNA-Cy5 and both FAM-conjugated proteins (Figure 3-11). A model was developed for the competitive exchange between ssDNA and protein on the SWCNT surface (Equations 3-1 and 3-2). In the model, unbound ssDNA (D) and protein (P) adsorb and desorb reversibly to SWCNT surface sites (*):

$$D + * \underset{k_2}{\overset{k_1}{\rightleftarrows}} D* \tag{3-1}$$

$$P + * \underset{k_4}{\overset{k_3}{\rightleftarrows}} P* \tag{3-2}$$

Total concentration of SWCNT surface sites ($[*]_T$) was fixed, given by a site balance (Equation 3-3), where *, D*, and P* refer to vacant sites, sites occupied by bound ssDNA, and sites occupied by bound protein, respectively:

$$[*]_T = [*] + [D*] + [P*] \tag{3-3}$$

Bound ssDNA and bound protein concentrations were calculated by species conservation, where total ssDNA was the amount added during ssDNA-SWCNT synthesis, total protein was the injected protein quantity, and total sites ($[*]_T$) was a fit parameter. Rate constants k_1, k_2 for ssDNA binding/unbinding, k_3, k_4 for protein binding/unbinding, and the total concentration of binding sites $[*]_T$ were computed using a least squares curve fit of Equations 3-4 and 3-5 to experimental data (see section 3.5.5).

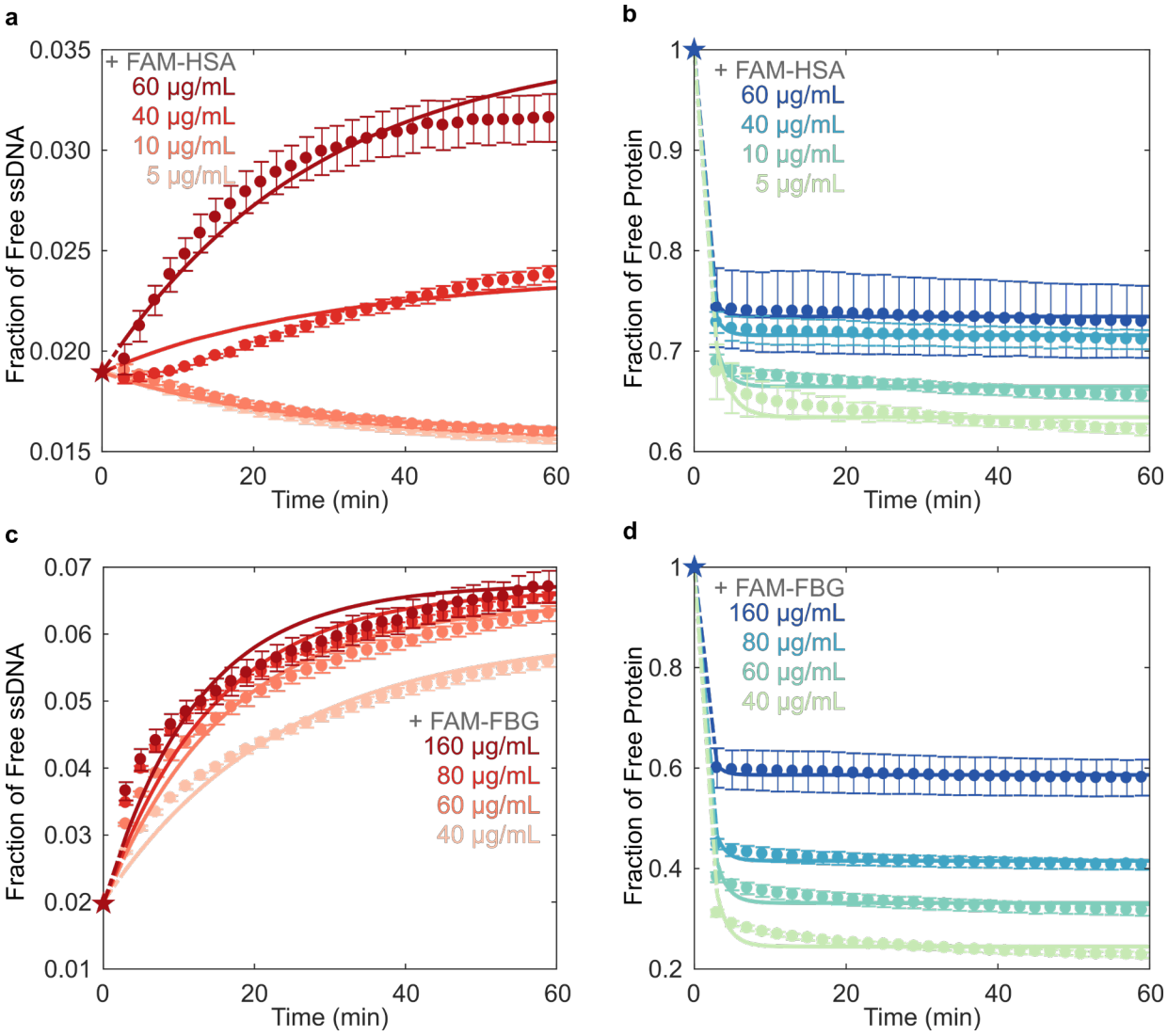

Figure 3-3. Kinetic model of competitive exchange between ssDNA and protein on SWCNTs fit to fluorescence data to extract rate constants. Fraction of (a) $(GT)_6$-Cy5 ssDNA and (b) FAM-labeled albumin (FAM-HSA) protein free in solution for varying concentrations of FAM-HSA injected into 5 µg/mL $(GT)_6$-Cy5-SWCNT solution. Fraction of (c) $(GT)_6$-Cy5 ssDNA and (d) FAM-labeled fibrinogen (FAM-FBG) protein free in solution for varying concentrations of FAM-FBG injected into $(GT)_6$-Cy5-SWCNT solution. Star data points represent initial conditions used for solving model differential equations. Error bars represent standard error between experimental replicates (N = 3).

Table 3-1. Range of kinetic model fit parameters.

Protein	k_1 x 10^6 (mL µg^{-1} s^{-1})	k_2 x 10^6 (s^{-1})	k_3 x 10^6 (mL µg^{-1} s^{-1})	k_4 x 10^6 (s^{-1})	$[*]_T$ (µg mL^{-1})
Albumin	1.10 - 1.54	8.40 - 20.7	7.86 - 9.44	5,850 - 12,000	365 - 526
Fibrinogen	1.15 - 2.30	42.7 - 90.9	11.8 - 16.9	2,610 - 9,150	486 - 620

Experimental data of FAM-HSA or FAM-FBG added to $(GT)_6$-Cy5-SWCNTs was fit to this model for each concentration tested (Figure 3-3). All mean relative errors comparing fits to experimental data were < 5% (Table 3-3). The model recapitulates the experimental observation that FBG has a higher affinity for SWCNTs (Figure 3-3d) than HSA (Figure 3-3b), where average $k_{3,\,FBG} = 1.43 \times 10^{-5} > k_{3,\,HSA} = 8.88 \times 10^{-6}$ mL μg $^{-1}$ s^{-1} (Table 3-1, with full fit parameter results in Table 3-3). These k values are in relative agreement with previous literature assessing the kinetic parameters for ssDNA desorption from SWCNTs[42] and protein binding to nanoparticles.[43] At the same initial FAM-protein concentration of 40 μg/mL added to 5 μg/mL $(GT)_6$-Cy5-SWCNTs, FBG adsorbed to a higher fraction of bound protein (0.756) than HSA (0.284) after 1 hour. Final solution-phase concentrations of FAM-FBG and FAM-HSA were 9.04 and 28.5 μg/mL, respectively, compared to concentrations of 13.8 and 36.4 μg/mL determined by PAGE (Figure 3-10d). Solution-phase concentrations of $(GT)_6$-Cy5 upon addition of FAM-FBG and FAM-HSA increased from 0.106 to 0.301 μg/mL and from 0.101 to 0.128 μg/mL, respectively, compared to concentration changes of 0.331 to 0.388 μg/mL and 0.688 to 0.767 μg/mL determined by PAGE (Figure 3-10c). The discrepancy in concentrations across the two approaches may be due to technical differences between methods, where gel electrophoresis is limited in both sensitivity and temporal resolution.

Addition of FAM-FBG into solution with $(GT)_6$-Cy5-SWCNTs led to ssDNA desorption for all tested concentrations of injected FAM-FBG Figure 3-3c), as compared to only ≥ 40 μg/mL of injected FAM-HSA led to measurable ssDNA desorption (Figure 3-3a). Adsorption of ssDNA was observed upon addition of PBS or low concentrations of FAM-HSA (≤ 20 μg/mL) to $(GT)_6$-Cy5-SWCNTs, indicating an initial excess of unbound ssDNA in bulk solution. Interestingly, the intermediate concentration of FAM-HSA (40 μg/mL) added to $(GT)_6$-Cy5-SWCNTs resulted in sigmoidal ssDNA desorption behavior that is not fully described by the model. This behavior fundamentally implies that the assumption of independent reactions made in Equations 3-1 and 3-2 may not hold for intermediate concentrations of FAM-HSA. Specifically, the dependence of ssDNA dissociation constant k_2 on total protein concentration indicates that the rate of ssDNA desorption is a function of adsorbed or free protein concentration (Table 3-3, Figure 3-12). This higher-order desorption process may account for the discrepancy between experimental data and model fit for $(GT)_6$-Cy5 desorption induced by addition of 40 μg/mL FAM-HSA.

For all concentrations tested, protein adsorption proceeded significantly faster than ssDNA desorption dynamics, indicating that protein adsorption precedes ssDNA desorption and suggesting that the two phenomena may be decoupled in time. This difference in exchange timescales may be due to the large concentration of total SWCNT surface binding sites (with average fit values of $[*]_{T,FBG} = 572$ μg mL^{-1} and $[*]_{T,HSA} = 472$ μg mL^{-1}) relative to the total ssDNA and protein concentrations. We hypothesize a low initial ssDNA surface coverage, or large accessible SWCNT surface area, is a likely reason for the difference in exchange timescales. Furthermore, in the case of FAM-FBG with $(GT)_6$-Cy5-SWCNTs, while amount of adsorbed FBG reaches an apparent steady-state value within ~5 minutes (Figure 3-3d), ssDNA continues to gradually desorb over time at a rate seemingly independent of injected protein concentration (Figure 3-3c). Continued ssDNA desorption may be caused by a surface rearrangement process in the adsorbed FBG layer,[254] where protein spreading could be responsible for this observed ssDNA displacement over longer timescales.[235,251] Hydrophobic interactions are posited to be the driving force for protein spreading on the SWCNT surface[182] and consequently interfacial denaturation is

presumed to be the dominant relaxation process, in addition to a smaller contribution from molecular reorientations.[250]

From the kinetic model fitting, the mass of protein adsorbed on the SWCNTs was consistently higher for FBG as compared to HSA for the same initial concentration of 40 μg/mL FAM-protein with 5 μg/mL $(GT)_6$-Cy5-SWCNTs. Previous studies of differential protein adsorption to hydrophobic surfaces has demonstrated that fibrinogen forms well-packed layers, whereas more weakly adsorbed albumin forms less tightly packed, more mobile adsorption layers.[182] Accordingly, we hypothesize that the seemingly higher protein surface coverage on the SWCNT points to the more tightly packed, if not multilayer formation, of FBG on the SWCNT surface.

Some potential shortcomings of our methodology include that the proposed elementary steps only approximate the true exchange mechanism, or that there are nonidealities present in the protein and/or ssDNA sorption behavior. Two alternative models to account for protein binding to surface-adsorbed ssDNA or protein were also attempted, but not pursued due to the poor quality of the fits (see section 3.5.5). Constraining the total surface sites $[*]_T$ during model fitting was also pursued, whereby $[*]_T$ would presumably be constant across different concentrations of protein added. Although the model fits to the experimental data are reasonable (Table 3-5, Figure 3-13), we decided to fit the data with varying $[*]_T$ to capture the effect of concentration-dependent nonidealities in the system, such as nanotube-nanotube interactions, on all fit parameters. Finally, we note that the system is not truly equilibrated, therefore, a thermodynamic analysis was not pursued.[161]

3.4 Conclusions

Protein adsorption to nanoparticle surfaces is a major hindrance to the successful application of nanotechnologies *in vivo.* We have shown that incubation of two high-abundance blood plasma proteins, human serum albumin and fibrinogen, with ssDNA-SWCNT dopamine sensors causes significantly different degrees of sensor response attenuation. Developing an understanding of protein-sensor interactions is vital in circumventing this issue and establishing better practices for testing nanotechnologies for *in vivo* use. Previously established techniques to evaluate these effects implement surface-immobilized nanoparticles or exploit the intrinsic nIR fluorescence changes of SWCNTs. Yet, these methods do not track the fate of adsorbates and cannot quantify the fraction of free biomolecules in real-time, thus precluding quantitative and temporally resolved studies of the SWCNT protein corona composition. Though the SDBS-induced solvatochromic shift assay successfully identifies FBG as a protein of interest, this assay provides no mechanistic information on FBG binding, nor can it distinguish between HSA and PBS control responses.

We have addressed these limitations in developing a method to quantitatively probe the kinetics of SWCNT corona exchange between ssDNA and protein adsorbates by monitoring fluorescence quenching of conjugated fluorophores in close proximity to SWCNT surfaces. Concentration curves were fit to a competitive adsorption model to extract kinetic parameters. Our method reveals that reduction of dopamine sensor performance correlates with quantity of adsorbed protein, where fibrinogen adsorbs to ssDNA-SWCNTs 168% more than albumin at the same concentration, and consequently leads to 26% more sensor attenuation. We demonstrate significantly greater SWCNT binding affinities for longer repeating ssDNA sequences, and for fibrinogen over albumin. These

results bear significance in that albumin is the highest abundance blood protein and is therefore commonly regarded as an important component of the SWCNT corona. However, our results show that lower abundance proteins with higher SWCNT affinities may disproportionately contribute to the SWCNT corona, as has been previously suggested in orthogonal protein corona-nanoparticle studies.[56,255] Preliminary findings from blood plasma and serum samples normalized to 40 μg/mL total protein concentration show that plasma and serum both caused significant attenuation of dopamine response in $(GT)_6$-Cy5-SWCNTs, with 81.0 ± 0.9% and 80.7 ± 1.4% reduction in response, respectively (Figure 3-14a). However, plasma—which contains fibrinogen—caused a higher degree of ssDNA desorption, with plasma inducing a 1.64 ± 0.01 fold increase in $(GT)_6$-Cy5 fluorescence vs. a 1.39 ± 0.03 fold increase by serum (Figure 3-14b). Our results motivate the necessity to test SWCNT-based and other nanobiotechnologies in more representative bio-environments, i.e. blood plasma rather than serum.

The method presented herein enables the study of corona formation dynamics of multiple biomolecular entities, with standard laboratory equipment, under varying solution conditions (e.g. ionic strength and pH). The generalizability of this assay allows for study of diverse corona exchange phenomena occurring on the surface of carbon nanotubes between a variety of biomolecular species. We demonstrate that RNA, phospholipids, and peptoids— molecules commonly used in SWCNT-mediated delivery, imaging, and sensing[39,174,231,256] —all exhibit varying degrees of corona exchange with ssDNA-SWCNTs (Figure 3-15 and see section 3.6.2.1). Furthermore, we can examine the competitive adsorption of multiple fluorophore-conjugated proteins, such as FAM-HSA and Cy5-FBG onto ssDNA-SWCNTs, where increasing mass ratios of FBG to HSA results in reduced adsorption of the latter (Figure 3-16). Careful selection of fluorophores may enable further multiplexing, allowing tracking of more than two distinct molecular species simultaneously. Rationally designed labeling methodologies such as FRET may also enable the study of more complex interactions such as protein denaturation on the SWCNT surface. Implementation of this assay will facilitate more thorough deconvolution of factors driving protein corona formation and accordingly inform design principles for nanotechnologies resistant to protein corona-based biofouling and performance attenuation. In summary, the corona exchange assay we have developed will serve to enhance our still deficient understanding of how noncovalently bound polymers exchange on nanoparticle surfaces and, accordingly, enable the design and testing of nanobiotechnologies toward effective implementation *in vivo*.

3.5 Materials and Methods

3.5.1 Preparation of ssDNA-SWCNT Complexes

Single-stranded DNA with single-walled carbon nanotube (ssDNA-SWCNT) suspensions were prepared by combining 0.2 mg of mixed-chirality SWCNTs (small diameter HiPco™ SWCNTs, NanoIntegris) and 20 μM of ssDNA (custom ssDNA oligos with standard desalting, Integrated DNA Technologies, Inc.) in 1 mL of 0.01 M phosphate-buffered saline (PBS). Solutions were probe-tip sonicated for 10 minutes in an ice bath (3 mm probe tip set at 50% amplitude, 5-6 W, Cole-Parmer Ultrasonic Processor). Samples were centrifuged to pellet insoluble SWCNT bundles and contaminants (16,100 cfg for 30 minutes). Supernatant containing the product was collected. ssDNA-SWCNT solutions were stored at 4°C until use. ssDNA-SWCNT concentration was determined via sample absorbance at 910 nm and the corresponding extinction coefficient ε_{910nm} =

0.02554 mL μg^{-1} cm^{-1}.[257] ssDNA-SWCNTs were diluted to a working concentration of 10 µg/mL in 0.1 M PBS.

Cyanine 5 (Cy5) was chosen as the ssDNA fluorophore label, with excitation maximum at 648 nm and emission maximum at 668 nm. The same suspension protocol was employed for preparation of fluorophore-labeled ssDNA-SWCNT complexes, using ssDNA-Cy5 (3' or internally labeled Cy5-labeled custom ssDNA oligos with HPLC purification, Integrated DNA Technologies, Inc.) in place of unlabeled ssDNA. Internally labeled ssDNA-Cy5 includes Cy5 conjugated to the thymine at nucleotide position 6 (GTGTGT/iCy5/GTGTGT).

Total ssDNA adsorbed to SWCNTs was determined by a heat/surfactant elution process. This molar ratio of ssDNA:SWCNT was required to calculate the fraction of free vs. bound ssDNA throughout the exchange process. Optimized elution conditions were achieved with salt and surfactant in the combination of 0.1 M PBS/0.1% (m/v) sodium dodecylbenzene sulfonate (SDBS), in agreement with prior literature demonstrating that SDBS disperses SWCNTs most effectively[240,258] and without chirality bias.[259] Freshly prepared ssDNA-Cy5-SWCNTs were diluted to a final concentration of 5 µg/mL in elution buffer, with a final volume of 150 µL in a PCR tube. Samples were heated at 95°C for 1 hour in a PCR thermocycler, transferred to a clean test-tube, and centrifuged (16,100 cfg for 30 minutes) to pellet insoluble SWCNT bundles. 120 µL of supernatant containing the eluted ssDNA-Cy5 was collected. Fluorescence in the Cy5 channel was measured (see section 3.5.3) and compared to a standard curve of known ssDNA-Cy5 concentrations (ranging 0.01 - 1 µM) to correlate the Cy5 fluorescence measurement to ssDNA eluted concentration. This resulted in a mole ratio of 364 ± 2 $(GT)_6$:SWCNT and 140 ± 7 $(GT)_{15}$:SWCNT (both N = 8), in relative agreement with previous literature for (6,5) single chirality SWCNTs.[196]

3.5.2 Fluorophore-Labeling of Proteins

N-Hydroxysuccinimide (NHS) ester chemistry was used to label proteins via conjugation to primary amine groups. Fluorescein (FAM) was chosen as the protein fluorophore label, with excitation maximum at 494 nm and emission maximum at 520 nm (FAM NHS ester 6-isomer, Lumiprobe). Lyophilized proteins were purchased: human serum albumin (HSA; from human plasma, ≤0.02% Fatty acids, Lot #SLBZ2785, Millipore Sigma) and fibrinogen (FBG; from human plasma, 20 mM sodium citrate-HCl pH 7.4, Lot #3169957, Millipore Sigma). FAM-proteins were prepared with 10 mg of protein reconstituted in 900 µL of 0.1 M sodium bicarbonate (pH 8.5) and 8-fold molar excess of FAM NHS ester solubilized in 100 µL DMSO. Solutions were combined, covered in foil, and incubated on a test-tube rotator for 4 hours. FAM-protein conjugates were twice purified to remove free FAM (Zeba™ 2 mL spin desalting columns with 40 kDa MWCO, Thermo Fisher Scientific) by washing with 0.1 M PBS three times (1,000 cfg for 2 minutes), centrifuging with sample (1,000 cfg for 3 minutes), and retaining sample in flow-through solution (repeating all steps twice with a new spin column). Protein concentration and degree of labeling (DOL) were determined by measuring the absorbance of the FAM-protein conjugate at the protein absorbance maximum, 280 nm (A_{280}), and the fluorophore emission maximum, 494 nm (A_{494}). Protein absorbance was corrected for the contribution of the fluorophore to A_{280} by subtracting A_{494} weighted by the correction factor (CF), an empirical constant of 0.17 for free FAM (from manufacturer). Protein and FAM concentrations were determined by the Beer-Lambert Law using

either A_{280} for protein or A_{494} for FAM, with the corresponding extinction coefficients of $\varepsilon_{280nm,HSA}$ = 43,824 $(M\ cm)^{-1}$,[260] $\varepsilon_{280nm,FBG}$ = 513,400 $(M\ cm)^{-1}$,[261] and $\varepsilon_{494nm,FAM}$ = 75,000 $(M\ cm)^{-1}$ (from manufacturer). DOL was then calculated as the ratio of FAM to protein molar concentrations, yielding $DOL_{FAM\text{-}HSA}$ = 2.773 and $DOL_{FAM\text{-}FBG}$ = 0.608.

Free FAM NHS ester remaining after purification was quantified by polyacrylamide gel electrophoresis (PAGE) run according to the Laemmli protocol[203] (adapted in Bio-Rad Mini-PROTEAN Tetra Cell manual). Briefly, purified FAM-protein conjugates were added to sodium dodecyl sulfate (SDS) reducing buffer (2% SDS, 5% β-mercaptoethanol, 0.066 M Tris-HCl) in a 1:2 ratio of sample to buffer. Samples were diluted such that 100 ng of FAM-HSA, 100 ng of FAM NHS ester, or 30 ng of FAM-FBG (due to lower labeling reaction yield) per 20 µL volume was applied per well. PAGE separation was carried out in 1 mm vertical mini gel format (Bio-Rad Mini-PROTEAN Tetra Cell) with a discontinuous buffer system under denaturing conditions. Gel composition was 12% acrylamide (total monomer), 0.375 M Tris-HCl, 0.1% SDS, 0.05% APS, 0.05% TEMED for the resolving gel and 12% acrylamide (total monomer), 0.125 M Tris-HCl, 0.1% SDS, 0.05% APS, 0.1% TEMED for the stacking gel. Electrode buffer was 25 mM Tris, 192 mM glycine, and 3.5 mM SDS (pH 8.3). Separation was run with 200 V for 35 minutes, gels were extracted, and the FAM label was visualized with a gel imager (Typhoon FLA 9500, 473 nm laser, General Electric) (Figure 3-7). The FAM-protein conjugate is the higher band (approximately 66 kDa for FAM-HSA, 52-95 kDa for FAM-FBG) and the free, lighter molecular weight FAM NHS ester is the lower band (approximately 0.475 kDa). FAM fluorescence intensity was quantified with ImageJ (Table 3-2).

3.5.3 Visible Fluorescence Measurements

Equal volumes of $(GT)_6$-Cy5-SWCNT and FAM-tagged protein at 2X working concentration were added to a 96-well PCR plate (Bio-Rad) to a total volume of 50 µL. The plate was sealed using an optically transparent adhesive seal (Bio-Rad) and briefly spun down on a benchtop centrifuge. Fluorescence time series readings were taken using a Bio-Rad CFX96 Real Time qPCR System, scanning all manufacturer set color channels (FAM, HEX, Texas Red, Cy5, Quasar 705) every 30 s at 22.5 °C (lid heating off). Fluorescence time series were analyzed without default background correction. Note that concentration ranges of FAM-HSA (5-60 µg/mL) and FAM-FBG (40-160 µg/mL) were chosen to be in the linear fluorescence regime of the qPCR.

3.5.4 Near-Infrared Fluorescence Measurements

Fluorescence spectra were collected with an inverted Zeiss microscope (20x objective, Axio Observer.D1) containing a custom filter cube set (800 nm SP FESH0800, 900 nm LP dichroic DMLP900R, 900 nm LP FELH900, ThorLabs) coupled to a Princeton Instruments spectrometer (SCT 320) and liquid nitrogen cooled Princeton Instruments InGaAs detector (PyLoN-IR 1024/1.7). Fluorescence measurements were done with a beam-expanded 721 nm laser (10-500 mW, OptoEngine LLC) excitation light source and 800 - 1400 nm emission wavelength range. Solution-phase measurements were acquired in a 384 well-plate format (1 s exposure time, 1 mW laser power). Protein solutions (final concentration 40 µg/mL) or PBS control were incubated with $(GT)_6$-SWCNTs (final concentration 5 µg/mL in 0.1 M PBS). For each time point, an aliquot of these incubation solutions was added to a well (40 µL total volume) and an initial fluorescence spectrum was acquired. 10 µL of dopamine was added to a final concentration of 200 µM prior to

the second fluorescence acquisition. Fluorescence fold change was measured by taking the ratio of fluorescence intensities at 1200 nm between post- and pre-addition of dopamine spectra.

Similarly, surfactant-induced solvatochromism was performed by collecting nIR fluorescence spectra pre- and 1-minute post-addition of 0.5% (w/v) SDBS. Fluorescence fold change was defined as the ratio of integrated fluorescence intensity (800 to 1400 nm) between post- and pre-addition of SDBS. Wavelength shift was measured relative to the wavelength of the (7,6) SWCNT chirality peak emission (initially 1130 nm) post-SDBS.

3.5.5 Kinetic Model

Corona exchange kinetics were modeled by a system of simultaneous adsorption/desorption reactions. The model assumes that both ssDNA and protein adsorb/desorb reversibly to a fixed number of vacant SWCNT surface sites (Equations 3-1 and 3-2). Note that all modeling was done on a mass basis. This is in agreement with the general use of volume fractions in polymer thermodynamics.[262] Here, we add the additional assumption that the biomolecules are of similar density. Modeling on a mass basis accounts for the widely varying molecular sizes between the two types of protein (HSA, 66.5 kDa, globular vs. FBG, 340 kDa, long) and ssDNA ($(GT)_6$, 3.7 kDa). The time-dependent differential equations governing ssDNA desorption and protein adsorption are as follows:

$$\frac{d}{dt}[D] = -k_1[*]_T[D] + (k_1[D] + k_2)([D]_T - [D]) + k_1[D]([P]_T - [P]) \qquad 3\text{-}4$$

$$\frac{d}{dt}[P] = -k_3[*]_T[P] + (k_3[P] + k_4)([P]_T - [P]) + k_3[P]([D]_T - [D]) \qquad 3\text{-}5$$

A least-squares regression was used to fit the model to fluorescence data and iterate model parameters. MATLAB 2019A's ode15s solver was implemented to solve Equations 3-4 and 3-5 for free protein and DNA concentration curves given fit rate constants k_1, k_2, k_3, k_4, and the total concentration of open sites, $[*]_T$. Relative error between the model fit and experimental data was calculated and averaged over all data points to yield mean relative error (MRE). Sensitivity analysis on initial conditions was performed to minimize this fit error. 48 unique combinations of rate parameter initial conditions were analyzed as inputs to the nonlinear least-squares solver (lsqcurvefit) in our MATLAB model. The optimal set of initial conditions for each protein was chosen as that which yielded a low MRE between fit and experimental data and a low standard error among fit parameters for each of the four protein concentrations. Each rate parameter was individually fit to each experiment, yielding 20 total fit parameters from each initial condition (Table 3-3). Final ssDNA and protein fit MRE were all < 5% (Table 3-3). Optimized initial conditions and resultant rate parameters for HSA and FBG are reported in Table 3-4.

Two alternative models were also attempted: in Model 2, protein was able to bind to surface-adsorbed ssDNA and in Model 3, protein was able to bind to surface-adsorbed protein. However, these models both produced significantly higher error in fits. Model 2 addressed the possibility of protein binding on top of ssDNA bound directly to the SWCNT. For FBG experiments fit with Model 2, most fits overestimated FBG adsorption and many fits displayed incorrect concavity for

the ssDNA desorption. For HSA experiments fit with Model 2, the protein data was generally fit well but the ssDNA fits exhibited either a maximum or produced linear fits. Model 3 addressed the possibility of protein binding on top of protein bound directly to the SWCNT. For FBG experiments, Model 3 overestimated both protein adsorption and ssDNA desorption. For HSA experiments, Model 3 generally fit the protein data well, yet did not capture ssDNA dynamics as a function of concentration. Although the higher errors associated with Model 2 and 3 do not rule out these nanoscale mechanistic possibilities, the simple model of independent binding does overall fit the data much more closely between both protein and ssDNA curves within the same experiment, as well as binding dynamics as a function of varying concentration.

3.6 Chapter Supporting Information

3.6.1 Supplementary Figures and Tables

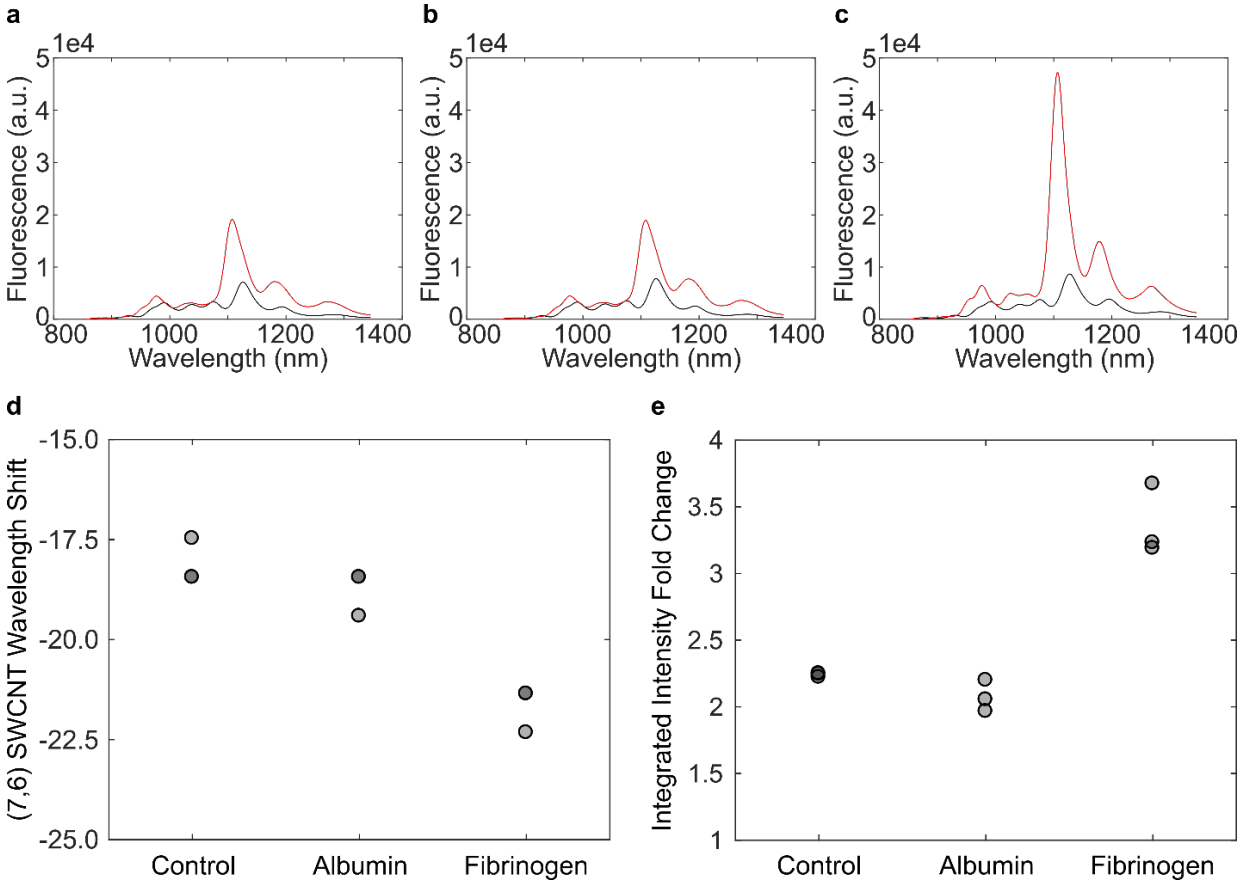

Figure 3-4. Surfactant-induced fluorescence change of ssDNA-SWCNTs incubated with protein. Near-infrared (nIR) spectra of 5 µg/mL $(GT)_6$-SWCNTs before (black) and after (red) addition of 0.5% (w/v) SDBS. (b-c) nIR spectra of 5 µg/mL $(GT)_6$-SWCNTs incubated with 40 µg/mL (b) albumin or (c) fibrinogen for 40 min before (black) and after (red) addition of 0.5% (w/v) SDBS. Change in (d) (7,6) SWCNT wavelength of peak emission and (e) integrated fluorescence intensity (800-1400 nm) observed 1 min after addition of SDBS (N = 3). Nanosensor excitation was with 721 nm light.

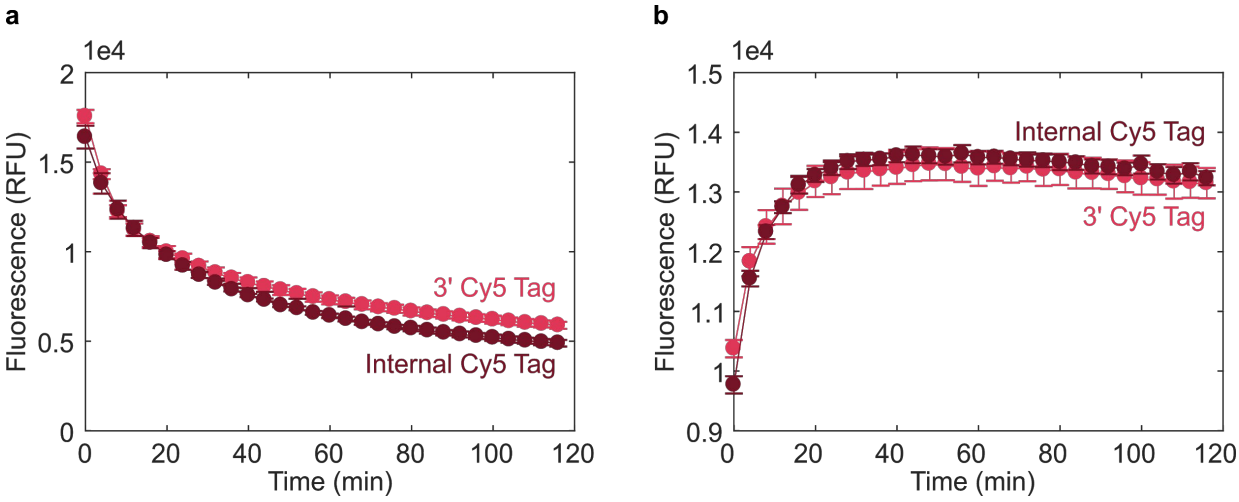

Figure 3-5. Effect of Cy5 tag location on ssDNA adsorption and protein-induced desorption. (a) Cy5 fluorescence tracking of 0.4 µM 3'- or internal-Cy5 tagged $(GT)_6$ ssDNA added to 5 µg/mL unlabeled $(GT)_6$-SWCNT. (b) Cy5 fluorescence tracking upon addition of 160 µg/mL fibrinogen, 3 h post-incubation with $(GT)_6$-Cy5. Error bars represent standard error between experimental replicates (N = 3).

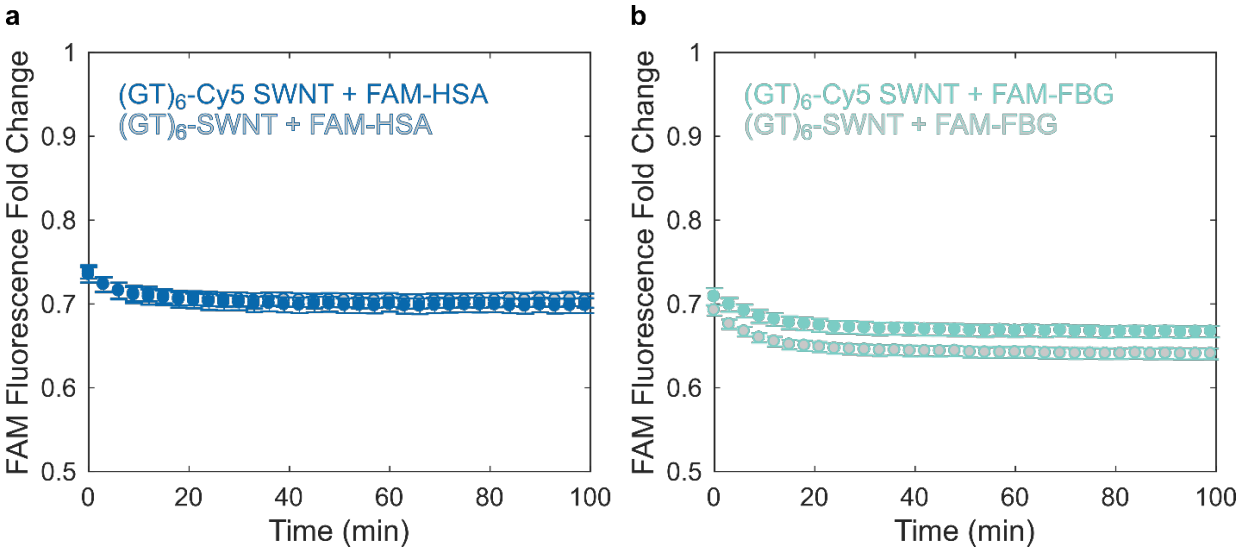

Figure 3-6. Effect of Cy5 ssDNA tag on protein adsorption. Quenching of FAM-protein upon addition of 40 µg/mL (a) FAM-HSA or (b) FAM-FBG to 5 µg/mL $(GT)_6$-Cy5-SWCNTs or $(GT)_6$-SWCNTs. Error bars represent standard error between experimental replicates (N = 3).

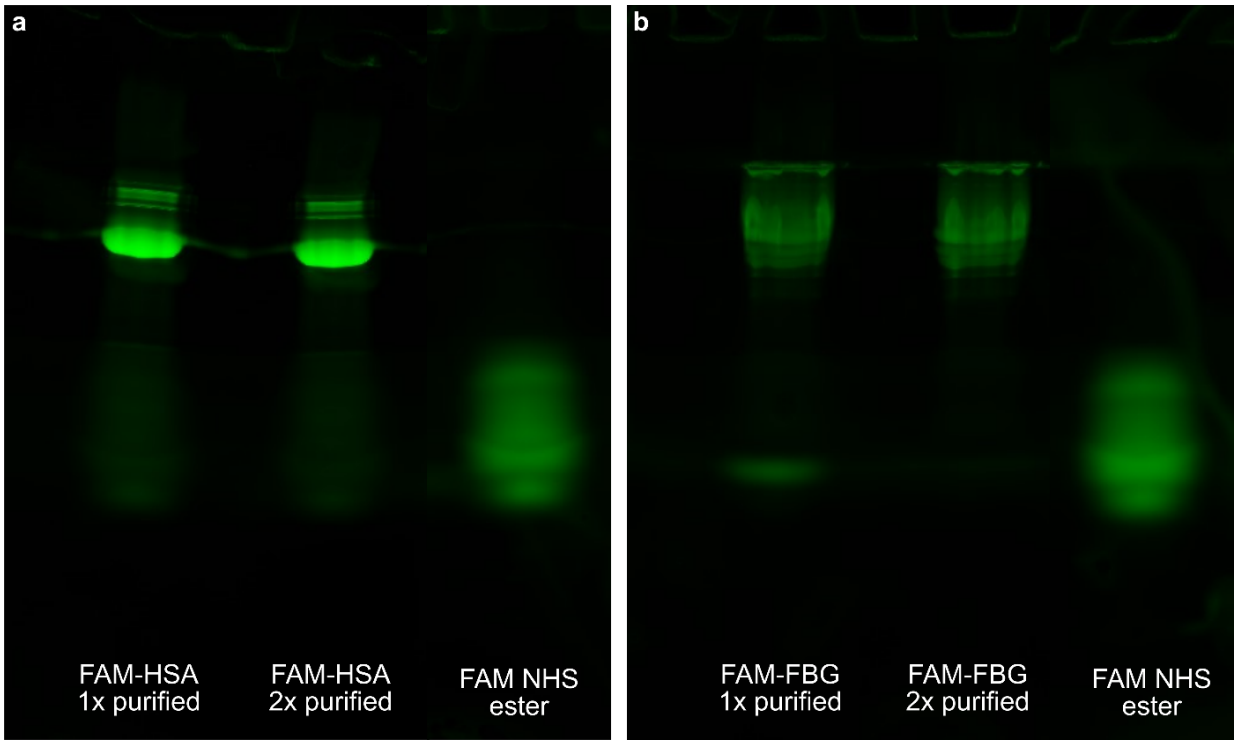

Figure 3-7. Polyacrylamide gel electrophoresis (PAGE) to quantify purification of labeled FAM-protein solutions. 12% acrylamide (total monomer) gel images of FAM-labeled (a) albumin (FAM-HSA) and (b) fibrinogen (FAM-FBG) post-purification to assess amount of free FAM remaining.

Table 3-2. Quantification of free FAM remaining in labeled FAM-protein solutions. Molar percentages of FAM-protein and free FAM are calculated based on gel band intensity and protein degree of labeling for (a) FAM-HSA and (b) FAM-FBG.

a

Sample	Band ID	Mole %
FAM-HSA, 1x pure	FAM-Protein	69.7%
	FAM	30.3%
FAM-HSA, 2x pure	FAM-Protein	67.8%
	FAM	32.2%
FAM	FAM	100.0%

b

Sample	Band ID	Mole %
FAM-FBG, 1x pure	FAM-Protein	70.5%
	FAM	29.5%
FAM-FBG, 2x pure	FAM-Protein	86.2%
	FAM	13.8%
FAM	FAM	100.0%

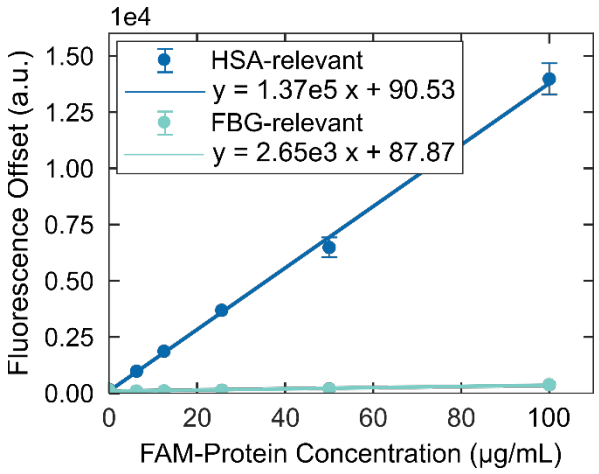

Figure 3-8. Fluorescence offset due to free FAM binding to SWCNT surface. FAM NHS ester was injected into solution with or without SWCNTs to quantify free fluorophore binding to the SWCNT. Free FAM concentrations tested were calculated based on molar percentage of free fluorophore at FAM-HSA or FAM-FBG concentrations between 0 and 100 µg/mL. Fluorescence offset was calculated as the difference between FAM fluorescence in the presence and absence SWCNTs. Offset is incorporated for all data conversion from fluorescence to concentration. Error bars represent standard deviation between technical replicates (N = 3).

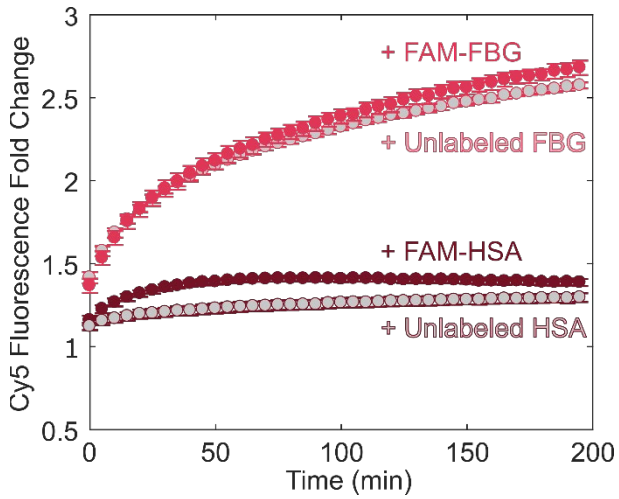

Figure 3-9. Desorption of ssDNA-Cy5 from SWCNT induced by FAM-labeled vs unlabeled protein. Dequenching of $(GT)_6$-Cy5 due to desorption from SWCNT upon addition of 40 µg/mL FAM-protein or unlabeled protein. Error bars represent standard error between experimental replicates (N = 3).

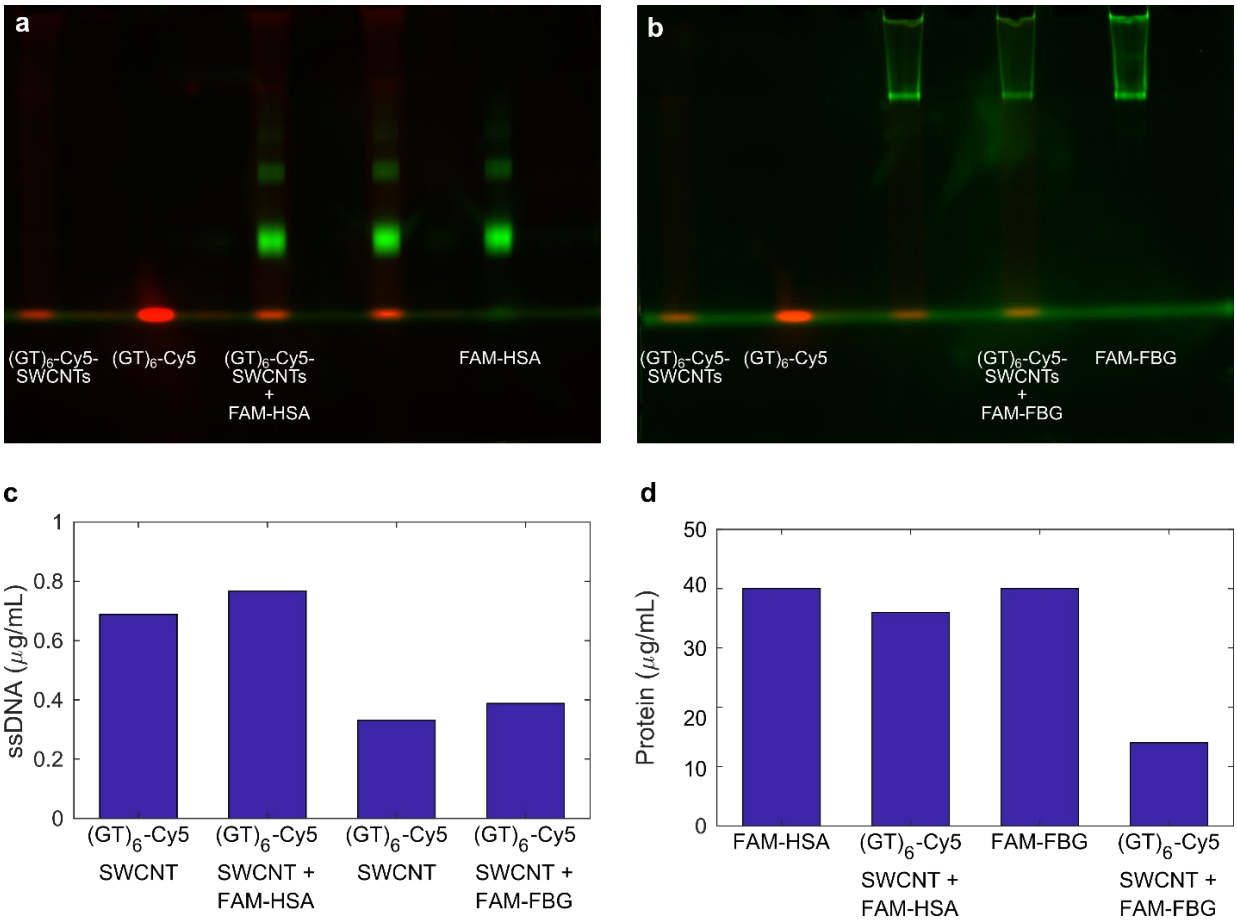

Figure 3-10. Native polyacrylamide gel electrophoresis (PAGE) to quantify ssDNA and protein exchange. Incubation of (a) FAM-HSA or (b) FAM-FBG proteins with $(GT)_6$-Cy5-SWCNTs for 1 h (final concentrations 5 μg/mL of $(GT)_6$-Cy5-SWCNTs with 40 μg/mL of either FAM-HSA or FAM-FBG). Quantification of concentration via fluorescence for (c) Cy5 bands (red) and (d) FAM bands (green).

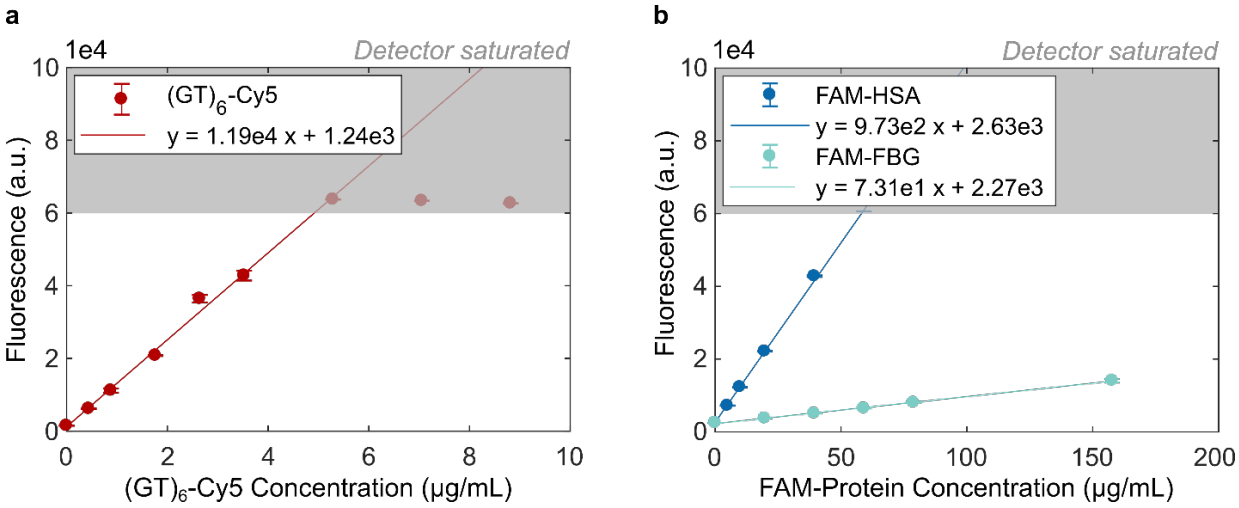

Figure 3-11. Conversion of fluorescence to concentration. Standard curves correlating fluorescence to fluorophore-labeled entity concentration for (a) Cy5-labeled $(GT)_6$ and (b) FAM-labeled proteins, FAM-HSA and FAM-FBG. Error bars represent standard deviation between technical replicates (N = 3).

Table 3-3. Full kinetic model fit parameters and mean relative errors (MREs).

Protein	Concentration (μg/mL)	k_1 (mL μg^{-1} s^{-1})	k_2 (s^{-1})	k_3 (mL μg^{-1} s^{-1})	k_4 (s^{-1})	$[*]_T$ (μg mL^{-1})	MRE protein	MRE ssDNA
Albumin	5	1.54E-06	8.40E-06	9.44E-06	5.9E-03	364.60	1.21%	0.25%
	10	1.41E-06	1.18E-05	7.86E-06	8.1E-03	525.60	0.83%	0.90%
	40	1.10E-06	1.34E-05	8.87E-06	1.1E-02	514.26	0.35%	3.01%
	60	1.22E-06	2.07E-05	9.34E-06	1.2E-02	483.76	0.41%	2.53%
Fibrinogen	40	1.15E-06	4.27E-05	1.38E-05	2.6E-03	619.82	4.71%	2.96%
	60	2.18E-06	6.64E-05	1.69E-05	3.7E-03	485.72	2.98%	3.47%
	80	2.09E-06	7.65E-05	1.48E-05	5.4E-03	562.90	1.37%	4.14%
	160	2.30E-06	9.09E-05	1.18E-05	9.2E-03	617.74	0.74%	4.74%

Table 3-4. Sensitivity analysis in kinetic fitting and resultant optimized initial conditions.

	k_1 (mL μg^{-1} s^{-1})	k_2 (s^{-1})	k_3 (mL μg^{-1} s^{-1})	k_4 (s^{-1})	$[*]_T$ (μg mL^{-1})
Range of Initial Conditions Tested	1.0E-03 1.0E-04 1.0E-05	1.0E-02 1.0E-03	1.0E-03 1.0E-04	1.0 0.1	1000 100
Albumin Optimized Initial Conditions	1.0E-04	1.0E-02	1.0E-03	1.0	100
Fibrinogen Optimized Initial Conditions	1.0E-04	1.0E-02	1.0E-04	0.1	100

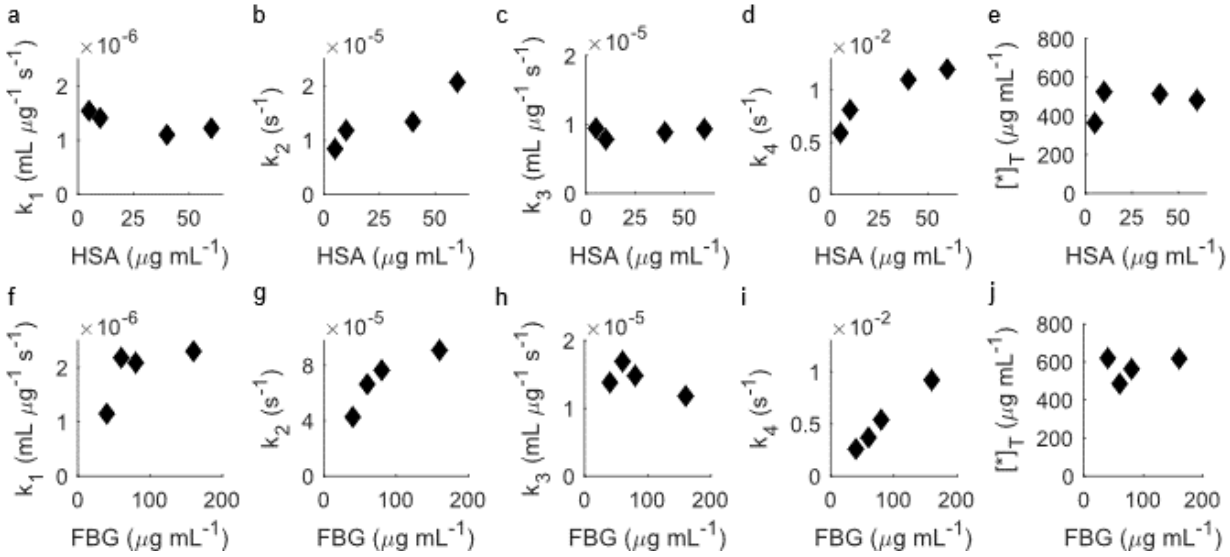

Figure 3-12. Full kinetic model fit parameters as functions of added protein concentrations. Fit parameters of (a) k_1 (ssDNA adsorption rate constant), (b) k_2 (ssDNA desorption rate constant), (c) k_3 (protein adsorption rate constant), (d) k_4 (protein desorption rate constant), and (e) $[*]_T$ (total SWCNT surface site concentration) for HSA in the top row and (f-j) the respective values for FBG in the bottom row.

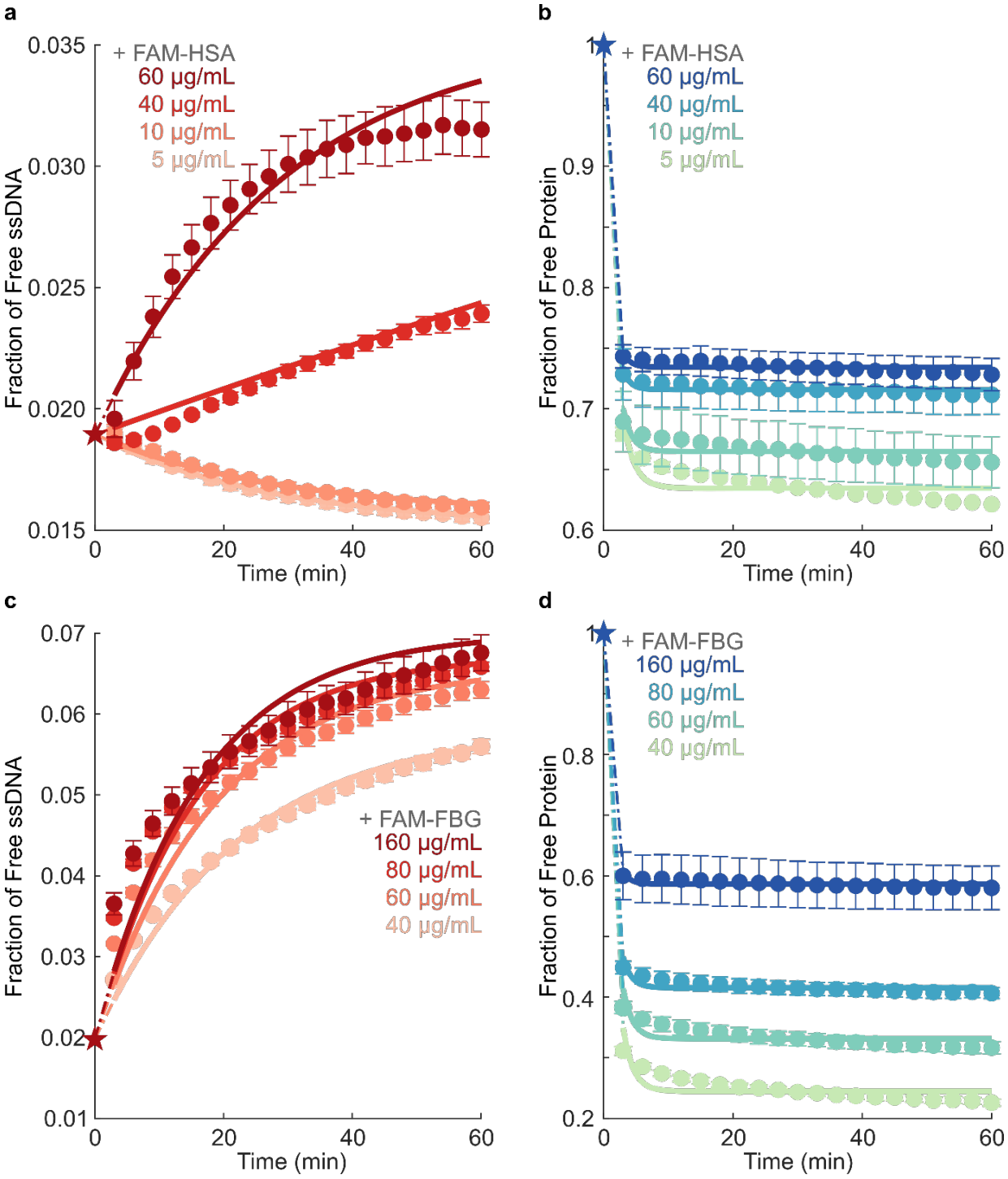

Figure 3-13. Kinetic model of competitive exchange between ssDNA and protein on SWCNTs fit to fluorescence data to extract rate constants, with constrained SWCNT surface site concentration. Fraction of (a) $(GT)_6$-Cy5 ssDNA and (b) FAM-labeled albumin (FAM-HSA) protein free in solution for varying concentrations of FAM-HSA injected into 5 µg/mL $(GT)_6$-Cy5-SWCNT solution. Fraction of (c) $(GT)_6$-Cy5 ssDNA and (d) FAM-labeled fibrinogen (FAM-FBG) protein free in solution for varying concentrations of FAM-FBG injected into $(GT)_6$-Cy5-SWCNT solution. Star data points represent initial conditions used for solving model

differential equations. Curves were fit with constrained $[*]_T$ per protein. Error bars represent standard error between experimental replicates (N = 3).

Table 3-5. Full kinetic model fit parameters and mean relative errors (MREs) for fitting with constrained SWCNT surface site concentration.

Protein	Concentration (μg/mL)	k_1 (mL μg^{-1} s^{-1})	k_2 (s^{-1})	k_3 (mL μg^{-1} s^{-1})	k_4 (s^{-1})	$[*]_T$ (μg mL^{-1})	MRE protein	MRE ssDNA
Albumin	5	1.47E-06	9.58E-06	8.74E-06	6.41E-03	429.69	1.24%	0.37%
	10	1.38E-06	9.25E-06	9.92E-06	8.29E-03		0.84%	0.63%
	40	6.93E-08	2.18E-06	1.06E-05	1.11E-02		0.35%	1.83%
	60	1.35E-06	2.04E-05	1.06E-05	1.19E-02		0.41%	2.66%
Fibrinogen	40	8.51E-07	4.41E-05	9.73E-06	2.64E-03	871.49	4.76%	2.52%
	60	1.01E-06	5.91E-05	9.14E-06	3.74E-03		3.00%	4.06%
	80	1.19E-06	7.04E-05	9.34E-06	5.43E-03		1.38%	4.46%
	160	1.20E-06	7.22E-05	7.96E-06	9.03E-03		0.74%	5.64%

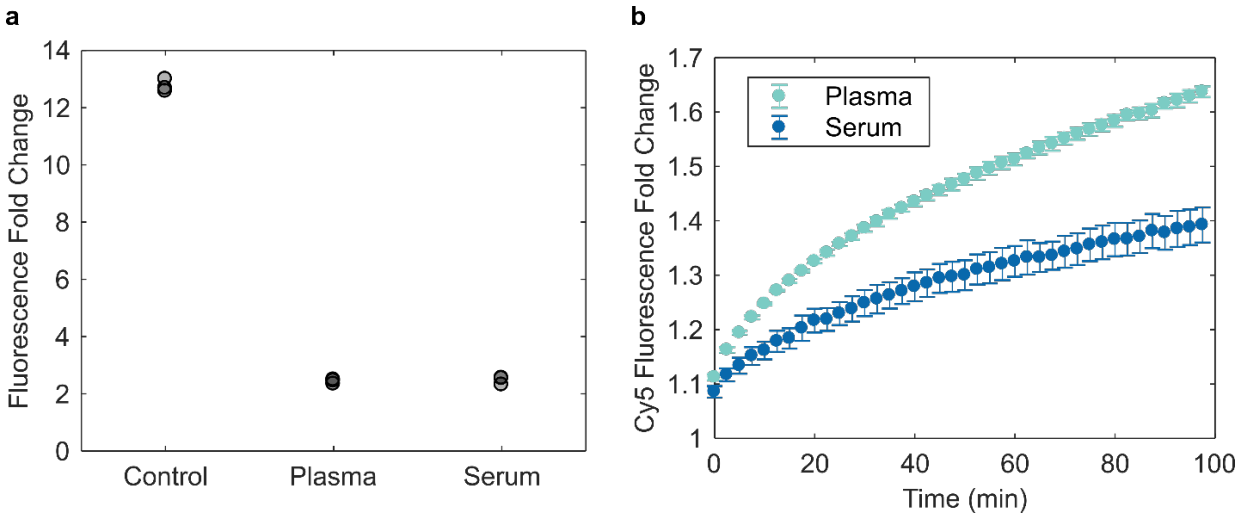

Figure 3-14. Comparison of plasma- vs serum-induced effects on ssDNA-SWCNTs. (a) Change in 1200 nm fluorescence intensity of 5 μg/mL $(GT)_6$-SWCNTs, pre-incubated for 40 min with PBS, plasma, or serum normalized to 40 μg/mL total protein concentration, before and after addition of 200 μM dopamine (N = 3). Nanosensor excitation was with 721 nm light. (b) $(GT)_6$-Cy5 fluorescence fold change upon desorption from 5 μg/mL SWCNTs induced by addition of plasma or serum, 40 μg/mL total protein concentration. Error bars represent standard error between experimental replicates (N = 3).

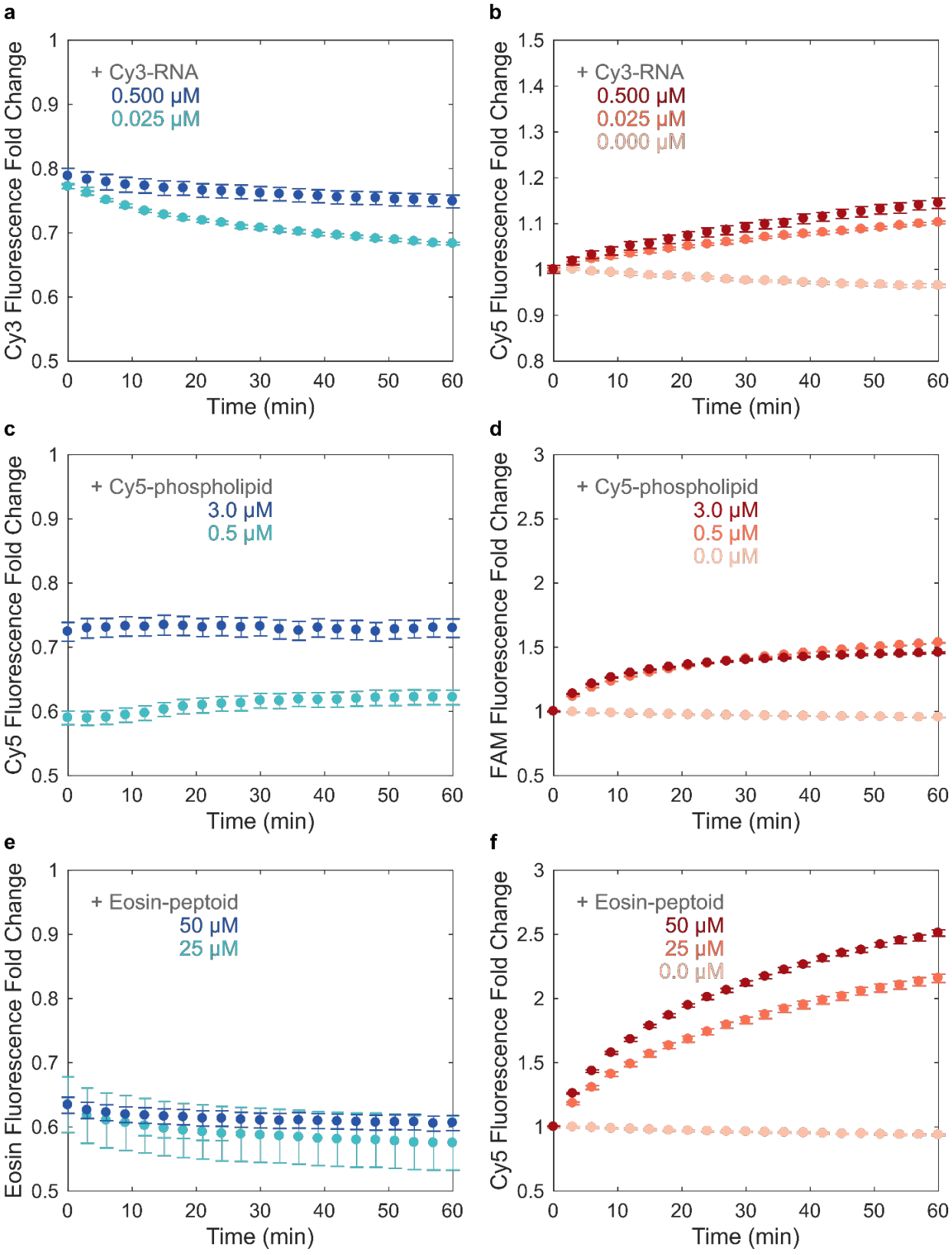
a
+ Cy3-RNA
0.500 μM
0.025 μM
Cy3 Fluorescence Fold Change
Time (min)
b
+ Cy3-RNA
0.500 μM
0.025 μM
0.000 μM
Cy5 Fluorescence Fold Change
Time (min)
c
+ Cy5-phospholipid
3.0 μM
0.5 μM
Cy5 Fluorescence Fold Change
Time (min)
d
+ Cy5-phospholipid
3.0 μM
0.5 μM
0.0 μM
FAM Fluorescence Fold Change
Time (min)
e
+ Eosin-peptoid
50 μM
25 μM
Eosin Fluorescence Fold Change
Time (min)
f
+ Eosin-peptoid
50 μM
25 μM
0.0 μM
Cy5 Fluorescence Fold Change
Time (min)

Figure 3-15. Adsorption of various fluorophore-tagged biomolecular species to ssDNA-SWCNTs. Adsorption of varying concentrations of biomolecules (as listed in figure) to 5 μg/mL $(GT)_6$-SWCNTs. (Column 1) Quenching of fluorophore-tagged biomolecules adsorbing to $(GT)_6$-SWCNTs: (a) Cy3-RNA, (c) Cy5-phospholipid (DSPE-PEG(2000)-N-Cy5), and (e) eosin-peptoid ($(Nae–Npe)_9$-$(Nce–Npe)_9$). (Column 2) Corresponding dequenching of fluorophore-tagged $(GT)_6$ ssDNA desorbing from SWCNT surface: (b) $(GT)_6$-Cy5, (d) $(GT)_6$-FAM, and (f) $(GT)_6$-Cy5. Error bars represent standard error between experimental replicates (N = 3).

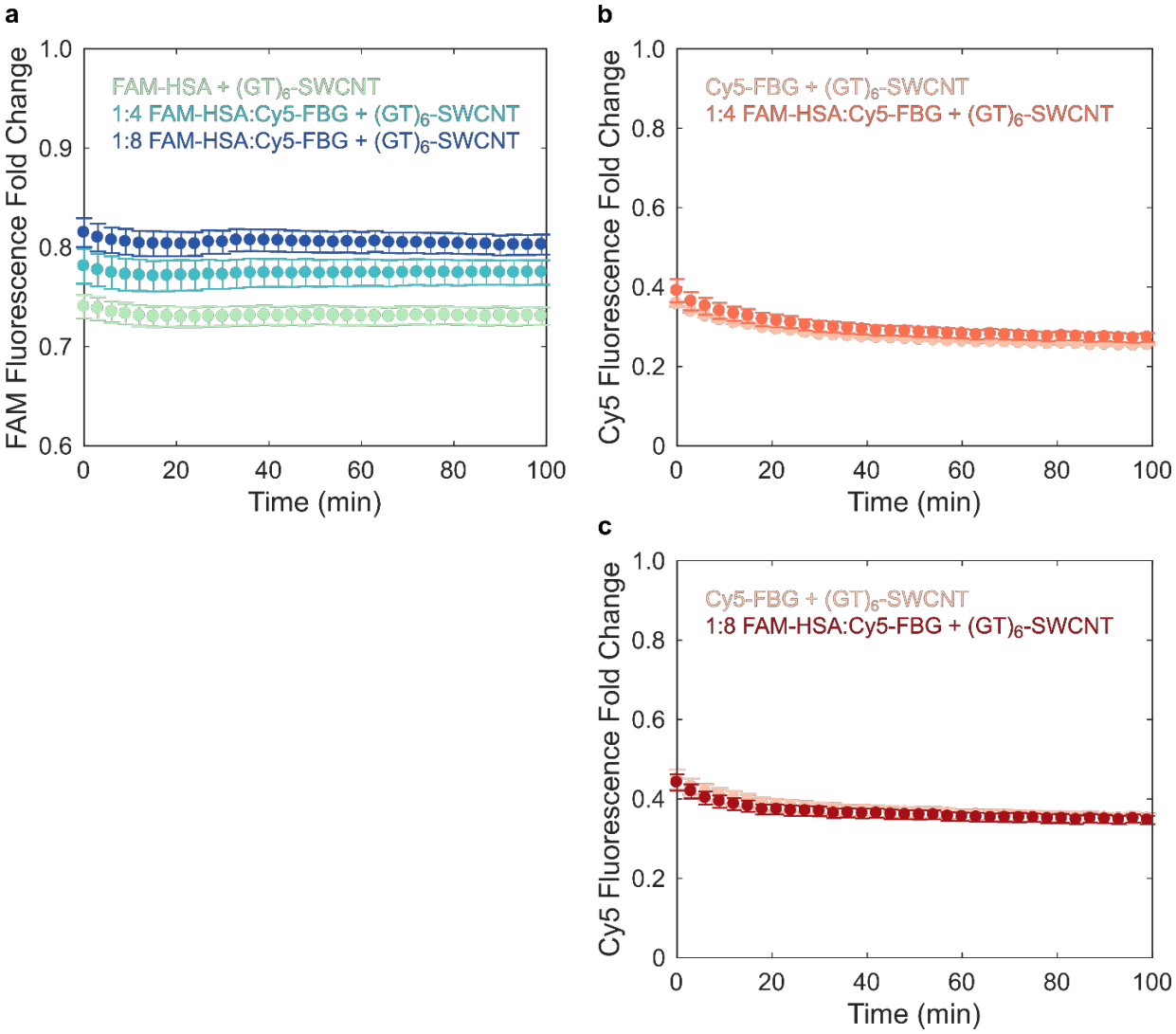

Figure 3-16. Tracking competitive adsorption of two protein species onto SWCNT surface. (a) Adsorption of 20 µg/mL FAM-HSA to 5 µg/mL $(GT)_6$ SWCNTs tracked by FAM quenching in the presence of Cy5-conjugated FBG at 0, 80, and 160 µg/mL. (b-c) Comparison of Cy5-FBG adsorption in the presence and absence of 20 µg/mL FAM-HSA, with Cy5-FBG concentrations of (b) 80 µg/mL and (c) 160 µg/mL. Error bars represent standard error between experimental replicates (N = 3).

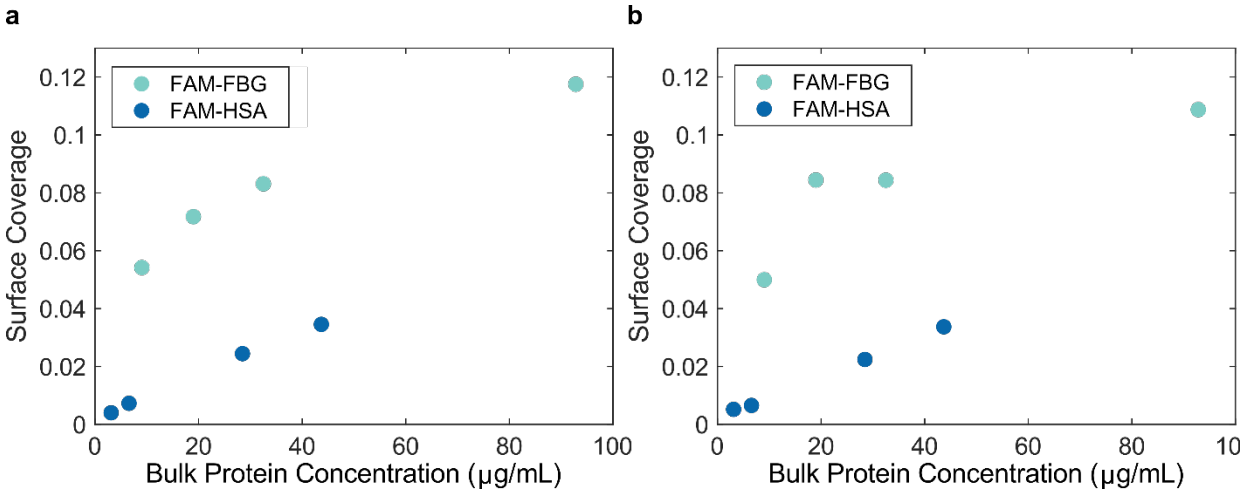

Figure 3-17. Surface coverage of protein on SWCNTs in end-state corona. Isotherm-type plots of surface coverage vs. bulk protein concentration for the end-state (2 h post-injection) of each tested protein concentration reveals higher surface coverage of FBG than HSA on the SWCNT surface for all tested concentrations. Surface coverage was calculated as the ratio of bound protein to total SWCNT surface site concentration, normalized to either (a) average surface site concentration or (b) individually fit surface site concentration. Bulk protein concentration is the remaining free protein in solution at the end-state.

Figure 3-17 gives rise to protein:SWCNT molar ratios of 32.7 and 20.5 for albumin and fibrinogen, respectively. These molar ratios are in comparison to the theoretical close-packed monolayer calculations of 98.2 (side-on) and 28 (end-on) for albumin and 6.7 (side-on) and 62.8 (end-on) for fibrinogen, indicating mixed orientations and/or multiple layers of each respective protein present on the SWCNT surface. In previous literature, protein packing on SWCNTs was found to result in high suspension yield (characterizing solubilized SWCNTs via absorbance) yet low dispersion quality (characterizing individually stabilized SWCNTs via fluorescence) for 1:1 molar ratios, and vice versa above a threshold of approximately 5:1.[263] As such, the calculated protein loadings in the current study reveal high protein loading on SWCNTs that may increase dispersion quality, leading to the observation of retained SWCNT fluorescence (due to the individually protein-solubilized SWCNTs) even upon entering colloidally unstable regimes that result in visible aggregation.

3.6.2 Extended Methods for PAGE to Quantify ssDNA and Protein Exchange

To validate the corona exchange assay, we performed polyacrylamide gel electrophoresis (PAGE) to quantify the unbound DNA and protein after 1-h incubation period of $(GT)_6$-Cy5-SWCNTs with either FAM-labeled human serum albumin (HSA) or fibrinogen (FBG) proteins. FAM-proteins were incubated with $(GT)_6$-Cy5-SWCNTs (final concentrations of 5 µg/mL of $(GT)_6$-Cy5-SWCNT with 40 µg/mL of either FAM-HSA or FAM-FBG) for 1 h, then free protein and ssDNA were quantified by PAGE run according to the Ornstein-Davis protocol[264] (adapted in Bio-Rad Mini-PROTEAN Tetra Cell manual). Samples were added to PAGE sample buffer (0.0625 M Tris-HCl, 30% glycerol) in a 1:2 ratio of sample to buffer. 20 µL total sample volume was applied per well. PAGE separation was carried out in 1 mm vertical mini gel format (Bio-Rad Mini-PROTEAN Tetra Cell) with a discontinuous buffer system under native conditions. Gel

composition was 8% acrylamide (total monomer), 0.375 M Tris-HCl, 0.05% APS, 0.05% TEMED for the resolving gel and 4% acrylamide (total monomer), 0.125 M Tris-HCl, 0.05% APS, 0.1% TEMED for the stacking gel. Electrode buffer was 25 mM Tris and 192 mM glycine (pH 8.3). Separation was run with 200 V for 30 min, gels were extracted, and the FAM and Cy5 labels were visualized with a gel imager (Typhoon FLA 9500, 473 nm and 635 nm lasers for FAM and Cy5, respectively, General Electric). FAM and Cy5 fluorescence intensities were quantified with ImageJ. Control PAGE experiments were done to validate that (i) all bands are resolvable on separate color channels and (ii) there are negligible interactions between proteins and ssDNA. The band structure for HSA run on native PAGE was confirmed by previous literature,[265–267] therefore HSA bands were quantified by summing the 3 bands. FBG was quantified by the sole band that entered the gel. The uniform lower green band is accounted for by diffusion of the small free FAM molecule across the wells upon sample loading and prior to electric field turn-on (as confirmed by control gels).

3.6.2.1 Extended Materials for Biomolecule Corona Exchange Assay

Cy3-RNA: UUC CGU AUG UUG CAU CAC CTT (5' Cy3-labeled custom RNA oligo with HPLC purification, Integrated DNA Technologies, Inc.). This particular RNA sequence was chosen because it serves as the antisense strand in a SWCNT-mediated plant delivery study.[268] Exchange was monitored with $(GT)_6$-Cy5-SWCNTs.

Cy5-phospholipid: 1,2-distearoyl-sn-glycero-3-phosphoethanolamine-N-[amino(polyethylene glycol)-2000]-N-(Cyanine 5), abbreviated DSPE-PEG(2000)-N-Cy5 (Avanti Polar Lipids, Inc.). This phospholipid was chosen because it has been previously used to functionalize SWCNT for brain imaging applications.[174] Exchange was monitored with $(GT)_6$-FAM-SWCNTs.

Eosin-peptoid: $(Nae–Npe)_9$-$(Nce–Npe)_9$): N-(2-aminoethyl) glycine (Nae) and N-(2-phenethyl) glycine (Npe) units, abbreviated $(Nae–Npe)_9$, and N-(2-carboxyethyl) glycine (Nce) and Npe, abbreviated $(Nce–Npe)_9$.[269] This peptoid sequence was chosen because it has been used to construct a SWCNT-based nanosensor.[270] Exchange was monitored with $(GT)_6$-Cy5-SWCNTs.

3.6.3 Calculation of ssDNA-Protein Exchange Energies on SWCNTs

3.6.3.1 Calculation of ssDNA-SWCNT Binding Energy

For this analysis, we use adsorption energies of nucleotides to SWCNTs from Johnson et al.'s solvent-explicit, all-atom MD simulations of nucleotide hetero- and homo-polymers to SWCNTs.[271] Individual nucleotide energies (Table 3-6) are used to calculate the total binding energy of $(GT)_6$ ssDNA to SWCNTs as **-166.0 kcal/mol**. This total energy of $(GT)_6$-SWCNT binding is in close agreement with values calculated from other sources by various methods: (i) Das et al.,[272] calculated from density functional theory (DFT) and experimentally from isothermal titration calorimetry (ITC) (-149.4 kcal/mol) and (ii) Gowtham et al.,[273] calculated from a first principles model (-114.8 kcal/mol) (Table 3-6).

Table 3-6. Adsorption energies of individual nucleotide to SWCNTs.

Nucleotide	Energy (kcal/mol)[271]	Energy (kcal/mol)[272]	Energy (kcal/mol)[273]
A	-13.84	-11.30	-8.994
G	-14.99	-13.14	-11.30
C	-11.07	-6.918	-6.688
T	-12.68	-11.76	-7.841
$(GT)_6$	-166.0	-149.4	-114.8

3.6.3.2 Calculation of Protein-SWCNT Binding Energy

For the analogous protein-SWCNT binding energies, we use an approximate value of -10 kcal/mol per amino acid residue based on the following studies: (i) Shen et al.[274] performed solvent-explicit MD simulations of human serum albumin (HSA) helices on SWCNTs, with an average of -13.51 kcal/mol per residue and (ii) DFT calculations of aromatic acids on SWCNTs reveal an average energy of ~-10 kcal/mol per residue.[275,276]

3.6.3.3 *Exchange of ssDNA and Protein on SWCNT*

We analyze the exchange of $(GT)_6$ ssDNA, originally adsorbed on the SWCNT surface, to protein that will adsorb to an equivalent surface area on the SWCNT. The contact area of $(GT)_6$ on SWCNTs has been previously determined by our lab via MD simulations as **2800 Å^2**.[42] As an estimate for how many amino acid residues would occupy this same surface area, we use dimensions for protein beta sheets as a proxy for peptides adsorbing to SWCNTs. Lengthwise, beta sheet spacing is 3.25 Å per residue, therefore X residues occupy a length of 3.25*X Å. The lateral dimension is approximated as twice the residue's variable R-group dimension, based on beta sheet geometry. Assuming aromatic residues primarily interact with SWCNTs (as determined previously in literature[275–277] as well as our lab's protein corona compositional studies), the average R-group lateral dimension is 5.69 Å, so 2*5.69 = 11.38 Å. Thus, contact area per residue is $SA_{residue}$ = (3.25*X Å)*(11.38 Å) = 36.99*X Å^2. For the $(GT)_6$ surface area of 2800 Å^2, this translates to 75.71 amino acids occupying the same surface area on the SWCNT surface. Thus, the total binding energy of protein to SWCNTs is 75.71*-10 kcal/mol = **-757.1 kcal/mol**. This is in order-of-magnitude agreement with Lu et al.'s[278] MD simulation of HSA adsorption to carboxylated-SWCNTs, with total energy ~-500 kcal/mol.

We assume independent binding of ssDNA and protein to the SWCNT surface, as done with the corona exchange kinetic model. This assumption is also in agreement with the literature values, where the "initial" state is the SWCNT in solvent and the "final" state is bound ssDNA or protein to SWCNTs. We note that it is energetically unfavorable to expose the hydrophobic SWCNT surface to solvent, accounting for a *positive* unbinding energy (unfavorable; ssDNA removed from SWCNT surface) and a corresponding *negative* binding energy (favorable; protein added to SWCNT surface). Finally, the Gibbs free energy of exchange from ssDNA to protein on the SWCNT surface can be written as:

$$\Delta G_{exchange} = \Delta G_{protein-SWCNT} + \Delta G_{ssDNA-SWCNT} \quad 3\text{-}6$$

$$\Delta G_{exchange} = \left(-757.1\ \frac{kcal}{mol}\right) + \left(+166.0\,\frac{kcal}{mol}\right) = \boldsymbol{-591.0\,\frac{kcal}{mol}}$$

This analysis emphasizes the energetically favorable displacement of ssDNA on the SWCNT surface by replacement with protein adsorption. This negative net change in free energy in favor of protein-SWCNT binding over ssDNA-SWCNT binding holds across a range of previously reported literature values.

4 Colloid Theory of Interactions Between DNA-Functionalized Carbon Nanotubes and Proteins in Solution

4.1 Chapter Abstract

Applications of nanotechnologies to probe and alter biological systems requires the stability of the nanoparticles within such biomolecule-rich environments. Single-stranded DNA-functionalized single-walled carbon nanotubes (ssDNA-SWCNTs) act as both a molecular-sensing platform and an effective route for genetic cargo delivery. Although experimental studies show that interactions between ssDNA-SWCNTs and surrounding proteins in bioenvironments decrease nanoparticle effectiveness, the theoretical basis of these interactions requires further study. Herein, we adopt a modified DLVO approach to understand interfacial interactions between functionalized nanoparticles with proteins in aqueous solution. The ssDNA-SWCNT is treated as a hollow cylinder, interacting with a protein modeled as either a cylindrical or spherical body, each possessing constant, asymmetric potentials. The influence of nanoparticle and protein parameters on the total potential of mean force is investigated, including colloid geometry (size, shape, fill) and surface morphology (solvation and electrostatics). We explore the interactions of ssDNA-SWCNTs with representative high- and low-binding affinity proteins (fibrinogen and albumin, respectively), as determined by experiment. Finally, the model is extended to study the interactions of ssDNA-SWCNTs with a panel of proteins of varying binding kinetics to ssDNA-SWCNTs. With this better understanding of parameters that govern the interactions between proteins and ssDNA-SWCNTs, nanoparticles may be better designed to resist protein adsorption and subsequent biofouling when applied in protein-rich, *in vivo* environments. [**]

4.2 Introduction

Engineered nanoparticles are an advantageous platform for biological sensing, imaging, and delivery applications due to their distinctive optical and physical properties.[10] For example, a nanoparticle's fluorescence enables optical tracking of the nanoparticle's location or signaling of the presence of target molecules. Moreover, nanoparticles exist at the length scale of fundamental biological processes occurring at the molecular and cellular level. In particular, single-walled carbon nanotubes (SWCNTs) are a promising nanoparticle platform due to their intrinsic near-infrared fluorescence that occurs in the tissue transparency window (NIR-II, 950 – 1700 nm) and is photostable, unlike conventional fluorophores that undergo photobleaching (i.e. degradation due to repeated optical stimulation).[27] These optical characteristics render SWCNTs as an ideal nanoparticle for long time-course *in vivo* imaging through tissue that is otherwise impermeable to visible light. Further, SWCNTs possess a high aspect ratio (~1 nm diameter by ~100-1000 nm length), giving rise to a high surface area available for cargo loading in genetic delivery applications, as well as the ability to penetrate through plant cell walls.[231]

[**] In preparation as Pinals, R. L.; Radke, C.; Landry, M. P. Interactions between DNA-Functionalized Carbon Nanotubes and Proteins in Solution.

SWCNTs, however, are extremely hydrophobic, as they are composed of a graphene sheet (monomolecular, aromatic carbon) in a cylindrical geometry. Functionalization is necessary to disperse SWCNTs for application in aqueous, biological environments. Noncovalent functionalization with amphiphilic polymers is often implemented to disperse SWCNTs, where the hydrophobic portion of the polymer coats the hydrophobic SWCNT surface and the hydrophilic portion of the polymer interacts with the surrounding aqueous solvent.[32] This adsorption process requires the energy input of ultrasonication to initially de-bundle the SWCNTs, then the polymers adsorb and provide both electrostatic and steric stabilization to prevent SWCNT re-aggregation. Polymers that solubilize SWCNTs include nucleic acids (DNA, RNA),[41,268] surfactants (both biological, such as phospholipids, and nonbiological, such as sodium dodecyl sulfate, sodium cholate, etc.),[39,240,279] and peptides (both natural and synthetic, called peptoids).[256,280] In particular, a single-stranded DNA sequence of $(GT)_6$ (i.e. a sequence of the nucleotides guanine, G, and thymine, T, repeated six times) adsorbed onto single-walled carbon nanotubes stabilizes the SWCNT in solution and selectively recognizes the neurotransmitter, dopamine.[40,41,43] Dopamine specifically binds to the surface-constrained $(GT)_6$ that in turn perturbs the local SWCNT electronic environment and modulates the SWCNT fluorescence emission spectrum. Similarly, biomolecules with natural recognition abilities for target analytes can be grafted to the nanotube surface, such that the SWCNT serves as the transducer upon molecular recognition.[38,281,282]

Despite the promise of such ssDNA-SWCNT platforms, SWCNTs become destabilized when introduced into biological environments. Competitive adsorption of surrounding biomolecules to the SWCNT surface, most notably proteins, cause this destabilization. Adsorption of proteins to SWCNTs results in adverse outcomes including unpredictable nanoparticle functionality, aggregation, and often toxicity. Accordingly, understanding interactions of nanoparticles and biomolecules in solution remains an important problem in successfully implementing nanotechnologies within biological systems.

Our previous work has investigated the composition and dynamics of the adsorbed protein layer formed on the ssDNA-SWCNTs, termed the "protein corona".[82] Two representative proteins emerged from this study: fibrinogen, which adsorbs to ssDNA-SWCNTs with a high affinity, and albumin, which adsorbs to ssDNA-SWCNTs with a low affinity. The adsorption of fibrinogen to nanoparticles is not surprising, as it binds with numerous other surfaces on the nano- and macro-scales.[158,180,183] However, the low abundance of albumin adsorbed in the protein corona is interesting, in that it is the most abundant blood protein in blood plasma, ~55% of total blood proteins by mass,[220] compared to ~4% of fibrinogen in blood plasma.[248] Our previous proteomic mass spectrometry, solution depletion experiments, isothermal titration calorimetry, and in-solution small-angle x-ray scattering confirmed the enrichment of fibrinogen on the ssDNA-SWCNT surface in comparison to albumin.

In addition to protein adsorption, DNA originally adsorbed on the SWCNT surface exchanges with various proteins from a bulk solution.[118] To study this exchange, we developed an assay that monitors different visible fluorophores tagged onto the ssDNA and protein molecules as a function of time (fluorophores of cyanine 5, Cy5, on DNA and fluorescein, FAM, on protein). The SWCNT surface quenches the fluorophore emission when the tagged molecule is in close proximity. Hence, a quenched fluorescence readout indicates the molecule is bound to the SWCNT, while a bright fluorescence readout indicates the molecule is free in solution. We selected a panel of proteins

based on the proteomic mass spectrometry study, and the higher binding affinity of fibrinogen on ssDNA-SWCNTs over albumin was again recapitulated.

This work applies the colloidal framework established by Derjaguin, Landau, Verwey, and Overbeek (DLVO)[283] to model interactions between proteins and DNA-functionalized carbon nanotubes in aqueous electrolyte. DLVO theory characterizes the total potential of mean force (PMF) as the sum of contributions from repulsive Born, repulsive electrostatic double-layer, and attractive dispersion (i.e. van der Waals) interactions. Previous computational and theoretical studies modeled the dispersion stability of surfactants on SWCNTs, invoking molecular dynamics simulations and DLVO theory.[284–286] Such work quantified the interaction energies between the coated nanomaterials in solution, from which energetic barriers preventing coagulation arise.
Other work has examined interaction potentials between two-dimensional graphene sheets in solution, pinpointing strongly attractive dispersion (or van der Waals) interactions as the driving force for aggregation and thus instability.[287,288] However, the asymmetric interaction between a surface-adsorbed molecule on the SWCNT with a distinct second body in solution has not been pursued. Curvature differentiates DNA adsorption on carbon nanotubes to that on other similar materials, such as planar nanoscale graphene, where DNA adsorbs with lower affinity.[285,289,290] Therefore, we expect curvature of both the SWCNT and protein to modulate interactions in the current model. Moreover, the SWCNT is a hollow (low density) substrate, whereby the surface is a single graphene layer that contributes attractive dispersion interactions with the protein far less than a filled nanoparticle case. This work also builds on previous studies of protein-protein PMF modeled by DLVO theory, toward understanding phenomena such as the "salting-out" effect of protein precipitation. These approaches adopted close-range protein-protein interactions that account for the energetic penalty of desolvating the portions of the protein that become solvent inaccessible.[291]

Herein, we compute PMF profiles for a ssDNA-SWCNT interacting with a protein in the dilute solution limit of a two-body interaction. PMF contributions include DLVO energies (i.e. long-range electrostatic repulsion, long-range attractive dispersion forces, and short-range steric repulsion) and non-DLVO energies (short-range desolvation repulsion). Proteins are modeled as either a spherical or cylindrical particle, where albumin is a globular protein approximated as a sphere and fibrinogen has an elongated form treated as a cylinder. To differentiate carbon nanotube-protein interactions from analogous carbon nanoparticle-protein interactions, this study assesses the effect of nanoparticle geometry and fill. This work investigates the impact of varying carbon nanotube solvation energy (to account for varying DNA coverage or other adsorbates) and protein properties (including surface potential, size, and shape). We compare each PMF contribution for the case of albumin interacting with ssDNA-SWCNT (sphere-cylinder) and fibrinogen interacting with ssDNA-SWCNT (cylinder-cylinder). Finally, we compute total PMFs between ssDNA-SWCNTs and various proteins identified by proteomic mass spectrometry as binding vs. nonbinding. This model presents an initial attempt to provide some mechanistic insight as to why different proteins preferentially adsorb to DNA-functionalized carbon nanotubes in solution.

4.3 Methods

4.3.1 DLVO Interactions for Sphere-Cylinder

DLVO electrostatic and dispersion interactions between a sphere and a cylinder are modeled by the surface element integration (SEI) technique expressions derived by Li *et al*.[292] Briefly, SEI incorporates curvature effects integrating interaction potentials over the projection planes of each body (Equation 4-1):

$$V(r) = \int_A \mathbf{n_2 k_2} \frac{\mathbf{n_1} \cdot \mathbf{k_1}}{|\mathbf{n_1} \cdot \mathbf{k_1}|} V_{\text{plates}}(D) dA \qquad 4\text{-}1$$

where r is the distance between the sphere and cylinder, $\mathbf{n}_1$ and $\mathbf{n}_2$ are outward unit vectors normal to the surfaces, $\mathbf{k}_1$ and $\mathbf{k}_2$ are unit vectors directed toward the positive z axes of each body-fixed coordinate system set such that the xy planes are parallel with z axes facing each other, $V_{\text{plates}}(D)$ is the interaction energy per unit area between the two flat projection plates separated by distance D (note that D denotes spacing between plates and r denotes spacing between objects), and A is the projected area of the body on the xy plane. The SEI technique is chosen over Derjaguin's approximation because the latter assumes that interacting bodies are locally flat, or that the interaction distance is shorter than the radius of curvature of the particle, enabling the approximation of differential rings interacting. However, this is not valid for this system, where the particles are nanoscale with high local curvature. Previous work compared the electrostatic PMF SEI solution for an interacting sphere and cylinder to Derjaguin's approximation, revealing equivalent behavior for low curvature bodies, but a diverging PMF at low cylinder to sphere radius ratios (R_c/R_s = 0.1). The dispersion PMF SEI solution for an interacting sphere and cylinder is comparable to Hamaker's solution derived by summing pairwise molecular interactions, revealing the same limiting behavior.

The electrostatic PMF invokes the constant potential assumption with asymmetric charges. This is consistent with previous work for similar systems.[283] The Hogg-Healy-Fuerstenau equation for two planar surfaces of low constant potentials in 1:1 electrolyte (Equation 4-2) is implemented as the electrostatic potential for the SEI method in Equation 4-1:[293]

$$V_{\text{EDL,plates}}(D) = \varepsilon_r \varepsilon_0 \kappa \left[\frac{2\psi_{01}\psi_{02} - \left(\psi_{01}{}^2 + \psi_{02}{}^2\right) e^{-\kappa D}}{e^{+\kappa D} - e^{-\kappa D}} \right] \qquad 4\text{-}2$$

where ε_r is the relative permittivity of the solution, ε_0 is the permittivity of vacuum, κ is the inverse Debye length, ψ_{01} and ψ_{02} are the surface potentials of interacting bodies 1 and 2, respectively, and D is the separation distance between the two plates. The surface potential of colloids is set to the measured zeta potential, in this case in phosphate-buffered saline (PBS).

For the dispersion PMF, the non-retarded dispersion energy per unit area between two flat plates separated by a distance D (Equation 4-3) is used within the SEI method in Equation 4-1:

$$V_{\text{AD,plates}}(D) = -\frac{A_H}{12\pi D^2} \qquad 4\text{-}3$$

where A_H is the Hamaker constant of the two interacting bodies. The SWCNT is then "hollowed out" by subtracting out the PMF contribution from the inner cylinder of radius $R_{c,in}$. Experiment estimate ssDNA-SWCNT dimensions (AFM for the additional DNA height added upon SWCNT adsorption)[197] and per the manufacturer's specifications (small diameter HiPco™ SWCNTs, NanoIntegris). Equations 4-10 and 4-11 in the Appendix give electrostatic and dispersion PMF expressions, respectively, derived from the SEI technique. These equations are for the case of $R_c < R_s$ that is valid for all proteins currently under study. Parameters of all interacting bodies, with their corresponding sources, are tabulated in the Appendix, Table 4-1.

4.3.2 DLVO Interactions for Sphere-Sphere

A sphere-sphere geometry is adopted for albumin interacting with a spherical nanoparticle. Derjaguin's approximation for two spheres models DLVO electrostatic interactions, given by Israelachvili (Equation 4-4)**:**[283]

$$V_{\mathrm{EDL,sph}}(r) = 2\pi\left(\frac{R_{\mathrm{s1}}R_{\mathrm{s2}}}{R_{\mathrm{s1}} + R_{\mathrm{s2}}}\right)\int_r^{\infty} V_{\mathrm{EDL,plates}}(D)dD \qquad 4\text{-}4$$

where R_{s1} and R_{s2} are the radii of spheres 1 and 2, respectively, $V_{\mathrm{EDL,plates}}(D)$ is the electrostatic potential per unit area between two flat plates separated by distance D, and r is the separation distance between the two spheres. The Hogg-Healy-Fuerstenau expression (Equation 4-2) for asymmetric, constant potential interaction provides the electrostatic contribution, $V_{\mathrm{EDL,plates}}(D)$. Israelachvili gives the dispersion interaction for two spheres, following Hamaker's approach of summing molecular pairwise interactions over the exact geometry :[283]

$$V_{AD,sph}(r) = -\frac{A_H}{6r}\left(\frac{R_{s1}R_{s2}}{R_{s1} + R_{s2}}\right) \qquad 4\text{-}5$$

4.3.3 DLVO Interactions for Cylinder-Cylinder

In the case of fibrinogen interacting with ssDNA-SWCNT, a cylinder-cylinder geometry is adopted. Derjaguin's approximation for two parallel cylinders models DLVO electrostatic interactions, following Ohshima *et al.* (Equation 4-6):[294]

$$V_{\mathrm{EDL,cyl}}(r) = \sqrt{\frac{2R_{\mathrm{c1}}R_{\mathrm{c2}}}{R_{\mathrm{c1}} + R_{\mathrm{c2}}}}L_{\mathrm{c2}}\int_r^{\infty} V_{\mathrm{EDL,plates}}(D)\frac{dD}{\sqrt{D-r}} \qquad 4\text{-}6$$

where R_{c1} and R_{c2} are the radii of cylinder 1 and 2, respectively, L_{c2} is the length of the shorter cylinder (in this case, the protein), and the asymmetric $V_{\mathrm{EDL,plate}}$ is from Equation 4-2. The dispersion interaction for two parallel cylinders from Hamaker's approach (Equation 4-7) is:[283]

$$V_{\mathrm{AD,cyl}}(r) = -\frac{A_{\mathrm{H}}L_{\mathrm{c2}}}{12\sqrt{2}r^{3/2}}\left(\frac{R_{\mathrm{c1}}R_{\mathrm{c2}}}{R_{\mathrm{c1}} + R_{\mathrm{c2}}}\right)^{1/2} \qquad 4\text{-}7$$

4.3.4 Non-DLVO Interactions

We adapt the solvation PMF from Curtis *et al.*, originally derived for the case of spherical protein-protein interactions within a DLVO framework.[291] Briefly, the protein-protein PMF includes the free energy of desolvating the protein surface made inaccessible to the solvent as proteins approach:

$$V_{\mathrm{SOLV}}(r) = -\left[A_1(r)\left(\frac{SE}{SASA}\right)_1 + A_2(r)\left(\frac{SE}{SASA}\right)_2\right] \qquad 4\text{-}8$$

where *A(r)* is the surface area inaccessible to solvent, *SE* is the solvation energy, and *SASA* is the total protein solvent accessible surface area. For the current study, this PMF contribution accounts for protein-SWCNT and/or protein-DNA interactions at very short separation distances. Solvation energy here is defined as the hypothetical work to transfer a protein from an ideal gas into an aqueous solution. Previously, Melander-Horvath salting out theory expressed protein solubility in terms of the solvation free energy of the protein, yet this theory applies to desolvating the entire protein.[295] Instead, Curtis's PMF includes only the free energy required to desolvate the surface area of the protein that is inaccessible to solvent due to protein-protein two-body interaction, governed by the separation distance of solvent diameter.[291] We adapt this geometric derivation, done for two spheres of equivalent radius, to derive expressions for *A(r)* in the sphere-sphere, sphere-cylinder, and cylinder-cylinder geometries with nonequivalent radii (included in the Appendix, Equation 4-12). Specifically, for the case of fibrinogen interacting with a ssDNA-SWCNT, the interaction of the two cylinders occurs lengthwise based on previous experimental and computational results confirming this orientation.[82,180] The solvation forces invoke the additivity assumption, the sum of hydration forces (to desolvate polar residues) and hydrophobic forces (to desolvate nonpolar residues), with the respective surface-exposed fractions. This work calculates these solvation energies and solvent accessible surface areas using the GETAREA program, based on atomic solvation parameters derived from empirical vapor-to-water free energies of transfer of amino acid side-chain analogs and analytical calculation based on the protein structure, respectively.[296] For the ssDNA-SWCNT, a combination of two previous DFT studies estimates the solvation energy: the first, provides the solvation energy of C_{540} per unit area,[297] the second study to corrects for the polar $(GT)_6$ molecules on the SWCNT surface.[298] The number of $(GT)_6$ per SWCNT was previously determined by experiment, as described elsewhere.[118]

4.3.5 Total PMF

With the last component of the total PMF as the Born repulsive interaction, a step-function at a separation distance of zero, the total PMF is then given by Equatin 4-9. The temperature is set at T = 22.5°C in PBS, pH 7.4 (137 mM NaCl, 2.7 mM KCl, 10 mM Na_2HPO_4, and 1.8 mM KH_2PO_4; net ionic strength 162.7 mM, Debye length 0.754 nm).

$$V_{\mathrm{total}}(r) = V_{\mathrm{SOLV}}(r) + V_{\mathrm{AD}}(r) + V_{\mathrm{EDL}}(r), \qquad \text{for } r > 0 \qquad 4\text{-}9$$

Here, V_{SOLV} is zero for $r < 2r_{\mathrm{solv}}$ for solvent radius r_{solv}. The model is used to investigate interactions of other approximately globular proteins with ssDNA-SWCNTs by changing the spherical body parameters of surface potential, radius of gyration, solvation energy, and solvent accessible surface

area, with parameters in the Appendix, Table 4-1. These proteins are chosen to model interactions with ssDNA-SWCNT based on previous experiments and the availability of the protein structure from the Protein Data Bank, which is required to extract information on the radius of gyration, solvent accessible surface area, and solvation energy. Further, zeta potentials for the individual proteins other than albumin and fibrinogen are estimated to be – 10 mV in PBS and will be confirmed experimentally in the future.

4.4 Results and Discussion

Contributions to the total potential of mean force (PMF) between protein and ssDNA-SWCNT include long-range electrostatic repulsion, long-range attractive dispersion forces, short-range desolvation repulsion (beginning at separation distance equivalent to one solvent diameter), and short-range steric repulsion (at zero separation distance) (Equation 4-9). Computed PMF profiles for varying cases of protein approaching ssDNA-SWCNT in solution exhibit several interesting, general features. First, the long-range electrostatic repulsion contributes only weakly to the total PMF. This may be expected due to prevalent charge screening at the relatively high ionic strength of biological environments (I = 162.7 mM). Accordingly, the barrier to adsorption is the high energetic cost of desolvation encountered at very close approach between the two bodies ($r < 2.75$ Å). This primary maximum in the PMF signifies a stable colloidal dispersion, as this barrier prevents the aggregation of proteins onto ssDNA-SWCNTs that would otherwise occur due to the large attractive dispersion interactions between the two bodies. Experimentally, however, high protein concentrations in bulk solution often leads to ssDNA-SWCNT aggregation. There are two minima in the PMF, where the primary minimum at closest approach is due to the steep drop-off of attractive dispersion forces and the secondary minimum is just beyond where repulsion due to solvation energy occurs at small separation distance.

This study first investigates the impact of varying nanoparticle geometry and fill for the case of a carbon nanoparticle with albumin (held with constant parameters). Figure 4-1 shows the calculated PMF between the different nanoparticles and albumin. The PMF is computed for four cases: a cylindrical nanoparticle, either filled or hollowed, interacting with albumin (Equations 4-1, 4-2, 4-3, and 4-8) and a spherical nanoparticle, either filled or hollowed, interacting with albumin (Equations 4-4, 4-5, and 4-8). Inner and outer radii are held constant between the differing carbon nanoparticle geometries (see all parameters listed in Table 4-1) and the average cylinder length is approximately 350 nm, as experimentally determined by atomic force microscopy and analytical ultracentrifugation for surfactant-coated SWCNTs.[299] Although the principle nanoparticle of interest here, ssDNA-SWCNT, possesses a hollow cylindrical geometry, the other case studies are relevant to closely related and relevant nanoparticle-protein interaction systems. Here, a "carbon-filled" cylinder better approximates a multi-walled carbon nanotube or carbon fiber, a carbon-filled sphere represents a carbon dot, and a hollow sphere represents a fullerene (such as a buckeyball, C_{60}). In Figure 4-1, the PMF maximum increases (~2-2.5 k_BT) as the carbon nanoparticle is hollowed out due to the lessening role of attractive dispersion forces. The interaction between albumin and the carbon nanoparticle is more attractive with the cylindrical geometry, for both filled and hollowed out centers, due to the larger surface area of interaction for attractive dispersion forces. Although the larger surface area slightly raises the repulsive solvation force, deconvoluting each contribution to the total PMF reveals that this repulsive component is outweighed by increasing attractive dispersion forces that ultimately drive the PMF maximum

down. The colloidal suspension is highly unstable in the case of a filled carbon sphere interacting with albumin, as the attractive dispersion interactions drive the energetic barrier close to zero (0.3 k_BT). This PMF indicates that adsorption of albumin on the ssDNA-SWCNT will occur, although with a larger energetic barrier than adsorption to filled nanoparticles. The suspension would be expected to rapidly aggregate in the case of a filled carbon cylinder interacting with albumin because the primary maximum disappears (-0.8 k_BT). This highlights the role of additive van der Waals interactions between the nanoparticle material layers and the solubilized protein, absent for shell-like, single-layer materials such as SWCNTs and fullerenes.

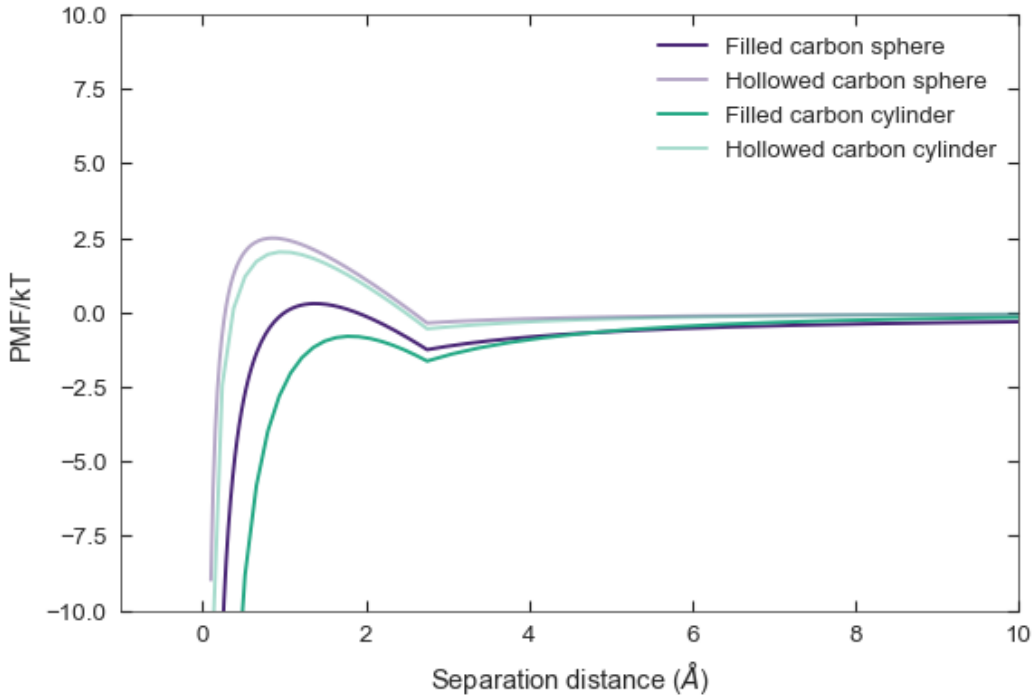

Figure 4-1. Effect of varying carbon nanoparticle fill and geometry on total PMF of interaction with albumin. Total PMF is plotted as the sum of contributions from repulsive Born, repulsive desolvation, repulsive electrostatic double-layer, and attractive dispersion interactions. Carbon nanoparticle properties are varied while parameters for albumin (approximated as a sphere) are kept constant. The spherical carbon nanoparticle interacting with albumin (purple) is either filled (dark purple) or hollowed (light purple). The cylindrical carbon nanoparticle interacting with albumin (green) is either filled (dark green) or hollowed (light green).

Figure 4-2 plots the calculated PMF between the carbon nanotube and albumin for varying nanoparticle solvation energy (Equations 4-1, 4-2, 4-3, and 4-8). Varying solvation energies arises from different surface coverages of DNA on SWCNTs, where lower DNA coverage exposes more hydrophobic SWCNT surface thus lowers the energy required to desolvate, and vice versa. Note that the solvation energy is set as a constant for each PMF calculation, despite DNA being in dynamic equilibrium between the surface-adsorbed and bulk phases.[118,199] For this dilute solution case (one protein with one ssDNA-SWCNT) and this short timescale, however, a constant solvation energy is assumed. The coating identity on the SWCNT also modulates the construct solvation energy, such as other nucleic acids, surfactants, and peptides. For reference, the ssDNA-

SWCNT solvation energy per unit solvent accessible surface area is -4.72 mJ/m^2 for all other calculations. The solvation energy is taken as the value for C_{540} corrected by the contribution of $(GT)_6$ (determined by DFT[297,298]; coverage of $(GT)_6$ per SWCNT determined experimentally[118]). Other values encountered in the literature include: -46.7 mJ/m^2 and -83 mJ/m^2 for graphene (measured by contact angle[300] and surface force balance,[301] respectively), and -62.1 mJ/m^2 for graphene oxide (measured by contact angle[300]). To capture this range of possible values, the solvation energy of the SWCNT is varied over the range of -1 to -100 mJ/m^2. In Figure 4-2, the PMF maximum decreases as the energy required to desolvate the SWCNT surface lowers in magnitude, becoming less unfavorable. Thus, the SWCNT construct possessing the highest solvation energy remains the most stable in solution, with a maximum of nearly 26 k_BT, and albumin is not able to adsorb.

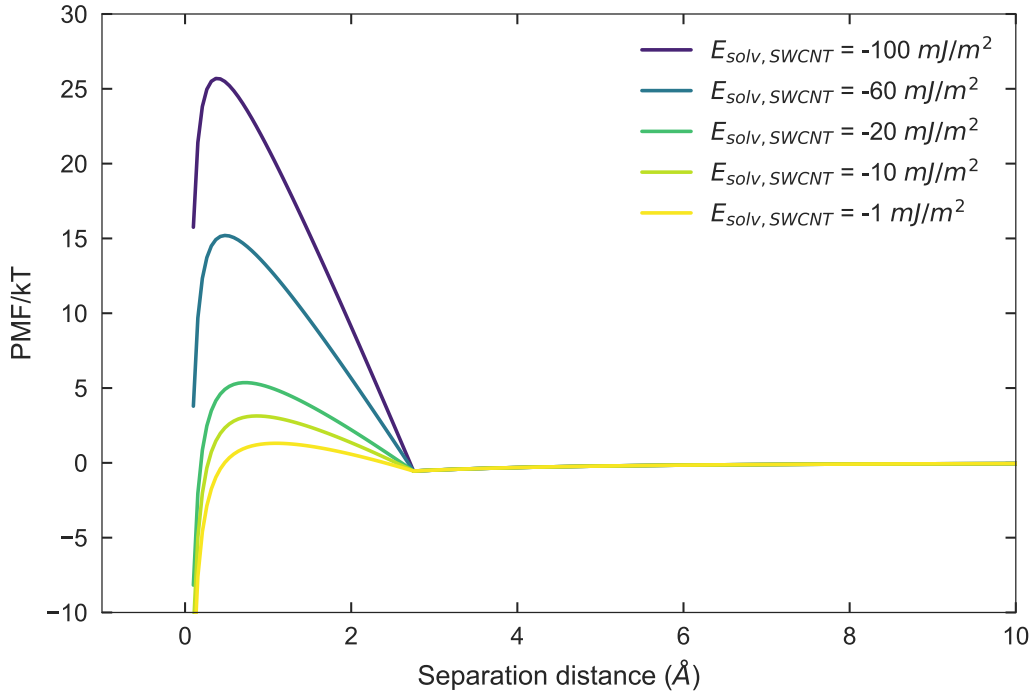

Figure 4-2. Effect of varying carbon nanoparticle solvation energy on total PMF of interaction with albumin. Carbon nanoparticle solvation energy is varied (decreasing negative magnitude moving from purple to yellow) while parameters for albumin (approximated as a sphere) are kept constant.

To understand the role of electrostatics on protein- ssDNA-SWCNT interactions, Figure 4-3 plots the PMF between ssDNA-SWCNT and a protein with various surface potentials (Equations 4-1, 4-2, 4-3, and 4-8). However, the result reveals some unexpected (or non-physical) effects of surface potential on the total PMF. Specifically, the electrostatic contribution to the PMF becomes attractive when surface potentials are the same sign but widely dissimilar magnitudes, at close distances of approach. This same phenomenon arises when one of the surface potentials is zero while the other is finite. These trends are shown in Figure 4-3, where increasing the negative magnitude of the protein surface potential from -1 through -20 mV increases the primary maximum to ~2 k_BT, highlighting increased colloidal stability between the two negatively charged bodies

(DNA-SWCNT is kept at a surface potential of -19.4 mV, determined experimentally). However, as the protein surface potential magnitude increases further to -60 mV, the trend reverses, and the maximum disappears for a surface potential of -100 mV. This result is suspect because the Hogg-Healy-Fuerstenau equation is rigorously valid only for low surface potentials (Equation 4-2).[302] Most proteins are not expected to have zeta potentials at such an extreme, yet this nonmonotonic trend must be recognized as a potential limitation of the current model.

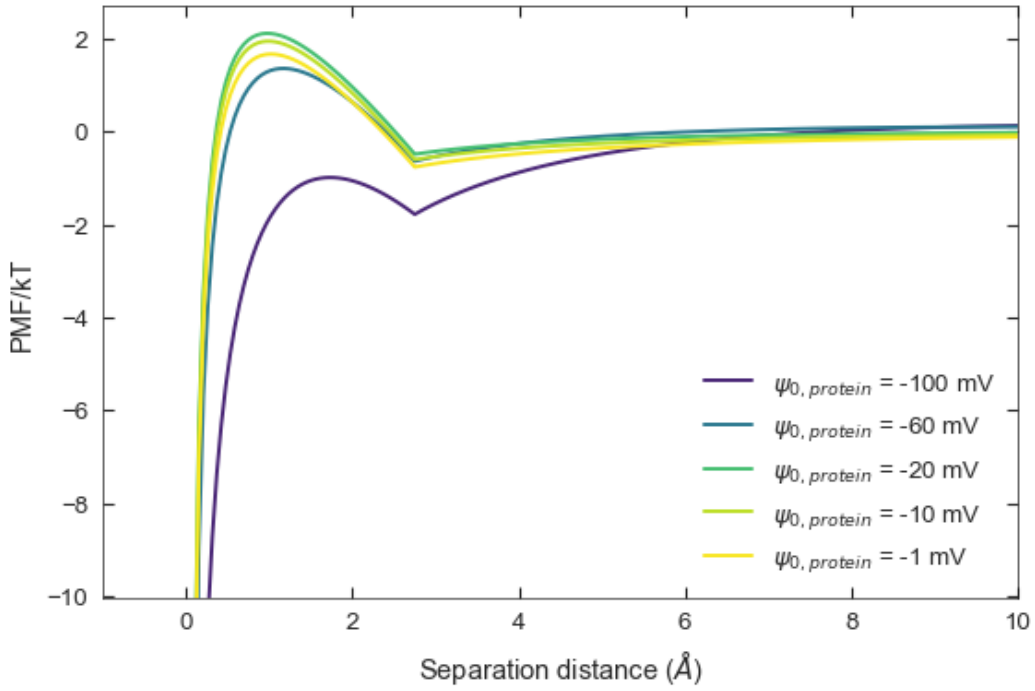

Figure 4-3. Effect of varying protein surface potential on total PMF of interaction with ssDNA-SWCNT. Albumin surface potential is varied (decreasing negative magnitude moving from purple to yellow) while parameters for the ssDNA-SWCNT (modeled as a hollow cylinder) are kept constant. Note the nonmonotonic trend in the PMF maximum, as explained in the text.

Figure 4-4 examines the influence of protein size and geometry by plotting the PMF between cylindrical ssDNA-SWCNT with either a cylindrical protein of radius 10 nm, 5 nm, or 1 nm (Equations 4-6, 4-7, and 4-8), or a spherical protein of radius 10 nm, 5 nm, or 1 nm (Equations 4-1, 4-2, 4-3, and 4-8). All other protein properties besides shape and size are those of albumin. Cylindrical proteins inherently have larger barriers between the primary and secondary minima than spherical proteins because there is more surface area to desolvate upon their approach to the nanoparticle. For the cylindrical protein, decreasing the radius lowers the primary maximum from ~25 k_BT to ~22 k_BT. As the cylinder radius decreases, the curvature increases, resulting in less surface area becoming desolvated at the close approach of the protein to the ssDNA-SWCNT. This lowers the energetic peak caused by the potential of desolvation. However, for the spherical protein, the opposite trend occurs, as decreasing the radius increases the primary maximum to the point of entering a colloidally stable regime of ~2.5 k_BT. This trend occurs because as the radius decreases, attractive dispersion forces decrease. Here, the solvation energy is less of an energetic

penalty because the sphere is inherently more solvated than a cylindrical geometry at the same spacing from the ssDNA-SWCNT.

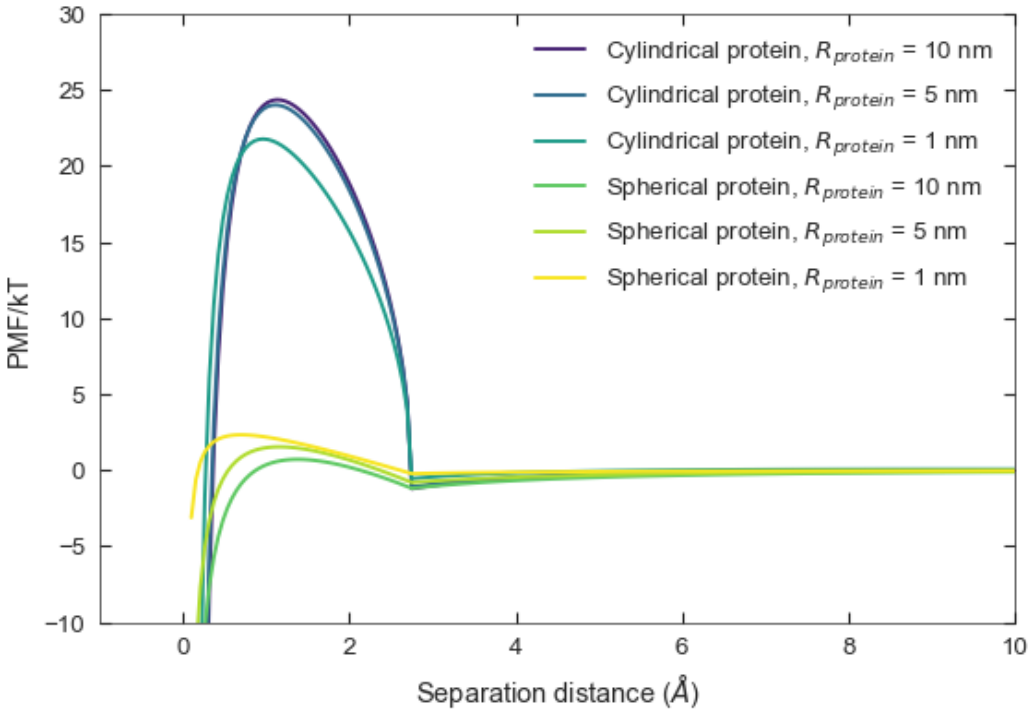

Figure 4-4. Effect of varying protein size and geometry on total PMF of interaction with ssDNA-SWCNT. Albumin size and shape are varied, while parameters for the ssDNA-SWCNT (modeled as a hollow cylinder) are kept constant. PMFs are plotted for cylindrical protein (purple-blue) radius decreasing from 10 nm (purple) to 1 nm (blue), interacting with ssDNA-SWCNT. PMFs are plotted for spherical protein (green-yellow) radius decreasing from 10 nm (green) to 1 nm (yellow), interacting with ssDNA-SWCNT.

Figure 4-5 shows the computed PMFs between the DNA-SWNCT and two model proteins, each with the total PMF decomposed into the respective contribution (Equation 4-9). Based on previous experiments, this study chooses albumin as the model low-binding protein (Figure 4-5a) and fibrinogen as the model high-binding protein to ssDNA-SWCNTs (Figure 4-5b). Electrostatic double-layer interactions play a minor role in this weakly charged system as shown by its low contribution. This is due to the low magnitude surface potentials and high charge screening from salt. Moreover, the double-layer interaction remains largely invariant to changing geometry, always decaying exponentially with distance of a characteristic decay length equal to the Debye length.[283] The importance of the desolvation potential is highlighted in comparing the two proteins, where desolvating fibrinogen requires over an order of magnitude more energy than albumin. Yet, the significantly more favorable attractive dispersion forces for fibrinogen with ssDNA-SWCNT than albumin provide some offset for this high energetic cost of desolvating. Nonetheless, the primary maximum is ~80 k_BT vs. 2 k_BT for fibrinogen and albumin, respectively, indicating that albumin would preferentially adsorb to the ssDNA-SWCNT. However, the secondary minimum is ten-fold lower for fibrinogen than albumin. Proteins may adsorb to ssDNA-SWCNT in a

solvated state, in which case fibrinogen would be predicted to interact more readily with ssDNA-SWCNT over albumin because of the more attractive potential well prior to desolvation, consistent with experiments.

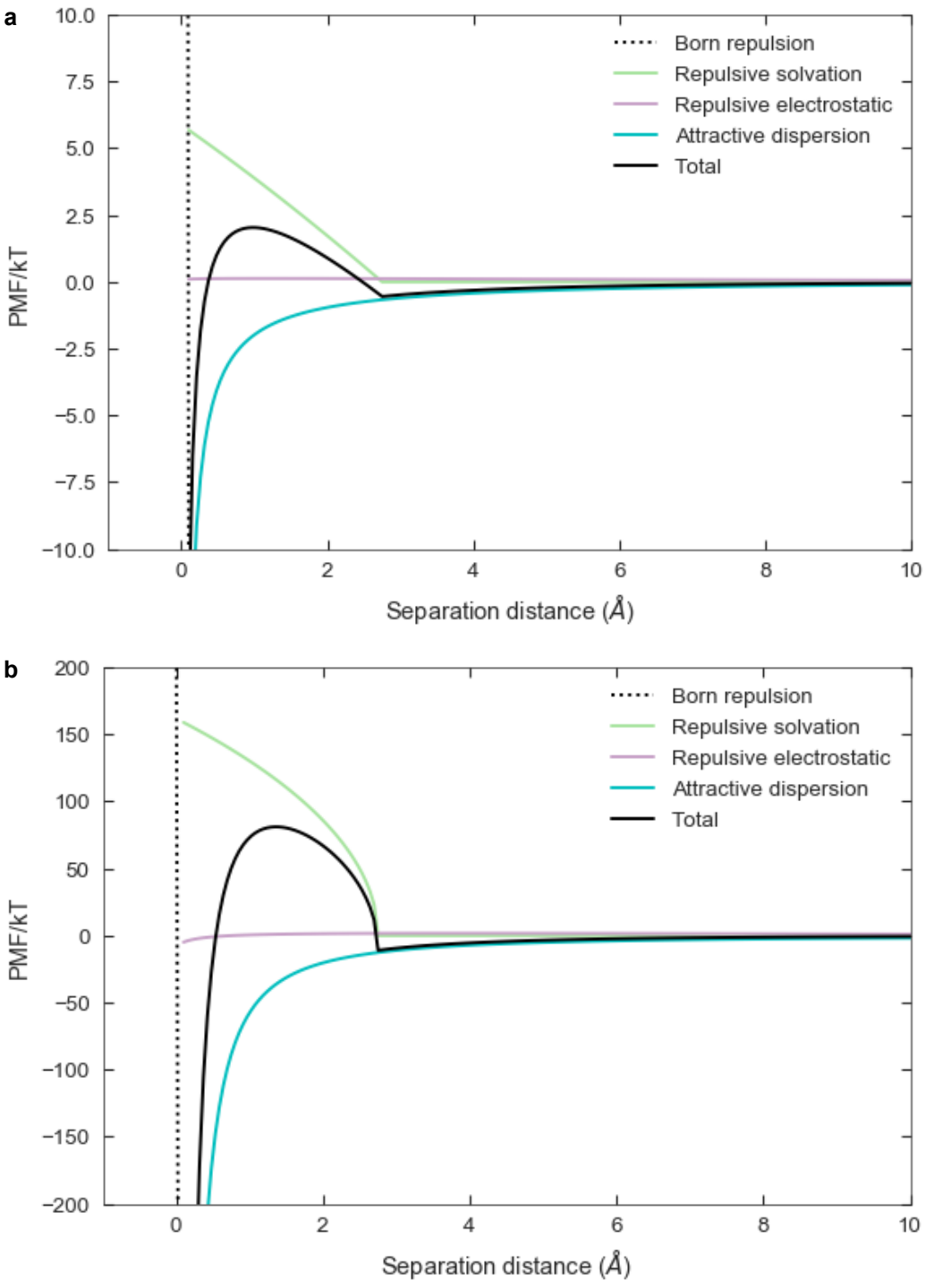

Figure 4-5. Total PMF for proteins interacting with ssDNA-SWCNT, decomposed into each contributing term. Total PMF (solid black) is plotted as the sum of PMF contributions from repulsive Born (dashed black), repulsive desolvation (green), repulsive electrostatic double-layer (purple), and attractive dispersion (blue) interactions. PMFs are included for a ssDNA-SWCNT interacting with either (a) albumin, approximated as a sphere, and (b) fibrinogen, approximated as a cylinder.

To pursue this hypothesis regarding the role of the secondary minimum, Figure 4-6b plots the calculated total PMFs (Equation 4-9) for ssDNA-SWCNT with various proteins identified as interacting with DNA-SWNCT by proteomic mass spectrometry. The corona exchange assay measures DNA florescence as a function of time, as Figure 4-6a shows. This experiment indicates that the expected order of protein binding is apolipoprotein A-I > fibrinogen > complement C3 > immunoglobulin G > albumin. In Figure 4-6a only the Cy5-labeled DNA is monitored. This is due to the nonuniform FAM fluorophore labeling of this protein panel. Cy5-labeled DNA is tracked as a proxy for protein adsorption, whereby a higher increase in free $(GT)_6$-Cy5 indicates more DNA desorption and more protein adsorption to the SWCNT surface. Total PMFs are calculated between each protein and ssDNA-SWCNT, where all proteins besides fibrinogen (approximated as a cylinder) are roughly globular in solution and are treated as spheres. The different order of magnitude in primary maximum for fibrinogen (~80 k_BT) as compared to all other proteins (~2.5 k_BT) highlights the importance of geometry, where fibrinogen again requires significantly more desolvation prior to reaching the primary minimum state. The same general trend with the secondary minimum holds, where proteins that are more likely to bind exhibit a more negative (more attractive) secondary minimum. From the total PMFs, this predicted trend is fibrinogen > apolipoprotein A-I ≈ complement C3 ≈ immunoglobulin G > albumin. This trend captures the higher binding affinity of fibrinogen over albumin. Further experiments would be necessary to fully investigate the role of this secondary minimum in predicting protein adsorption on ssDNA-SWCNTs.

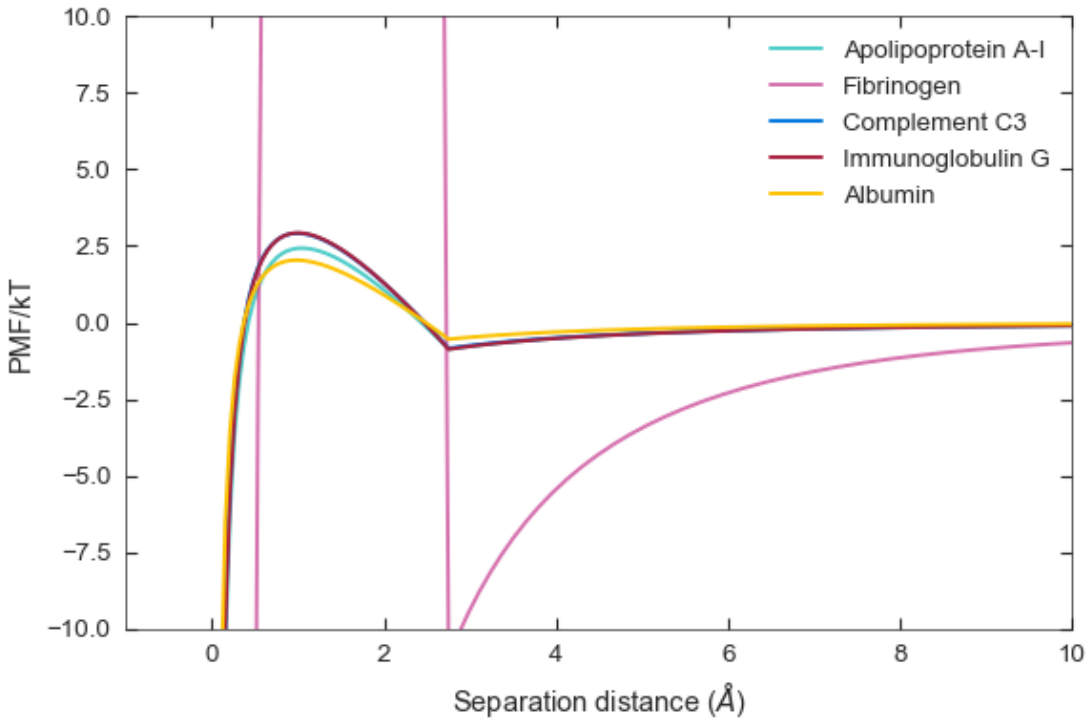

Figure 4-6. Interactions of varying proteins with ssDNA-SWCNT. Total PMF for varying proteins interacting with ssDNA-SWCNT. Protein size, shape, surface potential, and solvation energy are varied, while parameters for the ssDNA-SWCNT (modeled as a hollow cylinder) are kept constant. PMFs are plotted for apolipoprotein A-I (light blue), fibrinogen (light pink), complement C3 (dark blue), immunoglobulin (dark red), and albumin (yellow). Note that the y-range was chosen to highlight the secondary minima of the majority of proteins, while the primary maximum for fibrinogen extends up to ~80 k_BT.

In closing, we discuss some shortcomings of the proposed modified DLVO approach. First, all bodies are modeled as smooth, rigid spheres and cylinders. It has been demonstrated that surface roughness can increase the excluded volume of the protein by 1.7-fold, which is significant in the solvation PMF term.[303] Surface charge is spread out over the entire surface,[283] which disregards the distinctly patterned solvent-exposed residues on proteins (mostly polar) and varying attractive/repulsive potential energy "pockets" that DNA creates on SWCNT surfaces.[42] The conformations of both initial (DNA) and final (protein) entities on the SWCNT surface are assumed to be static, which disregards rearrangement on the SWCNT surface and, particularly for the protein, the likely denaturation that occurs in the bound state. These bodies are immersed in a continuous dielectric medium containing point charges to represent ions, which disregards interactions that arise in considering the salt ion identities (e.g. chaotropic vs. kosmotropic salts).[304] However, such salt-dependent effects on protein solubility are not expected to be observed until approximately 1 M salt concentration (an order of magnitude higher).[291] Finally, we note that the assumptions of DLVO may not fully hold at the nanometer scale, such as the additivity assumption not accounting for contributions from nanoparticle polarizability leading to coupling effects between various interactions.[3]

4.5 Conclusions

In sum, this paper presents a model of the interaction between a protein and ssDNA-SWCNT in solution within a modified DLVO framework. Proteins were modeled as either cylindrical or spherical bodies interacting with a hollow, cylindrical ssDNA-SWCNT. The effects of varying protein and ssDNA-SWCNT parameters on the total PMF and the individual PMF contributions were studied. Proteins of known high- and low-binding affinity revealed the potential importance of the secondary, rather than primary, PMF minimum in guiding selective adsorption. This simple model provides some understanding on what forces drive the process of protein corona formation on ssDNA-SWCNTs when they are introduced into biological environments. Future work could involve extending the model to a non-dilute system, wherein other PMF contributions would include attractive bridging between proteins and DNA adsorbed on different SWCNT substrates, repulsive steric forces between the soft surfaces, among others. The model may be improved by better representing the DNA and protein as soft, flexible polymers rather than a fixed surface potential on SWCNT and a rigid spherical body, respectively. The solvation energy could then be set as a function of adsorbed DNA and bulk protein in proximity to the SWCNT surface. For the SWCNT, a solvent-filled cylinder may be incorporated rather than a fully hollow cylinder, as water has been shown by both experiment and computation to fill the SWCNT upon ultrasonication dispersion.[305] Finally, quartz crystal microbalance with dissipation monitoring (QCM-d) experiments could be pursued toward experimental validation of protein-graphene binding rates. Previous work relates the sum of the PMFs of self-interacting bodies directly to the experimentally accessible second virial coefficient, measured by static light scattering.[291] However, for the current system under study, this relation would have to be adapted by considering the heterogeneity of different interacting bodies. With this framework, the complementary problem may be pursued, namely, the protein adsorbed on the SWCNT exchanging with DNA in solution. Then, a heterogeneous aggregation rate constant can capture the differing kinetics of proteins interacting with the ssDNA-SWCNT.[302] The fraction of bound DNA or protein on the SWCNT surface provides another experimentally accessible parameter to verify the model with.

4.6 Chapter Supporting Information

4.6.1 Full Mathematical Forms

For $R_c < R_s$, the SEI technique for the electrostatic interaction between a sphere and cylinder yields:

$$V_{\mathrm{EDL,sph-cyl}}(r) = 4\varepsilon_r\varepsilon_0\kappa\psi_{01}\psi_{02}\int_0^{\frac{\pi}{2}}\int_0^{R_c}\frac{y\alpha_c}{R_c} \tag{4-10}$$

$$\times\begin{Bmatrix}\operatorname{csch}[\kappa(r+R_s-\alpha_s+R_c-\alpha_c]\\ -\operatorname{csch}[\kappa(r+R_s+\alpha_s+R_c-\alpha_c]\\ -\operatorname{csch}[\kappa(r+R_s-\alpha_s+R_c+\alpha_c]\\ +\operatorname{csch}[\kappa(r+R_s+\alpha_s+R_c+\alpha_c]\end{Bmatrix}$$

$$+\frac{{\psi_{01}}^2+{\psi_{02}}^2}{2\psi_{01}\psi_{02}}\begin{bmatrix}-\coth[\kappa(r+R_s-\alpha_s+R_c-\alpha_c]\\ +\coth[\kappa(r+R_s+\alpha_s+R_c-\alpha_c]\\ +\coth[\kappa(r+R_s-\alpha_s+R_c+\alpha_c]\\ -\coth[\kappa(r+R_s+\alpha_s+R_c+\alpha_c]\end{bmatrix}\Bigg\}dyd\theta$$

$$+\ 4\varepsilon_r\varepsilon_0\kappa\psi_{01}\psi_{02}\int_{R_c}^{R_s}\int_0^{\arcsin(R_c/y)}\frac{y\alpha_c\alpha_s}{R_sR_c}$$

$$\times\begin{Bmatrix}\operatorname{csch}[\kappa(r+R_s-\alpha_s+R_c-\alpha_c]\\ -\operatorname{csch}[\kappa(r+R_s+\alpha_s+R_c-\alpha_c]\\ -\operatorname{csch}[\kappa(r+R_s-\alpha_s+R_c+\alpha_c]\\ +\operatorname{csch}[\kappa(r+R_s+\alpha_s+R_c+\alpha_c]\end{Bmatrix}$$

$$+\frac{{\psi_{01}}^2+{\psi_{02}}^2}{2\psi_{01}\psi_{02}}\begin{bmatrix}-\coth[\kappa(r+R_s-\alpha_s+R_c-\alpha_c]\\ +\coth[\kappa(r+R_s+\alpha_s+R_c-\alpha_c]\\ +\coth[\kappa(r+R_s-\alpha_s+R_c+\alpha_c]\\ -\coth[\kappa(r+R_s+\alpha_s+R_c+\alpha_c]\end{bmatrix}\Bigg\}d\theta dy$$

where $\alpha_c = \sqrt{R_c^2 - y^2\sin^2\theta}$

$\alpha_s = \sqrt{R_s^2 - y^2}$

For $R_c < R_s$, the SEI technique for the dispersion interaction between a sphere and cylinder yields:

$$V_{AD,\mathrm{sph-cyl}}(r) = -\frac{A_H}{3\pi}\int_0^{\frac{\pi}{2}}\int_0^{R_c}\frac{y\alpha_c}{R_c} \times \begin{Bmatrix} {}^{1}/_{(r+R_s-\alpha_s+R_c-\alpha_c)^2} \\ -{}^{1}/_{(r+R_s+\alpha_s+R_c-\alpha_c)^2} \\ -{}^{1}/_{(r+R_s-\alpha_s+R_c+\alpha_c)^2} \\ +{}^{1}/_{(r+R_s+\alpha_s+R_c+\alpha_c)^2} \end{Bmatrix} dyd\theta - \frac{A_H}{3\pi}\int_{R_c}^{R_s}\int_0^{\arcsin(R_c/y)}\frac{y\alpha_c}{R_c} \times \begin{Bmatrix} {}^{1}/_{(r+R_s-\alpha_s+R_c-\alpha_c)^2} \\ -{}^{1}/_{(r+R_s+\alpha_s+R_c-\alpha_c)^2} \\ -{}^{1}/_{(r+R_s-\alpha_s+R_c+\alpha_c)^2} \\ +{}^{1}/_{(r+R_s+\alpha_s+R_c+\alpha_c)^2} \end{Bmatrix} d\theta dy \quad \text{4-11}$$

where $\alpha_c = \sqrt{R_c^2 - y^2\sin^2\theta}$ and $\alpha_s = \sqrt{R_s^2 - y^2}$

Surface area inaccessible to solvent *A(r)* (in Equation 4-8) can be derived for the geometries:

$$\begin{aligned} &\text{I. Sphere} - \text{Sphere/Cylinder} && A(r) = 2\pi R_s\left(R_s - \sqrt{{R_s}^2 - h(r)^2}\right) \\ &\text{II. Cylinder} - \text{Sphere} && A(r) = 4hR_c\sin^{-1}\left(\frac{h(r)}{R_c}\right) \\ &\text{II. Cylinder} - \text{Cylinder} && A(r) = 2RL_{\min}\sin^{-1}\left(\frac{h(r)}{R}\right) \end{aligned} \quad \text{4-12}$$

where R_s is the sphere radius, R_c is the cylinder radius, and R is either for cylinder 1 or 2; L_{min} is the minimum cylinder length, here the lengthwise protein dimension; and *h(r)* is the height of the trapezoid formed between the two shape radii R_1 and R_2, the center-to-center distance r_c = r + R_1 + R_2, and the solvent diameter r_{solv}:

$$h(r) = \frac{\sqrt{(2r_{solv} - r_c + R_1 - R_2)(2r_{solv} - r_c - R_1 + R_2)(2r_{solv} - r_c + R_1 + R_2)(-2r_{solv} + r_c + R_1}}{2(r_c - 2r_{solv})}$$

Table 4-1. Model parameters.

Parameter	Entity	Value	Source
Surface potential	DNA-SWCNT	-19.4 mV	Experiment
	Albumin	-14.27 mV	Experiment
	Fibrinogen	-8.50 mV	Ref.[306]
	All other proteins	-10.0 mV	Estimated; will be confirmed by experiment
Radius	DNA-SWCNT (inner, outer)	(0.427, 0.750) nm	(Estimated from experiment and manufacturer, Ref.[197])
	Albumin	2.740 nm	Ref.[307]
	Fibrinogen	3.067 nm	Ref.[306]
	Apolipoprotein A-I	4.839 nm	Calculated with Ref.[308] and PDB ID: 1AV1[309]
	Complement C3	4.592 nm	Calculated with Ref.[308] and PDB ID: 2A73[310]
	Immunoglobulin G	4.869 nm	Calculated with Ref.[308] and PDB ID: 1HZH[311]
Hamaker constant	DNA-SWCNT + protein	4 k_BT	Ref.[291] (estimated as typical protein-protein A_H value); approximately in line with Ref.[312] (nanoparticles in plants) and Ref.[287] (graphene oxide and reduced graphene oxide nanosheets)
Solvation energy per unit solvent accessible surface area	DNA-SWCNT	-4.724 mJ/m^2	Adapted from Refs.[297,298]
	Albumin	-19.973 mJ/m^2	Calculated with Ref.[296]
	Fibrinogen	-7.750 mJ/m^2	Calculated with Ref.[296]
	Apolipoprotein A-I	-26.448 mJ/m^2	Calculated with Ref.[296]
	Complement C3	-29.157 mJ/m^2	Calculated with Ref.[296]
	Immunoglobulin G	-29.642 mJ/m^2	Calculated with Ref.[296]

5 Supervised Learning Model to Predict Protein Adsorption to Engineered Carbon Nanotubes

5.1 Chapter Abstract

Engineered nanoparticles are an advantageous platform for developing sensors and delivery vehicles toward numerous biotechnology applications. To date, testing the compatibility of nanotechnologies in biological systems requires a heuristic approach, where unpredictable biofouling and off-target effects often prevent effective implementation. Such biofouling effects are the result of spontaneous adsorption of proteins to the nanoparticle surface, forming the "protein corona" and altering the physicochemical properties, and thus intended function, of the nanotechnology. To better apply engineered nanoparticles in biological applications and aid in rational protein-nanoparticle construct design, we aim to gain predictive power over which proteins preferentially adsorb to the nanoparticle surface to form the protein corona. In this work, we develop a random forest classifier (RFC) trained using proteomic mass spectrometry data to model which proteins populate the corona of a candidate optical nanosensor composed of single-walled carbon nanotubes (SWCNTs) functionalized with single-stranded DNA (ssDNA). Using amino acid sequence information from a publicly available protein database, the RFC is designed to predict the propensity for specific proteins to adsorb to the SWCNT surface. We characterize the classifier performance against other models and then apply the classifier to rapidly identify new proteins with high binding affinity to SWCNTs, experimentally testing adsorption of these proteins with a fluorescence-based corona exchange assay to evaluate the predictive power of the model. We further determine protein features associated with SWCNT binding, where proteins high in glycine and disordered domain content are more likely to adsorb to ssDNA-SWCNTs, while proteins high in leucine and beta sheet domain content are less likely to adsorb to ssDNA-SWCNTs. The classifier presented herein provides an important tool to undertake the otherwise intractable problem of predicting protein-nanoparticle interactions, which is needed for more rapid and effective translation of nanobiotechnologies from *in vitro* synthesis to *in vivo* use.[††]

5.2 Introduction

Engineered nanoparticles are poised to transform how we undertake biological sensing,[12,313,314] imaging,[4,5,315] and delivery:[15,316,317] nanoparticle size on the nanoscale enables localization within otherwise inaccessible biological environments, together with highly tunable physicochemical properties to optimize function. Different nanoparticle platforms offer application-dependent advantages, such as near-infrared fluorescent nanoparticles for through-tissue imaging[175,318] or biodegradable nanoparticles for *in vivo* delivery.[319–321] In particular, single-walled carbon nanotubes (SWCNTs) are suited for biological sensing and imaging due to the tissue-transparent and photostable near-infrared fluorescence that they exhibit, in addition to the tunable and sizable surface that they possess.[322,27,10] As such, SWCNTs have been functionalized with biomolecules

[††] In preparation as Pinals, R. L.;* Ouassil, N.;* Bonis-O'Donnell, J. T. D.; Wang, J.; Landry, M. P. Supervised Learning Model to Predict Protein Adsorption to Engineered Carbon Nanotubes.

including single-stranded DNA to create neurotransmitter nanosensors,[40,41,323] synthetic peptides (known as peptoids) to form protein nanosensors,[324] and proteins to construct viral nanosensors.[325] Similarly, biomolecule-functionalized SWCNTs have been demonstrated as an advantageous delivery platform, whereby the high SWCNT aspect ratio promotes access to cellular environments and the large SWCNT surface area enables high-yield cargo loading.[30,231,326,327] Optimizing these biomolecule-nanoparticle interactions is key in enhancing nanotechnology function, and a deeper understanding of such nano-bio interactions would enable more rational conjugate designs.

Yet, functionalized SWCNTs and these nanotechnologies more broadly suffer from unpredictable and often unfavorable interactions with the biological environments in which they are applied. When engineered nanoparticles are introduced into biological systems, endogenous proteins rapidly bind to the nanoparticle surfaces.[160,328,329] This phenomenon is known as protein corona formation. Protein adsorption often leads to surface biofouling and colloidal instability that decreases the ability of the nanoparticle to interact with its surrounding environment, such as sensing nearby analytes or navigating biological barriers.[330,331] For sensing applications, protein corona formation sterically hinders access of target analytes to the nanosensor surface or unpredictably changes the sensor baseline readout.[54,118,332] For imaging and delivery applications, the corona can reduce the efficiency with which nanoparticle-based contrast agents or cargo-filled vehicles reach their intended locations.[130,333,334] Consequently, the *in vivo* trafficking, biodistribution, biocompatibility, and overall functionality of nanotechnologies are often drastically modified by the protein corona.[335,336] Knowledge of the proteins adsorbed in this corona phase would enable better prediction of the biological identity, and thus fate, of the applied nanotechnologies.[337,338] Passivation with anti-biofouling ligands such as polyethylene glycol (PEG) is a promising technique to reduce such protein-binding effects on foreign surfaces and to retain the pristine, as-designed nanoparticle properties.[38,65,334,339–341] Still, the protein corona remains as a complex and poorly understood phenomenon limiting the efficacious application of nanotechnologies in biological systems. Limitations in our understanding are rooted in the highly variable binding profiles of proteins on nanoparticles, arising as a convolution of properties of both the nanoparticles (dominated by surface characteristics) and the biological environments of interest.[38,328] Experimental testing to fully characterize the protein corona on all synthesized nanoparticle constructs within all intended biological environments is laborious and costly, now commonly relying on mass spectrometry-based proteomics.[38,342] Recent work has made headway toward higher-throughput experimental methods.[343,344] However, such techniques remain limited to a subset of nanoparticle systems, excluding classes of nanoparticles such as soft lipid nanoparticles. The ability to predict the protein corona that will ultimately form on nanoparticles *in vivo* remains a challenge that, if overcome, would move the field to *a priori* nanoparticle design.

Pattern recognition techniques, including those of machine learning, offer a route to characterize protein-nanoparticle interactions in a high-throughput manner across this extensive design space of nanoparticles applied in different biological systems. Previous work pioneering this idea applied random forest classification to predict what proteins adsorb to silver nanoparticles in biologically relevant environments.[342] However, the thresholding of whether a protein is classified as in or out of the corona stands to be refined, as well as extension to other nanoparticle types and establishment of a method for classifying proteins based solely on the readily accessible amino acid sequence for each protein. Additional work has examined a new physical descriptor to assess protein surface availability in the nanoparticle-bound state toward *in silico* prediction of protein

corona formation on a panel of nanoparticles, though issues in this methodology arise in characterizing fluorophore interactions on graphene-based substrates that are not easily controlled for.[345] More broadly, most predictive modeling efforts involving nanoparticles applied in biology consider cellular- or organism-level responses, such as cellular association,[59,346] toxicity,[347] *in vivo* fate,[338] and therapeutic efficacy.[346,348] Toward protein-SWCNT conjugate design, some predictive modeling has informed protein candidates that exhibit natural affinity for the graphitic SWCNT surface, across various intended applications.[30] Di Giosia *et al.* have implemented a molecular docking model to determine a panel of proteins that interact with the carbon nanotube surface, yet experimental validation is done in a dried state rather than in the more relevant solubilized state, due to difficulties in studying such interactions.[349]

Herein, we develop a classifier to predict protein-nanotube association based solely on physicochemical properties of proteins. Our purpose is two-fold: as one objective, we aim to predict protein-SWCNT interactions to expect in full biological environments. This knowledge will inform implementation of anti-biofouling strategies toward effective biological application of nanoparticles. Secondly, we intend to predict high-affinity protein binders to SWCNTs and protein features associated with such binding affinity, to improve the process of protein-nanoparticle construct design.[30] This capability would aid in design of nano-bio constructs by eliminating the need to experimentally test innate interactions of each protein with the nanoparticle of interest. Toward these ends, we build our classifier based on mass spectrometry-based proteomic data that quantitatively characterizes the protein corona on our SWCNT-based nanosensors in two relevant bioenvironments: the intravenous environment (blood plasma) and the brain environment (cerebrospinal fluid).[82] We focus on protein adsorption to $(GT)_{15}$-SWCNTs due to their demonstrated applicability for dopamine sensing, however, the work is generalizable to varying nanoparticles.[40,41] Using widely available protein data, we construct a database consisting of physicochemical properties for each corona protein. We train and validate a random forest classifier to predict whether proteins adsorb to nanoparticles, then test our classifier with a set of new experimental proteins. We find that our classifier can precisely target a small number of proteins that adsorb to our nanoparticle. Furthermore, we identify distribution changes among some of the most important protein properties to gain insight on how our classifier identifies positive targets. Namely, high content of glycine residues and intrinsically disordered domains lead to favorable SWCNT binding, whereas high content of leucine and planar beta sheet domains lead to unfavorable SWCNT binding. We conduct experimental validation by means of a corona exchange assay to track real-time, in-solution protein binding to our SWCNT-based nanosensors. In sum, we see this classifier as a valuable method to both overcome the high failure rate in translating nanotechnologies from *in vitro* validation to *in vivo* deployment, and to aid in rational design of future nano-bio tools.

5.3 Results and Discussion

5.3.1 Experimental Protein Corona Composition on $(GT)_{15}$-SWCNTs

The training data was experimentally generated from a selective adsorption assay that quantifies proteins present on $(GT)_{15}$-SWCNT nanoparticles incubated in either blood plasma or cerebrospinal fluid (CSF) of the brain, characterized using liquid chromatography tandem mass spectrometry (LC-MS/MS).[82] This experimental dataset reveals the corona components with quantitative protein amounts. The absolute protein abundance and relative enrichment or depletion

(compared to the control sample of the biofluid alone) was used to indicate whether a particular protein was considered to be in the corona, as will be described in a later section. We included four training datasets: $(GT)_{15}$-SWCNTs in either blood plasma, cerebrospinal fluid, total biofluid datasets, and total naïve. Total and total naïve only differ by one variable, namely, the former contains the biofluid phase from which the protein came from. Although we focus on protein corona characterization with one nanoparticle type, it is worthwhile to note that these protein datasets do not require any information regarding the nanoparticle itself, thus lending this methodology well to extension across various nanoparticles. The only location where nanoparticle data is included is the named class (i.e., in or out of the corona).

5.3.2 Database Development based on Physicochemical Protein Properties

We next curated a protein property database to use with our classifier. We used the amino acid sequence of each protein from the annotated protein database, UniProt,[350] to construct an array of physicochemical protein properties with the BioPython package (Table 5-3).[351] Our protein property database requires knowledge of and access to only the amino acid sequence, enabling expansion to new proteins as needed for future experimental datasets or nanoparticle-binding proteins of interest. Although UniProt also provides biological protein properties, such as gene ontology, sequence annotations, and specific functional regions, our final classifier was based solely on amino acid sequence data to avoid potential issues of less well-studied proteins that have no annotated features. Importantly, developing a database in this manner expands the number of possible proteins that can be tested because the classifier does not require prior information on the annotated protein sequence nor interactions between the protein and nanoparticle.

The amino acid sequence of a protein provides valuable information including the percentage of a specific amino acid within the full protein; however, spatial organization is disregarded. To complement the sequence-derived dataset, we added the parameter of solvent accessibility that estimates the exposed protein surface area. We implemented NetSurfP 1.1[352] to quantify the number of exposed residues of a particular protein using the amino acid sequence, normalized by either the total number of amino acids or the total number of exposed amino acids. These two choices of normalization provide information on amino acid content on the surface relative to the full protein or relative to only other surface-exposed residues, respectively. To collate this data, we programmatically created submissions from UniProt and rapidly collected data, aligning with our goal of creating an easily expandable database.

5.3.3 Thresholding to Determine Placement In or Out of the Corona

The decision of whether a protein was categorized as in or out of the corona was informed from the protein abundance data as determined by LC-MS/MS experiments. Proteins were placed into the corona based on two criteria: relative change and an abundance threshold (5-1). First, if a protein was more abundant in the nanoparticle-bound case than it was in the control solution of the native biofluid without any nanoparticles present, then it was classified as belonging in the corona. The remaining proteins were ordered by abundance and fit to an exponential distribution. Increasing the power of the exponential leads to a lower in-corona threshold, placing more proteins in the corona. Importantly, this thresholding approach reflects that depletion of a protein in the corona (relative to the protein amount in the biofluid alone) does not necessarily qualify a protein

as being out of the corona, as a protein that is significantly depleted may still be present in the corona with a high absolute quantity.

$$A_{Relative,\ normalized} > 1 \quad \textit{and} \quad A_{normalized} > A_{threshold} \qquad 5\text{-}1$$

$$\gamma_{protein} = |\{n\,|A_n > A_{threshold}\}|$$

$$n_{low\ abundance} \approx exp\ (-power)$$

5.3.4 Random Forest Classifier Development using Established Protein Property Database

In line with previously published work, we implemented a random forest classifier (RFC) to classify the proteins as in or out of the corona phase on $(GT)_{15}$-SWCNTs. We chose to pursue ensemble methods due to the concern of overfitting the classifier. To confirm the choice of RFC over other potential classifiers, we tested an assortment of classifier types (Figure 5-7). The highest performing classifiers were the RFC and an AdaBoost classifier using decision trees. We selected the RFC for this study because the corresponding precision (0.654) and accuracy (0.744) values were superior to that of the AdaBoost tree, while retaining similar area under the receiver operating curve (AUC; 0.700). However, the AdaBoost tree did perform better than the RFC in recall (0.608). After the results of all classifiers were tabulated, it was confirmed that the RFC was our best choice, as the RFC had one of the highest accuracies and AUCs. Moreover, the RFC provided the highest precision, or positive predictive value, giving the experimenter confidence in the results of this classifier.

During model validation, there was a central problem in selecting proteins that were substantially different from those that were clearly expressed in the dataset. Due to the imbalance of proteins in our LC-MS/MS experimental dataset that were considered present in the corona, we up-sampled our minority class (in corona) to ensure that each time the classifier was trained, we were able to recover an appropriate amount of the minority class. For this reason, the classifier was validated using a stratified shuffle split repeated 100 times. Moreover, we noticed that generalization of this classifier could also be quite poor, especially when considering recall which was below 0.5. To address this issue, a synthetic minority over-sampling technique (SMOTE)[353] was implemented to generate new "proteins" in the minority class (in corona). This analysis revealed that the most precise and accurate results for our classifier were obtained when the minority/majority ratio in SMOTE was 0.6/1.0 (Figure 5-8). The recall of our classifier was improved over 11%. The introduction of the described methods widely expanded the number of proteins that were placed in the corona, thus enhancing the classifiers generalization ability.

5.3.5 RFC Verification

Using an RFC, classification tests were run on the data marked in or out of the corona and classifier performance was scored (Figure 5-1). With the above-described method, datasets were iterated through that were identical except for which proteins were marked in the corona. The classifier was then refreshed and the standard protocol for training the classifier was repeated to gather metrics related to classification: accuracy, area under the receiver operating curve (AUC), precision, and recall. The metrics were recorded up until a thresholding power of 3.5, at which point higher powers no longer changed the number of proteins counted as in the corona, in intervals

of 0.25. We ultimately decided on selecting a power of 2.0 because this provided the highest values for precision (0.628), AUC (0.697), and accuracy (0.734), while only suffering slightly in recall (0.573). All reported results for the remainder of this work use a power of 2.0 for placing proteins in the corona.

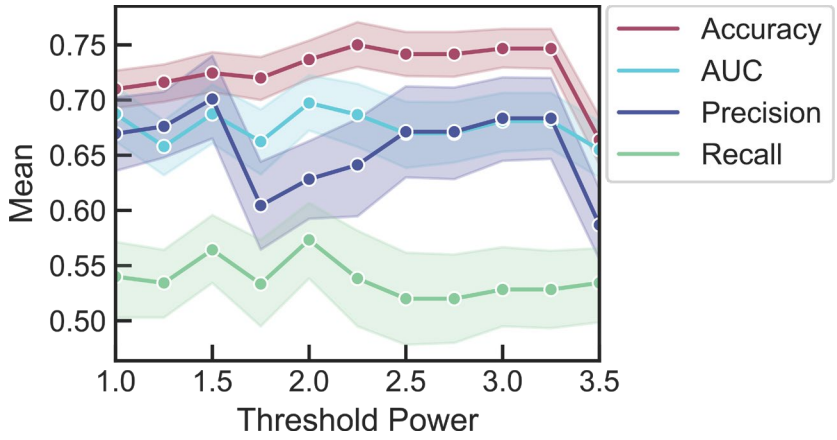

Figure 5-1. Random forest classifier (RFC) metrics of accuracy, area under the receiver operating curve (AUC), precision, and recall as a function of threshold power for classifying proteins as in vs. out of the corona phase on $(GT)_{15}$-SWCNTs. A threshold power value of 2.0 was selected for subsequent analyses due to the optimal combination of the recorded metrics. Error bars are a 95% confidence interval.

During the development of our classifier, k-fold validation was used to check the success of our classifier regarding accuracy, area under the receiver operating curve, recall, and precision. The dataset was divided into a training and test set at the beginning of each k-fold, then the training data was fit to an untrained classifier. Next, the test set was used to make predictions and compared with our true answers. The result of this classifier was saved then the process was repeated, with the classifier naïve at the beginning of each iteration. This process is graphically depicted in Figure 5-2. This method was used to ensure that the subset of proteins generated more accurate metrics for the classifier, considering each protein revolves into the testing set during one of the folds. Statistics represented in this work are generated from the k trials used in this verification step.

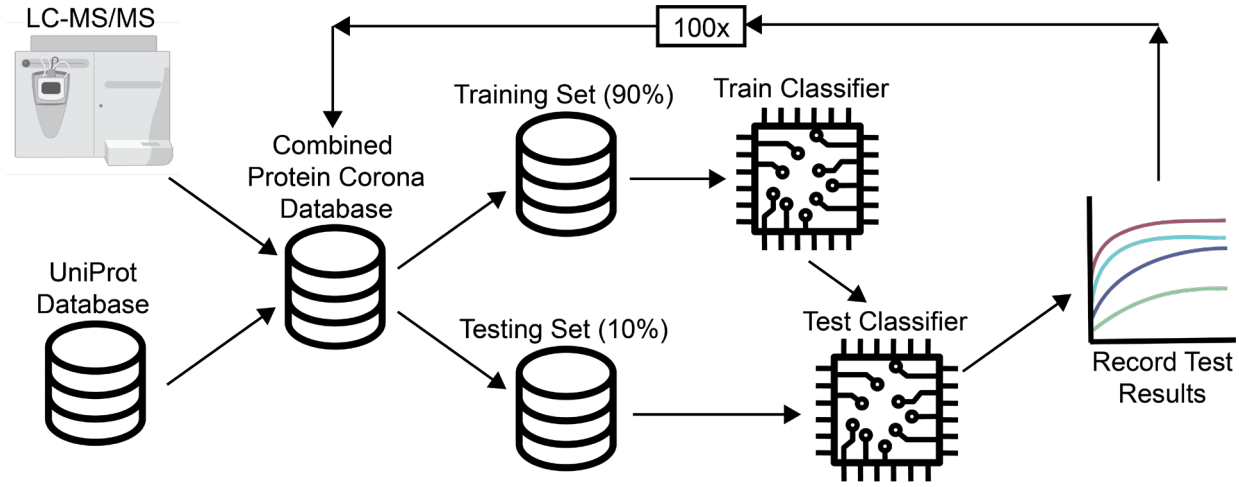

Figure 5-2. Random forest classifier (RFC) workflow used in splitting-based predictions.

Throughout this process, results were collated from each round of the classifier. The first trial was the difference of two datasets, total vs. total naïve (Figure 5-3). The only difference between these two sets is the inclusion of one Boolean column that dictates which biofluid dataset this protein came from. We observe that the inclusion of this information does not provide any significant improvement to our classification ability on our complete dataset. Thus, we deemed this column unnecessary to include for future runs. Moreover, keeping this column would have led to a natural problem when selecting new proteins that may not be present in blood plasma or CSF.

We next trained the classifier on corona proteins present in one biofluid and attempted to predict corona proteins present in another biofluid. For this case, instead of splitting the training data, the classifier was trained on one complete dataset, then the second dataset was subset into a testing set. We repeated this 100 times to generate statistics for the classifier. We notice similar results in AUC (CSF: 0.642, plasma: 0.678), accuracy (CSF: 0.666, plasma: 0.687) and recall (CSF: 0.598, plasma: 0.587) regardless of what biofluid the classifier was trained on (Figure 5-3). However, there is a visible difference between precision (CSF: 0.523, plasma: 0.649) of each of these classifiers. The difference in these metrics arises from the inclusion of a few of proteins that are present in the corona of one biofluid and are not present in the corona of the other (e.g., apolipoprotein A-I and haptoglobin). This highlights that our dataset does not contain any information about the biofluid. Due to this limitation, our classifier has no way of adjusting to this discrepancy. However, this problem only appears to affect a few proteins.

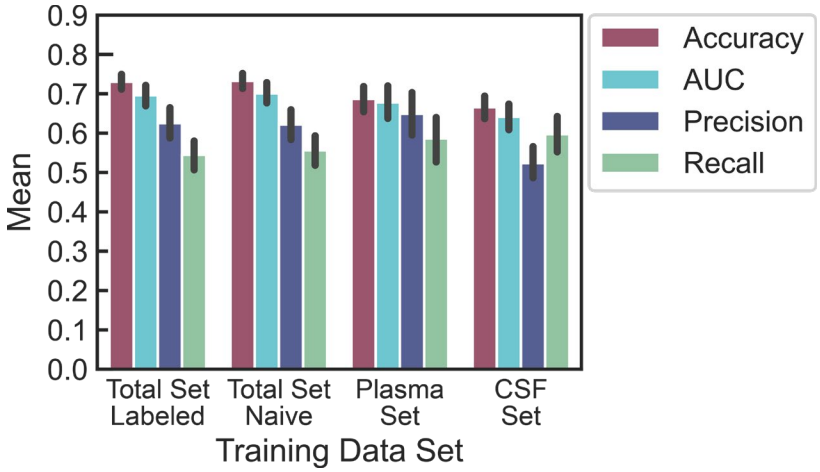

Figure 5-3. Classifier results on varied biofluid (plasma or cerebrospinal fluid, CSF) training datasets. Negligible differences arise between the RFC's ability to classify the total set with or without the biofluid label. Training the RFC on one biofluid and testing against the second biofluid produced similar metrics except for precision, attributable to a few proteins labeled in the corona of one biofluid but not the other. Error bars are a 95% confidence interval.

5.3.6 Feature Analysis for Importance and Correlation with Class Predictions

During the development of our model, 86 protein features were mined as potentially important to classify these proteins as in vs. out of the nanoparticle corona (Table 5-3). Each feature was examined for the extent of contribution to the overall classification ability of the system using an ANOVA test. Features were added in one-by-one until the classifier had scored all 86 features (Figure 5-4). This analysis indicates that there is a minimum number of features of approximately 10 to result in a sufficient classification ability. We also note that use of approximately 30 features provides a maximum for recall and AUC metrics, however, we are not near the maximum for precision at this point. If we extend out to 86 features, we see an increase in the precision ability of our classifier with only a marginal decrease in AUC and recall. We ultimately decided to retain all features because precision is slightly more important for our classifier: providing more precise results will allow this tool to be more accurate for experimenters who are using this tool to look for new targets.

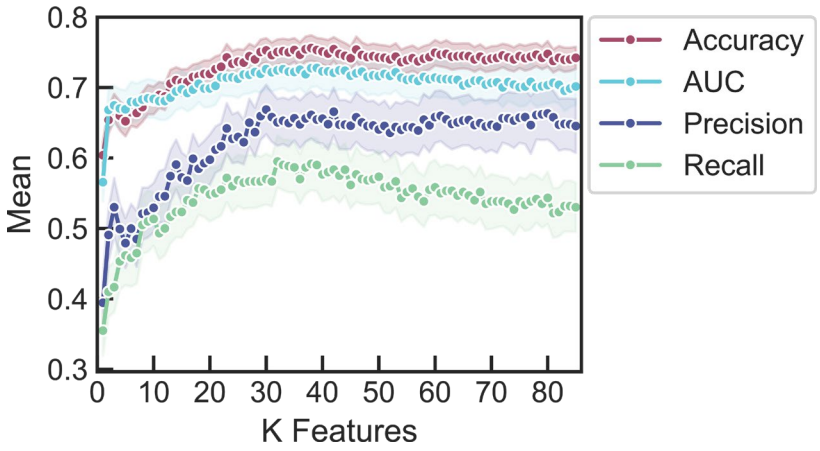

Figure 5-4. Classifier results on the total naïve set with reduced protein features, ranked by ANOVA.

Using the feature ranking by ANOVA, the ten most important protein features were identified (Table 5-1). For the top four most important features, we calculated basic kernel density estimates on distributions of these features, sorted by whether the protein was in or out of the corona. Since RFCs do not provide correlational information (i.e., whether a high value leads to a positive outcome), we examined how distributions of these features changed to hypothesize correlations (Figure 5-5). We find that percent amino acid glycine and percent disordered secondary structure are features that correlate more positively with being in the corona. Conversely, the percent amino acid leucine and percent beta sheet secondary structure correlate more negatively with being in the corona. Previously, we linearly regressed the log-fold change (of protein amount in the corona vs. in the native biofluid) against physicochemical protein properties to understand protein features that govern corona formation, using these same nanoparticle and biofluid data sets.[82] High leucine content was similarly determined to be less favorable for protein adsorption. High glycine content was found to be associated with more favorable protein adsorption when included in the regression analysis. However, glycine contribution was not evaluated in the original regression due to correlation of this independent variable with other protein features, as the calculated variance inflation factor was greater than the set threshold value.[82] As such, glycine content impact could not be deconvoluted from other protein properties. This analysis highlights a benefit of the current RFC over the previously applied linear regression approach, where co-dependent variables must be proactively excluded in the latter case. It should further be noted that secondary structure features were not included in the protein property database for the linear regression analysis due to the data sparsity, a problem that is overcome with the current study by implementing BioPython to calculate such features from the amino acid sequence without relying on protein sequence annotations.

Our analysis of top protein features promoting corona binding indicates that more flexible proteins to bind to $(GT)_{15}$-SWCNTs, as inferred by high glycine content and less strict secondary structural domains. This result is in agreement with previous experimental work demonstrating that peptides and small molecule ligands possessing more conformational flexibility bind more readily to carbon nanotubes.[277,354] Increased adsorption propensity suggests that more flexible proteins are able to maximize favorable surface contacts with the highly curved SWCNT, in comparison to rigid

proteins with energetic penalties for adopting new surface-adsorbed conformations. Examining these top-binding features individually in comparison to previous literature, interestingly, glycine displays a relatively low yet favorable free energy change upon binding to pristine SWCNTs, as determined by enhanced sampling molecular dynamics.[355] Intrinsically disordered proteins have been demonstrated to disperse SWCNTs stably in the aqueous phase even under mild sonication conditions, and of note, a fraction of the disordered chain was found to adopt a helical structure upon SWCNT binding.[356]

In contrast, our analysis of top protein features that deter corona binding reveals that proteins high in the aliphatic, hydrophobic amino acid leucine and proteins with more planar beta sheet content are not expected to bind to $(GT)_{15}$-SWCNTs. The finding that hydrophobic leucine does not increase SWCNT binding is not necessarily intuitive, considering that the SWCNT surface is highly hydrophobic. However, this result recapitulates prior literature that nonspecific hydrophobic interactions alone do not drive corona binding;[277,355,357,358] rather, aromatic, hydrophobic amino acids, especially tryptophan, are repeatedly found to be the highest binders to SWCNTs.[277,357–360] This raises the point that the RFC did not highlight any aromatic amino acid contents (tryptophan, tyrosine, or phenylalanine) as key features for corona binding. Therefore, although aromatic amino acids seemingly drive adsorption via π–π interactions with the SWCNT surface when studying the isolated amino acid or short peptide sequences, in the full protein context, these π–π interactions may not be sufficient to drive initial protein contact with the SWCNT surface, as these hydrophobic amino acids are expected to be shielded from solvent in the folded protein core. Finally, the finding that high beta sheet content leads to low protein adsorption to SWCNTs reveals the difficulty for planar protein secondary structures to adapt to highly curved surface. This result is in line with previous work demonstrating that the extremely high curvature of carbon nanotubes must be aligned at the amino acid level of proteins, much less the secondary structure level:[277,357] typical amino acid side chain lengths are on the order of 0.1-0.5 nm, in comparison to the SWCNT diameter of approximately 1 nm. Overall, the identification of these features is important in helping to predict high biofouling protein types or rationally selecting proteins to bind to nanoparticles prior to testing them experimentally.

Table 5-1. Ordered importance of protein features by ANOVA.

Ranking	Feature
1	Amino acid % - glycine
2	Amino acid % - leucine
3	Secondary structure % - sheet
4	Secondary structure % - disordered
5	Fraction exposed / total exposed amino acids - glycine
6	Fraction exposed / total amino acids – glycine
7	Secondary structure % - turn
8	Amino acid % - alanine
9	Fraction exposed / total amino acids - isoleucine
10	Secondary structure % - helix

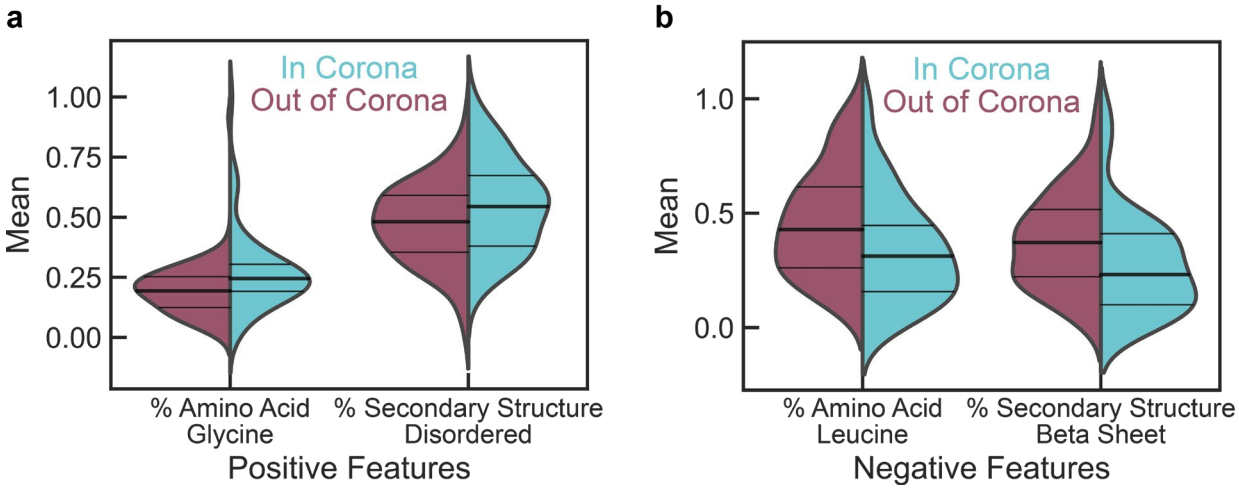

Figure 5-5. Distribution of top four normalized feature values for proteins characterized as out of the corona phase (red) vs. in the corona phase (blue) on $(GT)_{15}$-SWCNTs. Protein features that (a) positively influence or (b) negatively influence probability of protein being classified as in the corona are denoted by distribution shifts toward 1 or 0, respectively.

5.3.7 Experimental Validation with the Corona Exchange Assay

To test the predictive value of our classifier, we next applied our classifier to rank new nanotube-binding proteins and experimentally tested the expected binding order. The classifier was used to predict interaction affinity of $(GT)_{15}$-SWCNTs with a list of over 2,000 total cytoplasmic proteins and nuclear proteins (available for batch download through the UniProt database[350]), readily accessible proteins, and proteins of interest for developing brain-based nanosensors or targeted delivery nanocarriers. Importantly, these proteins are distinct from those present in the plasma and CSF training datasets. Protein binding propensity was determined with associated binding probabilities, as summarized in Table 5-4. We then implemented a corona exchange assay to measure real-time, in-solution binding dynamics on the nanotube surface, as described previously.[118] Briefly, the ssDNA originally adsorbed on the SWCNT surface is fluorescently labeled with a Cy5 fluorophore. When near the SWCNT surface, the fluorophore is in a quenched state. Upon addition of proteins, proteins will differentially bind to the SWCNT and cause various degrees of ssDNA desorption, as denoted by de-quenching of the attached Cy5 fluorophore. Thus, fluorescence tracking of the Cy5-ssDNA provides a proxy for protein binding on the SWCNT. This assay was used to test a panel of proteins predicted to be in the corona (probability > ~0.5) vs. out of the corona (probability < 0.5). Specifically, we tested the protein panel: transgelin, TAR DNA-binding protein 43 (TDP-43), CD44 antigen, and lysozyme C (predicted to adsorb to $(GT)_{15}$-SWCNTs) and L-lactate dehydrogenase A chain (LDH-A), ribonuclease pancreatic (RNase A), glutathione S-transferase (GST), and syntenin-1 (predicted to not adsorb to $(GT)_{15}$-SWCNTs) (classifier results listed in in Table 5-4. We). The relative ordering of protein adsorption based on the end-state value was predominantly in line with predicted outcomes of in vs. out of corona: injection of TDP-43 and CD44 antigen both resulted in sizeable ssDNA desorption from the SWCNT surface, whereas LDH-A, RNase A, GST, and syntenin produced less ssDNA desorption (Figure 5-6a). However, deviations from predicted outcomes arose for both transgelin and lysozyme C. Transgelin and lysozyme C were predicted to be in the corona phase (with probabilities of 62.58% and 47.76%, respectively), yet caused low amounts of ssDNA desorption

and therefore are concluded to undergo low levels of SWCNT binding. To provide a metric of predicted vs. measured monotonicity, the Spearman's rank-order correlation coefficient was calculated to be 0.4048, in comparison with 0.7500 for a previous protein panel comparing DNA desorption end-state vs. proteomic mass spectrometry-derived end-state (Figure 5-6c).[82] Predicted protein binding probabilities were also compared to rate constants fit to the ssDNA desorption dynamics for each protein (kinetic model and fits in SI, Figure 5-9). However, there is poor correlation between the RFC-predicted end-state and experimental dynamics of protein-SWCNT interactions, which may be reconciled with the fact that the RFC was trained on the end-state protein corona rather than the corona composition at earlier time points.

Experimental validation was repeated for the protein panel with Cy5-$(GT)_6$-SWCNTs, as the shorter ssDNA oligomer is displaced more readily and thus displays a greater spread in desorption rates and values between protein species (Figure 5-6b). The resultant protein panel binding order was largely the same as that of Cy5-$(GT)_{15}$-SWCNTs, although LDH-A underwent substantially less binding, in closer agreement with the RFC model. The calculated Spearman's correlation coefficient of 0.3810 is similar to that of $(GT)_{15}$-SWCNTs (Figure 5-6d). Comparison of predicted in-corona probabilities vs. fit rate constants is again less informative, yet in this case, it is easier to note different early-time dynamics that give rise to this lack of correlation (Figure 5-6b).

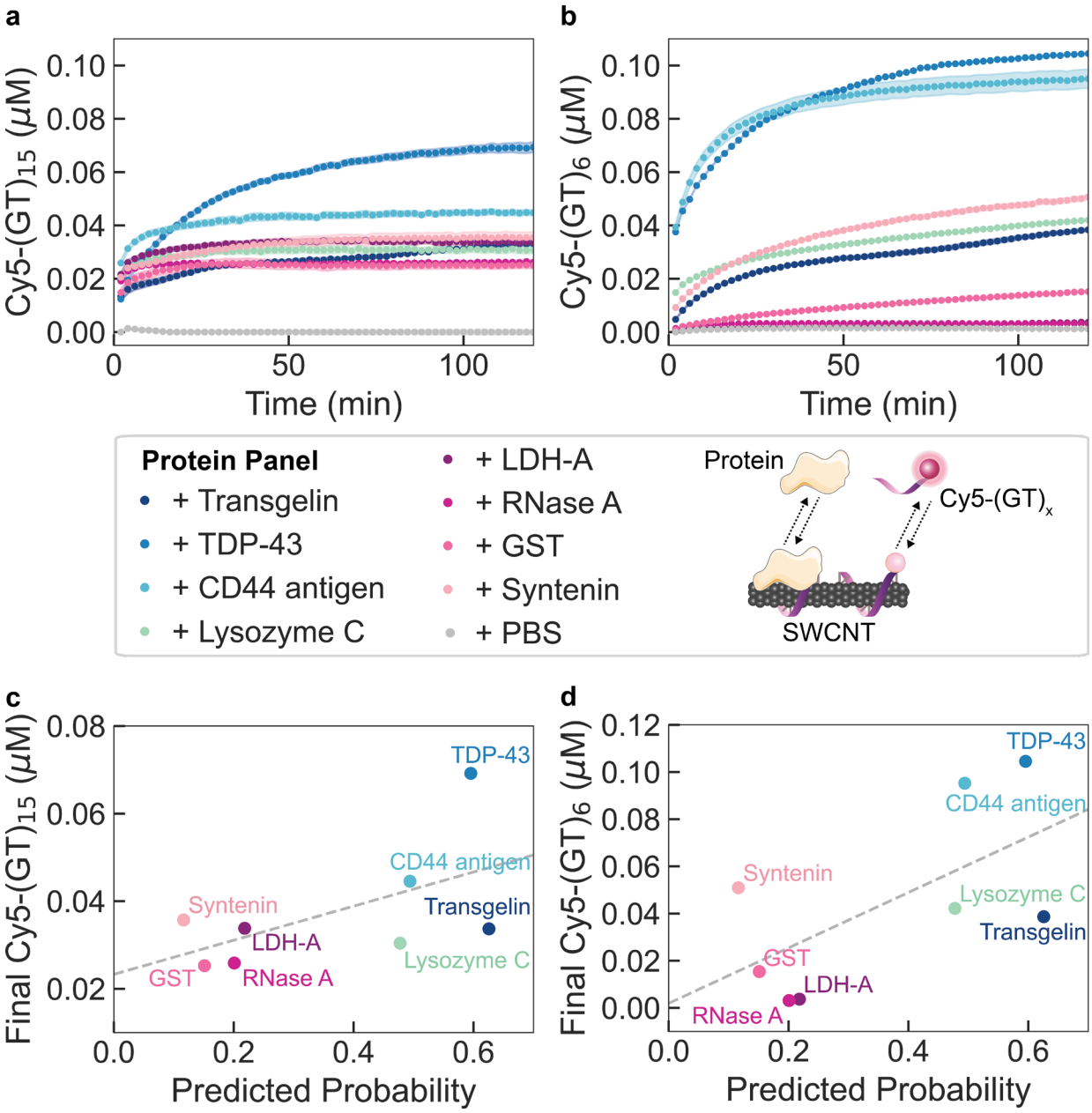

Figure 5-6. Protein corona dynamics assessed for binding of predicted proteins to $(GT)_x$-SWCNTs. (a-b) A corona exchange assay is employed to determine binding of a protein panel (each at 80 mg L^{-1} final concentration) to (a) $(GT)_{15}$-SWCNTs or (b) $(GT)_6$-SWCNTs (each at 5 mg L^{-1} final concentration). ssDNA desorption from the SWCNT serves as a proxy for protein adsorption. Proteins are predicted by the RFC to be in the corona (probability > ~0.5; blue-green colors) or out of the corona (probability < 0.5; purple-pink colors). The protein panel includes: TAR DNA-binding protein 43 (TDP-43), CD44 antigen, and lysozyme C (predicted to be in the corona) and L-lactate dehydrogenase A chain (LDH-A), ribonuclease pancreatic (RNase A), glutathione S-transferase (GST), and syntenin-1 (predicted to be out of the corona). Phosphate-buffered saline (PBS) is injected as a control and desorbed ssDNA is normalized to this initial value. Shaded error bars indicate standard error between experimental replicates (N = 3). (c-d)

End-state desorbed ssDNA is compared to the RFC predicted in-corona probability for (c) $(GT)_{15}$-SWCNTs and (d) $(GT)_6$-SWCNTs.

Examining the protein identities, it is interesting to note that lysozyme has previously been demonstrated to strongly interact with and disperse pristine carbon nanotubes, whereby hydrophobic aromatic amino acids (tryptophan and tyrosine) and cationic amino acids (arginine and lysine) are hypothesized to drive adsorption.[361–365] Yet, here we find that lysozyme interacts less with pre-dispersed ssDNA-SWCNTs based on the corona exchange results. Therefore, strong lysozyme-SWCNT interaction may hinge upon energetic input employed during the initial SWCNT dispersion process. Another protein of note is CD44, which is overexpressed in cancerous states including upregulation in cancer stem cells.[366] The innate affinity for CD44 to the SWCNT surface could be applied to construct a CD44-cell targeted nanotube delivery system.

5.4 Conclusions

In sum, we have developed a classifier to predict protein adsorption on ssDNA-functionalized SWCNTs. We expand upon prior predictive protein corona work by (i) leveraging quantitative protein corona data[82] and experimental confirmation of adsorption by a high-throughput, low-material usage corona exchange assay,[118] (ii) redefining conventions thresholding whether a protein is classified as in or out of the corona, with corresponding prediction probabilities, and (iii) establishing a method for classifying proteins based solely off of the amino acid sequence of the protein of interest. The use of machine learning algorithms allows us to quicky parse protein properties from a publicly available database to determine protein features of interest for corona formation, in turn informing heuristics to rationally select proteins for nanoparticle complexation in the future. Ensemble methods performed better in the corona classification task and a random forest classifier scheme was ultimately chosen and optimized. We find that no single nor small group of protein physicochemical features best determine placement in the corona. Rather, over 80 features are optimal for classification. The classifier enables rapid determination of proteins predicted to enter the corona phase, as validated with the corona exchange assay. Using kernel density estimates, we elucidate protein feature correlation with proteins binding or not binding to SWCNTs. Interestingly, proteins with high glycine content and more disordered secondary structure content (serving as proxies for protein flexibility) are found to bind in the corona, while proteins with high leucine content and beta sheet secondary structure content are not.

Future work will expand *in silico* protein corona prediction and ensure generalizability to capture a wider range of nanoparticles in bioenvironments, such that nanoparticle implementation can be expanded to new systems without the need for mass spectrometry-based proteomic experimental characterization and analysis. In the extension of this work, nanoparticle features may be included to further enhance classification ability on different nanoparticles. However, such nanoparticle features must be readily accessible to retain the triviality of classifying new systems. Recent advances in prediction of protein properties from protein sequences alone are promising toward refinement of the protein database we have curated for this classifier, additionally enabling inclusion of biological protein properties that are not reliant on experimental study.[367] The ability to predict adsorption of specific proteins will enable connection to downstream cellular responses, toxicity outcomes, and overall technology functionality. The developed classifier provides a tool

for rapid prescreening protein candidates for rationally designed nanobiotechnologies as well as predicting key proteins expected to take part in *in vivo* biofouling.

5.5 Materials and Methods

5.5.1 Database Development

Protein information was downloaded from UniProt,[350] including amino acid sequences and sequence annotations. Amino acid sequences were used to generate a series of physicochemical protein properties using BioPython's Protein Analysis module.[351] Amino acid sequences were additionally analyzed by NetSurfP 1.1[352] to determine solvent accessibility, including relative solvent accessibility (RSA), absolute solvent accessibility (ASA), and fractions of each amino acid exposed surface area relative to either all amino acids or only other exposed amino acid surface area. The resulting data was processed and merged with the BioPython analysis. The complete database was run normalized with a Min Max Scalar from Scikit-Learn[368] before being subset and fit to the classification model. This database development method was chosen to enable facile expansion with new protein datasets. Code for this and all subsequent sections can be found in the GitHub link provided.

5.5.2 Criteria for In-Corona Placement

Using the method described previously for protein corona studies by LC-MS/MS,[82] data was obtained for proteins adsorbing to $(GT)_{15}$-SWCNTs in two different human biofluids: blood plasma and cerebrospinal fluid. First, proteins with relative normalized abundances that were increased over the control (proteins in biofluids alone) were placed in the corona. Second, proteins were ranked in order of normalized abundance by decaying an exponential distribution with a particular power to set a threshold to determine which proteins were marked in vs. out of the corona. To select the appropriate power for in vs. out of corona demarcation, powers were tested ranging from 0 to 3.5 in increments of 0.25 and validated using the method outlined in the Classifier Selection section. We found the power of 2 to have the best results regarding accuracy and precision for our system (Figure 5-1), therefore this value was held for the remainder of the analysis.

5.5.3 Classifier Selection

The use of a random forest classifier (RFC), logistic regression, bagging classifier, gradient boosting classifier, AdaBoost classifier, XGBoost classifier, and neural networks were evaluated. The RFC, logistic regression, bagging classifier, gradient boosting classifier, and AdaBoost classifier were imported from Scikit-Learn.[368] The XGBoost classifier was imported from XGBoost[369] for use with Scikit-Learn. Neural networks were imported and developed in TensorFlow 2.0[370] with the Keras API. AdaBoost and bagging classifiers were tested with an underlying support vector machine, decision tree, and logistic regression. The gradient boosting classifier was tested with an underlying decision tree. XGBoost was tested with an underlying decision tree as well as 100 parallel trees. Neural networks were set up in three sizes: small, medium, and large, with 1,665, 13,889, and 832,513 trainable parameters, respectively.

As expected from previous literature, better performance was demonstrated with the RFC and this classifier was accordingly chosen for the remainder of the work. The classifier was next validated

using a stratified shuffle split (100 repeats) validation to ensure high levels of the minority class. The minority class here is the in-corona class which has less proteins than the out-of-corona class. The shuffle split retained 10% of the dataset for corona validation. Results were collected for each fold.

5.5.4 Hyperparameter Tuning

Using Scikit-Learn's GridSearchCV,[368] a wide range of hyperparameters, such as number or depth of trees, were tested with the classifier. With each set of hyperparameters the model was validated using the method dictated in the Classifier Selection section and scored. The classifier was chosen with the hyperparameters optimized for precision using GridSeachCV.

5.5.5 Dimensionality Reduction

To understand the effects of each feature (i.e. variable describing the protein of interest) on the total system, features were ranked using Scikit-Learn's SelectKBest function.[368] Using the ranking established from SelectKBest, the database features were unmasked one-by-one running the classifier as described in the Classifier Selection section until all features had been added in. Metric results were saved, and statistics were calculated.

5.5.6 New Prediction Targets

The classifier was tested against a list of 996 cytoplasmic proteins and 999 nuclear proteins (available for batch download through the UniProt database[350]), together with 42 readily accessible proteins or proteins of interest for SWCNT-based sensing and delivery applications. Amino acid sequences for these proteins were downloaded from UniProt and processed through the database development workflow described above. This new complete protein database was then processed through the classifier k+1 times. The first k times were completed through the described k-fold validation using the combined datasets for $(GT)_{15}$-SWCNTs in plasma and cerebrospinal fluid as the training and verification data. Predictions were recorded at the end of each fold. The last time new proteins were run, all available data was used to train the classifier; this last classifier then provided predictions on the new proteins, as listed in Table 5-4.

5.5.7 Synthesis of ssDNA-SWCNTs

Suspensions of single-walled carbon nanotube (SWCNTs) with fluorophore-labeled single-stranded DNA (Cy5-$(GT)_{15}$ or Cy5-$(GT)_6$) were prepared with 0.2 mg of mixed-chirality SWCNTs (small diameter HiPco™ SWCNTs, NanoIntegris) and 20 μM of ssDNA (3' Cy5-labeled custom ssDNA oligos with HPLC purification, Integrated DNA Technologies, Inc.; excitation 648 nm, emission 668 nm) added in 1 mL total volume of 0.1X phosphate-buffered saline (PBS; note 1X is 137 mM NaCl, 2.7 mM KCl, 10 mM Na_2HPO_4, 1.8 mM KH_2PO_4).[118] This mixture was probe-tip sonicated for 10 min in an ice bath (3 mm probe tip at 50% amplitude, 5-6 W, Cole-Parmer Ultrasonic Processor). Cy5-ssDNA-SWCNT suspensions were centrifuged to pellet insoluble SWCNT bundles and contaminants (16.1 krcf, 30 min). The supernatant containing product was collected and Cy5-ssDNA-SWCNT concentration was calculated with measured sample absorbance at 910 nm (NanoDrop One, Thermo Scientific) and the empirical extinction coefficient, ε_{910nm}=0.02554 L mg^{-1} cm^{-1}.[257] Cy5-ssDNA-SWCNTs were stored at 4°C until use, at

which point the solution was diluted to a working concentration of 10 mg L^{-1} in 1X PBS ≥ 2 h prior to use.

5.5.8 Preparation of Proteins

Proteins were sourced as listed in Table 5-2. Lyophilized proteins were reconstituted to the listed concentration in PBS, tilting intermittently to dissolve for 15 min, and filtering with 0.2 μm syringe filters (cellulose acetate membrane, VWR International). All proteins were purified with desalting columns (Zeba Spin Desalting Columns, 0.5 mL with 7 kDa MWCO, Thermo Fisher Scientific) by washing with PBS three times (centrifuging 1500 rcf, 1 min), centrifuging with sample (1500 rcf, 2 min), and retaining sample in flow-through solution. Resulting protein concentration was measured with the Qubit Protein Assay (Thermo Fisher Scientific).

5.5.9 Corona Exchange Assay

Corona dynamics were measured as described previously.[118] Briefly, equal volumes (25 μL) of ssDNA-Cy5-SWCNT and FAM-protein at 2X working concentration were added via multichannel pipette into a 96-well PCR plate (Bio-Rad) and mixed by pipetting. The PCR plate was sealed with an optically transparent adhesive seal (Bio-Rad) and briefly spun down on a benchtop centrifuge. Fluorescence was measured as a function of time using a Bio-Rad CFX96 Real Time qPCR System, scanning all manufacturer set color channels (FAM, HEX, Texas Red, Cy5, Quasar 705) every 30 s at 22.5 °C, with lid heating off. Fluorescence time series were analyzed without default background correction.

Table 5-2. Purchased protein specifications.

Protein	Manufacturer	Catalog #	Lot #	Source
TAR DNA-binding protein 43 (TDP-43)	R&D Systems	AP-190	22675420A	Recombinant human, expressed in E. coli
CD44 antigen	Acro Biosystems	CD4-H5226	616-784F1-G8	Human, expressed in HEK293
Lysozyme C	Sigma	L2879	SLCF2361	From chicken egg white
L-lactate dehydrogenase A chain (LDH-A)	Sigma-Aldrich	10127230001	42032824	
Ribonuclease pancreatic (RNase A)	New England BioLabs	T3018L		Purified from cow pancreas
Glutathione S-transferase (GST)	Abcam	ab86775	GR3377596-1	Recombinant mouse, expressed in E. coli
Syntenin-1	Novus Biologicals	NBP1-50893	1082301	Recombinant human, expressed in E. coli

5.6 Chapter Supporting Information

5.6.1 Supplementary Figures and Tables

Table 5-3. Protein property list.

Protein Property	Implementation in Code
Fraction of Amino Acid - alanine (A)	frac_aa_A
Fraction of Amino Acid - cysteine (C)	frac_aa_C
Fraction of Amino Acid - aspartic acid (D)	frac_aa_D
Fraction of Amino Acid - glutamic acid (E)	frac_aa_E
Fraction of Amino Acid - phenylalanine (F)	frac_aa_F
Fraction of Amino Acid - glycine (G)	frac_aa_G
Fraction of Amino Acid - histidine (H)	frac_aa_H
Fraction of Amino Acid - isoleucine (I)	frac_aa_I
Fraction of Amino Acid - lysine (K)	frac_aa_K
Fraction of Amino Acid - leucine (L)	frac_aa_L
Fraction of Amino Acid - methionine (M)	frac_aa_M
Fraction of Amino Acid - asparagine (N)	frac_aa_N
Fraction of Amino Acid - proline (P)	frac_aa_P
Fraction of Amino Acid - glutamine (Q)	frac_aa_Q
Fraction of Amino Acid - arginine (R)	frac_aa_R
Fraction of Amino Acid - serine (S)	frac_aa_S
Fraction of Amino Acid - threonine (T)	frac_aa_T
Fraction of Amino Acid - valine (V)	frac_aa_V
Fraction of Amino Acid - tryptophan (W)	frac_aa_W
Fraction of Amino Acid - tyrosine (Y)	frac_aa_Y
Molecular Weight	molecular_weight
Aromaticity	aromaticity
Instability Index	instability_index
Flexibility - Mean	flexability_mean
Flexibility - Standard Deviation	flexability_std
Flexibility - Variance	flexability_var
Flexibility - Max	flexability_max
Flexibility - Min	flexability_min
Flexibility - Median	flexability_median
Isoelectric Point	isoelectric_point
Secondary Structure Fraction - Helix	secondary_structure_fraction_helix
Secondary Structure Fraction - Turn	secondary_structure_fraction_turn
Secondary Structure Fraction - Sheet	secondary_structure_fraction_sheet
Secondary Structure Fraction - Disordered	secondary_structure_fraction_disordered
Length	length
Mass	mass
Fraction of Amino Acids Exposed	fraction_exposed
Fraction of Amino Acids Buried	fraction_buried

Fraction of Exposed Nonpolar Amino Acids / Total Amino Acids	fraction_exposed_nonpolar_total
Fraction of Exposed Nonpolar Amino Acids / Exposed	fraction_exposed_nonpolar_exposed
Relative Surface Area (RSA) - Mean	rsa_mean
Relative Surface Area - Median	rsa_median
Relative Surface Area - Standard Deviation	rsa_std
Absolute Surface Area (ASA) - Sum	asa_sum
Fraction of Exposed Amino Acid A / Total Amino Acids	fraction_total_exposed_A
Fraction of Exposed Amino Acid C / Total Amino Acids	fraction_total_exposed_C
Fraction of Exposed Amino Acid D / Total Amino Acids	fraction_total_exposed_D
Fraction of Exposed Amino Acid E / Total Amino Acids	fraction_total_exposed_E
Fraction of Exposed Amino Acid F / Total Amino Acids	fraction_total_exposed_F
Fraction of Exposed Amino Acid G / Total Amino Acids	fraction_total_exposed_G
Fraction of Exposed Amino Acid H / Total Amino Acids	fraction_total_exposed_H
Fraction of Exposed Amino Acid I / Total Amino Acids	fraction_total_exposed_I
Fraction of Exposed Amino Acid K / Total Amino Acids	fraction_total_exposed_K
Fraction of Exposed Amino Acid L / Total Amino Acids	fraction_total_exposed_L
Fraction of Exposed Amino Acid M / Total Amino Acids	fraction_total_exposed_M
Fraction of Exposed Amino Acid N / Total Amino Acids	fraction_total_exposed_N
Fraction of Exposed Amino Acid P / Total Amino Acids	fraction_total_exposed_P
Fraction of Exposed Amino Acid Q / Total Amino Acids	fraction_total_exposed_Q
Fraction of Exposed Amino Acid R / Total Amino Acids	fraction_total_exposed_R
Fraction of Exposed Amino Acid S / Total Amino Acids	fraction_total_exposed_S
Fraction of Exposed Amino Acid T / Total Amino Acids	fraction_total_exposed_T
Fraction of Exposed Amino Acid V / Total Amino Acids	fraction_total_exposed_V
Fraction of Exposed Amino Acid W / Total Amino Acids	fraction_total_exposed_W
Fraction of Exposed Amino Acid Y / Total Amino Acids	fraction_total_exposed_Y
Fraction of Exposed Amino Acid A / Total Exposed	fraction_exposed_exposed_A
Fraction of Exposed Amino Acid C / Total Exposed	fraction_exposed_exposed_C
Fraction of Exposed Amino Acid D / Total Exposed	fraction_exposed_exposed_D
Fraction of Exposed Amino Acid E / Total Exposed	fraction_exposed_exposed_E
Fraction of Exposed Amino Acid F / Total Exposed	fraction_exposed_exposed_F
Fraction of Exposed Amino Acid G / Total Exposed	fraction_exposed_exposed_G
Fraction of Exposed Amino Acid H / Total Exposed	fraction_exposed_exposed_H
Fraction of Exposed Amino Acid I / Total Exposed	fraction_exposed_exposed_I
Fraction of Exposed Amino Acid K / Total Exposed	fraction_exposed_exposed_K
Fraction of Exposed Amino Acid L / Total Exposed	fraction_exposed_exposed_L
Fraction of Exposed Amino Acid M / Total Exposed	fraction_exposed_exposed_M
Fraction of Exposed Amino Acid N / Total Exposed	fraction_exposed_exposed_N
Fraction of Exposed Amino Acid P / Total Exposed	fraction_exposed_exposed_P
Fraction of Exposed Amino Acid Q / Total Exposed	fraction_exposed_exposed_Q
Fraction of Exposed Amino Acid R / Total Exposed	fraction_exposed_exposed_R
Fraction of Exposed Amino Acid S / Total Exposed	fraction_exposed_exposed_S
Fraction of Exposed Amino Acid T / Total Exposed	fraction_exposed_exposed_T
Fraction of Exposed Amino Acid V / Total Exposed	fraction_exposed_exposed_V

Fraction of Exposed Amino Acid W / Total Exposed	fraction_exposed_exposed_W
Fraction of Exposed Amino Acid Y / Total Exposed	fraction_exposed_exposed_Y
Sum of Absolute Surface Area Normalized to MW	asa_sum_normalized

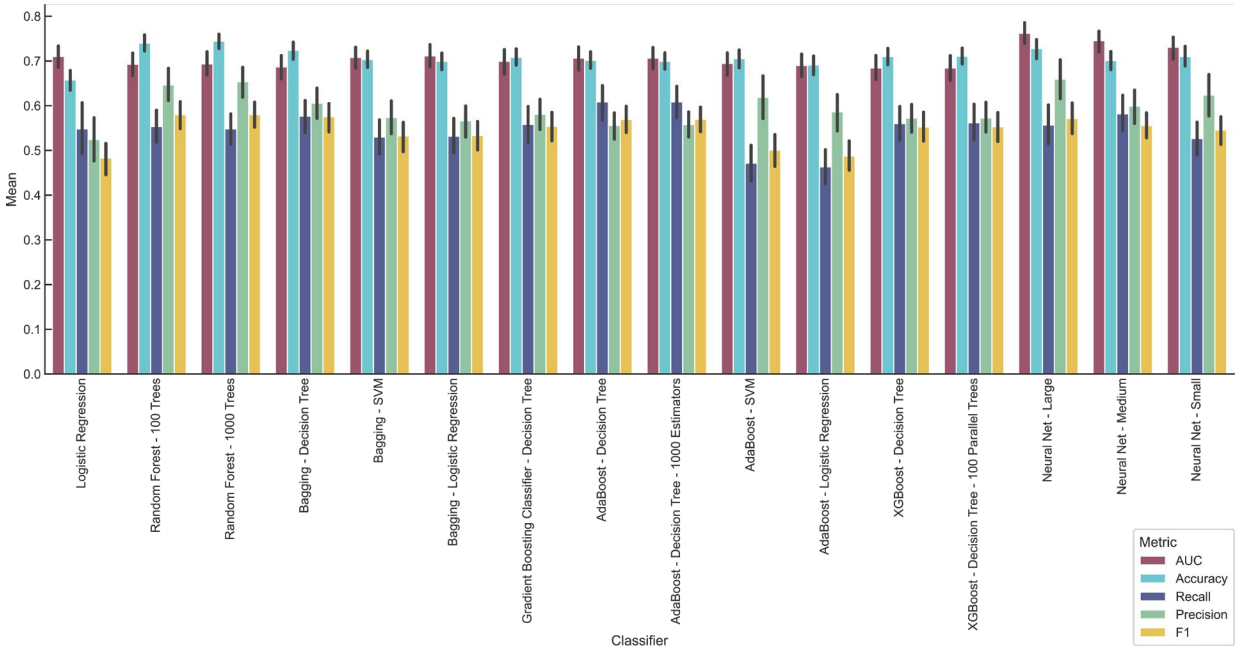

Figure 5-7. Comparison of output metrics for a panel of classifiers. Classifiers tested: logistic regression, random forest (100 or 1000 trees), bagging (decision tree, SVM, logistic regression), gradient boosting classifier (decision tree), AdaBoost (decision tree and with 1000 estimators, SVM, logistic regression), XGBoost (decision tree and with 100 parallel trees), neural net (large, medium, and small sizes). Corresponding classifier metrics are reported for each: accuracy, area under the receiver operating curve (AUC), precision, and recall.

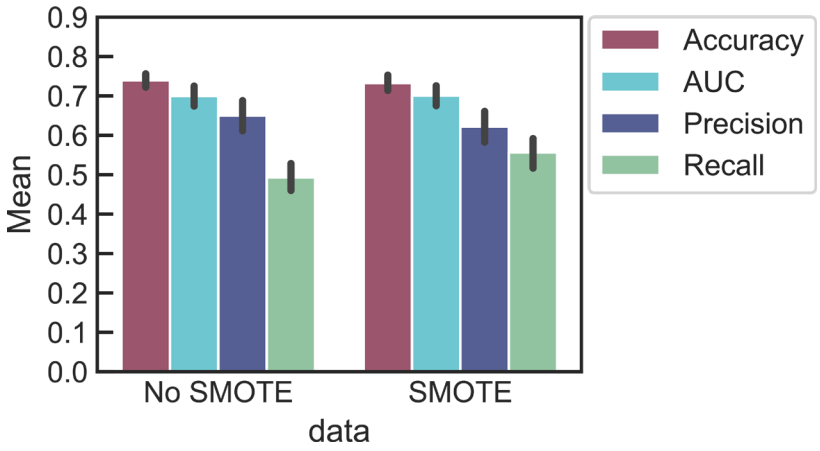

Figure 5-8. Comparison of classifier performance prior to and upon introducing a synthetic minority over-sampling technique (SMOTE).

Table 5-4. Classifier predictions of high- vs. low-binding proteins on $(GT)_{15}$-SWCNTs.

Ranking	Protein	Probability
In 1	Transgelin	62.58%
In 2	TAR DNA-binding protein 43 (TDP-43)	59.55%
In 3	CD44 antigen	49.39%
In 4	Lysozyme C	47.76%
Out 1	L-lactate dehydrogenase A chain (LDH-A)	21.82%
Out 2	Ribonuclease pancreatic (RNase A)	20.09%
Out 3	Glutathione S-transferase (GST)	15.12%
Out 4	Syntenin-1	11.64%

A simple kinetic model was fit to the ssDNA desorption data from the corona exchange assay:

$$D + * \underset{k_2}{\overset{k_1}{\rightleftarrows}} D* \qquad 5\text{-}2$$

Rate constants k_1, k_2, and total concentration of SWCNT surface sites $[*]_{tot}$ were fit using an ordinary least-squares regression (Figure 5-9).

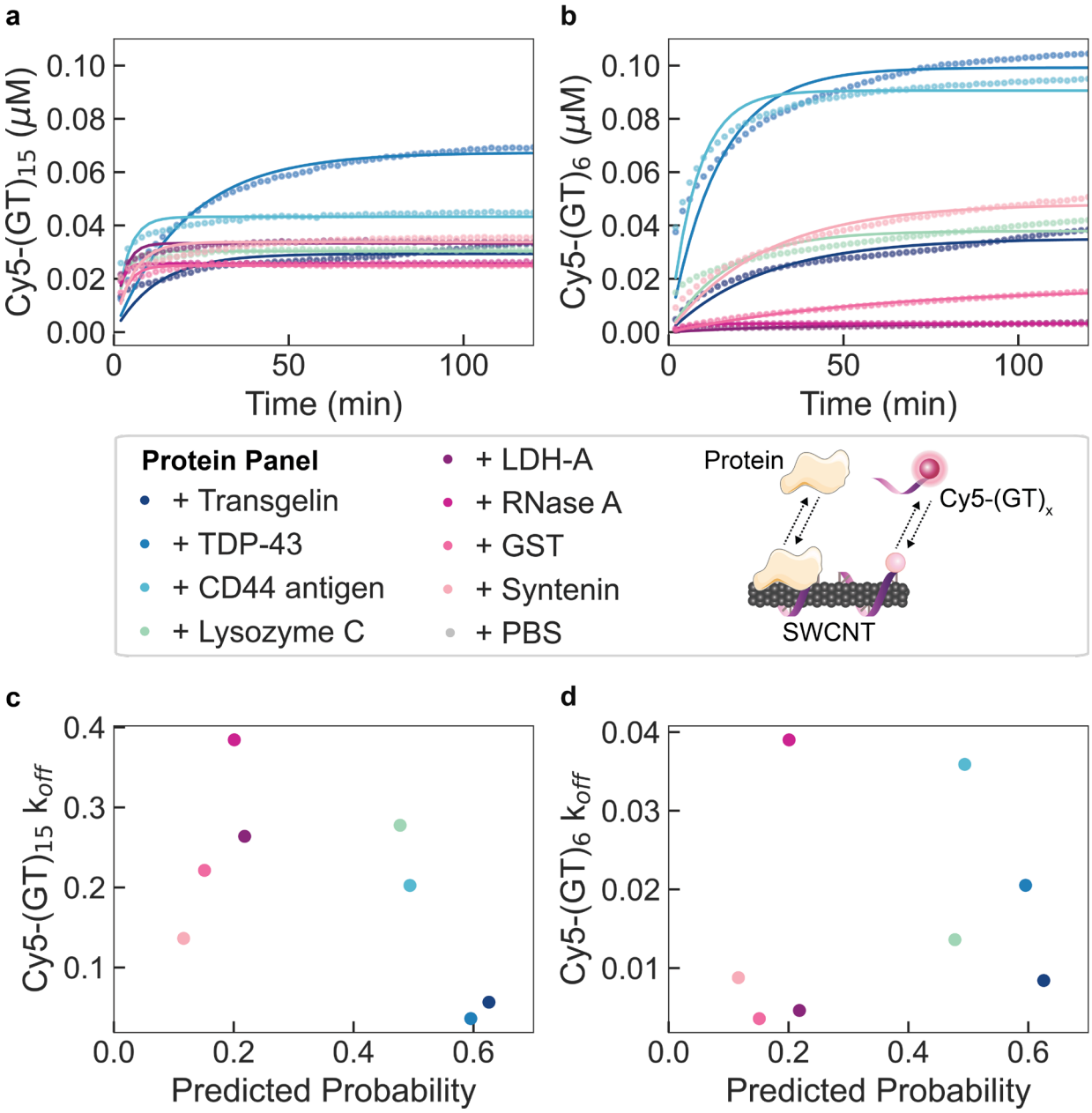

Figure 5-9. Protein corona dynamics assessed for binding of predicted proteins to $(GT)_x$-SWCNTs. (a-b) A corona exchange assay is employed to determine binding of a protein panel (each at 80 mg L^{-1} final concentration) to (a) $(GT)_{15}$-SWCNTs or (b) $(GT)_6$-SWCNTs (each at 5 mg L^{-1} final concentration). ssDNA desorption from the SWCNT serves as a proxy for protein adsorption. Proteins are predicted by the RFC to be in the corona (probability > ~0.5; blue-green colors) or out of the corona (probability < 0.5; purple-pink colors). The protein panel includes: TAR DNA-binding protein 43 (TDP-43), CD44 antigen, and lysozyme C (predicted to be in the corona) and L-lactate dehydrogenase A chain (LDH-A), ribonuclease pancreatic (RNase A), glutathione S-transferase (GST), and syntenin-1 (predicted to be out of the corona). Phosphate-buffered saline (PBS) is injected as a control and desorbed ssDNA is normalized to this initial value. Shaded error bars indicate standard error between experimental replicates (N = 3). (c-d)

Rate constants of ssDNA desorption are compared to the RFC predicted in-corona probability for (c) $(GT)_{15}$-SWCNTs and (d) $(GT)_6$-SWCNTs.

6 Graphene Quantum Dot Oxidation Governs Noncovalent Biopolymer Adsorption

6.1 Chapter Abstract

Graphene quantum dots (GQDs) are an allotrope of carbon with a planar surface amenable for functionalization and nanoscale dimensions that confer photoluminescence.[‡‡] Collectively, these properties render GQDs an advantageous platform for nanobiotechnology applications, including optical biosensing and delivery. Toward this end, noncovalent functionalization offers a route to reversibly modify and preserve the pristine GQD substrate, however, a clear paradigm has yet to be realized. Herein, we demonstrate the feasibility of noncovalent polymer adsorption to GQD surfaces, with a specific focus on single-stranded DNA (ssDNA). We study how GQD oxidation level affects the propensity for polymer adsorption by synthesizing and characterizing four types of GQD substrates ranging ~60-fold in oxidation level, then investigating noncovalent polymer association to these substrates. Adsorption of ssDNA quenches intrinsic GQD fluorescence by 31.5% for low-oxidation GQDs and enables aqueous dispersion of otherwise-insoluble no-oxidation GQDs. ssDNA-GQD complexation is confirmed by atomic force microscopy, by inducing ssDNA desorption, and with molecular dynamics simulations. ssDNA is determined to adsorb strongly to no-oxidation GQDs, weakly to low-oxidation GQDs, and not at all for heavily oxidized GQDs. Finally, we reveal the generality of the adsorption platform and assess how the GQD system is tunable by modifying polymer sequence and type.

6.2 Introduction

Graphene is a two-dimensional hexagonal carbon lattice that possesses a host of unique properties, including exceptional electronic conductivity, mechanical strength, and adsorptive capacity.[371–373] However, graphene is a zero-bandgap material, and this lack of bandgap limits its use in semiconducting applications.[374] To engineer a bandgap, the lateral dimensions of graphene must be restricted to the nanoscale, resulting in spatially confined structures such as graphene quantum dots (GQDs).[375] The bandgap of GQDs is attributed to quantum confinement,[376,377] edge effects,[378] and localized electron-hole pairs.[379] Accordingly, this gives rise to tunable fluorescence properties based upon GQD size, shape, and exogenous atomic composition. In comparison to conventional semiconductor quantum dots, GQDs are an inexpensive and less environmentally harmful alternative.[380,381] Moreover, for biological applications, GQDs are a low toxicity, biocompatible, and photostable material that offer a large surface-to-volume ratio for bioconjugation.[381,382]

Exploiting the distinct material properties of graphene often requires or benefits from exogenous functionalization. The predominant mechanism for graphene or graphene oxide (GO)

[‡‡] Published as Pinals, R. L.;* Jeong, S.;* Dharmadhikari, B.; Song, H.; Kalluri, A.; Debnath, D.; Wu, Q.; Ham, M.-H.; Patra, P.; Landry, M. P. Graphene Quantum Dot Oxidation Governs Noncovalent Biopolymer Adsorption. *Scientific Reports* **2020**, *10* (1), 1–14. https://doi.org/10.1038/s41598-020-63769-z.

functionalization is via covalent linkage to a polymer. However, noncovalent adsorption of polymers to carbon substrates is desirable in applications requiring reversibility for solution-based manipulation and tunable ligand exchange,[232] and preservation of the pristine atomic structure to maintain nanoscale graphene's fluorescence characteristics.[32] Functionalization of graphene and GO has proven valuable for sensing and delivery applications. Optical sensors based on DNA-graphene or DNA-GO hybrids have been developed for the detection of nucleic acids,[383,384] proteins,[385] small molecules,[386,387] and metal ions.[388] Modifications to GO for drug delivery applications include PEGylation for higher biocompatibility,[389,390] covalent modification with functional groups for water solubility,[391] covalent linking of antibodies,[392] and noncovalent loading of anticancer drugs.[389,391] Noncovalent adsorption of polymers to graphene and GO has been predicted by theory and simulations,[393,394] and has occasionally been demonstrated experimentally.[395] In particular, single-stranded DNA (ssDNA) of varying lengths has been experimentally shown to noncovalently attach to graphene and GO, with hydrophobic and aromatic, π-π stacking electronic interactions posited to drive assembly.[396,397] Molecular dynamics (MD) simulations and density functional theory (DFT) modeling of these systems has enabled validation and mechanistic insight into the corresponding experimental findings.[398,399]

While noncovalent adsorption of DNA and various other polymers has been proposed by simulation and theory, and experimentally established as feasible for graphene and GO substrates, noncovalent polymer adsorption has not been fully investigated for their nanoscale counterparts: GQDs.[400] Noncovalent functionalization of GQDs with biopolymers offers the advantages of reversible binding and preserving the fluorescent substrate properties, while reducing graphene dimensions to the nanoscale enables two-dimensional carbon applications at the molecular scale, of relevance to study biological processes.[401] Herein, we present a facile protocol for noncovalent complexation of biopolymers to GQDs, with a focus on ssDNA. We explore the effects of GQD oxidative surface chemistry on the strength of binding interactions between surface-adsorbed polymers and GQDs, while preserving, or in some cases enabling, intrinsic GQD fluorescence. Ultimately, these results can serve as the basis for the design and optimization of polymer-GQD conjugates in various nanobiotechnology applications.

6.3 Results and Discussion

6.3.1 GQD Synthesis and Characterization

We prepared and characterized four distinct GQD substrates of varying oxidation levels: no-oxidation GQDs (no-ox-GQDs) were fabricated by coronene condensation,[402] low-oxidation GQDs (low-ox-GQDs) by intercalation-based exfoliation,[375] medium-oxidation GQDs (med-ox-GQDs) by thermal decomposition of citric acid,[403] and high-oxidation GQDs (high-ox-GQDs) by carbon fiber cutting (Figure 6-1a).[382] X-ray photoelectron spectroscopy (XPS) was employed to quantify the differing oxidation levels among the GQD samples (Figure 6-1b). The high-resolution carbon 1s (C1s) XPS signal was deconvoluted into four individual peaks attributed to sp^2 carbon-carbon bonds (284.5 eV), hydroxyl and epoxide groups (286.1 eV), carbonyl groups (287.5 eV), and carboxyl groups (288.7 eV) (Figure 6-7).[404] The peak area ratio of oxidized carbon (A_{CO}) to sp^2 carbon (A_{CC}) decreases in the order of high-ox-GQDs (A_{CO}/A_{CC}=1.5) > med-ox-GQDs (0.45) > low-ox-GQDs (0.14) > no-ox-GQDs (0). Of note, no-ox-GQDs possessed only sp^2 carbon, no oxidized carbon, in the C1s XPS spectrum. Atomic force microscopy (AFM) images of the GQDs revealed heights of high-ox-GQDs distributed between 0.5-3 nm, corresponding to 1-5 graphene

layers, and heights of med- and low-ox-GQDs between 0.5-1 nm, indicating the presence of a single graphene layer (Figure 6-8). The morphology of no-ox-GQDs was separately characterized by matrix-assisted laser desorption/ionization time-of-flight mass spectroscopy (MALDI-TOF MS) due to aggregation of no-ox-GQDs during AFM sample preparation hindering equivalent AFM analysis. The single graphene layer structure of no-ox-GQDs was determined by discrete peaks in the size distribution from MALDI-TOF MS, attributed to the presence of planar dimer, trimer, tetramer, pentamer, and hexamer fused-coronene structures (Figure 6-9). Next, the fluorescence and absorbance spectra of low-, med-, and high-ox-GQDs were observed under 320 nm excitation in water (Figure 6-1c and Figure 6-10). The fluorescence maximum near 400 nm is described in previous literature as the intrinsic emission wavelength of GQDs with low oxidation, which is in close agreement with our own GQD samples.[380] GQD fluorescence peaks are observed at shorter wavelength as the GQD oxidation level decreases. As previously reported, longer wavelength emission emerges due to the presence of extrinsic, defect states.[375,405] No-ox-GQDs were insoluble in water due to the absence of oxygen-containing functional groups, and accordingly, aggregation led to self-quenched fluorescence. Instead, fluorescence of no-ox-GQDs was measured in hexane (Figure 6-1c) and the fluorescence spectrum exhibits multiple peaks originating from the size distribution of no-ox-GQD multimers. The GQD excitation-emission profiles demonstrate that the optical characteristics of low-, med-, and high-ox-GQDs depend on the excitation wavelength, where the maximum fluorescence wavelength is red-shifted as the excitation is moved to longer wavelengths. However, the fluorescence of no-ox-GQDs does not show this spectral shift (Figure 6-11). This excitation-wavelength dependence is commonly found in oxidized GQDs as a result of surface trap states introduced by functional groups and oxygen-related defects.[406] The no-ox-GQDs do not exhibit this excitation-dependency because they do not possess oxygen-containing functional groups.

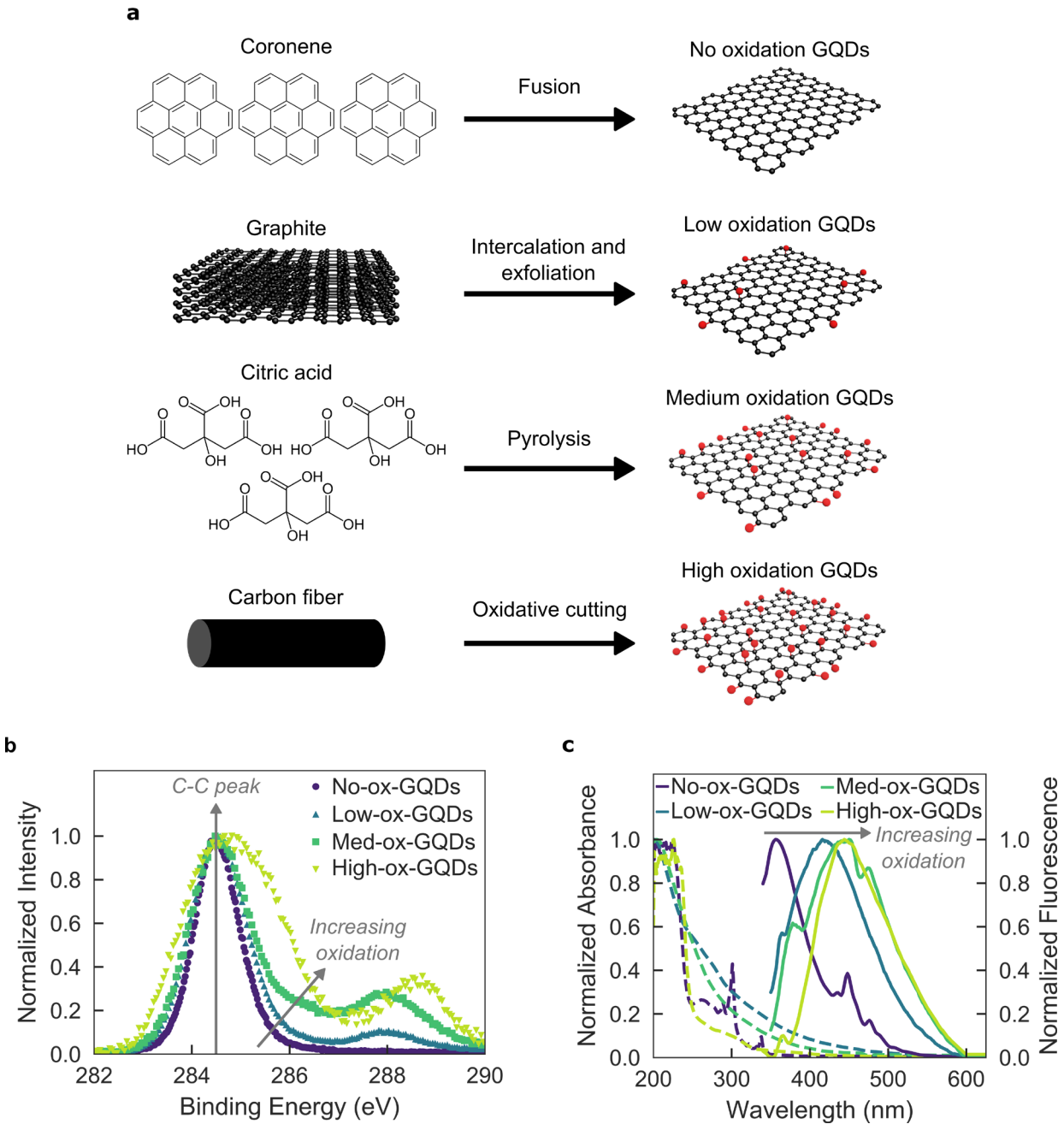

Figure 6-1. Four synthesis techniques are employed to produce graphene quantum dot (GQD) substrates of varying oxidation level. (a) Schematic illustration of synthesis techniques to produce no-oxidation GQDs (no-ox-GQDs), low-oxidation GQDs (low-ox-GQDs), medium-oxidation GQDs (med-ox-GQDs), and high-oxidation GQDs (high-ox-GQDs). (b) Normalized X-ray photoelectron spectroscopy (XPS) data of no-, low-, med-, and high-ox-GQDs. Arrows indicate the center of the C1s carbon-carbon (C-C) bond at 284.5 eV and increasing oxidation via contributions of various carbon-oxygen bonds (see Figure 6-7 for deconvolutions and peak ratios). (c) Normalized absorbance (dashed) and fluorescence emission (solid) spectra of no-ox-

GQDs in hexane solution and low-, med-, and high-ox-GQDs in water. All GQDs were excited at 320 nm.

6.3.2 Noncovalent Functionalization of GQDs with Single-Stranded DNA (ssDNA)

We next studied adsorption of the ssDNA sequence $(GT)_{15}$ onto GQDs of varying oxidation levels (Figure 6-2a). This ssDNA oligomer was chosen for initial adsorption studies based on its known π-π stacking adsorptive properties to the surface of pristine carbon nanotubes,[40,41] an analogous one-dimensional nanoscale substrate. For low-, med-, and high-ox-GQDs, ssDNA was added to GQDs in deionized (DI) water, the water was removed by vacuum evaporation to facilitate adsorption of $(GT)_{15}$ onto the GQDs, then the GQD-ssDNA complexes were resuspended in water (mix-and-dry protocol). For no-ox-GQDs, an alternative complexation technique was employed because the as-synthesized no-ox-GQDs were insoluble in aqueous solution. Instead, the mixture of $(GT)_{15}$ and solid no-ox-GQDs was probe-tip sonicated in phosphate-buffered saline (PBS) to disperse the hydrophobic GQD aggregates and enable ssDNA adsorption.

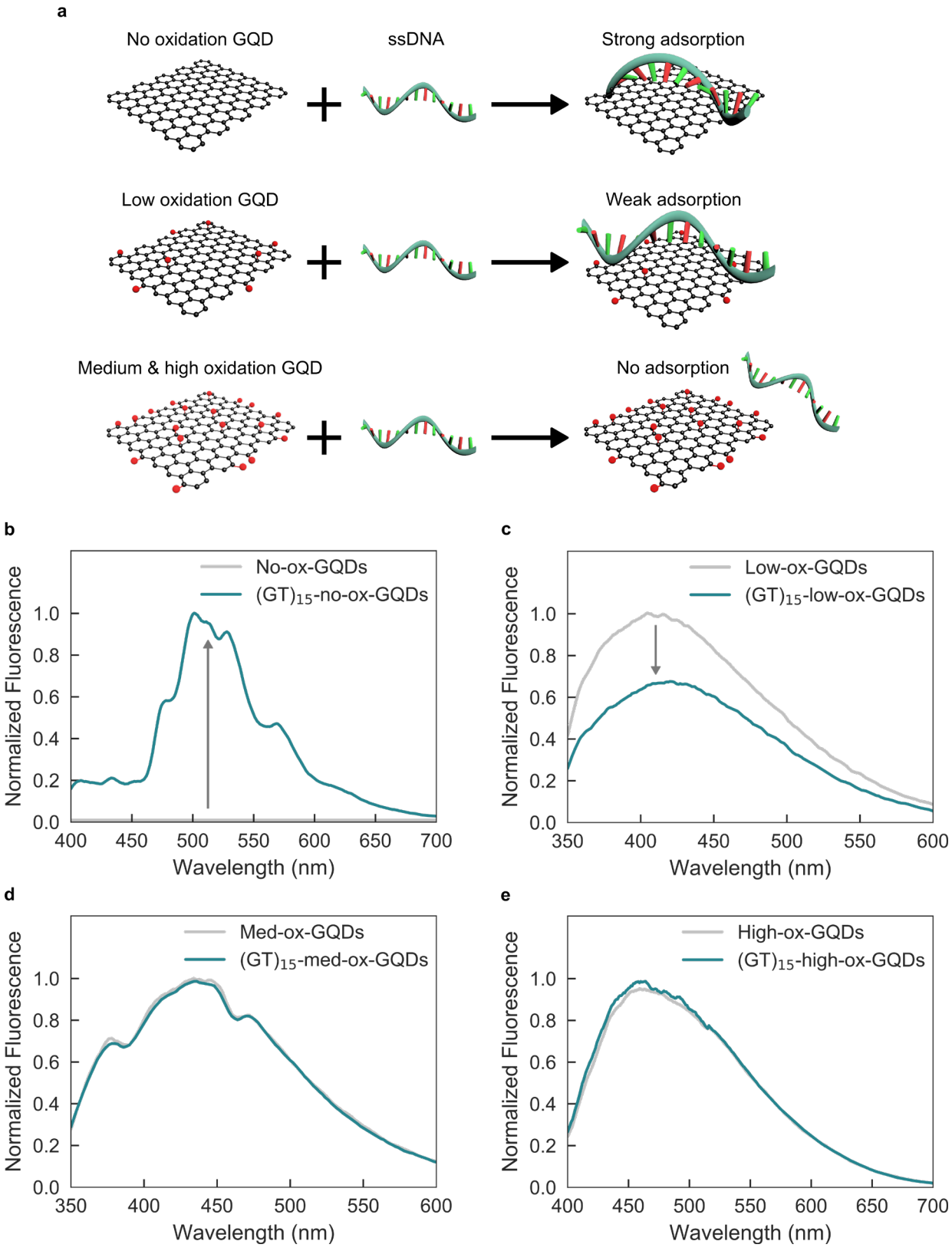

Figure 6-2. Single-stranded DNA (ssDNA)-GQD noncovalent interaction is governed by GQD oxidation level. (a) Schematic illustration of GQD oxidation level and resulting strength of

ssDNA-GQD interaction. The noncovalent interaction between ssDNA and no-ox-GQDs is stronger than that of ssDNA and low-ox-GQDs. ssDNA does not adsorb to either med- or high-ox-GQDs. (b-e) Adsorption of $(GT)_{15}$ ssDNA on the GQD surface results in GQD fluorescence modulation from before (gray) to after (blue) attempted adsorption of $(GT)_{15}$ ssDNA for (b) no-ox-GQDs, (c) low-ox-GQDs, (d) med-ox-GQDs, and (e) high-ox-GQDs. The presence of ssDNA on the no-ox-GQDs is confirmed by an increase in fluorescence emission intensity from the initially insoluble no-ox-GQDs. The presence of ssDNA on the low-ox-GQDs results in a decrease in fluorescence intensity from the initially soluble low-ox-GQDs. No fluorescence intensity changes are observed for the med- and high-ox-GQDs, suggesting absence of ssDNA adsorption. Fluorescence spectra are normalized by the absorbance at 320 nm.

$(GT)_{15}$ adsorption was verified by modulation of the intrinsic GQD fluorescence. For the initially soluble GQDs (low-, med-, and high-ox-GQDs), polymer adsorption manifests as fluorescence quenching from the original fluorescent state, whereas for the initially insoluble no-ox-GQDs, polymer adsorption manifests as fluorescence brightening from the original non-fluorescent, aggregated GQD state (Figure 6-2). Fluorescence quenching was observed for low-ox-GQDs with $(GT)_{15}$, but negligible fluorescence change was shown in the case of med- and high-ox-GQDs. These results suggest that $(GT)_{15}$ does not adsorb to GQDs of higher oxidation levels. Additionally, increased quenching of low-ox-GQD fluorescence was demonstrated with a higher mass ratio of $(GT)_{15}$ to low-ox-GQD (Figure 6-12). Fluorescence quenching of low-ox-GQDs was not a result of Förster resonance energy transfer (FRET) because there is no spectral overlap between GQD emission and ssDNA absorption. $(GT)_{15}$ adsorption also elicits a 15 nm red-shift of the low-ox-GQD fluorescence emission peak, resulting from either changing polarity proximal to the GQD surface or enrichment of larger GQDs (that display longer peak emission wavelengths) upon ssDNA adsorption (Figure 6-13). This bathochromic shift is consistent for all biopolymers interacting with low-ox-GQDs. Interestingly, the simple mixing of $(GT)_{15}$ with GQDs in the absence of drying results in only marginal fluorescence quenching for low-ox-GQDs (Figure 6-14) and was accordingly ineffective in promoting ssDNA adsorption to GQDs. We hypothesize that the dehydration step is required to overcome electrostatic repulsion present in solution and enable close approach of the negatively charged ssDNA to the negatively charged oxidized GQDs. Moreover, water molecules solvating the low-ox-GQD surface may hinder initial contact of ssDNA with low-ox-GQDs.[407] We also investigated the effect of NaCl salt on ssDNA-GQD adsorption. For large GO, high salt concentration enhances ssDNA adsorption due to screening of repulsive electrostatic interactions between negatively charged GO and ssDNA, and among surface-adsorbed ssDNA.[408] However, NaCl does not facilitate adsorption of ssDNA onto high-ox-GQDs, and seems to disrupt adsorption onto low-ox-GQDs (Figure 6-15). We hypothesize that the repulsive interactions between negatively charged GQDs and ssDNA is lessened due to the lower prevalence of oxidative functional groups in comparison to conventional GO. Moreover, repulsion among adsorbed ssDNA is less relevant for GQDs due to the smaller lateral dimensions as compared to GO sheets, resulting in fewer ssDNA molecules per GQD.

The $(GT)_{15}$-no-ox-GQDs show a fluorescence increase from the initially non-fluorescent no-ox-GQD aggregates in aqueous solution and display the multiple absorption and emission peaks characteristic of the hexane-solubilized no-ox-GQDs (Figure 6-1c). Thus, probe-tip sonication of no-ox-GQDs with $(GT)_{15}$ was successful in dispersing no-ox-GQDs in PBS buffer by disrupting GQD aggregates and enabling the amphiphilic ssDNA to adsorb onto the exposed hydrophobic

GQD surface, conferring water solubility to the complex. Without ssDNA, probe-tip sonication of no-ox-GQDs in solution does not result in a stable colloidal suspension. Presence of the ssDNA on no-ox-GQDs enabled AFM analysis of no-ox-GQDs and revealed heights distributed between 0.3-0.7 nm, corresponding to single graphene layer morphology (Figure 6-8a).

6.3.3 Characterization of Surface-Bound ssDNA on GQDs

To verify the presence of ssDNA on low-ox-GQDs, we conducted AFM studies utilizing the well-known biotin-streptavidin interaction to impart a measurable change in the ssDNA-GQD height profile. This assay was required because the change in height due to ssDNA adsorption alone on the GQD surface is below the limit of detection by AFM. Biotin (or vitamin H) is a small molecule with a specific and strong binding affinity for the protein streptavidin ($K_d \sim 10^{-14}$ mol/L). Biotinylated-$(GT)_{15}$ was adsorbed to low-ox-GQDs with the mix-and-dry procedure to form Bio-$(GT)_{15}$-low-ox-GQDs. Streptavidin was then mixed with the Bio-$(GT)_{15}$-low-ox-GQDs in a 1:1 ratio of biotin:streptavidin (Bio-$(GT)_{15}$-low-ox-GQDs + Strep) and the height profile of the resulting complexes was examined by AFM. Control samples of streptavidin mixed with non-biotinylated-$(GT)_{15}$-low-ox-GQDs ($(GT)_{15}$-low-ox-GQDs + Strep), biotinylated-$(GT)_{15}$-low-ox-GQD only (Bio-$(GT)_{15}$-low-ox-GQDs), and streptavidin only (Strep) were prepared for AFM analysis. Large biotin-streptavidin structures were frequently observed in the AFM images of Bio-$(GT)_{15}$-low-ox-GQDs + Strep, and rarely found in the $(GT)_{15}$-low-ox-GQDs + Strep sample, suggesting selective binding of streptavidin to the Bio-$(GT)_{15}$-low-ox-GQDs (Figure 6-3). Height distribution analysis reveals the percentage of structures larger than 1.8 nm is 20.3 ± 7.3% (mean ± standard deviation) for Bio-$(GT)_{15}$-low-ox-GQDs + Strep, compared to only 0.5 ± 0.7% for $(GT)_{15}$-low-ox-GQDs + Strep, 0% for Bio-$(GT)_{15}$-low-ox-GQDs, and 6.9 ± 5.0% for Strep. Here, the threshold value of 1.8 nm is the experimental sum of the GQD average height (0.6 nm) and streptavidin average height (1.2 nm). Accordingly, this confirms the formation of specific streptavidin-biotin-$(GT)_{15}$-low-ox-GQD complexes, and thus suggests the successful noncovalent adsorption of ssDNA on the surface of low-ox-GQDs. Absence of $(GT)_{15}$ adsorption onto med-ox-GQDs was also demonstrated with this assay by preparing a mixture of biotinylated-$(GT)_{15}$ and med-ox-GQDs (Bio-$(GT)_{15}$-med-ox-GQDs) by the same method and adding streptavidin (Bio-$(GT)_{15}$-med-ox-GQDs + Strep). Height distribution analysis reveals the percentage of structures >1.8 nm is 9.9 ± 0.6% for Bio-$(GT)_{15}$-med-ox-GQDs + Strep, close to the control value of 7.5 ± 2.6% obtained for non-specific adsorption of streptavidin onto med-ox-GQDs and $(GT)_{15}$ lacking biotin (Figure 6-16). This result, in corroboration with the lack of fluorescence quenching, verifies that ssDNA does not form stable adsorbed structures with med-ox-GQDs.

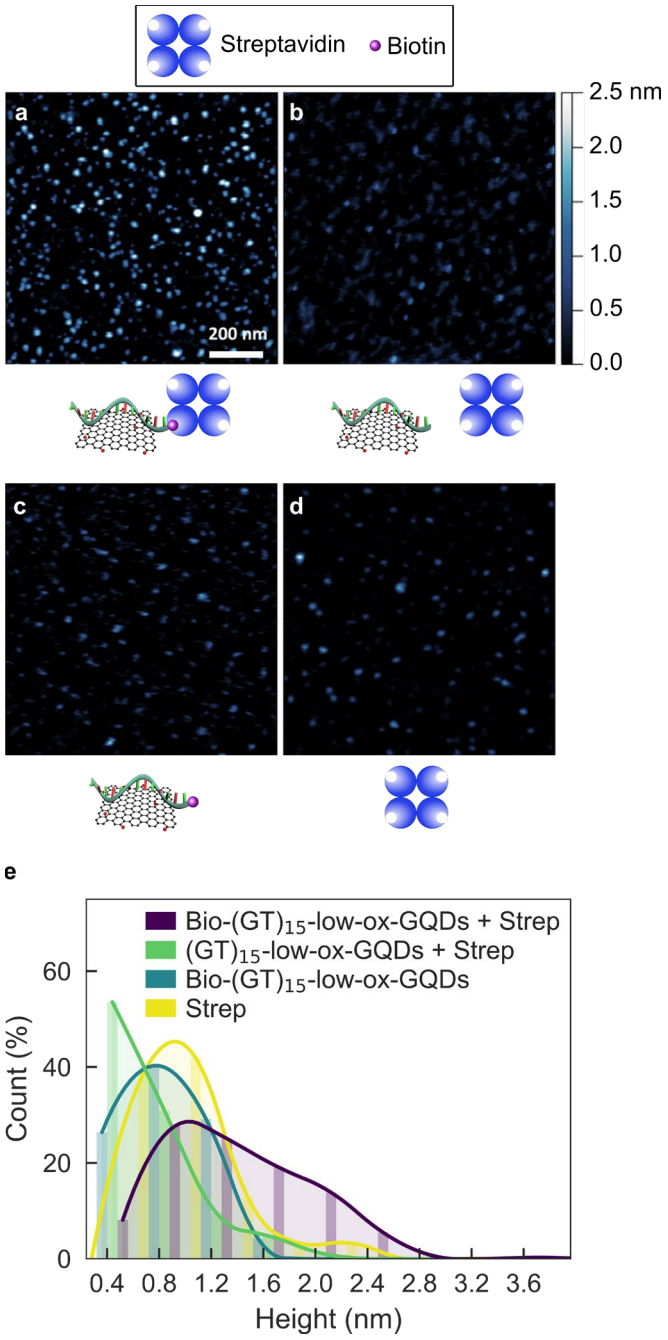

Figure 6-3. ssDNA adsorption to low-ox-GQDs is verified by atomic force microscopy (AFM). AFM images and accompanying schematics for (a) biotinylated-$(GT)_{15}$-low-ox-GQDs and streptavidin (Bio-$(GT)_{15}$-low-ox-GQD + Strep), (b) $(GT)_{15}$-low-ox-GQDs and streptavidin ($(GT)_{15}$-low-ox-GQD + Strep), (c) biotinylated-$(GT)_{15}$-low-ox-GQDs (Bio-$(GT)_{15}$-low-ox-GQD), and (d) streptavidin (Strep). Significantly larger heights in (A) are likely due to biotin-streptavidin binding via the biotinylated-ssDNA, which is adsorbed to the low-ox-GQD surface, absent in (b), (c), and (d). (e) Corresponding height distribution histograms. Bin width is 0.4 nm and curve fits are added to guide the eye.

6.3.4 Sequence-Dependent Adsorption of ssDNA onto the GQD Surface

To examine the effect of ssDNA nucleotide sequence on GQD adsorption affinity, we investigated the adsorption affinities of three ssDNA oligomers of the same length but different nucleotide identities: poly-adenine, A_{30}; poly-cytosine, C_{30}; and poly-thymine, T_{30}. Poly-guanine, G_{20}, a shorter ssDNA oligomer than other ssDNA candidates, was used as the poly-G model case because of commercial unavailability of longer poly-G ssDNA oligomers. To adsorb ssDNA polymers to low-ox-GQDs, each A_{30}, C_{30}, G_{20} and T_{30} ssDNA oligomer was mixed and dried with low-ox-GQDs to form ssDNA-GQD complexes: A_{30}-low-ox-GQDs, C_{30}-low-ox-GQDs, G_{20}-low-ox-GQDs, and T_{30}-low-ox-GQDs. Following ssDNA adsorption, the integrated fluorescence intensity of low-ox-GQDs decreased to 76.1 ± 8.2% (mean ± standard deviation) for A_{30}, 85.1 ± 1.9% for G_{20}, 72.0 ± 6.9% for T_{30} on average, and maintained the original value for C_{30} (Figure 6-4a and Figure 6-17). These results suggest that A_{30}, G_{20}, and T_{30} adsorb onto the low-ox-GQD surface, while C_{30} does not adsorb. We repeated the AFM studies with low-ox-GQD substrates to which we adsorbed biotinylated-C_{30} and mixed this construct with streptavidin (Bio-C_{30}-low-ox-GQDs + Strep) to further investigate whether C_{30} adsorbs to low-ox-GQDs. As a positive control for adsorption, biotinylated-T_{30} was prepared and incubated with streptavidin (Bio-T_{30}-low-ox-GQDs + Strep). AFM imaging of the biotinylated-ssDNA, low-ox-GQD, and streptavidin mixture demonstrated that Bio-C_{30}-low-ox-GQDs and Strep were observed as separate structures, while Bio-T_{30}-low-ox-GQDs + Strep displayed heights consistent with the larger, assembled complex. Specifically, the height distribution analysis shows the percentage of structures >1.8 nm is 1.6 ± 0.4% for Bio-C_{30}-low-ox-GQDs and Strep, which is significantly lower than the value of 12.6 ± 8.5% for Bio-T_{30}-low-ox-GQDs + Strep (Figure 6-4b-d). These results, consistent with our fluorescence quenching assay, suggest that C_{30} does not adsorb onto the low-ox-GQD surface.

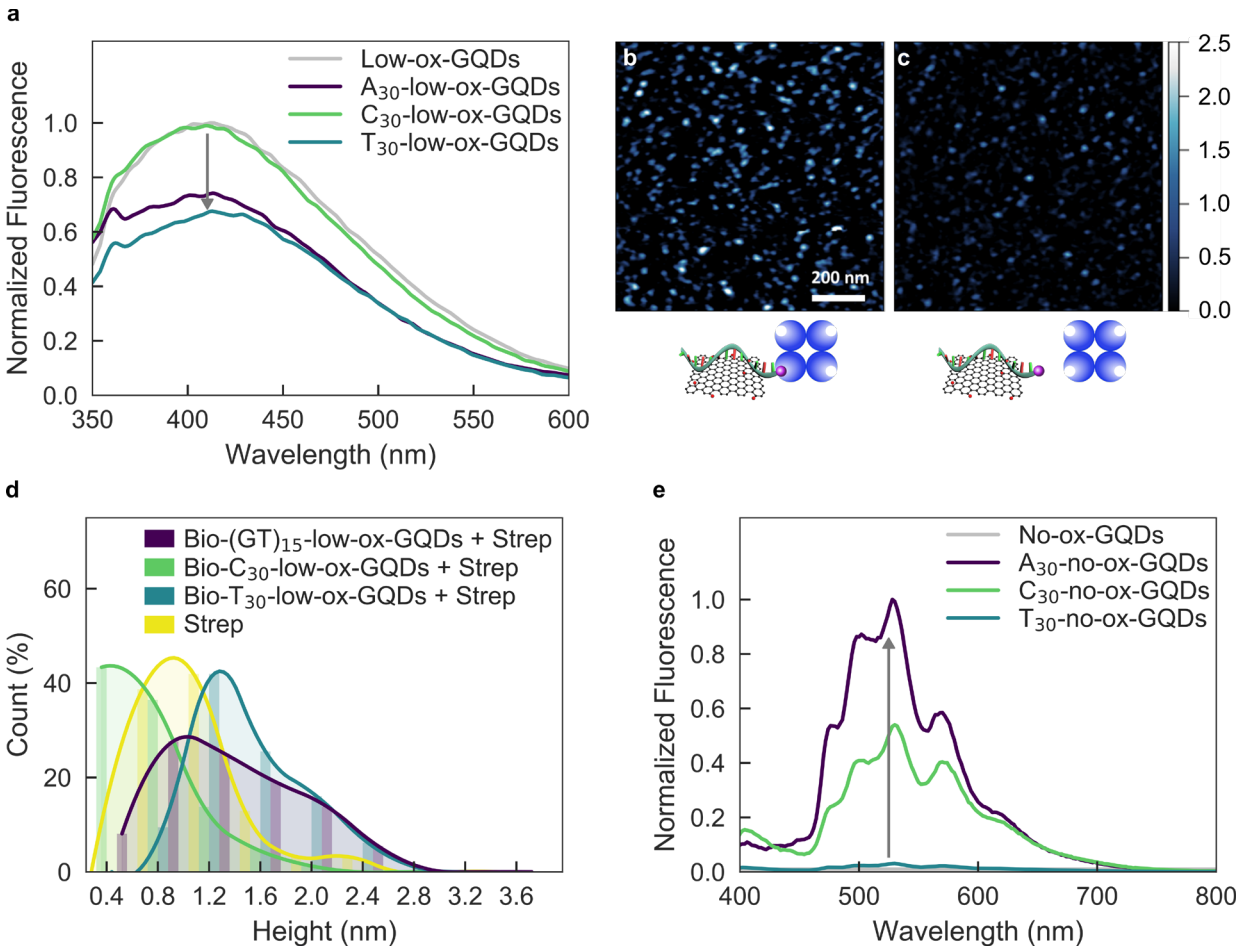

Figure 6-4. Propensity of ssDNA adsorption to low- and no-ox-GQDs depends on ssDNA sequence. (a) Fluorescence spectra of low-ox-GQDs (gray) and low-ox-GQDs with either A_{30}, C_{30}, or T_{30} adsorbed by the mix-and-dry process. AFM images and accompanying schematics for (b) biotinylated-T_{30}-low-ox-GQDs and streptavidin (Bio-T_{30}-GQD + Strep) and (c) biotinylated-C_{30}-low-ox-GQDs and streptavidin (Bio-C_{30}-GQD + Strep). (d) Corresponding height distribution histograms. Bin width is 0.4 nm and curve fits are added to guide the eye. (e) Fluorescence spectra of no-ox-GQDs (gray) and no-ox-GQDs with either A_{30}, C_{30}, or T_{30} adsorbed by probe-tip sonication. All GQD fluorescence spectra are normalized by the absorbance at 320 nm.

To further understand the sequence dependence of ssDNA adsorption to GQD substrates, we studied ssDNA adsorption affinity of A_{30}, C_{30}, and T_{30} ssDNA oligomers to no-ox-GQDs. A_{30}, C_{30}, and T_{30} ssDNA oligomers were probe-tip sonicated with water-insoluble no-ox-GQDs. All three ssDNA sequences resulted in stable colloidal dispersions of ssDNA-coated no-ox-GQDs. The relative fluorescence intensities normalized by the absorbance at the excitation wavelength (320 nm) establishes the fluorescence quantum yield order as $A_{30} > C_{30} > T_{30}$ (Figure 6-4d). However, it is noteworthy that this order does not directly reflect the adsorption affinity of each polynucleotide, as the fluorescence intensity is correlated to both nucleotide-specific adsorption affinity and quenching ability. Yet, this result still implies higher adsorption proclivity for C_{30} on no-ox-GQDs over low-ox-GQDs.

6.3.5 Strength of ssDNA-GQD Interactions

Next, we investigated ssDNA desorption from ssDNA-coated low-ox-GQDs and no-ox-GQDs by using high temperature and complementary ssDNA (cDNA) methods. To study the effect of high temperature, ssDNA-GQD samples of A_{30}, C_{30}, and T_{30} on either no- or low-ox-GQDs were prepared. Fluorescence of each GQD sample was measured at room temperature before and after heating samples to 50°C for 2 hours to attempt desorption of ssDNA from GQDs (Figure 6-18a-b). As expected, no fluorescence change was observed after heating pristine low-ox-GQDs and C_{30}-low-ox-GQDs because these samples did not initially have surface-adsorbed ssDNA. Fluorescence intensity of A_{30}- and T_{30}-low-ox-GQDs increased after heating, indicating that 47.4% of A_{30} and 30.7% of T_{30} desorbed from the low-ox-GQD surface upon heating to 50°C. In comparison, all ssDNA-no-ox-GQDs maintained their initial fluorescence intensity after heating to 50°C, suggesting this heat treatment was insufficient to desorb ssDNA from the pristine no-ox-GQD carbon lattice. When ssDNA-no-ox-GQDs were instead heated to 95°C for 2 hours, fluorescence intensities of all groups significantly decreased, indicating that 41.9% of A_{30}, 43.6% of C_{30}, and 39.3% of T_{30} desorbed from the no-ox-GQD surface (Figure 6-20). This difference in temperature stability implies that the adsorption affinity of ssDNA on the GQD surface is stronger for no-ox-GQDs than for low-ox-GQDs. A recent MD simulation study reported that the estimated binding free energy between T_{20} ssDNA and GO increased significantly when the oxygen content of GO was reduced to below 10%.[398] Accordingly, we hypothesize that GQD oxidation level is directly related to the adsorption affinity between ssDNA and GQDs. Stronger adsorption affinity of ssDNA on no-ox-GQDs results from increased sp^2 graphitic carbon content available for π-π stacking interactions with ssDNA and reduced negative GQD surface charge for electrostatic repulsion.

Adsorption stability of ssDNA on GQDs was also studied with a hybridization assay, where ssDNA complementary to the adsorbed sequence, cDNA, hybridizes in solution phase with the GQD surface-adsorbed ssDNA. It is known that double-stranded DNA has a low adsorption affinity for GO surfaces, and this property has been previously used to study the adsorption affinity of ssDNA by cDNA-induced desorption.[408] The cDNA oligomer $(AC)_{15}$ was added to either $(GT)_{15}$-low-ox-GQD or $(GT)_{15}$-no-ox-GQD solutions in five-fold excess relative to $(GT)_{15}$. Resulting fluorescence profiles were measured 2 hours following addition of $(AC)_{15}$ and compared with the initial fluorescence profile (Figure 6-18c-d). Fluorescence of low-ox-GQDs decreased to 68% upon initial $(GT)_{15}$ adsorption, then recovered to 88% of the initial low-ox-GQD fluorescence due to ssDNA desorption in the presence of cDNA. On the other hand, fluorescence of $(GT)_{15}$-no-ox-GQDs maintained the initial fluorescence value after adding cDNA. The addition of non-complementary T_{30} ssDNA onto $(GT)_{15}$-low-ox-GQDs did not induce the desorption of $(GT)_{15}$ (Figure 6-19). These results further substantiate our conclusion that ssDNA adsorbs to no-ox-GQDs more strongly than to low-ox-GQDs.

6.3.6 Molecular Dynamics Simulation of ssDNA-GQD Interactions

To understand the time-dependent energetics and structures of the ssDNA-GQD binding process, we performed MD simulations of ssDNA oligomers adsorbing to GQDs of varying oxidation levels. To investigate how GQD surface polarity affects ssDNA adsorption, we analyzed non-bonding interaction energies between A_{30} ssDNA and differentially oxidized GQDs during a 100

ns MD simulation. We utilized three types of GQDs, with 0%, 2.28%, and 17.36% oxidation (denoted as GQD-0%, GQD-2%, and GQD-17%, respectively), calculated as the ratio of oxidized carbon to sp^2 carbon. Overall, our results indicate that ssDNA physisorption is driven by a combination of van der Waals's (vdW) interactions and hydrogen bonding (H-bonding) to the GQD. Based on the contact area of ssDNA on the GQD surface, center-of-mass distance, and number of atoms within 5 Å of the GQD surface, A_{30} is more closely adsorbed on less oxidized GQD surfaces, such as GQD-0% and GQD-2%, as compared to the more highly oxidized surface of GQD-17% (Figure 6-5a and Figure 6-21a-b). These results indicate that vdW interactions are the sole contributor to the adsorption of A_{30} on GQD-0%, whereas H-bonding marginally contributes to the adsorption of A_{30} on GQD-2% and GQD-17% in addition to dominant vdW interactions (Figure 6-5b, Figure 6-21c). These interactions further support the less significant role of hydrogen bonds between the ssDNA and oxygen groups on the GQDs. In the simulation for GQD-17%, A_{30} showed negligible contact with the GQD until 70 ns, in comparison with A_{30} contact within 20 ns for the less oxidized GQD cases. After 70 ns, transient contact of A_{30} with GQD-17% was observed, as signified by the fluctuating center-of-mass distances, the latter suggesting highly unstable physisorption of A_{30} on GQD-17%. These MD results suggest more stable adsorption of A_{30} onto less oxidized GQDs (GQD-0% and GQD-2%) as compared to GQD-17%, and agree with experimentally determined selective adsorption of ssDNA on no- and low-ox-GQDs, which is not observed in the case of med- and high-ox-GQDs.

We next investigated the dependency of ssDNA-GQD adsorption on nucleotide sequence by performing MD simulations of A_{30}, C_{30}, and T_{30} ssDNA onto GQD-0% and GQD-2% (Figure 6-22 and Figure 6-23). While A_{30} and T_{30} displayed similar adsorption dynamics onto GQD-0% and GQD-2%, C_{30} adsorbed more weakly onto GQD-0% and GQD-2%, in alignment with previous studies regarding the interaction of homopolynucleotides with graphite.[31,32] For the GQD-0% case, the simulation shows that only the 5' end of C_{30} interacts with the GQD-0% surface, while the other end attempts self-hybridization and consequently unfolds. C_{30} does not show any attractive interaction with GQD-2%, corroborating experimental results that C_{30} does not quench low-ox-GQD fluorescence and was not found in appreciable quantities on the low-ox-GQD surface by AFM. Overall, the MD simulations recapitulate experimental findings that GQD oxidation level determines the ssDNA interaction with and conformation on the GQD surface, and that the ssDNA-GQD-2% interaction is strongly dependent on the nucleotide sequence.

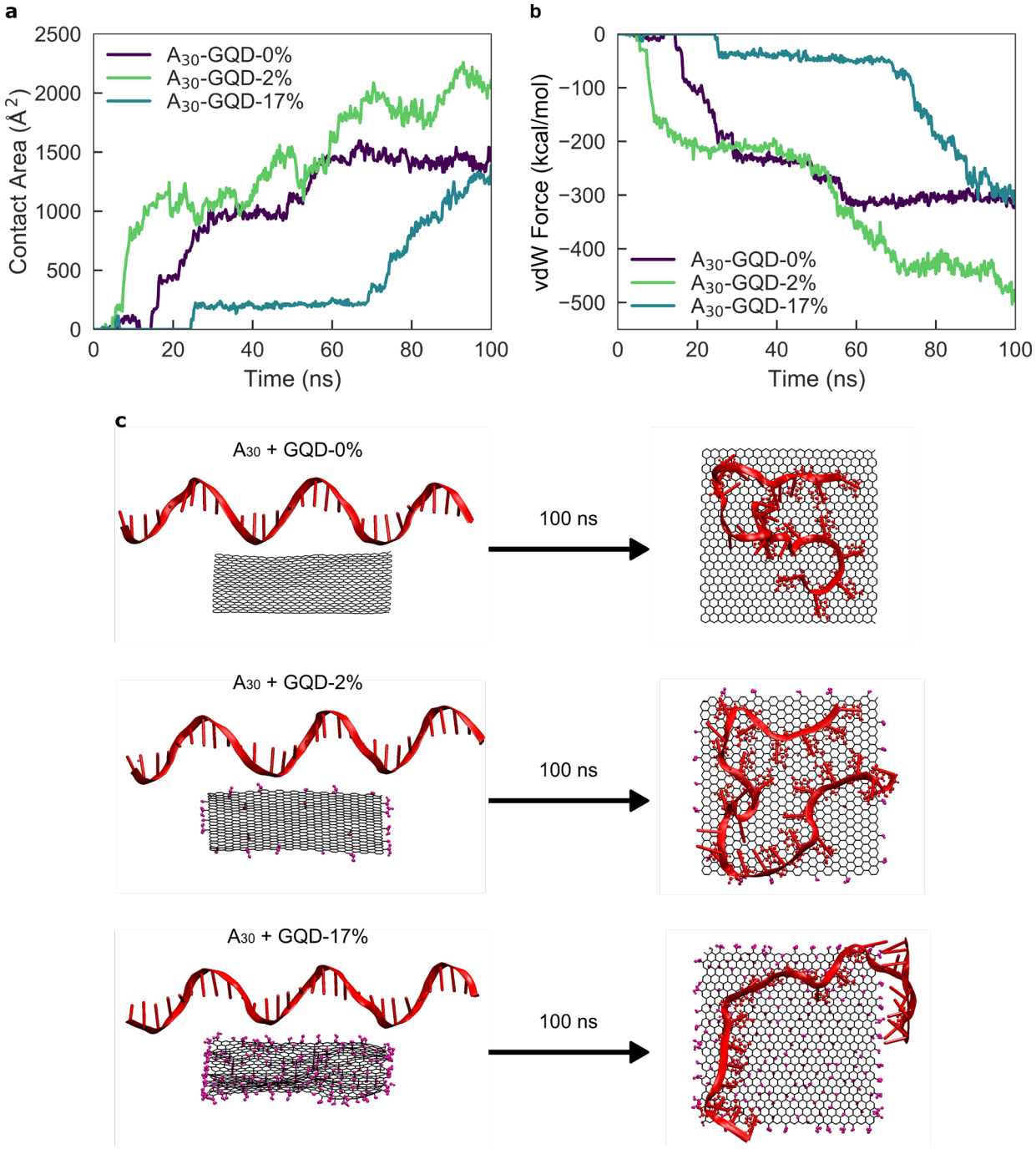

Figure 6-5. Molecular dynamics simulations confirm A_{30} ssDNA adsorption dependency on GQD oxidation level. Time-dependent (a) contact area and (b) van der Waals interactions for A_{30} ssDNA adsorbing to GQD-0%, GQD-2%, and GQD-17%. (c) Initial (left) and final (right) configurations of A_{30} ssDNA with GQD-0%, GQD-2%, and GQD-17% for a 100 ns simulation.

6.3.7 Platform extension to other biomolecule-GQD constructs

Finally, we demonstrate that this noncovalent adsorption platform is extendable to other biomolecules on GQDs. We hypothesized that planar sheet- or bilayer-forming molecules would

be amenable for adsorption onto a two-dimensional GQD substrate.[409] Accordingly, we attempted and successfully created biopolymer-GQD constructs with two such structure-forming biomolecules, phospholipids and peptoids. The phospholipid, 1,2-distearoyl-sn-glycero-3-phosphoethanolamine-N-diethylenetriaminepentaacetic acid (14:0 PE-DTPA), was adsorbed onto low-ox-GQDs with the same mix-and-dry protocol as ssDNA, and resulted in the expected fluorescence quenching of low-ox-GQDs that confirms adsorption (Figure 6-6a). As is the case with ssDNA adsorption, this fluorescence quenching may be due to a charge transfer mechanism between the GQD and adsorbed polymer.[410]

A peptoid is a synthetic peptide in which the variable group is attached to the amine rather than the alpha carbon, resulting in a loss of the chiral center.[411] In particular, 36-mer peptoids with alternating ionic and hydrophobic sidechains have been designed as amphiphilic, sheet-forming peptoids.[269] Two peptoid sequences were tested: Peptoid-1 is a diblock of alternating N-(2-aminoethyl) glycine (Nae) and N-(2-phenethyl) glycine (Npe) units, abbreviated $(Nae–Npe)_9$, and N-(2-carboxyethyl) glycine (Nce) and Npe, abbreviated $(Nce–Npe)_9$. Electrostatic interactions between the amine and carboxyl groups drive solution-phase self-assembly of these 36-mers into nanosheet morphology. Peptoid-2 is simply $(Nce–Npe)_{18}$, with only the carboxyl sidechain present. Therefore, no amine-carboxyl ionic interactions are available to initiate assembly and this peptoid is incapable of forming stable nanosheets by itself. Probe-tip sonication of no-ox-GQDs with Peptoid-1, $(Nae–Npe)_9$-$(Nce–Npe)_9$, resulted in a stable Peptoid-1-no-ox-GQD suspension (Figure 6-6b). The phenyl sidechains are posited to π-π stack with the no-ox-GQD basal plane in the same manner as ssDNA, thus resulting in stable constructs. Peptoid-2, $(Nce–Npe)_{18}$, was not able to suspend the no-ox-GQDs, most likely due to the absence of electrostatic interactions between the peptoids required to form stable sheet nanostructures and presumably also a GQD surface coating.

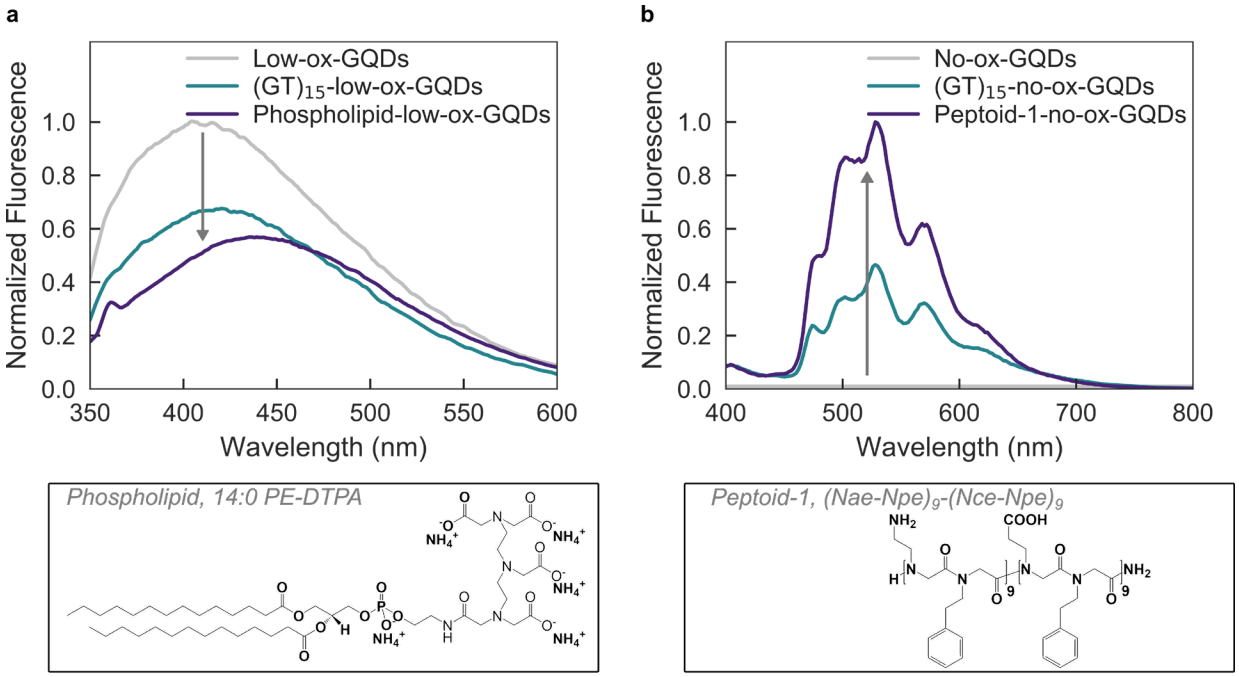

Figure 6-6. Noncovalent surface adsorption of biopolymers to low- and no-ox-GQDs is demonstrated by fluorescence modulation upon adsorption of phospholipid (14:0 PE-DTPA) and Peptoid-1 ((Nae–Npe)$_9$-(Nce–Npe)$_9$), respectively. (a) Normalized fluorescence emission spectra of low-ox-GQDs taken before (gray) and after (purple) the mix-and-dry process with phospholipid, 14:0 PE-DTPA. (b) Normalized fluorescence emission spectra of no-ox-GQDs taken before (gray) and after (purple) probe-tip sonication with Peptoid-1, (Nae-Npe)$_9$-(Nce-Npe)$_9$. The (GT)$_{15}$-no-ox-GQDs spectrum (blue) is included for comparison. All GQD fluorescence spectra are normalized by the absorbance at 320 nm.

6.4 Conclusions

We have demonstrated the feasibility of, and developed procedures for, noncovalent adsorption of ssDNA, phospholipids, and peptoid polymers to GQDs (summarized in Table 6-1). To the best of our knowledge, this is the first experimental realization of the noncovalent physisorption of these biomolecules on GQDs, which has not been previously investigated due to challenges arising from the small size and variable oxidation of GQD substrates.[383] We have confirmed the perturbative role of GQD oxidation on ssDNA adsorption, and further investigated the varying adsorption and desorption properties of ssDNA based on the GQD oxidation level and ssDNA sequence. To this end, four types of photoluminescent GQDs with different oxidation levels were fabricated. Characterization of the four GQD types reveals that changing GQD oxidation level allows tuning the optical fingerprints. This presents opportunities in creating a library of GQDs displaying unique photoluminescent properties or the ability to identify GQDs by means of fluorescence profiles. ssDNA adsorption to the GQD substrates is assessed by photoluminescence modulation and morphological characterization. Specifically, adsorption of ssDNA on low-ox-GQDs is confirmed by fluorescence quenching and AFM studies, and the adsorption affinity is evaluated by high temperature desorption and by hybridization. Adsorption of ssDNA on no-ox-GQDs is confirmed by producing stable colloidal suspensions with fluorescence emission, and the higher

adsorption affinity resists disruption by high temperature and cDNA. Thus, GQD oxygen content determines ssDNA adsorption affinity, where ssDNA can adsorb on no- and low-ox-GQD surfaces but not on med- nor high-ox-GQDs. This preferential ssDNA adsorption implies that ssDNA adsorbs more favorably onto graphene-like carbon domains rather than oxidized carbon domains,[408] underscoring the role of interfacial π-π electronic interactions between the GQD and aromatic ssDNA nitrogenous bases contributing more than hydrogen bonds between oxygen groups on the GQD with the ssDNA. Likewise, the surface roughness and electrostatic repulsion created by oxygen groups on the med- and high-ox-GQDs could prevent effective π-π stacking interactions of nucleobases with the graphitic surface, consequently inhibiting adsorption.

ssDNA attachment on low-ox-GQDs is sequence-dependent: poly-A, G, T do adsorb to low-ox-GQDs, while poly-C does not adsorb. Previously, Sowerby et. al. reported adsorption affinities of the four DNA bases on graphite (as determined by column chromatography) in decreasing order of G > A > T > C,[412] in accordance with our results showing a low adsorption affinity of cytosine to GQDs. Likewise, for pyrimidine homopolymers studied with chemical force microscopy, T_{50} required a much stronger peeling force of 85.3 pN from graphite as compared 60.8 pN for C_{50}.[413] Conversely, a recent study suggests that poly-C interacts with a carboxylated GO surface more strongly than poly-T or poly-A.[414] This result is attributed to the fact that poly-C ssDNA readily forms secondary structures, enabling hydrogen bonding interactions between the folded ssDNA and GO that drive the adsorption process.[398] However, our low-ox-GQDs contain significantly less oxidative functional groups available for hydrogen bonding (A_{CO}/A_{CC}=0.14) in comparison to common GO (A_{CO}/A_{CC}~0.36),[415] therefore we conclude that C_{30} was not able to interact with the same binding modalities as shown with non-nanoscale GO. From our MD simulations, C_{30} again does not show any attractive interaction with GQD-2% and shows some adsorption to GQD-0%. Another recent study has discovered that unfolded poly-C, rather than the i-motif secondary structure, has higher affinity for graphene oxide surfaces.[416] Accordingly, we posit that π-π stacking interactions between the aromatic portions of ssDNA and pristine graphitic areas of GQDs can overcome intramolecular forces holding together the C_{30} secondary structure, resulting in some adsorption of unfolded C_{30} to GQD-0%. Thus, contact with pristine GQDs may prompt poly-C unfolding and result in selective adsorption, whereas oxidized GQDs may be unable to disrupt potential C_{30} secondary structures to support stable surface adsorption.

In sum, the effect of graphene-based substrate size on biomolecule adsorption for nanoscale GQDs in comparison to micro-/macroscale GO sheets is best established by considering (1) solution ionic strength and (2) biopolymer sequence dependency. Toward (1), introduction of salt precludes ssDNA adsorption onto low-ox-GQDs, yet not onto no-ox-GQDs, whereas salt is known to assist ssDNA adsorption onto GO. Toward (2), we find differing ssDNA sequence dependencies on GQDs in comparison to their GO counterparts, particularly for poly-C.

Applications of graphene-based nanomaterials are vast, and a better understanding of parameters that affect adsorption of polymers to GQDs are needed to enable future applications in diagnostics, biomolecule delivery, and sensing. Our noncovalent attachment protocols to synthesize ssDNA-GQD complexes can lead to new opportunities in developing GQD-based nucleic acid detection platforms and further biological molecular sensing and imaging applications. Moreover, we show the adsorption protocols developed for ssDNA are generic to adsorb other biopolymers, such as phospholipids and peptoids, to GQDs. Successful synthesis of the Peptoid-1-GQD construct

motivates future developments in biopolymer-GQD-based detection platforms with peptoid-mediated protein recognition.[256] The noncovalent adsorption of biopolymers beyond ssDNA to GQDs provides a route to tune the GQD system not only by choice of GQD color and oxidation level, but additionally by polymer sequence and type. The platform developed here can be leveraged to expand the current possibilities of designing and applying GQD-based nanotechnologies.

6.5 Materials and Methods

6.5.1 Preparation of No-Oxidation GQDs (no-ox-GQDs)

No-ox-GQDs were prepared according to previous literature.[402] Briefly, 20 mg of coronene (95%, Acros) was vacuum-sealed in a glass ampule and annealed at 500°C for 20 hours. After cooling to room temperature, the product was loaded into a quartz tube and annealed at 500°C for 30 min under H_2 and Ar atmosphere (10 and 200 sccm, respectively) to remove unreacted coronene.

6.5.2 Preparation of Low-Oxidation GQDs (low-ox-GQDs)

Low-ox-GQDs were prepared by an intercalation-based exfoliation method.[375] 20 mg of graphite powder (natural, briquetting grade, -100 mesh, 99.9995%, UCP-1 grade, Ultra "F" purity, Alfa Aesar) and 300 mg of potassium sodium tartrate tetrahydrate (>99%, Sigma-Aldrich) were ground in a mortar and pestle. The powder was transferred to a glass tube and heated in a tube furnace at 250°C for 24 hours under Ar gas. The product powder was dispersed in 30 mL of deionized (DI) water and ultrasonicated for 10 min (Branson Ultrasonic 1800). The translucent, brown solution was centrifuged at 3220 g for 30 min and the supernatant was collected. For desalting and size selection, the solution was spin-filtered using a 100 kDa molecular weight cutoff (MWCO) centrifugal filter (Amicon Ultra-15, Ultracel, Millipore) at 3220 g for 30 min and the eluent solution was collected. The final product solution was spin-filtered with a 3 kDa centrifugal filter at 3220 g for 30 min to remove residual salts, repeated six times, and the remnant solution was collected.

6.5.3 Preparation of Medium-Oxidation GQDs (med-ox-GQDs)

Med-ox-GQDs were prepared according to previous literature.[403] 2 g of citric acid (>99.5%, ACS reagent, Sigma-Aldrich) was added to a 20 mL vial and heated to 200°C in a heating mantle for 30 min until citric acid liquified into an orange solution. The solution was cooled to room temperature and added dropwise into 100 mL of 10 mg/mL NaOH solution while stirring. The pH of the med-ox-GQDs solution was neutralized to pH 7 by adding NaOH. The final product solution was spin-filtered with a 3 kDa centrifugal filter at 3220 g for 30 min to remove residual salts, repeated six times, and the remnant solution was collected.

6.5.4 Preparation of High-Oxidation GQDs (high-ox-GQDs)

High-ox-GQDs were prepared according to previous literature.[382] Briefly, 0.3 g of carbon fibers (>95%, carbon fiber veil, Fibre Glast) was added into a mixture of concentrated H_2SO_4 (60 mL) and HNO_3 (20 mL). The mixture was ultrasonicated for two hours and stirred for 24 hours at 120°C. The solution was cooled to room temperature and diluted with DI water (800 mL). The pH of the high-ox-GQDs solution was adjusted to pH 8 by adding Na_2CO_3. The final product solution

was spin-filtered with a 3 kDa centrifugal filter at 3220 g for 30 min to remove residual salts, repeated six times, and the remnant solution was collected.

6.5.5 Fabrication of ssDNA-GQD Complex by Mix-and-Dry Process

10 μg of GQDs were mixed with 10 nmol of ssDNA dissolved in 0.2 mL DI water. The mixture was dried for 4 hours in a 1.5 mL microcentrifuge tube under moderate vacuum (~5 torr). The dried solid was re-dispersed in 1 mL DI water.

6.5.6 Fabrication of ssDNA-no-ox-GQD Complex by Probe-Tip Sonication Process

1 mg of no-ox-GQDs and 100 nmol of ssDNA was dispersed in 1 mL PBS buffer at pH 7.4. The mixture was ultrasonicated for 2 min and probe-tip sonicated for 30 min at 5 W power in an ice bath (Cole Parmer Ultrasonic Processor, 3 mm tip diameter). The product was centrifuged at 3300 g for 10 minutes to remove unsuspended no-ox-GQDs and the supernatant was collected. The suspension was centrifuged at 16000 g for 1 hour to remove free ssDNA and the precipitate was collected. This purification step was repeated three times until no ssDNA was observed in the supernatant solution by absorption spectroscopy.

6.5.7 GQD Characterization

XPS spectra were collected with a PHI 5600/ESCA system equipped with a monochromatic Al Kα radiation source (hν = 1486.6 eV). High-resolution XPS spectra were deconvoluted with MultiPak software (Physical Electronics) by centering the C-C peak to 284.5 eV, constraining peak centers to ±0.1 eV the peak positions reported in previous literature,[404] constraining full width at half maxima (FWHM) ≤1.5 eV, and applying Gaussian-Lorentzian curve fits with the Shirley background. AFM images were collected with an MFP-3D system (Asylum) in tapping mode with an NCL-20 AFM tip (force constant = 48 N/m, Nanoworld). Optical properties of the GQDs were studied with absorbance spectroscopy (UV-3600 Plus, SHIMADZU), photoluminescence spectroscopy (Quantamaster Master 4 L-format, Photon Technologies International), and excitation-emission profiles (Cary Eclipse, Varian). MALDI-TOF mass spectra were acquired on an Autoflex Max (Bruker) with a 355-nm laser, in the positive reflectron mode. Samples were added to CHCA matrix.

6.5.8 Verification of ssDNA-GQD Complexes by AFM

Biotinylated-$(GT)_{15}$-low-ox-GQDs (Bio-$(GT)_{15}$-low-ox-GQDs) were prepared by the mix-and-dry process using 5'-biotinylated-$(GT)_{15}$ and low-ox-GQDs. To form the biotin-streptavidin complex, Bio-$(GT)_{15}$-low-ox-GQDs, containing 10 pmol of biotinylated-$(GT)_{15}$ and 10 pmol of streptavidin were mixed in 0.02 mL DI water. The 50-fold diluted solution was drop cast onto a mica substrate and dried by N_2 flow. As a negative control, $(GT)_{15}$-low-ox-GQDs were also mixed with streptavidin in the same way. AFM analysis was performed in tapping mode and the height of the GQD complex was determined as the maximum height at the GQD region in the AFM image. Average and standard deviation of the relative portion of structures >1.8 nm were calculated from the height count data of multiple AFM images.

6.5.9 Molecular Dynamics (MD) Simulations

MD simulations of ssDNA adsorption on GQDs were performed by NAMD[417,418] using CHARMM27 and CHARMM36[419] force field parameters for 100 ns. Obtained trajectories were visualized and analyzed using VMD.[420] Crystallographic data coordinates of A_{30}, C_{30}, and T_{30} ssDNA as pdb files were generated using 3-D DART software.[421] 5 nm x 5 nm GQDs with sp^2 hybridized carbon atoms were generated using the VMD plug-in, "nanotube-builder". Hydroxyl, carbonyl, and carboxyl groups were placed randomly on the GQD surface and edges with VEGA ZZ software.[422] Minimum distance between ssDNA and GQDs was set to 1.4 nm to maintain several ordered water layers that reduced the effects by initial status. The ssDNA and GQDs were then solvated using TIP3P water model[423] with 150 mM sodium and chloride ions. The water box size was $130 \times 80 \times 60$ Å^3. Initial ssDNA position and orientation were the same in all simulations.

All computations were performed at constant temperature (300 K) and constant pressure (1 atm). Lennard–Jones potential parameters were set to study the cross-interaction between non-bonded atoms of ssDNA-GQD, GQD-water, and ssDNA-water. All atoms, including hydrogen, were defined explicitly in all simulations. CHARMM force field parameter files were specified to control the interaction between non-bonded atoms of ssDNA-GQD, GQD-water, and ssDNA-water. Exclude parameter was set to scaled1-4, such that all atom pairs directly connected via a linear bond and bonded to a common third atom along with all pairs connected by a set of two bonds were excluded. Electrostatic interactions for the above pairs were modified by the constant factor defined by 1-4scaling, set to 1. Cutoff distance and switching distance function were set to 14 and 10, respectively, and switching parameter set to on, such that the van der Waals energy was smoothly truncated at the cutoff distance starting at the switching distance specified. Pair list distance (pairlistdist) was set to 14 to calculate electrostatic and van der Waals interaction between atoms within a 14 Å radial distance. Integration timestep was set to 2 fs. Each hydrogen atom and the atom to which it was bonded were similarly constrained and water molecules were made rigid. Timesteps between non-bonded evaluation (nonbondedFreq) were set to 1, specifying how often short-range, non-bonded interactions were calculated. Number of timesteps between each full electrostatic evaluation (fullElectFrequency) was set to 2. Number of steps per cycle was set to 10. Langevin dynamics parameter (langevinDamping) was set to 1 to drive each atom in the system to the target temperature. Periodic boundary conditions were specified. Periodic cell center was defined in cellOrigin, to which all coordinates wrapped when wrapAll was set on. Particle Mesh Ewald (PME), applicable only to periodic simulations, was employed as an efficient full electrostatics method that is more accurate and less expensive than larger cutoffs. PME grid dimensions corresponding to the size of the periodic cell were specified. Group-based pressure was used to control the periodic cell fluctuations. Dynamical properties of the barostat and target pressure were controlled by parameters of the Nosé-Hoover Langevin piston. To initiate the simulation, energy minimization for 5000 steps at constant temperature and pressure was performed for all systems that contained ssDNA, GQD, water molecules, and NaCl ions. After minimization, all systems underwent equilibration for 100 ns.

In all MD simulation figures, GQDs are displayed by line representations and black coloring method. ssDNA secondary structures are displayed by New Cartoon representations. Adsorbed residue atoms and oxidation groups on GQDs are displayed by the CPK drawing method with red, green, blue, and magenta coloring for A_{30}, C_{30}, T_{30}, and oxidation groups, respectively.

6.6 Chapter Supporting Information

6.6.1 Supplementary Figures and Tables

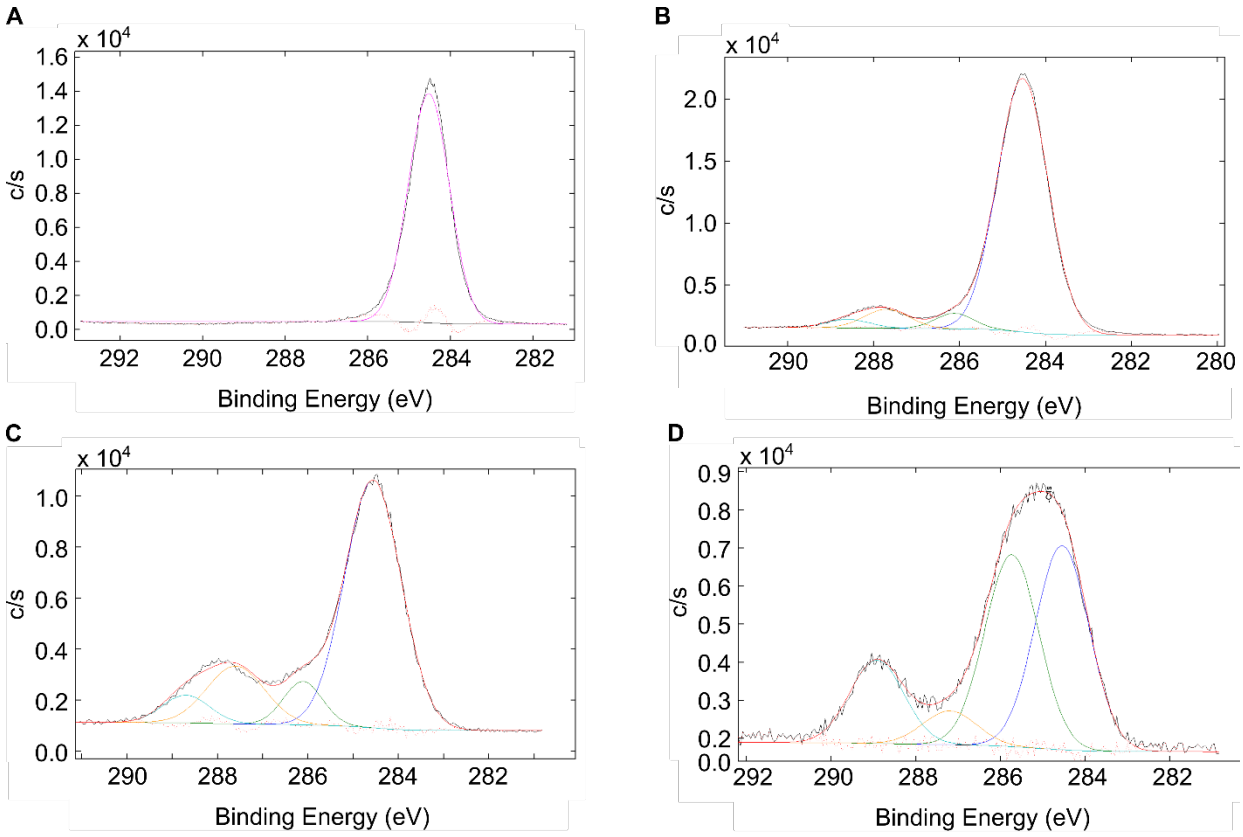

E

Sample	C-C (284.5 eV)	C-O (286.1 eV)	C=O (287.5 eV)	O-C=O (288.7 eV)
No-ox-GQD	100	0	0	0
Low-ox-GQD	87.55	4.06	5.84	2.56
Med-ox-GQD	68.95	8.31	16.36	6.38
High-ox-GQD	39.78	37.4	6.57	16.24

Figure 6-7. Deconvoluted carbon 1s (C1s) X-ray photoelectron spectroscopy (XPS) characterization of GQDs. (a) no-ox-GQD, (b) low-ox-GQD, (c) med-ox-GQD, and (d) high-ox-GQD samples included in Figure 6-1b. (e) Relative peak areas for C1s chemical bonds in each sample.

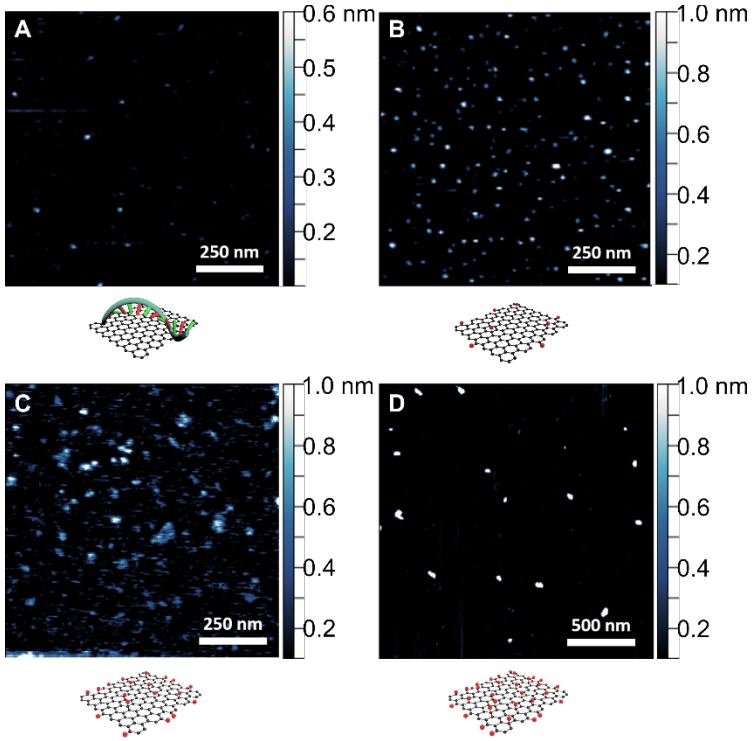

Figure 6-8. AFM characterization of GQDs. AFM images and accompanying schematics for (a) $(GT)_{15}$-no-ox-GQDs, (b) low-ox-GQDs, (c) med-ox-GQDs, and (d) high-ox-GQDs. Average height of each type of GQD is 0.35 ± 0.10, 0.83 ± 0.28, 0.82 ± 0.75, and 2.0 ± 0.91 nm for $(GT)_{15}$-no-ox-GQDs, low-ox-GQDs, med-ox-GQDs, and high-ox-GQDs, respectively.

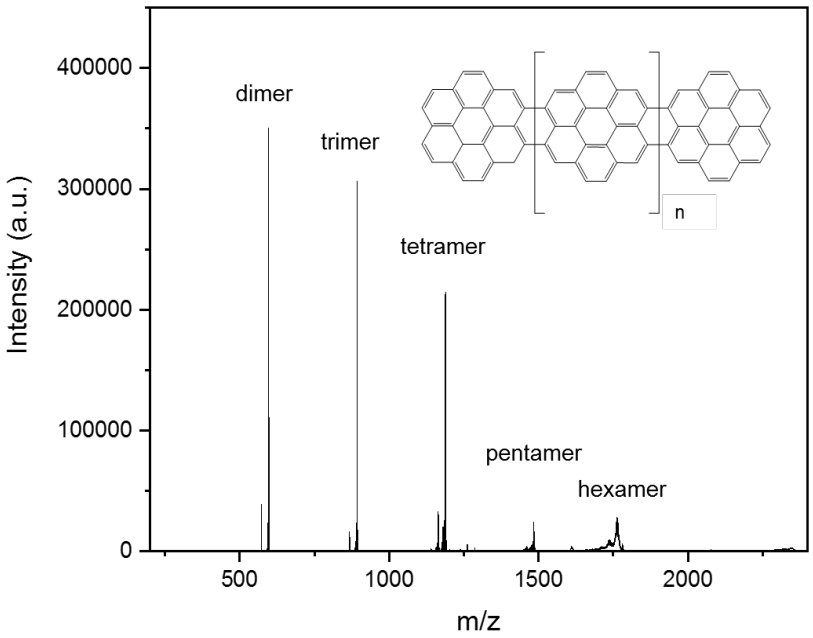

Figure 6-9. Matrix-assisted laser desorption/ionization time-of-flight mass spectroscopy (MALDI-TOF MS) characterization of no-ox-GQDs. Peak bands observed at m/z = 596, 892, 1188, 1484, and 1780 are attributed to planar coronene dimer, trimer, tetramer, and pentamer, and hexamer structures, respectively.

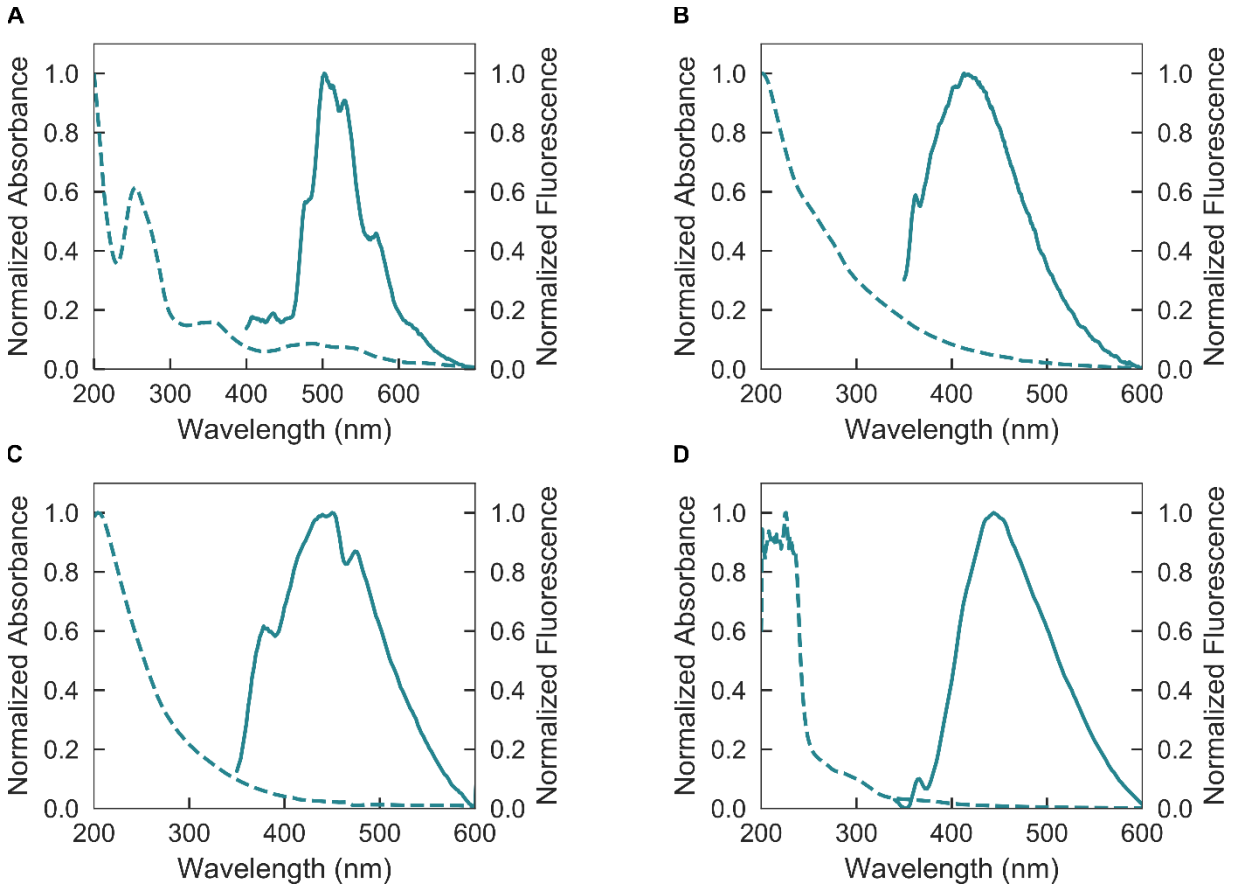

Figure 6-10. Optical absorption and emission characterization of GQDs. Normalized absorption (dashed) and fluorescence emission (solid) spectra of (a) $(GT)_{15}$-no-ox-GQDs (excitation 340 nm), (b) low-ox-GQDs (excitation 320 nm), (c) med-ox-GQDs (excitation 320 nm), and (d) high-ox-GQDs (excitation 340 nm) in water.

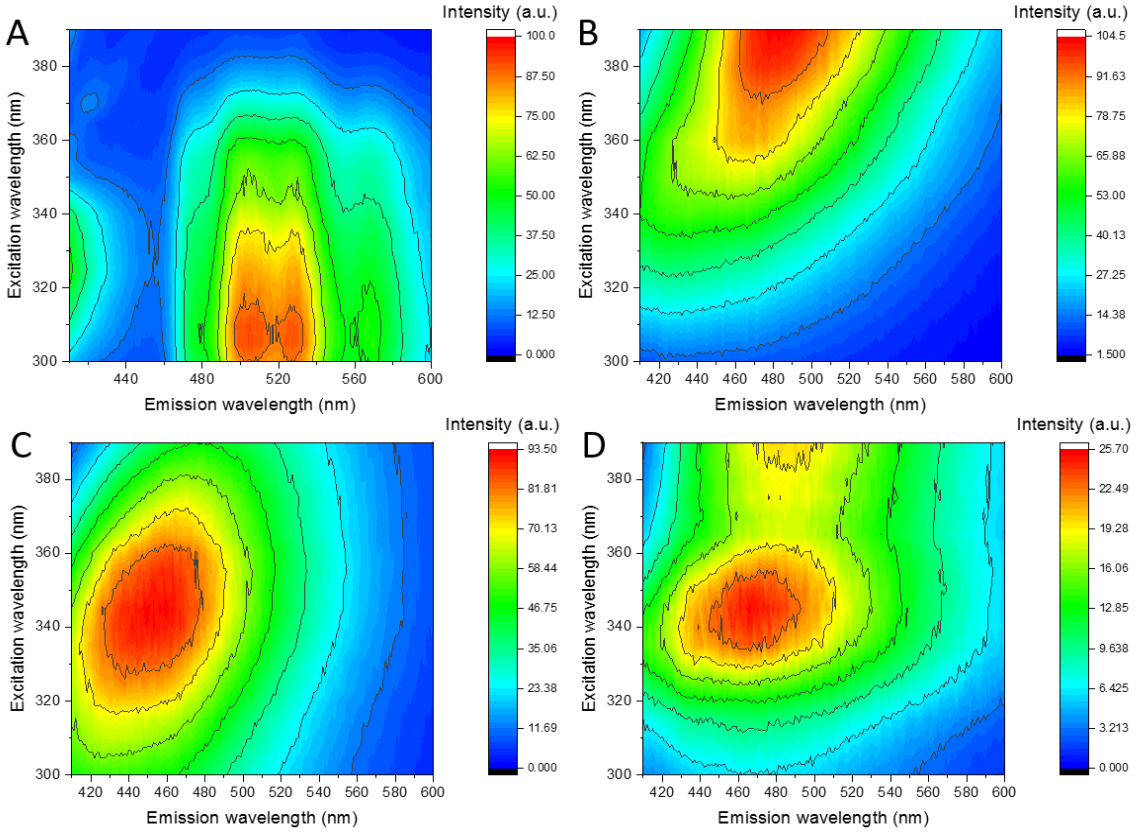

Figure 6-11. Excitation-emission profiles of GQDs. (a) $(GT)_{15}$-no-ox-GQDs, (b) low-ox-GQDs, (c) med-ox-GQDs, and (d) high-ox-GQDs in water. All spectra were collected in intervals of 5 nm for excitation wavelength.

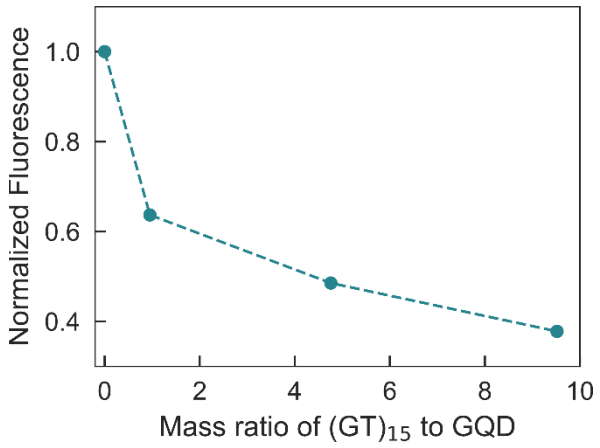

Figure 6-12. Fluorescence intensity of $(GT)_{15}$-low-ox-GQDs depends on the mass ratio of $(GT)_{15}$ to low-ox-GQD. Integrated, normalized fluorescence intensities upon $(GT)_{15}$ ssDNA adsorption to low-ox-GQDs, with curve fits added to guide the eye.

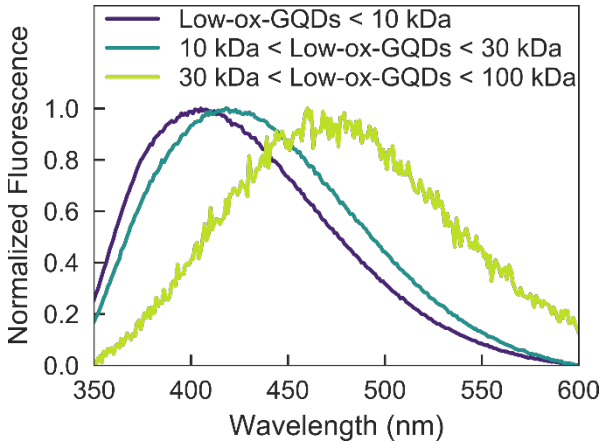

Figure 6-13. Low-ox-GQD fluorescence as a function of GQD size. Normalized fluorescence spectra demonstrate that larger low-ox-GQDs exhibit redshifted peak emission in comparison to smaller low-ox-GQDs. GQDs were size sorted by filtering with varying molecular weight cutoff (MWCO) centrifugal filters (Amicon Ultra-15, Ultracel, Millipore; 10 kDa, 30 kDa, and 100 kDa MWCO) at 3220 g for 30 min.

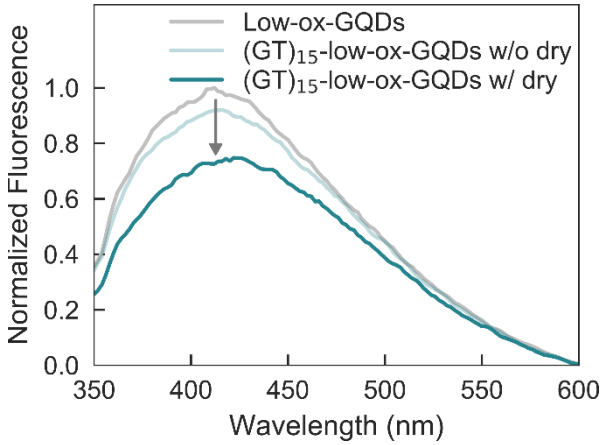

Figure 6-14. Effectiveness of vacuum drying for ssDNA adsorption to low-ox-GQDs. Normalized fluorescence emission spectra of low-ox-GQDs after vacuum evaporation (gray), $(GT)_{15}$ and low-ox-GQD mixture without vacuum evaporation (light blue), and $(GT)_{15}$ and low-ox-GQD mixture with vacuum evaporation (dark blue). Concentrations of all low-ox-GQD samples are equivalent.

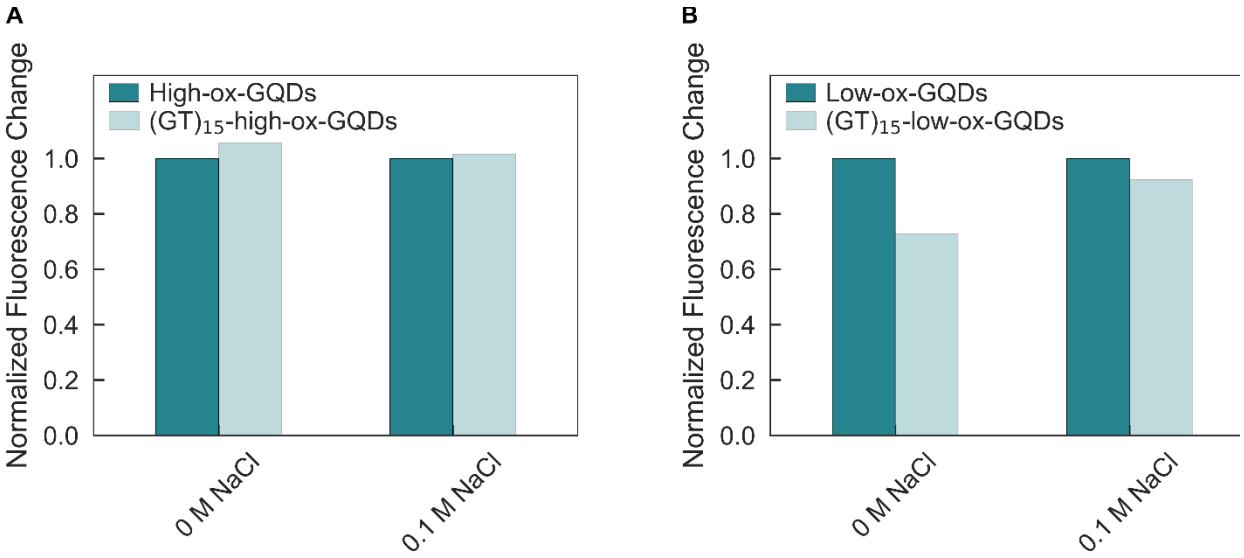

Figure 6-15. Impact of ionic strength on ssDNA adsorption to GQDs. Normalized fluorescence change of (a) $(GT)_{15}$-high-ox-GQDs and (b) $(GT)_{15}$-low-ox-GQDs in water vs. in 100 mM NaCl, demonstrating the lack of stability of ssDNA-coated low-ox-GQDs in higher salt conditions.

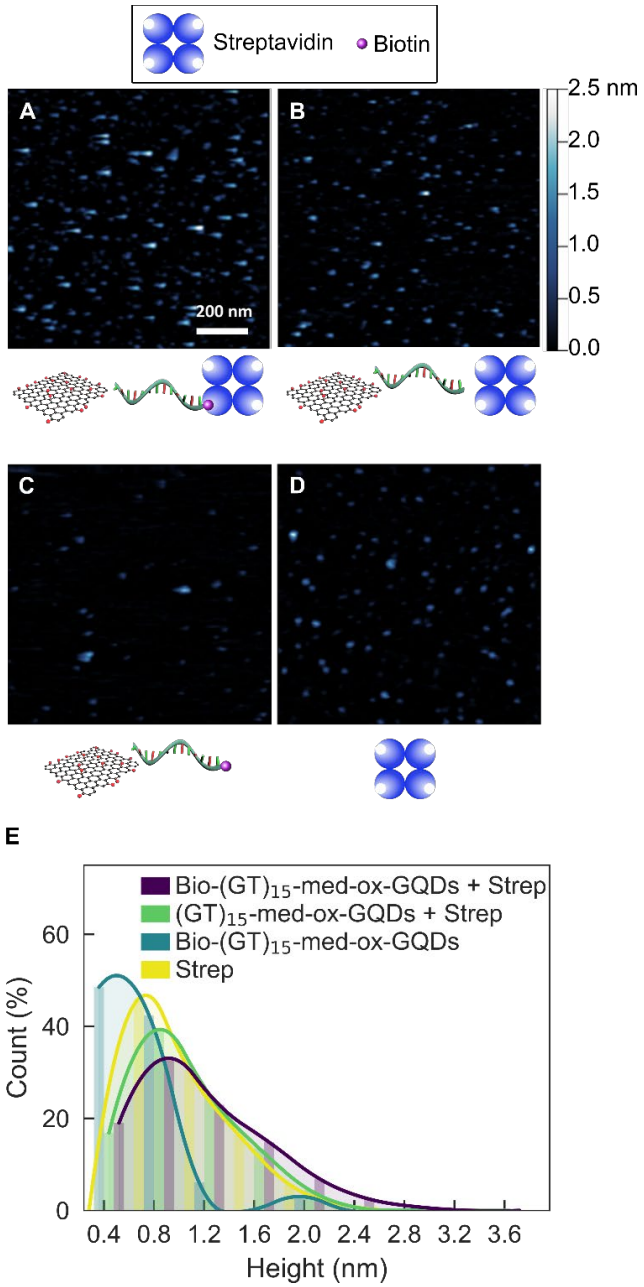

Figure 6-16. AFM verification of no ssDNA adsorption on med-ox-GQDs. AFM images and accompanying schematics for (a) biotinylated-$(GT)_{15}$-med-ox-GQDs and streptavidin (Bio-$(GT)_{15}$-med-ox-GQD + Strep), (b) $(GT)_{15}$-med-ox-GQDs and streptavidin ($(GT)_{15}$-med-ox-GQD + Strep), (c) biotinylated-$(GT)_{15}$-med-ox-GQDs (Bio-$(GT)_{15}$-med-ox-GQD), and (d) streptavidin (Strep). (e) Corresponding height distribution histograms. Bin width is 0.4 nm and curve fits are added to guide the eye.

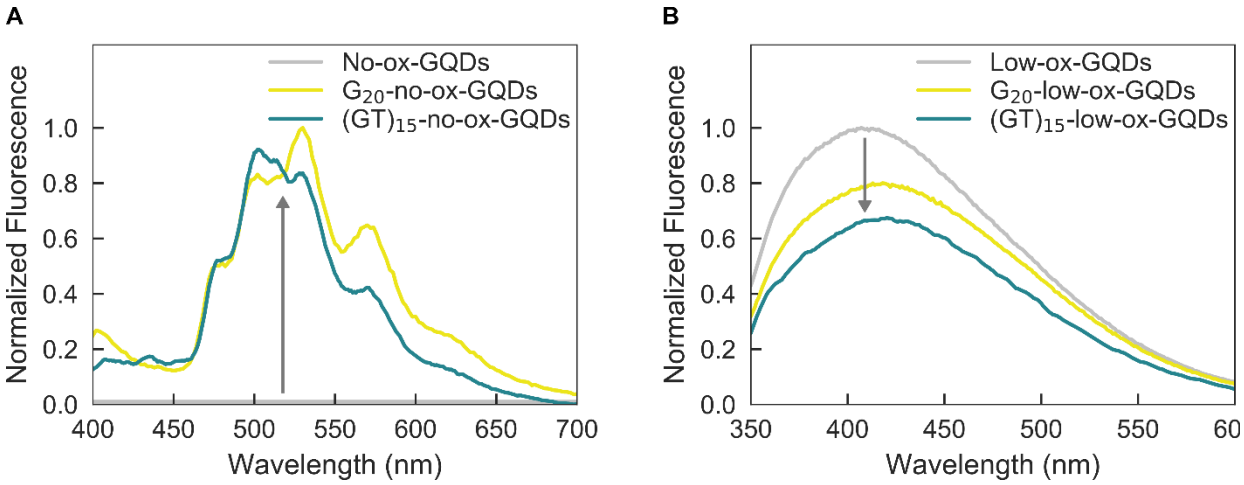

Figure 6-17. Normalized fluorescence emission spectra to probe ssDNA sequence dependence for adsorption to GQDs. Fluorescence of G_{20}-GQDs (yellow) compared to $(GT)_{15}$-GQDs (blue) for (a) no-ox-GQDs and (b) low-ox-GQDs. All GQD fluorescence spectra are normalized by the absorbance at 320 nm.

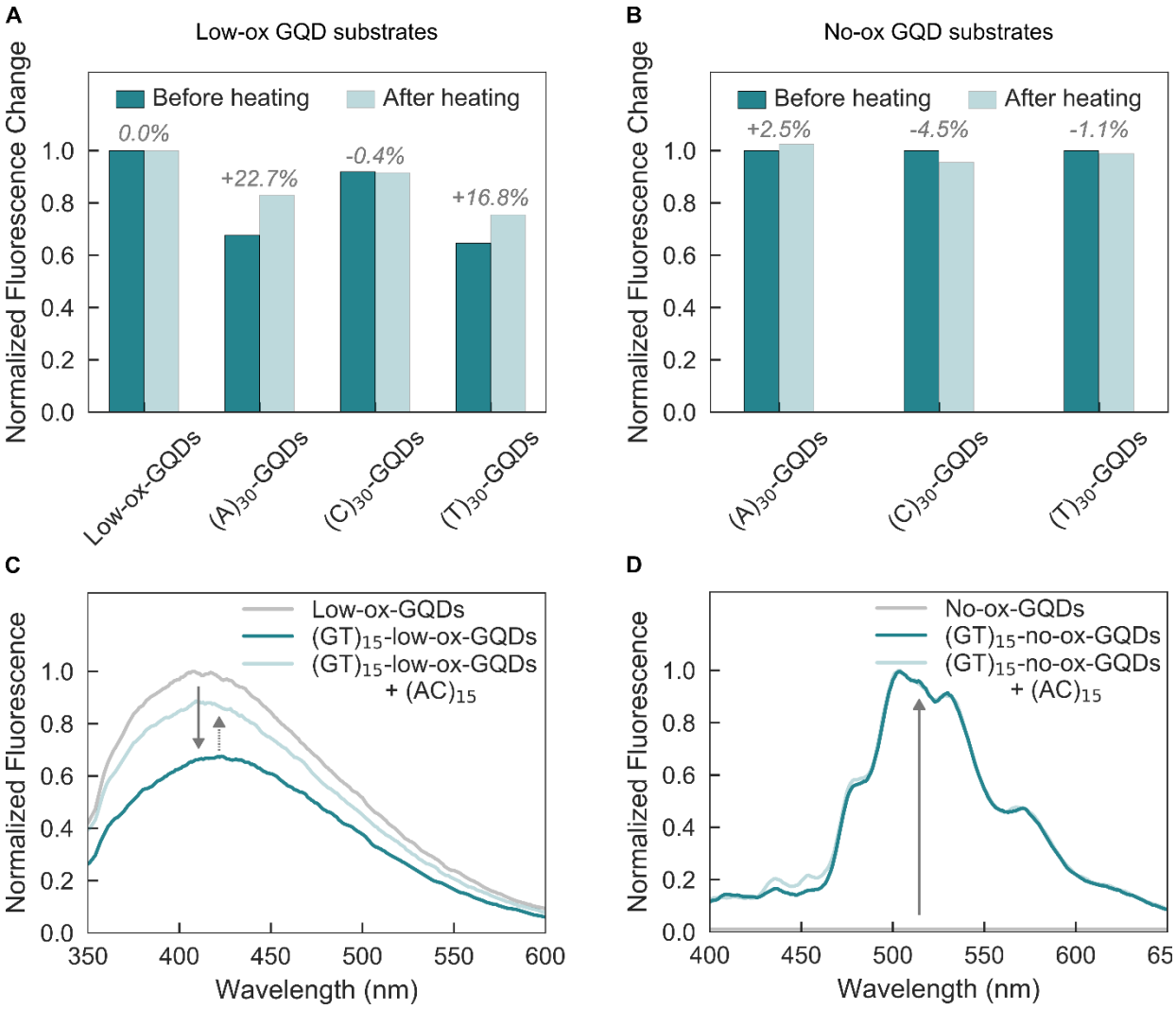

Figure 6-18. ssDNA desorption from low- and no-ox-GQDs indicates strength of noncovalent binding interactions is inversely proportional to GQD oxidation level. Fluorescence-intensity change of (a) ssDNA-low-ox-GQDs and (b) ssDNA-no-ox-GQDs induced by thermal desorption of ssDNA after heating ssDNA-GQD samples (in water) at 50 °C for 2 hours. Normalized fluorescence emission spectra of (c) $(GT)_{15}$-low-ox-GQDs and (d) $(GT)_{15}$-no-ox-GQDs, after adding five-fold excess of complementary ssDNA, $(AC)_{15}$ (in water). All GQD fluorescence spectra are normalized by the absorbance at 320 nm.

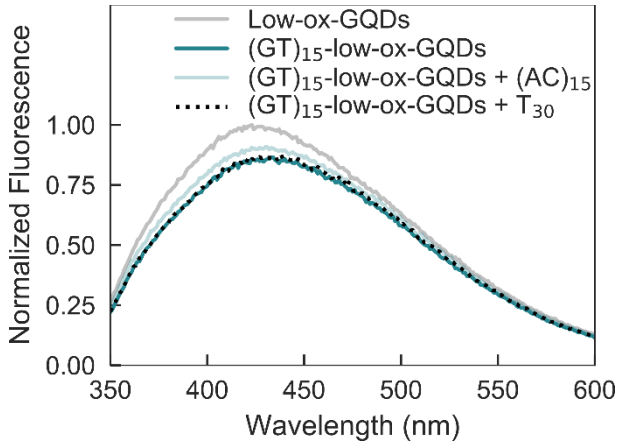

Figure 6-19. Effect of non-complementary ssDNA addition to $(GT)_{15}$-low-ox-GQD. Normalized fluorescence spectra of $(GT)_{15}$-low-ox-GQD in water after the addition of complementary $(AC)_{15}$ and T_{30} ssDNA.

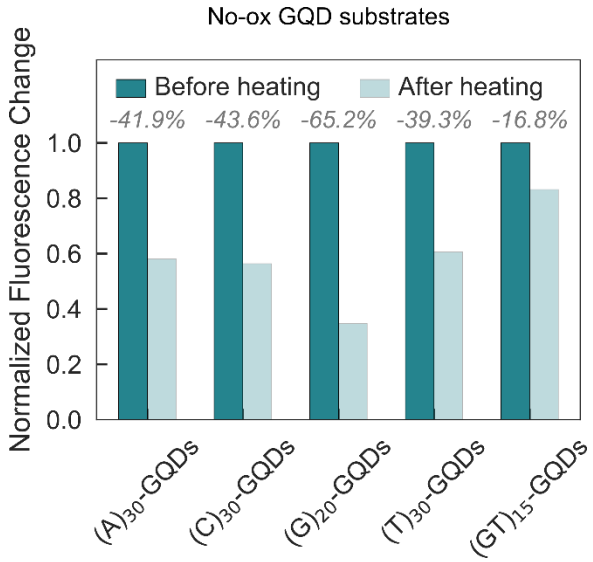

Figure 6-20. Thermally induced ssDNA desorption from ssDNA-no-ox-GQDs. Fluorescence-intensity change of ssDNA-no-ox-GQDs induced by thermal desorption of ssDNA after heating the mixture at 95 ℃ for 2 hours.

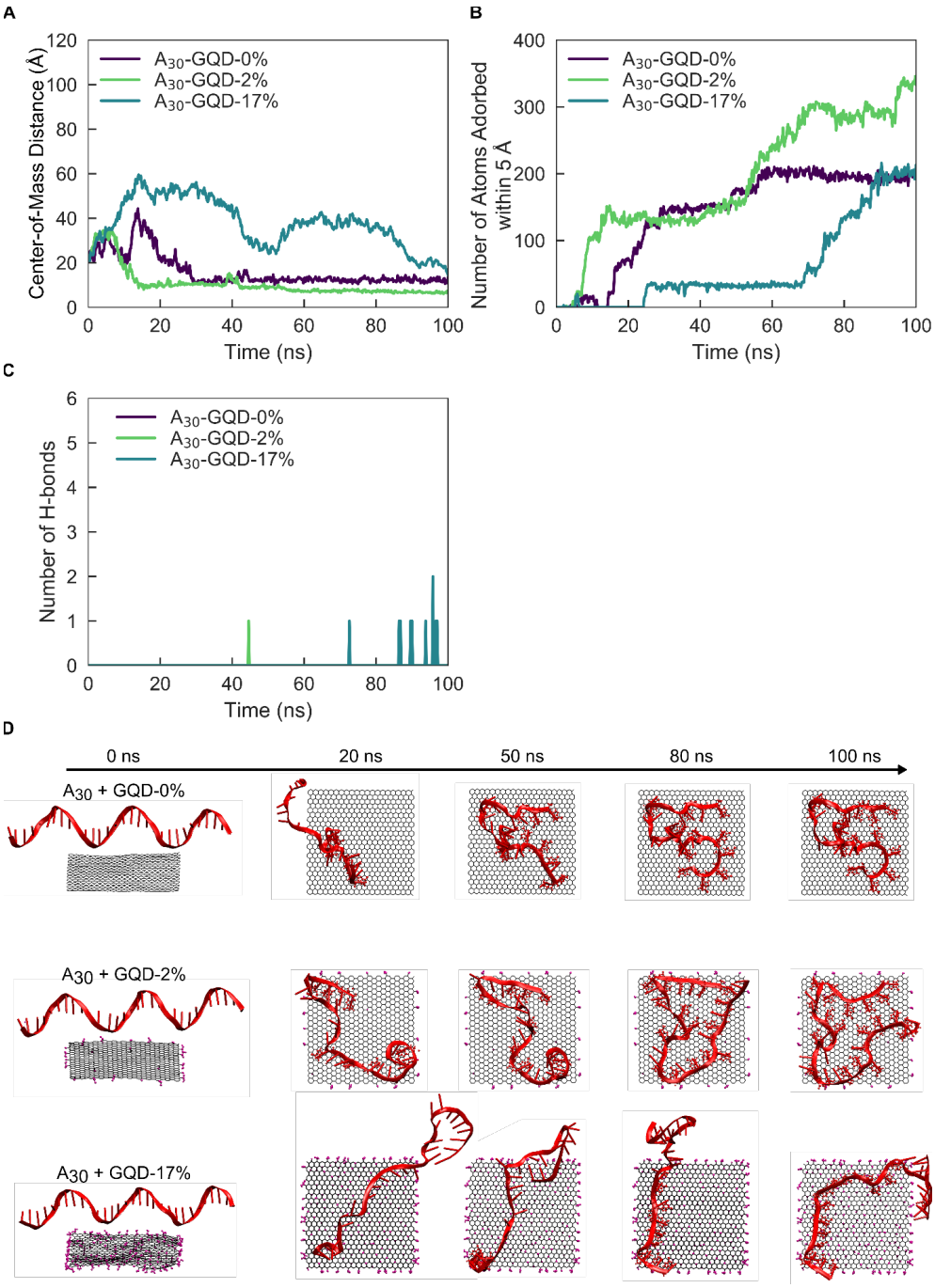

Figure 6-21. Molecular dynamics simulations of A_{30} ssDNA adsorbing to GQDs of varying oxidation levels. Time-dependent (a) center-of-mass distance, (b) number of atoms adsorbed within 5 Å of the GQD surface, and (c) number of hydrogen bonds for A_{30} ssDNA adsorbing to GQD-0%, GQD-2%, and GQD-17%. (d) Initial (left) and final (right) configurations of A_{30} ssDNA with GQD-0%, GQD-2%, and GQD-17% for a 100 ns simulation.

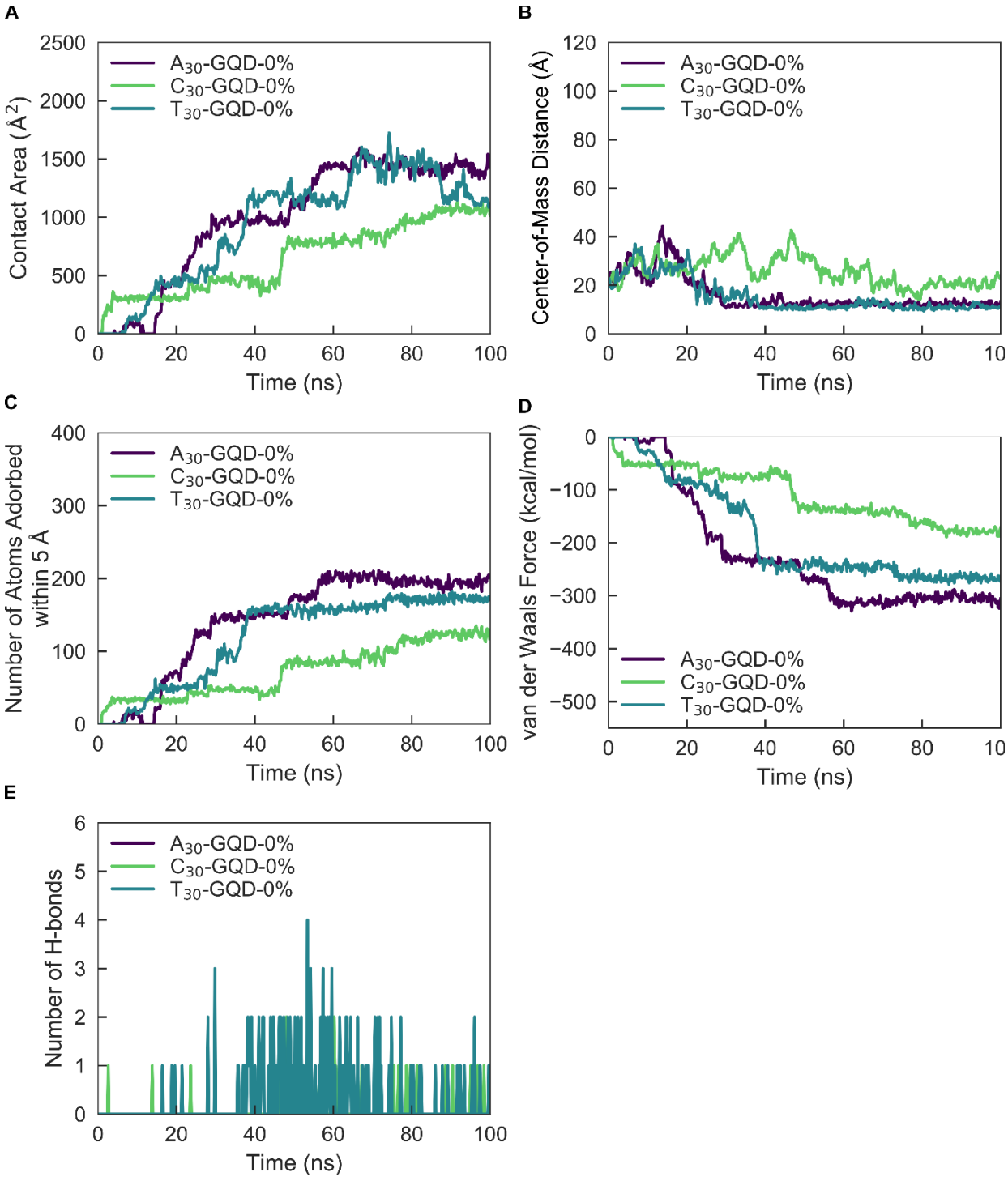
A
Contact Area (Å²)
2500
2000
1500
1000
500
0
0
20
40
60
80
100
Time (ns)
A30-GQD-0%
C30-GQD-0%
T30-GQD-0%
B
Center-of-Mass Distance (Å)
120
100
80
60
40
20
0
0
20
40
60
80
10
Time (ns)
A30-GQD-0%
C30-GQD-0%
T30-GQD-0%
C
Number of Atoms Adorbed within 5 Å
400
300
200
100
0
0
20
40
60
80
100
Time (ns)
A30-GQD-0%
C30-GQD-0%
T30-GQD-0%
D
van der Waals Force (kcal/mol)
0
−100
−200
−300
−400
−500
0
20
40
60
80
10
Time (ns)
A30-GQD-0%
C30-GQD-0%
T30-GQD-0%
E
Number of H-bonds
6
5
4
3
2
1
0
0
20
40
60
80
100
Time (ns)
A30-GQD-0%
C30-GQD-0%
T30-GQD-0%

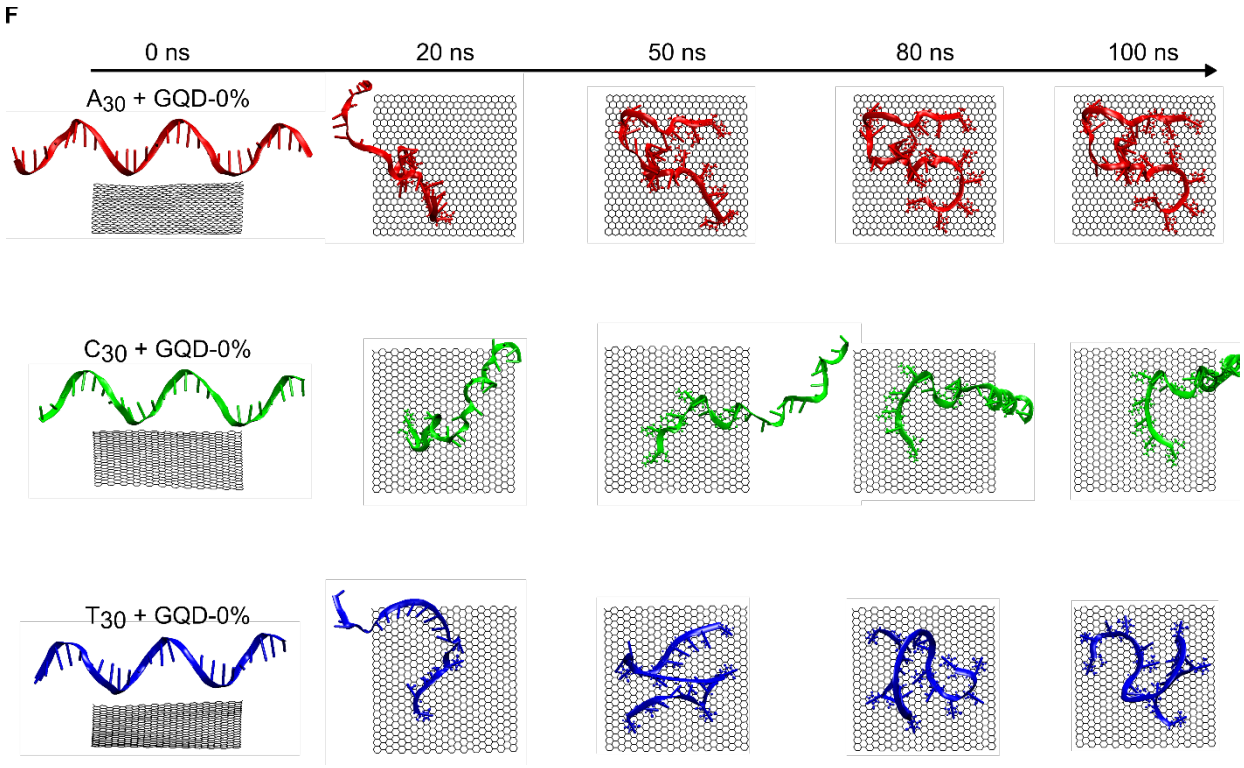

Figure 6-22. Molecular dynamics simulations of A_{30}, C_{30}, and T_{30} ssDNA adsorbing to GQDs without oxidation, GQD-0%. Time-dependent (a) contact area, (b) center-of-mass distance, (c) number of atoms adsorbed within 5 Å of the GQD surface, (d) van der Waals interactions, and (e) number of hydrogen bonds for A_{30}, C_{30}, and T_{30} ssDNA adsorbing to GQD-0%. (F) Initial (left) and final (right) configurations of ssDNA with GQD-0% for a 100 ns simulation.

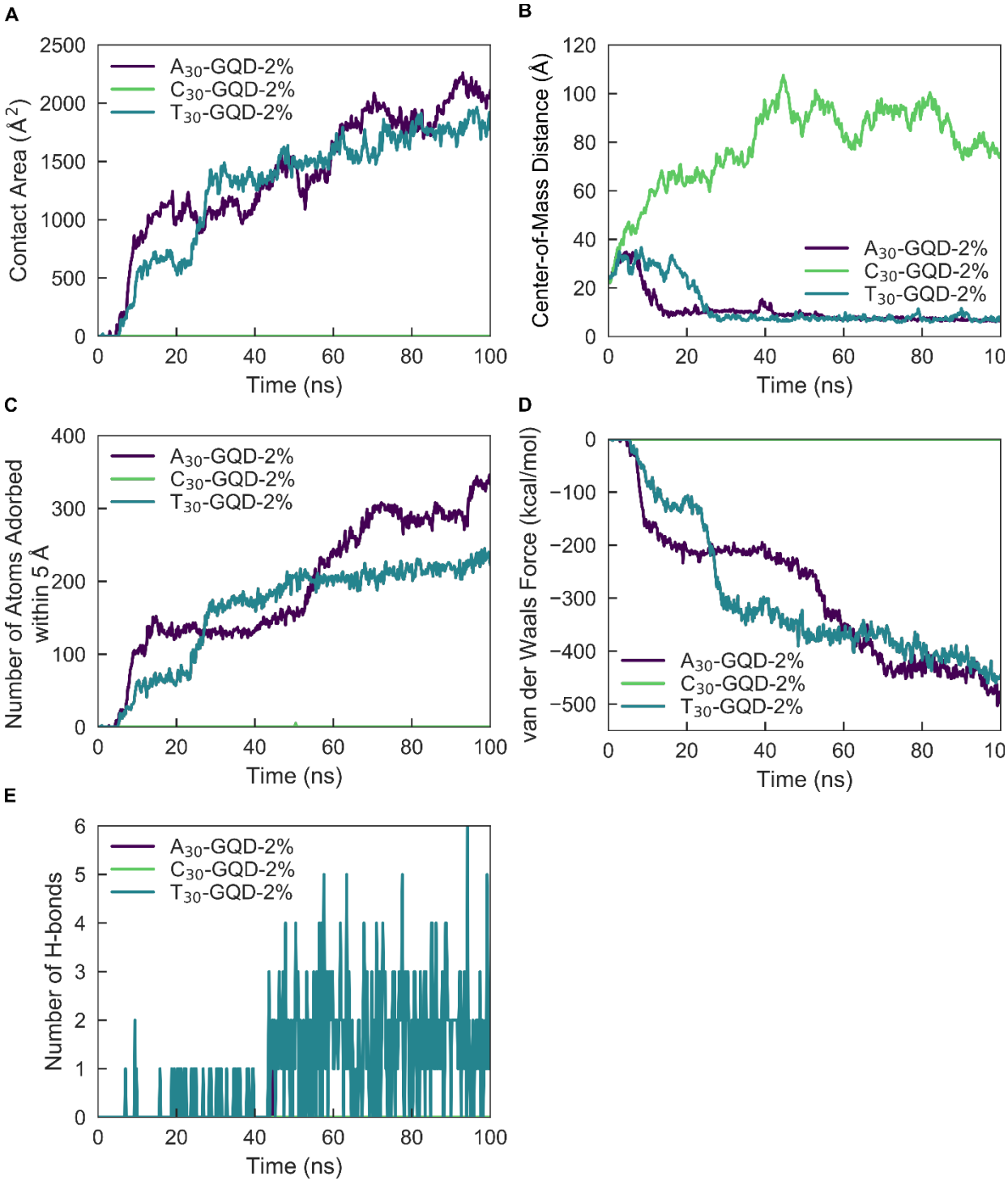
A
Contact Area (Å²)
Time (ns)
A30-GQD-2%
C30-GQD-2%
T30-GQD-2%
B
Center-of-Mass Distance (Å)
Time (ns)
C
Number of Atoms Adorbed within 5 Å
Time (ns)
D
van der Waals Force (kcal/mol)
Time (ns)
E
Number of H-bonds
Time (ns)

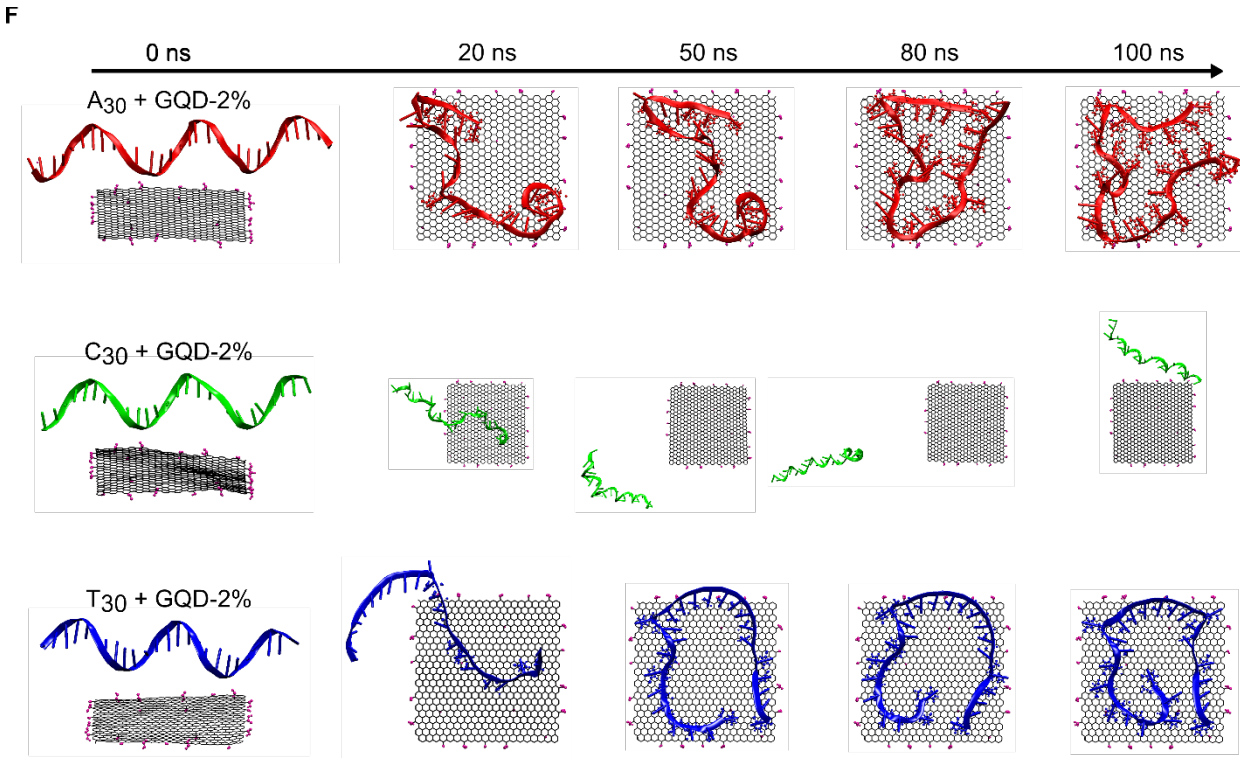

Figure 6-23. Molecular dynamics simulations of A_{30}, C_{30}, and T_{30} ssDNA adsorbing to GQDs low oxidation, GQD-2%. Time-dependent (a) contact area, (b) center-of-mass distance, (c) number of atoms adsorbed within 5 Å of the GQD surface, (d) van der Waals interactions, and (e) number of hydrogen bonds for A_{30}, C_{30}, and T_{30} ssDNA adsorbing to GQD-2%. (F) Initial (left) and final (right) configurations of ssDNA with GQD-2% for a 100 ns simulation. Note zoomed-out view of C_{30} due to larger distance of ssDNA to GQD surface; GQD size is the same throughout.

Table 6-1. Biomolecule adsorption on GQDs is dependent on GQD oxidation level.

Biopolymer Adsorbate Type	Biopolymer Sequence	GQD Adsorbent Type
ssDNA	$(GT)_{15}$	No-ox-GQD > Low-ox-GQD
	T_{30}	No-ox-GQD > Low-ox-GQD
	A_{30}	No-ox-GQD > Low-ox-GQD
	G_{20}	No-ox-GQD > Low-ox-GQD
	C_{30}	No-ox-GQD
Phospholipid	14:0 PE-DTPA	Low-ox-GQD
Peptoid	$(Nae\text{-}Npe)_9\text{-}(Nce\text{-}Npe)_9$	No-ox-GQD
	$(Nce\text{-}Npe)_9$	None

7 Harnessing the Protein Corona toward Nanoparticle Design and Function

7.1 Chapter Abstract

Unpredictable and uncontrollable protein adsorption on nanoparticles remains a considerable challenge to achieving effective application of nanotechnologies within biological environments. Nevertheless, engineered nanoparticles offer unprecedented functionality and control in probing and altering biological systems. Herein, recent advances are highlighted in harnessing the "protein corona" formed on nanoparticles as a handle to tune functional properties of the protein-nanoparticle complex. Toward this end, we review recent literature detailing corona-mediated functionalities, including stealth to avoid immune recognition and sequestration while in circulation, targeting of predetermined *in vivo* locations, and controlled activation once localized to the intended biological compartment. We conclude with a discussion of biocompatibility outcomes for these protein-nanoparticle complexes applied *in vivo*. While formation of the nanoparticle-corona complex may impede our control over its use for the projected nanobiotechnology application, it concurrently presents an opportunity to create improved protein-nanoparticle architectures by exploiting natural or guiding selective protein adsorption to the nanoparticle surface.[§§]

7.2 Introduction

When engineered nanoparticles are introduced into a biological medium, proteins swiftly adsorb to and coat the nanoparticle surfaces. This phenomenon is at present well-established, duly termed formation of the nanoparticle's "protein corona" to provoke imagery of the corona surrounding the sun during a solar eclipse, with tendrils of light (or rather, adsorbed proteins) reaching outwards. As our repertoire of engineered nanoparticles becomes ever-more diverse, these nanoparticles are continually applied for broader functions across vastly differing biological environments. A comprehensive understanding of the protein corona remains one of the greatest challenges in successfully developing and implementing nanobiotechnologies.

We begin by discussing how recent work has employed the protein corona toward *a priori* design of corona-mediated functionalities. Our review is centered on *in vivo* applications of corona-mediated nanoparticle stealth, targeting, and activation, with a corresponding discussion of nanoparticle construct biocompatibility to follow.

7.3 Corona-based Nanoparticle Development

7.3.1 Nanoparticle-Corona Complexation Considerations and Techniques

Development of functional protein-nanoparticle constructs requires special attention to the packing, conformation, and orientation of proteins on the nanoparticle surface. As detailed in

[§§] Portions of section 7 published as Pinals, R. L.; Chio, L.; Ledesma, F.; Landry, M. P. Engineering at the Nano-Bio Interface: Harnessing the Protein Corona towards Nanoparticle Design and Function. *Analyst* **2020**, *145* (15), 5090–5112. https://doi.org/10.1039/D0AN00633E.

section 1.3, less tightly packed proteins may experience damaging post-adsorptive transitions including spreading, reorientation, and denaturation.[85,86,140] This control over interfacial protein conformation is critical, in that denatured proteins are generally not functional and increase the risk of triggering nanoparticle aggregation or immune system recognition and clearance.[95,116] In turn, packing densities and patterns of biomolecules on nanoparticles can significantly affect targeting abilities[78] and clearance pathways.[120] Protein orientation on the surface also directly impacts protein function, in that particular protein domains must be outwardly displayed in solution, such as enzymatic active sites and targeting moieties for receptor or molecular recognition.[113,126,140]

Protein adsorption on nanoparticle surfaces is accomplished by either noncovalent or covalent means. Within the subset of noncovalent corona formation techniques, we describe both *post factum* and *ab initio* routes of protein corona formation. With *post factum* corona formation, the *in vivo* corona formed on nanoparticles is characterized, and this knowledge is applied to the advantage of the construct toward specific means.[88] For example, spontaneous apolipoprotein adsorption onto peptide-functionalized liposomes assists in brain targeting of drug-loaded liposomes.[424] The *ab initio* protein corona is achieved by initially pre-coating nanoparticles with the desired protein, resulting in noncovalent attachment of the protein on the nanoparticle. Examples of passive incubation to pre-coat nanoparticles with functional protein coronas include: albumin for extended circulation or biobarrier crossing;[123,145] antibodies for targeted cell uptake;[145] apolipoprotein E for extended circulation or brain targeting;[95,147] and transferrin for cancer cell targeting.[425] Proteins may also be actively adsorbed, i.e. requiring energy input, such as high-intensity sonication to disperse hydrophobic carbon nanotubes with various plasma protein coatings.[141,142] Another aim of passive *ab initio* corona formation is to passivate exposed nanoparticle surface for biocompatibility,[136] or retain the folded protein conformation or orientation of the functional corona components.[85]

Noncovalent methodologies are simple and rapid, yet inherently less stable than a covalent attachment and thus prone to exchange with other proteins in solution.[426] When Zhang *et al.* probed pre-coated protein stability on spherical nucleic acids, they discovered that ~45% of the initial corona is removed upon exposure to blood serum.[145] Additionally, passive incubation techniques generally lack control over the resulting spatial distribution and functional orientation of proteins on nanoparticle surfaces.[108,132] It is difficult to control monolayer vs. multilayer protein corona formation on nanoparticles, where monolayers may be desired, but multilayers often result from a combination of the hard and soft coronas.[116] To overcome unpredictable corona organization, Mout *et al.* present a rational design strategy taking advantage of directed electrostatic assembly to form hierarchical protein-nanoparticle superstructures via co-engineering recombinant proteins with ligand-tagged nanoparticles.[138] Noncovalent assembly is also ideal in some cases for preserving the intrinsic nanoparticle properties.[142,427] A clever bridge between retaining nanoparticle properties and enabling controlled protein attachment has been done by Mann *et al.*, where DNA is noncovalently adsorbed on the surface of single-walled carbon nanotubes, then nanobodies are covalently attached to the DNA.[427] This strategy preserves the intrinsic, near-infrared fluorescence of the underlying nanotube by avoiding protein-nanotube covalent attachment chemistries, and simultaneously confers more controlled protein orientation and packing that in turn enables successful nanobody targeting.

Covalent conjugation of proteins to nanoparticles offers another attachment route. While covalent functionalization is more stable and controlled than noncovalent adsorption, the former requires introducing new covalent bonds on both the nanoparticle surface and the protein. Examples of covalent corona attachment methods include maleimide-thiol chemistry,[91,99,110] photochemical cross-linking,[79] N-hydroxysuccinimide (NHS) active ester reactions,[76,126] and thiol-ene click chemistry.[108] These chemistries can be applied sequentially, such as gold nanoparticle-thiol surface chemistry followed by NHS ester chemistry with a linker to tether the protein.[125] New conjugation protocols such as those from Lee *et al.* offer promising, facile chemistries for more direct gold nanoparticle-PEG linker-peptide attachments.[91] New covalent chemistries have also enabled protein attachment to carbon nanotubes, with re-aromatization of the graphitic sidewalls to retain the desired near-infrared fluorescence for nanosensor readout.[428]

7.4 Development of Stealth Nanoparticles

After creation and *in vitro* characterization of nanoparticle-corona complexes, several challenges still lie between administration and successful use of nanoparticles *in vivo*. Many such obstacles stem from the recognition of these synthetic nanomaterials by the body. Nanoparticles often trigger an immune response, resulting in immune cell recruitment, antibody and chemokine release, and activation of the mononuclear phagocytic system (MPS) (Figure 7-1a). Briefly, the MPS entails the recognition, engulfment, and subsequent clearance of nanoparticles from blood circulation through the action of phagocytic cells, such as Kupffer cells in the liver, dendritic cells in major organs, microglia in the nervous system, and alveolar macrophages in the air spaces of the lungs.[429] Consequently, nanoparticles are often found to accumulate in the liver and spleen. Numerous studies have shown that the protein corona plays a critical role in modulating the MPS.[108,426,430] Specifically, proteins termed opsonins promote phagocytosis, and include complement proteins and immunoglobulins (IgG, IgA, and IgM). Conversely, dysopsonins are proteins that aid evasion of phagocytosis, and include albumin and apolipoproteins. The protein corona can thus be tuned to mediate challenges that the nanoparticle faces from injection to localization.

To prevent activation of the immune response and nanoparticle recognition by the body, several strategies can be implemented to provide nanoparticles with stealth properties. In literature, "stealth" is often used to indicate resistance to biofouling, referring to the low nonspecific adsorption of proteins on nanoparticles. Although less adsorption of certain proteins such as opsonins correlates with better biological compatibility, more factors are involved in nanoparticle stealth for biological applications.[426] We therefore refer to stealth herein as the ability to evade recognition by the body. In the discussion to follow, we highlight studies that report longer nanoparticle retention time *in vivo* and lower titer of biomolecules that indicate immune response. Studies have demonstrated this phenomenon through the design of the nanoparticle corona using polymer, protein, or biomimetic coatings (Figure 7-1b).

7.4.1 Polymer Coatings for Stealth

Attachment of polymers to nanoparticle surfaces provides a facile approach to modify hydrophilicity, size, and other nanomaterial properties, as detailed in section 1.3, that may modify protein corona formation in comparison to the bare nanoparticle and confer stealth *in vivo*.

7.4.1.1 Polyethylene Glycol Coatings for Stealth

Polyethylene glycol (PEG) is one of the most studied polymer coatings for use as a stealth agent on nanoparticles, and we point readers to previous reviews with more in-depth discussion on the efforts of PEG use in biological settings.[431,432] PEG is water soluble and capable of extending the half-lives of nanoparticle carriers in circulation,[99,433] presumably due to the water solvation effect whereby it is less energetically favorable for proteins to exchange with water adsorbed to the highly hydrophilic PEG chains. One important consideration is the PEG grafting density on the nanoparticle surface, which controls surface roughness and PEG orientation, and subsequently impacts protein corona formation. PEG in a dense, brush conformation better repels protein adsorption than a less dense, mushroom conformation.[97,100,101] Recent work implemented a two-layer PEG system, where the first layer is a dense polymer brush to prevent protein adsorption, followed by a second layer that approaches the mushroom-to-brush transition to reduce liver uptake.[97] This study also highlights that certain aspects of the PEG-driven stealth mechanism are still under investigation. It was originally thought that PEG enables nanoparticle stealth by repressing protein adsorption that in turn triggers MPS clearance. However, recent work shows that PEGylated nanoparticle surfaces can exhibit substantial adsorption of proteins, and it is the repressed adsorption of specific opsonin proteins and enhanced adsorption of dysopsonin proteins that enables stealth (referred to as the PEG "harvesting" effect).[101,106,434] In the case of polystyrene nanocarriers, a PEGylated surface enriched selective binding of a dysopsonin protein clusterin, which results in shielding of the nanoparticles from macrophage uptake.[434] Thus, PEGylation could serve to recruit selective proteins to the nanoparticle surface toward desired applications, such as avoiding macrophage internalization as shown here. [106,434]

Recent studies are moving away from the use of PEG as a stealth agent, as fundamental challenges of using PEG-nanoparticle conjugates come to light. The ubiquitous use of PEG in nanomedicine has led to the formation of anti-PEG antibodies in the body and rapid clearance of PEGylated nanoparticles from the body, termed the "accelerated blood clearance" phenomenon.[435,436] Furthermore, use of PEG does not necessarily suppress unfavorable protein adsorption onto all nanoparticles,[83,437] such as nanosomes with PEG linkers shown to irreversibly aggregate after protein corona formation in whole serum.[128] Due to these findings, researchers are investigating other polymer coatings for nanoparticle stealth.[432]

7.4.1.2 Zwitterionic Polymer Coatings for Stealth

Zwitterionic polymers, containing both positive and negative charges, are promising for stealth nanoparticle applications because they behave similarly to PEG in preventing protein corona formation *in vitro*.[73,127,426] It is known that surface charge affects *in vivo* nanoparticle fate: cationic polymer coatings promote cellular adhesion and uptake, yet exhibit higher clearance as compared to their anionic and zwitterionic counterparts.[93] Zwitterionic polymer coatings, such as sulfobetaines,[89,94] phosphorylcholine,[426,438] and peptides[439,440] have been increasingly investigated and have shown efficacy *in vivo*. A zwitterionic peptide coating of alternating negatively charged glutamic acid and positively charged lysine on gold nanoparticles showed prolonged circulation *in vivo* in tumor-bearing nude mice.[440] Compared to PEG-coated gold nanoparticles, these zwitterionic peptide-coated nanoparticles were inert to the immune system and did not elicit elevated levels of immune proteins, such as IgM and IgG. Similarly, a gold nanocage system functionalized with acylsulfonamide-based pH responsive zwitterionic ligands showed four-fold

longer circulation lifetime and tumor accumulation in BALB/c mice bearing 4T1 murine breast tumors than a neutrally charged polyvinylpyrrolidone-functionalized gold nanocage.[127]

7.4.1.3 Carbohydrate Coatings for Stealth

Researchers are increasingly turning to biologically derived polymers, such as carbohydrate coatings, to prolong nanoparticle circulation *in vivo*. Hydroxyethyl starch (HES)-linked nanoparticles have created drug nanocarriers with prolonged *in vivo* circulation half-life of several hydrophobic chemotherapy drugs.[107,441] HES-conjugated polydopamine nanoparticles were shown to have similar circulation half-life and drug-loading capability as PEGylated polydopamine mannosylated PPE-nanocarriers were shown to avoid protein adsorption and better target dendritic cells for immunotherapy.[442] This noncovalent PPE adsorption and sugar passivation is generalizable to other nanocarrier systems, and as different sugar-coated systems are shown to have varying responses in the body, there is a need for further investigation on how carbohydrate polymers interact with the protein corona to modulate stealth.[74]

7.4.2 Protein Coatings for Stealth

Another solution toward constructing stealth nanoparticles is to engineer the protein corona itself to avoid triggering the immune system and MPS detection.[80] As all nanoparticles are expected to develop coronas *in vivo* and the existence of these coronas often promotes immune cell association,[426] directed adsorption of dysopsonins and/or reduced adsorption of opsonins on the nanoparticle surface can be employed to reduce clearance of nanoparticles.[152]

Nanoparticle surface properties may be altered to direct adsorption of desired proteins or repel unwanted proteins. In a study of peptide-embedded liposomes, it was shown that the adsorption of IgM correlates with rapid clearance through MPS and accumulation in the lymph nodes.[436] By modifying the length of the peptide displayed on the liposome, adsorption of IgM decreased, leading to longer nanoparticle half-life in circulation. To encourage dysopsonin adsorption, nanogels were created using molecular imprinting, a method that templated nanogels to bear a binding site for native dysopsonin protein: albumin.[154] Upon injection into a tumor xenograft model, it was shown that the molecularly imprinted nanogels (MIP-NGs) had a higher half-life in blood (6.8 hours), compared to the non-imprinted nanogels (3 hours). Furthermore, these MIP-NGs were observed to circulate in the liver without aggregation or capture for over 10 hours, demonstrating that nanoparticle surface modifications can be utilized to adsorb necessary stealth proteins.

Protein corona shields can be made through the design of the nanoparticle surface *a priori*. Oh *et al.* created a protein corona shield for mesoporous silica nanoparticles using a recombinant fusion protein of glutathione-S-transferase genetically combined with Her2-binding affibody.[108] This outer corona shield led to the reduction of protein corona formation and subsequent higher retention in plasma. In another study, pre-incubation of charged polystyrene nanoparticles in IgG-depleted plasma formed a corona enriched in vitronectin and fibrinogen on negatively charged polystyrene nanoparticles or enriched in clusterin and hemopexin on positively charged polystyrene nanoparticles.[442] These nanoparticle-corona complexes showed reduced uptake by RAW264.7 macrophages and remained stable when reintroduced into whole plasma. Preincubation with the dysopsonin apolipoprotein E on graphene, gold nanoparticles, and iron

oxide nanoparticles showed markedly improved blood circulation and better biocompatibility than opsonin IgE-coated nanoparticles.[95] Using the growing database of corona proteins, it is increasingly possible to tailor nanoparticle surfaces for avoidance of premature clearance.

7.4.3 Biomimetic Coronas for Stealth

Similar to plasma-derived protein coatings for stealth applications, other biomimetic solutions to maintain nanoparticle biocompatibility include employing cell membrane proteins to shield nanoparticles from recognition. To keep nanoparticles in circulation and curtail recognition from immune cells, blood cells are a template for nanoparticle stealth. Corbo *et al.* have utilized white blood cell (leukocyte) proteins, such as macrophage receptors, to decorate liposomes and produce a new class of nanoparticles called leukosomes.[132] They showed that leukosomes have lower accumulation in MPS organs and have reduced uptake by macrophages. Similarly, Meng *et al.* extract red blood cell membranes to coat immunomagnetic micro and nanoparticles.[137] This coating prevents the formation of a protein corona in whole blood for better retention.

The use of biomimetic coronas could also accelerate the development of personalized nanomedicine with low immunogenicity. Personalized protein nanoparticles can be made from patient-derived proteins extracted from a variety of human sources such as serum, tears, saliva, or breast milk.[79] The proteins are initially cast on a metal nanoparticle core, then extracted to create a biodegradable nanoparticle made up of only proteins. These protein nanoparticles were used *in vivo* without any inflammation or immune cell recruitment. Biomimetic solutions in creating stealth nanoparticles leverage specific cell-type proteins or personalized proteins to evade detection.

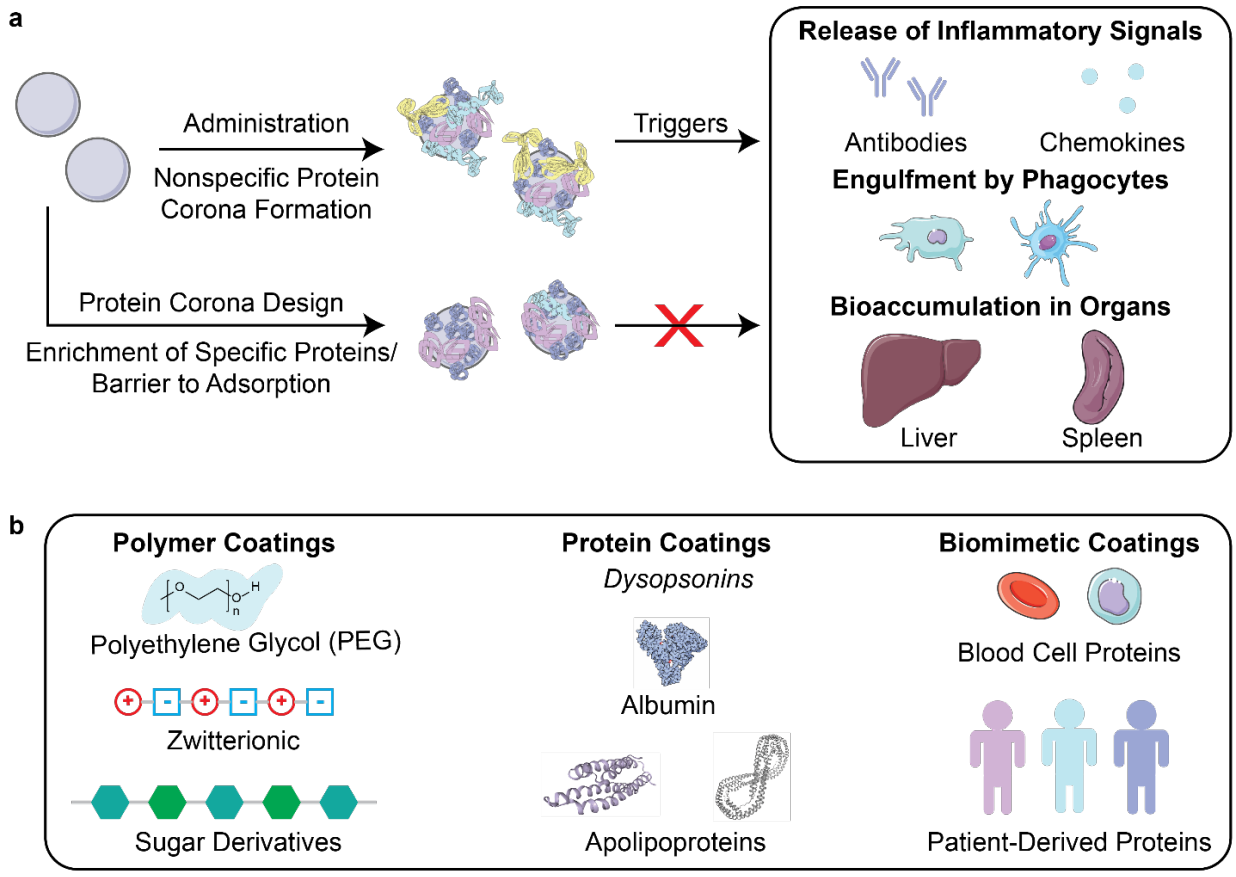

Figure 7-1. Nanoparticle stealth, strategies and outcomes. (a) Administration of nanoparticles into the body leads to formation of the protein corona that can trigger an immune response or clearance of nanoparticles. Rational design of the protein corona can promote the enrichment of favorable, dysopsonin proteins or mitigate the adsorption of unfavorable, opsonin proteins to promote nanoparticle stealth. (b) Strategies that utilize polymer, protein, or biomimetic coatings have been developed to design the protein corona for better nanoparticle stealth. Protein images are from the RCSB PDB (rcsb.org) of PDB ID 1E7I, 1LE2, and 1AV1.[443–445]

7.5 Targeting and Activation of Functional Nanoparticles to Biological Systems

After bypassing recognition and clearance from circulation, nanoparticles must overcome additional barriers to achieve successful localization and function. As such, targeted delivery of nanoparticles remains a major challenge in the clinical adoption of nanomedicine, and recent literature reveals that efficacious nanoparticles can manipulate protein corona engineering toward this purpose. In this section, we discuss the targeting strategies of nanoparticles and subsequent activation of nanoparticles once they arrive at a biological target of interest.

7.5.1 Challenges and Considerations in Nanoparticle Targeting

Nanoparticle surfaces can be engineered for targeting through the addition of different synthetic and biological ligands, such as small molecules, peptides, and antibodies. However, nanoparticle

targeting elements incorporated on bare nanoparticle surfaces and validated *in vitro* may show different functionality *in vivo*, where the formation of the protein corona upon administration could inhibit the accessibility of these targeting ligands.[130] Some studies show that cellular uptake of nanoparticles is controlled by the outermost protein corona as opposed to the surface ligands meant to target receptor-expressing cells.[102,446] A notable exception of this phenomenon was seen in poly(beta-aminoester) polymer nanoparticles with variable terminal targeting peptides.[446] The nanoparticles were coated with retinol, a hepatic targeting moiety, and the protein corona formed dictated organ biodistribution, yet cellular uptake was determined by the terminal peptides independent of the corona. For many other cases, however, the *in vivo* protein corona attenuates the targeting properties of nanoparticles. Serum proteins were shown to decrease association of transferrin-labeled liposomes with glioblastoma cancer cells, although transferrin-labeled liposomes still exhibited better association, tumor uptake, and tumor growth inhibition than unlabeled liposomes.[425] There is currently a dearth of literature on the mechanism of these targeting moieties *post factum*, and work is moving toward understanding the strategies for *ab initio* nanoparticle design. Certain properties such as size, conformation, and mobility of targeting ligand have come to light as important design parameters for targeting applications.

Size of targeting ligands could play a substantial role in targeting potency. An example is transferrin, an 80-kilodalton glycoprotein used in many targeting studies for its well documented ability to promote clathrin-mediated endocytosis, and subsequent intracellular trafficking through recycling pathways.[447] Transferrin, peptide LT7 (CHAIYPRH), and DT7 (the d-amino acid analogue of LT7) are all targeting ligands for transferrin receptors that are overexpressed in several cancer types.[133,447] Investigation of targeting and uptake of polystyrene nanoparticles functionalized with these ligands revealed that the transferrin-passivated nanoparticles out-performed the peptide-passivated ones.[133] Analysis of the protein corona formed around each of these nanoparticles revealed differences in composition, and underscored a size and conformation effect on ligand targeting.

As introduced in section 7.4, the conformation of targeting ligands on nanoparticle surfaces can affect the ability of the nanoparticle to carry out its intended function.[78,113] Fibronectin, a protein that binds cell-adhesion receptors called integrins and extracellular matrix components, can undergo pronounced conformational changes when adsorbed onto bare gold nanoparticle surfaces compared to when adsorbed to the nanoparticle surface through protein-protein interactions, leading to loss of function in the former.[116,448] The function of targeting modalities on nanoparticles must be preserved in the surface-adsorbed state and during *in vivo* application. Finally, beyond simply optimizing ligand avidity toward the intended target, Figueroa *et al.* highlights how increasing mobility of ligands tethered to nanoparticle surfaces drives more elevated cellular uptake.[449]

7.5.2 Protein Corona Strategies in Nanoparticle Targeting

Several nanoparticle targeting schemes are validated with applications *in vivo*. Cancer therapies often require targeted approaches because treatments, such as chemotherapy, are cytotoxic to both cancerous and non-diseased cells and have a limited dosing range. Hence, most literature examples of nanoparticle targeting are devoted to designing nanoparticles for cancer therapy. These design principles could be extended to other diseases and tissue types. This section highlights some

targeting modalities that can be attached to a variety of nanoparticles through different conjugation chemistries.

Targeting strategies that activate transport pathways or bind overexpressed biomarkers are promising for *in vivo* applications because they increase uptake of the nanoparticles by the target cell. To activate transport pathways, nanoparticle surfaces can be functionalized with ligands that bind to requisite receptors or proteins on the target cell (Figure 7-2a). The use of polypeptides is frequently employed to deliver nanomedicine to tumor cells, such as the arginine-glycine-aspartic acid (RGD) peptide motif that binds to integrin transmembrane proteins.[433,450,451] Other ligands include synthetically malleable polymers that are readily incorporated through bioconjugation chemistry or layer-by-layer synthesis; a prominent example is hyaluronic acid that binds to CD44 receptors overexpressed in many cancers.[168] Additionally, the use of hyaluronic acid is shown to reduce the immunogenicity through the selective adsorption of anti-inflammatory proteins to the formed protein corona.[452]

Dual stealth and targeting surface functionalization prevent the adsorption of plasma proteins and thus retains nanoparticle targeting capability. Koide and colleagues designed nanosomes, consisting of core metals covered by an anti-adhesive mixed self-assembled monolayer, capable of preventing protein adsorption while outwardly displaying n-acetylglucosamine (GlcNAc).[128] This outer layer triggered uptake through the cancer-specific GlcNAc salvage pathway, and resulted in body circulation, accumulation in the tumor, and reduced tumor size. Similarly, mesoporous silica nanoparticles with a protein shield of glutathione-S-transferase fused with Her2-binding affibodies were shown to adsorb few corona proteins and resulted in increased uptake and growth inhibition of breast cancer *in vivo* in SK-BR3 xenograft mice.[108] Corona proteins adsorbed during nanoparticle transport can also be used for targeting, and as mentioned in section 7.4, redirecting accumulation from the liver and spleen leads to better accumulation of nanoparticles in other organs. An interesting case of nanoparticles for cancer therapy is blood-triggered generation of platinum nanoparticles as anti-cancer agents. Platinum, originating from the chemotherapy drug cisplatin, is triggered by albumin to assemble *in vivo* to function as an anti-cancer agent.[143] This native corona of albumin then promotes targeting tumors with better efficacy in leukemia xenograft mice than commercial albumin-platinum conjugates.

7.5.3 Protein Corona Strategies in Nanoparticle Passage Across Biological Barriers

Targeting also aids efficient delivery of nanoparticles through biological barriers such as the blood-brain barrier (BBB), mucous membranes, and epithelial barriers (Figure 7-2b). These barriers impose certain limitations on the physical characteristics of the nanoparticles, as introduced in section 1.3. For example, the BBB excludes passage on the basis of size and surface properties including charge and hydrophilicity.[130,453] Nanoparticles have been shown to pass the BBB via transcytosis-mediated routes, mediated by immune cells[454,455] or the presence of apolipoproteins,[147,424] transferrin,[110] or other proteins within the adsorbed corona (as reviewed extensively elsewhere[453,456,457]). Importantly, traversing biological barriers can lead to alterations in the nanoparticle corona. A study of the nanoparticle protein corona was conducted in an *in vitro* cellular transwell model of the BBB, demonstrating evolution of the protein corona as well as a stabilizing effect after BBB crossing.[129] It is shown for gold nanoparticles that only 9 of the 20 most abundant proteins in the corona are retained after passage through this BBB model, where serum albumin and α-2-macroglobulin remain abundant, with enrichment of complement C9. For

efficient design of targeting elements to cross biological barriers, it is important to ensure stable attachment such that targeting functionality can be maintained across different environments.

Strategies exist at the intersection of nanoparticle surface design and biological environment considerations in designing nanoparticles for targeted biological barrier crossing. For oral delivery, nanocarriers must withstand acidic pH, enzymatic degradation, and differing surface charge requirements during passage through the mucous membrane and intestinal epithelium. Passage across the negatively charged mucus barrier is best achieved with neutral, hydrophobic molecules, while passage across the intestinal epithelium is optimal with cationic, hydrophobic molecules. With these system constraints in mind, Wang *et al.* aimed to overcome this issue of ineffective oral administration and uptake of insulin through rational corona design.[123] Ultimately, pre-coating albumin on cationic liposomes enabled increased penetration across both mucosal and epithelial barriers: the protein coating is enzymatically hydrolyzed as the liposomes cross the mucus layer, resulting in exposure of the underlying positively charged liposome that subsequently improves transepithelial transport. *In vivo* experiments show that the uptake amounts and transepithelial permeability of these liposomes carrying insulin were 3.24- and 7.91-fold higher, respectively, than that of free insulin. Continuing this same idea, Zeng *et al.* suggest that the presence of other proteins such as protease inhibitors in the nanoparticle corona, in addition to pre-loaded albumin, serves the role of protecting albumin from hydrolysis prior to reaching the intended destination (in this case, tumors).[143]

7.5.4 Activation of Nanoparticle Functions upon Localization

As discussed in previous sections, nanoparticle systems can be designed to increase their bioavailability, circulation time, and ability to target and localize to desired areas such as specific organs or tumors. However, surface functionalizations that prove beneficial for these purposes can be detrimental once these nanoparticles arrive at their target site.[458] It is thus desirable to alter nanoparticle composition in a controlled manner through various cleavable bonds and mechanisms upon nanoparticle localization. Several environmental triggers have been used for this purpose in recent years, with pH, light, enzymes, and redox environments being the most common (Figure 7-2c). Other triggers including temperature[459] and electrostimulation[460] have been demonstrated, but are less common due to the inherent difficulty of applying these external stimuli to *in vivo* systems in a controlled manner to avoid unintended side effects.

7.5.4.1 pH-Responsive Nanoparticles

The use of pH as a trigger stems from the range of distinct pH values that occur within the body: blood has a pH of 7.4,[127] tumor environments range from pH 6.5-7,[450] the gastrointestinal tract fluctuates from 5.7-7.4,[123] and lysosomes have a pH ~5.[461] These characteristic pHs have been exploited to design activatable nanoparticles in several examples over recent years. As introduced in section 7.4.1.1, PEGylation of nanoparticles often confers low-biofouling properties to nanoparticles desirable for circulation, however, the "PEG dilemma" arises in that the same properties that help biotransport also render the constructs less susceptible to cell internalization once localized.[458] Toward this problem, Lim *et al.* employed mesoporous silica nanoparticles conjugated to the chemotherapy drug doxorubicin via a pH-sensitive hydrazine linker.[462] These nanoparticles were encapsulated with a polyaspartamide-PEG-biotin coating to inhibit burst drug release, increase hydrophilicity, and increase cell penetration, respectively. Once these

nanoparticles were endocytosed by MCF-7 breast cancer cells, the acidic lysosome environment promoted cleavage of the hydrazine linker and released doxorubicin, resulting in decreased cell viability than free doxorubicin. Likewise, Wang *et al.* designed polymeric nanoparticles to shed their protective PEG coating, needed for stable transit, upon exposure to the acidic tumoral microenvironment, exposing a targeting iRGD peptide to facilitate tumor penetration and cellular uptake of the doxorubicin prodrug.[450]

In addition to dePEGylation, other modes of pH activation have been leveraged in recent years. Li *et al.* developed a peptide-assembling nanoparticle system loaded with immune checkpoint inhibitors to both effectively target breast cancer cells and release the cargo once internalized.[463] This result was achieved by designing a peptide polymer with cholesterol, a histidine domain for endosomal escape, and a targeting peptide sequence. Once the drug-loaded nanoparticle was endocytosed, the drop in pH led to protonation of the histidine domain, which facilitated endosomal escape and resulted in successful *in vivo* drug release. Naidu *et al.* showed different release kinetics of ion channel antagonists from transferrin-functionalized polymeric nanoparticles in various pH environments, finding faster drug release at lower pH.[110] This result suggests that pH-responsive systems can be beneficial for treatment of neurotrauma by maintaining drug cargo within the nanoparticles until they enter the acidic (pH ~5) endosomal environment of damaged central nervous system cells. Overall, these nanoparticle-drug systems benefit from pH activation by controlling drug release to occur at the predetermined location.

7.5.4.2 Light-Activated Nanoparticles

Light-activation has also been implemented to enhance the efficacy of nanoparticle systems because external light triggers offer greater spatiotemporal control of activation compared to other methods.[464] Zhou *et al.* demonstrated the utility of near-infrared-(NIR)-triggered dePEGylation of polymeric nanoparticles to both decrease the nanoparticle size, aiding tumor penetration, and expose RGD peptides, for enhanced tumor uptake.[433] Kong *et al.* analogously used UV light-triggered dePEGylation of liposomal nanoparticles functionalized with cancer-targeting peptide E.[98] Their findings showed that the PEGylated nanoparticles remained freely circulating within the zebrafish xenograft cancer cell model until triggered dePEGylation caused accumulation and uptake by cancer cells due to the targeting peptide. Further, Feng and co-workers used NIR irradiation to produce reactive oxygen species (ROS) that cleaved a thioketal bond between a cancer prodrug and a PEG moiety adsorbed onto a self-assembled nanoparticle composed of a photosensitizer and an immunoinhibitory compound.[465]

Taking advantage of a protein corona stealth effect rather than that of PEG, Yeo *et al.* evaluated the use of gold nanorods coated with mouse serum proteins and the photosensitizer molecule Chlorin e6 to accumulate in and subsequently eliminate tumors in mice.[136] The serum protein corona effectively shielded the nanoparticles from immune system clearance and increased their bioavailability. Once accumulated at the tumor site, visible-light laser irradiation induced the production of ROS by Chlorin e6 which, when combined with the temperature increase of the nanorods themselves, led to complete tumor regression within 19 days and no significant regrowth after 31 days. Also utilizing the nanoparticle-adsorbed protein corona, Fukuda *et al.* demonstrated the potential of single-walled carbon nanotubes suspended in apolipoprotein A-I to produce ROS under NIR illumination.[141] These ROS led to both lower HeLa cancer cell viability and disintegration of the neurotoxic peptide aggregate amyloid beta, which is implicated in

neurodegenerative diseases such as Alzheimer's. As light can be easily controlled both spatially and temporally, these light-activated systems show promise for effective *in vivo* applications.

7.5.4.3 Enzyme-Activated Nanoparticles

Enzymatic activation has been demonstrated to be an effective method to trigger nanoparticle function, as nanoparticles encounter various intracellular and extracellular enzymes including proteases, phospholipases, and glycosidases. Rodriguez-Quijada *et al.* observed enzymatic degradation of the protein corona formed on doxorubicin-loaded gold nanoparticles by matrix metalloproteinases, in turn affecting the doxorubicin release rate into pancreatic cancer cells.[35] Various corona proteins were degraded at different rates, leading to varying levels of cytotoxicity depending on the identity of the *in vitro* pre-formed corona proteins. Matrix metalloproteinases were also used by Gao *et al.* to dePEGylate their prodrug nanoparticles once accumulated at the target tumor site.[466] Another enzyme of interest is cathepsin B, used frequently in the realm of antibody-drug conjugates. Cathepsin B has the potential to augment nanoparticle efficacy through its abundance in lysosomes and consistent activity. Han *et al.* used a dual enzyme strategy to increase the efficacy of their drug-loaded quantum dots. First, they used the aforementioned matrix metalloproteinases to dePEGylate their quantum dots and expose a cyclic RGD targeting peptide, simultaneously increasing cellular targeting and uptake. Once within the lysosome, native cathepsin B cleaved the cancer drug gemcitabine from the quantum dot surface, thereby increasing drug release into the cell and thus nanoparticle efficacy.[451] There remains further work to be done in this area to utilize the array of endogenous enzymes found within biological systems of interest for enzyme-activation of nanoparticles.

7.5.4.4 Redox-Responsive Nanoparticles

Redox chemistry offers another trigger to activate nanoparticle systems, as the nanoparticle travels between oxidative and reductive environments found in the extracellular and intracellular spaces, respectively. For example, the second component of the cleavable system used by Feng *et al.* takes advantage of redox chemistry with a photosensitizer and an immunoinhibitory compound linked by a reducible disulfide bond. Once within the cellular environment, the abundant antioxidant, glutathione, reduces the disulfide bond and causes release of the nanoparticle components, proving effective for tumor ablation during *in vivo* mouse studies.[465] Nanoparticle dePEGylation has also been accomplished by a reducible disulfide attachment that is cleaved to release drug cargo once internalized.[467,468] Similarly, Yu *et al.* demonstrated the utility of ceria nanoparticles encapsulated by a poly(lactic-co-glycolic acid) (PLGA)-PEG coating linked by a thioketal bond and loaded with the kidney injury drug, atorvastatin.[469] The PEG coating was removed by thioketal bond cleavage once nanoparticles accumulated at the kidney injury site where ROS production was elevated, resulting in the release of atorvastatin for treatment. Interestingly, the ceria nanoparticles were also functionalized with triphenylphosphine to target the injured cell's mitochondria and scavenge the ROS produced by the injured mitochondria. The use of redox-responsive activation in nanoparticle systems gives rise to multifunctional modalities that would be more efficacious when used synergistically.

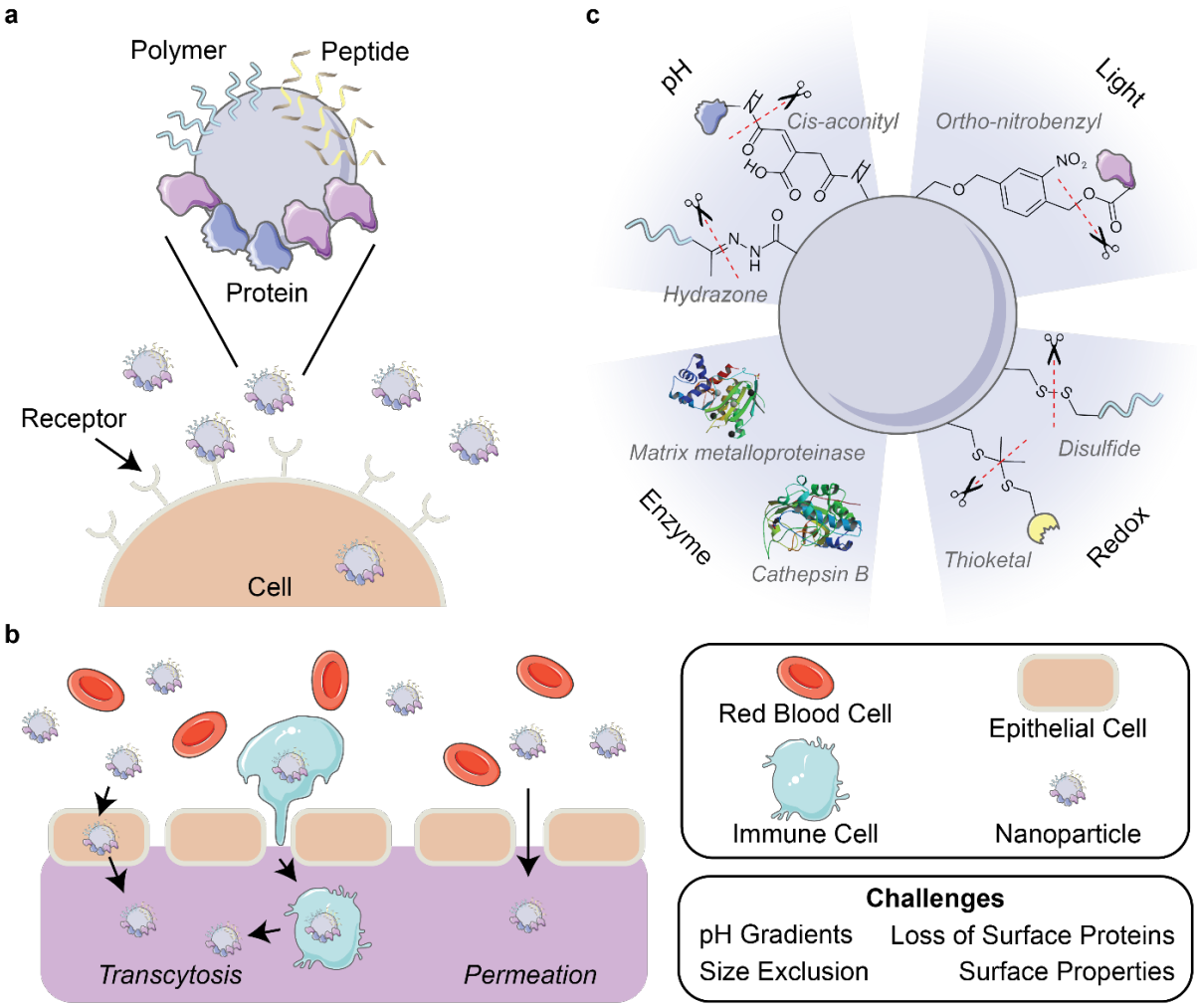

Figure 7-2. Corona-mediated targeting and activation. (a) Nanoparticles can be targeted to cell receptors through the surface decoration of ligands such as polymers, peptides, and proteins. (b) Delivery of nanoparticles through biological barriers is difficult due to environmental factors such as pH gradients and physical forces that destabilizes the outer protein corona. Nanoparticles can pass through barriers by permeation or the targeting of nanoparticles to cells for transcytosis. (c) Strategies for the activation of nanoparticles include the use of pH, light, enzymes, and redox reactions. Protein images are from the RCSB PDB (rcsb.org) of PDB ID 5UE3 and 3AI8.[470,471]

7.6 Biocompatibility

The presence of foreign objects such as bacteria, viruses, and nanoparticles within the body can induce a response by the immune system. Depending on the nanoparticle's properties, this immune response can both render the nanoparticles ineffective and also lead to inflammation and systemic complications.[472] Although many advancements have been made in preventing this response as detailed in section 7.4, it is still important to understand the scope of possible interactions between nanoparticles and the immune system to ensure nanoparticle efficacy and inform rational design of the protein corona (Figure 7-3).

The human immune system is composed of two branches: the innate immune system and the adaptive immune system. The innate immune system is composed of the complement system and the mononuclear phagocyte system (MPS) working in tandem to identify and eliminate pathogens. This process is activated almost immediately after an infection is detected. The adaptive immune system uses lymphocytes known as T cells and B cells in combination with antibodies to eliminate foreign and native infected cells. In contrast to the innate immune system, the adaptive response requires about one-week post-infection to fully develop. Due to this discrepancy in time scale, the innate immune response is the body's first line of defense against perceived foreign invaders and is canonically observed in assaying nanoparticle biocompatibility. Improper nanoparticle design that neglects the innate immune system could lead to untimely clearance, unintended immune response, and complications including systemic toxicity.[473] Conversely, over-use of nanoparticle coatings such as PEG can generate anti-PEG antibodies by the adaptive immune system as discussed in section 7.4.1.1. It is thus of great importance to consider the potential mounted immune responses, particularly the innate response, when designing nanoparticle systems for use *in vivo*.

7.6.1 Immune System Activation and Suppression

The involvement of nanoparticles with the innate immune system can be categorized into immune activation and suppression. Activation is better studied than suppression due to it being easier to elicit with nanoparticles, although both have been demonstrated in recent years.[61,474] Immune activation can be further divided into unintended activation via the complement system and intended activation through elevated cytokine levels and leukocyte activation. Immunosuppression aims to mitigate the immune response by depleting inflammatory cytokine levels and limiting leukocyte migration, which can result in longer nanoparticle circulation time from lower MPS clearance and reduced inflammation in hypersensitive systems.[475,476]

7.6.1.1 Complement Activation

It is generally accepted that nanoparticles possessing different physicochemical properties will activate different innate immune response pathways.[83,472] As part of the innate immune response, the complement system is composed of a series of soluble proteins produced by hepatocytes in the liver that amplify or "complement" the function of antibodies in the adaptive immune system. Complement proteins often contribute to the formation of the *in vivo* protein corona when a nanoparticle enters the body, which places the complement system at the forefront of the immune response to nanoparticles.[81] The complement system can be activated by three different pathways: classical, lectin, and alternative. The classical pathway is activated by the binding of antibodies to antigens present on the surface of pathogens. The lectin pathway is initiated by the binding of mannan-binding lectin with mannose and fucose residues found in the cell wall of bacteria. The alternative pathway is activated by the binding of complement protein C3 to the pathogen. All three pathways converge at the point where this C3 protein is cleaved into anaphylatoxins C3a and C3b, which leads the complement cascade to ultimately recruit phagocytes and lymphocytes to the site of infection. Nanoparticles typically activate the classical and alternative pathways, as their surfaces provide ample area for antibodies and complement proteins to bind and trigger the respective cascades.[477,478]

Nanoparticle surface properties are key to eliciting immune activation. For instance, Coty *et al.* demonstrated that dextran-coated poly(isobutylcyanoacrylate) nanoparticles activate different complement pathways depending on the architecture of the dextran coating itself.[472] They concluded that the density and length of the dextran coating modulated the ability of different complement proteins such as C3 and mannose-binding lectin to bind to the nanoparticle surface, in turn affecting which pathway was activated. Fülöp *et al.* explored the complement activation effect of various coating materials on superparamagnetic iron oxide nanoparticles (SPIONs), similarly determining that dextran coating leads to complement activation, in this case by the alternative pathway.[473] They incubated SPIONs noncovalently adsorbed to starch, carboxymethyldextran, chitosan, phosphatidylcholine, citric acid, and dextran coatings with human serum samples *in vitro* and measured the levels of the complement pathway-specific marker SC5b-9. Phosphatidylcholine and chitosan showed no reaction, starch and carboxymethyldextran showed minor effects, and dextran caused massive complement activation. Escamilla-Rivera *et al.* conducted a similar study, comparing complement activation of iron oxide nanoparticles with bare surfaces, with a polyvinylpyrrolidone (PVP) coating, and with a PEG coating.[83] Interestingly, the PEG coating resulted in doubled complement protein adsorption levels *in vitro* and higher levels of inflammatory cytokines *in vivo*, while the bare and PVP-coated nanoparticles showed no significant increase in either case. Quach and Kah studied the effect of gold nanoparticle size, shape, and polyelectrolyte ligand on complement activation.[81] By detecting the endpoint complement marker SC5b-9 concentration, they determined that polyethyleneimine ligand induced the most complement activation and that there is a negative correlation between nanoparticle surface hydrophilicity and complement activation. Based on the literature, there is little predictability with which nanoparticle materials or coatings will elicit an immune response, necessitating that each be tested individually.[479] Due to the importance of the complement pathway in understanding the biocompatibility of nanoparticle systems, more studies are required to fully understand the mechanisms and dependencies of this cascade within the context of nanoparticle activation.

7.6.1.2 Immunostimulation

Rather than avoiding immune activation, nanoparticles can also be applied to stimulate an immune response. Immunostimulation is beneficial in the context of harnessing the immune system to clear infected cells, including cancer cells, and combating immunodeficiency.[474] Since the protein corona influences the interactions between nanoparticles and cells of the immune system, it plays a crucial role in mediating this stimulatory response. For example, Dai *et al.* explored the effect of different *in vitro* protein coronas formed on poly(methylacrylic acid) (PMA) nanoparticles on cytokine production in THP-1 monocytes.[480] In particular, they found that serum-incubated PMA nanoparticles showed increased levels of inflammatory cytokines including interleukin-8 and interleukin-1ß, demonstrating the importance of the protein corona in immunostimulation responses to nanoparticle introduction.

Several nanoparticle systems in recent years have been designed to purposefully leverage the protein corona to activate the immune system. Mo *et al.* exploited the serum protein corona formed on black phosphorus nanosheets to polarize M0 macrophages into M1 macrophages, stimulating the immune system to eliminate cancer cells.[474] Similarly, Kouser *et al.* investigated the inflammatory response of functionalized carbon nanotubes with adsorbed human properdin, a protein that upregulates the alternative complement pathway.[150] The authors adsorbed either the

full properdin protein or only the binding domain, thrombospondin type I repeat 4 and 5 (TSR4+5), to cellulose-coated and oxidized carbon nanotubes. Upon *in vitro* incubation in blood serum, TSR4+5-coated nanotubes inhibited complement activation due to the lack of available surface area for native properdin to adsorb, while properdin-nanotubes maintained complement activation. Furthermore, pre-adsorbed properdin enhanced the uptake of carbon nanotubes by THP-1 macrophages, stimulating the production of pro-inflammatory cytokines, while pre-adsorbed TSR4+5 was ineffective in producing this immunostimulatory response. Taken together, these various studies demonstrate the potential design of nanoparticles to either stimulate immune cell activation directly or rationally engage immunostimulation through the complement system.

Employing nanoparticles that produce ROS can induce an oxidative stress response in cells as another form of immunostimulation. These ROS include hydrogen peroxide, superoxide anion radicals, singlet oxygen, and free hydroxyl radicals, which lead to a variety of oxidative stress responses, including inflammation, apoptosis, DNA damage, and lipid peroxidation.[481] While nanoparticles themselves can produce an oxidative stress response, Jayaram *et al.* demonstrated that the *in vitro* protein corona also plays a role in the oxidative stress experienced by cells.[482] In this study, titanium dioxide nanoparticles were found to produce ROS that caused oxidation of corona proteins, including complement C3, serum albumin, and plasminogen. The oxidized corona proteins subsequently caused downregulation of peroxiredoxin expression, enzymes responsible for clearing peroxide species, thus resulting in an oxidative stress response to the cell. They also concluded that an increase in nanoparticle surface defects exacerbates the oxidative stress effect. Due to the potential of the protein corona to produce an oxidative stress response in cells, it is important to further study nanoparticles in this light in addition to other immunological effects.

7.6.1.3 Immunosuppression

Nanoparticles can also function to limit activation of the immune system by suppressing cytokine levels to lower MPS activity and reduce inflammatory effects.[483] Cai *et al.* connected the nanoparticle protein corona to a decrease in cytokine production by macrophages, showing a decrease in level of proinflammatory cytokine, interleukin-6 (IL-6), produced due to the presence of the protein corona.[61] Similarly, Dai *et al.* discovered that their PMA nanoparticles had immunosuppressive effects in THP-1 monocytes depending on the source of their *in vitro* protein corona.[480] They found that PMA nanoparticles incubated with HeLa cell-conditioned media reduced the production of IL-6, IL-1b, IL-8, and TNF-a cytokines. In addition to reducing cytokine production, nanoparticles can also suppress an overactive immune system by targeting and eliminating specific immune cell populations. In certain autoimmune diseases, B cells can become overactive, leading to the destruction of healthy cells. Luk *et al.* demonstrated the possibility of targeting these hypersensitive B cells by coating polymeric nanoparticles with red blood cell membranes containing B cell receptor-targeted antigens.[476] By purposefully designing the protein corona of this nanoparticle system, the authors were able to successfully target and visualize autoimmune B cells, opening the door to the development of targeted immunosuppressive treatments. Overall, these findings demonstrate the ability of the protein corona to induce an immunosuppressive response *in vivo*.

7.6.2 Cytotoxicity Assays

The assessment of these various immune activation and suppression functionalities, and more broadly the extent to which a nanoparticle is deemed biocompatible, relies on cytotoxicity assays. These assay outputs depend not only on the nanoparticle properties and interactions, but also on the specific assay used in the study. Common techniques for toxicity assessment include nanoparticle incubation with representative cell systems, such as HeLa cancer cells and THP-1 monocytes to assess cell viability,[99] endpoint cytokine level measurements to determine inflammation,[81,136] and live mice and rat models to compare *in vitro* analysis with *in vivo* for characterization, literature increasingly suggests that the adaptation of standardized *in vitro* toxicity assays to assessing nanoparticle outcomes must be done with care. For example, common cell viability assays include the MTT,[462,469,482] LDH,[484,485] Trypan Blue,[483] and CCK-8 assays.[61,141] However, nanoparticles have been shown to interfere with such assays by either adsorbing the reagent or readout molecules, or in the case of colorimetric assays, absorbing or contributing to the output signal being quantified.[484–486] This leads to false cytotoxicity or efficacy predictions because the nanoparticle presence alone vastly modulates the assay output, often confirmed by seeing negligible *in vitro* toxicity yet drastic changes in cell morphology. As such, it is imperative to include the necessary controls for these assays and run multiple, orthogonal assays to avoid reporting misleading results.

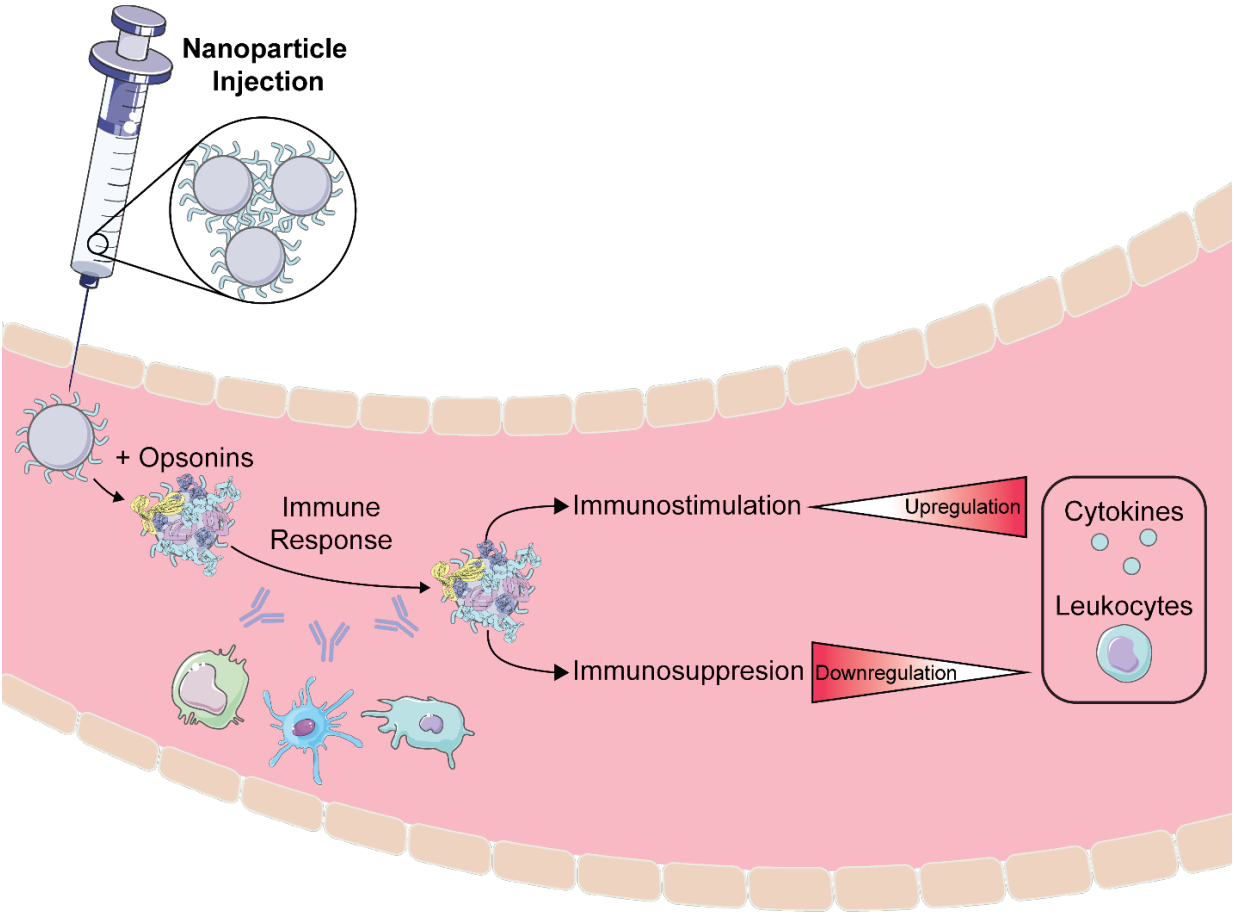

Figure 7-3. Biocompatibility considerations for nanoparticle administration. Proteins known as opsonins often adsorb to nanoparticles *in vivo* and elicit an immune response. This response involves the innate immune system (complement and mononuclear phagocyte systems) and/or adaptive immune system (lymphocytes and antibodies). Protein corona design can be employed to guide immunostimulation (increase in cytokine and leukocyte levels), whereby the immune system is activated intentionally toward eliminating harmful cells or combatting immunodeficiency. Conversely, the nanoparticle-corona construct can be manipulated to promote immunosuppression (decrease in cytokine and leukocyte levels), and nanoparticle clearance or an inflammatory response are avoided.

7.7 Conclusions

Nanoparticles offer a promising platform to study and manipulate biological systems. Yet, formation of the protein corona on nanoparticle surfaces upon introduction into biological environments remains a considerable barrier between *in vitro* design and *in vivo* application. Beyond characterizing the protein corona formed on varying nanomaterials, recent developments have sought to elegantly exploit and rationally design the protein corona to achieve improved nanomaterial functionality.

Corona-mediated nanoparticle functionalities include stealth, targeting, and activation. Stealth continues to be mechanistically explored, as more studies demonstrate the difficulty in fully eradicating protein corona formation. Instead, achieving stealth seems to rely on adsorption of specific proteins to mask the foreign nanoparticle presence. While common strategies rely on hydrophilic, zwitterionic, or carbohydrate shells, new work recognizes the promise of protein or biomimetic coatings toward attaining stealth. It is increasingly recognized that controlling, instead of eliminating, protein adsorption will further benefit stealth aims in nanomedicine. After evading recognition during circulation, targeting enables specific localization. Nanoparticle targeting stands to benefit from the remarkable molecular specificity of protein interactions by taking advantage of endogenous protein interactions with their target ligands. Finally, activatable properties have been applied to induce or guide specific nanoparticle function within the targeted area. Activation of nanoparticle function typically relies on biological or externally applied triggers, though future work is required to use such cleavable strategies synergistically with the protein corona. Combining such concepts, recent work has demonstrated modular nanoparticle constructs that are capable of tumor targeting (with cleavable reporters to indicate success) and gene delivery.[487] Other exciting work has moved to multiplexed testing of the targeting and function of many nanoparticle chemistries simultaneously via DNA-barcoding.[488] Finally, biocompatibility of such nanoparticle-corona constructs has inspired uses in both immune stimulation (both intended and unintended) and immune suppression, where the assays to assess biocompatibility stand to be refined. In sum, design of the protein corona on nanoparticles presents a functional handle to tune construct properties and attain improved outcomes toward *in vivo* stealth, targeting, and function.

8 Rapid SARS-CoV-2 Spike Protein Detection by Carbon Nanotube-Based Near-Infrared Nanosensors

8.1 Chapter Abstract

To effectively track and eliminate COVID-19, it is critical to develop tools for rapid and accessible diagnosis of actively infected individuals. Here, we introduce a single-walled carbon nanotube (SWCNT)-based optical sensing approach toward these ends. We construct a nanosensor based on SWCNTs noncovalently functionalized with ACE2, a host protein with high binding affinity for the SARS-CoV-2 spike protein. Presence of the SARS-CoV-2 spike protein elicits a robust, two-fold nanosensor fluorescence increase within 90 min of spike protein exposure. We characterize the nanosensor stability and sensing mechanism, and passivate the nanosensor to preserve sensing response in saliva and viral transport medium. We further demonstrate that these ACE2-SWCNT nanosensors retain sensing capacity in a surface-immobilized format, exhibiting a 73% fluorescence turn-on response within 5 s of exposure to 35 mg/L SARS-CoV-2 virus-like particles. Our data demonstrate that ACE2-SWCNT nanosensors can be developed into an optical tool for rapid SARS-CoV-2 detection.[***]

8.2 Introduction

The World Health Organization deemed COVID-19 a global pandemic on March 11, 2020. As of February 14, 2021, SARS-CoV-2 has infected over 108 million people and caused over 2.3 million deaths worldwide.[489] It is estimated that over 70% of infected individuals under the age of 60 are asymptomatic, yet can still transmit the virus to others.[490] Early estimates placed the basic reproductive number (R0) at 2.2, which represents the average number of people an infected person will spread the disease to.[491] Taken together, these findings underscore the need for advancements in testing and containment efforts to end the pandemic.

Current SARS-CoV-2 testing strategies can be grouped into two categories: molecular tests and serological tests. Molecular tests remain the status quo for diagnosing active CoV-2 infections by detecting CoV-2 RNA in patient samples, including sputum and nasal fluid. Molecular tests primarily use real-time reverse transcription polymerase chain reaction (RT-PCR), and are thus expensive ($5-10 per test), time-consuming (2-3 hours), and require laboratory processing.[492–495] Yet, RT-PCR tests possess high sensitivity in identifying viral nucleic material, with the limit of detection (LOD) reported between 1-10 viral RNA copies necessary to produce a positive result.[492] Serological tests detect the presence of IgG and IgM antibodies in patient blood serum and provide important surveillance data of past viral infections, yet do not identify active cases. As such,

[***] Published as Pinals, R. L.; Ledesma, F.; Yang, D.; Navarro, N.; Jeong, S.; Pak, J. E.; Kuo, L.; Chuang, Y.-C.; Cheng, Y.-W.; Sun, H.-Y.; Landry, M. P. Rapid SARS-CoV-2 Spike Protein Detection by Carbon Nanotube-Based Near-Infrared Nanosensors. *Nano Lett.* **2021**, *21* (5), 2272–2280. https://doi.org/10.1021/acs.nanolett.1c00118.

detection of viral RNA by molecular tests is to-date the preferred testing mode to diagnose active CoV-2 cases. However, the complexity of the process necessitates the use of expensive equipment and trained personnel, limiting the testing capability in rural and lower income regions.[496] Altogether, these factors amount to a large enough backlog in RT-PCR testing capabilities such that the United States is at 52% of its daily testing target to mitigate the spread of the virus as of November 1, 2020.[497] Several non-PCR-based methods of viral RNA detection have been developed recently, implementing techniques such as loop-mediated isothermal amplification (LAMP),[498] localized surface plasmon resonance (LSPR),[499] and CRISPR machinery[500] to avoid the expensive equipment required for the heating and cooling cycles of PCR. However, these techniques are not as sensitive as PCR and still require between 30 minutes to 1 hour of processing time per sample.[501] Antigen testing has emerged with great potential for rapid diagnostics, possessing the key strength that active virus is detected. This contrasts with RT-PCR tests, which are merely detecting the presence of viral RNA and can consequently lead to cases of RT-PCR positivity in the absence of any viable virus.[502] Such rapid tests are faster and cheaper, yet possess lower sensitivity.[502]

There has been a strong drive to find other viral testing targets and methodologies for simpler and faster diagnostics due to extended processing time and equipment restrictions associated with viral RNA detection. SARS-CoV-2 is a coronavirus, a family of viruses termed as such due to the halo or "corona" of proteins surrounding the virus in electron microscopy images. These outwardly protruding spike (S) proteins bind to the angiotensin-converting enzyme 2 (ACE2) receptor on the surface of human respiratory endothelial cells, facilitating viral entry.[503,504] The viral S protein is also the primary antigen that human monoclonal antibodies bind to prevent host cell entry and mark the virus for clearance.[505] With approximately 100 S protein trimers per SARS-CoV-2 virion, the S protein has become a prime target for live virus detection.[506] For example, Seo et al. developed a field-effect transistor-based sensor by functionalizing graphene sheets with SARS-CoV-2 S protein antibodies to detect SARS-CoV-2 at a LOD of 242 copies/mL in crude, nasopharyngeal swab clinical samples.[507] Several promising nanotechnology-based sensors for SARS-CoV-2 detection have also emerged for both nucleic acid- and antigen-based detection and diagnosis of COVID-19, including platforms based on gold nanoparticles and quantum dots.[499,508–511] Such technologies will be crucial in working toward sensitive tests that do not rely on specialized equipment for signal readout and controlled laboratory environments for sample processing.[501]

Single-walled carbon nanotubes (SWCNTs) have shown much utility for biological analyte sensing.[27,32,40] SWCNTs are intrinsically near-infrared (nIR) fluorescent and can be functionalized with various sensing moieties to develop stable biological sensors with rapid fluorescence-change readouts. Unlike conventional fluorophores, SWCNTs do not photobleach, giving rise to their potential long-term use.[27] Importantly, the SWCNT near-infrared emission is minimally absorbed and scattered by biomolecules,[27] providing a readout that can penetrate optically occluded patient samples, thus eliminating the need for sample purification that limits the throughput of other viral testing modes. Furthermore, SWCNTs offer facile incorporation into portable form factors such as immobilization in paper or hydrogels[512,513] with detection of the nIR SWCNT signal by a Raspberry Pi and charge-coupled device (CCD) camera system, of similar form factor to a smartphone.[514]

Herein we demonstrate the development and characterization of a nanosensor to detect SARS-CoV-2 by exploiting the innate ability of host proteins to bind virion components, coupled to a SWCNT substrate that provides a fluorescence readout of the protein recognition events. This concept of a hybrid nano-bio sensor harnesses the natural recognition abilities of proteins acting as sensing moieties, together with SWCNTs as signal transducers, to enable targeted biological sensing. Considering the difficulties of preserving protein activity once tethered to nanomaterials, few previous protein-SWCNT conjugate sensors have been developed, and most have used enzymes to detect their small molecule substrates[30,281,322] or protein A to detect antibodies.[282,515] Here, we introduce a protein-SWCNT construct that uses human host cell membrane protein ACE2 to bind to the CoV-2 spike protein receptor-binding domain (S RBD) protruding from the virion surface, enabling protein detection in a rapid, label-free manner. We constructed nanosensors by immobilizing ACE2 proteins on the surface of SWCNTs, where this noncovalent modification strategy is advantageous in retaining the intact SWCNT surface lattice that is necessary for fluorescence.[30,38] Upon S protein binding to ACE2-functionalized SWCNTs, the change in exciton dynamics of the SWCNTs leads to a modulation in the nIR SWCNT fluorescence. We demonstrate that ACE2-functionalized SWCNT nanosensors can achieve a LOD of 12.6 nM S RBD, can be passivated for detection of S protein in saliva and viral transport medium, and can be imaged for rapid detection of S protein or virus-like CoV-2 virions within seconds.

8.3 Results and Discussion

8.3.1 Nanosensor Platform Generation and Characterization

To generate nanosensors, we first solubilized SWCNTs by probe-tip sonication with single-stranded DNA (ssDNA), $(GT)_6$ (see section 8.5.1). Direct probe-tip sonication of ACE2 with pristine SWCNTs did not lead to a stable suspension and further raises the likelihood for disruption of the native ACE2 protein conformation, and hence loss of sensing ability for S RBD. The ssDNA sequence of $(GT)_6$ was chosen based on high SWCNT suspension yield. The short ssDNA sequence length (12 nucleotides) was informed by previous work demonstrating that shorter ssDNA desorbs faster, and to a greater extent, from SWCNTs in the presence of proteins.[82,118] $(GT)_6$-SWCNTs (2.5 mg/L final concentration) were incubated with ACE2 sensing protein (6.25 mg/L final concentration) in phosphate-buffered saline (PBS) solution to noncovalently passivate the SWCNT surface with protein, schematically represented in Figure 8-1a.[82] This ratio of ACE2 sensing protein to SWCNT substrate was calculated to be approximately above the close-packing threshold to minimize protein surface-denaturation and colloidal aggregation, then this calculated value was experimentally optimized (see details in section 8.6.1 and Figure 8-5, Figure 8-6). ACE2 adsorption to $(GT)_6$-SWCNTs manifested as a nearly instantaneous quenching of the SWCNT fluorescence, leveling off to -37% integrated-fluorescence fold change ($\Delta F/F_0$) within 5 min (Figure 8-1b). This fluorescence quenching exhibited excellent time stability over the course of 2 h (Figure 8-1c). Comparing the time-dependent quenching behavior of ACE2 with $(GT)_6$- vs. $(GT)_{15}$-SWCNTs affirmed the faster "leaving group" behavior of the shorter ssDNA, $(GT)_6$, stabilizing within 10 minutes, as compared to $(GT)_{15}$, requiring at least 60 minutes (Figure 8-7). Noncovalent ACE2 adsorption, as opposed to covalent modification, was confirmed by retention of SWCNT absorbance peaks representing various SWCNT chiralities' electronic transitions (Figure 8-8). These results of decreased nIR SWCNT fluorescence emission while the absorption peaks remain unchanged demonstrate that ACE2 adsorption on SWCNTs leads to exciton

quenching, involving a decreased exciton recombination frequency and/or increased nonradiative decay pathways.[516]

The affinity of ACE2 for the ssDNA-wrapped SWCNT surface was assessed by the corona exchange assay.[118] For this assay, Cy5-labeled $(GT)_6$ ssDNA was tracked as it desorbed from the SWCNT surface and thus de-quenched in the presence of ACE2. ACE2 displayed high affinity for the SWCNT surface, as ACE2 adsorption led to an 80.5% increase in Cy5 fluorescence, denoting free ssDNA, 1 h post addition of ACE2 (Figure 8-1d) in an ACE2 concentration-dependent manner (Figure 8-9). We further assessed the stability of the ACE2-SWCNT interface with a surfactant displacement assay, which confirmed strong and stable adsorption of ACE2 to the SWCNT (Figure 8-10).[42,198] Taken together, these results suggest that ACE2 adsorbs to the SWCNT surface, displaces ssDNA originally on the SWCNT surface, and forms a stable ACE2-SWCNT conjugate that can be tested for its utility as a CoV-2 nanosensor.

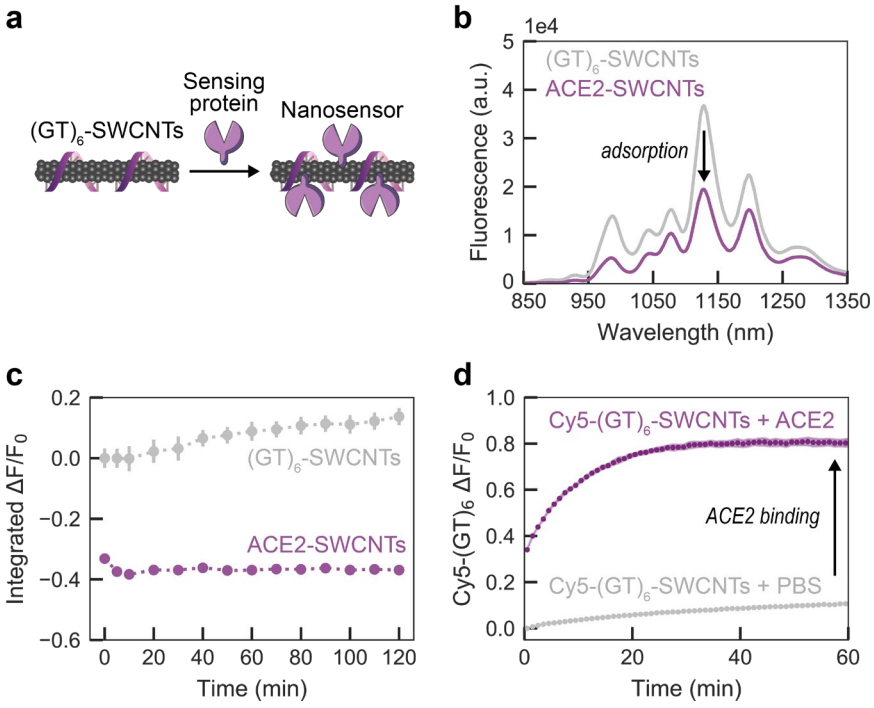

Figure 8-1. Adsorption of ACE2 sensing proteins to $(GT)_6$-SWCNTs. (a) Schematic depiction of ACE2-SWCNT nanosensor formation, with sensing protein ACE2 adsorbing to $(GT)_6$-SWCNTs. (b) ACE2-SWCNT complexation was observed as quenching of the intrinsic SWCNT near-infrared fluorescence following 1 h incubation of 6.25 mg/L ACE2 with 2.5 mg/L $(GT)_6$-SWCNTs (final concentrations). (c) ACE2-SWCNT construct demonstrated time-stable quenched fluorescence. All fluorescence measurements were obtained with 721 nm laser excitation. Gray bars represent standard error between experimental replicates (N = 3). (d) Adsorption of ACE2 on the SWCNT surface led to $(GT)_6$ desorption, tracked by Cy5-labeled ssDNA following addition of 6.25 mg/L ACE2 with 2.5 mg/L Cy5-$(GT)_6$-SWCNTs (final concentrations). The increase in Cy5-$(GT)_6$ fluorescence from the initial quenched state on the SWCNT serves as a proxy for ACE2 adsorption. Shaded error bars represent standard error between experimental replicates (N = 3).

8.3.2 Nanosensor Response to SARS-CoV-2 Spike Protein

We analyzed the fluorescence response of ACE2-SWCNT nanosensors to the SARS-CoV-2 S RBD analyte, schematically represented in Figure 8-2a. Recognition of the CoV-2 S RBD by the nanosensor elicited a strong turn-on fluorescence response upon addition of 10 mg/L final concentration of CoV-2 S RBD to the nanosensor (formed by adsorbing 6.25 mg/L ACE2 to 2.5 mg/L $(GT)_6$-SWCNTs) (Figure 8-2b). The normalized change in fluorescence of the 1130 nm SWCNT emission peak instantaneously increased to $\Delta F/F_0 = 21.1\%$, reaching $\Delta F/F_0 = 99.6\%$ after 90 min (Figure 8-2c). This fluorescence modulation was verified to arise from the S RBD analyte itself rather than any impurities remaining post-gel filtration chromatography (see section 8.5.2) by testing the filtrate of S RBD solution below a 3 kDa molecular weight cutoff centrifugal filter (Figure 8-11), which showed a negligible change in fluorescence above that of adding PBS. The concentration-dependent nanosensor response to S RBD (Figure 8-2d) gives rise to a 12.6 nM nanosensor LOD (see calculation in section 8.6.1). Further, approximate values for the nanosensor kinetic parameters were determined by fitting the 90-minute nanosensor response to this analyte concentration series to the Hill Equation (cooperative binding model).[40] Here, the integrated-fluorescence fold change of the nanosensor was correlated to the concentration of the S RBD analyte as shown in Figure 8-2e, resulting in an equilibrium dissociation constant (K_d) of 4.22 μM^{-1}. These fit values represent conservative estimates for the nanosensor kinetic parameters by using the full integrated-fluorescence fold change. Moreover, this model implicates the assumption that the bulk analyte concentration remains constant (i.e., only a small fraction of total injected analyte is bound by the nanosensor). Importantly, the response of ACE2-SWCNT nanosensors for S RBD was confirmed by showing insignificant $(GT)_6$ DNA desorption that does not scale with injected S RBD analyte concentration (Figure 8-12a). Furthermore, addition of S RBD to $(GT)_6$-SWCNTs alone (without ACE2 sensing moiety) resulted in aggregation, as the ssDNA displaced from the SWCNT surface continues to increase linearly over 6 h (Figure 8-12b).

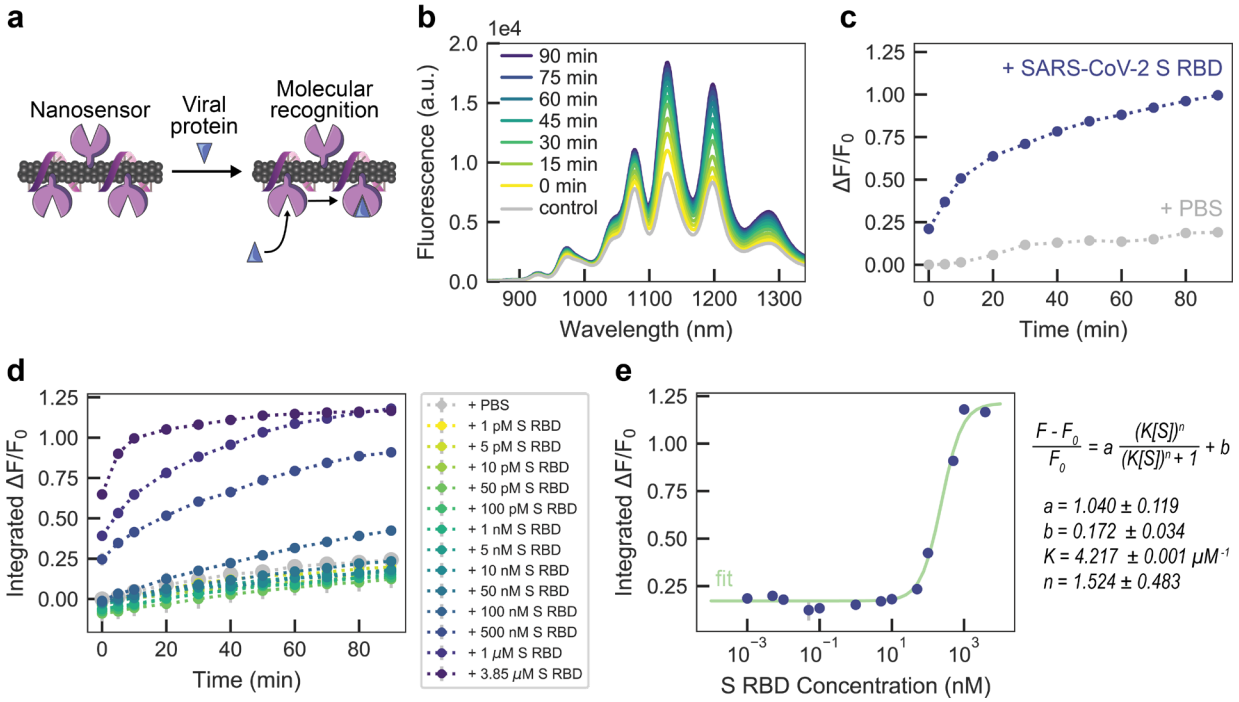

Figure 8-2. ACE2-SWCNT nanosensor response to SARS-CoV-2 spike protein receptor-binding domain (S RBD). (a) Schematic depiction of ACE2-SWCNT nanosensor interacting with viral protein S RBD. Addition of 10 mg/L S RBD (final concentration) to ACE2-SWCNTs (formed by 6.25 mg/L ACE2 and 2.5 mg/L $(GT)_6$-SWCNTs) yielded a strong turn-on fluorescence response, as shown by (b) the full fluorescence spectrum and (c) the normalized change in fluorescence ($\Delta F/F_0$) of the 1130 nm SWCNT emission peak as a function of time, over 90 min. (d) Varying S RBD concentrations were injected into ACE2-SWCNTs and the integrated-fluorescence fold change ($\Delta F/F_0$) was monitored over 90 min. (e) Integrated $\Delta F/F_0$ values at time = 90 min for varying S RBD concentrations were fit to a cooperative binding model to quantify nanosensor kinetic parameters. Fit parameters are listed with 95% confidence intervals evaluated using the t-distribution. All fluorescence measurements were obtained with 721 nm laser excitation. (c-e) Gray bars represent standard error between experimental replicates (N = 3).

Nanosensor colloidal stability was verified by demonstrating that the nanosensor response to S RBD persisted after centrifugation (16.1 krcf, 30 min; Figure 8-13a) and overnight incubation at ambient conditions (Figure 8-13b). Repeating the surfactant displacement experiment with the ACE2-SWCNT nanosensor in the presence of S RBD showed that the bound receptor-ligand state further stabilized the nanosensor surface to surfactant perturbations (Figure 8-10e-f). This latter result, together with the retained solution stability of the analyte-bound state, indicates ACE2 was not removed from the SWCNT surface upon S RBD binding. As such, we postulate that S RBD binding to ACE2 induces a conformational change pinning ACE2 to the SWCNT surface, thus simultaneously increasing SWCNT fluorescence emission via exciton de-quenching and stabilizing the SWCNT surface against surfactant interaction.

8.3.3 Nanosensor Analyte Selectivity and Bioenvironment Robustness

We next investigated the selectivity of ACE2-SWCNT nanosensors to a panel of viral spike-like proteins. This viral analyte panel was composed of the SARS-CoV-2 S RBD in addition to the SARS-CoV-1 S RBD, MERS S RBD, and FLU hemagglutinin subunit (HA1). Serum albumin (HSA) was also included as a protein abundant in bioenvironments and in viral transport medium (VTM; 2% Fetal Bovine Serum, 100 µg/mL Gentamicin, 0.5 µg/mL Amphotericin in a Hanks Balanced salt solution base). Viral proteins were normalized on a mass basis (10 mg/L final concentration) to account for varying molecular weights. SARS-CoV-2 S RBD elicited the largest nanosensor response of $\Delta F/F_0$ = 99.6% at the 1130 nm SWCNT emission peak after 90 min (Figure 8-3a), followed by SARS-CoV-1 S RBD ($\Delta F/F_0$ = 88.4%). This cross-reactivity is expected, as ACE2 is also the cell membrane protein that binds to CoV-1 S RBD, although at ~10 to 20-fold lower affinity.[517,518] MERS and FLU spike-like proteins naturally interact with different cell membrane receptors, accounting for this lower magnitude fluorescence response with our ACE2-SWCNT nanosensors.

Nanosensor compatibility in biofluids was assessed by testing the nanosensor response to CoV-2 S RBD in 1% relevant biological fluids, including viral transport medium (VTM), human saliva, human nasal fluid, and human sputum (treated with sputasol) (biofluid details in Table 8-1). Although the nanosensor response was maintained in PBS and VTM, the response was diminished in the other biofluids, with a $\Delta F/F_0$ = 3.2% in saliva, 7.8% in nasal fluid, and 6.3% in sputum (Figure 8-3b). The attenuation of nanosensor response seems to arise from biofluid protein adsorption to the nanosensor surface that raises the baseline fluorescence and obfuscates viral analyte interaction, whereby the nanosensor fluorescence in the biofluids alone is stable with an increased baseline fluorescence (Figure 8-13c).

To mitigate the unfavorable effects of biofouling that lead to this diminished nanosensor response, we pursued a passivation strategy involving phosphatidylethanolamine phospholipid with a 5000 Da PEG chain attached to the head group (PE-PEG), schematically represented in Figure 8-3c.[339] The PE-PEG passivated nanosensor response to 500 nM CoV-2 S RBD was $\Delta F/F_0$ = 19.9% in 10% VTM (otherwise absent without passivation) and $\Delta F/F_0$ = 12.4% in 1% saliva (otherwise 3.2% without passivation), suggesting PE-PEG nanosensor passivation enables partial mitigation of nanosensor biofouling.

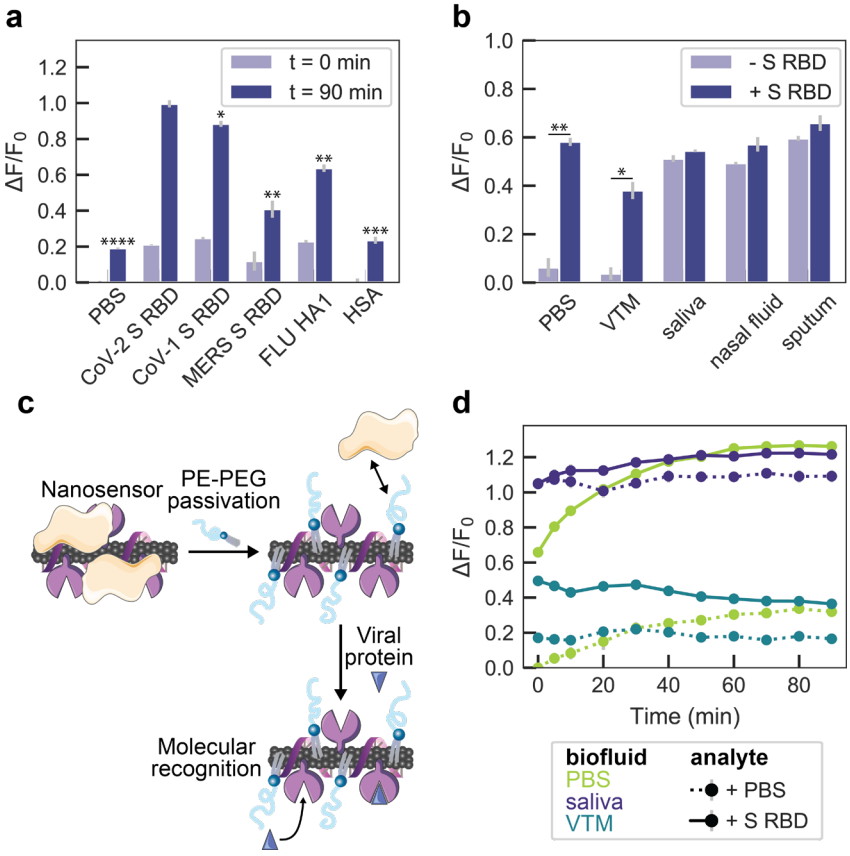

Figure 8-3. ACE2-SWCNT nanosensor selectivity and sensitivity in biofluid environments. (a) Normalized change in fluorescence ($\Delta F/F_0$) of the 1130 nm SWCNT emission peak for the ACE2- SWCNT nanosensor 0 min and 90 min after exposure to 10 mg/L of viral protein panel: SARS-CoV-2 spike receptor-binding domain (S RBD), SARS-CoV-1 S RBD, MERS S RBD, and FLU hemagglutinin subunit (HA1). ****P = 0.0006 (PBS), ***P = 0.0014 (HSA), **P = 0.0065 (FLU) and 0.0076 (MERS), and *P = 0.0503 (SARS-CoV-1) in independent two-sample t-tests, for each analyte $\Delta F/F_0$ response at t = 90 min in comparison to SARS-CoV-2 S RBD $\Delta F/F_0$ response at t = 90 min. (b) ACE2-SWCNT nanosensor response 90 min after exposure to 1 µM S RBD in the presence of 1% relevant biofluids: viral transport medium (VTM), saliva, nasal fluid, and sputum (treated with sputasol). **P = 0.0065 (PBS) and *P = 0.0161 (VTM) in independent two-sample t-tests, for $\Delta F/F_0$ response in biofluids compared before vs. after S RBD addition. (c) Schematic depiction of nanosensor biofouling with proteins present in relevant biofluids, mitigated upon passivation with phosphatidylethanolamine phospholipid with a 5000 Da PEG chain (PE-PEG). (d) Response of PE-PEG passivated nanosensor to 500 nM S RBD in the presence of PBS, 10% VTM, or 1% saliva. Surface passivation with a hydrophilic polymer improved the nanosensor response that was otherwise greatly attenuated, as shown in (b). All fluorescence measurements were obtained with 721 nm laser excitation. Gray bars represent standard error between experimental replicates (N = 3).

8.3.4 Immobilized Nanosensor Response to Spike Protein and Virus-Like Particles

We next translated the nanosensors from in-solution sensing to a surface-immobilized format for imaging. ACE2-SWCNTs (formed by adsorbing 12.5 mg/L ACE2 to 5 mg/L $(GT)_6$-SWCNTs)

were immobilized on a glass-bottom microwell dish and imaged with a 100x oil immersion objective (Figure 8-4). Addition of PBS at 60 s did not cause a change in fluorescence signal, as anticipated based on solution-based nanosensor control experiments (Figure 8-2). Upon injection of 2 μM (final concentration) S RBD, the average integrated-fluorescence intensity change was $\Delta F/F_0$ = 65.1% within 5 s (Figure 8-4a-c). This experiment was repeated using virus-like particles (VLPs), which are formed by co-expressing all four SARS-CoV-2 structural proteins (spike, membrane, nucleocapsid, and envelope proteins). Addition of 10% sucrose (the VLP buffer) at 60 s slightly increased the baseline fluorescence. Injection of 35 mg/L VLPs increased the average integrated-fluorescence intensity by $\Delta F/F_0$ = 72.8% within 5 s (Figure 8-4d-f). This concentration of VLPs corresponds to approximately 17 nM S RBD. To evaluate the specificity of the observed nanosensor response, we then tested VLPs produced with and without S protein co-expressed. We found that the immobilized nanosensor exhibited a response of $\Delta F/F_0$ = 19.4% within 5 s for the VLPs without S protein, compared to a response of $\Delta F/F_0$ = 70.7% for the VLPs with S protein (Figure 8-14).

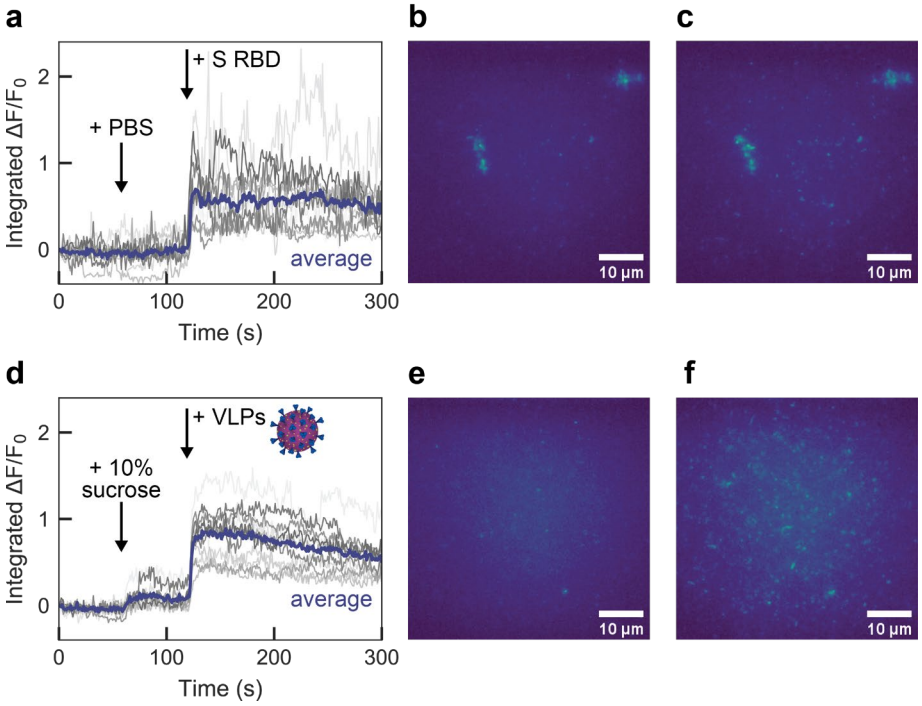

Figure 8-4. Surface-immobilized ACE2-SWCNT nanosensor response to SARS-CoV-2 spike protein receptor-binding domain (S RBD) and virus-like particles (VLPs). Microscopy traces of ACE2-SWCNTs (formed by 12.5 mg/L ACE2 and 5 mg/L $(GT)_6$-SWCNTs) immobilized on a glass-bottom microwell dish exhibited a fluorescence response to both S RBD and VLPs, for single regions of interest (gray; 12 total per image) and the average intensity (purple). (a-c) Addition of PBS at 60 s caused no change in fluorescence, as expected, and addition of 2 μM S RBD (final concentration) at 120 s yielded a turn-on fluorescence response, as shown by (a) the integrated-fluorescence fold change ($\Delta F/F_0$) over 5 min and entire field-of-view at (b) time = 0 s and (c) time = 125 s. (d-f) Addition of 10% sucrose buffer (to match VLP buffer) at 60 s caused a slight increase in fluorescence and addition of 35 mg/L VLPs (final concentration) at 120 s yielded a turn-on fluorescence response, as shown by (d) the integrated-fluorescence fold change ($\Delta F/F_0$) over 5 min and entire field-of-view at (e) time = 0 s and (f) time = 125 s. All fluorescence images were obtained with 721 nm laser excitation and a 100x oil immersion objective. VLP adapted with permission from an image by Maya Peters Kostman for the Innovative Genomics Institute.

8.4 Conclusions

In summary, we have developed an optical SWCNT-based nanosensor capable of detecting SARS-CoV-2 via S protein recognition. Our protein-SWCNT design concept can be extended to incorporate other proteins of interest and for applications beyond biological sensing, such as the label-free study of protein-protein interactions. To construct these nanosensors, ACE2 was noncovalently adsorbed to the SWCNT surface and, in the presence of the viral S protein analyte, binding elicited a modulation of the intrinsic SWCNT fluorescence. We studied ACE2 adsorption to SWCNTs by employing corona exchange and surfactant displacement assays, which confirmed stable adsorption of ACE2 to SWCNTs, and subsequently confirmed S RBD binding to the ACE2-SWCNT nanosensor. The resulting nanosensors displayed excellent colloidal stability and retained

binding capability to CoV-2 S RBD when surface-immobilized. Nanosensors exhibited a 100% turn-on response in fluorescence upon addition of 1 μM CoV-2 S RBD, with response scaling as a function of concentration. Fitting to a cooperative binding model gave rise to kinetic parameter estimates to quantify nanosensor performance. Although the solution-phase LOD (12.6 nM S RBD) remains above that of realistic samples (viral loads ranging from ~10^1-10^4 viral copies per μL,[519–522] translating to ~0.005-5 pM S RBD), the surface-immobilized nanosensor can achieve a $\Delta F/F_0$ = 73% within 5 s of exposure to 35 mg/L VLPs as a mimic of the full SARS-CoV-2 virion, with detection able to reach down to ~10^4-10^6 viral copies per μL (Figure 8-15). The lower magnitude response for VLPs without S protein ($\Delta F/F_0$ = 19%) supports our hypothesis that molecular recognition is enabled by the specific ACE2-S protein interaction. Furthermore, solution-phase nanosensor passivation with a hydrophilic polymer (PEG) attached to phospholipids (PE) provided some improvement of nanosensor response to S protein in 10% VTM and 1% saliva. However, additional strategies must be pursued to further mitigate biofouling while retaining the fluorescence response, thus increasing the feasibility of these nanosensors to function in crude biofluids. Such strategies may include varying the anti-biofouling polymers attached to the phospholipids, such as incorporating zwitterionic polymers,[38,523] or covalently linking polymers directly to the SWCNT surface.[428,524] Future work will also improve nanosensor sensitivity and selectivity to the CoV-2 S protein necessary for clinical application (comparisons in Table 8-2), potentially by incorporating a more specific sensing protein than ACE2, which serves as a receptor for other viral and endogenous proteins.[525] Such sensing proteins could include antibodies[526] or nanobodies,[527,528] as well as other viral biomarker binding moieties. Moreover, various protein-anchoring[277,529] and SWCNT pre-coating[339,530] strategies can be pursued to give rise to a more pre-quenched initial nanosensor fluorescence, thus leading to a larger magnitude increase in the presence of the viral analyte. Incorporating nanosensors in form factors such as paper or hydrogel may enable locally concentrating viral analytes to elicit a greater fluorescence response, or immobilizing nanosensors in a flow channel may allow an accumulation mode of function. Finally, patient biofluids may undergo a facile filtering step to concentrate proteins.[531]

Early and frequent testing is key to trace and control the spread of COVID-19. However, current diagnostics suffer from insufficient supply and throughput, where our reliance on tests with long turnaround times leads to delays in patients receiving test results. A technology capable of rapidly detecting active infections in crude biofluids is needed. Taken together, our data show that SWCNT-based nanosensors noncovalently functionalized with the human ACE2 receptor can detect the SARS-CoV-2 S protein in relevant patient biofluids and can be immobilized and imaged on microfluidic surfaces. Though less sensitive than PCR-based testing, the rapid nanosensor response to SARS-CoV-2 VLPs in the surface-immobilized state has distinct advantages in enabling on-site testing, and has the potential to detect SARS-CoV-2 without patient biofluid sample processing and purification due to the SWCNT nIR fluorescence. Ultimately, these nanosensors can be incorporated into a point-of-care device for rapid diagnosis of individuals actively infected with SARS-CoV-2, using accessible equipment from a different supply chain than that of current testing modes.

8.5 Materials and Methods

8.5.1 Synthesis of ssDNA-SWCNTs

Suspensions of single-walled carbon nanotube (SWCNTs) with single-stranded DNA (ssDNA) were prepared by mixing 0.2 mg of mixed-chirality SWCNTs (small diameter HiPco™ SWCNTs, NanoIntegris) with 250 μM of ssDNA (custom ssDNA oligos with standard desalting, Integrated DNA Technologies, Inc.) in 1 mL, 0.1X phosphate-buffered saline (PBS; note 1X is 137 mM NaCl, 2.7 mM KCl, 10 mM Na_2HPO_4, 1.8 mM KH_2PO_4). This mixture was bath sonicated for 30 min (Branson Ultrasonic 1800) then probe-tip sonicated for 10 min in an ice bath (3 mm probe tip at 50% amplitude, 5-6 W, Cole-Parmer Ultrasonic Processor). Suspensions were centrifuged to pellet insoluble SWCNT bundles and contaminants (16.1 krcf, 90 min). Supernatant was collected and ssDNA-SWCNT concentration was calculated with measured sample absorbance at 632 nm (NanoDrop One, Thermo Scientific) and the empirical extinction coefficient ε_{632nm}=0.036 L mg^{-1} cm^{-1}.[532] ssDNA-SWCNTs were stored at 4°C and diluted to a working concentration of 10 mg L^{-1} in 1X PBS at ambient temperature ≥ 2 h prior to use.

8.5.2 Preparation of Proteins and Biofluids

Proteins were sourced and reconstituted as listed in Table 8-1. All viral protein analytes were purified with desalting columns to remove impurities (Zeba Spin Desalting Columns, 0.5 mL with 7 kDa MWCO, Thermo Fisher Scientific) by washing with PBS three times (1500 rcf for 1 min), centrifuging with sample (1500 rcf for 2 min), and retaining sample in flow-through solution. Resulting protein concentration was measured with the Qubit Protein Assay (Thermo Fisher Scientific) and proteins were diluted in PBS to 10X the intended final analyte concentration.

Biofluids were prepared by centrifuging to remove any large contaminants (1000 rcf for 5 min) then diluting in PBS to 10X the intended final concentration. Sputasol (Oxoid) was used to liquify sputum prior to use, used according to manufacturer's instructions.

8.5.3 Synthesis of ACE2-ssDNA-SWCNT Nanosensors

Nanosensors were made by preparing solutions of 10 mg/L $(GT)_6$-SWCNTs and 25 mg/L ACE2, mixing in equal volumes, incubating for 30 min, diluting by half with PBS, and incubating for an additional 30 min. Final concentrations of components are thus 2.5 mg/L $(GT)_6$-SWCNTs and 6.25 mg/L ACE2. Removal of unbound ACE2 remaining in solution was attempted by centrifugal filtration (Amicon Ultra-0.5 mL centrifugal filters with 100 kDa MWCO, Millipore Sigma), however, this led to embedding of nanosensors in the filter membrane and negligible nanosensor yield. Downstream testing confirmed necessity of the bound ACE2-SWCNT complex for SARS-CoV-2 spike protein sensing, therefore, presence of free ACE2 was not a concern. For the stability test of nIR fluorescence as a function of time, $(GT)_6$-SWCNTs and ACE2 were injected together to these final concentrations and measured immediately.

For passivation of nanosensors with phospholipid-PEG, the protocol was slightly modified to incorporate first adsorption of the sensing protein (ACE2) then passivation of remaining exposed SWCNT surface by phospholipid-PEG (saturated 16:0 phosphatidylethanolamine-PEG 5000 Da, or PE-PEG). Passivated nanosensors were made by preparing solutions of 10 mg/L $(GT)_6$-SWCNTs and 25 mg/L ACE2, mixing in equal volumes, incubating for 15 min, adding PE-PEG

to a final concentration of 2.5 mg/L, diluting by half with PBS, bath sonicating for 15 min, and incubating for an additional 30 min.

8.5.4 Preparation of SARS-CoV-2 S RBD Analyte

Plasmid encoding for SARS-CoV-2 S RBD[533] was transiently transfected into suspension Expi293 cells at 0.5-1 L scale. Three days after transfection, cell culture supernatants were clarified and purified by Ni-NTA affinity chromatography as previously described[534] and the eluted protein was dialyzed extensively against PBS prior to storage at -80C.

8.5.5 Synthesis and Purification of SARS-CoV-2 VLPs

To prepare the SARS-CoV-2 VLPs, two plasmids pcDNA3.1-Spike and pIRES2-MNE were synthesized based on the sequence of the Wuhan-Hu-1 strain (GenBank: MN908947.3). The spike protein was stabilized with the furin cleavage (residues 682-685) abrogated and the consecutive residue 986 and 987 substituted with prolines.[518,535] The VLPs were synthesized by co-transfecting HEK293 or HEK293T cells with plasmids using HyFect transfection reagent (Leadgene Biomedical Inc., Taiwan) or JetOptimus (Polyplus-transfection, USA). To generate VLPs without S protein, cells were transfected with pIRES2-MNE only. The harvested supernatant was first concentrated with a 100 kDa MWCO centrifugal filter (Pall Corporation) then laid over discontinuous 20%-60% sucrose or Opti-prep (BioVision Inc.) gradients followed with centrifugation at 30,000 rpm for 4 hours. Purified VLPs were resuspended in PBS pH 7.4 and frozen at -80°C for storage.

8.5.6 Nanosensor Optical Characterization and Analyte Screening

Fluorescence was measured with an inverted Zeiss microscope (Axio Observer.D1, 10X objective) coupled to a Princeton Instruments spectrometer (SCT 320) and liquid nitrogen-cooled Princeton Instruments InGaAs detector (PyLoN-IR). Samples were excited with a triggered 721 nm laser (OptoEngine LLC) and emission was collected in the 800 – 1400 nm wavelength range, with samples in a polypropylene 384 well-plate format (30 μL total sample volume; Greiner Bio-One microplate).

For nIR fluorescence screens, 27 μL of nanosensor was added per well and 3 μL of 10X-concentrated viral protein analytes in PBS (or buffer alone) were injected per well using a microchannel pipette (in triplicate), with brief mixing by pipetting. The plate was sealed with an adhesive seal (Bio-Rad) and spun down for 15 sec with a benchtop well plate centrifuge. Fluorescence spectra were recorded at time points of 0 min, 5 min, 10 min, and every subsequent 10 min until the max time point.

For surfactant stability tests, the screening protocol was modified as follows: 24 μL of nanosensor, 3 μL of 2.5 w/v% sodium cholate (SC), then 3 μL of 10X-concentrated viral protein analytes in PBS (or buffer alone) were added per well. Wavelength shifts were calculated by translating fluorescence spectra in 1 nm wavelength increments such that the correlation coefficient was maximized with respect to the reference state. Data processing in this manner captures the full spectrum shifting behavior.

Absorbance was measured by UV-VIS-nIR spectrophotometer (Shimadzu UV-3600 Plus) with samples in a 50 μL volume, black-sided quartz cuvette (Thorlabs, Inc.).

For surface-immobilized nanosensor experiments, ACE2-SWCNTs were immobilized on MatTek glass-bottom microwell dishes (35 mm petri dish with 10 mm microwell) as follows: the dish was washed twice with 150 μL PBS, 100 μL of nanosensor (formed by 12.5 mg/L ACE2 with 5 mg/L $(GT)_6$-SWCNT pre-incubated for 40 min) was added and incubated for 20 min, nanosensor solution was removed, and the dish was washed twice again with 150 μL PBS. Surface-immobilized nanosensors were imaged on an epifluorescence microscope (100x oil immersion objective) with an excitation of 721 nm and a Ninox VIS-SWIR 640 camera (Raptor). For each imaging experiment, 120 μL PBS was added prior to recording and the z-plane was refocused. Images were collected with a 950 ms exposure time and 1000 ms repeat cycle over 5 min. 15 μL buffer was added at frame 60 and 15 μL analyte was added at frame 120. Images were processed in ImageJ by applying a median filter (0.5-pixel radius) and rolling ball background subtraction (300-pixel radius), then using the ROI analyzer tool (Multi Measure).

8.5.7 Corona Exchange Assay

Corona dynamic studies were done as described previously.[118] Briefly, the same ssDNA-SWCNT suspension protocol was employed, instead using fluorophore-labeled ssDNA-Cy5 (3' Cy5-labeled custom ssDNA oligos with HPLC purification, Integrated DNA Technologies, Inc.). Fluorescently labeled ssDNA was tracked and the displacement of ssDNA from the SWCNT surface (monitored as in increase in Cy5 fluorescence) was used as a proxy for protein adsorption. To assess $(GT)_6$-Cy5 desorption from SWCNTs in the presence of ACE2, 25 μL of 12.5 mg L^{-1} ACE2 was added to 25 μL of 5 mg L^{-1} $(GT)_6$-Cy5-SWCNTs. To assess $(GT)_6$-Cy5 desorption from nanosensors in the presence of S RBD, 5 μL of 10X-concentrated S RBD was injected into 45 μL of ACE2-$(GT)_6$-Cy5-SWCNTs. Solutions were added via microchannel pipette into a 96-well PCR plate (Bio-Rad) and mixed by pipetting. The plate was sealed with an optically transparent adhesive seal (Bio-Rad) and briefly spun down on a benchtop centrifuge. Fluorescence time series readings were measured in a Bio-Rad CFX96 Real Time qPCR System by scanning the Cy5 channel every 30 s at 22.5°C.

Table 8-1. Purchased biofluid and protein specifications.

Purpose	Protein	Manufacturer	Lot #	Source	Form	Concentration
Sensing protein	Angiotensin-converting enzyme 2 (ACE2)	Ray Biotech	04U24020GC	Recombinant, (HEK293 cell expression system; C-terminal His-tag)	Liquid (PBS)	2.8 g/L
Control	SARS CoV-1 spike protein receptor-binding domain (CoV-1 S RBD)	ACROBiosystems	3558c-203KF1-R7	Recombinant (HEK293 cell expression system; C-terminal His-tag)	Lyophilized from PBS, 10% Trehalose	Reconstituted in 167 µL PBS, 30 min at room temperature with occasional gentle mixing
Control	MERS spike protein receptor-binding domain (MERS S RBD)	MyBioSource	0110YB	Recombinant (HEK293 cell expression system; C-terminal His-tag)	Liquid (PBS, 0.1% sodium azide)	1 g/L
Control	Influenza hemagglutinin subunit (FLU HA1)	MyBioSource	95-101-1104	Recombinant (E. coli expression; N-terminal His-tag and strepll-tag)	Liquid (PBS, 0.1% SDS, 0.02% sodium azide)	1 g/L
Control	Human serum albumin (HSA)	Sigma-Aldrich	#SLBZ2785	Human plasma	Lyophilized, fatty acid and globulin free	Reconstituted in PBS, 30 min at room temperature with occasional gentle mixing
Biofluid	Viral transport medium	Innovative Research	31975	Standard CDC-recommended formulation: 2% FBS, 100 µg/mL Gentamicin, 0.5 µg/mL Amphotericin in a Hanks Balanced salt solution base	Liquid	N/A
Biofluid	Saliva	Lee Biosolutions	W205820	Human, pooled, normal	Liquid	N/A
Biofluid	Nasal fluid	Lee Biosolutions	18-05-538	Human, single donor, normal	Liquid	N/A
Biofluid	Sputum	Lee Biosolutions	18-03-594	Human, single donor, normal	Liquid	N/A

8.6 Chapter Supporting Information

8.6.1 Supplementary Figures and Tables

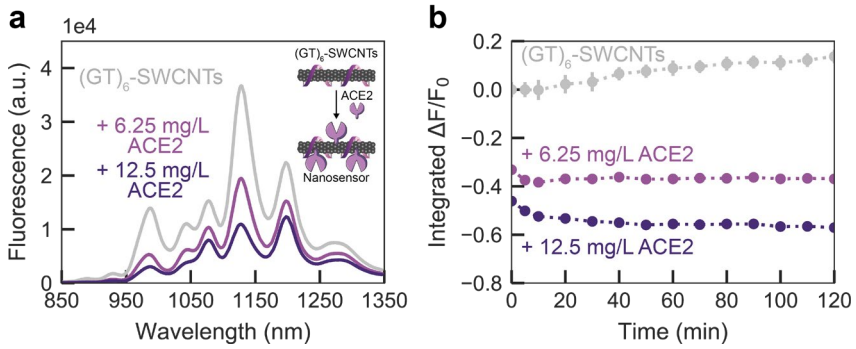

Figure 8-5. Adsorption of different ratios of ACE2 on $(GT)_6$-SWCNTs. ACE2-SWCNT complexation quenched intrinsic SWCNT near-infrared fluorescence, shown by (a) the full fluorescence spectrum after 1 h incubation of 6.25 mg/L or 12.5 mg/L ACE2 with 2.5 mg/L $(GT)_6$-SWCNTs (final concentrations) and (b) the integrated-fluorescence change as a function of time over 2 h. Both ratios exhibit stable quenched fluorescence, however, the lower ratio of protein to SWCNT exhibited better colloidal stability. Gray bars represent standard error between experimental replicates (N = 3).

The ratio of ACE2 to $(GT)_6$-SWCNTs was chosen based on a protein footprint estimation that 28.6 ACE2 dimers fit per SWCNT in the close-packed limit (using ACE2 dimer dimensions as determined by cryo-EM[536]). This calculation translates to a mass ratio of 2.36 ACE2:SWCNT. The actual mass ratio of 2.5 ACE2:SWCNT was chosen to be just above this theoretical close-packed limit in an attempt to minimize protein spreading that arises from a large excess of nanoparticle surface available for proteins.[38] Extending to twice this mass ratio produces more quenching in the SWCNT fluorescence (Figure 8-5), yet reduced sensing ability (Figure 8-6) and colloidal stability. Thus, the mass ratio of 2.5 ACE2:SWCNT was experimentally determined to be best suited for S RBD sensing (Figure 8-6).

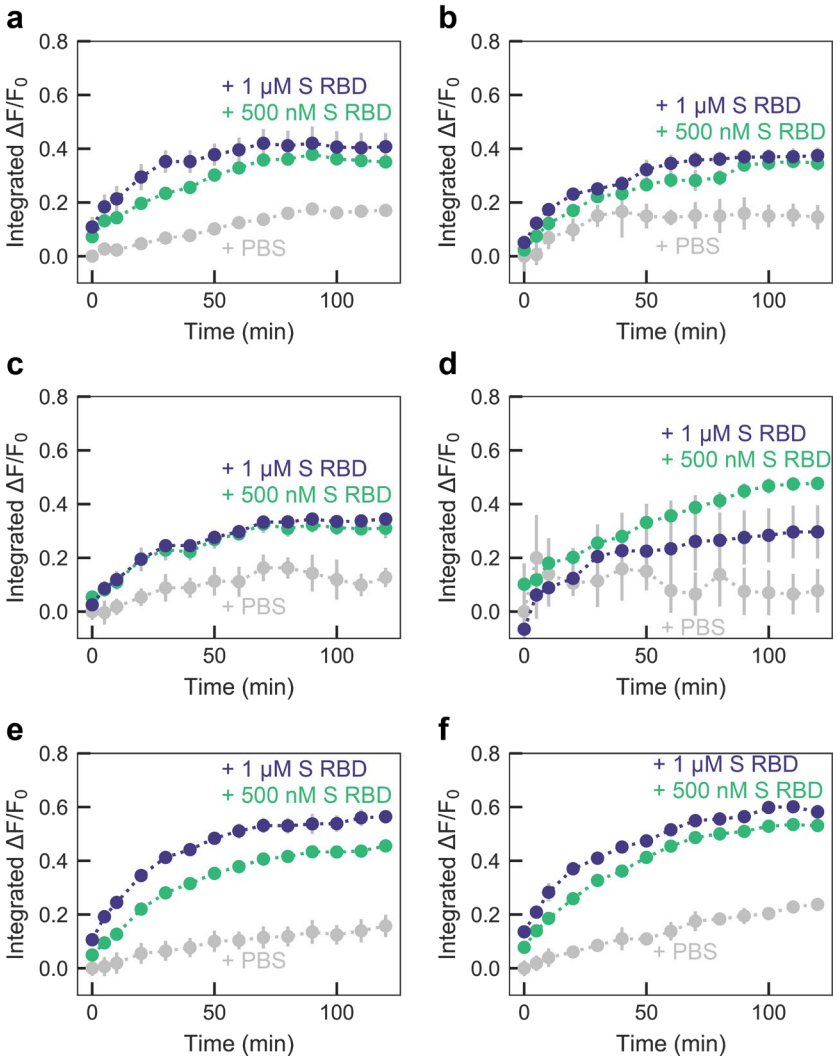

Figure 8-6. Response of different ratios ACE2:$(GT)_6$-SWCNTs to S RBD. Integrated-fluorescence fold change as a function of time over 120 min upon addition of PBS, 500 nM S RBD, or 1 μM S RBD to nanosensor formed by (a) 6.25 mg/L ACE2 and 2.5 mg/L $(GT)_6$-SWCNTs incubated 1 h, (b) 12.5 mg/L ACE2 and 2.5 mg/L $(GT)_6$-SWCNTs incubated 1 h, (c) 6.25 mg/L ACE2 and 2.5 mg/L $(GT)_6$-SWCNTs incubated 3 h, (d) 12.5 mg/L ACE2 and 2.5 mg/L $(GT)_6$-SWCNTs incubated 3 h, (e) 6.25 mg/L ACE2 and 2.5 mg/L $(GT)_6$-SWCNTs incubated 30 min, diluted by half in PBS, and incubated an additional 30 min, and (f) 12.5 mg/L ACE2 and 2.5 mg/L $(GT)_6$-SWCNTs incubated 30 min, diluted by half in PBS, and incubated an additional 30 min. Gray bars represent standard error between experimental replicates (N = 3).

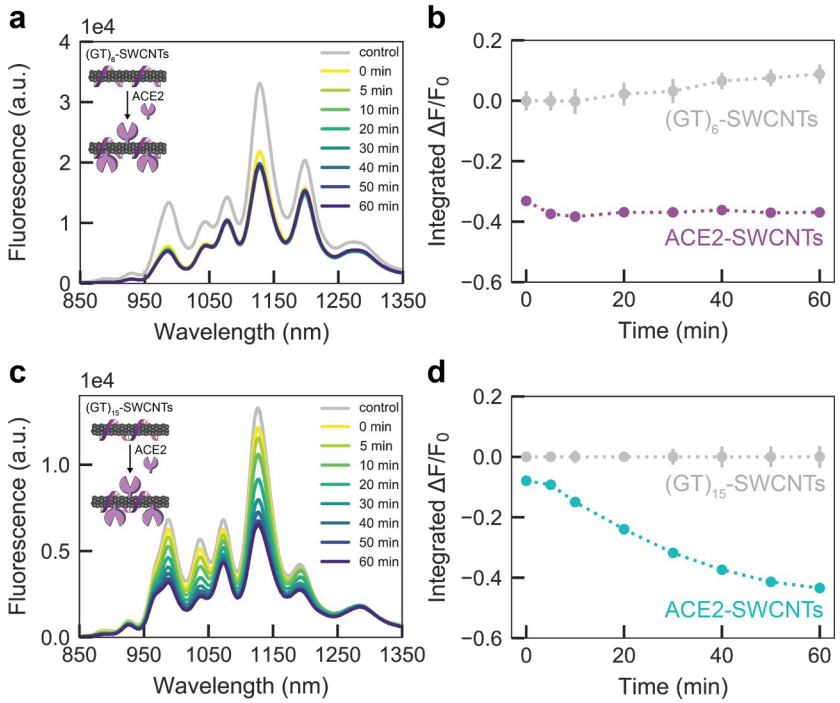

Figure 8-7. Adsorption of ACE2 to $(GT)_6$- vs. $(GT)_{15}$-SWCNTs. ACE2-SWCNT complexation rapidly quenched intrinsic SWCNT near-infrared fluorescence, shown by (a) the full fluorescence spectrum and (b) the integrated-fluorescence fold change as a function of time over 1 h, upon incubation of 6.25 mg/L ACE2 with 2.5 mg/L $(GT)_6$-SWCNTs (final concentrations). ACE2-SWCNT complexation quenched intrinsic SWCNT near-infrared fluorescence at a slower rate, shown by (c) the full fluorescence spectrum and (d) the integrated-fluorescence fold change as a function of time over 1 h, upon incubation of 6.25 mg/L ACE2 with 2.5 mg/L $(GT)_{15}$-SWCNTs (final concentrations). Gray bars represent standard error between experimental replicates (N = 3).

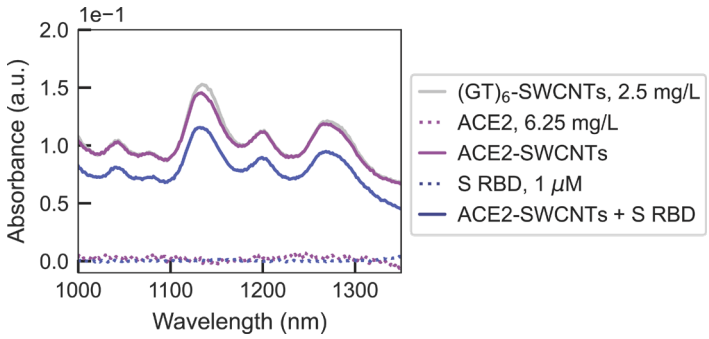

Figure 8-8. Absorbance of $(GT)_6$-SWCNTs with ACE2 sensing protein and S RBD analyte. Retention of near-infrared SWCNT absorbance peaks in the presence of ACE2 adsorption and S RBD analyte binding confirms solution-stable noncovalent passivation, rather than covalent modification, of the SWCNT surface.

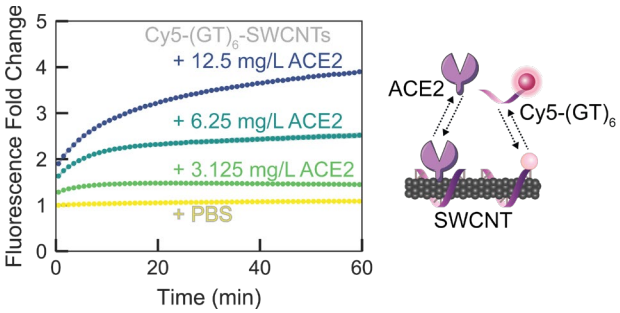

Figure 8-9. Displacement of Cy5-$(GT)_6$ ssDNA from SWCNT as a function of passivating ACE2 concentration. Adsorption of ACE2 on the SWCNT surface led to $(GT)_6$ desorption, tracked by Cy5-labeled ssDNA, in a concentration-dependent manner upon addition of varying ACE2 concentrations with 2.5 mg/L Cy5-$(GT)_6$-SWCNTs (final concentrations). The increase in Cy5-$(GT)_6$ fluorescence from the initial quenched state on the SWCNT serves as a proxy for ACE2 adsorption. Shaded error bars represent standard error between experimental replicates (N = 3).

To test the stability of the ACE2-functionalized SWCNT construct, we implemented a solvatochromic shift assay.[42,198] This methodology is based upon addition of surfactant (sodium cholate, SC) that coats any solvent-exposed SWCNT surface and can displace low-affinity molecules from the SWCNT surface. SC adsorption causes exclusion of water from the SWCNT surface, producing a large increase in fluorescence and solvatochromic shift to lower emission wavelengths. Prior to ACE2 incubation, SC elicited both a large blue-shift (-16 nm) and sizeable increase in fluorescence (70.2%) for $(GT)_6$-SWCNTs alone (Figure 8-10a-b). However, upon passivation with ACE2, these spectral changes were reduced to -10 nm and 10.3%, respectively (Figure 8-10c-d), suggesting a mechanism in which ACE2 adsorbs to the SWCNT surface and causes $(GT)_6$ ssDNA desorption. Moreover, we show that addition of S RBD analyte to the ACE2-SWCNT complex further stabilizes the nanosensor, whereby addition of SC produced a brief blue-shift of -6 nm yet a complete return to baseline by 70 min, and similarly, a minimal change in fluorescence of -3.9% (Figure 8-10e-f).

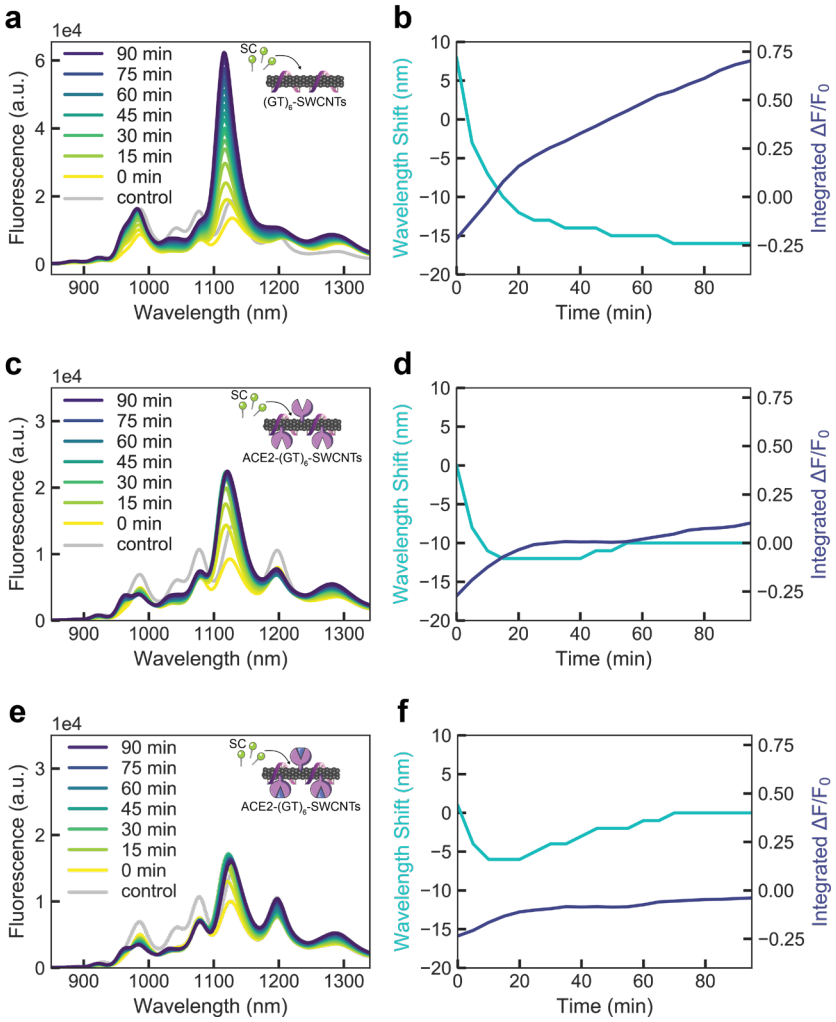

Figure 8-10. Surfactant displacement experiment to probe the stability of $(GT)_6$-SWCNTs with ACE2 sensing protein and S RBD analyte. Full fluorescence spectrum (left) and time-dependent wavelength shift and integrated-fluorescence fold change (right) for (a-b) 2.5 mg/L $(GT)_6$-SWCNTs alone, (c-d) ACE2-SWCNT nanosensors (formed by 6.25 mg/L ACE2 and 2.5 mg/L $(GT)_6$-SWCNTs), and (e-f) ACE2-SWCNT nanosensors with 500 nM S RBD, each upon addition of 0.25 w/v% sodium cholate (SC, final concentration). Decreasing blue-shift and fluorescence fold change due to ACE2 implies ACE2 covers and stabilizes the SWCNT surface, with further stabilization upon addition of S RBD analyte.

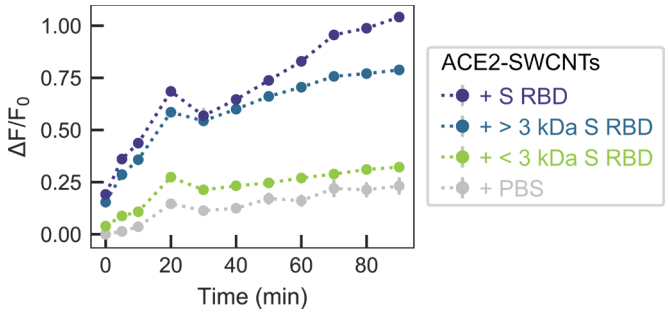

Figure 8-11. ACE2-SWCNT nanosensor response to controls. Addition of 500 nM S RBD (final concentration) to ACE2-SWCNTs (formed by 6.25 mg/L ACE2 and 2.5 mg/L $(GT)_6$-SWCNTs) yielded a significant turn-on fluorescence response. This response is maintained for S RBD > 3 kDa MWCO centrifugal filter and absent for S RBD < 3 kDa. Gray bars represent standard error between experimental replicates (N = 3).

The limit of detection (*LOD*) of the ACE2-SWNT nanosensor for S RBD analyte is defined as the lowest analyte concentration that can be determined to be statistically different from the blank:[537]

$$LOD = mean_{blank} + 3\,SD_{blank} \qquad 8\text{-}1$$

where the mean and standard deviation (*SD*) are in terms of the measured fluorescence fold change ($\Delta F/F_0$). For the concentration series of S RBD analyte tested (Figure 8-2d-e), the *LOD* is calculated to be $\Delta F/F_0 = 0.3456$. This corresponds to an S RBD concentration of 12.59 nM based on the cooperative binding model fit.

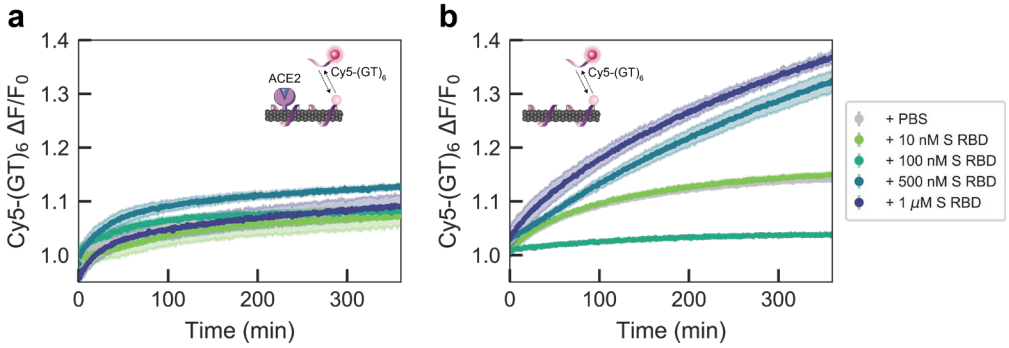

Figure 8-12. Displacement of Cy5-$(GT)_6$ ssDNA from SWCNT in the presence or absence of ACE2 sensing protein, as a function of S RBD analyte concentration. Addition of varying concentrations of S RBD analyte to (a) ACE2-Cy5-$(GT)_6$-SWCNT nanosensors (formed by 6.25 mg/L ACE2 and 2.5 mg/L $(GT)_6$-SWCNTs) and (b) Cy5-$(GT)_6$-SWCNTs alone (2.5 mg/L). Shaded error bars represent standard error between experimental replicates (N = 3).

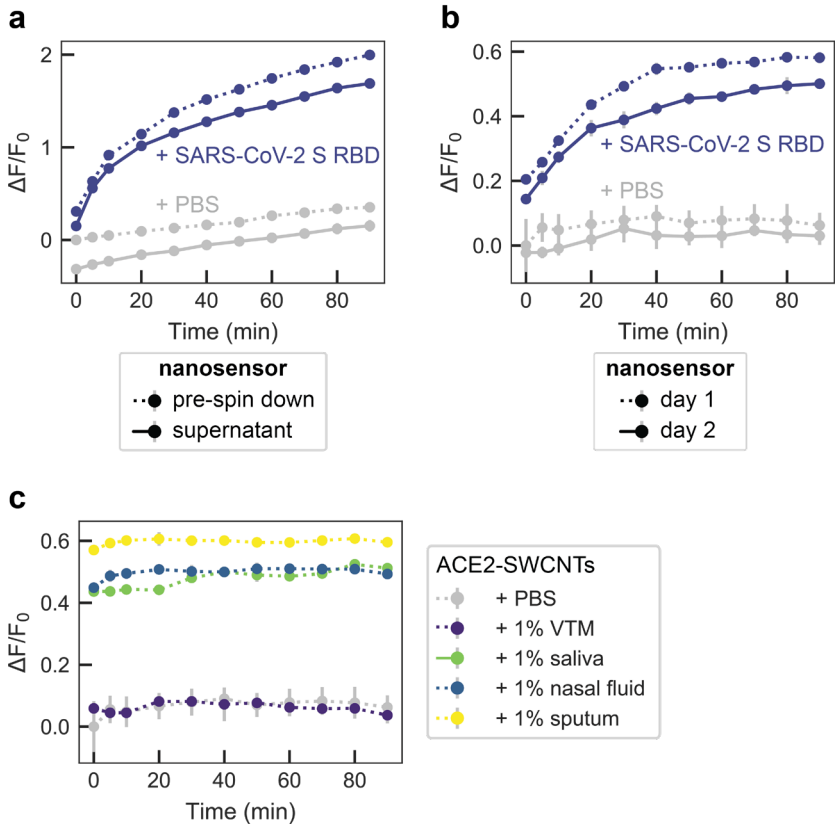

Figure 8-13. ACE2-SWCNT nanosensor controls for assessing stability. Response of ACE2-SWCNTs (formed by 6.25 mg/L ACE2 and 2.5 mg/L $(GT)_6$-SWCNTs) to S RBD was preserved (a) before and after centrifugation (16.1 krcf, 30 min; 500 nM S RBD) and (b) before and after overnight incubation at ambient conditions (1 μM S RBD). (c) Stability of ACE2-SWCNT nanosensors in different biofluids. Normalized change in fluorescence of the 1130 nm SWCNT emission peak for the ACE2-SWCNT sensor as a function of time in 1% relevant biofluids: viral transport medium (VTM), saliva, nasal fluid, and sputum (treated with sputasol). Nanosensor fluorescence in biofluids demonstrated stability yet elevated magnitudes. Gray bars represent standard error between experimental replicates (N = 3).

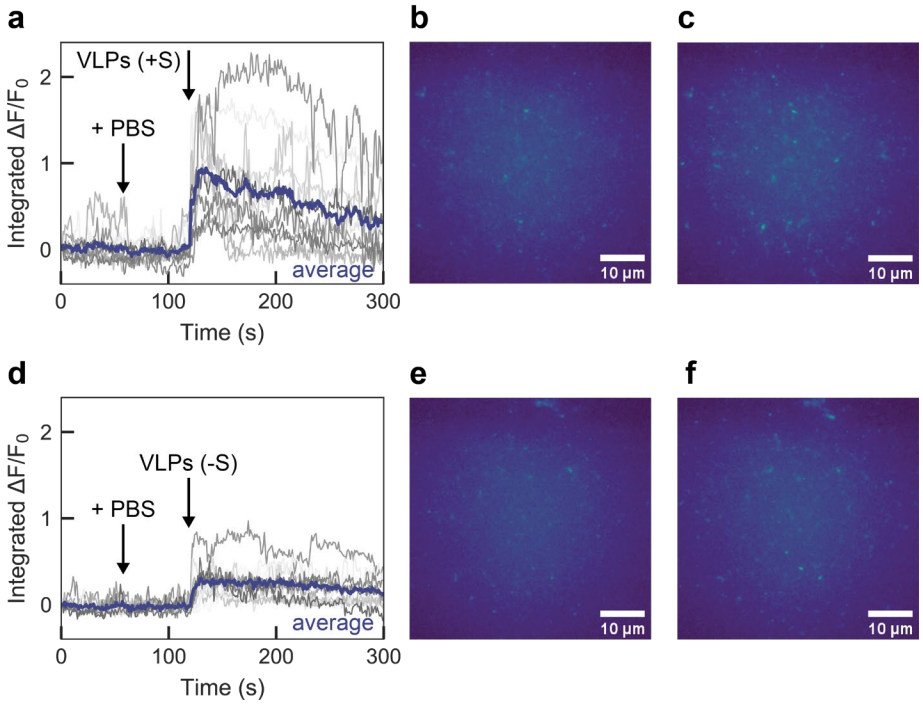

Figure 8-14. Surface-immobilized ACE2-SWCNT nanosensor response to SARS-CoV-2 virus-like particles (VLPs) with and without S protein. Microscopy traces of ACE2-SWCNTs (formed by 12.5 mg/L ACE2 and 5 mg/L $(GT)_6$-SWCNTs) immobilized on a glass-bottom microwell dish exhibited a larger fluorescence response to VLPs expressing S protein, for single regions of interest (gray; 12 total per image) and the average intensity (purple). (a-c) Addition of PBS at 60 s caused no change in fluorescence, as expected, and addition of 50 mg/L VLPs (with S protein) at 120 s yielded a large turn-on fluorescence response, as shown by (a) the integrated-fluorescence fold change ($\Delta F/F_0$) over 5 min and entire field-of-view at (b) time = 100 s and (c) time = 125 s. (d-f) Addition of PBS at 60 s caused no change in fluorescence, as expected, and addition of 50 mg/L VLPs (no S protein) at 120 s yielded a minor turn-on fluorescence response, as shown by (d) the integrated-fluorescence fold change ($\Delta F/F_0$) over 5 min and entire field-of-view at (e) time = 100 s and (f) time = 125 s. All fluorescence images were obtained with 721 nm laser excitation and a 100x oil immersion objective.

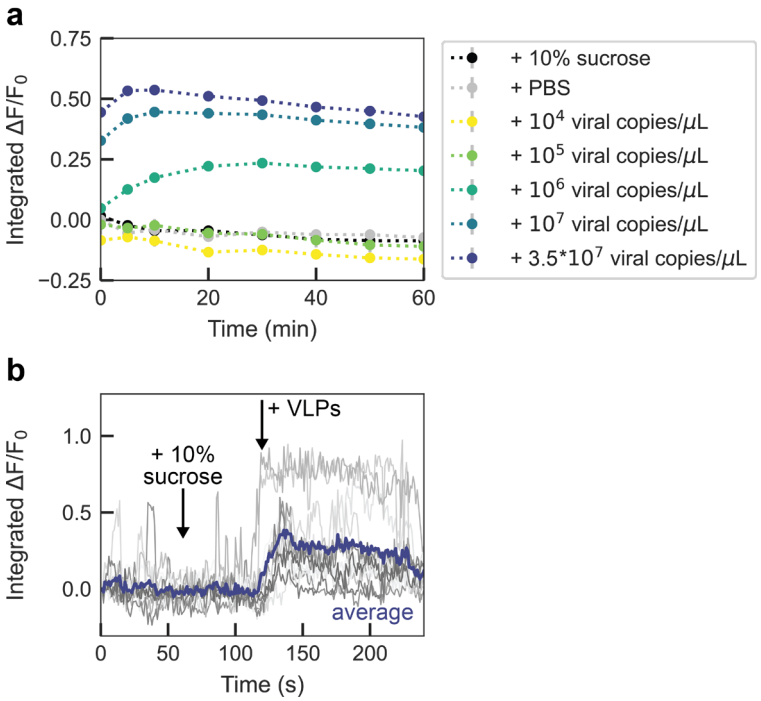

Figure 8-15. ACE2-SWCNT nanosensor response to lower concentrations of SARS-CoV-2 virus-like particles (VLPs). (a) Varying SARS-CoV-2 VLP concentrations were injected into ACE2-SWCNTs (formed by 6.25 mg/L ACE2 and 2.5 mg/L $(GT)_6$-SWCNTs) and the integrated-fluorescence fold change ($\Delta F/F_0$) was monitored over 60 min. Gray bars represent standard error between experimental replicates (N = 3). (b) Microscopy traces of ACE2-SWCNTs (formed by 12.5 mg/L ACE2 and 5 mg/L $(GT)_6$-SWCNTs) immobilized on a glass-bottom microwell dish exhibited a fluorescence response to 0.035 mg/L VLPs, for single regions of interest (gray; 12 total per image) and the average intensity (purple). Addition of 10% sucrose buffer (to match VLP buffer) at 60 s caused no change in fluorescence and addition of 0.035 mg/L VLPs (final concentration) at 120 s yielded a turn-on fluorescence response, as shown by the integrated-fluorescence fold change ($\Delta F/F_0$) over 4 min. Fluorescence spectra and images were obtained with 721 nm laser excitation, with (a) 10X and (b) 100X oil immersion objectives.

This platform for nanosensor design was expanded to attempt passivation of $(GT)_6$-SWCNTs with an antibody for SARS-CoV-1 S RBD that has been previously verified to bind CoV-2 S RBD.[538] Interestingly, the anti-S sensing protein did not exhibit any modulation in intrinsic SWCNT fluorescence, nor did addition of the S RBD analyte provoke a fluorescence response. This result, implying a lack of interaction between anti-S and the SWCNT surface, is in line with our previous work that implies antibodies exhibit minimal adsorption to ssDNA-SWCNTs.[82] Thus, alternative attachment strategies must be pursued for sensing proteins with no intrinsic affinity for the SWCNT surface.

Table 8-2. Comparison of sensor performance to current SARS-CoV-2 diagnostic technologies.

Type of test	Test name	Minimum detectable RNA (copies/μL)	Time per run (min)	Reference
Molecular				
RT-PCR	CDC PCR test	1	<180	[539,540]
	GenMark ePlex test	1	90	[541]
	Cepheid Xpert Xpress test	<1	45	[541]
Isothermal amplification	Abbott ID NOW test	20	15	[541]
	iLACO	10	20–40	[498]
(+CRISPR-based detection)	Mammoth Biosciences DETECTR	10	45	[500]
(+CRISPR-based detection)	Sherlock Biosciences CRISPR-based test	10	60	[542]
Next-generation sequencing	Nanopore Targeted Sequencing	<1	360-600	[543]
Antigen	Sofia 2, Quidel	595 (viral particles)	15	[539]
	FET biosensor	<1 (viral particles) / ~10^{-17} M - 10^{-15} (S)	<1	[507]
	OECT biosensor	~10^{-14} M (S RBD)	10	[544]
	SWCNT-based nanosensor	~10^{4} - 10^{6} (viral particles) / ~10^{-8} M (S RBD)	<1 (surface-immobilized) / 90 (well-plate)	this study

Note that prior work has established viral RNA load in SARS-CoV-2 infected human samples typically ranging from 10^{1}-10^{4} viral copies per μL.[519–522] These viral loads translate to approximately 10^{-15}-10^{-12} M S RBD.

9 Concluding Remarks and Suggested Future Directions

Understanding how nanoparticles function in their intended biological environments is essential to developing successful nanotechnologies for biological sensing, imaging, and delivery applications. Moreover, a fundamental knowledge of such nano-bio interactions will aid rational design of future nanobiotechnologies. In this work, I develop a joint experimental and theoretical framework for studying and employing advantageous nano-bio interactions. This framework provides a quantitative approach to determine protein corona composition, driving forces, dynamics, and morphology on nanoparticles. I have completed experimental protein corona work using conventional analysis techniques, together with the development and application of facile, new techniques. Single-stranded DNA (ssDNA)-functionalized single-walled carbon nanotubes (SWCNTs) are the primary nanoparticle studied in this work due to the numerous desirable optical and physical properties that they possess for a nanobiotechnology platform. The methodology and analysis are generalizable to other nanoparticles within various biological environments. These ideas are extended to probe interactions of ssDNA with an analogous graphene-based nanomaterial from that of the quasi-one-dimensional SWCNT: two-dimensional graphene quantum dots (GQDs). Finally, the experimental techniques and insights on protein-nanoparticle interactions are harnessed to develop a SARS-CoV-2 sensor. This nano-bio construct design takes advantage of the incredible molecular recognition abilities of proteins, in conjunction with nanoparticles to transduce binding events and provide an effective signal readout.

Individual chapters provide detailed conclusions for each portion of the work. Here, I briefly present prevailing themes:

(1) The protein corona that forms on ssDNA-SWCNTs is selective, in that protein abundance in the corona does not scale with that in the full biofluid. The selectivity of protein corona formation on ssDNA-SWCNTs contrasts with that on polystyrene nanoparticles, where most proteins adsorb in some capacity.
(2) Interactions driving corona formation are dependent on the corona layer (e.g., outer vs. inner), whereby electrostatic screening facilitates formation of the soft corona while hydrophobic interactions are posited to drive formation of the hard corona.
(3) Protein features including aromatic amino acid content (from the linear regression analysis) and flexibility (from the supervised learning model) promote protein binding to ssDNA-SWCNTs. However, the favorability of other protein physicochemical properties in promoting corona binding depends on the full biofluid context, highlighting the collective nature of such interactions occurring at the nano-bio interface.
(4) The end-state protein corona formed on ssDNA-SWCNTs from a whole biofluid context is indicative of individual protein binding. Deviations from this trend indicates the role of cooperativity effects for certain proteins to enter the corona phase.
(5) Techniques previously developed to probe the kinetics and thermodynamics of proteins binding to macroscopic surfaces are in some cases adaptable to the problem of studying protein-nanoparticle interactions. However, this unique problem of proteins and nanoparticles, being of similar size and both solubilized, necessitates development of new techniques to provide relevant information on the system, as demonstrated with the simple corona exchange assay.

(6) In turn, this fluorescence-based assay has revealed the more biologically relevant corona exchange process, whereby proteins adsorb and prompt ssDNA desorption from the SWCNT surface. This result provides insight on nanosensor failure mechanisms and led to the development of a more robust nanosensor with a phospholipid passivation scheme to deter unwanted protein adsorption.[339]
(7) *In vitro*-characterized nanoparticle charge is less important in driving protein adsorption than generally thought. From a theory-based approach, we recognize that nanoparticle and protein charge are highly screened in an intravenous blood plasma environment. Accordingly, the absence of electrostatic screening drastically alters protein corona formation. More broadly, nanoparticle charge and size are widely used as characterization parameters prior to the nanoparticles entering a biological environment (determined via zeta potential and dynamic light scattering measurements, respectively). Yet, nanoparticle charge is screened, and nanoparticle size is rapidly changed with biomolecule adsorption. As such, these parameters may not be the most critical in predicting nanoparticle success in biological environments.
(8) Proteins with high affinity for the SWCNT surface can be harnessed to develop hybrid nano-bio constructs toward sensing analytes of interest, as demonstrated with the protein-SWCNT sensor for SARS-CoV-2.

This chapter concludes by presenting some outstanding questions and suggested future directions:

(1) Nanomaterial synthesis and characterization *in vitro* are becoming increasingly well established, yet translation of these technologies outside of the test tube faces a high failure rate.[11,68,69,71] Despite studies aimed at cataloging protein adsorption on nanoparticles, the field remains mired by case-dependent variation and lacks broadly translational and predictive design rules.[122,329,545] A mechanistic understanding of protein corona formation is required to inform parameters upon which to build quantitative models. First-principles approaches offer valuable insight on nano-bio interactions and driving forces, yet inherently require simplified systems and assumptions that, although tractable, are of less relevance to the complexity of a full biological system.[546,547] Empirical correlations present the opportunity of tractability and predictability, however, require extensive experimental datasets with systematically varied, well-characterized parameters.[341,546,548] Ultimately, such models will ideally require individual properties of nanoparticles and biological environments, eliminating the need to characterize the nano-bio complex on a case-by-case basis. To this end, future work will be directed toward establishing quantitative models that identify actionable design principles for engineering nanoparticles capable of functioning in highly complex biological media. In parallel, property predictors of protein corona formation and subsequent *in vivo* outcomes will be used to inform high-throughput screens (experimental and/or computational) and thus facilitate improved nanotechnology-development pipelines.
(2) The protein corona formed around soft nanoparticles is understudied and highly relevant, in light of the multiple mRNA-based SARS-CoV-2 vaccines packaged in lipid nanoparticles.[19–23] Future work will expand upon preliminary studies on the protein corona formed around lipid nanoparticles[88,224,549–551] and liposomes,[437,552,553] employing a slightly modified protein corona isolation procedure to accommodate the more fragile nanoparticle constructs. Exploring the nature and dynamics of the *in vivo*-relevant biomolecular surface coating will provide insight into nanoparticle delivery efficiency and translated protein yield. Of specific relevance to the

intramuscularly dosed mRNA-based SARS-CoV-2 vaccine, such studies should interrogate the protein corona formed in the muscle and lymph node environment, in contrast to the more widely studied protein corona formed from the intravenous environment. A tangential outstanding question that this may address is then – what is the role of nanoparticle stiffness in protein corona formation? For instance, how translatable will the protein corona findings be from these soft lipid nanoparticles to stiff carbon nanotubes that possess the same outer lipid coating? More simply, how will the protein corona differ on solvent-filled liposomes compared to lipid-filled lipid nanoparticles? Chapter 4 revealed a considerable effect of hollowed vs. filled carbon nanoparticles interacting with proteins, yet this theoretical modeling is done only for carbon nanomaterials in the dilute protein-nanoparticle interaction limit. Thus, it is of interest to experimentally test the role of nanoparticle stiffness and fill in guiding interactions with complex mixtures of many proteins present in full biofluids.

(3) Biological environments of relevance to nanoparticle contact extend outside that of the human body. For instance, nanotechnologies are under development for genetic cargo delivery and sensing applications in plants,[231,268,317,554] in which nanoparticle substrates would encounter the metabolite-rich environment unique to plants.[555] More broadly, nanoparticles are becoming ubiquitously used in commercial products and unintentionally released into natural environments, encountering aquatic and terrestrial environments and impacting their inhabitants.[545,546,556–559] This motivates extension from the paradigm of the protein corona to the ecological, or eco-, corona composed of additional biomolecules such as small molecule metabolites and natural organic matter.[545,559–561] Nevertheless, the same framework of probing and understanding nano-bio interactions remains applicable. Although the eco-corona is expected to impact the fate and transformation of nanoparticles deposited in ecosystems, we lack understanding of how exactly the eco-corona affects the nanoparticle's environmental distribution, residence time upon partitioning, subsequent interactions with organisms and corresponding trophic transfer, and propagation of nanotoxicity within larger systems.[545,546,560–563] A poignant case is that of nanoplastics accumulating in marine environments such as coral reefs, originating from mechanically or chemically degraded bulk plastic waste in the ocean, in addition to other human sources such as leaching from sunscreen-covered swimmers.[563–567] Future work must develop a deeper knowledge of the eco-corona and move us toward minimizing the nanoparticle-mediated damage inflicted on these natural systems.

(4) Morphological studies of the protein-nanoparticle complex are improving alongside technological developments. Future work will further employ techniques such as small-angle x-ray scattering (SAXS) to capture the in-solution morphology and *in situ* binding behavior of the protein corona.[82,138,336,568] Due to the relatively low scattering capacity of such biological molecules, small metallic nanoparticle tags can be added to assist in characterizing biomolecule conformation and packing in the nanoparticle-adsorbed state.[569] Additionally, cryo-electron microscopy provides a tool to visualize the close-to-solubilized state of the bound protein-nanoparticle complex.[132,144,570]

(5) Formation of the nanoparticle-corona complex can pose an obstacle toward effectively deploying nanotechnologies, yet concurrently presents a unique opportunity as a functional handle to tune and enhance auxiliary nanoparticle properties. This concept is relevant in mediating nanoparticle delivery: while significant work has focused on employing PEG as a corona-mitigating coating (alongside others including zwitterionic coatings becoming further developed[94,440,523,571,572]), nanoparticles need not avoid all protein adsorption, merely adsorb

the “correct” proteins in the “correct” orientation for the desired function.[38,108,573–575] Future work establishing such design rules correlating surface coatings with appropriate adsorbed-protein profiles will be impactful toward predictable delivery outcomes. For sensing and imaging applications, the hybrid nano-bio construct design paradigm presented in developing the SARS-CoV-2 nanosensor can be expanded to create additional nanoparticle-corona architectures. This design strategy combines the molecular recognition capabilities of proteins to impart chemical specificity, together with the highly tunable and spatially localizable features of nanoparticles to serve as signal transducers. Rationally designed nano-bio constructs will be impactful for sensing and imaging fundamental studies, clinical diagnostics, and more. Future work will identify candidate sensing proteins with intrinsic nanoparticle adsorption affinities and optimize nano-bio linkages in the absence of such innate affinities.

10 References

(1) Alivisatos, P. The Use of Nanocrystals in Biological Detection. *Nature Biotechnology* **2004**, *22* (1), 47–52. https://doi.org/10.1038/nbt927.

(2) Bao, G.; Mitragotri, S.; Tong, S. Multifunctional Nanoparticles for Drug Delivery and Molecular Imaging. *Annual Review of Biomedical Engineering* **2013**, *15* (1), 253–282. https://doi.org/10.1146/annurev-bioeng-071812-152409.

(3) Batista, C. A. S.; Larson, R. G.; Kotov, N. A. Nonadditivity of Nanoparticle Interactions. *Science* **2015**, *350* (6257). https://doi.org/10.1126/science.1242477.

(4) Smith, B. R.; Gambhir, S. S. Nanomaterials for In Vivo Imaging. *Chem. Rev.* **2017**, *117* (3), 901–986. https://doi.org/10.1021/acs.chemrev.6b00073.

(5) Del Bonis-O'Donnell, J. T.; Chio, L.; Dorlhiac, G. F.; McFarlane, I. R.; Landry, M. P. Advances in Nanomaterials for Brain Microscopy. *Nano Res.* **2018**, *11* (10), 5144–5172. https://doi.org/10.1007/s12274-018-2145-2.

(6) Kirtane, A. R.; Verma, M.; Karandikar, P.; Furin, J.; Langer, R.; Traverso, G. Nanotechnology Approaches for Global Infectious Diseases. *Nature Nanotechnology* **2021**, 1–16. https://doi.org/10.1038/s41565-021-00866-8.

(7) Shin, M. D.; Shukla, S.; Chung, Y. H.; Beiss, V.; Chan, S. K.; Ortega-Rivera, O. A.; Wirth, D. M.; Chen, A.; Sack, M.; Pokorski, J. K.; Steinmetz, N. F. COVID-19 Vaccine Development and a Potential Nanomaterial Path Forward. *Nature Nanotechnology* **2020**, *15* (8), 646–655. https://doi.org/10.1038/s41565-020-0737-y.

(8) Alvarez, M. M.; Aizenberg, J.; Analoui, M.; Andrews, A. M.; Bisker, G.; Boyden, E. S.; Kamm, R. D.; Karp, J. M.; Mooney, D. J.; Oklu, R.; Peer, D.; Stolzoff, M.; Strano, M. S.; Trujillo-de Santiago, G.; Webster, T. J.; Weiss, P. S.; Khademhosseini, A. Emerging Trends in Micro- and Nanoscale Technologies in Medicine: From Basic Discoveries to Translation. *ACS Nano* **2017**, *11* (6), 5195–5214. https://doi.org/10.1021/acsnano.7b01493.

(9) Batty, C. J.; Bachelder, E. M.; Ainslie, K. M. Historical Perspective of Clinical Nano and Microparticle Formulations for Delivery of Therapeutics. *Trends in Molecular Medicine* **2021**. https://doi.org/10.1016/j.molmed.2021.04.002.

(10) Liu, Z.; Tabakman, S.; Welsher, K.; Dai, H. Carbon Nanotubes in Biology and Medicine: In Vitro and in Vivo Detection, Imaging and Drug Delivery. *Nano Res.* **2009**, *2* (2), 85–120. https://doi.org/10.1007/s12274-009-9009-8.

(11) Park, S.; Aalipour, A.; Vermesh, O.; Yu, J. H.; Gambhir, S. S. Towards Clinically Translatable in Vivo Nanodiagnostics. *Nature Reviews Materials* **2017**, *2* (5), 1–20. https://doi.org/10.1038/natrevmats.2017.14.

(12) Gloag, L.; Mehdipour, M.; Chen, D.; Tilley, R. D.; Gooding, J. J. Advances in the Application of Magnetic Nanoparticles for Sensing. *Advanced Materials* **2019**, *31* (48), 1904385. https://doi.org/10.1002/adma.201904385.

(13) Howes, P. D.; Chandrawati, R.; Stevens, M. M. Colloidal Nanoparticles as Advanced Biological Sensors. *Science* **2014**, *346* (6205). https://doi.org/10.1126/science.1247390.

(14) Mitchell, M. J.; Billingsley, M. M.; Haley, R. M.; Wechsler, M. E.; Peppas, N. A.; Langer, R. Engineering Precision Nanoparticles for Drug Delivery. *Nat Rev Drug Discov* **2020**. https://doi.org/10.1038/s41573-020-0090-8.

(15) Poon, W.; Kingston, B. R.; Ouyang, B.; Ngo, W.; Chan, W. C. W. A Framework for Designing Delivery Systems. *Nature Nanotechnology* **2020**, *15* (10), 819–829. https://doi.org/10.1038/s41565-020-0759-5.
(16) Al-Jamal, W. T.; Kostarelos, K. Liposomes: From a Clinically Established Drug Delivery System to a Nanoparticle Platform for Theranostic Nanomedicine. *Acc. Chem. Res.* **2011**, *44* (10), 1094–1104. https://doi.org/10.1021/ar200105p.
(17) Shi, J.; Kantoff, P. W.; Wooster, R.; Farokhzad, O. C. Cancer Nanomedicine: Progress, Challenges and Opportunities. *Nature Reviews Cancer* **2017**, *17* (1), 20–37. https://doi.org/10.1038/nrc.2016.108.
(18) Bangham, A. D.; Horne, R. W. Negative Staining of Phospholipids and Their Structural Modification by Surface-Active Agents as Observed in the Electron Microscope. *Journal of Molecular Biology* **1964**, *8* (5), 660-IN10. https://doi.org/10.1016/S0022-2836(64)80115-7.
(19) Krammer, F. SARS-CoV-2 Vaccines in Development. *Nature* **2020**, *586* (7830), 516–527. https://doi.org/10.1038/s41586-020-2798-3.
(20) Corbett, K. S.; Edwards, D. K.; Leist, S. R.; Abiona, O. M.; Boyoglu-Barnum, S.; Gillespie, R. A.; Himansu, S.; Schäfer, A.; Ziwawo, C. T.; DiPiazza, A. T.; Dinnon, K. H.; Elbashir, S. M.; Shaw, C. A.; Woods, A.; Fritch, E. J.; Martinez, D. R.; Bock, K. W.; Minai, M.; Nagata, B. M.; Hutchinson, G. B.; Wu, K.; Henry, C.; Bahl, K.; Garcia-Dominguez, D.; Ma, L.; Renzi, I.; Kong, W.-P.; Schmidt, S. D.; Wang, L.; Zhang, Y.; Phung, E.; Chang, L. A.; Loomis, R. J.; Altaras, N. E.; Narayanan, E.; Metkar, M.; Presnyak, V.; Liu, C.; Louder, M. K.; Shi, W.; Leung, K.; Yang, E. S.; West, A.; Gully, K. L.; Stevens, L. J.; Wang, N.; Wrapp, D.; Doria-Rose, N. A.; Stewart-Jones, G.; Bennett, H.; Alvarado, G. S.; Nason, M. C.; Ruckwardt, T. J.; McLellan, J. S.; Denison, M. R.; Chappell, J. D.; Moore, I. N.; Morabito, K. M.; Mascola, J. R.; Baric, R. S.; Carfi, A.; Graham, B. S. SARS-CoV-2 MRNA Vaccine Design Enabled by Prototype Pathogen Preparedness. *Nature* **2020**, *586* (7830), 567–571. https://doi.org/10.1038/s41586-020-2622-0.
(21) Jackson, L. A.; Anderson, E. J.; Rouphael, N. G.; Roberts, P. C.; Makhene, M.; Coler, R. N.; McCullough, M. P.; Chappell, J. D.; Denison, M. R.; Stevens, L. J.; Pruijssers, A. J.; McDermott, A.; Flach, B.; Doria-Rose, N. A.; Corbett, K. S.; Morabito, K. M.; O'Dell, S.; Schmidt, S. D.; Swanson, P. A.; Padilla, M.; Mascola, J. R.; Neuzil, K. M.; Bennett, H.; Sun, W.; Peters, E.; Makowski, M.; Albert, J.; Cross, K.; Buchanan, W.; Pikaart-Tautges, R.; Ledgerwood, J. E.; Graham, B. S.; Beigel, J. H. An MRNA Vaccine against SARS-CoV-2 — Preliminary Report. *New England Journal of Medicine* **2020**, *383* (20), 1920–1931. https://doi.org/10.1056/NEJMoa2022483.
(22) Mulligan, M. J.; Lyke, K. E.; Kitchin, N.; Absalon, J.; Gurtman, A.; Lockhart, S.; Neuzil, K.; Raabe, V.; Bailey, R.; Swanson, K. A.; Li, P.; Koury, K.; Kalina, W.; Cooper, D.; Fontes-Garfias, C.; Shi, P.-Y.; Türeci, Ö.; Tompkins, K. R.; Walsh, E. E.; Frenck, R.; Falsey, A. R.; Dormitzer, P. R.; Gruber, W. C.; Şahin, U.; Jansen, K. U. Phase I/II Study of COVID-19 RNA Vaccine BNT162b1 in Adults. *Nature* **2020**, *586* (7830), 589–593. https://doi.org/10.1038/s41586-020-2639-4.
(23) Polack, F. P.; Thomas, S. J.; Kitchin, N.; Absalon, J.; Gurtman, A.; Lockhart, S.; Perez, J. L.; Pérez Marc, G.; Moreira, E. D.; Zerbini, C.; Bailey, R.; Swanson, K. A.; Roychoudhury, S.; Koury, K.; Li, P.; Kalina, W. V.; Cooper, D.; Frenck, R. W.; Hammitt, L. L.; Türeci, Ö.; Nell, H.; Schaefer, A.; Ünal, S.; Tresnan, D. B.; Mather, S.; Dormitzer, P. R.; Şahin,

U.; Jansen, K. U.; Gruber, W. C. Safety and Efficacy of the BNT162b2 MRNA Covid-19 Vaccine. *New England Journal of Medicine* **2020**, *383* (27), 2603–2615. https://doi.org/10.1056/NEJMoa2034577.

(24) Barenholz, Y. (Chezy). Doxil® — The First FDA-Approved Nano-Drug: Lessons Learned. *Journal of Controlled Release* **2012**, *160* (2), 117–134. https://doi.org/10.1016/j.jconrel.2012.03.020.

(25) Blanco, E.; Shen, H.; Ferrari, M. Principles of Nanoparticle Design for Overcoming Biological Barriers to Drug Delivery. *Nat Biotechnol* **2015**, *33* (9), 941–951. https://doi.org/10.1038/nbt.3330.

(26) Bruchez, M.; Moronne, M.; Gin, P.; Weiss, S.; Alivisatos, A. P. Semiconductor Nanocrystals as Fluorescent Biological Labels. *Science* **1998**, *281* (5385), 2013–2016. https://doi.org/10.1126/science.281.5385.2013.

(27) Boghossian, A. A.; Zhang, J.; Barone, P. W.; Reuel, N. F.; Kim, J.-H.; Heller, D. A.; Ahn, J.-H.; Hilmer, A. J.; Rwei, A.; Arkalgud, J. R.; Zhang, C. T.; Strano, M. S. Near-Infrared Fluorescent Sensors Based on Single-Walled Carbon Nanotubes for Life Sciences Applications. *ChemSusChem* **2011**, *4* (7), 848–863. https://doi.org/10.1002/cssc.201100070.

(28) Saha, K.; Agasti, S. S.; Kim, C.; Li, X.; Rotello, V. M. Gold Nanoparticles in Chemical and Biological Sensing. *Chem. Rev.* **2012**, *112* (5), 2739–2779. https://doi.org/10.1021/cr2001178.

(29) Dresselhaus, M. S.; Dresselhaus, G.; Eklund, P. C. *Science of Fullerenes and Carbon Nanotubes: Their Properties and Applications*; Elsevier, 1996.

(30) Antonucci, A.; Kupis-Rozmysłowicz, J.; Boghossian, A. A. Noncovalent Protein and Peptide Functionalization of Single-Walled Carbon Nanotubes for Biodelivery and Optical Sensing Applications. *ACS Appl. Mater. Interfaces* **2017**, *9* (13), 11321–11331. https://doi.org/10.1021/acsami.7b00810.

(31) Chen, R. J.; Bangsaruntip, S.; Drouvalakis, K. A.; Kam, N. W. S.; Shim, M.; Li, Y.; Kim, W.; Utz, P. J.; Dai, H. Noncovalent Functionalization of Carbon Nanotubes for Highly Specific Electronic Biosensors. *PNAS* **2003**, *100* (9), 4984–4989. https://doi.org/10.1073/pnas.0837064100.

(32) Zhang, J.; Landry, M. P.; Barone, P. W.; Kim, J.-H.; Lin, S.; Ulissi, Z. W.; Lin, D.; Mu, B.; Boghossian, A. A.; Hilmer, A. J.; Rwei, A.; Hinckley, A. C.; Kruss, S.; Shandell, M. A.; Nair, N.; Blake, S.; Şen, F.; Şen, S.; Croy, R. G.; Li, D.; Yum, K.; Ahn, J.-H.; Jin, H.; Heller, D. A.; Essigmann, J. M.; Blankschtein, D.; Strano, M. S. Molecular Recognition Using Corona Phase Complexes Made of Synthetic Polymers Adsorbed on Carbon Nanotubes. *Nature Nanotechnology* **2013**, *8* (12), 959–968. https://doi.org/10.1038/nnano.2013.236.

(33) Barone, P. W.; Baik, S.; Heller, D. A.; Strano, M. S. Near-Infrared Optical Sensors Based on Single-Walled Carbon Nanotubes. *Nature Materials* **2005**, *4* (1), 86–92. https://doi.org/10.1038/nmat1276.

(34) O'Connell, M. J.; Bachilo, S. M.; Huffman, C. B.; Moore, V. C.; Strano, M. S.; Haroz, E. H.; Rialon, K. L.; Boul, P. J.; Noon, W. H.; Kittrell, C.; Ma, J.; Hauge, R. H.; Weisman, R. B.; Smalley, R. E. Band Gap Fluorescence from Individual Single-Walled Carbon Nanotubes. *Science* **2002**, *297* (5581), 593–596. https://doi.org/10.1126/science.1072631.

(35) Carlson, L. J.; Krauss, T. D. Photophysics of Individual Single-Walled Carbon Nanotubes. *Acc. Chem. Res.* **2008**, *41* (2), 235–243. https://doi.org/10.1021/ar700136v.

(36) Heller, D. A.; Baik, S.; Eurell, T. E.; Strano, M. S. Single-Walled Carbon Nanotube Spectroscopy in Live Cells: Towards Long-Term Labels and Optical Sensors. *Advanced Materials* **2005**, *17* (23), 2793–2799. https://doi.org/10.1002/adma.200500477.

(37) Dai, Q.; Bertleff-Zieschang, N.; Braunger, J. A.; Björnmalm, M.; Cortez-Jugo, C.; Caruso, F. Particle Targeting in Complex Biological Media. *Advanced Healthcare Materials* **2018**, *7* (1), 1700575. https://doi.org/10.1002/adhm.201700575.

(38) Pinals, R. L.; Chio, L.; Ledesma, F.; Landry, M. P. Engineering at the Nano-Bio Interface: Harnessing the Protein Corona towards Nanoparticle Design and Function. *Analyst* **2020**, *145* (15), 5090–5112. https://doi.org/10.1039/D0AN00633E.

(39) Bisker, G.; Dong, J.; Park, H. D.; Iverson, N. M.; Ahn, J.; Nelson, J. T.; Landry, M. P.; Kruss, S.; Strano, M. S. Protein-Targeted Corona Phase Molecular Recognition. *Nature Communications* **2016**, *7*, 10241. https://doi.org/10.1038/ncomms10241.

(40) Kruss, S.; Landry, M. P.; Vander Ende, E.; Lima, B. M. A.; Reuel, N. F.; Zhang, J.; Nelson, J.; Mu, B.; Hilmer, A.; Strano, M. Neurotransmitter Detection Using Corona Phase Molecular Recognition on Fluorescent Single-Walled Carbon Nanotube Sensors. *Journal of the American Chemical Society* **2014**, *136* (2), 713–724. https://doi.org/10.1021/ja410433b.

(41) Beyene, A. G.; Delevich, K.; Bonis-O'Donnell, J. T. D.; Piekarski, D. J.; Lin, W. C.; Thomas, A. W.; Yang, S. J.; Kosillo, P.; Yang, D.; Prounis, G. S.; Wilbrecht, L.; Landry, M. P. Imaging Striatal Dopamine Release Using a Nongenetically Encoded near Infrared Fluorescent Catecholamine Nanosensor. *Science Advances* **2019**, *5* (7), eaaw3108. https://doi.org/10.1126/sciadv.aaw3108.

(42) Beyene, A. G.; Alizadehmojarad, A. A.; Dorlhiac, G.; Goh, N.; Streets, A. M.; Král, P.; Vuković, L.; Landry, M. P. Ultralarge Modulation of Fluorescence by Neuromodulators in Carbon Nanotubes Functionalized with Self-Assembled Oligonucleotide Rings. *Nano Lett.* **2018**, *18* (11), 6995–7003. https://doi.org/10.1021/acs.nanolett.8b02937.

(43) Beyene, A. G.; McFarlane, I. R.; Pinals, R. L.; Landry, M. P. Stochastic Simulation of Dopamine Neuromodulation for Implementation of Fluorescent Neurochemical Probes in the Striatal Extracellular Space. *ACS Chem. Neurosci.* **2017**, *8* (10), 2275–2289. https://doi.org/10.1021/acschemneuro.7b00193.

(44) Kruss, S.; Salem, D. P.; Vuković, L.; Lima, B.; Vander Ende, E.; Boyden, E. S.; Strano, M. S. High-Resolution Imaging of Cellular Dopamine Efflux Using a Fluorescent Nanosensor Array. *Proceedings of the National Academy of Sciences* **2017**, *114* (8), 1789–1794. https://doi.org/10.1073/pnas.1613541114.

(45) Monopoli, M. P.; Åberg, C.; Salvati, A.; Dawson, K. A. Biomolecular Coronas Provide the Biological Identity of Nanosized Materials. *Nature Nanotechnology* **2012**, *7* (12), 779–786. https://doi.org/10.1038/nnano.2012.207.

(46) Nel, A. E.; Mädler, L.; Velegol, D.; Xia, T.; Hoek, E. M. V.; Somasundaran, P.; Klaessig, F.; Castranova, V.; Thompson, M. Understanding Biophysicochemical Interactions at the Nano–Bio Interface. *Nature Materials* **2009**, *8* (7), 543–557. https://doi.org/10.1038/nmat2442.

(47) Monopoli, M. P.; Walczyk, D.; Campbell, A.; Elia, G.; Lynch, I.; Baldelli Bombelli, F.; Dawson, K. A. Physical−Chemical Aspects of Protein Corona: Relevance to in Vitro and in Vivo Biological Impacts of Nanoparticles. *J. Am. Chem. Soc.* **2011**, *133* (8), 2525–2534. https://doi.org/10.1021/ja107583h.

(48) Cedervall, T.; Lynch, I.; Lindman, S.; Bergg\a ard, T.; Thulin, E.; Nilsson, H.; Dawson, K. A.; Linse, S. Understanding the Nanoparticle–Protein Corona Using Methods to Quantify Exchange Rates and Affinities of Proteins for Nanoparticles. *Proceedings of the National Academy of Sciences* **2007**, *104* (7), 2050–2055.

(49) Karajanagi, S. S.; Vertegel, A. A.; Kane, R. S.; Dordick, J. S. Structure and Function of Enzymes Adsorbed onto Single-Walled Carbon Nanotubes. *Langmuir* **2004**, *20* (26), 11594–11599. https://doi.org/10.1021/la047994h.

(50) Deng, Z. J.; Liang, M.; Monteiro, M.; Toth, I.; Minchin, R. F. Nanoparticle-Induced Unfolding of Fibrinogen Promotes Mac-1 Receptor Activation and Inflammation. *Nature Nanotechnology* **2011**, *6* (1), 39–44. https://doi.org/10.1038/nnano.2010.250.

(51) Aggarwal, P.; Hall, J. B.; McLeland, C. B.; Dobrovolskaia, M. A.; McNeil, S. E. Nanoparticle Interaction with Plasma Proteins as It Relates to Particle Biodistribution, Biocompatibility and Therapeutic Efficacy. *Advanced Drug Delivery Reviews* **2009**, *61* (6), 428–437. https://doi.org/10.1016/j.addr.2009.03.009.

(52) Owens, D. E.; Peppas, N. A. Opsonization, Biodistribution, and Pharmacokinetics of Polymeric Nanoparticles. *International Journal of Pharmaceutics* **2006**, *307* (1), 93–102. https://doi.org/10.1016/j.ijpharm.2005.10.010.

(53) Dutta, D.; Sundaram, S. K.; Teeguarden, J. G.; Riley, B. J.; Fifield, L. S.; Jacobs, J. M.; Addleman, S. R.; Kaysen, G. A.; Moudgil, B. M.; Weber, T. J. Adsorbed Proteins Influence the Biological Activity and Molecular Targeting of Nanomaterials. *Toxicol Sci* **2007**, *100* (1), 303–315. https://doi.org/10.1093/toxsci/kfm217.

(54) Gravely, M.; Safaee, M. M.; Roxbury, D. Biomolecular Functionalization of a Nanomaterial To Control Stability and Retention within Live Cells. *Nano Lett.* **2019**, *19* (9), 6203–6212. https://doi.org/10.1021/acs.nanolett.9b02267.

(55) Salvati, A.; Pitek, A. S.; Monopoli, M. P.; Prapainop, K.; Bombelli, F. B.; Hristov, D. R.; Kelly, P. M.; Åberg, C.; Mahon, E.; Dawson, K. A. Transferrin-Functionalized Nanoparticles Lose Their Targeting Capabilities When a Biomolecule Corona Adsorbs on the Surface. *Nature Nanotechnology* **2013**, *8* (2), 137–143. https://doi.org/10.1038/nnano.2012.237.

(56) Tenzer, S.; Docter, D.; Kuharev, J.; Musyanovych, A.; Fetz, V.; Hecht, R.; Schlenk, F.; Fischer, D.; Kiouptsi, K.; Reinhardt, C.; Landfester, K.; Schild, H.; Maskos, M.; Knauer, S. K.; Stauber, R. H. Rapid Formation of Plasma Protein Corona Critically Affects Nanoparticle Pathophysiology. *Nat Nanotechnol* **2013**, *8* (10), 772–781. https://doi.org/10.1038/nnano.2013.181.

(57) Röcker, C.; Pötzl, M.; Zhang, F.; Parak, W. J.; Nienhaus, G. U. A Quantitative Fluorescence Study of Protein Monolayer Formation on Colloidal Nanoparticles. *Nature Nanotechnology* **2009**, *4* (9), 577–580. https://doi.org/10.1038/nnano.2009.195.

(58) Lundqvist, M.; Stigler, J.; Elia, G.; Lynch, I.; Cedervall, T.; Dawson, K. A. Nanoparticle Size and Surface Properties Determine the Protein Corona with Possible Implications for Biological Impacts. *Proceedings of the National Academy of Sciences* **2008**, *105* (38), 14265–14270.

(59) Walkey, C. D.; Olsen, J. B.; Song, F.; Liu, R.; Guo, H.; Olsen, D. W. H.; Cohen, Y.; Emili, A.; Chan, W. C. W. Protein Corona Fingerprinting Predicts the Cellular Interaction of Gold and Silver Nanoparticles. *ACS Nano* **2014**, *8* (3), 2439–2455. https://doi.org/10.1021/nn406018q.

(60) Walkey, C. D.; Olsen, J. B.; Guo, H.; Emili, A.; Chan, W. C. W. Nanoparticle Size and Surface Chemistry Determine Serum Protein Adsorption and Macrophage Uptake. *J. Am. Chem. Soc.* **2012**, *134* (4), 2139–2147. https://doi.org/10.1021/ja2084338.

(61) Cai, R.; Ren, J.; Ji, Y.; Wang, Y.; Liu, Y.; Chen, Z.; Farhadi Sabet, Z.; Wu, X.; Lynch, I.; Chen, C. Corona of Thorns: The Surface Chemistry-Mediated Protein Corona Perturbs the Recognition and Immune Response of Macrophages. *ACS Appl. Mater. Interfaces* **2020**, *12* (2), 1997–2008. https://doi.org/10.1021/acsami.9b15910.

(62) Cox, A.; Andreozzi, P.; Dal Magro, R.; Fiordaliso, F.; Corbelli, A.; Talamini, L.; Chinello, C.; Raimondo, F.; Magni, F.; Tringali, M.; Krol, S.; Jacob Silva, P.; Stellacci, F.; Masserini, M.; Re, F. Evolution of Nanoparticle Protein Corona across the Blood–Brain Barrier. *ACS Nano* **2018**. https://doi.org/10.1021/acsnano.8b03500.

(63) Hadjidemetriou, M.; Al-Ahmady, Z.; Mazza, M.; Collins, R. F.; Dawson, K.; Kostarelos, K. In Vivo Biomolecule Corona around Blood-Circulating, Clinically Used and Antibody-Targeted Lipid Bilayer Nanoscale Vesicles. *ACS Nano* **2015**, *9* (8), 8142–8156. https://doi.org/10.1021/acsnano.5b03300.

(64) Kristensen, K.; Engel, T. B.; Stensballe, A.; Simonsen, J. B.; Andresen, T. L. The Hard Protein Corona of Stealth Liposomes Is Sparse. *Journal of Controlled Release* **2019**, *307*, 1–15. https://doi.org/10.1016/j.jconrel.2019.05.042.

(65) Klibanov, A. L.; Maruyama, K.; Torchilin, V. P.; Huang, L. Amphipathic Polyethyleneglycols Effectively Prolong the Circulation Time of Liposomes. *FEBS Letters* **1990**, *268* (1), 235–237. https://doi.org/10.1016/0014-5793(90)81016-H.

(66) Sacchetti, C.; Motamedchaboki, K.; Magrini, A.; Palmieri, G.; Mattei, M.; Bernardini, S.; Rosato, N.; Bottini, N.; Bottini, M. Surface Polyethylene Glycol Conformation Influences the Protein Corona of Polyethylene Glycol-Modified Single-Walled Carbon Nanotubes: Potential Implications on Biological Performance. *ACS Nano* **2013**, *7* (3), 1974–1989. https://doi.org/10.1021/nn400409h.

(67) Gal, N.; Schroffenegger, M.; Reimhult, E. Stealth Nanoparticles Grafted with Dense Polymer Brushes Display Adsorption of Serum Protein Investigated by Isothermal Titration Calorimetry. *J. Phys. Chem. B* **2018**, *122* (22), 5820–5834. https://doi.org/10.1021/acs.jpcb.8b02338.

(68) Wilhelm, S.; Tavares, A. J.; Dai, Q.; Ohta, S.; Audet, J.; Dvorak, H. F.; Chan, W. C. W. Analysis of Nanoparticle Delivery to Tumours. *Nature Reviews Materials* **2016**, *1* (5), 1–12. https://doi.org/10.1038/natrevmats.2016.14.

(69) He, H.; Liu, L.; Morin, E. E.; Liu, M.; Schwendeman, A. Survey of Clinical Translation of Cancer Nanomedicines—Lessons Learned from Successes and Failures. *Acc. Chem. Res.* **2019**, *52* (9), 2445–2461. https://doi.org/10.1021/acs.accounts.9b00228.

(70) Venditto, V. J.; Szoka, F. C. Cancer Nanomedicines: So Many Papers and so Few Drugs! *Adv Drug Deliv Rev* **2013**, *65* (1), 80–88. https://doi.org/10.1016/j.addr.2012.09.038.

(71) Rosenblum, D.; Joshi, N.; Tao, W.; Karp, J. M.; Peer, D. Progress and Challenges towards Targeted Delivery of Cancer Therapeutics. *Nature Communications* **2018**, *9* (1), 1410. https://doi.org/10.1038/s41467-018-03705-y.

(72) R. Findlay, M.; N. Freitas, D.; Mobed-Miremadi, M.; E. Wheeler, K. Machine Learning Provides Predictive Analysis into Silver Nanoparticle Protein Corona Formation from Physicochemical Properties. *Environmental Science: Nano* **2018**, *5* (1), 64–71. https://doi.org/10.1039/C7EN00466D.

(73) Perng, W.; Palui, G.; Wang, W.; Mattoussi, H. Elucidating the Role of Surface Coating in the Promotion or Prevention of Protein Corona around Quantum Dots. *Bioconjugate Chem.* **2019**, *30* (9), 2469–2480. https://doi.org/10.1021/acs.bioconjchem.9b00549.

(74) Stepien, G.; Moros, M.; Pérez-Hernández, M.; Monge, M.; Gutiérrez, L.; Fratila, R. M.; las Heras, M. de; Menao Guillén, S.; Puente Lanzarote, J. J.; Solans, C.; Pardo, J.; de la Fuente, J. M. Effect of Surface Chemistry and Associated Protein Corona on the Long-Term Biodegradation of Iron Oxide Nanoparticles In Vivo. *ACS Appl. Mater. Interfaces* **2018**, *10* (5), 4548–4560. https://doi.org/10.1021/acsami.7b18648.

(75) Zhu, Y.; Meng, T.; Tan, Y.; Yang, X.; Liu, Y.; Liu, X.; Yu, F.; Wen, L.; Dai, S.; Yuan, H.; Hu, F. Negative Surface Shielded Polymeric Micelles with Colloidal Stability for Intracellular Endosomal/Lysosomal Escape. *Mol. Pharmaceutics* **2018**, *15* (11), 5374–5386. https://doi.org/10.1021/acs.molpharmaceut.8b00842.

(76) Zhao, J.; Wu, S.; Qin, J.; Shi, D.; Wang, Y. Electrical-Charge-Mediated Cancer Cell Targeting via Protein Corona-Decorated Superparamagnetic Nanoparticles in a Simulated Physiological Environment. *ACS Appl. Mater. Interfaces* **2018**, *10* (49), 41986–41998. https://doi.org/10.1021/acsami.8b15098.

(77) Lai, W.; Wang, Q.; Li, L.; Hu, Z.; Chen, J.; Fang, Q. Interaction of Gold and Silver Nanoparticles with Human Plasma: Analysis of Protein Corona Reveals Specific Binding Patterns. *Colloids and Surfaces B: Biointerfaces* **2017**, *152*, 317–325. https://doi.org/10.1016/j.colsurfb.2017.01.037.

(78) Simonelli, F.; Rossi, G.; Monticelli, L. Role of Ligand Conformation on Nanoparticle–Protein Interactions. *J. Phys. Chem. B* **2019**, *123* (8), 1764–1769. https://doi.org/10.1021/acs.jpcb.8b11204.

(79) Lazarovits, J.; Chen, Y. Y.; Song, F.; Ngo, W.; Tavares, A. J.; Zhang, Y.-N.; Audet, J.; Tang, B.; Lin, Q.; Tleugabulova, M. C.; Wilhelm, S.; Krieger, J. R.; Mallevaey, T.; Chan, W. C. W. Synthesis of Patient-Specific Nanomaterials. *Nano Lett.* **2019**, *19* (1), 116–123. https://doi.org/10.1021/acs.nanolett.8b03434.

(80) Giulimondi, F.; Digiacomo, L.; Pozzi, D.; Palchetti, S.; Vulpis, E.; Capriotti, A. L.; Chiozzi, R. Z.; Laganà, A.; Amenitsch, H.; Masuelli, L.; Mahmoudi, M.; Screpanti, I.; Zingoni, A.; Caracciolo, G. Interplay of Protein Corona and Immune Cells Controls Blood Residency of Liposomes. *Nat Commun* **2019**, *10* (1), 3686. https://doi.org/10.1038/s41467-019-11642-7.

(81) Quach, Q. H.; Kah, J. C. Complement Activation by Gold Nanoparticles Passivated with Polyelectrolyte Ligands. *RSC Adv.* **2018**, *8* (12), 6616–6619. https://doi.org/10.1039/C7RA13325A.

(82) Pinals, R. L.; Yang, D.; Rosenberg, D. J.; Chaudhary, T.; Crothers, A. R.; Iavarone, A. T.; Hammel, M.; Landry, M. P. Quantitative Protein Corona Composition and Dynamics on Carbon Nanotubes in Biological Environments. *Angewandte Chemie International Edition* **2020**, *59* (52), 23668–23677. https://doi.org/10.1002/anie.202008175.

(83) Escamilla-Rivera, V.; Solorio-Rodriguez, A.; Uribe-Ramirez, M.; Lozano, O.; Lucas, S.; Chagolla-López, A.; Winkler, R.; De Vizcaya-Ruiz, A. Plasma Protein Adsorption on Fe_3O_4-PEG Nanoparticles Activates the Complement System and Induces an Inflammatory Response. *IJN* **2019**, *Volume 14*, 2055–2067. https://doi.org/10.2147/IJN.S192214.

(84) Lee, H. Effects of Nanoparticle Electrostatics and Protein–Protein Interactions on Corona Formation: Conformation and Hydrodynamics. *Small* **2020**, *16* (10), 1906598. https://doi.org/10.1002/smll.201906598.
(85) Warning, L. A.; Zhang, Q.; Baiyasi, R.; Landes, C. F.; Link, S. Nanoscale Surface-Induced Unfolding of Single Fibronectin Is Restricted by Serum Albumin Crowding. *J. Phys. Chem. Lett.* **2020**. https://doi.org/10.1021/acs.jpclett.9b03446.
(86) Mohammad-Beigi, H.; Hayashi, Y.; Zeuthen, C. M.; Eskandari, H.; Scavenius, C.; Juul-Madsen, K.; Vorup-Jensen, T.; Enghild, J. J.; Sutherland, D. S. Mapping and Identification of Soft Corona Proteins at Nanoparticles and Their Impact on Cellular Association. *bioRxiv* **2020**, 2020.02.05.924480. https://doi.org/10.1101/2020.02.05.924480.
(87) Wang, H.; Ma, R.; Nienhaus, K.; Nienhaus, G. U. Formation of a Monolayer Protein Corona around Polystyrene Nanoparticles and Implications for Nanoparticle Agglomeration. *Small* **2019**, *15* (22), 1900974. https://doi.org/10.1002/smll.201900974.
(88) Chen, D.; Parayath, N.; Ganesh, S.; Wang, W.; Amiji, M. The Role of Apolipoprotein- and Vitronectin-Enriched Protein Corona on Lipid Nanoparticles for *in Vivo* Targeted Delivery and Transfection of Oligonucleotides in Murine Tumor Models. *Nanoscale* **2019**, *11* (40), 18806–18824. https://doi.org/10.1039/C9NR05788A.
(89) Gupta, A.; Das, R.; Yesilbag Tonga, G.; Mizuhara, T.; Rotello, V. M. Charge-Switchable Nanozymes for Bioorthogonal Imaging of Biofilm-Associated Infections. *ACS Nano* **2018**, *12* (1), 89–94. https://doi.org/10.1021/acsnano.7b07496.
(90) Guo, P.; Liu, D.; Subramanyam, K.; Wang, B.; Yang, J.; Huang, J.; Auguste, D. T.; Moses, M. A. Nanoparticle Elasticity Directs Tumor Uptake. *Nat Commun* **2018**, *9* (1), 1–9. https://doi.org/10.1038/s41467-017-02588-9.
(91) Lee, J. C.; Donahue, N. D.; Mao, A. S.; Karim, A.; Komarneni, M.; Thomas, E. E.; Francek, E. R.; Yang, W.; Wilhelm, S. Exploring Maleimide-Based Nanoparticle Surface Engineering to Control Cellular Interactions. *ACS Appl. Nano Mater.* **2020**. https://doi.org/10.1021/acsanm.9b02541.
(92) Francia, V.; Montizaan, D.; Salvati, A. Interactions at the Cell Membrane and Pathways of Internalization of Nano-Sized Materials for Nanomedicine. *Beilstein J. Nanotechnol.* **2020**, *11* (1), 338–353. https://doi.org/10.3762/bjnano.11.25.
(93) Gafur, A.; Kristi, N.; Maruf, A.; Wang, G.; Ye, Z. Transforming Stealthy to Sticky Nanocarriers: A Potential Application for Tumor Therapy. *Biomater. Sci.* **2019**, *7* (9), 3581–3593. https://doi.org/10.1039/C9BM00724E.
(94) Affonso de Oliveira, J. F.; Scheffer, F. R.; Landis, R. F.; Teixeira Neto, É.; Rotello, V. M.; Cardoso, M. B. Dual Functionalization of Nanoparticles for Generating Corona-Free and Noncytotoxic Silica Nanoparticles. *ACS Appl. Mater. Interfaces* **2018**, *10* (49), 41917–41923. https://doi.org/10.1021/acsami.8b12351.
(95) Lu, X.; Xu, P.; Ding, H.-M.; Yu, Y.-S.; Huo, D.; Ma, Y.-Q. Tailoring the Component of Protein Corona via Simple Chemistry. *Nat Commun* **2019**, *10* (1), 4520. https://doi.org/10.1038/s41467-019-12470-5.
(96) Champanhac, C.; Simon, J.; Landfester, K.; Mailänder, V. Timing of Heparin Addition to the Biomolecular Corona Influences the Cellular Uptake of Nanocarriers. *Biomacromolecules* **2019**, *20* (10), 3724–3732. https://doi.org/10.1021/acs.biomac.9b00777.
(97) Zhou, H.; Fan, Z.; Li, P. Y.; Deng, J.; Arhontoulis, D. C.; Li, C. Y.; Bowne, W. B.; Cheng, H. Dense and Dynamic Polyethylene Glycol Shells Cloak Nanoparticles from Uptake by

Liver Endothelial Cells for Long Blood Circulation. *ACS Nano* **2018**, *12* (10), 10130–10141. https://doi.org/10.1021/acsnano.8b04947.

(98) Kong, L.; Chen, Q.; Campbell, F.; Snaar-Jagalska, E.; Kros, A. Light-Triggered Cancer Cell Specific Targeting and Liposomal Drug Delivery in a Zebrafish Xenograft Model. *Adv. Healthcare Mater.* **2020**, 1901489. https://doi.org/10.1002/adhm.201901489.

(99) Dancy, J. G.; Wadajkar, A. S.; Connolly, N. P.; Galisteo, R.; Ames, H. M.; Peng, S.; Tran, N. L.; Goloubeva, O. G.; Woodworth, G. F.; Winkles, J. A.; Kim, A. J. Decreased Nonspecific Adhesivity, Receptor-Targeted Therapeutic Nanoparticles for Primary and Metastatic Breast Cancer. *Science Advances* **2020**, *6* (3), eaax3931. https://doi.org/10.1126/sciadv.aax3931.

(100) Li, X.; Lu, C.; Xia, W.; Quan, G.; Huang, Y.; Bai, X.; Yu, F.; Xu, Q.; Qin, W.; Liu, D.; Pan, X. Poly(L-Glutamic Acid)-Based Brush Copolymers: Fabrication, Self-Assembly, and Evaluation as Efficient Nanocarriers for Cationic Protein Drug Delivery. *AAPS PharmSciTech* **2020**, *21* (3), 78. https://doi.org/10.1208/s12249-020-1624-4.

(101) Bertrand, N.; Grenier, P.; Mahmoudi, M.; Lima, E. M.; Appel, E. A.; Dormont, F.; Lim, J.-M.; Karnik, R.; Langer, R.; Farokhzad, O. C. Mechanistic Understanding of in Vivo Protein Corona Formation on Polymeric Nanoparticles and Impact on Pharmacokinetics. *Nat Commun* **2017**, *8* (1), 1–8. https://doi.org/10.1038/s41467-017-00600-w.

(102) Piloni, A.; Wong, C. K.; Chen, F.; Lord, M.; Walther, A.; Stenzel, M. H. Surface Roughness Influences the Protein Corona Formation of Glycosylated Nanoparticles and Alter Their Cellular Uptake. *Nanoscale* **2019**, *11* (48), 23259–23267. https://doi.org/10.1039/C9NR06835J.

(103) Gal, N.; Schroffenegger, M.; Reimhult, E. Stealth Nanoparticles Grafted with Dense Polymer Brushes Display Adsorption of Serum Protein Investigated by Isothermal Titration Calorimetry. *J. Phys. Chem. B* **2018**, *122* (22), 5820–5834. https://doi.org/10.1021/acs.jpcb.8b02338.

(104) Lima, T.; Bernfur, K.; Vilanova, M.; Cedervall, T. Understanding the Lipid and Protein Corona Formation on Different Sized Polymeric Nanoparticles. *Sci Rep* **2020**, *10* (1), 1129. https://doi.org/10.1038/s41598-020-57943-6.

(105) Shadmani, P.; Mehrafrooz, B.; Montazeri, A.; Naghdabadi, R. Protein Corona Impact on Nanoparticle-Cell Interactions: Toward an Energy-Based Model of Endocytosis. *J. Phys.: Condens. Matter* **2020**, *32* (11), 115101. https://doi.org/10.1088/1361-648X/ab5a14.

(106) Kari, O. K.; Ndika, J.; Parkkila, P.; Louna, A.; Lajunen, T.; Puustinen, A.; Viitala, T.; Alenius, H.; Urtti, A. In Situ Analysis of Liposome Hard and Soft Protein Corona Structure and Composition in a Single Label-Free Workflow. *Nanoscale* **2020**, *12* (3), 1728–1741. https://doi.org/10.1039/C9NR08186K.

(107) Yu, C.; Zhou, Q.; Xiao, F.; Li, Y.; Hu, H.; Wan, Y.; Li, Z.; Yang, X. Enhancing Doxorubicin Delivery toward Tumor by Hydroxyethyl Starch- *g* -Polylactide Partner Nanocarriers. *ACS Appl. Mater. Interfaces* **2017**, *9* (12), 10481–10493. https://doi.org/10.1021/acsami.7b00048.

(108) Oh, J. Y.; Kim, H. S.; Palanikumar, L.; Go, E. M.; Jana, B.; Park, S. A.; Kim, H. Y.; Kim, K.; Seo, J. K.; Kwak, S. K.; Kim, C.; Kang, S.; Ryu, J.-H. Cloaking Nanoparticles with Protein Corona Shield for Targeted Drug Delivery. *Nature Communications* **2018**, *9* (1), 4548. https://doi.org/10.1038/s41467-018-06979-4.

(109) Ho, Y. T.; Azman, N. 'Ain; Loh, F. W. Y.; Ong, G. K. T.; Engudar, G.; Kriz, S. A.; Kah, J. C. Y. Protein Corona Formed from Different Blood Plasma Proteins Affects the

Colloidal Stability of Nanoparticles Differently. *Bioconjugate Chem.* **2018**, *29* (11), 3923–3934. https://doi.org/10.1021/acs.bioconjchem.8b00743.

(110) Naidu, P. S. R.; Denham, E.; Bartlett, C. A.; McGonigle, T.; Taylor, N. L.; Norret, M.; Smith, Nicole. M.; Dunlop, S. A.; Iyer, K. S.; Fitzgerald, M. Protein Corona Formation Moderates the Release Kinetics of Ion Channel Antagonists from Transferrin-Functionalized Polymeric Nanoparticles. *RSC Adv.* **2020**, *10* (5), 2856–2869. https://doi.org/10.1039/C9RA09523C.

(111) Curtis, C.; Toghani, D.; Wong, B.; Nance, E. Colloidal Stability as a Determinant of Nanoparticle Behavior in the Brain. *Colloids and Surfaces B: Biointerfaces* **2018**, *170*, 673–682. https://doi.org/10.1016/j.colsurfb.2018.06.050.

(112) Visalakshan, R. M.; MacGregor, M. N.; Sasidharan, S.; Ghazaryan, A.; Mierczynska-Vasilev, A. M.; Morsbach, S.; Mailänder, V.; Landfester, K.; Hayball, J. D.; Vasilev, K. Biomaterial Surface Hydrophobicity-Mediated Serum Protein Adsorption and Immune Responses. *ACS Appl. Mater. Interfaces* **2019**, *11* (31), 27615–27623. https://doi.org/10.1021/acsami.9b09900.

(113) Wang, X.; Wang, M.; Lei, R.; Zhu, S. F.; Zhao, Y.; Chen, C. Chiral Surface of Nanoparticles Determines the Orientation of Adsorbed Transferrin and Its Interaction with Receptors. *ACS Nano* **2017**, *11* (5), 4606–4616. https://doi.org/10.1021/acsnano.7b00200.

(114) Palomba, R.; Palange, A. L.; Rizzuti, I. F.; Ferreira, M.; Cervadoro, A.; Barbato, M. G.; Canale, C.; Decuzzi, P. Modulating Phagocytic Cell Sequestration by Tailoring Nanoconstruct Softness. *ACS Nano* **2018**, *12* (2), 1433–1444. https://doi.org/10.1021/acsnano.7b07797.

(115) Anselmo, A. C.; Mitragotri, S. Impact of Particle Elasticity on Particle-Based Drug Delivery Systems. *Advanced Drug Delivery Reviews* **2017**, *108*, 51–67. https://doi.org/10.1016/j.addr.2016.01.007.

(116) Raoufi, M.; Hajipour, M. J.; Kamali Shahri, S. M.; Schoen, I.; Linn, U.; Mahmoudi, M. Probing Fibronectin Conformation on a Protein Corona Layer around Nanoparticles. *Nanoscale* **2018**, *10* (3), 1228–1233. https://doi.org/10.1039/C7NR06970G.

(117) Francia, V.; Yang, K.; Deville, S.; Reker-Smit, C.; Nelissen, I.; Salvati, A. Corona Composition Can Affect the Mechanisms Cells Use to Internalize Nanoparticles. *ACS Nano* **2019**, *13* (10), 11107–11121. https://doi.org/10.1021/acsnano.9b03824.

(118) Pinals, R. L.; Yang, D.; Lui, A.; Cao, W.; Landry, M. P. Corona Exchange Dynamics on Carbon Nanotubes by Multiplexed Fluorescence Monitoring. *J. Am. Chem. Soc.* **2020**, *142* (3), 1254–1264. https://doi.org/10.1021/jacs.9b09617.

(119) Weiss, A. C. G.; Kempe, K.; Förster, S.; Caruso, F. Microfluidic Examination of the "Hard" Biomolecular Corona Formed on Engineered Particles in Different Biological Milieu. *Biomacromolecules* **2018**, *19* (7), 2580–2594. https://doi.org/10.1021/acs.biomac.8b00196.

(120) Chen, F.; Wang, G.; Griffin, J. I.; Brenneman, B.; Banda, N. K.; Holers, V. M.; Backos, D. S.; Wu, L.; Moghimi, S. M.; Simberg, D. Complement Proteins Bind to Nanoparticle Protein Corona and Undergo Dynamic Exchange *in Vivo*. *Nature Nanotechnology* **2017**, *12* (4), 387–393. https://doi.org/10.1038/nnano.2016.269.

(121) Rodriguez-Quijada, C.; de Puig, H.; Sánchez-Purrà, M.; Yelleswarapu, C.; Evans, J. J.; Celli, J. P.; Hamad-Schifferli, K. Protease Degradation of Protein Coronas and Its Impact on Cancer Cells and Drug Payload Release. *ACS Appl. Mater. Interfaces* **2019**, *11* (16), 14588–14596. https://doi.org/10.1021/acsami.9b00928.

(122) Mahmoudi, M. Debugging Nano–Bio Interfaces: Systematic Strategies to Accelerate Clinical Translation of Nanotechnologies. *Trends in Biotechnology* **2018**, *36* (8), 755–769. https://doi.org/10.1016/j.tibtech.2018.02.014.
(123) Wang, A.; Yang, T.; Fan, W.; Yang, Y.; Zhu, Q.; Guo, S.; Zhu, C.; Yuan, Y.; Zhang, T.; Gan, Y. Protein Corona Liposomes Achieve Efficient Oral Insulin Delivery by Overcoming Mucus and Epithelial Barriers. *Adv. Healthcare Mater.* **2019**, *8* (12), 1801123. https://doi.org/10.1002/adhm.201801123.
(124) Nance, E. Brain-Penetrating Nanoparticles for Analysis of the Brain Microenvironment. In *Biomedical Nanotechnology*; Methods in Molecular Biology; Humana Press, New York, NY, 2017; pp 91–104. https://doi.org/10.1007/978-1-4939-6840-4_6.
(125) Reza Sepand, M.; Ghavami, M.; Zanganeh, S.; Stacks, S.; Ghasemi, F.; Montazeri, H.; Corbo, C.; Derakhshankhah, H.; Nasser Ostad, S.; Hossein Ghahremani, M.; Mahmoudi, M. Impact of Plasma Concentration of Transferrin on Targeting Capacity of Nanoparticles. *Nanoscale* **2020**. https://doi.org/10.1039/C9NR08784B.
(126) Tonigold, M.; Simon, J.; Estupiñán, D.; Kokkinopoulou, M.; Reinholz, J.; Kintzel, U.; Kaltbeitzel, A.; Renz, P.; Domogalla, M. P.; Steinbrink, K.; Lieberwirth, I.; Crespy, D.; Landfester, K.; Mailänder, V. Pre-Adsorption of Antibodies Enables Targeting of Nanocarriers despite a Biomolecular Corona. *Nature Nanotechnology* **2018**, *13* (9), 862–869. https://doi.org/10.1038/s41565-018-0171-6.
(127) Piao, J.-G.; Gao, F.; Li, Y.; Yu, L.; Liu, D.; Tan, Z.-B.; Xiong, Y.; Yang, L.; You, Y.-Z. PH-Sensitive Zwitterionic Coating of Gold Nanocages Improves Tumor Targeting and Photothermal Treatment Efficacy. *Nano Res.* **2018**, *11* (6), 3193–3204. https://doi.org/10.1007/s12274-017-1736-7.
(128) Koide, R.; Nishimura, S.-I. Antiadhesive Nanosomes Facilitate Targeting of the Lysosomal GlcNAc Salvage Pathway through Derailed Cancer Endocytosis. *Angew. Chem. Int. Ed.* **2019**, *58* (41), 14513–14518. https://doi.org/10.1002/anie.201907778.
(129) Cox, A.; Andreozzi, P.; Dal Magro, R.; Fiordaliso, F.; Corbelli, A.; Talamini, L.; Chinello, C.; Raimondo, F.; Magni, F.; Tringali, M.; Krol, S.; Jacob Silva, P.; Stellacci, F.; Masserini, M.; Re, F. Evolution of Nanoparticle Protein Corona across the Blood–Brain Barrier. *ACS Nano* **2018**, *12* (7), 7292–7300. https://doi.org/10.1021/acsnano.8b03500.
(130) Naidu, P. S. R.; Gavriel, N.; Gray, C. G. G.; Bartlett, C. A.; Toomey, L. M.; Kretzmann, J. A.; Patalwala, D.; McGonigle, T.; Denham, E.; Hee, C.; Ho, D.; Taylor, N. L.; Norret, M.; Smith, N. M.; Dunlop, S. A.; Iyer, K. S.; Fitzgerald, M. Elucidating the Inability of Functionalized Nanoparticles to Cross the Blood–Brain Barrier and Target Specific Cells in Vivo. *ACS Appl. Mater. Interfaces* **2019**, *11* (25), 22085–22095. https://doi.org/10.1021/acsami.9b01356.
(131) Palchetti, S.; Pozzi, D.; Capriotti, A. L.; Barbera, G. L.; Chiozzi, R. Z.; Digiacomo, L.; Peruzzi, G.; Caracciolo, G.; Laganà, A. Influence of Dynamic Flow Environment on Nanoparticle-Protein Corona: From Protein Patterns to Uptake in Cancer Cells. *Colloids and Surfaces B: Biointerfaces* **2017**, *153*, 263–271. https://doi.org/10.1016/j.colsurfb.2017.02.037.
(132) Corbo, C.; Molinaro, R.; Taraballi, F.; Toledano Furman, N. E.; Hartman, K. A.; Sherman, M. B.; De Rosa, E.; Kirui, D. K.; Salvatore, F.; Tasciotti, E. Unveiling the in Vivo Protein Corona of Circulating Leukocyte-like Carriers. *ACS Nano* **2017**, *11* (3), 3262–3273. https://doi.org/10.1021/acsnano.7b00376.

(133) Zhang, H.; Wu, T.; Yu, W.; Ruan, S.; He, Q.; Gao, H. Ligand Size and Conformation Affect the Behavior of Nanoparticles Coated with in Vitro and in Vivo Protein Corona. *ACS Appl. Mater. Interfaces* **2018**, *10* (10), 9094–9103. https://doi.org/10.1021/acsami.7b16096.

(134) Wang, C.; Wang, Z.; Dong, L. Translating Current Bioanalytical Techniques for Studying Corona Activity. *Trends in Biotechnology* **2018**. https://doi.org/10.1016/j.tibtech.2018.02.016.

(135) Silvestri, A.; Di Silvio, D.; Llarena, I.; Murray, R. A.; Marelli, M.; Lay, L.; Polito, L.; Moya, S. E. Influence of Surface Coating on the Intracellular Behaviour of Gold Nanoparticles: A Fluorescence Correlation Spectroscopy Study. *Nanoscale* **2017**, *9* (38), 14730–14739. https://doi.org/10.1039/C7NR04640E.

(136) Yeo, E. L. L.; Thong, P. S. P.; Soo, K. C.; Kah, J. C. Y. Protein Corona in Drug Delivery for Multimodal Cancer Therapy in Vivo. *Nanoscale* **2018**, *10* (5), 2461–2472. https://doi.org/10.1039/C7NR08509E.

(137) Meng, Q.-F.; Cheng, Y.-X.; Huang, Q.; Zan, M.; Xie, W.; Sun, Y.; Li, R.; Wei, X.; Guo, S.-S.; Zhao, X.-Z.; Rao, L.; Liu, W. Biomimetic Immunomagnetic Nanoparticles with Minimal Nonspecific Biomolecule Adsorption for Enhanced Isolation of Circulating Tumor Cells. *ACS Appl. Mater. Interfaces* **2019**, *11* (32), 28732–28739. https://doi.org/10.1021/acsami.9b10318.

(138) Mout, R.; Yesilbag Tonga, G.; Wang, L.-S.; Ray, M.; Roy, T.; Rotello, V. M. Programmed Self-Assembly of Hierarchical Nanostructures through Protein–Nanoparticle Coengineering. *ACS Nano* **2017**, *11* (4), 3456–3462. https://doi.org/10.1021/acsnano.6b07258.

(139) Carril, M.; Padro, D.; del Pino, P.; Carrillo-Carrion, C.; Gallego, M.; Parak, W. J. In Situ Detection of the Protein Corona in Complex Environments. *Nat Commun* **2017**, *8* (1), 1542. https://doi.org/10.1038/s41467-017-01826-4.

(140) Herda, L. M.; Hristov, D. R.; Lo Giudice, M. C.; Polo, E.; Dawson, K. A. Mapping of Molecular Structure of the Nanoscale Surface in Bionanoparticles. *J. Am. Chem. Soc.* **2017**, *139* (1), 111–114. https://doi.org/10.1021/jacs.6b12297.

(141) Fukuda, R.; Umeyama, T.; Tsujimoto, M.; Ishidate, F.; Tanaka, T.; Kataura, H.; Imahori, H.; Murakami, T. Sustained Photodynamic Effect of Single Chirality-Enriched Single-Walled Carbon Nanotubes. *Carbon* **2020**, *161*, 718–725. https://doi.org/10.1016/j.carbon.2020.02.002.

(142) Di Giosia, M.; Valle, F.; Cantelli, A.; Bottoni, A.; Zerbetto, F.; Fasoli, E.; Calvaresi, M. High-Throughput Virtual Screening to Rationally Design Protein - Carbon Nanotube Interactions. Identification and Preparation of Stable Water Dispersions of Protein - Carbon Nanotube Hybrids and Efficient Design of New Functional Materials. *Carbon* **2019**, *147*, 70–82. https://doi.org/10.1016/j.carbon.2019.02.043.

(143) Zeng, X.; Sun, J.; Li, S.; Shi, J.; Gao, H.; Leong, W. S.; Wu, Y.; Li, M.; Liu, C.; Li, P.; Kong, J.; Wu, Y.-Z.; Nie, G.; Fu, Y.; Zhang, G. Blood-Triggered Generation of Platinum Nanoparticle Functions as an Anti-Cancer Agent. *Nat Commun* **2020**, *11* (1), 1–12. https://doi.org/10.1038/s41467-019-14131-z.

(144) Kokkinopoulou, M.; Simon, J.; Landfester, K.; Mailänder, V.; Lieberwirth, I. Visualization of the Protein Corona: Towards a Biomolecular Understanding of Nanoparticle-Cell-Interactions. *Nanoscale* **2017**, *9* (25), 8858–8870. https://doi.org/10.1039/C7NR02977B.

(145) Zhang, W.; Meckes, B.; Mirkin, C. A. Spherical Nucleic Acids with Tailored and Active Protein Coronae. *ACS Cent. Sci.* **2019**, *5* (12), 1983–1990. https://doi.org/10.1021/acscentsci.9b01105.
(146) Weber, C.; Simon, J.; Mailänder, V.; Morsbach, S.; Landfester, K. Preservation of the Soft Protein Corona in Distinct Flow Allows Identification of Weakly Bound Proteins. *Acta Biomaterialia* **2018**, *76*, 217–224. https://doi.org/10.1016/j.actbio.2018.05.057.
(147) Dal Magro, R.; Albertini, B.; Beretta, S.; Rigolio, R.; Donzelli, E.; Chiorazzi, A.; Ricci, M.; Blasi, P.; Sancini, G. Artificial Apolipoprotein Corona Enables Nanoparticle Brain Targeting. *Nanomedicine: Nanotechnology, Biology and Medicine* **2018**, *14* (2), 429–438. https://doi.org/10.1016/j.nano.2017.11.008.
(148) Perera, Y. R.; Hill, R. A.; Fitzkee, N. C. Protein Interactions with Nanoparticle Surfaces: Highlighting Solution NMR Techniques. *Israel Journal of Chemistry* **2019**, *59* (11–12), 962–979. https://doi.org/10.1002/ijch.201900080.
(149) Ceccon, A.; Schmidt, T.; Tugarinov, V.; Kotler, S. A.; Schwieters, C. D.; Clore, G. M. Interaction of Huntingtin Exon-1 Peptides with Lipid-Based Micellar Nanoparticles Probed by Solution NMR and Q-Band Pulsed EPR. *J. Am. Chem. Soc.* **2018**, *140* (20), 6199–6202. https://doi.org/10.1021/jacs.8b02619.
(150) Kouser, L.; Paudyal, B.; Kaur, A.; Stenbeck, G.; Jones, L. A.; Abozaid, S. M.; Stover, C. M.; Flahaut, E.; Sim, R. B.; Kishore, U. Human Properdin Opsonizes Nanoparticles and Triggers a Potent Pro-Inflammatory Response by Macrophages without Involving Complement Activation. *Front. Immunol.* **2018**, *9*, 131. https://doi.org/10.3389/fimmu.2018.00131.
(151) Zhang, Y.; Wu, J. L. Y.; Lazarovits, J.; Chan, W. C. W. An Analysis of the Binding Function and Structural Organization of the Protein Corona. *J. Am. Chem. Soc.* **2020**, *142* (19), 8827–8836. https://doi.org/10.1021/jacs.0c01853.
(152) Simon, J.; Müller, L. K.; Kokkinopoulou, M.; Lieberwirth, I.; Morsbach, S.; Landfester, K.; Mailänder, V. Exploiting the Biomolecular Corona: Pre-Coating of Nanoparticles Enables Controlled Cellular Interactions. *Nanoscale* **2018**, *10* (22), 10731–10739. https://doi.org/10.1039/C8NR03331E.
(153) Prozeller, D.; Morsbach, S.; Landfester, K. Isothermal Titration Calorimetry as a Complementary Method for Investigating Nanoparticle–Protein Interactions. *Nanoscale* **2019**, *11* (41), 19265–19273. https://doi.org/10.1039/C9NR05790K.
(154) Takeuchi, T.; Kitayama, Y.; Sasao, R.; Yamada, T.; Toh, K.; Matsumoto, Y.; Kataoka, K. Molecularly Imprinted Nanogels Acquire Stealth In Situ by Cloaking Themselves with Native Dysopsonic Proteins. *Angew. Chem. Int. Ed.* **2017**, *56* (25), 7088–7092. https://doi.org/10.1002/anie.201700647.
(155) Park, J.; Park, J. E.; Hedrick, V. E.; Wood, K. V.; Bonham, C.; Lee, W.; Yeo, Y. A Comparative In Vivo Study of Albumin-Coated Paclitaxel Nanocrystals and Abraxane. *Small* **2018**, *14* (16), 1703670. https://doi.org/10.1002/smll.201703670.
(156) Feiner-Gracia, N.; Beck, M.; Pujals, S.; Tosi, S.; Mandal, T.; Buske, C.; Linden, M.; Albertazzi, L. Super-Resolution Microscopy Unveils Dynamic Heterogeneities in Nanoparticle Protein Corona. *Small* **2017**, *13* (41), 1701631. https://doi.org/10.1002/smll.201701631.
(157) Zhao, L.; Zhao, L.; Li, H.; Sun, P.; Wu, J.; Li, K.; Hu, S.; Wang, X.; Pu, Q. Facile Evaluation of Nanoparticle–Protein Interaction Based on Charge Neutralization with

Pulsed Streaming Potential Measurement. *Anal. Chem.* **2019**, *91* (24), 15670–15677. https://doi.org/10.1021/acs.analchem.9b03778.
(158) Horbett, T. A. Fibrinogen Adsorption to Biomaterials. *Journal of Biomedical Materials Research Part A* **2018**, *0* (ja). https://doi.org/10.1002/jbm.a.36460.
(159) Milani, S.; Baldelli Bombelli, F.; Pitek, A. S.; Dawson, K. A.; Rädler, J. Reversible versus Irreversible Binding of Transferrin to Polystyrene Nanoparticles: Soft and Hard Corona. *ACS Nano* **2012**, *6* (3), 2532–2541. https://doi.org/10.1021/nn204951s.
(160) Monopoli, M. P.; Åberg, C.; Salvati, A.; Dawson, K. A. Biomolecular Coronas Provide the Biological Identity of Nanosized Materials. *Nature Nanotechnology* **2012**, *7* (12), 779–786. https://doi.org/10.1038/nnano.2012.207.
(161) Latour, R. A. The Langmuir Isotherm: A Commonly Applied but Misleading Approach for the Analysis of Protein Adsorption Behavior. *J. Biomed. Mater. Res.* **2015**, *103* (3), 949–958. https://doi.org/10.1002/jbm.a.35235.
(162) Casalini, T.; Limongelli, V.; Schmutz, M.; Som, C.; Jordan, O.; Wick, P.; Borchard, G.; Perale, G. Molecular Modeling for Nanomaterial–Biology Interactions: Opportunities, Challenges, and Perspectives. *Front. Bioeng. Biotechnol.* **2019**, *7*. https://doi.org/10.3389/fbioe.2019.00268.
(163) Zhdanov, V. P. Formation of a Protein Corona around Nanoparticles. *Current Opinion in Colloid & Interface Science* **2019**, *41*, 95–103. https://doi.org/10.1016/j.cocis.2018.12.002.
(164) Malaspina, D. C.; Pérez-Fuentes, L.; Drummond, C.; Bastos-González, D.; Faraudo, J. Protein-Surface Interactions at the Nanoscale: Atomistic Simulations with Implicit Solvent Models. *Current Opinion in Colloid & Interface Science* **2019**, *41*, 40–49. https://doi.org/10.1016/j.cocis.2018.11.005.
(165) Brancolini, G.; Bellucci, L.; Maschio, M. C.; Di Felice, R.; Corni, S. The Interaction of Peptides and Proteins with Nanostructures Surfaces: A Challenge for Nanoscience. *Current Opinion in Colloid & Interface Science* **2019**, *41*, 86–94. https://doi.org/10.1016/j.cocis.2018.12.003.
(166) Brancolini, G.; Lopez, H.; Corni, S.; Tozzini, V. Low-Resolution Models for the Interaction Dynamics of Coated Gold Nanoparticles with B2-Microglobulin. *International Journal of Molecular Sciences* **2019**, *20* (16), 3866. https://doi.org/10.3390/ijms20163866.
(167) Tavanti, F.; Pedone, A.; Menziani, M. C. Multiscale Molecular Dynamics Simulation of Multiple Protein Adsorption on Gold Nanoparticles. *International Journal of Molecular Sciences* **2019**, *20* (14), 3539. https://doi.org/10.3390/ijms20143539.
(168) Correa, S.; Boehnke, N.; Barberio, A. E.; Deiss-Yehiely, E.; Shi, A.; Oberlton, B.; Smith, S. G.; Zervantonakis, I.; Dreaden, E. C.; Hammond, P. T. Tuning Nanoparticle Interactions with Ovarian Cancer through Layer-by-Layer Modification of Surface Chemistry. *ACS Nano* **2020**, *14* (2), 2224–2237. https://doi.org/10.1021/acsnano.9b09213.
(169) Cedervall, T.; Lynch, I.; Foy, M.; Berggård, T.; Donnelly, S. C.; Cagney, G.; Linse, S.; Dawson, K. A. Detailed Identification of Plasma Proteins Adsorbed on Copolymer Nanoparticles. *Angewandte Chemie International Edition* **2007**, *46* (30), 5754–5756. https://doi.org/10.1002/anie.200700465.
(170) Costa, P. M.; Bourgognon, M.; Wang, J. T.-W.; Al-Jamal, K. T. Functionalised Carbon Nanotubes: From Intracellular Uptake and Cell-Related Toxicity to Systemic Brain Delivery. *Journal of Controlled Release* **2016**, *241*, 200–219. https://doi.org/10.1016/j.jconrel.2016.09.033.

(171) Galassi, T. V.; Jena, P. V.; Shah, J.; Ao, G.; Molitor, E.; Bram, Y.; Frankel, A.; Park, J.; Jessurun, J.; Ory, D. S.; Haimovitz-Friedman, A.; Roxbury, D.; Mittal, J.; Zheng, M.; Schwartz, R. E.; Heller, D. A. An Optical Nanoreporter of Endolysosomal Lipid Accumulation Reveals Enduring Effects of Diet on Hepatic Macrophages in Vivo. *Science Translational Medicine* **2018**, *10* (461). https://doi.org/10.1126/scitranslmed.aar2680.

(172) Iverson, N. M.; Barone, P. W.; Shandell, M.; Trudel, L. J.; Sen, S.; Sen, F.; Ivanov, V.; Atolia, E.; Farias, E.; McNicholas, T. P.; Reuel, N.; Parry, N. M. A.; Wogan, G. N.; Strano, M. S. In Vivo Biosensing via Tissue-Localizable near-Infrared-Fluorescent Single-Walled Carbon Nanotubes. *Nature Nanotechnology* **2013**, *8* (11), 873–880. https://doi.org/10.1038/nnano.2013.222.

(173) Schöttler, S.; Becker, G.; Winzen, S.; Steinbach, T.; Mohr, K.; Landfester, K.; Mailänder, V.; Wurm, F. R. Protein Adsorption Is Required for Stealth Effect of Poly(Ethylene Glycol)- and Poly(Phosphoester)-Coated Nanocarriers. *Nature Nanotechnology* **2016**, *11* (4), 372–377. https://doi.org/10.1038/nnano.2015.330.

(174) Godin, A. G.; Varela, J. A.; Gao, Z.; Danné, N.; Dupuis, J. P.; Lounis, B.; Groc, L.; Cognet, L. Single-Nanotube Tracking Reveals the Nanoscale Organization of the Extracellular Space in the Live Brain. *Nature Nanotechnology* **2016**, *12* (3), 238–243. https://doi.org/10.1038/nnano.2016.248.

(175) Hong, G.; Diao, S.; Chang, J.; Antaris, A. L.; Chen, C.; Zhang, B.; Zhao, S.; Atochin, D. N.; Huang, P. L.; Andreasson, K. I.; Kuo, C. J.; Dai, H. Through-Skull Fluorescence Imaging of the Brain in a New near-Infrared Window. *Nature Photonics* **2014**, *8* (9), 723–730. https://doi.org/10.1038/nphoton.2014.166.

(176) Dinarvand, M.; Neubert, E.; Meyer, D.; Selvaggio, G.; Mann, F. A.; Erpenbeck, L.; Kruss, S. Near-Infrared Imaging of Serotonin Release from Cells with Fluorescent Nanosensors. *Nano Lett.* **2019**. https://doi.org/10.1021/acs.nanolett.9b02865.

(177) Salvador-Morales, C.; Flahaut, E.; Sim, E.; Sloan, J.; H. Green, M. L.; Sim, R. B. Complement Activation and Protein Adsorption by Carbon Nanotubes. *Molecular Immunology* **2006**, *43* (3), 193–201. https://doi.org/10.1016/j.molimm.2005.02.006.

(178) Pondman, K. M.; Sobik, M.; Nayak, A.; Tsolaki, A. G.; Jäkel, A.; Flahaut, E.; Hampel, S.; Ten Haken, B.; Sim, R. B.; Kishore, U. Complement Activation by Carbon Nanotubes and Its Influence on the Phagocytosis and Cytokine Response by Macrophages. *Nanomedicine* **2014**, *10* (6), 1287–1299. https://doi.org/10.1016/j.nano.2014.02.010.

(179) Lu, N.; Sui, Y.; Tian, R.; Peng, Y.-Y. Adsorption of Plasma Proteins on Single-Walled Carbon Nanotubes Reduced Cytotoxicity and Modulated Neutrophil Activation. *Chem. Res. Toxicol.* **2018**, *31* (10), 1061–1068. https://doi.org/10.1021/acs.chemrestox.8b00141.

(180) Ge, C.; Du, J.; Zhao, L.; Wang, L.; Liu, Y.; Li, D.; Yang, Y.; Zhou, R.; Zhao, Y.; Chai, Z.; others. Binding of Blood Proteins to Carbon Nanotubes Reduces Cytotoxicity. *Proceedings of the National Academy of Sciences* **2011**, *108* (41), 16968–16973.

(181) UniProt: A Worldwide Hub of Protein Knowledge. *Nucleic Acids Res* **2019**, *47* (D1), D506–D515. https://doi.org/10.1093/nar/gky1049.

(182) Wertz, C. F.; Santore, M. M. Effect of Surface Hydrophobicity on Adsorption and Relaxation Kinetics of Albumin and Fibrinogen: Single-Species and Competitive Behavior. *Langmuir* **2001**, *17* (10), 3006–3016. https://doi.org/10.1021/la0017781.

(183) Wertz, C. F.; Santore, M. M. Fibrinogen Adsorption on Hydrophilic and Hydrophobic Surfaces: Geometrical and Energetic Aspects of Interfacial Relaxations. *Langmuir* **2002**, *18* (3), 706–715. https://doi.org/10.1021/la011075z.

(184) Jeng, E. S.; Moll, A. E.; Roy, A. C.; Gastala, J. B.; Strano, M. S. Detection of DNA Hybridization Using the Near-Infrared Band-Gap Fluorescence of Single-Walled Carbon Nanotubes. *Nano Lett.* **2006**, *6* (3), 371–375. https://doi.org/10.1021/nl051829k.
(185) Schöppler, F.; Mann, C.; Hain, T. C.; Neubauer, F. M.; Privitera, G.; Bonaccorso, F.; Chu, D.; Ferrari, A. C.; Hertel, T. Molar Extinction Coefficient of Single-Wall Carbon Nanotubes. *J. Phys. Chem. C* **2011**, *115* (30), 14682–14686. https://doi.org/10.1021/jp205289h.
(186) Tsapikouni, T. S.; Missirlis, Y. F. PH and Ionic Strength Effect on Single Fibrinogen Molecule Adsorption on Mica Studied with AFM. *Colloids and Surfaces B: Biointerfaces* **2007**, *57* (1), 89–96. https://doi.org/10.1016/j.colsurfb.2007.01.011.
(187) Breiten, B.; Lockett, M. R.; Sherman, W.; Fujita, S.; Al-Sayah, M.; Lange, H.; Bowers, C. M.; Heroux, A.; Krilov, G.; Whitesides, G. M. Water Networks Contribute to Enthalpy/Entropy Compensation in Protein–Ligand Binding. *J. Am. Chem. Soc.* **2013**, *135* (41), 15579–15584. https://doi.org/10.1021/ja4075776.
(188) Dutta, A. K.; Rösgen, J.; Rajarathnam, K. Using Isothermal Titration Calorimetry to Determine Thermodynamic Parameters of Protein–Glycosaminoglycan Interactions. *Methods Mol Biol* **2015**, *1229*, 315–324. https://doi.org/10.1007/978-1-4939-1714-3_25.
(189) Prozeller, D.; Morsbach, S.; Landfester, K. Isothermal Titration Calorimetry as a Complementary Method for Investigating Nanoparticle–Protein Interactions. *Nanoscale* **2019**, *11* (41), 19265–19273. https://doi.org/10.1039/C9NR05790K.
(190) Chen, F.; Wang, G.; Griffin, J. I.; Brenneman, B.; Banda, N. K.; Holers, V. M.; Backos, D. S.; Wu, L.; Moghimi, S. M.; Simberg, D. Complement Proteins Bind to Nanoparticle Protein Corona and Undergo Dynamic Exchange *in Vivo*. *Nature Nanotechnology* **2017**, *12* (4), 387–393. https://doi.org/10.1038/nnano.2016.269.
(191) Mildner, D. F. R.; Hall, P. L. Small-Angle Scattering from Porous Solids with Fractal Geometry. *J. Phys. D: Appl. Phys.* **1986**, *19* (8), 1535–1545. https://doi.org/10.1088/0022-3727/19/8/021.
(192) Schaefer, D. W. Polymers, Fractals, and Ceramic Materials. *Science* **1989**, *243* (4894), 1023–1027. https://doi.org/10.1126/science.243.4894.1023.
(193) Schmidt, P. W. Small-Angle Scattering Studies of Disordered, Porous and Fraetal Systems. *J. Appl. Cryst.* **1991**, *24*, 414–435.
(194) Lazzari, S.; Nicoud, L.; Jaquet, B.; Lattuada, M.; Morbidelli, M. Fractal-like Structures in Colloid Science. *Advances in Colloid and Interface Science* **2016**, *235*, 1–13. https://doi.org/10.1016/j.cis.2016.05.002.
(195) Walkey, C. D.; Chan, W. C. W. Understanding and Controlling the Interaction of Nanomaterials with Proteins in a Physiological Environment. *Chem. Soc. Rev.* **2012**, *41* (7), 2780–2799. https://doi.org/10.1039/C1CS15233E.
(196) Nißler, R.; Mann, F. A.; Chaturvedi, P.; Horlebein, J.; Meyer, D.; Vuković, L.; Kruss, S. Quantification of the Number of Adsorbed DNA Molecules on Single-Walled Carbon Nanotubes. *J. Phys. Chem. C* **2019**, *123* (8), 4837–4847. https://doi.org/10.1021/acs.jpcc.8b11058.
(197) Safaee, M. M.; Gravely, M.; Rocchio, C.; Simmeth, M.; Roxbury, D. DNA Sequence Mediates Apparent Length Distribution in Single-Walled Carbon Nanotubes. *ACS Appl. Mater. Interfaces* **2019**, *11* (2), 2225–2233. https://doi.org/10.1021/acsami.8b16478.
(198) Alizadehmojarad, A. A.; Zhou, X.; Beyene, A. G.; Chacon, K. E.; Sung, Y.; Pinals, R. L.; Landry, M. P.; Vuković, L. Binding Affinity and Conformational Preferences Influence

Kinetic Stability of Short Oligonucleotides on Carbon Nanotubes. *Advanced Materials Interfaces* **2020**, *7* (15), 2000353. https://doi.org/10.1002/admi.202000353.
(199) Brunecker, F. K.; Schöppler, F.; Hertel, T. Interaction of Polymers with Single-Wall Carbon Nanotubes. *J. Phys. Chem. C* **2016**, *120* (18), 10094–10103. https://doi.org/10.1021/acs.jpcc.6b02198.
(200) Wiśniewski, J. R.; Zougman, A.; Nagaraj, N.; Mann, M. Universal Sample Preparation Method for Proteome Analysis. *Nat Methods* **2009**, *6* (5), 359–362. https://doi.org/10.1038/nmeth.1322.
(201) Simonsen, J. B.; Münter, R. Pay Attention to Biological Nanoparticles When Studying the Protein Corona on Nanomedicines. *Angewandte Chemie International Edition* **2020**, *59* (31), 12584–12588. https://doi.org/10.1002/anie.202004611.
(202) O'Farrell, P. H. High Resolution Two-Dimensional Electrophoresis of Proteins. *Journal of biological chemistry* **1975**, *250* (10), 4007–4021.
(203) Laemmli, U. K. Cleavage of Structural Proteins during the Assembly of the Head of Bacteriophage T4. *Nature* **1970**, *227* (5259), 680–685. https://doi.org/10.1038/227680a0.
(204) World-2DPAGE Constellation: SWISS-2DPAGE https://world-2dpage.expasy.org/swiss-2dpage/ (accessed Jul 29, 2018).
(205) Shliaha, P. V.; Bond, N. J.; Gatto, L.; Lilley, K. S. Effects of Traveling Wave Ion Mobility Separation on Data Independent Acquisition in Proteomics Studies. *J. Proteome Res.* **2013**, *12* (6), 2323–2339. https://doi.org/10.1021/pr300775k.
(206) Distler, U.; Kuharev, J.; Navarro, P.; Levin, Y.; Schild, H.; Tenzer, S. Drift Time-Specific Collision Energies Enable Deep-Coverage Data-Independent Acquisition Proteomics. *Nature Methods* **2014**, *11* (2), 167–170. https://doi.org/10.1038/nmeth.2767.
(207) Plumb, R. S.; Johnson, K. A.; Rainville, P.; Smith, B. W.; Wilson, I. D.; Castro-Perez, J. M.; Nicholson, J. K. UPLC/MSE; a New Approach for Generating Molecular Fragment Information for Biomarker Structure Elucidation. *Rapid Communications in Mass Spectrometry* **2006**, *20* (13), 1989–1994. https://doi.org/10.1002/rcm.2550.
(208) Neilson, K. A.; Ali, N. A.; Muralidharan, S.; Mirzaei, M.; Mariani, M.; Assadourian, G.; Lee, A.; Sluyter, S. C. van; Haynes, P. A. Less Label, More Free: Approaches in Label-Free Quantitative Mass Spectrometry. *PROTEOMICS* **2011**, *11* (4), 535–553. https://doi.org/10.1002/pmic.201000553.
(209) Nahnsen, S.; Bielow, C.; Reinert, K.; Kohlbacher, O. Tools for Label-Free Peptide Quantification. *Mol Cell Proteomics* **2012**, mcp.R112.025163. https://doi.org/10.1074/mcp.R112.025163.
(210) Silva, J. C.; Gorenstein, M. V.; Li, G.-Z.; Vissers, J. P. C.; Geromanos, S. J. Absolute Quantification of Proteins by LCMSE : A Virtue of Parallel Ms Acquisition. *Molecular & Cellular Proteomics* **2006**, *5* (1), 144–156. https://doi.org/10.1074/mcp.M500230-MCP200.
(211) Greene, W. H. *Econometric Analysis*; Pearson Education India, 2003.
(212) Thomas, P. D.; Campbell, M. J.; Kejariwal, A.; Mi, H.; Karlak, B.; Daverman, R.; Diemer, K.; Muruganujan, A.; Narechania, A. PANTHER: A Library of Protein Families and Subfamilies Indexed by Function. *Genome Res.* **2003**, *13* (9), 2129–2141. https://doi.org/10.1101/gr.772403.
(213) Benjamini, Y.; Hochberg, Y. Controlling the False Discovery Rate: A Practical and Powerful Approach to Multiple Testing. *Journal of the Royal Statistical Society: Series B*

(Methodological) **1995**, *57* (1), 289–300. https://doi.org/10.1111/j.2517-6161.1995.tb02031.x.

(214) Seabold, S.; Perktold, J. Statsmodels: Econometric and Statistical Modeling with Python. **2010**, 6.

(215) Classen, S.; Hura, G. L.; Holton, J. M.; Rambo, R. P.; Rodic, I.; Mcguire, P. J.; Dyer, K.; Hammel, M.; Meigs, G.; Frankel, K. A.; Tainer, J. A. Implementation and Performance of SIBYLS : A Dual Endstation Small-Angle X-Ray Scattering and Macromolecular Crystallography Beamline at the Advanced Light Source. *Journal of Applied Crystallography* **2013**, *46*, 1–13. https://doi.org/10.1107/S0021889812048698.

(216) Dyer, K. N.; Hammel, M.; Rambo, R. P.; Tsutakawa, S. E.; Rodic, I.; Classen, S.; Tainer, J. A.; Hura, G. L. *High-Throughput SAXS for the Characterization of Biomolecules in Solution : A Practical Approach*, Methods in.; Chen, Y. W., Ed.; Springer International Publishing, 2014; Vol. 1091. https://doi.org/10.1007/978-1-62703-691-7.

(217) Hura, G. L.; Menon, A. L.; Hammel, M.; Rambo, R. P.; Poole II, F. L.; Tsutakawa, S. E.; Jenney Jr, F. E.; Classen, S.; Frankel, K. A.; Hopkins, R. C.; Yang, S.; Scott, J. W.; Dillard, B. D.; Adams, M. W. W.; Tainer, J. A. Robust, High-Throughput Solution Structural Analyses by Small Angle X-Ray Scattering (SAXS). *Nature Methods* **2009**, *6* (8), 606–612. https://doi.org/10.1038/nmeth.1353.

(218) Streit, J. K.; Bachilo, S. M.; Sanchez, S. R.; Lin, C.-W.; Weisman, R. B. Variance Spectroscopy. *J. Phys. Chem. Lett.* **2015**, *6* (19), 3976–3981. https://doi.org/10.1021/acs.jpclett.5b01835.

(219) Gong, X.; Sharma, A. K.; Strano, M. S.; Mukhopadhyay, D. Selective Assembly of DNA-Conjugated Single-Walled Carbon Nanotubes from the Vascular Secretome. *ACS Nano* **2014**, *8* (9), 9126–9136. https://doi.org/10.1021/nn5026912.

(220) Anderson, N. L.; Anderson, N. G. The Human Plasma Proteome: History, Character, and Diagnostic Prospects. *Molecular & Cellular Proteomics* **2002**, *1* (11), 845–867. https://doi.org/10.1074/mcp.R200007-MCP200.

(221) Bisker, G.; Bakh, N. A.; Lee, M. A.; Ahn, J.; Park, M.; O'Connell, E. B.; Iverson, N. M.; Strano, M. S. Insulin Detection Using a Corona Phase Molecular Recognition Site on Single-Walled Carbon Nanotubes. *ACS Sens.* **2018**, *3* (2), 367–377. https://doi.org/10.1021/acssensors.7b00788.

(222) Harvey, J. D.; Baker, H. A.; Ortiz, M. V.; Kentsis, A.; Heller, D. A. HIV Detection via a Carbon Nanotube RNA Sensor. *ACS Sens.* **2019**, *4* (5), 1236–1244. https://doi.org/10.1021/acssensors.9b00025.

(223) Holt, B. D.; Dahl, K. N.; Islam, M. F. Quantification of Uptake and Localization of Bovine Serum Albumin-Stabilized Single-Wall Carbon Nanotubes in Different Human Cell Types. *Small* **2011**, *7* (16), 2348–2355. https://doi.org/10.1002/smll.201100437.

(224) Digiacomo, L.; Cardarelli, F.; Pozzi, D.; Palchetti, S.; A. Digman, M.; Gratton, E.; L. Capriotti, A.; Mahmoudi, M.; Caracciolo, G. An Apolipoprotein-Enriched Biomolecular Corona Switches the Cellular Uptake Mechanism and Trafficking Pathway of Lipid Nanoparticles. *Nanoscale* **2017**, *9* (44), 17254–17262. https://doi.org/10.1039/C7NR06437C.

(225) Rybak-Smith, M. J.; Sim, R. B. Complement Activation by Carbon Nanotubes. *Advanced Drug Delivery Reviews* **2011**, *63* (12), 1031–1041. https://doi.org/10.1016/j.addr.2011.05.012.

(226) Guggenheim, E. A. *Thermodynamics - An Advanced Treatment for Chemists and Physicists (7th Edition)*; 1985.
(227) Schön, A.; Clarkson, B. R.; Jaime, M.; Freire, E. Temperature Stability of Proteins: Analysis of Irreversible Denaturation Using Isothermal Calorimetry. *Proteins* **2017**, *85* (11), 2009–2016. https://doi.org/10.1002/prot.25354.
(228) Mildner, D. F. R.; Hall, P. L. Small-Angle Scattering from Porous Solids with Fractal Geometry. *J. Phys. D: Appl. Phys.* **1986**, *19* (8), 1535–1545. https://doi.org/10.1088/0022-3727/19/8/021.
(229) Putnam, C. D.; Hammel, M.; Hura, G. L.; Tainer, J. A. X-Ray Solution Scattering (SAXS) Combined with Crystallography and Computation: Defining Accurate Macromolecular Structures, Conformations and Assemblies in Solution. *Quarterly Reviews of Biophysics* **2007**, *40* (3), 191–285. https://doi.org/10.1017/S0033583507004635.
(230) Kikhney, A. G.; Svergun, D. I. A Practical Guide to Small Angle X-Ray Scattering (SAXS) of Flexible and Intrinsically Disordered Proteins. *FEBS Letters* **2015**, *589* (19, Part A), 2570–2577. https://doi.org/10.1016/j.febslet.2015.08.027.
(231) Demirer, G. S.; Zhang, H.; Matos, J. L.; Goh, N. S.; Cunningham, F. J.; Sung, Y.; Chang, R.; Aditham, A. J.; Chio, L.; Cho, M.-J.; Staskawicz, B.; Landry, M. P. High Aspect Ratio Nanomaterials Enable Delivery of Functional Genetic Material without DNA Integration in Mature Plants. *Nat. Nanotechnol.* **2019**, *14* (5), 456–464. https://doi.org/10.1038/s41565-019-0382-5.
(232) Zheng, M.; Jagota, A.; Semke, E. D.; Diner, B. A.; Mclean, R. S.; Lustig, S. R.; Richardson, R. E.; Tassi, N. G. DNA-Assisted Dispersion and Separation of Carbon Nanotubes. *Nature Materials* **2003**, *2* (5), 338–342. https://doi.org/10.1038/nmat877.
(233) Marchesan, S.; Prato, M. Under the Lens: Carbon Nanotube and Protein Interaction at the Nanoscale. *Chem. Commun.* **2015**, *51* (21), 4347–4359. https://doi.org/10.1039/C4CC09173F.
(234) Gravely, M.; Safaee, M. M.; Roxbury, D. Biomolecular Functionalization of a Nanomaterial To Control Stability and Retention within Live Cells. *Nano Lett.* **2019**, *19* (9), 6203–6212. https://doi.org/10.1021/acs.nanolett.9b02267.
(235) Dijt, J. C.; Cohen Stuart, M. A.; Fleer, G. J. Competitive Adsorption Kinetics of Polymers Differing in Length Only. *Macromolecules* **1994**, *27* (12), 3219–3228. https://doi.org/10.1021/ma00090a015.
(236) Landry, M. P.; Vuković, L.; Kruss, S.; Bisker, G.; Landry, A. M.; Islam, S.; Jain, R.; Schulten, K.; Strano, M. S. Comparative Dynamics and Sequence Dependence of DNA and RNA Binding to Single Walled Carbon Nanotubes. *The Journal of Physical Chemistry C* **2015**, *119* (18), 10048–10058. https://doi.org/10.1021/jp511448e.
(237) Silvera-Batista, C. A.; Wang, R. K.; Weinberg, P.; Ziegler, K. J. Solvatochromic Shifts of Single-Walled Carbon Nanotubes in Nonpolar Microenvironments. *Phys. Chem. Chem. Phys.* **2010**, *12* (26), 6990–6998. https://doi.org/10.1039/B927053A.
(238) Larsen, B. A.; Deria, P.; Holt, J. M.; Stanton, I. N.; Heben, M. J.; Therien, M. J.; Blackburn, J. L. Effect of Solvent Polarity and Electrophilicity on Quantum Yields and Solvatochromic Shifts of Single-Walled Carbon Nanotube Photoluminescence. *J. Am. Chem. Soc.* **2012**, *134* (30), 12485–12491. https://doi.org/10.1021/ja2114618.
(239) Choi, J. H.; Strano, M. S. Solvatochromism in Single-Walled Carbon Nanotubes. *Appl. Phys. Lett.* **2007**, *90* (22), 223114. https://doi.org/10.1063/1.2745228.

(240) Oh, H.; Sim, J.; Ju, S.-Y. Binding Affinities and Thermodynamics of Noncovalent Functionalization of Carbon Nanotubes with Surfactants. *Langmuir* **2013**, *29* (35), 11154–11162. https://doi.org/10.1021/la4022933.
(241) Harvey, J. D.; Jena, P. V.; Baker, H. A.; Zerze, G. H.; Williams, R. M.; Galassi, T. V.; Roxbury, D.; Mittal, J.; Heller, D. A. A Carbon Nanotube Reporter of MicroRNA Hybridization Events in Vivo. *Nature Biomedical Engineering* **2017**, *1* (4), 0041. https://doi.org/10.1038/s41551-017-0041.
(242) Shankar, A.; Mittal, J.; Jagota, A. Binding between DNA and Carbon Nanotubes Strongly Depends upon Sequence and Chirality. *Langmuir* **2014**, *30* (11), 3176–3183. https://doi.org/10.1021/la500013c.
(243) Roxbury, D.; Tu, X.; Zheng, M.; Jagota, A. Recognition Ability of DNA for Carbon Nanotubes Correlates with Their Binding Affinity. *Langmuir* **2011**, *27* (13), 8282–8293. https://doi.org/10.1021/la2007793.
(244) Jena, P. V.; Safaee, M. M.; Heller, D. A.; Roxbury, D. DNA–Carbon Nanotube Complexation Affinity and Photoluminescence Modulation Are Independent. *ACS Applied Materials & Interfaces* **2017**, *9* (25), 21397–21405. https://doi.org/10.1021/acsami.7b05678.
(245) Zheng, Y.; Bachilo, S. M.; Weisman, R. B. Enantiomers of Single-Wall Carbon Nanotubes Show Distinct Coating Displacement Kinetics. *J. Phys. Chem. Lett.* **2018**, 3793–3797. https://doi.org/10.1021/acs.jpclett.8b01683.
(246) Zhu, Z.; Yang, R.; You, M.; Zhang, X.; Wu, Y.; Tan, W. Single-Walled Carbon Nanotube as an Effective Quencher. *Anal Bioanal Chem* **2010**, *396* (1), 73–83. https://doi.org/10.1007/s00216-009-3192-z.
(247) Umemura, K.; Sato, S.; Bustamante, G.; Ye, J. Y. Using a Fluorescence Quenching Method to Detect DNA Adsorption onto Single-Walled Carbon Nanotube Surfaces. *Colloids and Surfaces B: Biointerfaces* **2017**, *160*, 201–206. https://doi.org/10.1016/j.colsurfb.2017.09.029.
(248) Lowe, G. D. O.; Rumley, A.; Mackie, I. J. Plasma Fibrinogen. *Ann Clin Biochem* **2004**, *41* (6), 430–440. https://doi.org/10.1258/0004563042466884.
(249) Foroozandeh, P.; Aziz, A. A. Merging Worlds of Nanomaterials and Biological Environment: Factors Governing Protein Corona Formation on Nanoparticles and Its Biological Consequences. *Nanoscale Research Letters* **2015**, *10* (1), 221. https://doi.org/10.1186/s11671-015-0922-3.
(250) Wertz, C. F.; Santore, M. M. Adsorption and Relaxation Kinetics of Albumin and Fibrinogen on Hydrophobic Surfaces: Single-Species and Competitive Behavior. *Langmuir* **1999**, *15* (26), 8884–8894. https://doi.org/10.1021/la990089q.
(251) Mubarekyan, E.; Santore, M. M. Adsorption and Exchange Dynamics in Aging Hydroxyethylcellulose Layers on Silica. *Journal of Colloid and Interface Science* **2000**, *227* (2), 334–344. https://doi.org/10.1006/jcis.2000.6899.
(252) Jungbauer, L. M.; Yu, C.; Laxton, K. J.; LaDu, M. J. Preparation of Fluorescently-Labeled Amyloid-Beta Peptide Assemblies: The Effect of Fluorophore Conjugation on Structure and Function. *Journal of Molecular Recognition* **2009**, *22* (5), 403–413. https://doi.org/10.1002/jmr.948.
(253) Albertorio, F.; Hughes, M. E.; Golovchenko, J. A.; Branton, D. Base Dependent DNA–Carbon Nanotube Interactions: Activation Enthalpies and Assembly–Disassembly

Control. *Nanotechnology* **2009**, *20* (39), 395101. https://doi.org/10.1088/0957-4484/20/39/395101.
(254) Dijt, J. C.; Cohen Stuart, M. A.; Fleer, G. J. Surface Exchange Kinetics of Chemically Different Polymers. *Macromolecules* **1994**, *27* (12), 3229–3237. https://doi.org/10.1021/ma00090a016.
(255) De Paoli, S. H.; Diduch, L. L.; Tegegn, T. Z.; Orecna, M.; Strader, M. B.; Karnaukhova, E.; Bonevich, J. E.; Holada, K.; Simak, J. The Effect of Protein Corona Composition on the Interaction of Carbon Nanotubes with Human Blood Platelets. *Biomaterials* **2014**, *35* (24), 6182–6194. https://doi.org/10.1016/j.biomaterials.2014.04.067.
(256) Chio, L.; Del Bonis-O'Donnell, J. T.; Kline, M. A.; Kim, J. H.; McFarlane, I. R.; Zuckermann, R. N.; Landry, M. P. Electrostatic Assemblies of Single-Walled Carbon Nanotubes and Sequence-Tunable Peptoid Polymers Detect a Lectin Protein and Its Target Sugars. *Nano Lett.* **2019**. https://doi.org/10.1021/acs.nanolett.8b04955.
(257) Roxbury, D.; Jena, P. V.; Shamay, Y.; Horoszko, C. P.; Heller, D. A. Cell Membrane Proteins Modulate the Carbon Nanotube Optical Bandgap via Surface Charge Accumulation. *ACS Nano* **2016**, *10* (1), 499–506. https://doi.org/10.1021/acsnano.5b05438.
(258) Moore, V. C.; Strano, M. S.; Haroz, E. H.; Hauge, R. H.; Smalley, R. E.; Schmidt, J.; Talmon, Y. Individually Suspended Single-Walled Carbon Nanotubes in Various Surfactants. *Nano Lett.* **2003**, *3* (10), 1379–1382. https://doi.org/10.1021/nl034524j.
(259) Okazaki, T.; Saito, T.; Matsuura, K.; Ohshima, S.; Yumura, M.; Iijima, S. Photoluminescence Mapping of "As-Grown" Single-Walled Carbon Nanotubes: A Comparison with Micelle-Encapsulated Nanotube Solutions. *Nano Lett.* **2005**, *5* (12), 2618–2623. https://doi.org/10.1021/nl051888y.
(260) Gill, S. C.; von Hippel, P. H. Calculation of Protein Extinction Coefficients from Amino Acid Sequence Data. *Analytical Biochemistry* **1989**, *182* (2), 319–326. https://doi.org/10.1016/0003-2697(89)90602-7.
(261) Marder, V. J.; Shulman, N. R.; Carroll, W. R. High Molecular Weight Derivatives of Human Fibrinogen Produced by Plasmin I. Physicochemical and Immunological Characterization. *J. Biol. Chem.* **1969**, *244* (8), 2111–2119.
(262) Flory, P. J. *Principles of Polymer Chemistry*; Cornell University Press, 1953.
(263) Holt, B. D.; McCorry, M. C.; Boyer, P. D.; Dahl, K. N.; Islam, M. F. Not All Protein-Mediated Single-Wall Carbon Nanotube Dispersions Are Equally Bioactive. *Nanoscale* **2012**, *4* (23), 7425–7434. https://doi.org/10.1039/C2NR31928D.
(264) Ornstein, L. Disc Electrophoresis-I Background and Theory*. *Annals of the New York Academy of Sciences* **1964**, *121* (2), 321–349. https://doi.org/10.1111/j.1749-6632.1964.tb14207.x.
(265) Braz, V. A.; Howard, K. J. Separation of Protein Oligomers by Blue Native Gel Electrophoresis. *Anal Biochem* **2009**, *388* (1), 170–172. https://doi.org/10.1016/j.ab.2009.02.019.
(266) Peters, T. Serum Albumin. In *Advances in Protein Chemistry*; Anfinsen, C. B., Edsall, J. T., Richards, F. M., Eds.; Academic Press, 1985; Vol. 37, pp 161–245. https://doi.org/10.1016/S0065-3233(08)60065-0.
(267) Carter, D. C.; Ho, J. X. Structure of Serum Albumin. In *Advances in Protein Chemistry*; Anfinsen, C. B., Edsall, J. T., Richards, F. M., Eisenberg, D. S., Eds.; Lipoproteins,

Apolipoproteins, and Lipases; Academic Press, 1994; Vol. 45, pp 153–203. https://doi.org/10.1016/S0065-3233(08)60640-3.
(268) Demirer, G. S.; Zhang, H.; Goh, N. S.; Pinals, R. L.; Chang, R.; Landry, M. P. Carbon Nanocarriers Deliver SiRNA to Intact Plant Cells for Efficient Gene Knockdown. *Science Advances* **2020**, *6* (26), eaaz0495. https://doi.org/10.1126/sciadv.aaz0495.
(269) Nam, K. T.; Shelby, S. A.; Choi, P. H.; Marciel, A. B.; Chen, R.; Tan, L.; Chu, T. K.; Mesch, R. A.; Lee, B.-C.; Connolly, M. D.; Kisielowski, C.; Zuckermann, R. N. Free-Floating Ultrathin Two-Dimensional Crystals from Sequence-Specific Peptoid Polymers. *Nature Materials* **2010**, *9* (5), 454–460. https://doi.org/10.1038/nmat2742.
(270) Chio, L.; Yang, D.; Landry, M. Surface Engineering of Nanoparticles to Create Synthetic Antibodies. In *Synthetic Antibodies*; Methods in Molecular Biology; Humana Press, New York, NY, 2017; pp 363–380. https://doi.org/10.1007/978-1-4939-6857-2_23.
(271) Johnson, R. R.; Johnson, A. T. C.; Klein, M. L. Probing the Structure of DNA−Carbon Nanotube Hybrids with Molecular Dynamics. *Nano Lett.* **2008**, *8* (1), 69–75. https://doi.org/10.1021/nl071909j.
(272) Das, A.; Sood, A. K.; Maiti, P. K.; Das, M.; Varadarajan, R.; Rao, C. N. R. Binding of Nucleobases with Single-Walled Carbon Nanotubes: Theory and Experiment. *Chemical Physics Letters* **2008**, *453* (4), 266–273. https://doi.org/10.1016/j.cplett.2008.01.057.
(273) Gowtham, S.; Scheicher, R. H.; Pandey, R.; Karna, S. P.; Ahuja, R. First-Principles Study of Physisorption of Nucleic Acid Bases on Small-Diameter Carbon Nanotubes. *Nanotechnology* **2008**, *19* (12), 125701. https://doi.org/10.1088/0957-4484/19/12/125701.
(274) Shen, J.-W.; Wu, T.; Wang, Q.; Kang, Y. Induced Stepwise Conformational Change of Human Serum Albumin on Carbon Nanotube Surfaces. *Biomaterials* **2008**, *29* (28), 3847–3855. https://doi.org/10.1016/j.biomaterials.2008.06.013.
(275) Yang, Z.; Wang, Z.; Tian, X.; Xiu, P.; Zhou, R. Amino Acid Analogues Bind to Carbon Nanotube via π-π Interactions: Comparison of Molecular Mechanical and Quantum Mechanical Calculations. *J. Chem. Phys.* **2012**, *136* (2), 025103. https://doi.org/10.1063/1.3675486.
(276) Rajesh, C.; Majumder, C.; Mizuseki, H.; Kawazoe, Y. A Theoretical Study on the Interaction of Aromatic Amino Acids with Graphene and Single Walled Carbon Nanotube. *J. Chem. Phys.* **2009**, *130* (12), 124911. https://doi.org/10.1063/1.3079096.
(277) Wang, S.; Humphreys, E. S.; Chung, S.-Y.; Delduco, D. F.; Lustig, S. R.; Wang, H.; Parker, K. N.; Rizzo, N. W.; Subramoney, S.; Chiang, Y.-M.; Jagota, A. Peptides with Selective Affinity for Carbon Nanotubes. *Nature Mater* **2003**, *2* (3), 196–200. https://doi.org/10.1038/nmat833.
(278) Lu, N.; Sui, Y.; Ding, Y.; Tian, R.; Li, L.; Liu, F. Adsorption of Human Serum Albumin on Functionalized Single-Walled Carbon Nanotubes Reduced Cytotoxicity. *Chemico-Biological Interactions* **2018**. https://doi.org/10.1016/j.cbi.2018.03.015.
(279) Gillen, A. J.; Siefman, D. J.; Wu, S.-J.; Bourmaud, C.; Lambert, B.; Boghossian, A. A. Templating Colloidal Sieves for Tuning Nanotube Surface Interactions and Optical Sensor Responses. *Journal of Colloid and Interface Science* **2020**, *565*, 55–62. https://doi.org/10.1016/j.jcis.2019.12.058.
(280) Mann, F. A.; Horlebein, J.; Meyer, N. F.; Meyer, D.; Thomas, F.; Kruss, S. Carbon Nanotubes Encapsulated in Coiled-Coil Peptide Barrels. *Chemistry – A European Journal* **2018**, *0* (0). https://doi.org/10.1002/chem.201800993.

(281) Zubkovs, V.; Schuergers, N.; Lambert, B.; Ahunbay, E.; Boghossian, A. A. Mediatorless, Reversible Optical Nanosensor Enabled through Enzymatic Pocket Doping. *Small* **2017**, *13* (42), 1701654. https://doi.org/10.1002/smll.201701654.
(282) Nelson, J. T.; Kim, S.; Reuel, N. F.; Salem, D. P.; Bisker, G.; Landry, M. P.; Kruss, S.; Barone, P. W.; Kwak, S.; Strano, M. S. Mechanism of Immobilized Protein A Binding to Immunoglobulin G on Nanosensor Array Surfaces. *Analytical Chemistry* **2015**, *87* (16), 8186–8193. https://doi.org/10.1021/acs.analchem.5b00843.
(283) Israelachvili, J. N. *Intermolecular and Surface Forces*; Academic press, 2011.
(284) Lin, S.; Shih, C.-J.; Sresht, V.; Govind Rajan, A.; Strano, M. S.; Blankschtein, D. Understanding the Colloidal Dispersion Stability of 1D and 2D Materials: Perspectives from Molecular Simulations and Theoretical Modeling. *Advances in Colloid and Interface Science* **2017**, *244*, 36–53. https://doi.org/10.1016/j.cis.2016.07.007.
(285) Tummala, N. R.; Striolo, A. SDS Surfactants on Carbon Nanotubes: Aggregate Morphology. *ACS Nano* **2009**, *3* (3), 595–602. https://doi.org/10.1021/nn8007756.
(286) Xu, Z.; Yang, X.; Yang, Z. A Molecular Simulation Probing of Structure and Interaction for Supramolecular Sodium Dodecyl Sulfate/Single-Wall Carbon Nanotube Assemblies. *Nano Lett.* **2010**, *10* (3), 985–991. https://doi.org/10.1021/nl9041005.
(287) Gudarzi, M. M. Colloidal Stability of Graphene Oxide: Aggregation in Two Dimensions. *Langmuir* **2016**, *32* (20), 5058–5068. https://doi.org/10.1021/acs.langmuir.6b01012.
(288) Shih, C.-J.; Lin, S.; Strano, M. S.; Blankschtein, D. Understanding the Stabilization of Liquid-Phase-Exfoliated Graphene in Polar Solvents: Molecular Dynamics Simulations and Kinetic Theory of Colloid Aggregation. *J. Am. Chem. Soc.* **2010**, *132* (41), 14638–14648. https://doi.org/10.1021/ja1064284.
(289) Jeong, S.; Pinals, R. L.; Dharmadhikari, B.; Song, H.; Kalluri, A.; Debnath, D.; Wu, Q.; Ham, M.-H.; Patra, P.; Landry, M. P. Graphene Quantum Dot Oxidation Governs Noncovalent Biopolymer Adsorption. *Scientific Reports* **2020**, *10* (1), 1–14. https://doi.org/10.1038/s41598-020-63769-z.
(290) Iliafar, S.; Mittal, J.; Vezenov, D.; Jagota, A. Interaction of Single-Stranded DNA with Curved Carbon Nanotube Is Much Stronger Than with Flat Graphite. *J. Am. Chem. Soc.* **2014**, *136* (37), 12947–12957. https://doi.org/10.1021/ja5055498.
(291) Curtis, R. A.; Ulrich, J.; Montaser, A.; Prausnitz, J. M.; Blanch, H. W. Protein–Protein Interactions in Concentrated Electrolyte Solutions. *Biotechnology and Bioengineering* **2002**, *79* (4), 367–380. https://doi.org/10.1002/bit.10342.
(292) Li, K.; Chen, Y. Evaluation of DLVO Interaction between a Sphere and a Cylinder. *Colloids and Surfaces A: Physicochemical and Engineering Aspects* **2012**, *415*, 218–229. https://doi.org/10.1016/j.colsurfa.2012.09.027.
(293) Hogg, R.; Healy, T. W.; Fuerstenau, D. W. Mutual Coagulation of Colloidal Dispersions. *Trans. Faraday Soc.* **1966**, *62* (0), 1638–1651. https://doi.org/10.1039/TF9666201638.
(294) Ohshima, H.; Hyono, A. Electrostatic Interaction between Two Cylindrical Soft Particles. *Journal of Colloid and Interface Science* **2009**, *333* (1), 202–208. https://doi.org/10.1016/j.jcis.2008.11.060.
(295) Melander, W.; Horváth, C. Salt Effects on Hydrophobic Interactions in Precipitation and Chromatography of Proteins: An Interpretation of the Lyotropic Series. *Archives of Biochemistry and Biophysics* **1977**, *183* (1), 200–215. https://doi.org/10.1016/0003-9861(77)90434-9.

(296) Fraczkiewicz, R.; Braun, W. Exact and efficient analytical calculation of the accessible surface areas and their gradients for macromolecules. *Journal of Computational Chemistry* **1998**, *19* (3), 319–333. https://doi.org/10.1002/(SICI)1096-987X(199802)19:3<319::AID-JCC6>3.0.CO;2-W.

(297) Hajgató, B.; Güryel, S.; Dauphin, Y.; Blairon, J.-M.; Lier, G. V.; Miltner, H. E.; Proft, F. D.; Geerlings, P. Solvation of Graphene Sheets vs. Dimerization: A Theoretical Study. *IJC-A Vol.53A(08-09) [August-September 2014]* **2014**.

(298) Alinezhad, H.; Ganji, M. D.; Soleymani, E.; Tajbakhsh, M. A Comprehensive Theoretical Investigation about the Bio-Functionalization Capability of Single Walled CNT, BNNT and SiCNT Using DNA/RNA Nucleobases. *Applied Surface Science* **2017**, *422*, 56–72. https://doi.org/10.1016/j.apsusc.2017.05.196.

(299) Silvera Batista, C. A.; Zheng, M.; Khripin, C. Y.; Tu, X.; Fagan, J. A. Rod Hydrodynamics and Length Distributions of Single-Wall Carbon Nanotubes Using Analytical Ultracentrifugation. *Langmuir* **2014**, *30* (17), 4895–4904. https://doi.org/10.1021/la404892k.

(300) Wang, S.; Zhang, Y.; Abidi, N.; Cabrales, L. Wettability and Surface Free Energy of Graphene Films. *Langmuir* **2009**, *25* (18), 11078–11081. https://doi.org/10.1021/la901402f.

(301) van Engers, C. D.; Cousens, N. E. A.; Babenko, V.; Britton, J.; Zappone, B.; Grobert, N.; Perkin, S. Direct Measurement of the Surface Energy of Graphene. *Nano Lett.* **2017**, *17* (6), 3815–3821. https://doi.org/10.1021/acs.nanolett.7b01181.

(302) Berg, J. C. *An Introduction to Interfaces & Colloids: The Bridge to Nanoscience*; World Scientific, 2010.

(303) Neal, B. L.; Lenhoff, A. M. Excluded Volume Contribution to the Osmotic Second Virial Coefficient for Proteins. *AIChE Journal* **1995**, *41* (4), 1010–1014. https://doi.org/10.1002/aic.690410432.

(304) Wendorf, J. R.; Radke, C. J.; Blanch, H. W. The Role of Electrolytes on Protein Adsorption at a Hydrophilic Solid–Water Interface. *Colloids and Surfaces B: Biointerfaces* **2010**, *75* (1), 100–106. https://doi.org/10.1016/j.colsurfb.2009.08.015.

(305) Cambré, S.; Santos, S. M.; Wenseleers, W.; Nugraha, A. R. T.; Saito, R.; Cognet, L.; Lounis, B. Luminescence Properties of Individual Empty and Water-Filled Single-Walled Carbon Nanotubes. *ACS Nano* **2012**, *6* (3), 2649–2655. https://doi.org/10.1021/nn300035y.

(306) Adamczyk, Z.; Bratek-Skicki, A.; Dąbrowska, P.; Nattich-Rak, M. Mechanisms of Fibrinogen Adsorption on Latex Particles Determined by Zeta Potential and AFM Measurements. *Langmuir* **2012**, *28* (1), 474–485. https://doi.org/10.1021/la2038119.

(307) Kiselev, M. A.; Gryzunov, I. u. A.; Dobretsov, G. E.; Komarova, M. N. Size of a Human Serum Albumin Molecule in Solution. *Biofizika* **2001**, *46* (3), 423–427.

(308) Jayaram, B. Filters for Globular Protein Evaluation - Radius of Gyration http://www.scfbio-iitd.res.in/software/proteomics/rgnew1.jsp (accessed May 3, 2020).

(309) Borhani, D. W.; Rogers, D. P.; Engler, J. A.; Brouillette, C. G. Crystal Structure of Truncated Human Apolipoprotein A-I Suggests a Lipid-Bound Conformation. *PNAS* **1997**, *94* (23), 12291–12296. https://doi.org/10.1073/pnas.94.23.12291.

(310) Janssen, B. J. C.; Huizinga, E. G.; Raaijmakers, H. C. A.; Roos, A.; Daha, M. R.; Nilsson-Ekdahl, K.; Nilsson, B.; Gros, P. Structures of Complement Component C3 Provide

Insights into the Function and Evolution of Immunity. *Nature* **2005**, *437* (7058), 505–511. https://doi.org/10.1038/nature04005.

(311) Saphire, E. O.; Parren, P. W. H. I.; Pantophlet, R.; Zwick, M. B.; Morris, G. M.; Rudd, P. M.; Dwek, R. A.; Stanfield, R. L.; Burton, D. R.; Wilson, I. A. Crystal Structure of a Neutralizing Human IgG Against HIV-1: A Template for Vaccine Design. *Science* **2001**, *293* (5532), 1155–1159. https://doi.org/10.1126/science.1061692.

(312) Su, Y.; Ashworth, V.; Kim, C.; S. Adeleye, A.; Rolshausen, P.; Roper, C.; White, J.; Jassby, D. Delivery, Uptake, Fate, and Transport of Engineered Nanoparticles in Plants: A Critical Review and Data Analysis. *Environmental Science: Nano* **2019**, *6* (8), 2311–2331. https://doi.org/10.1039/C9EN00461K.

(313) Taylor, A. B.; Zijlstra, P. Single-Molecule Plasmon Sensing: Current Status and Future Prospects. *ACS Sens.* **2017**, *2* (8), 1103–1122. https://doi.org/10.1021/acssensors.7b00382.

(314) Howes, P. D.; Chandrawati, R.; Stevens, M. M. Colloidal Nanoparticles as Advanced Biological Sensors. *Science* **2014**, *346* (6205). https://doi.org/10.1126/science.1247390.

(315) Hong, G.; Antaris, A. L.; Dai, H. Near-Infrared Fluorophores for Biomedical Imaging. *Nature Biomedical Engineering* **2017**, *1* (1), 1–22. https://doi.org/10.1038/s41551-016-0010.

(316) Mitchell, M. J.; Billingsley, M. M.; Haley, R. M.; Wechsler, M. E.; Peppas, N. A.; Langer, R. Engineering Precision Nanoparticles for Drug Delivery. *Nature Reviews Drug Discovery* **2020**, 1–24. https://doi.org/10.1038/s41573-020-0090-8.

(317) Wang, J. W.; Grandio, E. G.; Newkirk, G. M.; Demirer, G. S.; Butrus, S.; Giraldo, J. P.; Landry, M. P. Nanoparticle-Mediated Genetic Engineering of Plants. *Molecular Plant* **2019**, *12* (8), 1037–1040. https://doi.org/10.1016/j.molp.2019.06.010.

(318) Bruns, O. T.; Bischof, T. S.; Harris, D. K.; Franke, D.; Shi, Y.; Riedemann, L.; Bartelt, A.; Jaworski, F. B.; Carr, J. A.; Rowlands, C. J.; Wilson, M. W. B.; Chen, O.; Wei, H.; Hwang, G. W.; Montana, D. M.; Coropceanu, I.; Achorn, O. B.; Kloepper, J.; Heeren, J.; So, P. T. C.; Fukumura, D.; Jensen, K. F.; Jain, R. K.; Bawendi, M. G. Next-Generation in Vivo Optical Imaging with Short-Wave Infrared Quantum Dots. *Nature Biomedical Engineering* **2017**, *1* (4), 1–11. https://doi.org/10.1038/s41551-017-0056.

(319) Safari, H.; Kaczorowski, N.; Felder, M. L.; Brannon, E. R.; Varghese, M.; Singer, K.; Eniola-Adefeso, O. Biodegradable, Bile Salt Microparticles for Localized Fat Dissolution. *Science Advances* **2020**, *6* (49), eabd8019. https://doi.org/10.1126/sciadv.abd8019.

(320) Ball, R. L.; Hajj, K. A.; Vizelman, J.; Bajaj, P.; Whitehead, K. A. Lipid Nanoparticle Formulations for Enhanced Co-Delivery of SiRNA and MRNA. *Nano Lett.* **2018**, *18* (6), 3814–3822. https://doi.org/10.1021/acs.nanolett.8b01101.

(321) Xiao, L.; Lu, G.; Lu, Q.; Kaplan, D. L. Direct Formation of Silk Nanoparticles for Drug Delivery. *ACS Biomater. Sci. Eng.* **2016**, *2* (11), 2050–2057. https://doi.org/10.1021/acsbiomaterials.6b00457.

(322) Gillen, A. J.; Boghossian, A. A. Non-Covalent Methods of Engineering Optical Sensors Based on Single-Walled Carbon Nanotubes. *Front. Chem.* **2019**, *7*. https://doi.org/10.3389/fchem.2019.00612.

(323) Jeong, S.; Yang, D.; Beyene, A. G.; Bonis-O'Donnell, J. T. D.; Gest, A. M. M.; Navarro, N.; Sun, X.; Landry, M. P. High-Throughput Evolution of near-Infrared Serotonin Nanosensors. *Science Advances* **2019**, *5* (12), eaay3771. https://doi.org/10.1126/sciadv.aay3771.

(324) Chio, L.; Del Bonis-O'Donnell, J. T.; Kline, M. A.; Kim, J. H.; McFarlane, I. R.; Zuckermann, R. N.; Landry, M. P. Electrostatic Assemblies of Single-Walled Carbon Nanotubes and Sequence-Tunable Peptoid Polymers Detect a Lectin Protein and Its Target Sugars. *Nano Lett.* **2019**, *19* (11), 7563–7572. https://doi.org/10.1021/acs.nanolett.8b04955.

(325) Pinals, R. L.; Ledesma, F.; Yang, D.; Navarro, N.; Jeong, S.; Pak, J. E.; Kuo, L.; Chuang, Y.-C.; Cheng, Y.-W.; Sun, H.-Y.; Landry, M. P. Rapid SARS-CoV-2 Spike Protein Detection by Carbon Nanotube-Based Near-Infrared Nanosensors. *Nano Lett.* **2021**. https://doi.org/10.1021/acs.nanolett.1c00118.

(326) Boyer, P. D.; Ganesh, S.; Qin, Z.; Holt, B. D.; Buehler, M. J.; Islam, M. F.; Dahl, K. N. Delivering Single-Walled Carbon Nanotubes to the Nucleus Using Engineered Nuclear Protein Domains. *ACS Appl. Mater. Interfaces* **2016**, *8* (5), 3524–3534. https://doi.org/10.1021/acsami.5b12602.

(327) Demirer, G. S.; Zhang, H.; Goh, N. S.; Pinals, R. L.; Chang, R.; Landry, M. P. Carbon Nanocarriers Deliver SiRNA to Intact Plant Cells for Efficient Gene Knockdown. *Science Advances* **2020**, *6* (26), eaaz0495. https://doi.org/10.1126/sciadv.aaz0495.

(328) Nel, A. E.; Mädler, L.; Velegol, D.; Xia, T.; Hoek, E. M. V.; Somasundaran, P.; Klaessig, F.; Castranova, V.; Thompson, M. Understanding Biophysicochemical Interactions at the Nano–Bio Interface. *Nature Materials* **2009**, *8* (7), 543–557. https://doi.org/10.1038/nmat2442.

(329) Ke, P. C.; Lin, S.; Parak, W. J.; Davis, T. P.; Caruso, F. A Decade of the Protein Corona. *ACS Nano* **2017**, *11* (12), 11773–11776. https://doi.org/10.1021/acsnano.7b08008.

(330) Tenzer, S.; Docter, D.; Kuharev, J.; Musyanovych, A.; Fetz, V.; Hecht, R.; Schlenk, F.; Fischer, D.; Kiouptsi, K.; Reinhardt, C.; Landfester, K.; Schild, H.; Maskos, M.; Knauer, S. K.; Stauber, R. H. Rapid Formation of Plasma Protein Corona Critically Affects Nanoparticle Pathophysiology. *Nature Nanotechnology* **2013**, *8* (10), 772–781. https://doi.org/10.1038/nnano.2013.181.

(331) Gebauer, J. S.; Malissek, M.; Simon, S.; Knauer, S. K.; Maskos, M.; Stauber, R. H.; Peukert, W.; Treuel, L. Impact of the Nanoparticle–Protein Corona on Colloidal Stability and Protein Structure. *Langmuir* **2012**, *28* (25), 9673–9679. https://doi.org/10.1021/la301104a.

(332) Jiang, C.; Wang, G.; Hein, R.; Liu, N.; Luo, X.; Davis, J. J. Antifouling Strategies for Selective In Vitro and In Vivo Sensing. *Chem. Rev.* **2020**, *120* (8), 3852–3889. https://doi.org/10.1021/acs.chemrev.9b00739.

(333) Dai, Q.; Bertleff-Zieschang, N.; Braunger, J. A.; Björnmalm, M.; Cortez-Jugo, C.; Caruso, F. Particle Targeting in Complex Biological Media. *Advanced Healthcare Materials* **2018**, *7* (1), 1700575. https://doi.org/10.1002/adhm.201700575.

(334) Bertrand, N.; Grenier, P.; Mahmoudi, M.; Lima, E. M.; Appel, E. A.; Dormont, F.; Lim, J.-M.; Karnik, R.; Langer, R.; Farokhzad, O. C. Mechanistic Understanding of in Vivo Protein Corona Formation on Polymeric Nanoparticles and Impact on Pharmacokinetics. *Nat Commun* **2017**, *8* (1), 1–8. https://doi.org/10.1038/s41467-017-00600-w.

(335) Cai, K.; Wang, A. Z.; Yin, L.; Cheng, J. Bio-Nano Interface: The Impact of Biological Environment on Nanomaterials and Their Delivery Properties. *Journal of Controlled Release* **2017**. https://doi.org/10.1016/j.jconrel.2016.11.034.

(336) Giulimondi, F.; Digiacomo, L.; Pozzi, D.; Palchetti, S.; Vulpis, E.; Capriotti, A. L.; Chiozzi, R. Z.; Laganà, A.; Amenitsch, H.; Masuelli, L.; Peruzzi, G.; Mahmoudi, M.;

Screpanti, I.; Zingoni, A.; Caracciolo, G. Interplay of Protein Corona and Immune Cells Controls Blood Residency of Liposomes. *Nature Communications* **2019**, *10* (1), 3686. https://doi.org/10.1038/s41467-019-11642-7.

(337) Dawson, K. A.; Yan, Y. Current Understanding of Biological Identity at the Nanoscale and Future Prospects. *Nature Nanotechnology* **2021**, *16* (3), 229–242. https://doi.org/10.1038/s41565-021-00860-0.

(338) Lazarovits, J.; Sindhwani, S.; Tavares, A. J.; Zhang, Y.; Song, F.; Audet, J.; Krieger, J. R.; Syed, A. M.; Stordy, B.; Chan, W. C. W. Supervised Learning and Mass Spectrometry Predicts the in Vivo Fate of Nanomaterials. *ACS Nano* **2019**, *13* (7), 8023–8034. https://doi.org/10.1021/acsnano.9b02774.

(339) Yang, D.; Yang, S. J.; Del Bonis-O'Donnell, J. T.; Pinals, R. L.; Landry, M. P. Mitigation of Carbon Nanotube Neurosensor Induced Transcriptomic and Morphological Changes in Mouse Microglia with Surface Passivation. *ACS Nano* **2020**, *14* (10), 13794–13805. https://doi.org/10.1021/acsnano.0c06154.

(340) Ostuni, E.; Chapman, R. G.; Holmlin, R. E.; Takayama, S.; Whitesides, G. M. A Survey of Structure−Property Relationships of Surfaces That Resist the Adsorption of Protein. *Langmuir* **2001**, *17* (18), 5605–5620. https://doi.org/10.1021/la010384m.

(341) Wei, Q.; Becherer, T.; Angioletti-Uberti, S.; Dzubiella, J.; Wischke, C.; Neffe, A. T.; Lendlein, A.; Ballauff, M.; Haag, R. Protein Interactions with Polymer Coatings and Biomaterials. *Angewandte Chemie International Edition* **2014**, *53* (31), 8004–8031. https://doi.org/10.1002/anie.201400546.

(342) R. Findlay, M.; N. Freitas, D.; Mobed-Miremadi, M.; E. Wheeler, K. Machine Learning Provides Predictive Analysis into Silver Nanoparticle Protein Corona Formation from Physicochemical Properties. *Environmental Science: Nano* **2018**, *5* (1), 64–71. https://doi.org/10.1039/C7EN00466D.

(343) Poulsen, K. M.; Pho, T.; Champion, J. A.; Payne, C. K. Automation and Low-Cost Proteomics for Characterization of the Protein Corona: Experimental Methods for Big Data. *Anal Bioanal Chem* **2020**, *412* (24), 6543–6551. https://doi.org/10.1007/s00216-020-02726-1.

(344) Oliverio, R.; Liberelle, B.; Murschel, F.; Garcia-Ac, A.; Banquy, X.; De Crescenzo, G. Versatile and High-Throughput Strategy for the Quantification of Proteins Bound to Nanoparticles. *ACS Appl. Nano Mater.* **2020**, *3* (10), 10497–10507. https://doi.org/10.1021/acsanm.0c02414.

(345) Duan, Y.; Coreas, R.; Liu, Y.; Bitounis, D.; Zhang, Z.; Parviz, D.; Strano, M.; Demokritou, P.; Zhong, W. Prediction of Protein Corona on Nanomaterials by Machine Learning Using Novel Descriptors. *NanoImpact* **2020**, *17*, 100207. https://doi.org/10.1016/j.impact.2020.100207.

(346) Fourches, D.; Pu, D.; Tassa, C.; Weissleder, R.; Shaw, S. Y.; Mumper, R. J.; Tropsha, A. Quantitative Nanostructure−Activity Relationship Modeling. *ACS Nano* **2010**, *4* (10), 5703–5712. https://doi.org/10.1021/nn1013484.

(347) Bai, X.; Liu, F.; Liu, Y.; Li, C.; Wang, S.; Zhou, H.; Wang, W.; Zhu, H.; Winkler, D. A.; Yan, B. Toward a Systematic Exploration of Nano-Bio Interactions. *Toxicology and Applied Pharmacology* **2017**, *323*, 66–73. https://doi.org/10.1016/j.taap.2017.03.011.

(348) Yamankurt, G.; Berns, E. J.; Xue, A.; Lee, A.; Bagheri, N.; Mrksich, M.; Mirkin, C. A. Exploration of the Nanomedicine-Design Space with High-Throughput Screening and

Machine Learning. *Nature Biomedical Engineering* **2019**, *3* (4), 318–327. https://doi.org/10.1038/s41551-019-0351-1.
(349) Di Giosia, M.; Valle, F.; Cantelli, A.; Bottoni, A.; Zerbetto, F.; Fasoli, E.; Calvaresi, M. High-Throughput Virtual Screening to Rationally Design Protein - Carbon Nanotube Interactions. Identification and Preparation of Stable Water Dispersions of Protein - Carbon Nanotube Hybrids and Efficient Design of New Functional Materials. *Carbon* **2019**, *147*, 70–82. https://doi.org/10.1016/j.carbon.2019.02.043.
(350) The UniProt Consortium. UniProt: The Universal Protein Knowledgebase in 2021. *Nucleic Acids Research* **2021**, *49* (D1), D480–D489. https://doi.org/10.1093/nar/gkaa1100.
(351) Cock, P. J. A.; Antao, T.; Chang, J. T.; Chapman, B. A.; Cox, C. J.; Dalke, A.; Friedberg, I.; Hamelryck, T.; Kauff, F.; Wilczynski, B.; de Hoon, M. J. L. Biopython: Freely Available Python Tools for Computational Molecular Biology and Bioinformatics. *Bioinformatics* **2009**, *25* (11), 1422–1423. https://doi.org/10.1093/bioinformatics/btp163.
(352) Klausen, M. S.; Jespersen, M. C.; Nielsen, H.; Jensen, K. K.; Jurtz, V. I.; Sønderby, C. K.; Sommer, M. O. A.; Winther, O.; Nielsen, M.; Petersen, B.; Marcatili, P. NetSurfP-2.0: Improved Prediction of Protein Structural Features by Integrated Deep Learning. *Proteins: Structure, Function, and Bioinformatics* **2019**, *87* (6), 520–527. https://doi.org/10.1002/prot.25674.
(353) Chawla, N. V.; Bowyer, K. W.; Hall, L. O.; Kegelmeyer, W. P. SMOTE: Synthetic Minority Over-Sampling Technique. *Journal of Artificial Intelligence Research* **2002**, *16*, 321–357. https://doi.org/10.1613/jair.953.
(354) Liu, J.; Yang, L.; Hopfinger, A. J. Affinity of Drugs and Small Biologically Active Molecules to Carbon Nanotubes: A Pharmacodynamics and Nanotoxicity Factor? *Mol. Pharmaceutics* **2009**, *6* (3), 873–882. https://doi.org/10.1021/mp800197v.
(355) Saeedimasine, M.; Brandt, E. G.; Lyubartsev, A. P. Atomistic Perspective on Biomolecular Adsorption on Functionalized Carbon Nanomaterials under Ambient Conditions. *J. Phys. Chem. B* **2021**, *125* (1), 416–430. https://doi.org/10.1021/acs.jpcb.0c08622.
(356) Chaudhary, H.; Fernandes, R. M. F.; Gowda, V.; Claessens, M. M. A. E.; Furó, I.; Lendel, C. Intrinsically Disordered Protein as Carbon Nanotube Dispersant: How Dynamic Interactions Lead to Excellent Colloidal Stability. *Journal of Colloid and Interface Science* **2019**, *556*, 172–179. https://doi.org/10.1016/j.jcis.2019.08.050.
(357) Hirano, A.; Kameda, T. Aromaphilicity Index of Amino Acids: Molecular Dynamics Simulations of the Protein Binding Affinity for Carbon Nanomaterials. *ACS Appl. Nano Mater.* **2021**, *4* (3), 2486–2495. https://doi.org/10.1021/acsanm.0c03047.
(358) He, Z.; Zhou, J. Probing Carbon Nanotube–Amino Acid Interactions in Aqueous Solution with Molecular Dynamics Simulations. *Carbon* **2014**, *78*, 500–509. https://doi.org/10.1016/j.carbon.2014.07.031.
(359) Zorbas, V.; Smith, A. L.; Xie, H.; Ortiz-Acevedo, A.; Dalton, A. B.; Dieckmann, G. R.; Draper, R. K.; Baughman, R. H.; Musselman, I. H. Importance of Aromatic Content for Peptide/Single-Walled Carbon Nanotube Interactions. *J. Am. Chem. Soc.* **2005**, *127* (35), 12323–12328. https://doi.org/10.1021/ja050747v.
(360) Tomásio, S. M.; Walsh, T. R. Modeling the Binding Affinity of Peptides for Graphitic Surfaces. Influences of Aromatic Content and Interfacial Shape. *J. Phys. Chem. C* **2009**, *113* (20), 8778–8785. https://doi.org/10.1021/jp8087594.
(361) Davis, T. A.; Holland, L. A. Peptide Probe for Multiwalled Carbon Nanotubes: Electrophoretic Assessment of the Binding Interface and Evaluation of Surface

Functionalization. *ACS Appl. Mater. Interfaces* **2018**, *10* (13), 11311–11318. https://doi.org/10.1021/acsami.8b00022.
(362) Nepal, D.; Geckeler, K. E. PH-Sensitive Dispersion and Debundling of Single-Walled Carbon Nanotubes: Lysozyme as a Tool. *Small* **2006**, *2* (3), 406–412. https://doi.org/10.1002/smll.200500351.
(363) Horn, D. W.; Tracy, K.; Easley, C. J.; Davis, V. A. Lysozyme Dispersed Single-Walled Carbon Nanotubes: Interaction and Activity. *J. Phys. Chem. C* **2012**, *116* (18), 10341–10348. https://doi.org/10.1021/jp300242a.
(364) Holt, B. D.; McCorry, M. C.; Boyer, P. D.; Dahl, K. N.; Islam, M. F. Not All Protein-Mediated Single-Wall Carbon Nanotube Dispersions Are Equally Bioactive. *Nanoscale* **2012**, *4* (23), 7425–7434. https://doi.org/10.1039/C2NR31928D.
(365) Matsuura, K.; Saito, T.; Okazaki, T.; Ohshima, S.; Yumura, M.; Iijima, S. Selectivity of Water-Soluble Proteins in Single-Walled Carbon Nanotube Dispersions. *Chemical Physics Letters* **2006**, *429* (4), 497–502. https://doi.org/10.1016/j.cplett.2006.08.044.
(366) Zöller, M. CD44: Can a Cancer-Initiating Cell Profit from an Abundantly Expressed Molecule? *Nature Reviews Cancer* **2011**, *11* (4), 254–267. https://doi.org/10.1038/nrc3023.
(367) Rives, A.; Meier, J.; Sercu, T.; Goyal, S.; Lin, Z.; Liu, J.; Guo, D.; Ott, M.; Zitnick, C. L.; Ma, J.; Fergus, R. Biological Structure and Function Emerge from Scaling Unsupervised Learning to 250 Million Protein Sequences. *PNAS* **2021**, *118* (15). https://doi.org/10.1073/pnas.2016239118.
(368) Pedregosa, F.; Varoquaux, G.; Gramfort, A.; Michel, V.; Thirion, B.; Grisel, O.; Blondel, M.; Prettenhofer, P.; Weiss, R.; Dubourg, V.; Vanderplas, J.; Passos, A.; Cournapeau, D. Scikit-Learn: Machine Learning in Python. *The Journal of Machine Learning Research* **2011**, *12*, 2825–2830.
(369) XGBoost | Proceedings of the 22nd ACM SIGKDD International Conference on Knowledge Discovery and Data Mining https://dl.acm.org/doi/10.1145/2939672.2939785 (accessed Apr 11, 2021).
(370) Abadi, M.; Agarwal, A.; Barham, P.; Brevdo, E.; Chen, Z.; Citro, C.; Corrado, G. S.; Davis, A.; Dean, J.; Devin, M.; Ghemawat, S.; Goodfellow, I.; Harp, A.; Irving, G.; Isard, M.; Jia, Y.; Jozefowicz, R.; Kaiser, L.; Kudlur, M.; Levenberg, J.; Mane, D.; Monga, R.; Moore, S.; Murray, D.; Olah, C.; Schuster, M.; Shlens, J.; Steiner, B.; Sutskever, I.; Talwar, K.; Tucker, P.; Vanhoucke, V.; Vasudevan, V.; Viegas, F.; Vinyals, O.; Warden, P.; Wattenberg, M.; Wicke, M.; Yu, Y.; Zheng, X. TensorFlow: Large-Scale Machine Learning on Heterogeneous Distributed Systems. *arXiv:1603.04467 [cs]* **2016**.
(371) Novoselov, K. S.; Fal′ko, V. I.; Colombo, L.; Gellert, P. R.; Schwab, M. G.; Kim, K. A Roadmap for Graphene. *Nature* **2012**, *490* (7419), 192–200. https://doi.org/10.1038/nature11458.
(372) Gupta, V. K.; Saleh, T. A. Sorption of Pollutants by Porous Carbon, Carbon Nanotubes and Fullerene- An Overview. *Environ Sci Pollut Res* **2013**, *20* (5), 2828–2843. https://doi.org/10.1007/s11356-013-1524-1.
(373) Burakov, A. E.; Galunin, E. V.; Burakova, I. V.; Kucherova, A. E.; Agarwal, S.; Tkachev, A. G.; Gupta, V. K. Adsorption of Heavy Metals on Conventional and Nanostructured Materials for Wastewater Treatment Purposes: A Review. *Ecotoxicology and Environmental Safety* **2018**, *148*, 702–712. https://doi.org/10.1016/j.ecoenv.2017.11.034.

(374) Castro Neto, A. H.; Guinea, F.; Peres, N. M. R.; Novoselov, K. S.; Geim, A. K. The Electronic Properties of Graphene. *Rev. Mod. Phys.* **2009**, *81* (1), 109–162. https://doi.org/10.1103/RevModPhys.81.109.
(375) Yoon, H.; Chang, Y. H.; Song, S. H.; Lee, E.-S.; Jin, S. H.; Park, C.; Lee, J.; Kim, B. H.; Kang, H. J.; Kim, Y.-H.; Jeon, S. Intrinsic Photoluminescence Emission from Subdomained Graphene Quantum Dots. *Advanced Materials* **2016**, *28* (26), 5255–5261. https://doi.org/10.1002/adma.201600616.
(376) Li, L.; Yan, X. Colloidal Graphene Quantum Dots. *J. Phys. Chem. Lett.* **2010**, *1* (17), 2572–2576. https://doi.org/10.1021/jz100862f.
(377) Ponomarenko, L. A.; Schedin, F.; Katsnelson, M. I.; Yang, R.; Hill, E. W.; Novoselov, K. S.; Geim, A. K. Chaotic Dirac Billiard in Graphene Quantum Dots. *Science* **2008**, *320* (5874), 356–358. https://doi.org/10.1126/science.1154663.
(378) Fujii, S.; Enoki, T. Cutting of Oxidized Graphene into Nanosized Pieces. *J. Am. Chem. Soc.* **2010**, *132* (29), 10034–10041. https://doi.org/10.1021/ja101265r.
(379) Eda, G.; Lin, Y.-Y.; Mattevi, C.; Yamaguchi, H.; Chen, H.-A.; Chen, I.-S.; Chen, C.-W.; Chhowalla, M. Blue Photoluminescence from Chemically Derived Graphene Oxide. *Advanced Materials* **2010**, *22* (4), 505–509. https://doi.org/10.1002/adma.200901996.
(380) Song, S. H.; Jang, M.-H.; Chung, J.; Jin, S. H.; Kim, B. H.; Hur, S.-H.; Yoo, S.; Cho, Y.-H.; Jeon, S. Highly Efficient Light-Emitting Diode of Graphene Quantum Dots Fabricated from Graphite Intercalation Compounds. *Advanced Optical Materials* **2014**, *2* (11), 1016–1023. https://doi.org/10.1002/adom.201400184.
(381) Shen, J.; Zhu, Y.; Yang, X.; Li, C. Graphene Quantum Dots : Emergent Nanolights for Bioimaging, Sensors, Catalysis and Photovoltaic Devices. *Chemical Communications* **2012**, *48* (31), 3686–3699. https://doi.org/10.1039/C2CC00110A.
(382) Peng, J.; Gao, W.; Gupta, B. K.; Liu, Z.; Romero-Aburto, R.; Ge, L.; Song, L.; Alemany, L. B.; Zhan, X.; Gao, G.; others. Graphene Quantum Dots Derived from Carbon Fibers. *Nano letters* **2012**, *12* (2), 844–849.
(383) Zhang, H.; Wang, Y.; Zhao, D.; Zeng, D.; Xia, J.; Aldalbahi, A.; Wang, C.; San, L.; Fan, C.; Zuo, X.; others. Universal Fluorescence Biosensor Platform Based on Graphene Quantum Dots and Pyrene-Functionalized Molecular Beacons for Detection of MicroRNAs. *ACS applied materials & interfaces* **2015**, *7* (30), 16152–16156.
(384) He, S.; Song, B.; Li, D.; Zhu, C.; Qi, W.; Wen, Y.; Wang, L.; Song, S.; Fang, H.; Fan, C. A Graphene Nanoprobe for Rapid, Sensitive, and Multicolor Fluorescent DNA Analysis. *Advanced Functional Materials* **2010**, *20* (3), 453–459. https://doi.org/10.1002/adfm.200901639.
(385) Chang, H.; Tang, L.; Wang, Y.; Jiang, J.; Li, J. Graphene Fluorescence Resonance Energy Transfer Aptasensor for the Thrombin Detection. *Anal. Chem.* **2010**, *82* (6), 2341–2346. https://doi.org/10.1021/ac9025384.
(386) Jeon, S.-J.; Kwak, S.-Y.; Yim, D.; Ju, J.-M.; Kim, J.-H. Chemically-Modulated Photoluminescence of Graphene Oxide for Selective Detection of Neurotransmitter by "Turn-On" Response. *J. Am. Chem. Soc.* **2014**, *136* (31), 10842–10845. https://doi.org/10.1021/ja504276z.
(387) Wang, Y.; Tang, L.; Li, Z.; Lin, Y.; Li, J. In Situ Simultaneous Monitoring of ATP and GTP Using a Graphene Oxide Nanosheet–Based Sensing Platform in Living Cells. *Nat. Protocols* **2014**, *9* (8), 1944–1955. https://doi.org/10.1038/nprot.2014.126.

(388) Li, X.; Wang, G.; Ding, X.; Chen, Y.; Gou, Y.; Lu, Y. A "Turn-on" Fluorescent Sensor for Detection of Pb 2+ Based on Graphene Oxide and G-Quadruplex DNA. *Physical Chemistry Chemical Physics* **2013**, *15* (31), 12800–12804. https://doi.org/10.1039/C3CP00047H.

(389) Liu, Z.; Robinson, J. T.; Sun, X.; Dai, H. PEGylated Nanographene Oxide for Delivery of Water-Insoluble Cancer Drugs. *J. Am. Chem. Soc.* **2008**, *130* (33), 10876–10877. https://doi.org/10.1021/ja803688x.

(390) Luo, N.; Weber, J. K.; Wang, S.; Luan, B.; Yue, H.; Xi, X.; Du, J.; Yang, Z.; Wei, W.; Zhou, R.; Ma, G. PEGylated Graphene Oxide Elicits Strong Immunological Responses despite Surface Passivation. *Nature Communications* **2017**, *8*, 14537. https://doi.org/10.1038/ncomms14537.

(391) Zhang, L.; Xia, J.; Zhao, Q.; Liu, L.; Zhang, Z. Functional Graphene Oxide as a Nanocarrier for Controlled Loading and Targeted Delivery of Mixed Anticancer Drugs. *Small* **2010**, *6* (4), 537–544. https://doi.org/10.1002/smll.200901680.

(392) Sun, X.; Liu, Z.; Welsher, K.; Robinson, J. T.; Goodwin, A.; Zaric, S.; Dai, H. Nano-Graphene Oxide for Cellular Imaging and Drug Delivery. *Nano Res.* **2008**, *1* (3), 203–212. https://doi.org/10.1007/s12274-008-8021-8.

(393) Lee, J.-H.; Choi, Y.-K.; Kim, H.-J.; Scheicher, R. H.; Cho, J.-H. Physisorption of DNA Nucleobases on H-BN and Graphene: VdW-Corrected DFT Calculations. *J. Phys. Chem. C* **2013**, *117* (26), 13435–13441. https://doi.org/10.1021/jp402403f.

(394) Willems, N.; Urtizberea, A.; Verre, A. F.; Iliut, M.; Lelimousin, M.; Hirtz, M.; Vijayaraghavan, A.; Sansom, M. S. P. Biomimetic Phospholipid Membrane Organization on Graphene and Graphene Oxide Surfaces: A Molecular Dynamics Simulation Study. *ACS Nano* **2017**, *11* (2), 1613–1625. https://doi.org/10.1021/acsnano.6b07352.

(395) Li, X.; Wang, X.; Zhang, L.; Lee, S.; Dai, H. Chemically Derived, Ultrasmooth Graphene Nanoribbon Semiconductors. *Science* **2008**, *319* (5867), 1229–1232. https://doi.org/10.1126/science.1150878.

(396) Wu, M.; Kempaiah, R.; Huang, P.-J. J.; Maheshwari, V.; Liu, J. Adsorption and Desorption of DNA on Graphene Oxide Studied by Fluorescently Labeled Oligonucleotides. *Langmuir* **2011**, *27* (6), 2731–2738.

(397) Varghese, N.; Mogera, U.; Govindaraj, A.; Das, A.; Maiti, P. K.; Sood, A. K.; Rao, C. N. R. Binding of DNA Nucleobases and Nucleosides with Graphene. *ChemPhysChem* **2009**, *10* (1), 206–210.

(398) Kim, H. S.; Farmer, B. L.; Yingling, Y. G. Effect of Graphene Oxidation Rate on Adsorption of Poly-Thymine Single Stranded DNA. *Advanced Materials Interfaces* **2017**, *4* (8), 1601168. https://doi.org/10.1002/admi.201601168.

(399) Ranganathan, S. V.; Halvorsen, K.; Myers, C. A.; Robertson, N. M.; Yigit, M. V.; Chen, A. A. Complex Thermodynamic Behavior of Single-Stranded Nucleic Acid Adsorption to Graphene Surfaces. *Langmuir* **2016**, *32* (24), 6028–6034. https://doi.org/10.1021/acs.langmuir.6b00456.

(400) Lin, Y.; Chapman, R.; Stevens, M. M. Integrative Self-Assembly of Graphene Quantum Dots and Biopolymers into a Versatile Biosensing Toolkit. *Advanced Functional Materials* **2015**, *25* (21), 3183–3192. https://doi.org/10.1002/adfm.201500624.

(401) Lu, L.; Guo, L.; Wang, X.; Kang, T.; Cheng, S. Complexation and Intercalation Modes: A Novel Interaction of DNA and Graphene Quantum Dots. *RSC Adv.* **2016**, *6* (39), 33072–33075. https://doi.org/10.1039/C6RA00930A.

(402) Hayakawa, T.; Ishii, Y.; Kawasaki, S. Sodium Ion Battery Anode Properties of Designed Graphene-Layers Synthesized from Polycyclic Aromatic Hydrocarbons. *RSC Advances* **2016**, *6* (26), 22069–22073. https://doi.org/10.1039/C6RA00955G.
(403) Dong, Y.; Shao, J.; Chen, C.; Li, H.; Wang, R.; Chi, Y.; Lin, X.; Chen, G. Blue Luminescent Graphene Quantum Dots and Graphene Oxide Prepared by Tuning the Carbonization Degree of Citric Acid. *Carbon* **2012**, *50* (12), 4738–4743.
(404) Kundu, S.; Wang, Y.; Xia, W.; Muhler, M. Thermal Stability and Reducibility of Oxygen-Containing Functional Groups on Multiwalled Carbon Nanotube Surfaces: A Quantitative High-Resolution XPS and TPD/TPR Study. *The Journal of Physical Chemistry C* **2008**, *112* (43), 16869–16878. https://doi.org/10.1021/jp804413a.
(405) Jang, M.-H.; Ha, H. D.; Lee, E.-S.; Liu, F.; Kim, Y.-H.; Seo, T. S.; Cho, Y.-H. Is the Chain of Oxidation and Reduction Process Reversible in Luminescent Graphene Quantum Dots? *Small* **2015**, *11* (31), 3773–3781.
(406) LeCroy, G. E.; Messina, F.; Sciortino, A.; Bunker, C. E.; Wang, P.; Fernando, K. A. S.; Sun, Y.-P. Characteristic Excitation Wavelength Dependence of Fluorescence Emissions in Carbon "Quantum" Dots. *J. Phys. Chem. C* **2017**, *121* (50), 28180–28186. https://doi.org/10.1021/acs.jpcc.7b10129.
(407) Zheng, S.; Tu, Q.; Urban, J. J.; Li, S.; Mi, B. Swelling of Graphene Oxide Membranes in Aqueous Solution: Characterization of Interlayer Spacing and Insight into Water Transport Mechanisms. *ACS Nano* **2017**, *11* (6), 6440–6450. https://doi.org/10.1021/acsnano.7b02999.
(408) Lu, C.; Huang, P.-J. J.; Liu, B.; Ying, Y.; Liu, J. Comparison of Graphene Oxide and Reduced Graphene Oxide for DNA Adsorption and Sensing. *Langmuir* **2016**, *32* (41), 10776–10783. https://doi.org/10.1021/acs.langmuir.6b03032.
(409) Ip, A. C.-F.; Liu, B.; Huang, P.-J. J.; Liu, J. Oxidation Level-Dependent Zwitterionic Liposome Adsorption and Rupture by Graphene-Based Materials and Light-Induced Content Release. *Small* **2013**, *9* (7), 1030–1035. https://doi.org/10.1002/smll.201202710.
(410) Li, M.; Zhou, X.; Ding, W.; Guo, S.; Wu, N. Fluorescent Aptamer-Functionalized Graphene Oxide Biosensor for Label-Free Detection of Mercury(II). *Biosensors and Bioelectronics* **2013**, *41*, 889–893. https://doi.org/10.1016/j.bios.2012.09.060.
(411) Zuckermann, R. N.; Kerr, J. M.; Kent, S. B. H.; Moos, W. H. Efficient Method for the Preparation of Peptoids [Oligo(N-Substituted Glycines)] by Submonomer Solid-Phase Synthesis. *Journal of the American Chemical Society* **1992**, *114* (26), 10646–10647. https://doi.org/10.1021/ja00052a076.
(412) Sowerby, S. J.; Cohn, C. A.; Heckl, W. M.; Holm, N. G. Differential Adsorption of Nucleic Acid Bases: Relevance to the Origin of Life. *PNAS* **2001**, *98* (3), 820–822. https://doi.org/10.1073/pnas.98.3.820.
(413) Manohar, S.; Mantz, A. R.; Bancroft, K. E.; Hui, C.-Y.; Jagota, A.; Vezenov, D. V. Peeling Single-Stranded DNA from Graphite Surface to Determine Oligonucleotide Binding Energy by Force Spectroscopy. *Nano Letters* **2008**, *8* (12), 4365–4372. https://doi.org/10.1021/nl8022143.
(414) Huang, Z.; Liu, J. Length-Dependent Diblock DNA with Poly-Cytosine (Poly-C) as High-Affinity Anchors on Graphene Oxide. *Langmuir* **2018**, *34* (3), 1171–1177. https://doi.org/10.1021/acs.langmuir.7b02812.
(415) Yang, D.; Velamakanni, A.; Bozoklu, G.; Park, S.; Stoller, M.; Piner, R. D.; Stankovich, S.; Jung, I.; Field, D. A.; Ventrice, C. A.; Ruoff, R. S. Chemical Analysis of Graphene

Oxide Films after Heat and Chemical Treatments by X-Ray Photoelectron and Micro-Raman Spectroscopy. *Carbon* **2009**, *47* (1), 145–152. https://doi.org/10.1016/j.carbon.2008.09.045.

(416) Lopez, A.; Liu, B.; Huang, Z.; Zhang, F.; Liu, J. Fluorescein-Stabilized i-Motif DNA and Its Unfolding Leading to a Stronger Adsorption Affinity. *Langmuir* **2019**, *35* (36), 11932–11939. https://doi.org/10.1021/acs.langmuir.9b01606.

(417) Phillips, J. C.; Braun, R.; Wang, W.; Gumbart, J.; Tajkhorshid, E.; Villa, E.; Chipot, C.; Skeel, R. D.; Kalé, L.; Schulten, K. Scalable Molecular Dynamics with NAMD. *Journal of Computational Chemistry* **2005**, *26* (16), 1781–1802. https://doi.org/10.1002/jcc.20289.

(418) Kumar, S.; Huang, C.; Zheng, G.; Bohm, E.; Bhatele, A.; Phillips, J. C.; Yu, H.; Kale, L. V. Scalable Molecular Dynamics with NAMD on the IBM Blue Gene/L System. *IBM Journal of Research and Development* **2008**, *52* (1.2), 177–188. https://doi.org/10.1147/rd.521.0177.

(419) Brooks, B. R.; Bruccoleri, R. E.; Olafson, B. D.; States, D. J.; Swaminathan, S.; Karplus, M. CHARMM: A Program for Macromolecular Energy, Minimization, and Dynamics Calculations. *Journal of Computational Chemistry* **1983**, *4* (2), 187–217. https://doi.org/10.1002/jcc.540040211.

(420) Humphrey, W.; Dalke, A.; Schulten, K. VMD: Visual Molecular Dynamics. *Journal of Molecular Graphics* **1996**, *14* (1), 33–38. https://doi.org/10.1016/0263-7855(96)00018-5.

(421) van Dijk, M.; Bonvin, A. M. J. J. 3D-DART: A DNA Structure Modelling Server. *Nucleic Acids Res* **2009**, *37* (suppl_2), W235–W239. https://doi.org/10.1093/nar/gkp287.

(422) Pedretti, A.; Villa, L.; Vistoli, G. VEGA – An Open Platform to Develop Chemo-Bio-Informatics Applications, Using Plug-in Architecture and Script Programming. *J Comput Aided Mol Des* **2004**, *18* (3), 167–173. https://doi.org/10.1023/B:JCAM.0000035186.90683.f2.

(423) Jorgensen, W. L.; Chandrasekhar, J.; Madura, J. D.; Impey, R. W.; Klein, M. L. Comparison of Simple Potential Functions for Simulating Liquid Water. *J. Chem. Phys.* **1983**, *79* (2), 926–935. https://doi.org/10.1063/1.445869.

(424) Zhang, Z.; Guan, J.; Jiang, Z.; Yang, Y.; Liu, J.; Hua, W.; Mao, Y.; Li, C.; Lu, W.; Qian, J.; Zhan, C. Brain-Targeted Drug Delivery by Manipulating Protein Corona Functions. *Nat Commun* **2019**, *10* (1), 1–11. https://doi.org/10.1038/s41467-019-11593-z.

(425) Jhaveri, A.; Deshpande, P.; Pattni, B.; Torchilin, V. Transferrin-Targeted, Resveratrol-Loaded Liposomes for the Treatment of Glioblastoma. *Journal of Controlled Release* **2018**, *277*, 89–101. https://doi.org/10.1016/j.jconrel.2018.03.006.

(426) Weiss, A. C. G.; Kelly, H. G.; Faria, M.; Besford, Q. A.; Wheatley, A. K.; Ang, C.-S.; Crampin, E. J.; Caruso, F.; Kent, S. J. Link between Low-Fouling and Stealth: A Whole Blood Biomolecular Corona and Cellular Association Analysis on Nanoengineered Particles. *ACS Nano* **2019**, *13* (5), 4980–4991. https://doi.org/10.1021/acsnano.9b00552.

(427) Mann, F. A.; Lv, Z.; Grosshans, J.; Opazo, F.; Kruss, S. Nanobody Conjugated Nanotubes for Targeted Near-Infrared in Vivo Imaging and Sensing. *Angewandte Chemie International Edition* **2019**, *0* (ja). https://doi.org/10.1002/anie.201904167.

(428) Chio, L.; Pinals, R. L.; Murali, A.; Goh, N. S.; Landry, M. P. Covalent Surface Modification Effects on Single-Walled Carbon Nanotubes for Targeted Sensing and Optical Imaging. *Advanced Functional Materials* **2020**, *30* (17), 1910556. https://doi.org/10.1002/adfm.201910556.

(429) Hume, D. A.; Irvine, K. M.; Pridans, C. The Mononuclear Phagocyte System: The Relationship between Monocytes and Macrophages. *Trends in Immunology* **2019**, *40* (2), 98–112. https://doi.org/10.1016/j.it.2018.11.007.
(430) Cai, R.; Chen, C. The Crown and the Scepter: Roles of the Protein Corona in Nanomedicine. *Adv. Mater.* **2019**, *31* (45), 1805740. https://doi.org/10.1002/adma.201805740.
(431) Huckaby, J. T.; Lai, S. K. PEGylation for Enhancing Nanoparticle Diffusion in Mucus. *Advanced Drug Delivery Reviews* **2018**, *124*, 125–139. https://doi.org/10.1016/j.addr.2017.08.010.
(432) Sanchez-Cano, C.; Carril, M. Recent Developments in the Design of Non-Biofouling Coatings for Nanoparticles and Surfaces. *IJMS* **2020**, *21* (3), 1007. https://doi.org/10.3390/ijms21031007.
(433) Zhou, M.; Huang, H.; Wang, D.; Lu, H.; Chen, J.; Chai, Z.; Yao, S. Q.; Hu, Y. Light-Triggered PEGylation/DePEGylation of the Nanocarriers for Enhanced Tumor Penetration. *Nano Lett.* **2019**, *19* (6), 3671–3675. https://doi.org/10.1021/acs.nanolett.9b00737.
(434) Müller, J.; Bauer, K. N.; Prozeller, D.; Simon, J.; Mailänder, V.; Wurm, F. R.; Winzen, S.; Landfester, K. Coating Nanoparticles with Tunable Surfactants Facilitates Control over the Protein Corona. *Biomaterials* **2017**, *115*, 1–8. https://doi.org/10.1016/j.biomaterials.2016.11.015.
(435) Zhang, P.; Sun, F.; Liu, S.; Jiang, S. Anti-PEG Antibodies in the Clinic: Current Issues and beyond PEGylation. *Journal of Controlled Release* **2016**, *244*, 184–193. https://doi.org/10.1016/j.jconrel.2016.06.040.
(436) Guan, J.; Shen, Q.; Zhang, Z.; Jiang, Z.; Yang, Y.; Lou, M.; Qian, J.; Lu, W.; Zhan, C. Enhanced Immunocompatibility of Ligand-Targeted Liposomes by Attenuating Natural IgM Absorption. *Nat Commun* **2018**, *9* (1), 2982. https://doi.org/10.1038/s41467-018-05384-1.
(437) Papi, M.; Caputo, D.; Palmieri, V.; Coppola, R.; Palchetti, S.; Bugli, F.; Martini, C.; Digiacomo, L.; Pozzi, D.; Caracciolo, G. Clinically Approved PEGylated Nanoparticles Are Covered by a Protein Corona That Boosts the Uptake by Cancer Cells. *Nanoscale* **2017**, *9* (29), 10327–10334. https://doi.org/10.1039/C7NR03042H.
(438) Li, S.; Cai, Y.; Cao, J.; Cai, M.; Chen, Y.; Luo, X. Phosphorylcholine Micelles Decorated by Hyaluronic Acid for Enhancing Antitumor Efficiency. *Polym. Chem.* **2017**, *8* (16), 2472–2483. https://doi.org/10.1039/C6PY02032A.
(439) Zhang, C.; Lu, J.; Hou, Y.; Xiong, W.; Sheng, K.; Lu, H. Investigation on the Linker Length of Synthetic Zwitterionic Polypeptides for Improved Nonfouling Surfaces. *ACS Appl. Mater. Interfaces* **2018**, *10* (20), 17463–17470. https://doi.org/10.1021/acsami.8b02854.
(440) Zhao, J.; Qin, Z.; Wu, J.; Li, L.; Jin, Q.; Ji, J. Zwitterionic Stealth Peptide-Protected Gold Nanoparticles Enable Long Circulation without the Accelerated Blood Clearance Phenomenon. *Biomater. Sci.* **2018**, *6* (1), 200–206. https://doi.org/10.1039/C7BM00747G.
(441) Zhao, K.; Li, D.; Xu, W.; Ding, J.; Jiang, W.; Li, M.; Wang, C.; Chen, X. Targeted Hydroxyethyl Starch Prodrug for Inhibiting the Growth and Metastasis of Prostate Cancer. *Biomaterials* **2017**, *116*, 82–94. https://doi.org/10.1016/j.biomaterials.2016.11.030.
(442) Simon, J.; Bauer, K. N.; Langhanki, J.; Opatz, T.; Mailänder, V.; Landfester, K.; Wurm, F. R. Noncovalent Targeting of Nanocarriers to Immune Cells with Polyphosphoester-

Based Surfactants in Human Blood Plasma. *Adv. Sci.* **2019**, *6* (22), 1901199. https://doi.org/10.1002/advs.201901199.

(443) Bhattacharya, A. A.; Grüne, T.; Curry, S. Crystallographic Analysis Reveals Common Modes of Binding of Medium and Long-Chain Fatty Acids to Human Serum Albumin 1 1Edited by R. Huber. *Journal of Molecular Biology* **2000**, *303* (5), 721–732. https://doi.org/10.1006/jmbi.2000.4158.

(444) Wilson, C.; Mau, T.; Weisgraber, K. H.; Wardell, M. R.; Mahley, R. W.; Agard, D. A. Salt Bridge Relay Triggers Defective LDL Receptor Binding by a Mutant Apolipoprotein. *Structure* **1994**, *2* (8), 713–718. https://doi.org/10.1016/S0969-2126(00)00072-1.

(445) Borhani, D. W.; Rogers, D. P.; Engler, J. A.; Brouillette, C. G. Crystal Structure of Truncated Human Apolipoprotein A-I Suggests a Lipid-Bound Conformation. *Proceedings of the National Academy of Sciences* **1997**, *94* (23), 12291–12296. https://doi.org/10.1073/pnas.94.23.12291.

(446) Fornaguera, C.; Guerra-Rebollo, M.; Lázaro, M. Á.; Cascante, A.; Rubio, N.; Blanco, J.; Borrós, S. In Vivo Retargeting of Poly(Beta Aminoester) (OM-PBAE) Nanoparticles Is Influenced by Protein Corona. *Adv. Healthcare Mater.* **2019**, *8* (19), 1900849. https://doi.org/10.1002/adhm.201900849.

(447) Shen, Y.; Li, X.; Dong, D.; Zhang, B.; Xue, Y.; Shang, P. Transferrin Receptor 1 in Cancer: A New Sight for Cancer Therapy. *Am J Cancer Res* **2018**, *8* (6), 916–931. https://doi.org/2156-6976/ajcr0080015.

(448) Han, Z.; Lu, Z.-R. Targeting Fibronectin for Cancer Imaging and Therapy. *J. Mater. Chem. B* **2017**, *5* (4), 639–654. https://doi.org/10.1039/C6TB02008A.

(449) Figueroa, S. M.; Fleischmann, D.; Beck, S.; Goepferich, A. The Effect of Ligand Mobility on the Cellular Interaction of Multivalent Nanoparticles. *Macromolecular Bioscience* **2020**, *20* (4), 1900427. https://doi.org/10.1002/mabi.201900427.

(450) Wang, T.; Wang, D.; Liu, J.; Feng, B.; Zhou, F.; Zhang, H.; Zhou, L.; Yin, Q.; Zhang, Z.; Cao, Z.; Yu, H.; Li, Y. Acidity-Triggered Ligand-Presenting Nanoparticles To Overcome Sequential Drug Delivery Barriers to Tumors. *Nano Lett.* **2017**, *17* (9), 5429–5436. https://doi.org/10.1021/acs.nanolett.7b02031.

(451) Han, H.; Valdepérez, D.; Jin, Q.; Yang, B.; Li, Z.; Wu, Y.; Pelaz, B.; Parak, W. J.; Ji, J. Dual Enzymatic Reaction-Assisted Gemcitabine Delivery Systems for Programmed Pancreatic Cancer Therapy. *ACS Nano* **2017**, *11* (2), 1281–1291. https://doi.org/10.1021/acsnano.6b05541.

(452) Almalik, A.; Benabdelkamel, H.; Masood, A.; Alanazi, I. O.; Alradwan, I.; Majrashi, M. A.; Alfadda, A. A.; Alghamdi, W. M.; Alrabiah, H.; Tirelli, N.; Alhasan, A. H. Hyaluronic Acid Coated Chitosan Nanoparticles Reduced the Immunogenicity of the Formed Protein Corona. *Sci Rep* **2017**, *7* (1), 10542. https://doi.org/10.1038/s41598-017-10836-7.

(453) Agrahari, V.; Burnouf, P.-A.; Burnouf, T.; Agrahari, V. Nanoformulation Properties, Characterization, and Behavior in Complex Biological Matrices: Challenges and Opportunities for Brain-Targeted Drug Delivery Applications and Enhanced Translational Potential. *Advanced Drug Delivery Reviews* **2019**, *148*, 146–180. https://doi.org/10.1016/j.addr.2019.02.008.

(454) Wu, M.; Zhang, H.; Tie, C.; Yan, C.; Deng, Z.; Wan, Q.; Liu, X.; Yan, F.; Zheng, H. MR Imaging Tracking of Inflammation-Activatable Engineered Neutrophils for Targeted Therapy of Surgically Treated Glioma. *Nature Communications* **2018**, *9* (1), 1–13. https://doi.org/10.1038/s41467-018-07250-6.

(455) Xue, J.; Zhao, Z.; Zhang, L.; Xue, L.; Shen, S.; Wen, Y.; Wei, Z.; Wang, L.; Kong, L.; Sun, H.; Ping, Q.; Mo, R.; Zhang, C. Neutrophil-Mediated Anticancer Drug Delivery for Suppression of Postoperative Malignant Glioma Recurrence. *Nature Nanotechnology* **2017**, *12* (7), 692–700. https://doi.org/10.1038/nnano.2017.54.

(456) Tang, L.; Wang, Y.; Li, J. The Graphene/Nucleic Acid Nanobiointerface. *Chemical Society Reviews* **2015**, *44* (19), 6954–6980.

(457) Nabi, B.; Rehman, S.; Khan, S.; Baboota, S.; Ali, J. Ligand Conjugation: An Emerging Platform for Enhanced Brain Drug Delivery. *Brain Research Bulletin* **2018**, *142*, 384–393. https://doi.org/10.1016/j.brainresbull.2018.08.003.

(458) Zhu, Y.; Chen, C.; Cao, Z.; Shen, S.; Li, L.; Li, D.; Wang, J.; Yang, X. On-Demand PEGylation and DePEGylation of PLA-Based Nanocarriers *via* Amphiphilic MPEG- *TK* -Ce6 for Nanoenabled Cancer Chemotherapy. *Theranostics* **2019**, *9* (26), 8312–8320. https://doi.org/10.7150/thno.37128.

(459) Kwon, Y.; Choi, Y.; Jang, J.; Yoon, S.; Choi, J. NIR Laser-Responsive PNIPAM and Gold Nanorod Composites for the Engineering of Thermally Reactive Drug Delivery Nanomedicine. *Pharmaceutics* **2020**, *12* (3), 204. https://doi.org/10.3390/pharmaceutics12030204.

(460) Puiggalí-Jou, A.; del Valle, L. J.; Alemán, C. Encapsulation and Storage of Therapeutic Fibrin-Homing Peptides Using Conducting Polymer Nanoparticles for Programmed Release by Electrical Stimulation. *ACS Biomater. Sci. Eng.* **2020**. https://doi.org/10.1021/acsbiomaterials.9b01794.

(461) Yu, J.; Chu, X.; Hou, Y. Stimuli-Responsive Cancer Therapy Based on Nanoparticles. *Chem. Commun.* **2014**, *50* (79), 11614–11630. https://doi.org/10.1039/C4CC03984J.

(462) Lim, C.; Cho, E.-B.; Kim, D. PH-Triggered Intracellular Release of Doxorubicin from Polyaspartamide-Encapsulated Mesoporous Silica Nanoparticles. *Korean J. Chem. Eng.* **2019**, *36* (1), 166–172. https://doi.org/10.1007/s11814-018-0185-7.

(463) Li, G.; Gao, Y.; Gong, C.; Han, Z.; Qiang, L.; Tai, Z.; Tian, J.; Gao, S. Dual-Blockade Immune Checkpoint for Breast Cancer Treatment Based on a Tumor-Penetrating Peptide Assembling Nanoparticle. *ACS Appl. Mater. Interfaces* **2019**, *11* (43), 39513–39524. https://doi.org/10.1021/acsami.9b13354.

(464) Jin, G.; He, R.; Liu, Q.; Lin, M.; Dong, Y.; Li, K.; Tang, B. Z.; Liu, B.; Xu, F. Near-Infrared Light-Regulated Cancer Theranostic Nanoplatform Based on Aggregation-Induced Emission Luminogen Encapsulated Upconversion Nanoparticles. *Theranostics* **2019**, *9* (1), 246–264. https://doi.org/10.7150/thno.30174.

(465) Feng, B.; Hou, B.; Xu, Z.; Saeed, M.; Yu, H.; Li, Y. Self-Amplified Drug Delivery with Light-Inducible Nanocargoes to Enhance Cancer Immunotherapy. *Adv. Mater.* **2019**, *31* (40), 1902960. https://doi.org/10.1002/adma.201902960.

(466) Gao, A.; Chen, B.; Gao, J.; Zhou, F.; Saeed, M.; Hou, B.; Li, Y.; Yu, H. Sheddable Prodrug Vesicles Combating Adaptive Immune Resistance for Improved Photodynamic Immunotherapy of Cancer. *Nano Lett.* **2020**, *20* (1), 353–362. https://doi.org/10.1021/acs.nanolett.9b04012.

(467) Li, J.; Xu, R.; Lu, X.; He, J.; Jin, S. A Simple Reduction-Sensitive Micelles Co-Delivery of Paclitaxel and Dasatinib to Overcome Tumor Multidrug Resistance. *IJN* **2017**, *Volume 12*, 8043–8056. https://doi.org/10.2147/IJN.S148273.

(468) Yang, Z.; Guo, Q.; Cai, Y.; Zhu, X.; Zhu, C.; Li, Y.; Li, B. Poly(Ethylene Glycol)-Sheddable Reduction-Sensitive Polyurethane Micelles for Triggered Intracellular Drug

Delivery for Osteosarcoma Treatment. *Journal of Orthopaedic Translation* **2020**, *21*, 57–65. https://doi.org/10.1016/j.jot.2019.11.001.

(469) Yu, H.; Jin, F.; Liu, D.; Shu, G.; Wang, X.; Qi, J.; Sun, M.; Yang, P.; Jiang, S.; Ying, X.; Du, Y. ROS-Responsive Nano-Drug Delivery System Combining Mitochondria-Targeting Ceria Nanoparticles with Atorvastatin for Acute Kidney Injury. *Theranostics* **2020**, *10* (5), 2342–2357. https://doi.org/10.7150/thno.40395.

(470) Scannevin, R. H.; Alexander, R.; Haarlander, T. M.; Burke, S. L.; Singer, M.; Huo, C.; Zhang, Y.-M.; Maguire, D.; Spurlino, J.; Deckman, I.; Carroll, K. I.; Lewandowski, F.; Devine, E.; Dzordzorme, K.; Tounge, B.; Milligan, C.; Bayoumy, S.; Williams, R.; Schalk-Hihi, C.; Leonard, K.; Jackson, P.; Todd, M.; Kuo, L. C.; Rhodes, K. J. Discovery of a Highly Selective Chemical Inhibitor of Matrix Metalloproteinase-9 (MMP-9) That Allosterically Inhibits Zymogen Activation. *J. Biol. Chem.* **2017**, *292* (43), 17963–17974. https://doi.org/10.1074/jbc.M117.806075.

(471) Mirković, B.; Renko, M.; Turk, S.; Sosič, I.; Jevnikar, Z.; Obermajer, N.; Turk, D.; Gobec, S.; Kos, J. Novel Mechanism of Cathepsin B Inhibition by Antibiotic Nitroxoline and Related Compounds. *ChemMedChem* **2011**, *6* (8), 1351–1356. https://doi.org/10.1002/cmdc.201100098.

(472) Coty, J.-B.; Eleamen Oliveira, E.; Vauthier, C. Tuning Complement Activation and Pathway through Controlled Molecular Architecture of Dextran Chains in Nanoparticle Corona. *International Journal of Pharmaceutics* **2017**, *532* (2), 769–778. https://doi.org/10.1016/j.ijpharm.2017.04.048.

(473) Fülöp, T.; Nemes, R.; Mészáros, T.; Urbanics, R.; Kok, R. J.; Jackman, J. A.; Cho, N.-J.; Storm, G.; Szebeni, J. Complement Activation in Vitro and Reactogenicity of Low-Molecular Weight Dextran-Coated SPIONs in the Pig CARPA Model: Correlation with Physicochemical Features and Clinical Information. *Journal of Controlled Release* **2018**, *270*, 268–274. https://doi.org/10.1016/j.jconrel.2017.11.043.

(474) Mo, J.; Xu, Y.; Wang, X.; Wei, W.; Zhao, J. Exploiting the Protein Corona: Coating of Black Phosphorus Nanosheets Enables Macrophage Polarization *via* Calcium Influx. *Nanoscale* **2020**, *12* (3), 1742–1748. https://doi.org/10.1039/C9NR08570J.

(475) Gabizon, A.; Tzemach, D.; Mak, L.; Bronstein, M.; Horowitz, A. T. Dose Dependency of Pharmacokinetics and Therapeutic Efficacy of Pegylated Liposomal Doxorubicin (DOXIL) in Murine Models. *Journal of Drug Targeting* **2002**, *10* (7), 539–548. https://doi.org/10.1080/1061186021000072447.

(476) Luk, B. T.; Jiang, Y.; Copp, J. A.; Hu, C.-M. J.; Krishnan, N.; Gao, W.; Li, S.; Fang, R. H.; Zhang, L. Biomimetic Targeting of Nanoparticles to Immune Cell Subsets via Cognate Antigen Interactions. *Mol. Pharmaceutics* **2018**, *15* (9), 3723–3728. https://doi.org/10.1021/acs.molpharmaceut.8b00074.

(477) Pondman, K. M.; Sobik, M.; Nayak, A.; Tsolaki, A. G.; Jäkel, A.; Flahaut, E.; Hampel, S.; ten Haken, B.; Sim, R. B.; Kishore, U. Complement Activation by Carbon Nanotubes and Its Influence on the Phagocytosis and Cytokine Response by Macrophages. *Nanomedicine: Nanotechnology, Biology and Medicine* **2014**, *10* (6), 1287–1299. https://doi.org/10.1016/j.nano.2014.02.010.

(478) Wang, G.; Chen, F.; Banda, N. K.; Holers, V. M.; Wu, L.; Moghimi, S. M.; Simberg, D. Activation of Human Complement System by Dextran-Coated Iron Oxide Nanoparticles Is Not Affected by Dextran/Fe Ratio, Hydroxyl Modifications, and Crosslinking. *Front. Immunol.* **2016**, *7*. https://doi.org/10.3389/fimmu.2016.00418.

(479) Ding, T.; Sun, J. Formation of Protein Corona on Nanoparticle Affects Different Complement Activation Pathways Mediated by C1q. *Pharm Res* **2020**, *37* (1), 10. https://doi.org/10.1007/s11095-019-2747-8.
(480) Dai, Q.; Guo, J.; Yan, Y.; Ang, C.-S.; Bertleff-Zieschang, N.; Caruso, F. Cell-Conditioned Protein Coronas on Engineered Particles Influence Immune Responses. *Biomacromolecules* **2017**, *18* (2), 431–439. https://doi.org/10.1021/acs.biomac.6b01545.
(481) Ray, P. D.; Huang, B.-W.; Tsuji, Y. Reactive Oxygen Species (ROS) Homeostasis and Redox Regulation in Cellular Signaling. *Cellular Signalling* **2012**, *24* (5), 981–990. https://doi.org/10.1016/j.cellsig.2012.01.008.
(482) Jayaram, D. T.; Runa, S.; Kemp, M. L.; Payne, C. K. Nanoparticle-Induced Oxidation of Corona Proteins Initiates an Oxidative Stress Response in Cells. *Nanoscale* **2017**, *9* (22), 7595–7601. https://doi.org/10.1039/C6NR09500C.
(483) de Araújo, R. F.; de Araújo, A. A.; Pessoa, J. B.; Freire Neto, F. P.; da Silva, G. R.; Leitão Oliveira, A. L. C. S.; de Carvalho, T. G.; Silva, H. F. O.; Eugênio, M.; Sant'Anna, C.; Gasparotto, L. H. S. Anti-Inflammatory, Analgesic and Anti-Tumor Properties of Gold Nanoparticles. *Pharmacological Reports* **2017**, *69* (1), 119–129. https://doi.org/10.1016/j.pharep.2016.09.017.
(484) Gioria, S.; Caputo, F.; Urbán, P.; Maguire, C. M.; Bremer-Hoffmann, S.; Prina-Mello, A.; Calzolai, L.; Mehn, D. Are Existing Standard Methods Suitable for the Evaluation of Nanomedicines: Some Case Studies. *Nanomedicine* **2018**, *13* (5), 539–554. https://doi.org/10.2217/nnm-2017-0338.
(485) Riaz Ahmed, K. B.; Nagy, A. M.; Brown, R. P.; Zhang, Q.; Malghan, S. G.; Goering, P. L. Silver Nanoparticles: Significance of Physicochemical Properties and Assay Interference on the Interpretation of in Vitro Cytotoxicity Studies. *Toxicology in Vitro* **2017**, *38*, 179–192. https://doi.org/10.1016/j.tiv.2016.10.012.
(486) Wörle-Knirsch, J. M.; Pulskamp, K.; Krug, H. F. Oops They Did It Again! Carbon Nanotubes Hoax Scientists in Viability Assays. *Nano Lett.* **2006**, *6* (6), 1261–1268. https://doi.org/10.1021/nl060177c.
(487) Boehnke, N.; Correa, S.; Hao, L.; Wang, W.; Straehla, J. P.; Bhatia, S. N.; Hammond, P. T. Theranostic Layer-by-Layer Nanoparticles for Simultaneous Tumor Detection and Gene Silencing. *Angewandte Chemie International Edition* **2020**, *59* (7), 2776–2783. https://doi.org/10.1002/anie.201911762.
(488) Dahlman, J. E.; Kauffman, K. J.; Xing, Y.; Shaw, T. E.; Mir, F. F.; Dlott, C. C.; Langer, R.; Anderson, D. G.; Wang, E. T. Barcoded Nanoparticles for High Throughput in Vivo Discovery of Targeted Therapeutics. *PNAS* **2017**, *114* (8), 2060–2065. https://doi.org/10.1073/pnas.1620874114.
(489) WHO Coronavirus Disease (COVID-19) Dashboard https://covid19.who.int (accessed Feb 15, 2021).
(490) Poletti, P.; Tirani, M.; Cereda, D.; Trentini, F.; Guzzetta, G.; Sabatino, G.; Marziano, V.; Castrofino, A.; Grosso, F.; Del Castillo, G.; Piccarreta, R.; ATS Lombardy COVID-19 Task Force; Andreassi, A.; Melegaro, A.; Gramegna, M.; Ajelli, M.; Merler, S. Probability of Symptoms and Critical Disease after SARS-CoV-2 Infection. *arXiv:2006.08471 [q-bio]* **2020**.
(491) Li, Q.; Guan, X.; Wu, P.; Wang, X.; Zhou, L.; Tong, Y.; Ren, R.; Leung, K. S. M.; Lau, E. H. Y.; Wong, J. Y.; Xing, X.; Xiang, N.; Wu, Y.; Li, C.; Chen, Q.; Li, D.; Liu, T.; Zhao, J.; Liu, M.; Tu, W.; Chen, C.; Jin, L.; Yang, R.; Wang, Q.; Zhou, S.; Wang, R.; Liu, H.;

Luo, Y.; Liu, Y.; Shao, G.; Li, H.; Tao, Z.; Yang, Y.; Deng, Z.; Liu, B.; Ma, Z.; Zhang, Y.; Shi, G.; Lam, T. T. Y.; Wu, J. T.; Gao, G. F.; Cowling, B. J.; Yang, B.; Leung, G. M.; Feng, Z. Early Transmission Dynamics in Wuhan, China, of Novel Coronavirus-Infected Pneumonia. *The New England Journal of Medicine* **2020**, *382* (13), 1199–1207. https://doi.org/10.1056/NEJMoa2001316.

(492) Esbin, M. N.; Whitney, O. N.; Chong, S.; Maurer, A.; Darzacq, X.; Tjian, R. Overcoming the Bottleneck to Widespread Testing: A Rapid Review of Nucleic Acid Testing Approaches for COVID-19 Detection. *RNA (New York, N.Y.)* **2020**, *26* (7), 771–783. https://doi.org/10.1261/rna.076232.120.

(493) Mio, C.; Cifù, A.; Marzinotto, S.; Bergamin, N.; Caldana, C.; Cattarossi, S.; Cmet, S.; Cussigh, A.; Martinella, R.; Zucco, J.; Verardo, R.; Schneider, C.; Marcon, B.; Zampieri, S.; Pipan, C.; Curcio, F. A Streamlined Approach to Rapidly Detect SARS-CoV-2 Infection Avoiding RNA Extraction: Workflow Validation https://www.hindawi.com/journals/dm/2020/8869424/ (accessed Feb 15, 2021). https://doi.org/10.1155/2020/8869424.

(494) Sentmanat, M.; Kouranova, E.; Cui, X. One-Step RNA Extraction for RT-QPCR Detection of 2019-NCoV. *bioRxiv* **2020**, 2020.04.02.022384. https://doi.org/10.1101/2020.04.02.022384.

(495) Won, J.; Lee, S.; Park, M.; Kim, T. Y.; Park, M. G.; Choi, B. Y.; Kim, D.; Chang, H.; Kim, V. N.; Lee, C. J. Development of a Laboratory-Safe and Low-Cost Detection Protocol for SARS-CoV-2 of the Coronavirus Disease 2019 (COVID-19). *Experimental Neurobiology* **2020**, *29* (2), 107–119. https://doi.org/10.5607/en20009.

(496) McMinn, S.; Carlsen, A.; Jaspers, B.; Talbot, R.; Adeline, S. In Large Texas Cities, Access To Coronavirus Testing May Depend On Where You Live. *NPR*. May 27, 2020.

(497) Collins, K. Is Your State Doing Enough Coronavirus Testing? *The New York Times*.

(498) Yu, L.; Wu, S.; Hao, X.; Dong, X.; Mao, L.; Pelechano, V.; Chen, W.-H.; Yin, X. Rapid Detection of COVID-19 Coronavirus Using a Reverse Transcriptional Loop-Mediated Isothermal Amplification (RT-LAMP) Diagnostic Platform. *Clin Chem* **2020**, *66* (7), 975–977. https://doi.org/10.1093/clinchem/hvaa102.

(499) Qiu, G.; Gai, Z.; Tao, Y.; Schmitt, J.; Kullak-Ublick, G. A.; Wang, J. Dual-Functional Plasmonic Photothermal Biosensors for Highly Accurate Severe Acute Respiratory Syndrome Coronavirus 2 Detection. *ACS Nano* **2020**, *14* (5), 5268–5277. https://doi.org/10.1021/acsnano.0c02439.

(500) Broughton, J. P.; Deng, X.; Yu, G.; Fasching, C. L.; Servellita, V.; Singh, J.; Miao, X.; Streithorst, J. A.; Granados, A.; Sotomayor-Gonzalez, A.; Zorn, K.; Gopez, A.; Hsu, E.; Gu, W.; Miller, S.; Pan, C.-Y.; Guevara, H.; Wadford, D. A.; Chen, J. S.; Chiu, C. Y. CRISPR–Cas12-Based Detection of SARS-CoV-2. *Nature Biotechnology* **2020**, *38* (7), 870–874. https://doi.org/10.1038/s41587-020-0513-4.

(501) Guglielmi, G. The Explosion of New Coronavirus Tests That Could Help to End the Pandemic. *Nature* **2020**, *583* (7817), 506–509. https://doi.org/10.1038/d41586-020-02140-8.

(502) Guglielmi, G. Fast Coronavirus Tests: What They Can and Can't Do. *Nature* **2020**, *585* (7826), 496–498. https://doi.org/10.1038/d41586-020-02661-2.

(503) Du, L.; He, Y.; Zhou, Y.; Liu, S.; Zheng, B.-J.; Jiang, S. The Spike Protein of SARS-CoV — a Target for Vaccine and Therapeutic Development. *Nature Reviews Microbiology* **2009**, *7* (3), 226–236. https://doi.org/10.1038/nrmicro2090.

(504) Lan, J.; Ge, J.; Yu, J.; Shan, S.; Zhou, H.; Fan, S.; Zhang, Q.; Shi, X.; Wang, Q.; Zhang, L.; Wang, X. Structure of the SARS-CoV-2 Spike Receptor-Binding Domain Bound to the ACE2 Receptor. *Nature* **2020**, 1–6. https://doi.org/10.1038/s41586-020-2180-5.

(505) Sui, J.; Li, W.; Murakami, A.; Tamin, A.; Matthews, L. J.; Wong, S. K.; Moore, M. J.; Tallarico, A. S. C.; Olurinde, M.; Choe, H.; Anderson, L. J.; Bellini, W. J.; Farzan, M.; Marasco, W. A. Potent Neutralization of Severe Acute Respiratory Syndrome (SARS) Coronavirus by a Human MAb to S1 Protein That Blocks Receptor Association. *PNAS* **2004**, *101* (8), 2536–2541. https://doi.org/10.1073/pnas.0307140101.

(506) Bar-On, Y. M.; Flamholz, A.; Phillips, R.; Milo, R. SARS-CoV-2 (COVID-19) by the Numbers. *eLife* **2020**, *9*, e57309. https://doi.org/10.7554/eLife.57309.

(507) Seo, G.; Lee, G.; Kim, M. J.; Baek, S.-H.; Choi, M.; Ku, K. B.; Lee, C.-S.; Jun, S.; Park, D.; Kim, H. G.; Kim, S.-J.; Lee, J.-O.; Kim, B. T.; Park, E. C.; Kim, S. I. Rapid Detection of COVID-19 Causative Virus (SARS-CoV-2) in Human Nasopharyngeal Swab Specimens Using Field-Effect Transistor-Based Biosensor. *ACS Nano* **2020**, *14* (4), 5135–5142. https://doi.org/10.1021/acsnano.0c02823.

(508) Zhu, X.; Wang, X.; Han, L.; Chen, T.; Wang, L.; Li, H.; Li, S.; He, L.; Fu, X.; Chen, S.; Xing, M.; Chen, H.; Wang, Y. Multiplex Reverse Transcription Loop-Mediated Isothermal Amplification Combined with Nanoparticle-Based Lateral Flow Biosensor for the Diagnosis of COVID-19. *Biosensors and Bioelectronics* **2020**, *166*, 112437. https://doi.org/10.1016/j.bios.2020.112437.

(509) Udugama, B.; Kadhiresan, P.; Kozlowski, H. N.; Malekjahani, A.; Osborne, M.; Li, V. Y. C.; Chen, H.; Mubareka, S.; Gubbay, J. B.; Chan, W. C. W. Diagnosing COVID-19: The Disease and Tools for Detection. *ACS Nano* **2020**, *14* (4), 3822–3835. https://doi.org/10.1021/acsnano.0c02624.

(510) Moitra, P.; Alafeef, M.; Dighe, K.; Frieman, M. B.; Pan, D. Selective Naked-Eye Detection of SARS-CoV-2 Mediated by N Gene Targeted Antisense Oligonucleotide Capped Plasmonic Nanoparticles. *ACS Nano* **2020**, *14* (6), 7617–7627. https://doi.org/10.1021/acsnano.0c03822.

(511) Teengam, P.; Siangproh, W.; Tuantranont, A.; Vilaivan, T.; Chailapakul, O.; Henry, C. S. Multiplex Paper-Based Colorimetric DNA Sensor Using Pyrrolidinyl Peptide Nucleic Acid-Induced AgNPs Aggregation for Detecting MERS-CoV, MTB, and HPV Oligonucleotides. *Anal. Chem.* **2017**, *89* (10), 5428–5435. https://doi.org/10.1021/acs.analchem.7b00255.

(512) Salem, D. P.; Gong, X.; Liu, A. T.; Akombi, K.; Strano, M. S. Immobilization and Function of NIR-Fluorescent Carbon Nanotube Sensors on Paper Substrates for Fluidic Manipulation. *Anal. Chem.* **2020**, *92* (1), 916–923. https://doi.org/10.1021/acs.analchem.9b03756.

(513) Kozawa, D.; Cho, S.-Y.; Gong, X.; Nguyen, F. T.; Jin, X.; Lee, M. A.; Lee, H.; Zeng, A.; Xue, G.; Schacherl, J.; Gibson, S.; Vega, L.; Strano, M. S. A Fiber Optic Interface Coupled to Nanosensors: Applications to Protein Aggregation and Organic Molecule Quantification. *ACS Nano* **2020**, *14* (8), 10141–10152. https://doi.org/10.1021/acsnano.0c03417.

(514) Wong, M. H.; Giraldo, J. P.; Kwak, S.-Y.; Koman, V. B.; Sinclair, R.; Lew, T. T. S.; Bisker, G.; Liu, P.; Strano, M. S. Nitroaromatic Detection and Infrared Communication from Wild-Type Plants Using Plant Nanobionics. *Nature Materials* **2017**, *16* (2), 264–272. https://doi.org/10.1038/nmat4771.

(515) Salem, D. P.; Gong, X.; Lee, H.; Zeng, A.; Xue, G.; Schacherl, J.; Gibson, S.; Strano, M. S. Characterization of Protein Aggregation Using Hydrogel-Encapsulated NIR Fluorescent Nanoparticle Sensors. *ACS Sens.* **2020**, *5* (2), 327–337. https://doi.org/10.1021/acssensors.9b01586.

(516) Heller, D. A.; Pratt, G. W.; Zhang, J.; Nair, N.; Hansborough, A. J.; Boghossian, A. A.; Reuel, N. F.; Barone, P. W.; Strano, M. S. Peptide Secondary Structure Modulates Single-Walled Carbon Nanotube Fluorescence as a Chaperone Sensor for Nitroaromatics. *PNAS* **2011**, *108* (21), 8544–8549. https://doi.org/10.1073/pnas.1005512108.

(517) Tai, W.; He, L.; Zhang, X.; Pu, J.; Voronin, D.; Jiang, S.; Zhou, Y.; Du, L. Characterization of the Receptor-Binding Domain (RBD) of 2019 Novel Coronavirus: Implication for Development of RBD Protein as a Viral Attachment Inhibitor and Vaccine. *Cellular & Molecular Immunology* **2020**, *17* (6), 613–620. https://doi.org/10.1038/s41423-020-0400-4.

(518) Wrapp, D.; Wang, N.; Corbett, K. S.; Goldsmith, J. A.; Hsieh, C.-L.; Abiona, O.; Graham, B. S.; McLellan, J. S. Cryo-EM Structure of the 2019-NCoV Spike in the Prefusion Conformation. *Science* **2020**, *367* (6483), 1260–1263. https://doi.org/10.1126/science.abb2507.

(519) Zou, L.; Ruan, F.; Huang, M.; Liang, L.; Huang, H.; Hong, Z.; Yu, J.; Kang, M.; Song, Y.; Xia, J.; Guo, Q.; Song, T.; He, J.; Yen, H.-L.; Peiris, M.; Wu, J. SARS-CoV-2 Viral Load in Upper Respiratory Specimens of Infected Patients. *New England Journal of Medicine* **2020**, *382* (12), 1177–1179. https://doi.org/10.1056/NEJMc2001737.

(520) Pan, Y.; Zhang, D.; Yang, P.; Poon, L. L. M.; Wang, Q. Viral Load of SARS-CoV-2 in Clinical Samples. *The Lancet Infectious Diseases* **2020**, *20* (4), 411–412. https://doi.org/10.1016/S1473-3099(20)30113-4.

(521) To, K. K.-W.; Tsang, O. T.-Y.; Leung, W.-S.; Tam, A. R.; Wu, T.-C.; Lung, D. C.; Yip, C. C.-Y.; Cai, J.-P.; Chan, J. M.-C.; Chik, T. S.-H.; Lau, D. P.-L.; Choi, C. Y.-C.; Chen, L.-L.; Chan, W.-M.; Chan, K.-H.; Ip, J. D.; Ng, A. C.-K.; Poon, R. W.-S.; Luo, C.-T.; Cheng, V. C.-C.; Chan, J. F.-W.; Hung, I. F.-N.; Chen, Z.; Chen, H.; Yuen, K.-Y. Temporal Profiles of Viral Load in Posterior Oropharyngeal Saliva Samples and Serum Antibody Responses during Infection by SARS-CoV-2: An Observational Cohort Study. *The Lancet Infectious Diseases* **2020**, *20* (5), 565–574. https://doi.org/10.1016/S1473-3099(20)30196-1.

(522) Wyllie, A. L.; Fournier, J.; Casanovas-Massana, A.; Campbell, M.; Tokuyama, M.; Vijayakumar, P.; Warren, J. L.; Geng, B.; Muenker, M. C.; Moore, A. J.; Vogels, C. B. F.; Petrone, M. E.; Ott, I. M.; Lu, P.; Venkataraman, A.; Lu-Culligan, A.; Klein, J.; Earnest, R.; Simonov, M.; Datta, R.; Handoko, R.; Naushad, N.; Sewanan, L. R.; Valdez, J.; White, E. B.; Lapidus, S.; Kalinich, C. C.; Jiang, X.; Kim, D. J.; Kudo, E.; Linehan, M.; Mao, T.; Moriyama, M.; Oh, J. E.; Park, A.; Silva, J.; Song, E.; Takahashi, T.; Taura, M.; Weizman, O.-E.; Wong, P.; Yang, Y.; Bermejo, S.; Odio, C. D.; Omer, S. B.; Dela Cruz, C. S.; Farhadian, S.; Martinello, R. A.; Iwasaki, A.; Grubaugh, N. D.; Ko, A. I. Saliva or Nasopharyngeal Swab Specimens for Detection of SARS-CoV-2. *New England Journal of Medicine* **2020**, *383* (13), 1283–1286. https://doi.org/10.1056/NEJMc2016359.

(523) Shao, Q.; Jiang, S. Molecular Understanding and Design of Zwitterionic Materials. *Advanced Materials* **2015**, *27* (1), 15–26. https://doi.org/10.1002/adma.201404059.

(524) Kwon, H.; Furmanchuk, A.; Kim, M.; Meany, B.; Guo, Y.; Schatz, G. C.; Wang, Y. Molecularly Tunable Fluorescent Quantum Defects. *J. Am. Chem. Soc.* **2016**, *138* (21), 6878–6885. https://doi.org/10.1021/jacs.6b03618.

(525) Li, F. Structure, Function, and Evolution of Coronavirus Spike Proteins. *Annual Review of Virology* **2016**, *3* (1), 237–261. https://doi.org/10.1146/annurev-virology-110615-042301.

(526) Lv, H.; Wu, N. C.; Tsang, O. T.-Y.; Yuan, M.; Perera, R. A. P. M.; Leung, W. S.; So, R. T. Y.; Chan, J. M. C.; Yip, G. K.; Chik, T. S. H.; Wang, Y.; Choi, C. Y. C.; Lin, Y.; Ng, W. W.; Zhao, J.; Poon, L. L. M.; Peiris, J. S. M.; Wilson, I. A.; Mok, C. K. P. Cross-Reactive Antibody Response between SARS-CoV-2 and SARS-CoV Infections. *Cell Reports* **2020**, *31* (9). https://doi.org/10.1016/j.celrep.2020.107725.

(527) Schoof, M.; Faust, B.; Saunders, R. A.; Sangwan, S.; Rezelj, V.; Hoppe, N.; Boone, M.; Billesbølle, C. B.; Puchades, C.; Azumaya, C. M.; Kratochvil, H. T.; Zimanyi, M.; Deshpande, I.; Liang, J.; Dickinson, S.; Nguyen, H. C.; Chio, C. M.; Merz, G. E.; Thompson, M. C.; Diwanji, D.; Schaefer, K.; Anand, A. A.; Dobzinski, N.; Zha, B. S.; Simoneau, C. R.; Leon, K.; White, K. M.; Chio, U. S.; Gupta, M.; Jin, M.; Li, F.; Liu, Y.; Zhang, K.; Bulkley, D.; Sun, M.; Smith, A. M.; Rizo, A. N.; Moss, F.; Brilot, A. F.; Pourmal, S.; Trenker, R.; Pospiech, T.; Gupta, S.; Barsi-Rhyne, B.; Belyy, V.; Barile-Hill, A. W.; Nock, S.; Liu, Y.; Krogan, N. J.; Ralston, C. Y.; Swaney, D. L.; García-Sastre, A.; Ott, M.; Vignuzzi, M.; Consortium4‡, Q. S. B.; Walter, P.; Manglik, A. An Ultrapotent Synthetic Nanobody Neutralizes SARS-CoV-2 by Stabilizing Inactive Spike. *Science* **2020**, *370* (6523), 1473–1479. https://doi.org/10.1126/science.abe3255.

(528) Wrapp, D.; De Vlieger, D.; Corbett, K. S.; Torres, G. M.; Wang, N.; Van Breedam, W.; Roose, K.; van Schie, L.; Hoffmann, M.; Pöhlmann, S.; Graham, B. S.; Callewaert, N.; Schepens, B.; Saelens, X.; McLellan, J. S. Structural Basis for Potent Neutralization of Betacoronaviruses by Single-Domain Camelid Antibodies. *Cell* **2020**, *181* (5), 1004-1015.e15. https://doi.org/10.1016/j.cell.2020.04.031.

(529) Dunakey, S. J. G.; Coyle, B. L.; Thomas, A.; Xu, M.; Swift, B. J. F.; Baneyx, F. Selective Labeling and Decoration of the Ends and Sidewalls of Single-Walled Carbon Nanotubes Using Mono- and Bispecific Solid-Binding Fluorescent Proteins. *Bioconjugate Chem.* **2019**, *30* (3), 959–965. https://doi.org/10.1021/acs.bioconjchem.9b00097.

(530) Satishkumar, B. C.; Brown, L. O.; Gao, Y.; Wang, C.-C.; Wang, H.-L.; Doorn, S. K. Reversible Fluorescence Quenching in Carbon Nanotubes for Biomolecular Sensing. *Nature Nanotechnology* **2007**, *2* (9), 560–564. https://doi.org/10.1038/nnano.2007.261.

(531) Mohamed, R.; Campbell, J.-L.; Cooper-White, J.; Dimeski, G.; Punyadeera, C. The Impact of Saliva Collection and Processing Methods on CRP, IgE, and Myoglobin Immunoassays. *Clin Trans Med* **2012**, *1* (1), 19. https://doi.org/10.1186/2001-1326-1-19.

(532) Jeng, E. S.-H. The Investigation of Interactions between Single Walled Carbon Nanotubes and Flexible Chain Molecules. Thesis, Massachusetts Institute of Technology, 2010.

(533) Amanat, F.; Stadlbauer, D.; Strohmeier, S.; Nguyen, T. H. O.; Chromikova, V.; McMahon, M.; Jiang, K.; Arunkumar, G. A.; Jurczyszak, D.; Polanco, J.; Bermudez-Gonzalez, M.; Kleiner, G.; Aydillo, T.; Miorin, L.; Fierer, D. S.; Lugo, L. A.; Kojic, E. M.; Stoever, J.; Liu, S. T. H.; Cunningham-Rundles, C.; Felgner, P. L.; Moran, T.; García-Sastre, A.; Caplivski, D.; Cheng, A. C.; Kedzierska, K.; Vapalahti, O.; Hepojoki, J. M.; Simon, V.; Krammer, F. A Serological Assay to Detect SARS-CoV-2 Seroconversion in Humans. *Nature Medicine* **2020**, *26* (7), 1033–1036. https://doi.org/10.1038/s41591-020-0913-5.

(534) Robbiani, D. F.; Gaebler, C.; Muecksch, F.; Lorenzi, J. C. C.; Wang, Z.; Cho, A.; Agudelo, M.; Barnes, C. O.; Gazumyan, A.; Finkin, S.; Hägglöf, T.; Oliveira, T. Y.; Viant, C.; Hurley, A.; Hoffmann, H.-H.; Millard, K. G.; Kost, R. G.; Cipolla, M.; Gordon, K.; Bianchini, F.; Chen, S. T.; Ramos, V.; Patel, R.; Dizon, J.; Shimeliovich, I.; Mendoza, P.; Hartweger, H.; Nogueira, L.; Pack, M.; Horowitz, J.; Schmidt, F.; Weisblum, Y.; Michailidis, E.; Ashbrook, A. W.; Waltari, E.; Pak, J. E.; Huey-Tubman, K. E.; Koranda, N.; Hoffman, P. R.; West, A. P.; Rice, C. M.; Hatziioannou, T.; Bjorkman, P. J.; Bieniasz, P. D.; Caskey, M.; Nussenzweig, M. C. Convergent Antibody Responses to SARS-CoV-2 in Convalescent Individuals. *Nature* **2020**, *584* (7821), 437–442. https://doi.org/10.1038/s41586-020-2456-9.

(535) Walls, A. C.; Park, Y.-J.; Tortorici, M. A.; Wall, A.; McGuire, A. T.; Veesler, D. Structure, Function, and Antigenicity of the SARS-CoV-2 Spike Glycoprotein. *Cell* **2020**, *181* (2), 281-292.e6. https://doi.org/10.1016/j.cell.2020.02.058.

(536) Yan, R.; Zhang, Y.; Li, Y.; Xia, L.; Guo, Y.; Zhou, Q. Structural Basis for the Recognition of SARS-CoV-2 by Full-Length Human ACE2. *Science* **2020**, *367* (6485), 1444–1448. https://doi.org/10.1126/science.abb2762.

(537) Long, G. L.; Winefordner, J. D. Limit of Detection A Closer Look at the IUPAC Definition. *Analytical chemistry* **1983**, *55* (7), 712A-724A.

(538) Yuan, M.; Wu, N. C.; Zhu, X.; Lee, C.-C. D.; So, R. T. Y.; Lv, H.; Mok, C. K. P.; Wilson, I. A. A Highly Conserved Cryptic Epitope in the Receptor Binding Domains of SARS-CoV-2 and SARS-CoV. *Science* **2020**, *368* (6491), 630–633. https://doi.org/10.1126/science.abb7269.

(539) Guglielmi, G. The Explosion of New Coronavirus Tests That Could Help to End the Pandemic. *Nature* **2020**, *583* (7817), 506–509. https://doi.org/10.1038/d41586-020-02140-8.

(540) CDC 2019-Novel Coronavirus (2019-NCoV) Real-Time RT-PCR Diagnostic Panel.

(541) Zhen, W.; Smith, E.; Manji, R.; Schron, D.; Berry, G. J. Clinical Evaluation of Three Sample-to-Answer Platforms for Detection of SARS-CoV-2. *Journal of Clinical Microbiology* **2020**, *58* (8). https://doi.org/10.1128/JCM.00783-20.

(542) Zhang, F.; Abudayyeh, O. O.; Gootenberg, J. S. A Protocol for Detection of COVID-19 Using CRISPR Diagnostics. 8.

(543) Wang, M.; Fu, A.; Hu, B.; Tong, Y.; Liu, R.; Liu, Z.; Gu, J.; Xiang, B.; Liu, J.; Jiang, W.; Shen, G.; Zhao, W.; Men, D.; Deng, Z.; Yu, L.; Wei, W.; Li, Y.; Liu, T. Nanopore Targeted Sequencing for the Accurate and Comprehensive Detection of SARS-CoV-2 and Other Respiratory Viruses. *Small* **2020**, *16* (32), 2002169. https://doi.org/10.1002/smll.202002169.

(544) Guo, K.; Wustoni, S.; Koklu, A.; Díaz-Galicia, E.; Moser, M.; Hama, A.; Alqahtani, A. A.; Ahmad, A. N.; Alhamlan, F. S.; McCulloch, I.; Arold, S. T.; Grünberg, R.; Inal, S. A Nanobody-Functionalized Organic Electrochemical Transistor for the Rapid Detection of SARS-CoV-2 or MERS Antigens at the Physical Limit. *medRxiv* **2020**, 2020.11.12.20228874. https://doi.org/10.1101/2020.11.12.20228874.

(545) Docter, D.; Westmeier, D.; Markiewicz, M.; Stolte, S.; Knauer, S. K.; Stauber, R. H. The Nanoparticle Biomolecule Corona: Lessons Learned – Challenge Accepted? *Chem. Soc. Rev.* **2015**, *44* (17), 6094–6121. https://doi.org/10.1039/C5CS00217F.

(546) Louie, S. M.; Tilton, R. D.; Lowry, G. V. Critical Review: Impacts of Macromolecular Coatings on Critical Physicochemical Processes Controlling Environmental Fate of

Nanomaterials. *Environ. Sci.: Nano* **2016**, *3* (2), 283–310. https://doi.org/10.1039/C5EN00104H.
(547) Lane, L. A. Physics in Nanomedicine: Phenomena Governing the in Vivo Performance of Nanoparticles. *Applied Physics Reviews* **2020**, *7* (1), 011316. https://doi.org/10.1063/1.5052455.
(548) Xia, X.-R.; Monteiro-Riviere, N. A.; Riviere, J. E. An Index for Characterization of Nanomaterials in Biological Systems. *Nature Nanotechnology* **2010**, *5* (9), 671–675. https://doi.org/10.1038/nnano.2010.164.
(549) Miao, L.; Lin, J.; Huang, Y.; Li, L.; Delcassian, D.; Ge, Y.; Shi, Y.; Anderson, D. G. Synergistic Lipid Compositions for Albumin Receptor Mediated Delivery of MRNA to the Liver. *Nature Communications* **2020**, *11* (1), 2424. https://doi.org/10.1038/s41467-020-16248-y.
(550) Chen, D.; Ganesh, S.; Wang, W.; Amiji, M. The Role of Surface Chemistry in Serum Protein Corona-Mediated Cellular Delivery and Gene Silencing with Lipid Nanoparticles. *Nanoscale* **2019**, *11* (18), 8760–8775. https://doi.org/10.1039/C8NR09855G.
(551) Caracciolo, G.; Palchetti, S.; Colapicchioni, V.; Digiacomo, L.; Pozzi, D.; Capriotti, A. L.; La Barbera, G.; Laganà, A. Stealth Effect of Biomolecular Corona on Nanoparticle Uptake by Immune Cells. *Langmuir* **2015**, *31* (39), 10764–10773. https://doi.org/10.1021/acs.langmuir.5b02158.
(552) Weber, C.; Voigt, M.; Simon, J.; Danner, A.-K.; Frey, H.; Mailänder, V.; Helm, M.; Morsbach, S.; Landfester, K. Functionalization of Liposomes with Hydrophilic Polymers Results in Macrophage Uptake Independent of the Protein Corona. *Biomacromolecules* **2019**, *20* (8), 2989–2999. https://doi.org/10.1021/acs.biomac.9b00539.
(553) Caracciolo, G.; Pozzi, D.; Capriotti, A. L.; Cavaliere, C.; Piovesana, S.; Barbera, G. L.; Amici, A.; Laganà, A. The Liposome–Protein Corona in Mice and Humans and Its Implications for in Vivo Delivery. *J. Mater. Chem. B* **2014**, *2* (42), 7419–7428. https://doi.org/10.1039/C4TB01316F.
(554) Cunningham, F. J.; Goh, N. S.; Demirer, G. S.; Matos, J. L.; Landry, M. P. Nanoparticle-Mediated Delivery towards Advancing Plant Genetic Engineering. *Trends in Biotechnology*. https://doi.org/10.1016/j.tibtech.2018.03.009.
(555) Voke, E.; Pinals, R. L.; Goh, N. S.; Landry, M. P. In Planta Nanosensors: Understanding Bio-Corona Formation for Functional Design. *In preparation* **2021**.
(556) Oliveira, M.; Almeida, M.; Miguel, I. A Micro(Nano)Plastic Boomerang Tale: A Never Ending Story? *TrAC Trends in Analytical Chemistry* **2019**, *112*, 196–200. https://doi.org/10.1016/j.trac.2019.01.005.
(557) Bundschuh, M.; Filser, J.; Lüderwald, S.; McKee, M. S.; Metreveli, G.; Schaumann, G. E.; Schulz, R.; Wagner, S. Nanoparticles in the Environment: Where Do We Come from, Where Do We Go To? *Environ Sci Eur* **2018**, *30* (1). https://doi.org/10.1186/s12302-018-0132-6.
(558) Lehner, R.; Weder, C.; Petri-Fink, A.; Rothen-Rutishauser, B. Emergence of Nanoplastic in the Environment and Possible Impact on Human Health. *Environ. Sci. Technol.* **2019**, *53* (4), 1748–1765. https://doi.org/10.1021/acs.est.8b05512.
(559) Kihara, S.; Köper, I.; Mata, J. P.; McGillivray, D. J. Reviewing Nanoplastic Toxicology: It's an Interface Problem. *Advances in Colloid and Interface Science* **2021**, *288*, 102337. https://doi.org/10.1016/j.cis.2020.102337.

(560) Natarajan, L.; Jenifer, M. A.; Mukherjee, A. Eco-Corona Formation on the Nanomaterials in the Aquatic Systems Lessens Their Toxic Impact: A Comprehensive Review. *Environmental Research* **2021**, *194*, 110669. https://doi.org/10.1016/j.envres.2020.110669.
(561) Monikh, F. A.; Chupani, L.; Karkossa, I.; Gardian, Z.; Arenas-Logo, D.; von Bergen, M.; Schubert, K.; Piackova, V.; Zuskova, E.; Jiskoot, W.; Vijver, M. G.; Peijnenburg, W. J. G. M. An Environmental Ecocorona Influences the Formation and Evolution of the Biological Corona on the Surface of Single-Walled Carbon Nanotubes. *NanoImpact* **2021**, 100315. https://doi.org/10.1016/j.impact.2021.100315.
(562) Teles, M.; Balasch, J. C.; Oliveira, M.; Sardans, J.; Peñuelas, J. Insights into Nanoplastics Effects on Human Health. *Science Bulletin* **2020**, *65* (23), 1966–1969. https://doi.org/10.1016/j.scib.2020.08.003.
(563) Galloway, T. S.; Lewis, C. N. Marine Microplastics Spell Big Problems for Future Generations. *PNAS* **2016**, *113* (9), 2331–2333. https://doi.org/10.1073/pnas.1600715113.
(564) Ripken, C.; Khalturin, K.; Shoguchi, E. Response of Coral Reef Dinoflagellates to Nanoplastics under Experimental Conditions. *bioRxiv* **2020**, 2020.09.23.310847. https://doi.org/10.1101/2020.09.23.310847.
(565) Huang, W.; Chen, M.; Song, B.; Deng, J.; Shen, M.; Chen, Q.; Zeng, G.; Liang, J. Microplastics in the Coral Reefs and Their Potential Impacts on Corals: A Mini-Review. *Science of The Total Environment* **2021**, *762*, 143112. https://doi.org/10.1016/j.scitotenv.2020.143112.
(566) Al-Thawadi, S. Microplastics and Nanoplastics in Aquatic Environments: Challenges and Threats to Aquatic Organisms. *Arab J Sci Eng* **2020**, *45* (6), 4419–4440. https://doi.org/10.1007/s13369-020-04402-z.
(567) Wood, E. Impacts of Sunscreens on Coral Reefs. 21.
(568) Sanchez-Cano, C.; Alvarez-Puebla, R. A.; Abendroth, J. M.; Beck, T.; Blick, R.; Cao, Y.; Caruso, F.; Chakraborty, I.; Chapman, H. N.; Chen, C.; Cohen, B. E.; Conceição, A. L. C.; Cormode, D. P.; Cui, D.; Dawson, K. A.; Falkenberg, G.; Fan, C.; Feliu, N.; Gao, M.; Gargioni, E.; Glüer, C.-C.; Grüner, F.; Hassan, M.; Hu, Y.; Huang, Y.; Huber, S.; Huse, N.; Kang, Y.; Khademhosseini, A.; Keller, T. F.; Körnig, C.; Kotov, N. A.; Koziej, D.; Liang, X.-J.; Liu, B.; Liu, S.; Liu, Y.; Liu, Z.; Liz-Marzán, L. M.; Ma, X.; Machicote, A.; Maison, W.; Mancuso, A. P.; Megahed, S.; Nickel, B.; Otto, F.; Palencia, C.; Pascarelli, S.; Pearson, A.; Peñate-Medina, O.; Qi, B.; Rädler, J.; Richardson, J. J.; Rosenhahn, A.; Rothkamm, K.; Rübhausen, M.; Sanyal, M. K.; Schaak, R. E.; Schlemmer, H.-P.; Schmidt, M.; Schmutzler, O.; Schotten, T.; Schulz, F.; Sood, A. K.; Spiers, K. M.; Staufer, T.; Stemer, D. M.; Stierle, A.; Sun, X.; Tsakanova, G.; Weiss, P. S.; Weller, H.; Westermeier, F.; Xu, M.; Yan, H.; Zeng, Y.; Zhao, Y.; Zhao, Y.; Zhu, D.; Zhu, Y.; Parak, W. J. X-Ray-Based Techniques to Study the Nano–Bio Interface. *ACS Nano* **2021**. https://doi.org/10.1021/acsnano.0c09563.
(569) Hura, G. L.; Tsai, C.-L.; Claridge, S. A.; Mendillo, M. L.; Smith, J. M.; Williams, G. J.; Mastroianni, A. J.; Alivisatos, A. P.; Putnam, C. D.; Kolodner, R. D.; Tainer, J. A. DNA Conformations in Mismatch Repair Probed in Solution by X-Ray Scattering from Gold Nanocrystals. *PNAS* **2013**, *110* (43), 17308–17313. https://doi.org/10.1073/pnas.1308595110.
(570) Sheibani, S.; Basu, K.; Farnudi, A.; Ashkarran, A.; Ichikawa, M.; Presley, J. F.; Bui, K. H.; Ejtehadi, M. R.; Vali, H.; Mahmoudi, M. Nanoscale Characterization of the

Biomolecular Corona by Cryo-Electron Microscopy, Cryo-Electron Tomography, and Image Simulation. *Nature Communications* **2021**, *12* (1), 573. https://doi.org/10.1038/s41467-020-20884-9.

(571) Erfani, A.; Seaberg, J.; Aichele, C. P.; Ramsey, J. D. Interactions between Biomolecules and Zwitterionic Moieties: A Review. *Biomacromolecules* **2020**. https://doi.org/10.1021/acs.biomac.0c00497.

(572) García, K. P.; Zarschler, K.; Barbaro, L.; Barreto, J. A.; O'Malley, W.; Spiccia, L.; Stephan, H.; Graham, B. Zwitterionic-Coated "Stealth" Nanoparticles for Biomedical Applications: Recent Advances in Countering Biomolecular Corona Formation and Uptake by the Mononuclear Phagocyte System. *Small* **2014**, *10* (13), 2516–2529. https://doi.org/10.1002/smll.201303540.

(573) Park, J. H.; Jackman, J. A.; Ferhan, A. R.; Belling, J. N.; Mokrzecka, N.; Weiss, P. S.; Cho, N.-J. Cloaking Silica Nanoparticles with Functional Protein Coatings for Reduced Complement Activation and Cellular Uptake. *ACS Nano* **2020**. https://doi.org/10.1021/acsnano.0c05097.

(574) Fleischer, C. C.; Payne, C. K. Secondary Structure of Corona Proteins Determines the Cell Surface Receptors Used by Nanoparticles. *J. Phys. Chem. B* **2014**, *118* (49), 14017–14026. https://doi.org/10.1021/jp502624n.

(575) Dar, A. I.; Abidi, S. M. S.; Acharya, A. Nanomaterials at the Biological Interphase: Protein Corona Formation and Infusion Reactions. In *Nanomaterial - Based Biomedical Applications in Molecular Imaging, Diagnostics and Therapy*; Acharya, A., Ed.; Springer: Singapore, 2020; pp 159–183. https://doi.org/10.1007/978-981-15-4280-0_8.